Proceedings of the Sixteenth Annual Precise Time and Time Interval (PTTI) Applications and Planning Meeting

**A meeting held at the
NASA Goddard Space Flight Center
Greenbelt, Maryland
November 27-29, 1984**

NASA
National Aeronautics and
Space Administration

Proceedings of the Sixteenth Annual Precise Time and Time Interval (PTTI) Applications and Planning Meeting

A meeting held at the
NASA Goddard Space Flight Center
Greenbelt, Maryland
November 27-29, 1984

Sponsored by

Naval Observatory
NASA Goddard Space Flight Center
Naval Electronic Systems Command
Naval Research Laboratory
Defense Communications Agency
Chief of Naval Operations
National Bureau of Standards
Army Electronics Technology
and Devices Laboratory
Rome Air Development Center

EXECUTIVE COMMITTEE

Dr. William J. Klepczynski, Chairman
U. S. Naval Observatory

David W. Allan
National Bureau of Standards

James A. Buisson
Naval Research Laboratory

Jimmie B. Collie
Naval Electronic Systems Command

Sheila C. Faulkner
U. S. Naval Observatory

Hugh S. Fosque
NASA Headquarters

William M. Hocking
NASA Goddard Space Flight Center

Dr. Arthur O. McCoubrey
National Bureau of Standards

James A. Murray, Jr.
Naval Research Laboratory

Dr. Harris A. Stover
Defense Communications Agency

Dr. John R. Vig
Army Electronics Technology and Devices Laboratory

Dr. Gernot M. R. Winkler
U. S. Naval Observatory

Dr. Nicholas F. Yannoni
Rome Air Development Center

GENERAL CHAIRMAN

Dr. WILLIAM J. KLEPCZYNSKI
U. S. Naval Observatory

TECHNICAL PROGRAM COMMITTEE

DR. VICTOR S. REINHARDT, CHAIRMAN
Hughes Aircraft

Dr. HELMUT HELLWIG
Frequency and Time Systems

MARTIN BLOCH
Frequency Electronics

DR. JOHN KLOBUCHAR
Air Force Geophysical Lab

DAVID W. ALLAN
National Bureau of Standards

DR. ARTHUR O. McCOUBREY
National Bureau of Standards

JAMES BUISSON
Naval Research Lab

EDITORIAL COMMITTEE

DR. RICHARD L. SYDNOR, CHAIRMAN
Jet Propulsion Laboratory

MARK J. LISTER
Naval Research Laboratory

PAUL F. KUHNLE
Jet Propulsion Laboratory

DR. LUTFOLLAH MALEKI
Jet Propulsion Laboratory

PUBLICITY CHAIRMAN

SHEILA C. FAULKNER
U. S. Naval Observatory

SESSION CHAIRMEN

SESSION I

DR. HELMUT HELLWIG
Frequency and Time Systems

SESSION II

MARTIN BLOCH
Frequency Electronics

SESSION III

DR. JOHN KLOBUCHAR
Air Force Geophysical Lab

SESSION IV

DAVID W. ALLAN
National Bureau of Standards

SESSION V

DR. ARTHUR O. McCOUBREY
National Bureau of Standards

SESSION VI

JAMES BUISSON
Naval Research Laboratory

ARRANGEMENTS

William Hocking
Paul J. Kushmeider

FINANCE COMMITTEE

James A Buisson
James A. Murray, Jr.

TECHNICAL ASSISTANCE

John Arnold   Archie Brown
Fred Blanchette   Tom Stalder

RECEPTIONISTS

Elaine Bowers   Betty Jo Slaback
Shiela Faulkner   Betty Wardrip
Stella Scates   Frances Wrigh.

For information concerning availability of this document or previous proceedings contact:

FOREWORD

These proceedings contain the papers presented at the Sixteenth Annual Precise Time and Time Interval Applications and Planning Meeting which was held November 27-29, 1984 at Goddard Space Flight Center. The discussions following the presentations are also included. There were 215 registered attendees, of which 28 were from 12 foreign countries. Fourteen were from Europe, seven from Asia, one from the Pacific and six from the Western Hemisphere. Within the United States, 57 of the attendees were from west of the Mississippi and 130 from east of the Mississippi.

The objective of the meeting was to provide an opportunity for program planners to meet those who are engaged in research and development and to keep abreast of the state-of-the-art and latest technological developments. At the same time, it provided an opportunity for engineers to meet program planners. This objective is clearly reflected by the title of the meeting.

This year, the program emphasized the effects of ionospheric and tropospheric propagation on time and frequency transfer, advances in the generation of precise time and frequency, time transfer techniques and filtering and modeling.

The Session Chairmen and the Technical Program Committee are responsible for the excellent technical content of the meeting. The unstinting support of the sponsors and the volunteers make a meeting such as this possible. We are fortunate to have such dedicated people.

CONTENTS

CONTENTS (continued)

CONTENTS (continued)

SESSION VI

TIME TRANSFER TECHNIQUES
Chairman: James Buisson, Naval Research Lab

CONTENTS (continued)

PROSPECTS FOR ATOMIC FREQUENCY STANDARDS

by

C. Audoin

Laboratoire de l'Horloge Atomique
Equipe de Recherche du CNRS,
associée à l'Université Paris-Sud
Bât. 221 - Université Paris-Sud
91405 Orsay - France

ABSTRACT

We shall describe the potentialities of different ato-
mic frequency standards which are not yet into field
operation, for most of them, but for which preliminary
data, obtained in laboratory experiments, give confi-
dence that they may improve greatly the present state
of the art.

The review will mainly cover the following devices :
        - cesium beam frequency standards with opti-
          cal pumping and detection
        - optically pumped rubidium cells
        - magnesium beam
        - cold hydrogen masers
        - traps with stored and cooled ions.

1. PHYSICAL BACKGROUND

Atomic frequency standards are founded on the space and time invariance of the
energy difference between specified levels of atoms, at rest and in a given
acceleration field. This statement is to be related to the absence of experi-
mental evidence of a cosmological variation of the fundamental constants, at
least at the present level of our measurement ability.

However, there are two fundamental limits to the precision of the measurement
of the energy difference $h\nu_o$ between two atomic levels.

The first one is set by the Heisenberg uncertainty principle, $\Delta\nu \cdot \Delta t \simeq 1$,
which means that the linewidth cannot be smaller than the inverse of the ob-
servation time, about. This limit may be reached provided that appropriate
tricks eliminate as well as possible other sources of line broadening such
as the first order Doppler effect and the inhomogeneity of the static magne-
tic field, for instance.

1

Assuming that these spurious effects are unde sufficiently good control, the Heisenberg principle call for long interaction times such as in the hydrogen maser and in ion traps.

The second fundamental limit is determined by noise processes. In the case where the atomic resonance is monitored by a flux of particles, atoms or photons, shot noise is the annoying effect. The corresponding fractional fluctuations of the particle flux being inversely proportional to the mean flux value, it is desirable to monitor a high particle flux, in atomic beam devices for instance. In the hydrogen maser, where the atomic transition is detected whether as the creation (active operation), or the variation (passive operation), of a coherent electromagnetic field, thermal noise due to the brownian motion of electrons in the cavity wall perturbs the phase and the amplitude of the electromagnetic field. The most obvious solution -at least in principle- consists in the cooling of the cavity.

A more detailed analysis shows that the fractional frequency stability measure, $\sigma_y(\tau)$ [1], is given by :

$$\sigma_y(\tau) \simeq \frac{1}{Q \ S/B(\tau)}$$ (1)

where Q is the quality factor of the atomic line and $S/B(\tau)$ the signal to noise ratio of its observation, during the time interval τ. The best frequency stability is then obtained in devices where it is possible to realize both a large quality factor and a large signal to noise ratio. Of course, tradeoffs between the two factors are possible.

A high quality factor requires, among other demands, a sufficiently large transition frequency. At the present time, the largest one which has been used in experimental devices are that of the hyperfine transition of the mass 199 mercury ion, at 40.5 GHz, and that of a fine structure transition of the mass 24 magnesium atom at 601 GHz. At the present time, higher frequencies cannot be produced and/or measured in sufficiently reliable set-ups, so that we shall focus on microwave frequency standards, mainly.

The preceding remarks indicate the directions in which improvements of atomic frequency standards may be expected. They refer, in fact, to means of enhancing the short and medium term frequency stability. However, it is well known that other qualities are necessary to fulfill the present demand. Among them, the long term stability and the reproducibility are of prime importance in a num-

ber of applications. Similarily, improved accuracy is desired for the labora-
tory primary cesium beam frequency standards, which realize the definition of
the S.I. time unit. As we will see, the cited directions of work are also bene-
ficial to these very important characteristics. Their improvement motivates, in
particular, the present efforts to cool ions and to observe one of a few of them
almost at rest and isolated from spurious sources of frequency shifts.

A description of the principles and of the design of most of the existing fre-
quency standards has been given in review articles [2,3] and shall not be re-
peated here.

2. BASIC PROPERTIES OF THE USEFUL TRANSITIONS

Hyperfine transitions of atoms and ions in the ground state share in common
the following properties of interest :

    - the life-time of the hyperfine levels is very large, amounting to
years, due to the very low probability of spontaneous emission. This is mainly
related to the small energy difference $h\nu_c$ between the levels,

    - the Stark effect, i.e. the frequency shift   due to an electric field
E is of second order,

    - the Zeeman effect of some of the $\Delta F = 1$, $\Delta m_F = 0$ transitions is also of
second order. The sensitivity to the magnetic field of the fine structure tran-
sition in ^{24}Mg is very small. It is approximately equal to 10^{-4} times that of
cesium [4]. Table 1 gives some pertinent numerical values.

As a result of the small energy difference between the ground state hyperfine
levels, they are almost equally populated at thermal equilibrium, such as in an
atomic beam source. State selection is then mandatory to observe hyperfine tran-
sitions with a sufficient signal to noise ratio. This is accomplished either
by magnetic deflection or optical pumping.

In the case of the magnesium fine structure transition, atoms are produced in
a metastable state having three sublevels with different lifetimes. The popu-
lation difference follows from the fastest decay to the ground state of one of
them.

3. BEAM FREQUENCY STANDARDS WITH OPTICAL PUMPING AND DETECTION

3.1. Cesium Beam

    a) Experimental achievements

3

In 1950, A. Kastler [5] showed that it shoud be possible to optically enhance the population of certain atomic levels and to optically detect magnetic resonance transitions. He suggested that the strong and inhomogeneous magnetic field regions could be replaced by optical interaction region in the Rabi beam magnetic resonance machine. This possibility was confirmed in a Rb 87 beam using rubidium spectral lamps and a Ramsey-type microwave cavity [6]. However, at that time, the light sources were spectral lamps, and the energy density of the light beam was not large enough to provide efficient optical pumping and detection. More recently, the development of reliable semi-conductor laser light sources in the near infrared, at 0.852 μm, enabled the optical pumping of cesium atoms and the optical detection of the F = 4, m_F = 0 $\longleftrightarrow$ F = 3, m_F = 0 clock transition at 9.192 MHz produced in a Ramsey type microwave cavity [7].

Figure 1 shows the principle of optical pumping and detection. At the left of the figure an energy diagram is shown with two levels in the ground state and one in an excited state. A light beam excites the atoms from level 1 to 3. The population of the excited state decays by spontaneous emission with an equal probability on levels 1 and 2. Assuming that the energy density is large enough it follows that the level 2 is populated at the detriment of level 1, and a population difference is created by optical pumping. This three level configuration is also useful for the detection of a transition between levels 1 and 2. If this transition occurs, the level 2 becomes populated and the light beam may transfer one atom to level 3. Spontaneous emission creates one fluorescence photon which may be detected and used to monitor the 1 $\longleftrightarrow$ 2 transition. In that case, one photon at most is produced per atom. Another optical detection scheme is shown at the right of figure 1. Only two levels are involved. One fluorescence photon is emitted each time one photon of the incident light beam is absorbed by atoms in level 1. The life-time of the excited state being very small, one may then detect several photons per atom if the light beam energy density is sufficiently large. This transition is denoted as a cycling transition. Furthermore, the number of photons is proportional to the time spent by the atoms in the light beam, and, consequently, this method provides a narrowing of the line.

The configurations of figure 1 are included in the level energy diagram of the cesium atom, shown in figure 2, in a simplified form. Taking into account the selection rule ΔF = 0 or $\pm$ 1, one sees that the levels F = 3 and 4 of the ground state plus the level F' = 4 of the excited state, for

4

instance, may be considered for optical pumping and detection. The levels $F = 3$ and $F' = 2$, for instance, may be used for optical detection. It exists several such configurations, corresponding to a number of experimental arrangements.

In fact, the spectrum is even more complicated than shown in figure 2, because each hyperfine level has $2F + 1$ magnetic sublevels. In particular, the ground state has a total of sixteen sublevels which are equally populated at the atomic source exit.

The most simple experimental set-up is sketched in figure 3. A single semi-conductor laser, at 0.852 µm, illuminates a cesium beam, on each side of the Ramsey microwave cavity. A population difference is created in the first light atom interaction region and the microwave transition is detected in the second one. In that set-up, one of the two hyperfine levels, $F = 3$ or 4 of the ground state is emptied to the benefit of the other one, if the light intensity is sufficiently large in the first interaction region. The population of the $F = 3$, $m_F = 0$ or of the $F = 4$, $m_F = 0$ sublevel, depending on the arrangement, becomes 1/8 of the total population of the beam. This is twice what may be expected with magnetic state selectors, which deflects off the beam one of these $m_F = 0$ levels. Figure 4 shows the microwave spectrum observed [8] with the experimental set-up of figure 3.

Another interesting consequence of the selection rules has been suggested by L. Cutler, pointed out by Lewis and Feldman [9] and theoretically investigated by de Clercq et al [10]. It affords the possibility to transfer the population of the sixteen hyperfine magnetic sublevels of the ground state to either the $F = 3$, $m_F = 0$ or the $F = 4$, $m_F = 0$ level. For instance, one light beam tuned to the $F = 3 \longleftrightarrow F' = 4$ transition will populate all the sublevels of the state $F = 4$. The second light beam, tuned on the $F = 4 \longleftrightarrow F' = 4$ transition will empty the sublevels of the state $F = 4$, with the exception of the sublevel $F = 4$, $m_F = 0$ because the transition $F = 4$, $m_F = 0 \longleftrightarrow F' = 4$, $m_F = 0$ is forbidden if the light is linearly polarized, parallel to the static field. It is then possible, in principle, to concentrate all the atoms on the $F = 4$, $m_F = 0$ level, for instance, whose population becomes 100 % of that of the beam. This major improvement has been experimentally achieved in two experimental configurations [8, 11]. In the first one, the detection is accomplished by a light beam derived from one pumping beam, and in the second one a third laser is used for the detection by a cycling transition. In figure 5, one sees that the field dependent $\Delta m_F = 0$ transitions have almost disappeared correspon-

ding to an increase of the central Rabi-Ramsey central line. Figure 6 shows the central Ramsey fringe obtained in a three lasers configuration.

b) Prospects

Besides the simplification in the design and the manufacturing of the cesium beam tube, optical pumping and detection methods have an impact on both the frequency stability and the accuracy of cesium beam frequency standards.

The short and medium term frequency stability measure, $\sigma_y(\tau)$, is determined by shot noise, for $\tau \lesssim 1$ day. It is approximately given by :

$$\sigma_y(\tau) \simeq \frac{1}{Q} \frac{1}{(I\tau)^{1/2}} \tag{2}$$

where I is the flux of detected cesium atoms. The optical pumping method is able to make the most efficient use of the cesium beam :

- no atom is lost by velocity dependent magnetic deflection

- the atoms of the sixteen sublevels of the ground state can be accumulated on either the $F = 3$, $m_F = 0$ or the $F = 4$, $m_F = 0$ level

- wider beams may be used due to the absence of beam geometry limitations by magnet pole piece separation and hot wire detector width.

It is then very likely that the useful beam intensity I may be increased by a factor of the order of 100 and, thus, the frequency stability by a factor of about 10, so that a frequency stability figure approaching

$$\sigma_y(\tau) = 10^{-12} \tau^{-1/2} \tag{3}$$

appears feasible in manufactured units. Figure 7 compares this frequency stability with that of examples of presently manufactured cesium beam frequency standards. Among others, this achievement will require a suitable choice of the optical pumping and detection scheme and a proper design of the optical detection region in order to eliminate as well as possible spurious background light from the incident laser beam.

Systematic effects may also be greatly diminished, thereby improving the long term stability, reproducibility and accuracy

- the suppression of the field dependent side-bands of the microwave spectrum of the beam tube eliminates the frequency pulling by neighbouring lines [12]. As the separation between these side-bands depends on the applied static magnetic field, their absence allows to decrease its value and, consequently to decrease the sensitivity to ambiant magnetic field changes.

- the velocity distribution of the detected atoms is determined by the

interaction time with the light beams and the chosen method of optical detection. Well defined velocity distribution functions may be achieved [13], thus improving the knowledge of the second order Doppler effect.

- the absence of state selector magnets and the creation of a weak magnetic field all along the cesium beam cancel the probability of Majorana transitions, suppress the related frequency shift and ease the achievement of a better magnetic field uniformity.

- a better evaluation of the coupling between the velocity and the transverse position of atoms will enable a better averaging [14] of the transverse phase shift.

- the cesium beam may be designed symmetrical with an on-axis cesium oven at each end, thereby allowing a measurement and a correction of the cavity phase shift.

The light shift, which is inherent to optical methods is small here [15], because the optical and microwave interactions do not occur at the same place. It may be measured and kept constant to about one part in 10^{14}. As a consequence of a decrease, or a better control of systematic frequency shift, a frequency stability of the order of 1×10^{-14} may be expected over a year.

In addition, it is worth noting that it is of prime interest, from a fundamental point of view, to realize the S.I. time unit by significantly different means to verify that possible fundamental and apparatus effects have not been missed.

Use of slow atoms increase the line quality factor -which is inversely proportional to the velocity- and thus improve the short and medium term frequency stability ($\tau <$ 1 day) if the beam flux is not too much diminished. It also decreases the velocity dependent frequency shift and contributes to an increase of the long term frequency stability and to the accuracy. Slow atoms are already preferentially state selected in one of the primary cesium beam frequency standards [16]. In the same line, the interest in a fountain beam experiment [17] has been recently renewed [18]. Assuming that collisions do not scatter significantly the very slow atoms of a beam effusing from a properly designed over aperture, a possible accuracy of 10^{-15} has been anticipated for a machine, using 6 ms^{-1} optically pumped and detected Cs atoms.

Laser cooling is also studied [19,20], with the hope to produce intense and sufficiently well collimated beams of slow atoms.

3.2. Rubidium Beam Frequency Standard

One may consider the application of optical pumping and detection methods to a mass 87 rubidium beam [21], but using laser diode light sources instead of spectral lamps [6]. The wavelength of the D2 resonance transition, which is equal to 780 nm, is well suited, because it corresponds to that of light sources developed for the video-disc industry. However, besides that point, rubidium does not provide significant advantages for improved frequency standards.

- It has 8 hyperfine sublevels in the ground state, instead of 16 for cesium, but in both cases, then may be transferred to a single $m_F = 0$ by double wavelength optical pumping.

- Its mass is smaller than that of cesium. The line-width on the one hand and the velocity dependent frequency shift one the other hand would be slightly worse than for a cesium beam.

4. MAGNESIUM BEAM FREQUENCY STANDARD

As a consequence of their two valency electrons, earth alkaline atoms have singlet and triplet states. The ground state, $^1S_0$, is a singlet. The first triplet states, $^3P_{0,1,2}$, shown in the simplified energy diagram of Fig. 7, is metastable. The $^1S_0 \leftrightarrow ^3P_0$ and the $^1S_0 \leftrightarrow ^3P_2$ transitions are forbidden, for even isotopes, but the $^1S_0 \leftrightarrow ^3P_1$ transition is slightly allowed. Consequently, a large population difference may be created between the ^3P fine structure levels by spontaneous decay of the $^3P_1$ level [4].

The fine structure splitting is rather large. The $^3P_1 \leftrightarrow ^3P_0$ ones of Mg[22,23,24] and Ca are the smallest. They are given in Table 2, as well as the life time [25] of the $^3P_1$ level and the wavelength of the fluorescence light.

In a magnesium or a calcium beam frequency standard, the metastable $^3P_{0,1,2}$ levels are created in a discharge. At a distance downstream, which is of the order of 1 m for Mg, for instance, the population of the $^3P_1$ level is depleted by spontaneous decay. The dipole magnetic fine structure $^3P_0 \leftrightarrow ^3P_1$ transition is induced in a sub-millimeter cavity, so that the level $^3P_1$ is replenished. The fine structure transition is then monitored by the intensity of the fluorescence light which is emitted by the beam, after its passage in the cavity. As usual, the resonance signal is processed to enable the frequency control of the interrogation frequency. Such a device, using a magnesium beam has been successfully operated [24], with a Rabi-type cavity at the present time.

With a Ramsey type sub-millimeter cavity, the short-term frequency capability of such a device would be [24] :

$$\sigma_y(\tau) = 3 \times 10^{-13} \tau^{-1/2} \qquad (4)$$

for magnesium and 10 times better for calcium. This is mainly due i) to the high value of the line Q, of the order of 10^9, although limited by spontaneous decay of the $^3P_1$ level and ii) to the possibility to use wide atomic beams.

The very low sensitivity to magnetic fields and the absence of neighbouring transitions are positive points. But the long term stability, the reproducibility and the accuracy are limited to the 10^{-13} level by the second order Doppler effect [26] which is rather large due to the large velocity of light atoms forming a beam from a high temperature oven. It amounts to 2.5×10^{-12} for magnesium.

A magnesium beam machine must be several meters long to allow a sufficient decay of the $^3P_1$ level after the discharge region, and an efficient collection of the fluorescence light after the cavity. The length requirement is about 10 times less with Ca, according to the smallest life time of the $^3P_1$ level. The generation of the large interrogation frequency may cause technical problems.

5. RUBIDIUM CELL FREQUENCY STANDARDS

Spectral lamp optically pumped rubidium cell frequency standards are popular in applications where good short term stability, but relatively poor long term stability are compatible with small size, small power consumption and low cost.

A buffer gas is introduced in the cell containing mass 87 rubidium atoms to enhance the optical pumping efficiency [27]. Nitrogen quenches rubidium atoms in the excited state so that they make a non radiative transition to the ground state. Otherwise, the fluorescence light, which contains both hyperfine components, would decrease the attained population difference. In addition, the slow diffusion of atoms in the buffer gas greatly reduces the Doppler broadening[28], without requirement on the size of the cell compared to the microwave wavelength, so that the Doppler free hyperfine transition can be observed with a cell filling the microwave cavity *.

---

* In that case, the microwave cavity is not necessary. This Doppler free transition may be observed if the cell is placed in a travelling wave at the hyperfine transition frequency.

9

With a laser light source the optical pumping efficiency is highly increased, due to the much larger energy density at the proper wavelength. It would then be possible to suppress the buffer gas, provided i) that the cell does not extend to regions where the phase of the standing microwave magnetic field is reversed and ii) that a wall coating prevents strong relaxation on the glass wall. The great advantage would be the elimination of the large size buffer gas frequency shift and,mainly,of the inhomogeneous line broadening effects causing large power frequency shifts [28bis] due to the absence of motional averaging when a buffer gas is used. These inhomogeneous line broadening effects are produced by the progressive absorption of light along its path in the cell, causing a distributed light shift, and by inhomogeneous magnetic field. In that event, the buffer gas frequency shift would be replaced by a noticeably smaller wall shift.

One may then expect that the larger resonance signal increases the short term frequency stability and that the reduction of frequency offsets improves the medium and long term frequency stability. This assumes i) that the optical wavelength is tuned to that of the D_2 line, so that the light shift goes to zero and ii) that the amplitude and frequency noises [29] of the laser is sufficiently reduced so that they are not transduced into fluctuations of the frequency of the hyperfine transition. In the event that these requirements cannot be fulfilled, it would be possible to eliminate light shift related effects by performing sequential optical pumping and by observing hyperfine transition "in the dark".

Optical pumping of the rubidium maser by diodes may be considered as well, but with the same limitations.

6. THE HYDROGEN MASER

6.1. Standard Size Hydrogen Maser

The standard size hydrogen maser usually includes a TE_{011} microwave cavity, resonating at 1.42 GHz, with a thin walled teflon coated storage quartz bulb. A typical size is 12 x 7.7 x 5.3 dm^3. The device is able to sustain a self-oscillation, so that it is said active.

The standard size hydrogen maser is the most stable atomic frequency standard [30], as shown in Fig. 9. The medium term frequency stability 10 s < τ < 1 hour is determined by the thermal noise in the microwave cavity. We have :

$$\sigma_y(\tau) \simeq K_1 \frac{1}{Q} \left(\frac{kT}{2P\tau}\right)^{1/2} \tag{5}$$

where k is Boltzman constant, T the absolute temperature of the cavity, Q the atomic line-width and P the power delivered to the microwave cavity by the hydrogen atoms. K_1 is unity for active masers. An optimization of the operating parameters is possible [31] but would only improve very slightly the frequency stability, as shown in Fig. 10.

Short term frequency stability ($\tau < 10$ s) is mainly determined by the noise added in the first stage of the microwave receiver. We have, approximately :

$$\sigma_y(\tau) \simeq K_2 \left(\frac{kT}{P}\right)^{1/2} \frac{1}{\tau} \tag{6}$$

T is the noise temperature of the receiver and K_2 is a constant which depends on the noise bandwidth.

The long term frequency stability ($\tau > 1$ hour) is determined by environmental effects, which are mainly related to the cavity pulling effect [32,33]. If necessary, it would be possible to operate a fast autotuning system [34] to keep the resonant frequency of the cavity under control, thereby improving the long term frequency stability figure to values of the order of 10^{-15} without degrading the short and medium term stability.

The accuracy of the hydrogen maser is still limited by the lack of reproducibility of the wall shift. The best achieved accuracy [35] is 6 x 10^{-13} in a standard size maser. It seems difficult to improve it with teflon coatings. However, this is better than the accuracy and the reproducibility of presently manufactured cesium beam frequency standards. This does not cause serious problems in the main fields of application of the standard size hydrogen maser i.e. : very long base line radio-interferometry and navigation.

6.2. Small Size Hydrogen Masers

The key of size reduction is a decrease of the microwave cavity dimensions, its resonance frequency being kept equal to 1.42 GHz. This is achieved by using properly disposed dielectric materials [36] or conductors [37,38] as shown in Fig. 11. The achieved size of the maser is then of the order of 6 x 5 x 3.5 dm^3. However, the presence of materials in the cavity increases the losses and the quality factor becomes smaller than 10 000, which does not enable self-oscillation to occur anymore. The small size hydrogen masers may then be operated in two different ways : either passively [39] or actively [40]. In the last case, electronic feedback is used to enhance the cavity quality factor above oscil-

11

lation threshold. In both circumstances, the frequency stability is given by Eq. 5, but with K_1 larger than unity. The achieved frequency stability is very good [41(42)]. Fig. 12 shows the result obtained with a passively operated small size hydrogen maser of a particular design. The short and medium term frequency stability may still be improved by proper optimization of the operating parameters [31], as shown in Fig. 10. The long term stability happens to be excellent [42], of the order of 3×10^{-15} for $\tau = 10$ days, although the thermal coefficient of the loaded cavity is large. This shows that the achieved long term stability is due to the operation of an efficient electronic control of the cavity.

Actually, the small size hydrogen maser realizes an excellent trade-off between performance and size.

6.3. Cold Hydrogen Maser

The interest to cool the hydrogen maser has been recognized early in the history of this device. It was motivated by two different but complementary reasons : i) since the   achieved short and medium term frequency stability is determined by thermal noise, cooling must improve the short and medium term stability [43], as shown by Eq. 5 and 6 and ii) cooling provides a means of studying the properties of the wall coating [44,45] and to search for materials having more reproducible properties than teflon at room temperature. In that respect, the following materials have been studied : FEP 120 teflon down to 48 K [44-46] and tetrafluoromethane between 50 and 25 K [47].

At approximately the same time, fundamental studies aimed to achieve Bose-Einstein condensation of hydrogen atoms in a high density gas of spin polarized hydrogen atoms were engaged in several laboratories. This led to information on the interaction of hydrogen atoms with molecular hydrogen surfaces around 4 K [49,50]. A very significant breakthrough occured when it was discovered that ^{3}He and ^{4}He films are able to contain a high density of polarized hydrogen gas below 1 K [51].

This result opens very promising prospects for a cryogenic hydrogen maser frequency standard, for the following reasons, pointed out by Berlinsky and Hardy [52] :

- the binding energy of H on a ^{3}He or a ^{4}He surface is 0.4 K or 1.15 K, respectively, thus allowing low enough recombination rates at the surface at temperatures below 1 K.

- the total pressure shift in the gas plus wall shift shows a minimum around 0.2 K for ^{3}He and 0.5 K for ^{4}He. The frequency shift in a 15 cm diameter storage bulb is then of the same magnitude than with teflon at room temperature.

- the helium film is homogeneous and of high purity, and the pressure of the helium gas can be controlled well enough to expect a fractional frequency stability of the order of 10^{-18}.

- the spin exchange line broadening effect is 10^3 times smaller at very low temperature than at room temperature. This allows larger oscillation power to be obtained.

- the cavity pulling effect should be drastically reduced because materials have a very low expansion coefficient at low temperature and because it is possible to operate the cold maser at low values of the cavity quality factor.

- slow hydrogen atoms issued from a cold hydrogen source may be very easily state selected.

- magnetic shielding may be provided by superconductive materials.

- cooled GaAs FET amplifiers are available with noise temperature of 10 K.

From these statements, a fractional frequency capability of 2×10^{-18} for $\tau > 10^3$ s is anticipated [52]. One may add that the pressure and the wall shift been assumed reproducible, the accuracy should be very significantly increased too.

However difficulties arise, which are related to the background pressure of ^{4}He at 0.5 K, for instance, giving a mean free path of 1.4 cm. A means to introduce the hydrogen gas in the storage cell should be found. In addition, the motional averaging effect occuring in conventional hydrogen masers disappears which may cause severe requirements on the magnetic field homogeneity.

7. ION STORAGE

It is known, since several tens years that one may store charged particles in electric and magnetic fields [53] (Penning trap) or in a radiofrequency electric field [54] (r.f. trap). Storage may occur for hours, and the interest of this technique for high resolution -microwave spectroscopy, of ^{3}He$^+$ at first, has been demonstrated by Dehmelt [55].

It has been proved that it is possible to use a hyperfine structure transition, that of the mass 199 mercury ion, to realize an experimental model of a fre-

quency standard using ions stored in a radiofrequency trap [56-59].

In the following we shall mainly focus on the radiofrequency trap and the mercury ions frequency standard and we shall give indications on the potentialities of stored cooled ions [60].

7.1. Storage in a r.f. Trap

Let us consider the three electrodes system and the applied voltage shown in Fig. 13. Assuming that the electrodes have the proper hyperboloid shape, the axial and transverse components of the electric field are proportional to the distance from the center O of the trap, but they have opposite sⁱ...·. If the voltage is a constant, a charged particle will be submitted to . ·lsive force either in the axial or the transverse direction, according ; ·s sign, and no storage may occur.

The situation is different if the voltage is alternating, with frequency ν_c. The electric field forces a motion at the frequency ν_c, whose amplitude is small. It is called the micromotion. This motion is approximately sinusoïdal. As shown in Fig. 14, the axial and transverse micromotions are out of phase because the two components of the electric field have opposite signs. In its motion, the particle explores the electric field and, due to its non-uniformity, the acting electric force is not sinusoïdal. It follows that it has a non zero mean value and it may be shown that its two components tend to attract the particle towards the center of the trap. This central force imposes another harmonic motion of larger amplitude called the secular motion. Its frequency ν_s is in general noticeably smaller than ν_c. If the inner dimensions of the trap are of the order of 1 cm, ν_c equals 200 kHz and has an amplitude of 100 V, then ν_s is of the order of 20 kHz for the mercury ion and the amplitude of the macromotion is of the order of a few mm. Therefore, within conditions [61] which have not been considered here, the charged particle motion has a finite amplitude and the particle may stay inside the trap for very long times, provided that it does not suffer collisions with the background gas. It is worth noting that a stored ion cloud is very dilute as a consequence of the Coulomb repulsive forces leading to the so-called space charge effect. Usually the ion density is limited to about 10^6 per cubic centimeter.

Assume now that the ions are irradiated by an electromagnetic wave at frequen-

14

cy ν_0. According to their harmonic motion, they will see a Doppler frequency modulated wave composed of a carrier at frequency ν_0 and side-bands separated by ν_s, at least, from the carrier. If the ion atomic spectrum has a sharp line close to the frequency ν_0, only the carrier component of the wave will be effective and the condition of high resolution Doppler free spectroscopy is met.

These principles are implemented in the mercury ion frequency standard, for instance.

7.2. The Mercury Ion Frequency Standard

The mass 199 mercury ion has a hyperfine structure in the ground state shown in Fig. 15. One has $I = 1/2$, and the hyperfine structure is as simple as that of the hydrogen atom, but the hyperfine separation is large, equal to about 40.5 GHz (see Table 1). The hyperfine transition is observed by conventional optical pumping techniques owing to a favorable isotope shift of the mass 202 mercury ion. The experimental set-up is shown in Fig. 16. A lamp filled with ^{202}Hg emits the resonance light of the ionized mercury at 194 nm. This light is selectively absorbed by those stored ^{199}Hg$^+$ ions which are in the F = 1 hyperfine level. This level is depopulated to the benefit of the F = 2 level and the intensity of the fluorescence light is weak. If now the microwave transition at 40.5 GHz is induced, the level F = 1 is replenished and the intensity of the fluorescence light increases. This intensity is used to monitor the microwave hyperfine transition. Fig. 17 shows a power broadened hyperfine resonance pattern, corresponding to a line quality factor of 5 x 10^9. The high value of the quality factor compensates for the relatively poor signal to noise ratio. A quartz crystal frequency source has been frequency locked on such a transition and a short term frequency stability (10 s < τ < 3500 s) of

$$\sigma_y(\tau) = 3.6 \ 10^{-11} \tau^{-1/2} \tag{7}$$

has been obtained [58]. It is shown in Fig. 18.

A substantially narrower line, 0.85 Hz wide, has been achieved, in a different set-up [59,62] where the light broadening and frequency shift are eliminated by switching off periodically the pumping light and by interrogating the microwave transition in the dark.

Stored ions have a relatively large kinetic energy of about 1 eV and, conse-

quently a large second order Doppler shift, of $- 5 \times 10^{-12}$ per eV in the case of mercury. Models for the effect of the ion number, i.e. of the space charge effect on the ion motion and the ion kinetic energy have been established [62,63]. This has led to a measurement of the ion kinetic energy [63] and to the extrapolation to zero Doppler shift of the hyperfine transition frequency in a mercury ion cloud cooled by viscous drag with helium [62]. The cooling gas is efficient under very low pressure, of the order of 10^{-5} Torr, for which the pressure shift is about 6×10^{-14}.

The short and medium term capability of the mercury ion frequency standard is of $10^{-12} \tau^{-1/2}$ about [62,64]. A long term frequency stability of 2.2×10^{-14} and an accuracy of 2.5×10^{-13} are anticipated.

The mercury ion frequency standard can be built smaller than the presently manufactured cesium beam frequency standard. It is then a potential competitor of this device. However, technical problems related to the life-time of the $^{202}Hg^+$ lamp and to the control of the pressure of the background neutral mercury remains to be solved.

7.3. Microwave Spectroscopy in Radiofrequency Traps

The ground state hyperfine splitting of several ionized elements has been measured, with a precision of the order of 10^{-10} using the r.f. trap storage technique and a pulsed dye laser for optical pumping. They are $^{135}Ba^+$ (493 nm) at 7.18 GHz [65], $^{137}Ba^+$ (493 nm) at 8.04 GHz [66] and $^{171}Yb^+$ (369 nm) at 12.6 GHz [67], where the quantity within parenthesis is the wavelength used for optical pumping. A fractional linewidth up to 3.8×10^{11} has been obtained in such experiments, which shows their interest in the field of atomic frequency standards. An experimental set-up has been realized in which a quartz crystal oscillator has been frequency locked to the hyperfine transition of $^{137}Ba^+$ [68]. However, the drawback of these devices, compared to the mercury ion frequency standard is the requirement of a pulsed dye laser, at least at the present time.

7.4. Ion Cooling

In the absence of any collision, stored ions have an agitation energy which is larger than the room temperature thermal energy, especially in r.f. traps. As stated previously, collisions with the atoms of a rarefied light gas are

16

efficient to thermalize ions [61,69,70], in a r.f. trap with the additional benefit of an increase of the stored ion number and of their storage time.

However, the most efficient cooling is by means of side-band laser irradiation [71,72] which takes advantage of the Doppler effect. A schematical explanation is the following. Due to the harmonic motion in a trap, the absorption spectrum of the stored ions shows lower and upper sidebands. An ion can absorb a photon whose frequency, v_L coincides with a component of the lower sideband. We then have $v_L < v_0$, where v_0 is the transition frequency of the ion at rest. By spontaneous emission, the excited ion will emit a photon, with the frequency v_0 in the average. In that process the ion looses the energy $h(v_L - v_0)$ which decreases its kinetic energy. This process requires an ion having a short life time of the excited level in order to enable a large number of such cycles every second. Efficient cooling has been demonstrated, using Mg^+ ions, either in a Penning trap [73,74] or a r.f. trap [75], or using Ba^+ ions in a r.f. trap [76]. Temperatures as low as 5 mK have been observed with a single stored Mg^+ ion [75]. Due to zero point energy, the lowest attainable temperature is of the order of

$$T \simeq \frac{1}{2} \hbar \gamma / k \tag{8}$$

where γ is the natural linewidth of the transition. Typically, we have $T \simeq$ 1 mK.

One of the most impressive recent achievement has been the observation and the spectroscopy of single stored cooled Mg^+ [75,77] and Ba^+ ions [78].

7.5. Frequency Standards with Cooled Stored Ions

Precision microwave spectroscopy of $^{25}Mg^+$ [79] and $^9Be^+$ [80] ions confined in a Penning trap and laser cooled has been accomplished. In that experiments the magnetic field was stabilized to a value for which some of the hyperfine transitions show a minimum.

Following these experiments, a laboratory microwave frequency standard using $^9Be^+$ ions has been investigated [81]. Approximately 300 ions are stored in a Penning trap at a magnetic field of 0.82 T and laser cooled with a laser beam at a wavelength of 313 nm This laser beam is produced from the output of a single mode dye laser by the frequency doubling technique, in a non linear crystal. Although the transition frequency is small, equal to approximately

17

300 MHz, in that experiment, the very long storage time enabled to achieve a line-width as small as 10 mHz, and a line quality factor of 1.2×10^{10} has thus been obtained. A quartz crystal oscillator locked to a transition of the hyperfine manifold has a frequency stability given by :

$$\sigma_y(\tau) = 2 \times 10^{-11} \tau^{-1/2} \tag{9}$$

for 400 s < τ < 3200 s, of the same order as achieved in manufactured cesium beam frequency standards. The magnetic field instability contributes an uncertainty of 3×10^{-14} in this experiment and the second order Doppler shift is – 5×10^{-14} only, due to the cooling.

7.6. Prospects

Ion storage in a r.f. trap or a Penning trap has proved to be a promising technique for frequency standard applications. The r.f. trap is best suited to the realization of a portable clock. Laser cooling affords the possibility of a drastic reduction of velocity dependent frequency shifts, and of the most annoying of them, the second order Doppler frequency shift. In addition, the related very small spatial extension of the ion motion reduces the effects of magnetic field homogeneïty, accordingly. However, laser cooling is tributary upon suitable coherent c.w. light sources adapted to ions having a favorable energy level diagram, and it can be contemplated for Laboratory frequency standards only. In that respect, a mass 201 mercury ion frequency standard is being studied [82]. The required wavelength, at 194 nm has been coherently produced [83]. A frequency stability better than $10^{-16} \tau^{-1/2}$ and an accuracy better than 10^{-15} are expected. Another similar proposal refers to the use of $^{137}Ba^+$ [84].

Altlough this is out of the scope of this paper, it should be mentionned that laser cooled stored ions are being considered for optical frequency standards [85,86]. At optical frequencies, which are roughly 10^4 times larger than microwave frequencies, the line quality factor and, therefore the performances should be greatly enhanced. The most fascinating proposal is by Dehmelt [87]. He considers a single ion stored in a r.f. trap, such as the $^{205}Tl^+$ ion whose spectrum contains both a wide line and a very narrow line sharing in common one energy level. The very narrow line is used as the frequency reference feature. The broad line, corresponding to a short-lived excited state is used for efficient laser cooling and as a cycling transition providing about 10^6

photons each time the narrow line transition is induced. This yields an optical resolution capability of 1 part in 10^{18}. However, optical frequency generation and synthesis must be greatly improved, mainly in the UV part of the spectrum before such a potentiality can be experimentally verified.

8. CONCLUSION

It then appears that the performances of atomic frequency standards are open to significant improvement. Table 3 summarizes the potentialities* of some of the considered devices.

The cold hydrogen maser and the cooled trapped ions frequency standards using storage techniques show the best promise of frequency stability improvement. In a trap the storage process does not involve collisions either with a wall or a buffer gas. For cooled ions, almost at rest at the center of the trap, the confinement related frequency shifts are either extremely small (effect of the electric field) or calculable with a great precision (effect of the magnetic field). It follows that the expected accuracy is impressively good. The cold hydrogen maser and the cooled trapped ions frequency standards will be suited to applications in the field of fundamental research (experimental verification of Relativity theories, search for gravitational waves), to deep space navigation or to fundamental metrology.

Other devices such as the optically pumped portable cesium beam frequency standard, the small size hydrogen maser, the mercury ion frequency standard and the rubidium frequency standard have frequency stability capabilities very significantly better than achieved at present. They will remain of moderate size and cost and they will certainly find a number of technical applications such as in navigation systems.

It is worth reminding that application of optical methods to laboratory primary cesium beam frequency standards is being studied in a number of laboratories. This is of prime importance to verify that two different designs of the realization of the definition of the time unit, one using magnetic state selection and the other optical pumping and detection methods, yields the same result.

---

* The author is not familiar enough with Rb clocks to give pertinent figures for this device.

REFERENCES

(1) J.A. Barnes, A.R. Chi, L.S. Cutler, D.J. Healey, D.B. Leeson, T.E. Mc Gunigal, J.A. Mullen Jr., W.L. Smith, R.L. Sydnor, R.F.C. Vessot and G.M.R. Winkler, Proc. IEEE Trans. on Instr. and Meas. IM-20 (1971) p. 105

(2) H. Hellwig, Proc. of the IEEE 63 (1975) p. 212

(3) C. Audoin and J. Vanier, Journal de Physique E, Scientific Instruments 9 (1976) p. 697

(4) F. Strumia, Metrologia 8 (1972) p. 85

(5) A. Kastler, J. de Physique et le Radium 11 (1959) p. 255

(6) P. Cerez, M. Arditi and A. Kastler, Comptes-Rendus Acad. Sci. 266B (1968) p. 282

(7) M. Arditi and J.L. Picqué, J. de Physique Lettres 41 (1980) p. L-379

(8) G. Avila, E. de Clercq, M. de Labachelerie and P. Cérez, Conference on Precision Electromagnetic Measurement. Delft, the Netherlands, 1984

(9) L.L. Lewis and M. Feldmann, Proc. of the 35th Annual Frequency Control Symposium, Philadelphia, USA (1981), p. 612

(10) E. de Clercq, M. de Labachelerie, G. Avila, P. Cérez and M. Têtu, J. de Physique 45 (1984) p. 239

(11) E. de Clercq, G. Avila, M. de Labachelerie, P. Petit and P. Cérez, Congrès International de Chronométrie, Besançon, France, 1984

(12) A. de Marchi, G.D. Rovera and A. Premoli, Metrologia 20 (1984) p. 37

(13) P. Cérez, G. Avila, E. de Clercq, M. de Labachelerie and M. Têtu, Proc. of the 38th Annual Symposium on Frequency Control, Philadelphia, USA (1984)

(14) S. Jarvis, Jr., Metrologia 10 (1974) p. 87

(15) A. Brillet, Metrologia 17 (1981) p. 147

(16) G. Becker, IEEE Trans. on Instr. and Meas. IM-27 (1978) p. 319

(17) J.R. Zacharias, Phys. Rev. 94 (1954) p. 751

(18) A. de Marchi, Metrologia 18, (1982), p. 103

(19) J.V. Prodan, W.D. Philipps and H. Metcalf, Phys.Rev. Lett. 49 (1982) p. 1149

(20) V.O. Balykin, V.S. Letokhov and A.I. Sidorov, Optics Com. (1984) p. 248

(21) M. Feldmann, J.C. Bergquist, L.L. Lewis and F.L. Walls, Proc. of the 35 th Annual Frequency Control Symposium, Philadelphia, USA (1981) p. 625

(22) A. Godone, A. de Marchi, G.D. Rovera and E. Bava, Phys. Rev. A, 28 (1983) p. 2562

(23) E. Bava, A. de Marchi, A. Godone, G.D. Rovera and G. Giusfredi, Optics Com. 47 (1983) p. 193

(24) A. Godone, E. Bava, A. de Marchi, G.D. Rovera and G. Giusfredi, 21st General Assembly of URSI, Firenze, Italy (1984)

(25) H.S. Kwong, P.L. Smith and W.H. Parkinson, Phys. Rev. A, 25 (1982) p.2629

(26) A. de Marchi, E. Bava, A. Godone and G. Giusfredi, IEEE Trans. on Instr. and Meas. IM-32 (1983) p. 191

(27) P. Davidovits and R. Novick, Proc. of the IEEE 54 (1966) p. 155

(28) R.H. Dicke, Phys. Rev. 89 (1953) p. 472

(28bis) A. Risley, S. Jarvis Jr and J. Vanier, Proc. of the 33rd Annual Symposium on Frequency Control, Atlantic City, USA (1979) p. 477

(29) L.L. Lewis and M. Feldman, Proc. of the 35th Annual Frequency Control Symposium, Philadelphia, USA, (1981) p. 612

(30) M.W. Levine, R.F.C. Vessot and E.M. Mattison, Proc. of the 32nd Annual Symposium on Frequency Control, Atlantic City, USA (1978), p. 477

(31) C. Audoin, J. Viennet and P. Lesage, Journal de Physique 42, Supplément au n° 12 (1981) p. C8-159

(32) D. Kleppner, H.M. Goldenberg and N.F. Ramsey, Phys. Rev. 126 (1962) p. 603

(33) D. Kleppner, H.C. Berg, S.B. Crampton, N.F. Ramsey, R.F.C. Vessot, H.E. Peters and J. Vanier, Phys. Rev. A 138 (1965) p. 972

(34) C. Audoin, Revue de Physique Appliquée 16 (1981) p. 125 and 17 (1982) p. 273
also : H.E. Peters, Proc. of the 36th Annual Frequency Control Symposium, Philadelphia, USA (1982) p. 240

(35) P. Petit, M. Desaintfuscien and C. Audoin, Metrologia 16 (1980) p. 7

(36) D.A. Howe, F.L. Walls, H.E. Bell and H. Hellwig, Proc. of the 33rd Annual Symposium on Frequency Control, Atlantic City, USA (1979) p. 554

(37) H.E. Peters, Proc. of the 32nd Annual Frequency Control Symposium, Atlantic City, USA (1978) p. 469

(38) H.T.M. Wang, J.B. Lewis and S.B.Crampton, Proc. of the 33rd Annual Symposium on Frequency Control, Atlantic City, USA (1979) p. 543

(39) F.L. Walls and H. Hellwig, Proc. of the 39th Annual Symposium on Frequency Control, Atlantic City, USA (1978) p. 473

(40) H.T.M. Wang, Proc. of the 34th Annual Symposium on Frequency Control, Philadelphia, USA (1980) p. 364

(41) H.T.M. Wang, Proc. of the 36th Annual Symposium on Frequency Control, Philadelphia, USA (1982), p. 249

(42) F.L. Walls and K.B. Persson, Proc. of the 38th Annual Frequency Control Symposium, Philadelphia, USA (1984) p. 416

(43) R.F.C. Vessot, M.W. Levine and E.M. Mattison, Proc. of the 9th Annual PTTI. Applications and Planning Meeting, Greenbelt, USA (1978), p.549

(44) P.W. Zitzewitz and N.F. Ramsey, Phys. Rev. A $\underline{3}$ (1971) p. 51

(45) M. Desaintfuscien, J. Viennet and C. Audoin, Metrologia $\underline{13}$ (1977) p. 125

(46) R.F.C. Vessot, E.M. Mattison and E. Imbier, Proc. of the 37th Annual Symposium on Frequency Control, Philadelphia, USA (1983) p. 49

(47) R.F.C. Vessot, E.M. Mattison and E.L. Blomberg, Proc. of the 33rd Annual Symposium on Frequency Control, Atlantic City, USA (1979), p. 511
also : R.F.C. Vessot, E.M. Mattison, E. Imbier and Z.C. Zhai (1984), this conference

(48) S.B. Crampton, K.M. Jones, G. Nunes and S.P. Souza (1984), this conference

(49) S.B. Crampton, J.J. Krupczak and S.P. Souza, Phys. Rev. B $\underline{25}$ (1982) p. 4383

(50) W.N. Hardy, A.J. Berlinsky and L.A. Whitehead, Phys. Rev. Lett $\underline{42}$ (1979) p. 1042

(51) W.N. Hardy and M. Morrow, Journal de Physique, $\underline{42}$, supplément C8 (1981) p. 171 and quoted references

(52) A.J. Berlinsky and W.N. Hardy, Proc. of the 13th Annual PTTI. Applications and Planning Meeting, Washington D.C., USA (1981) p. 547

(53) F.M. Penning, Physica $\underline{3}$ (1936) p. 873

(54) W. Paul, O. Osberghaus and E. Fischer, Forschungber. Wirtsch. Verkehrsministerium Nordrhein-Westfalen n° 415 (1958)

(55) H.G. Dehmelt in Advances Atomic and Molecular Physics $\underline{3}$ (1967) p. 53 and $\underline{5}$ (1969) p. 109

(56) F.G. Major and G. Werth, Phys. Rev. Lett. $\underline{30}$ (1973) p. 1155

(57) M.D. Mc Guire, R. Petsch and G. Werth, Phys. Rev. A $\underline{17}$ (1978) p. 1999

(58) M. Jardino, M. Desaintfuscien and C. Audoin, Applied Physics 24 (1981) p. 167

(59) L.S. Cutler, R.P. Giffard and M.D. Mc Guire, Proc. of the 13th Annual PTTI. Applications and Planning Meeting, Washington, D.C., USA (1981), p. 563

(60) D.J. Wineland, Proc. of the 13th Annual PTTI. Applications and Planning Meeting, Washington D.C., USA (1981) p. 579

(61) F.G. Major and H.G. Dehmelt, Phys. Rev. 170 (1968) p. 91

(62) L.S. Cutler, R.P. Giffard and M.D. Mc Guire, Proc. of the 37th Annual Frequency Control Symposium, Philadelphia, USA (1983) p. 32

(63) M. Jardino, F. Plumelle, M. Desaintfuscien and J.L. Duchêne, Proc. of the 38th Annual Frequency Control Symposium, Philadelphia, USA (1984) p. 431

(64) M. Jardino, M. Desaintfuscien and F. Plumelle, Journal de Physique 42 Supplément au n° 12 (1981) p. C8-327

(65) W. Becker and G. Werth, Zeits.. für Physik A, 311 (1983) p. 41

(66) R. Blatt and G. Werth, Phys. Rev. A 25 (1982) p. 1476

(67) R. Blatt, H. Schnatz and G. Werth, Zeits. für Physik A 312 (1983) p. 143

(68) H. Knab, K.D. Niebling and G. Werth, Conference on Precision Electromagnetic Measurement, Delft, the Netherlands (1984)

(69) J. André and F. Vedel, Journal de Physique 38 (1977) p. 1381

(70) F. Plumelle, M. Desaintfuscien, J.L. Duchêne and C. Audoin, Optics Com. 34 (1980) p. 71

(71) D.J. Wineland and W.M. Itano, Phys. Rev. A 20 (1979) p. 1521 and quoted references

(72) D.J. Wineland and W.M. Itano, Phys. Rev. A 25 (1982) p. 35 and quoted references

(73) D.J. Winaland and R.E. Drullinger, Phys. Rev. Lett. 40 (1978) p. 1639

(74) F. Plumelle, private communication (1984)

(75) W. Nagourney, G. Janik and H. Dehmelt, Proc. Natl. Acad. Sci. (USA) 80 (1983) p. 643

(76) W. Neuhauser, M. Hohenstatt, P. Toschek and H. Dehmelt, Phys. Rev. Lett. 41 (1978) p. 233

(77) W. Neuhauser, M. Hohenstatt and P.E. Toschek, Phys. Rev. A 22 (1980) p. 1137

(78) D.J. Wineland and W.M. Itano, Physics Letters 82A (1982) p. 75

(79) W.M. Itano and D.J. Wineland, Phys. Rev. A 24 (1982) p. 1364

(80) J.J. Bollinger, D.J. Wineland, W.M. Itano and J.S. Wells in Laser
     Spectroscopy VI. Springer series optical sciences 4, p. 168

(81) J.J. Bollinger, W.M. Itano and D.J. Wineland, 37th Annual Frequency
     Control Symposium, Philadelphia, USA (1983) p. 37

(82) D.J. Wineland, W.M. Itano, J.C. Bergquist and F.L. Walls, Proc. of the
     35th Annual Symposium on Frequency Control, Philadelphia, USA (1981)
     p. 602

(83) H. Hammati, J.C. Bergquist and W.M. Itano, Optics Letters 8 (1983) p. 73

(84) F.L. Walls, D.J. Wineland and R.E. Drullinger, Proc. of the 32nd Annual
     Frequency Control Symposium, Atlantic City, USA (1978) p. 453

(85) P.L. Bender, J.L. Hall, R.H. Garstang, F.M.J. Pichanick, W.W. Smith,
     R.L. Barger and J.B. West, Bulletin Am. Phys. Soc. 21 (1976) p. 599

(86) D.J. Wineland, W.M. Itano and R.S. Van Dyck Jr. in Advances in Atomic and
     Molecular Physics 19, Academic Press (1983) and quoted references

(87) H.G. Dehmelt, IEEE Trans. on Instr. and Meas. IM-31 (1982) p. 83

	ν_o	$\Delta\nu_1/\nu_o$	$\Delta\nu_2/\nu_o$
^{133}Cs	9 192 631 770 Hz	$- 2.45 \times 10^{-20}$ E^2	4.64 B^2
^{1}H	1 420 405 751.770 $\pm$ 0.003 Hz::	$- 5.5 \times 10^{-23}$ E^2	195.3 B^2
^{87}Rb	6 834 682 612.8 $\pm$ 0.5 Hz	$- 1.8 \times 10^{-20}$ E^2	8.42 B^2
^{199}Hg$^+$	40 507 347 996.9 $\pm$ 0.3 Hz	$- 3 \times 10^{-22}$ E^2	0.24 B^2

TABLE 1. Property of the hyperfine transition of some elements. ν_o is the hyperfine transition frequency, expressed in Hz. $\Delta\nu_1$ and $\Delta\nu_2$ are the Stark frequency shift and the Zeeman frequency shift, respectively. E is expressed in Volt per meter and B in Tesla.
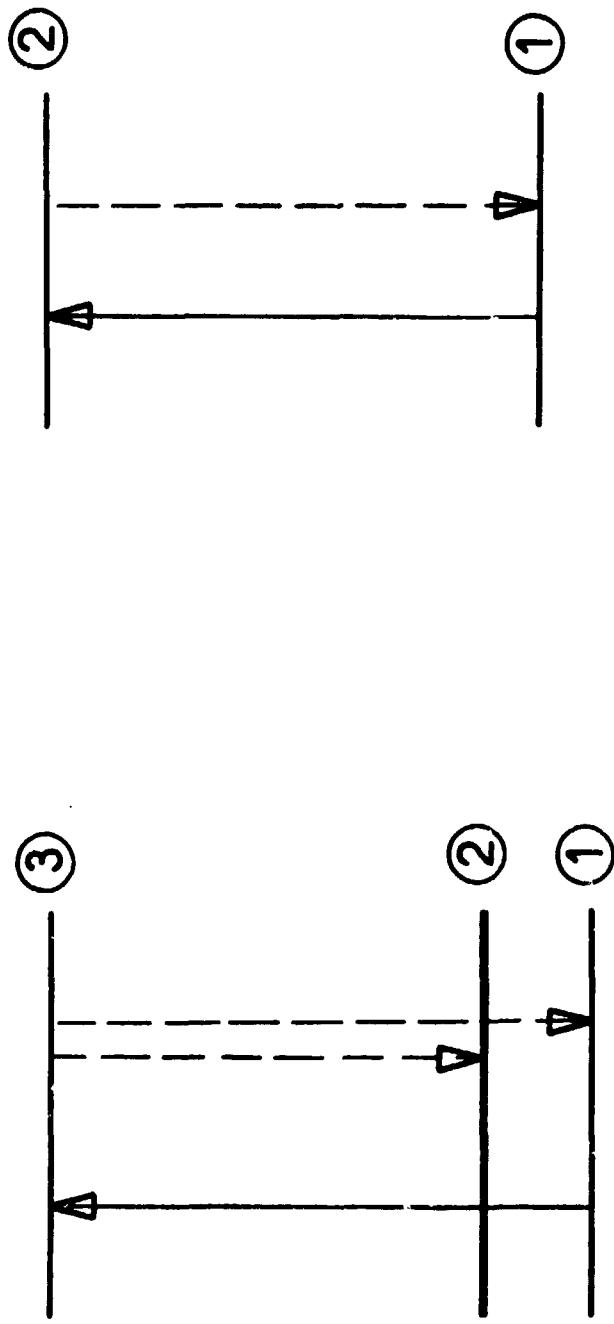
:: *Mean value of measurements in which the wall frequency shift has been measured at the same time as the hydrogen hyperfine transition frequency and in which the measurement uncertainty of the unperturbed transition of hydrogen was smaller than 4×10^{-3} Hz.*

	$\nu_0[Hz]$	$\tau[ms]$	$\lambda[nm]$
^{24}Mg	601. 27715833 (20)	4.6	457.1
^{26}Mg	601. 278866 (4)	4.6	457.1
^{40}Ca	1563. 6	0.55	657.3

TABLE 2. Property of fine structure transitions in magnesium and calcium. ν_0 is the frequency of the $^3P_1 \leftrightarrow {}^3P_0$ fine structure transition, τ is the life-time of the $^3P_1$ level and λ is the wavelength of the $^3P_{1,2,3} \rightarrow {}^1S_0$ fluorescence light.

Device	Short and medium term frequency stability	Accuracy	Possible technical difficulty
Optically pumped Cs (portable)	$10^{-12} \tau^{-1/2}$ 10^{-14} (year)	10^{-13}	Reliability of laser diodes
Small size H maser	$3 \times 10^{-13} \tau^{-1/2}$	10^{-12}	
Cold H maser	$[(2.9 \times 10^{-17} \tau^{-1/2})^2 + (1.2 \times 10^{-16} \tau^{-1/2})^2]^{1/2}$	$10^{-13}/10^{-14}$	Refrigeration, injection of atoms in the storage cell
Mg beam	$3 \times 10^{-13} \tau^{-1/2}$	10^{-13}	Sub-millimeter frequency source
$^{199}Hg^+$	$10^{-12} \tau^{-1/2}$	$1C^{-13}$	Life time of lamp, control of neutral mercury pressure
Cooled ions ($^{201}Hg^+$)	$10^{-16} \tau^{-1/2}$	10^{-15}	Cooling laser source

TABLE 3. Summary of the potentialities of some atomic frequency standards.

27
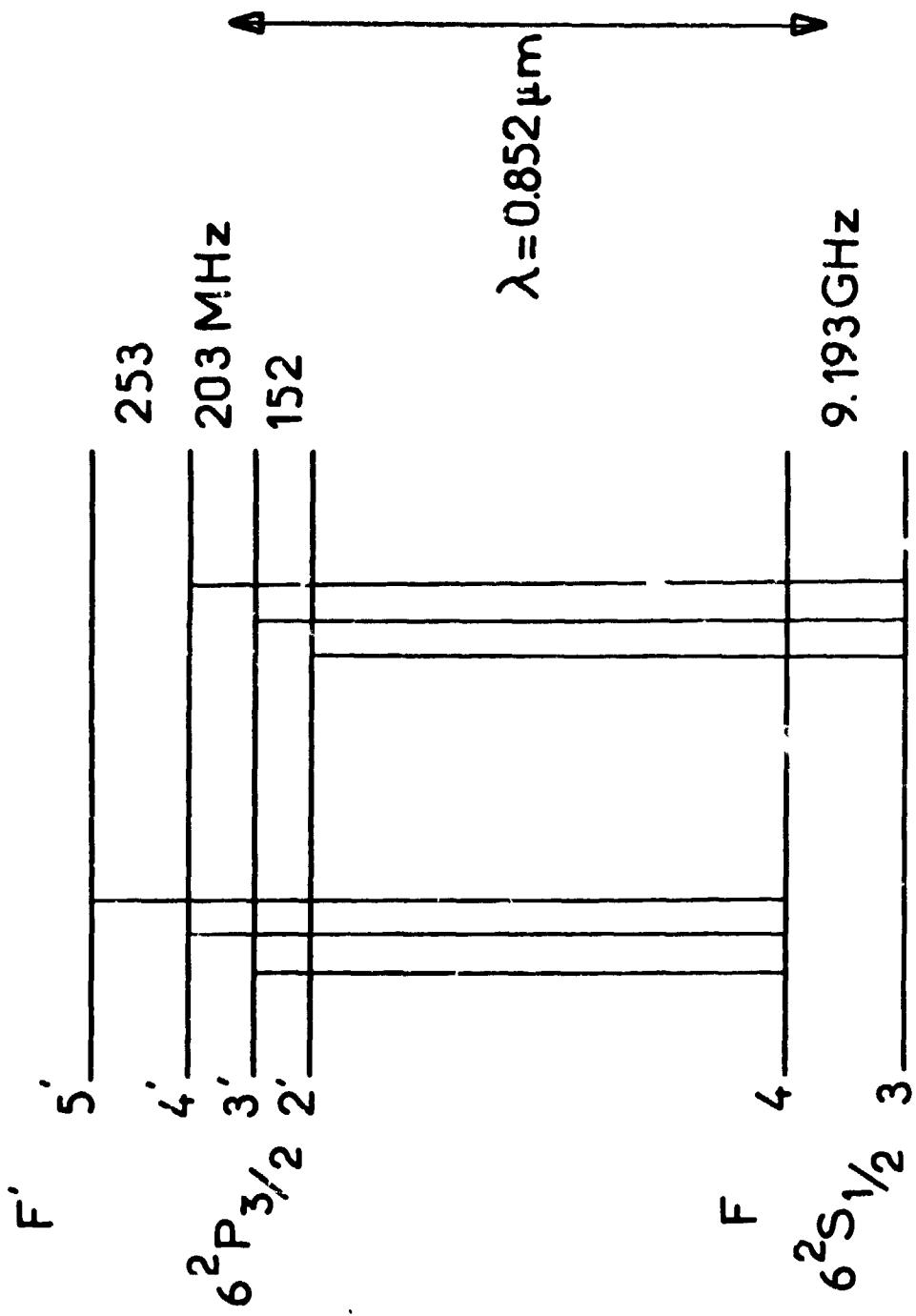
Optical Pumping   Optical Detection
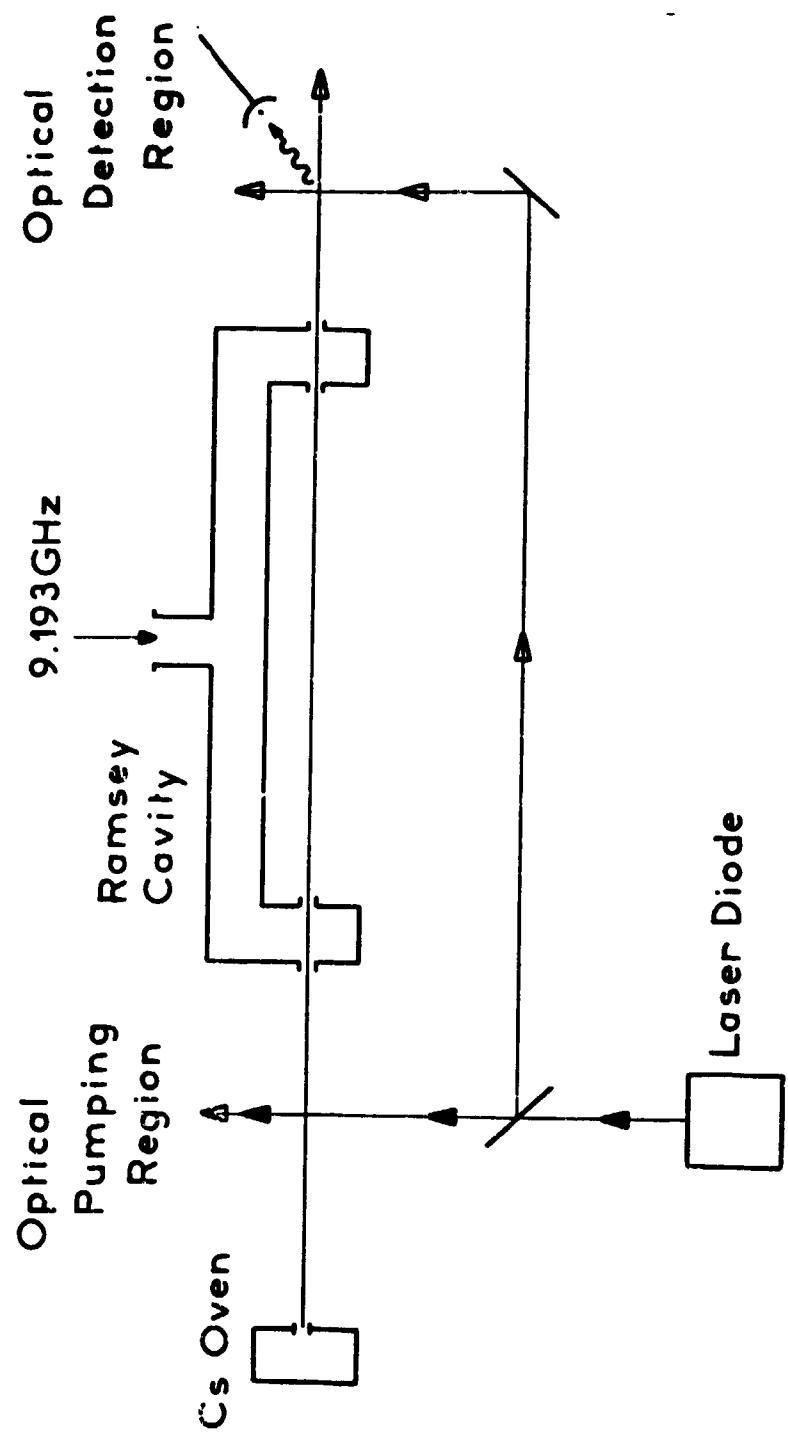
Schematic representation of optical pumping and detection methods.

Fig.1

F′

5′ — 253

4′ — 203 MHz

3′ — 152

2′

$6^2P_{3/2}$

λ=0.852μm

F

4 — 9.193GHz

3

$6^2S_{1/2}$

Fig.2

Simplified energy diagram of the cesium atom, with the hyperfine structure
of the $5^2S_{1/2}$ ground state and of the $6^2P_{3/2}$ second excited state. Magnetic
sub-levels are not shown. Vertical lines represent allowed transitions.
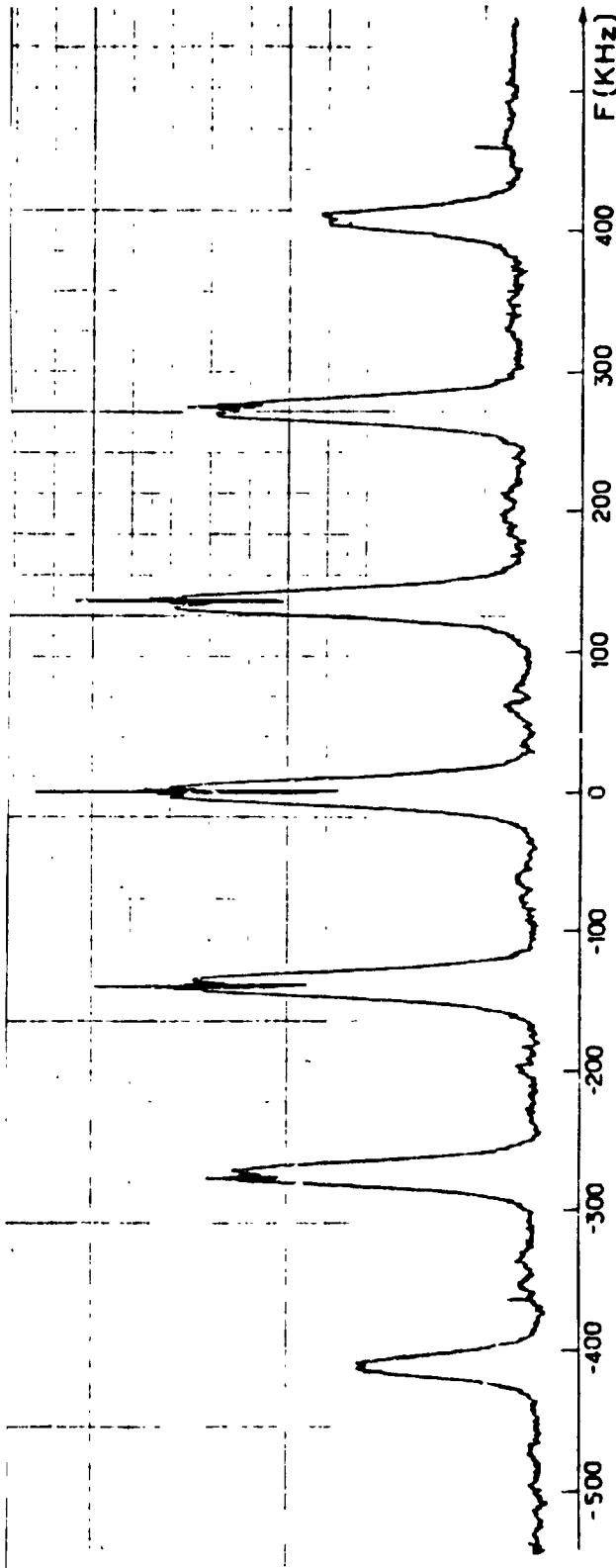
Cesium beam with one laser for optical pumping and detection.

Fig.3

30
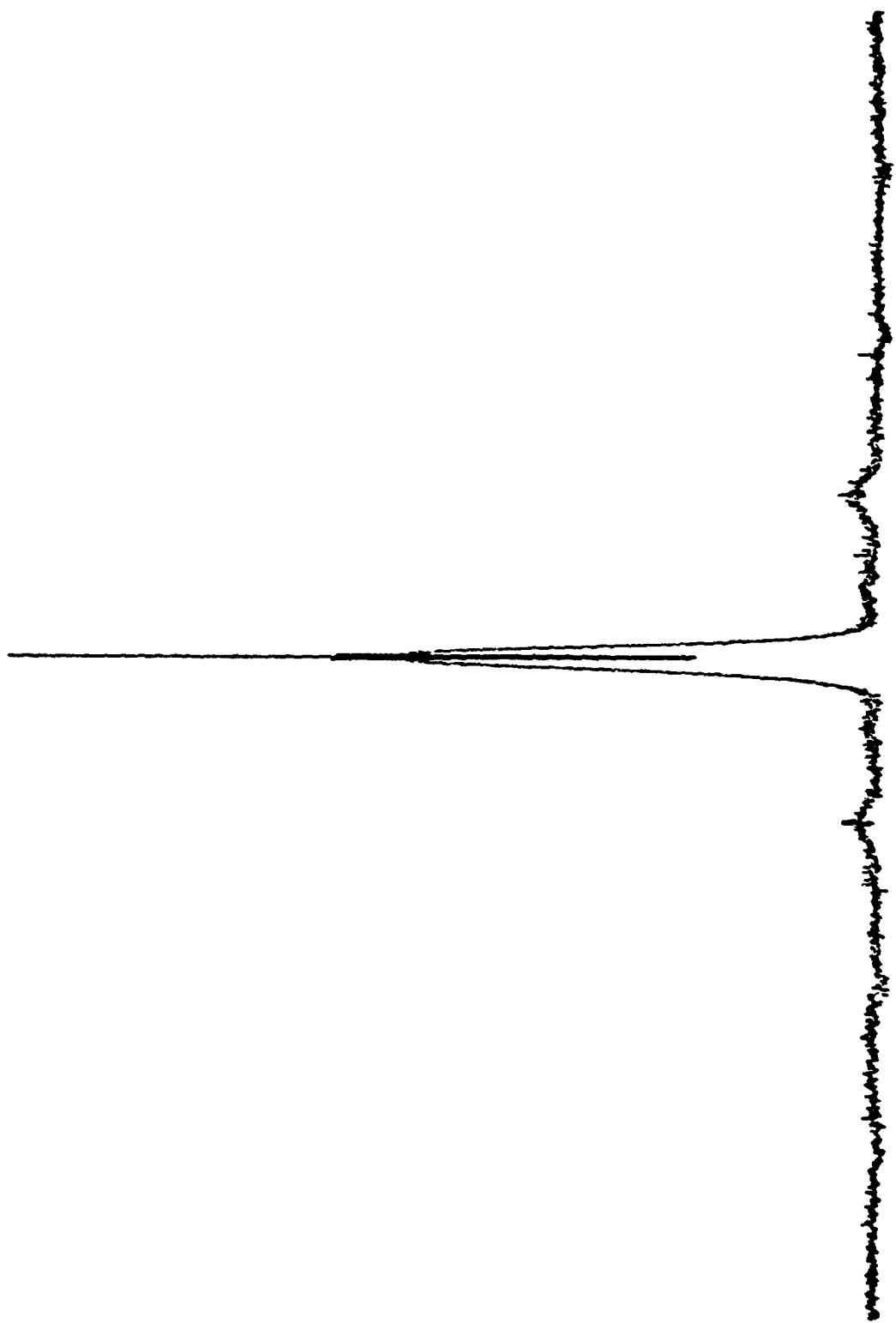
Microwave spectrum obtained with the one laser configuration.
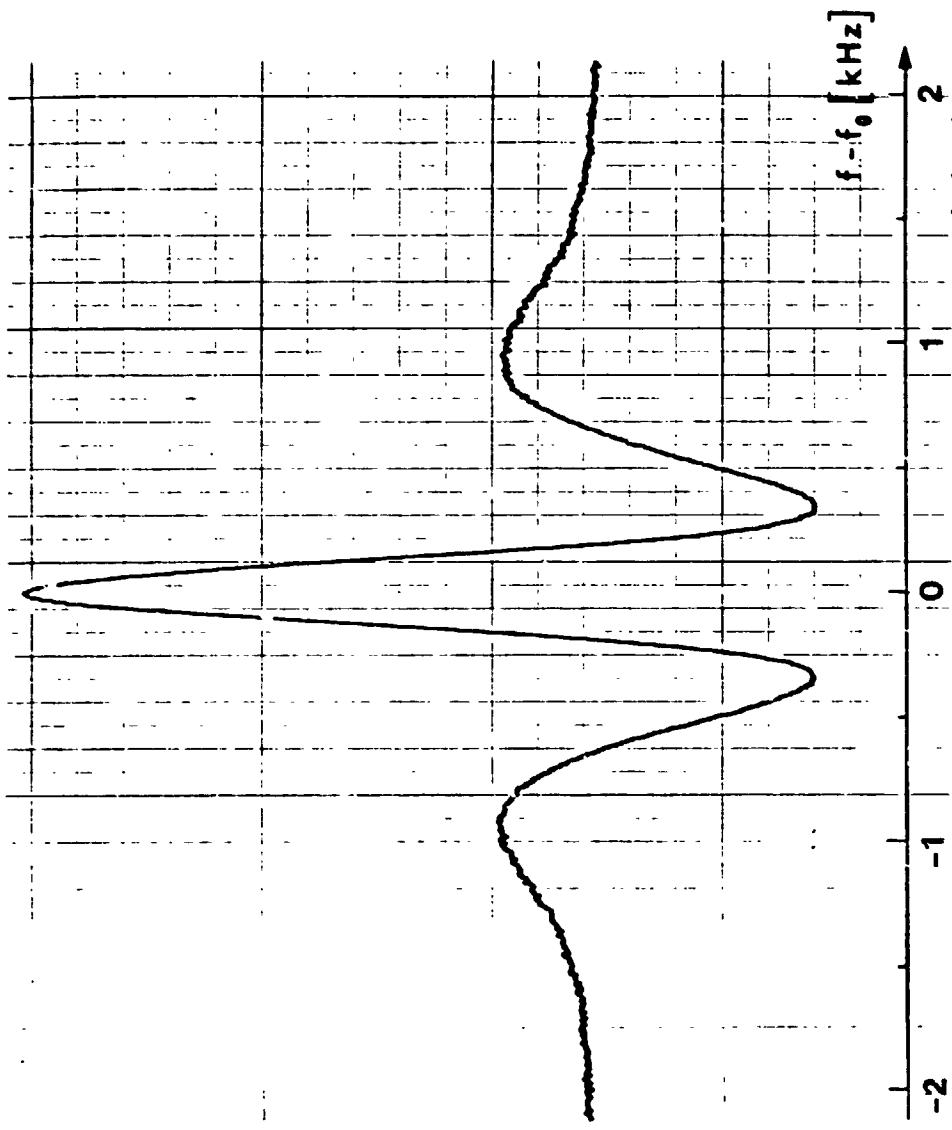
Fig.4

Microwave spectrum obtained with two lasers. Optical pumping : F = 3 ⟷
F' = 3 (π)and F = 4, F' = 3 (σ). Optical detection : F = 3, F' = 3 (o). Same
horizontal scale as in Fig. 4.   Fig.5
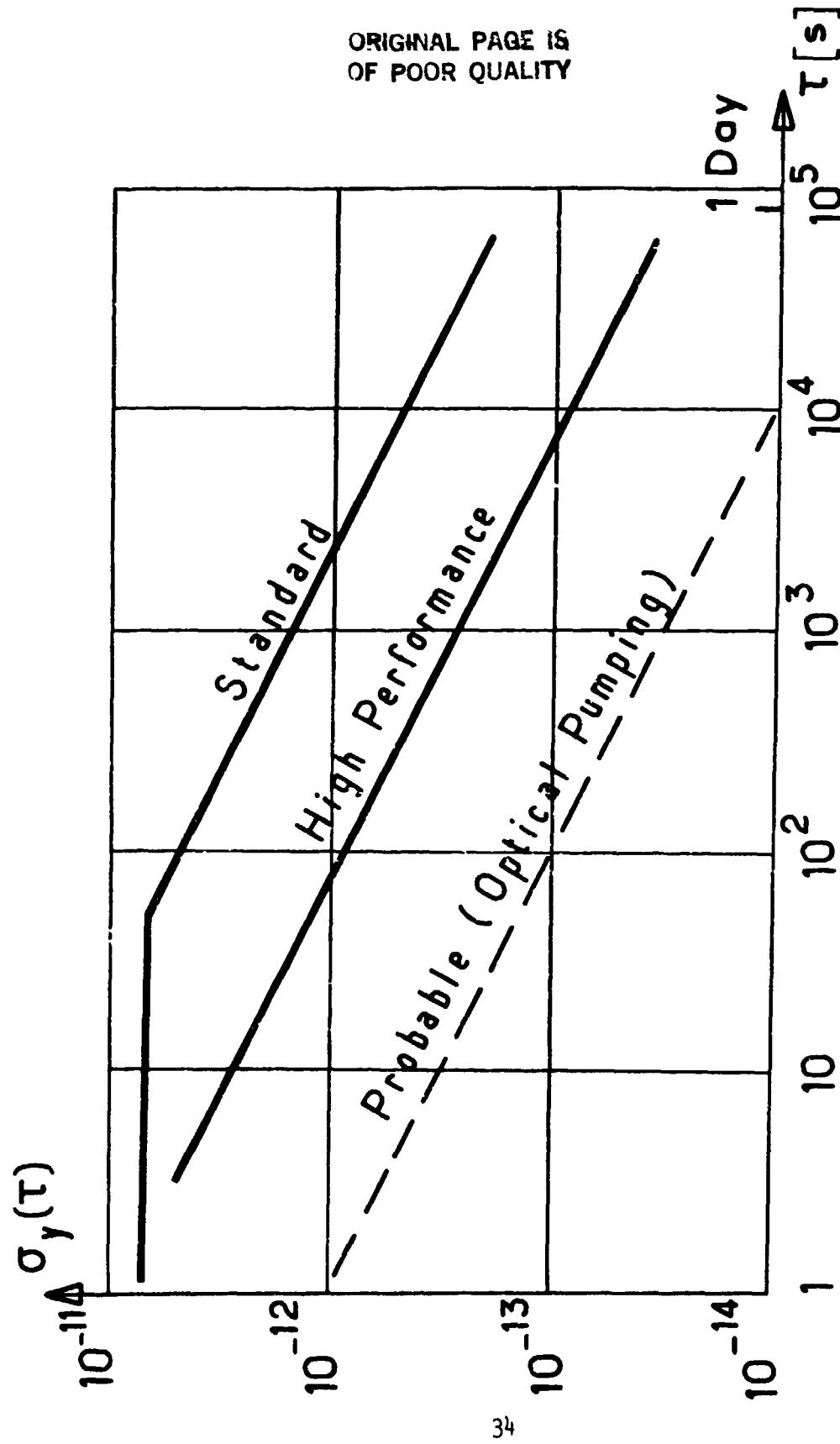
Central fringe of the Ramsey pattern obtained with two lasers for optical pumping and a third one for optical detection. We have : ℓ = 1 cm, L = 21,5 cm and about optimum microwave power. The linewidth is 290 Hz.
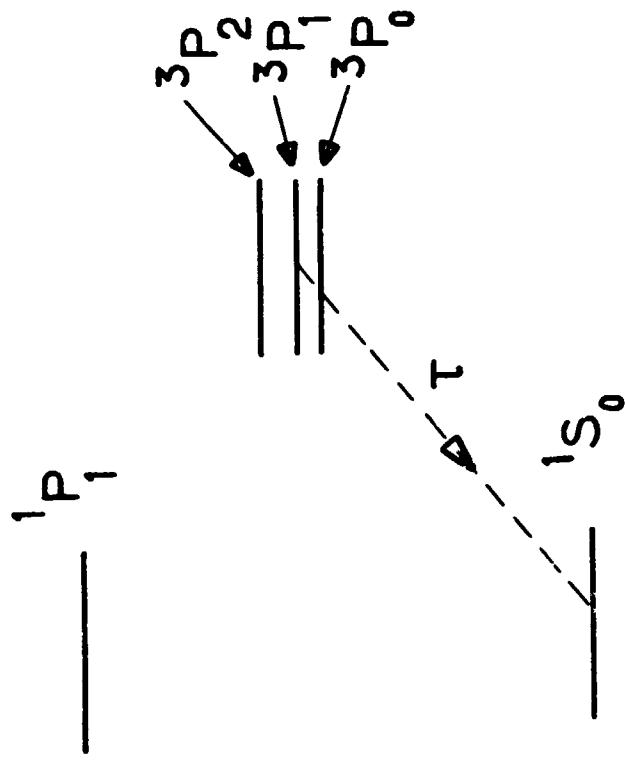
Fig.6
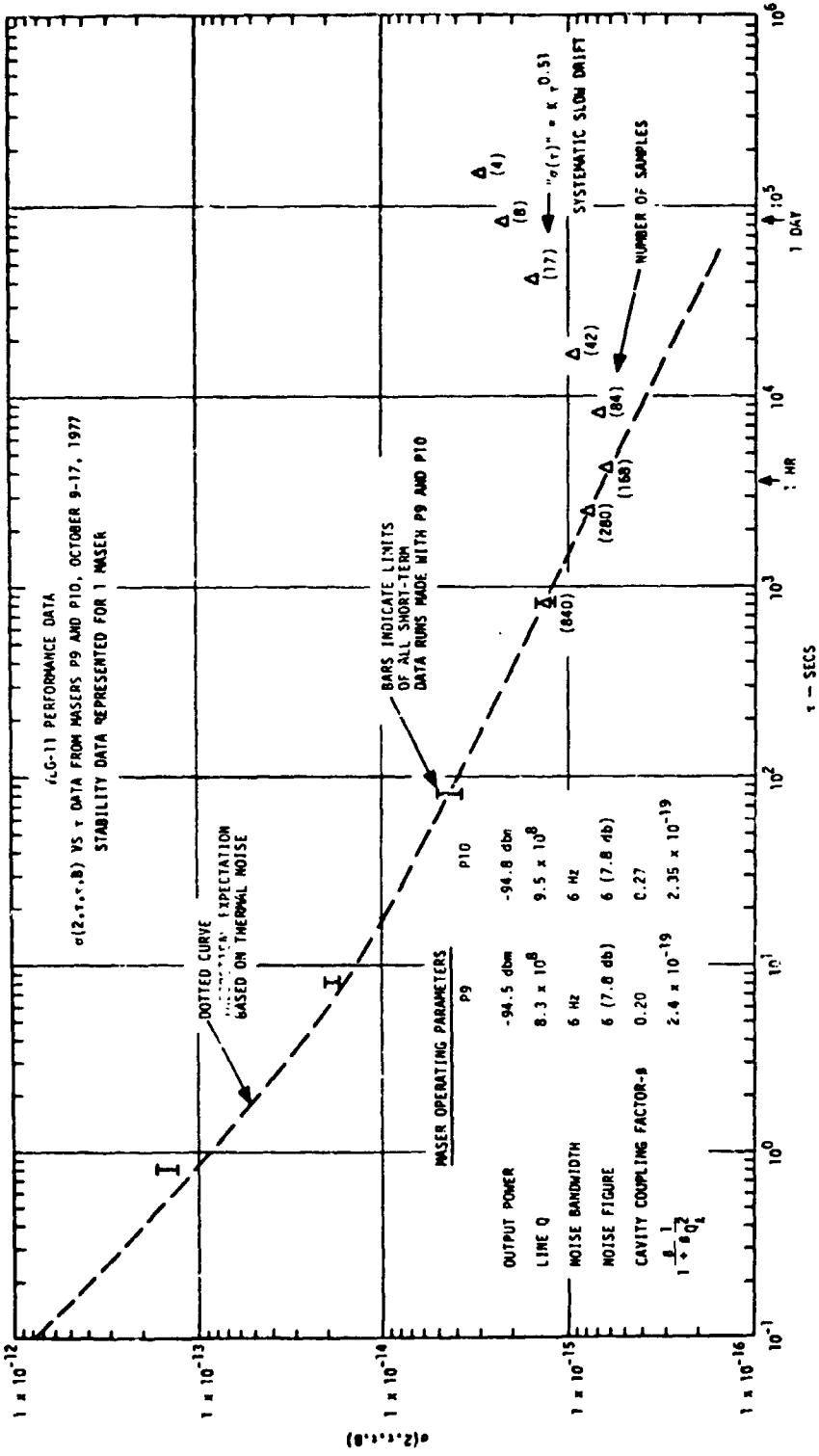
Example of frequency stability graph of two manufactured cesium beam frequency standards and expected frequency stability with optical pumping and detection methods. Standard:FTS 4050 model. High performance: HP 5061 A opt. 004 .

Fig.7
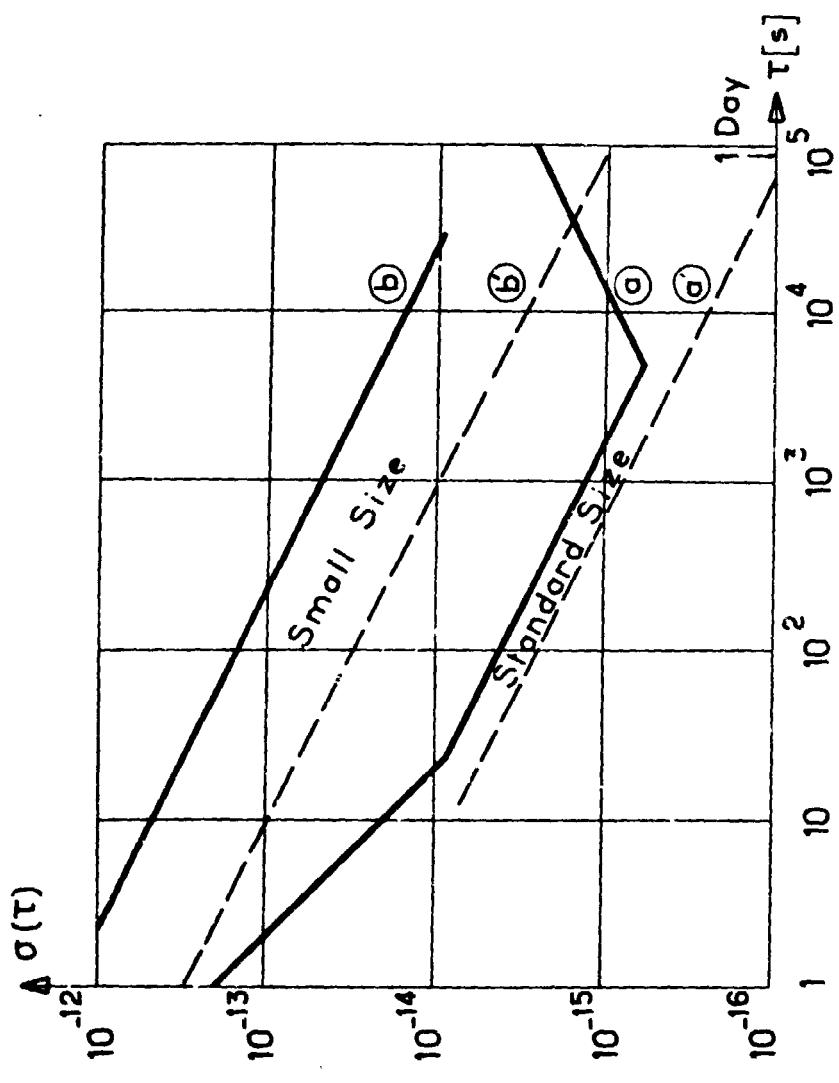
Simplified energy diagram of the first singlet and triplet levels of Mg and Ca. The life-time τ of the level $^3P_1$ is 4.6 ms for Mg and 0.55 ms for Ca.

Fig. 8

Fig.9

Frequency stability graph of standard size VLG 11 hydrogen maser (from reference 30).
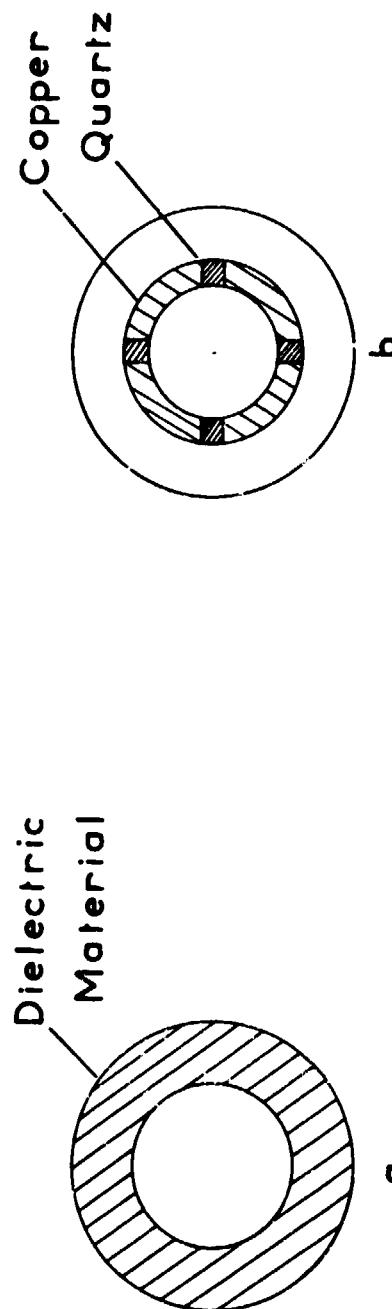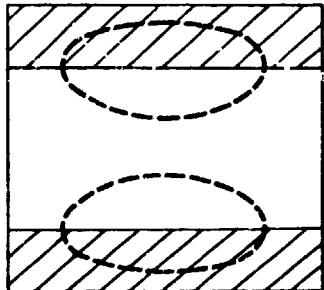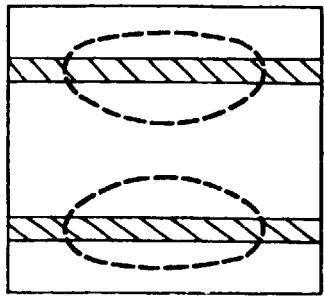
Frequency stability graph of hydrogen masers.

a. operational standard size hydrogen maser

a'. ultimate frequency stability of standard size hydrogen masers (room temperature)

b. operational small size hydrogen maser

b'. ultimate frequency stability of small size hydrogen masers (room temperature).

Fig. 10

Copper

Quartz

Dielectric
Material
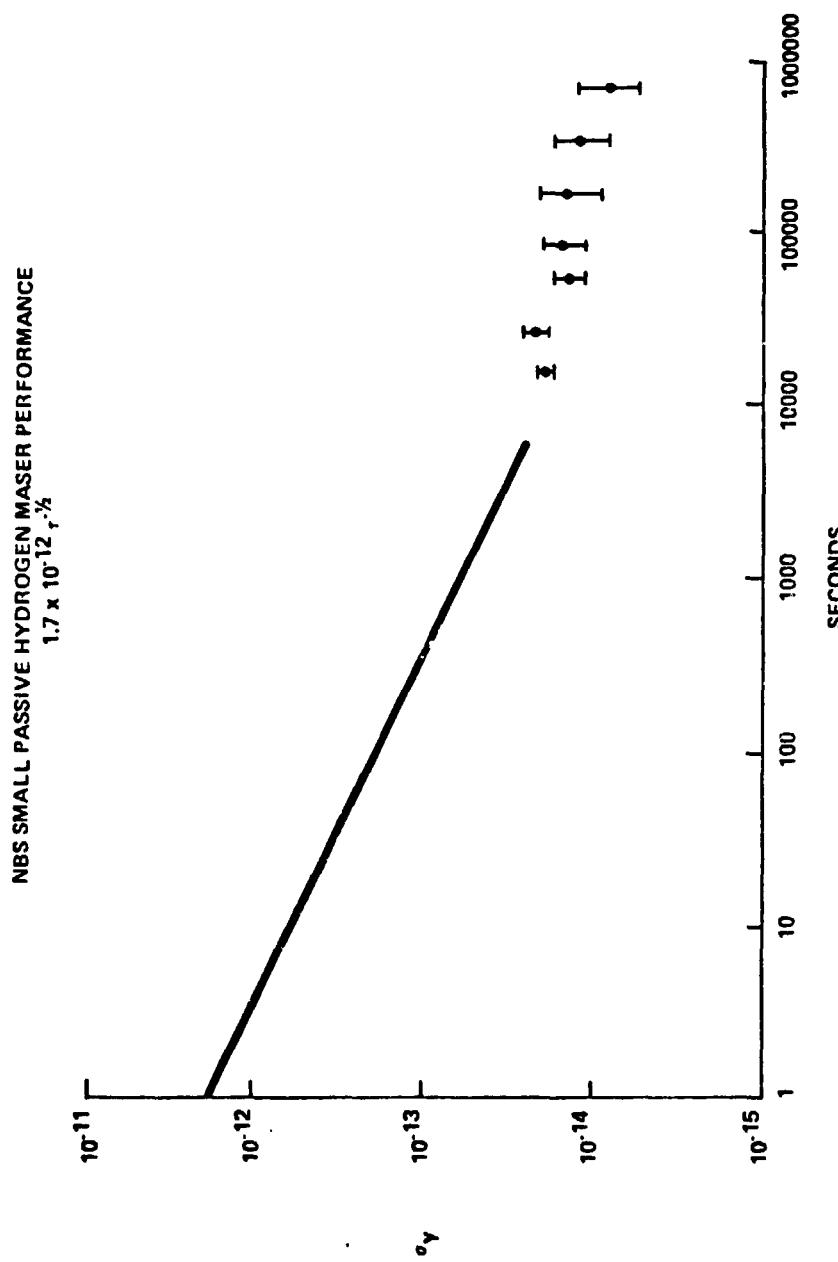
a   Resonant cavities for small size hydrogen masers
a. with a hollow cylinder of dielectric material
b. with conductors in the cavity.
   Dotted lines show the magnetic lines of force.

Fig.11

NBS SMALL PASSIVE HYDROGEN MASER PERFORMANCE
$1.7 \times 10^{-12} \tau^{-\frac{1}{2}}$
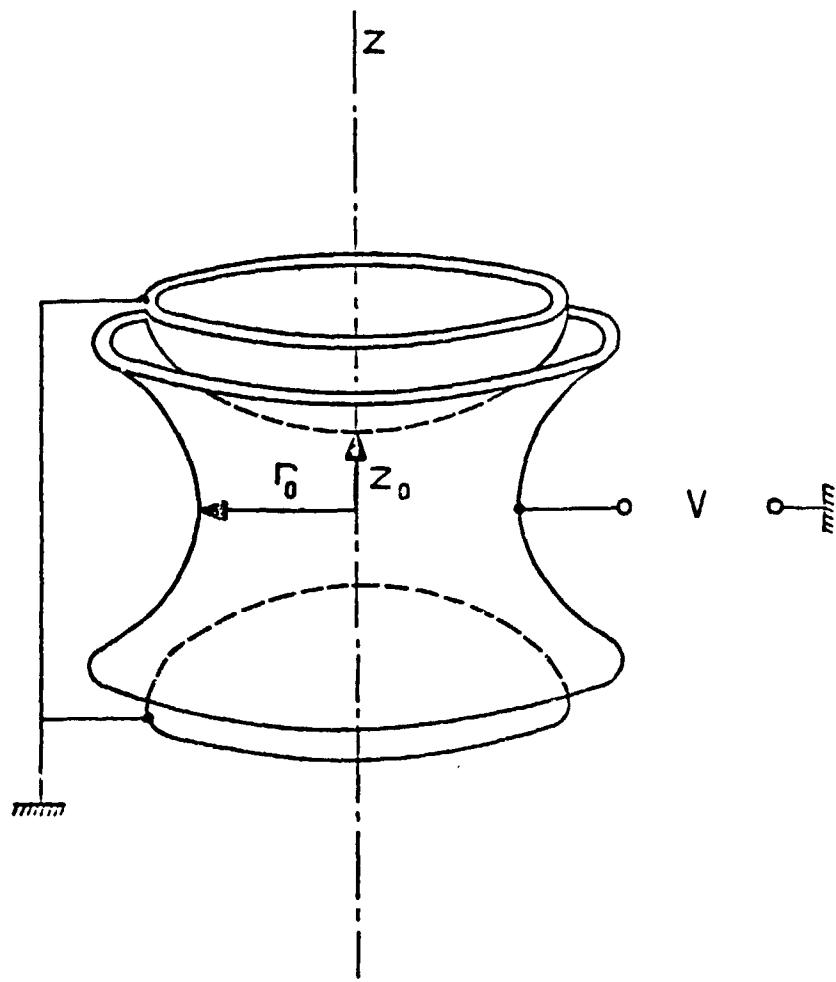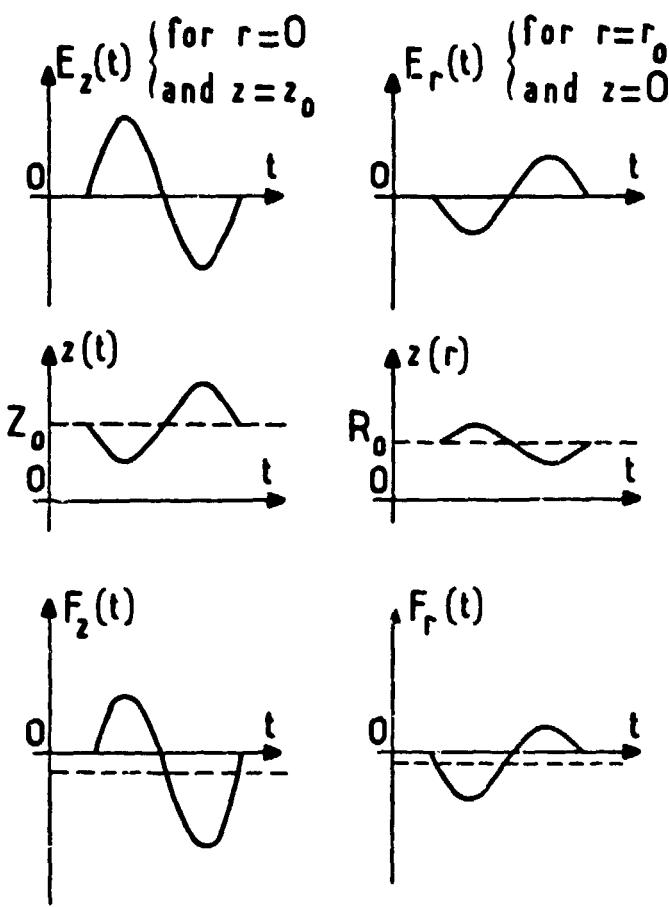
Frequency stability obtained with a passively operated small size hydrogen maser.

Fig. 12

39

Electrodes of a ion trap, assuming a hyperboloïd shape.

Fig.13
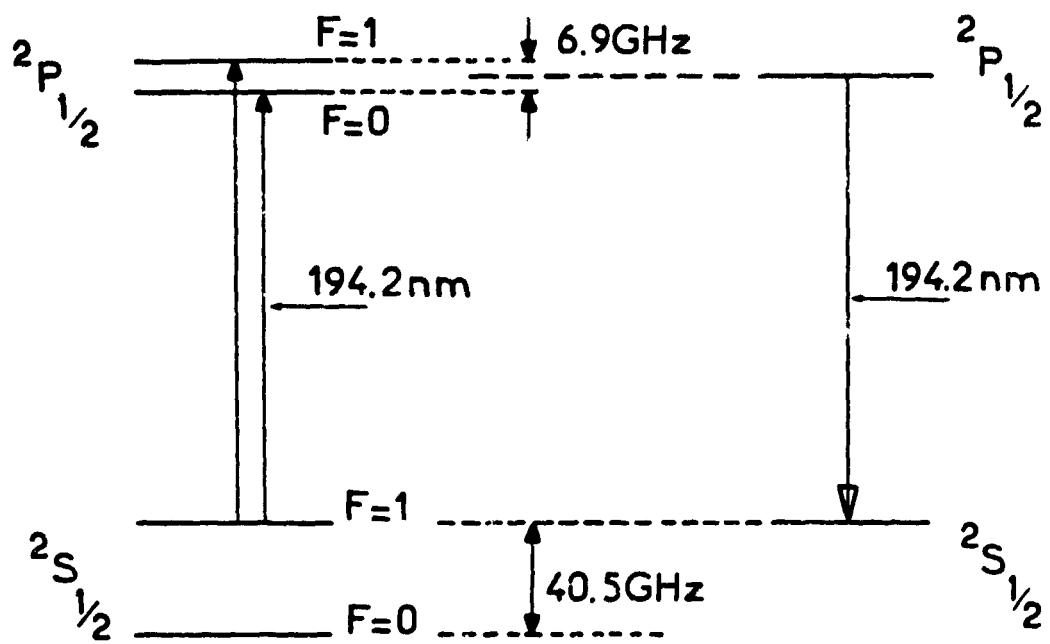
Radiofrequency trap : origin of the axial (left) and transverse (right) confinement forces.The ionic charge is assumed positive.

Top : periodic variation of the axial electric field at point $r = 0$ and $z = z_0$ and of the transverse electric field at point $r = r_0$ and $z = 0$

Middle : Forced motion (micromotion) of the ion in the vicinity of the considered points

Bottom : Due to the electric field inhomogeneity, the variation of the axial and transverse components of the electric force is not sinusoïdal. It follows that the mean value of this force is not zero and it is directed towards the center of the trap. It yields the macromotion.

Fig.14
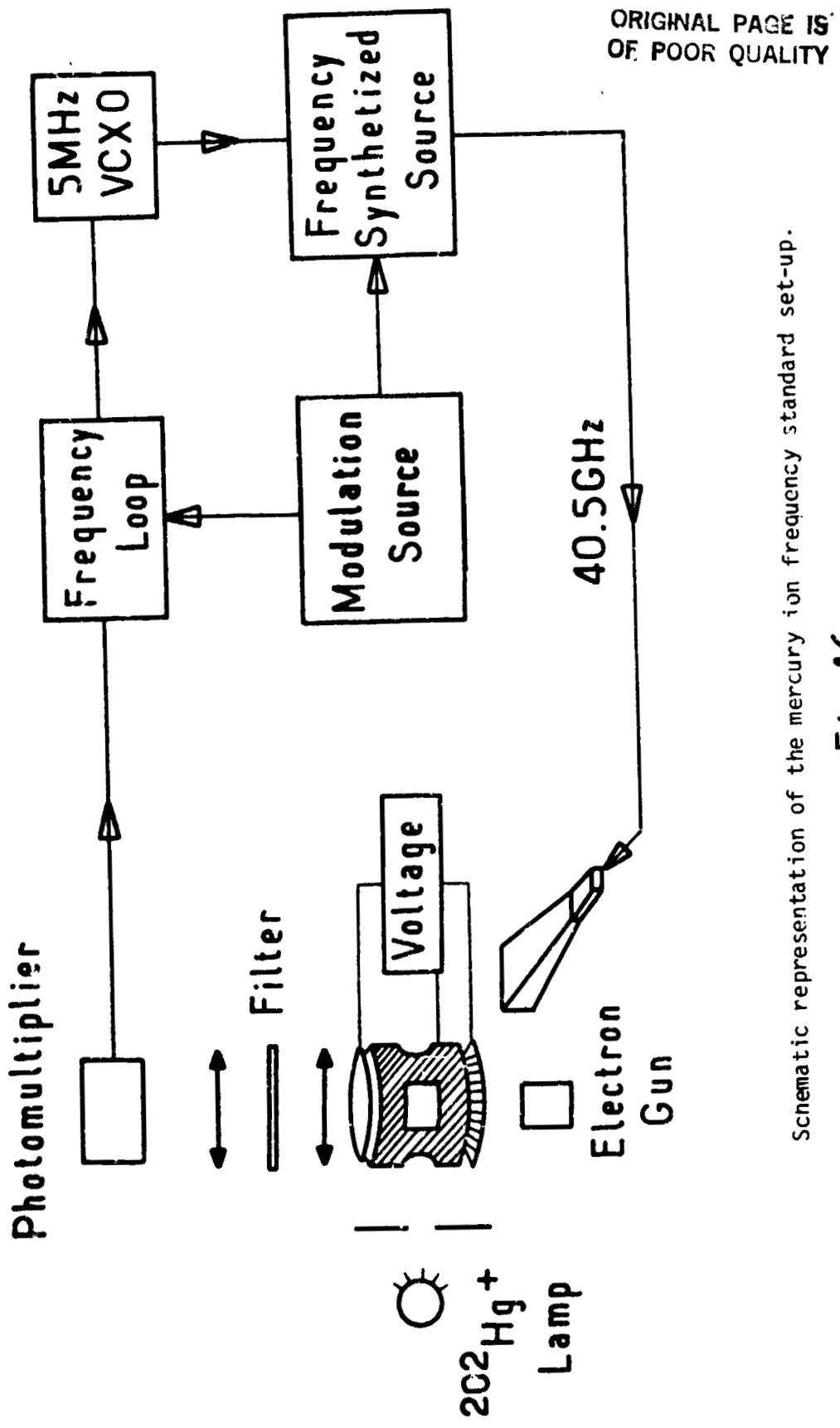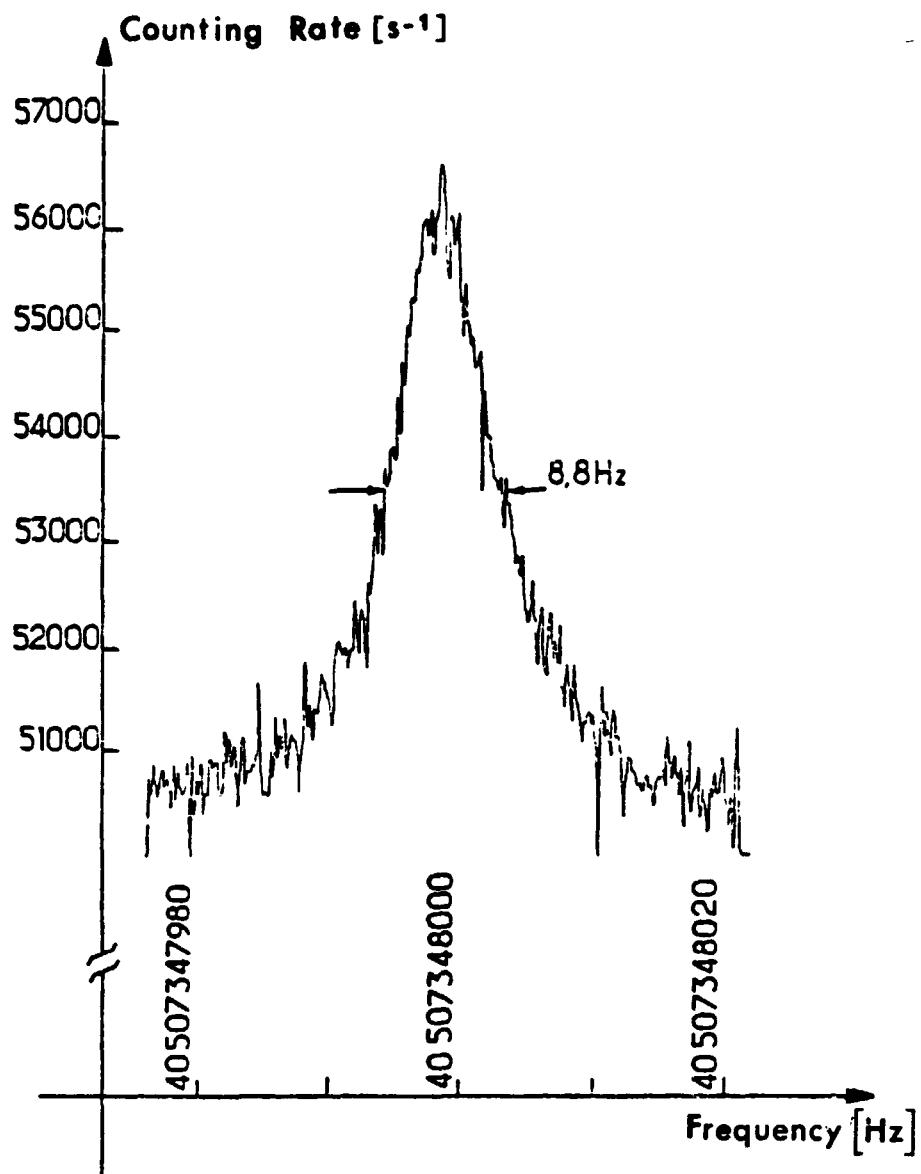
Simplified energy diagram of $^{199}Hg^+$ and $^{202}Hg^+$.

Fig.15
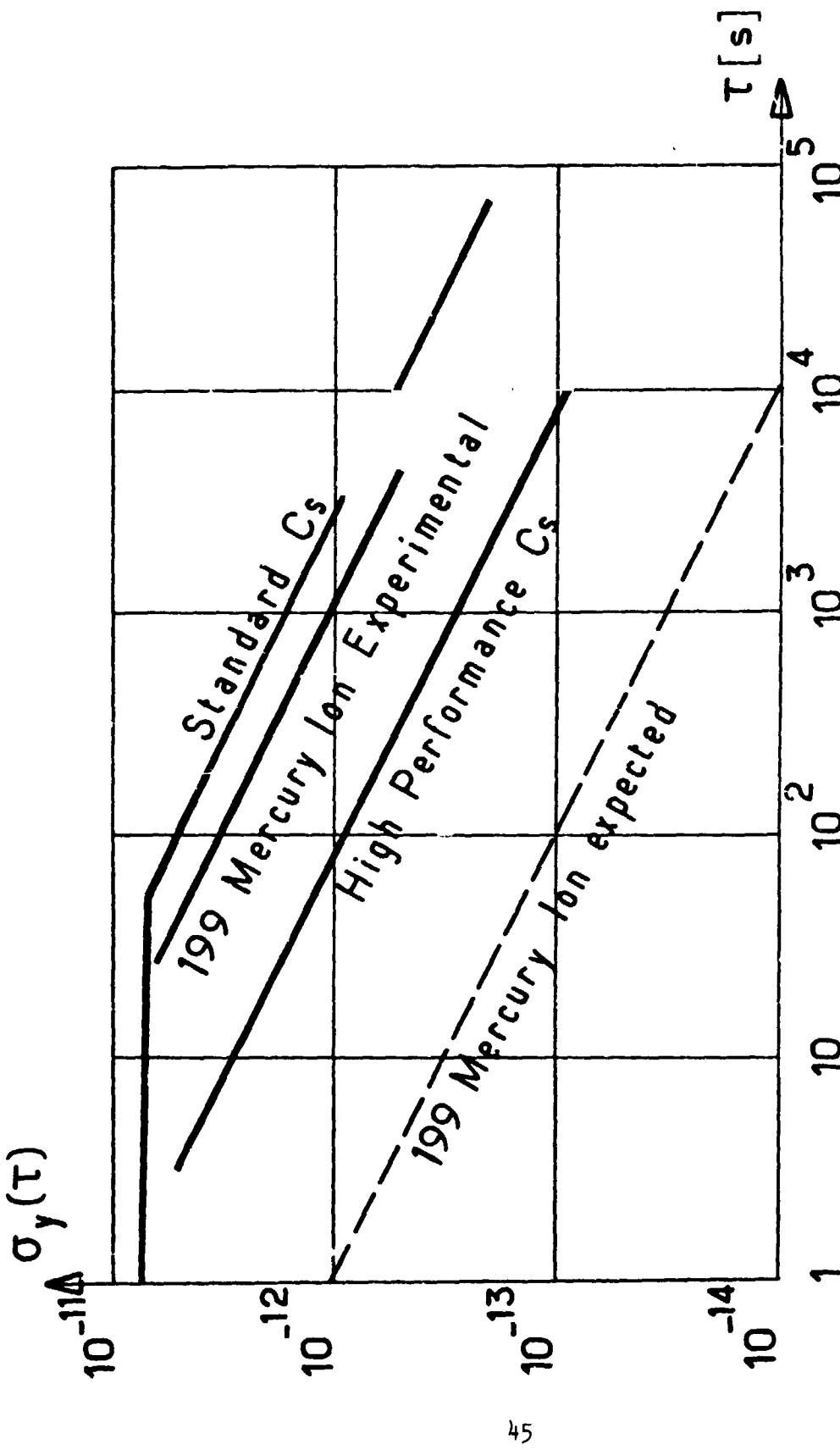
Schematic representation of the mercury ion frequency standard set-up.

Fig.16

43

Power broadened hyperfine resonance line of ^{199}Hg$^+$.

Fig.17

Frequency stability achieved in an experimental mercury ion frequency standard compared to portable cesium beam frequency standard. Dotted line : expected frequency stability.   Fig.18

STUART CRAMPTON, WILLIAMS COLLEGE: I have saved most of my comments for tomorrow, but I would like to make two comments about cold hydrogen masers. One is that they are inherently small, and it's not necessary to use feedback in order to get oscillation. The second is the possibility of trade-offs. At a sacrifice of somewhat increased wall shift, one can operate at a lower temperature with the liquid helium walls and thus avoid the background pressure problem. So there are some interesting prospects in the future for that kind of device.

MR. AUDOIN: Yes, at the low temperature the linewidth is very small. The Q of the microwave cavity may be made extremely large using superconducting walls, or even copper has low losses at low temperature, so it is possible to have an active maser.
    Also, it is possible to use, in principle, super conducting magnetic shields which reduce the problem of sensitivity to the magnetic field. So there are a lot of possibility of improvement.

VICTOR REINHARDT, HUGHES AIRCRAFT: Do you have any comments on the future possibility of a rubidium standard?

MR. AUDOIN: Yes, there is some indication in my manuscript on this, but I am not a specialist in rubidium clocks. Using optical pumping by diode lasers offers many new possibilities. As you know, in the present rubidium cells one uses a buffer gas for several purposes. One of them is to improve the optical pumping efficiency. But if you use a laser diode, the optical pumping efficiency will be large anyway, so we don't need the buffer gas. You may go to a wall coated cell, which will remove any difficulty due to that sense of motional variation in present rubidium cells. So, maybe one may expect improvements in that field, too.

MR. HELLWIG: Do you have any comment on the primary status of cesium versus the other techniques for the rest of the century?

MR. AUDOIN: Yes. The present level of performance of laboratory cesium standards is between one part in ten to the thirteenth and one part in ten to the fourteenth. I do not believe that it will be proved in this century that other devices have better accuracy. There are possibilities, ion storage gives the best promise in my view and there is a prospect with the cold hydrogen maser, but this has been proved with a different design of the device. I think that it will take time and I am confident that the definition will be attached to the cesium atom until the end of the century.

STEVE KNOWLES, NAVAL RESEARCH LABORATORY: While we are on the subject of frequency standards, I just wanted to mention the idea of frequency synchronization via phase length, via synchronous satellites. In a sense, this isn't a frequency standard at all, but if what one wants is worldwide frequency synchronization, this offers, I think, the possibility of accuracy on the order of

ten to the minus fifteenth, and since it's a true closed loop system, it has never been tested to see whether long term precision may be considerably lower than that.

MR. AUDOIN: Yes, but accuracy figure is attached to the device, not to the comprising system.

MR. KNOWLES: As I say, in a sense, I am not talking about the subject of your talk at all, but I wanted to say that if what one wants is worldwide frequency synchronization, then he can claim that this is equivalent to a secondary standard, and not a primary one.

MR. AUDOIN: Okay, these techniques allow comparison of standards.

FREQUENCY AND TIME STANDARDS BASED
ON STORED IONS†

J. J. Bollinger, D. J. Wineland, W. M. Itano, J. C. Bergquist,
and J. D. Prestage

National Bureau of Standards, Boulder, Colorado 80303

ABSTRACT

The method of ion storage provides a basis for excellent time and
frequency standards. This is due to the ability to confine ions for long
periods of time without the usual perturbations associated with
confinement (e.g. wall shifts). In addition, Doppler effects can be
greatly suppressed. The use of stored ions for microwave frequency
standards and the future possibilities for an optical frequency standard
based on stored ions are addressed.

INTRODUCTION

Since the pioneering work of Dehmelt and coworkers [1] it has been
realized that the techniques of ion storage provide some fundamental
advantages over other devices for improved frequency and time standards.
This assertion is based largely on the ability to confine ions for long
periods of time without the usual perturbations associated with confine-
ment. Samples of ions have been stored in electromagnetic traps for as
long as days. [1-3] This means that the interaction time for the ions can
be quite long which gives rise to large line Q (transition frequency
divided by the linewidth) and high spectral resolution. For example, the
linewidth of a cesium beam is limited by the transit time between the two
ends of the Ramsey cavity. Linewidths of 0.01 Hz have already been
observed for stored Mg^+ ions. [4] This would correspond to a cesium beam
tube of about 10 km length. The long term confinement also implies that
the average velocity $\langle \vec{v} \rangle$ of the ions approaches zero and first order
Doppler shifts can be made very small. [5] This characteristic, which is
also shared by rubidium clocks and hydrogen masers, gives an advantage over
atomic beam devices where a correction must be made for cavity phase shift
errors which are a form of residual first order Doppler effects. In
addition, typical confinement dimensions of < 1 cm imply that the Dicke
criterion [6] (confinement dimensions < wavelength) can be easily
satisfied in the microwave region of the spectrum. This nearly elimi..tes
any first order Doppler broadening of the microwave spectrum. It also
appears that the Dicke criterion can be met in the optical region of the
spectrum with laser cooling (to be described) on a single stored ion.

---

†Work of the US Government; not subject to US copyright.

The ion storage technique has the advantage that it lacks the usual perturbations associated with confinement. For example, the frequency shifts associated with collisions of atoms with identical atoms, buffer gases, or container walls such as in rubidium clocks or hydrogen masers are very small. Ions are often stored under conditions of ultrahigh vacuum so that frequency shifts due to ion collisions with background neutrals are negligible. Frequency shifts due to ion-ion collisions are caused by the electric fields of the Coulomb repulsion. These shifts as well as frequency shifts due to the electric fields of the trap can, in many cases, be made extremely small ($< 10^{-15}$). [5,7,8]

Two types of traps have so far been used for atomic clock experiments. The Paul [9] or rf trap uses inhomogeneous rf electric fields to provide confinement in a pseudopotential well [1]. It is the three dimensional analog of the Paul quadrupole mass filter. To see how it works we first note that in a (homogeneous) sinusoidal rf electric field, ion motion is sinusoidal but is 180 degrees out of phase with respect to the electric force. If the field is somewhat inhomogeneous, it is easy to show that the force on the ion averaged over one cycle of the driven motion is towards the region of weaker field. [1] Since an electric field minimum can exist in a charge free region, stable trapping can be accomplished. Such a trap is shown schematically in Fig. 1 where the three trap electrodes are shaped to provide an electric potential of the form (r^2-2z^2) inside the trap. For this "ideal" trap shape, an ion is bound in a nearly harmonic well.

The "ideal" Penning [10] trap uses the same electrode configuration as in Fig. 1 but uses static electric and magnetic fields. A harmonic potential well is provided along the "z" axis by static electric fields. This however results in a radial electric field which forces the ions towards the "ring" electrode. This effect can be overcome if a static magnetic field $\vec{B}$ is superimposed along the "z" axis. In this case the x - y motion of the ions is a composite of circular cyclotron orbits (primarily due to the $\vec{B}$ field) and a circular $\vec{E} \times \vec{B}$ drift ("magnetron" motion) about the trap axis.

FREQUENCY STANDARDS WITHOUT LASER COOLING

Several groups have sought to develop a microwave frequency standard based on the 40.5 GHz hyperfine splitting in $^{199}Hg^+$ ions stored in an rf trap. [11-15] The relatively small size of this device could make it a portable standard with potential commercial applications. The choice of the $^{199}Hg^+$ ion for a microwave frequency standard is based on its 40.5 GHz ground-state hyperfine separation, which is the largest of any ion which might easily be used in a frequency standard (hence high Q for given interrogation time), and its relatively large mass (hence small second order Doppler shift for a given temperature). In addition, a $^{202}Hg^+$ lamp source can be be used to optically pump the $^{199}Hg^+$ ground state. A fractional frequency stability comparable to that of commercial cesium

standards has been demonstrated. [13] In these experiments, the second order Doppler shift can be reduced by cooling the ions with a light neutral buffer gas (e.g. helium or hydrogen). With buffer gas pressures up to 10^{-2} Pa the secular motion of the ions in the psuedopotential well can be thermalized to the ambient temperature.[14] For Hg^+ at room temperature, the second order Doppler shift is about 2×10^{-13}. Unfortunately, the second order Doppler shift due to the micromotion of the ions can be much larger. [1,14] The size of the micromotion contribution to the 2nd order Doppler shift depends on the size of the ion cloud, or, for a given ion number density, on the total number of ions. Consequently in the performance of the $^{199}Hg^+$ frequency standard there is a tradeoff between systematic errors due to the 2nd order Doppler shift and signal-to-noise ratio.   For a cloud of $\sim 10^6$ ions an accuracy of 2×10^{-13} and fractional frequency stability of $\sigma_y(\tau) \cong 2 \times 10^{-12}\tau^{-1/2}$ appear accessible.[14] This would be about an order of magnitude improvement in accuracy and stability over commercially available cesium frequency standards.

In addition, optical microwave double resonance experiments on stored ions have been performed using tunable lasers as light sources. The ground-state hyperfine splittings of $^{137}Ba^+$, [16] $^{135}Ba^+$, [17] and $^{171}Yb^+$ [18] have been measured, using pulsed dye lasers and rf traps. Microwave resonances as narrow as 60 mHz were observed in $^{171}Yb^+$. This has a line Q of 2×10^{11}. In some cases, optical pumping out of the absorbing ground state prevents use of the double-resonance method. This problem may be overcome, however, with the use of collisional relaxation [16,19].

FREQUENCY STANDARDS WITH LASER COOLING

A fundamental limitation of the above ion trap experiments is the 2nd order Doppler shift. In 1975 proposals [20,21] were made which could further reduce the second order Doppler shift by a process called laser cooling (also called optical sideband cooling or radiation pressure cooling). Laser cooling is a method by which a beam of light can be used to damp the velocity of an atom or ion. The basic mechanism for cooling of a trapped ion by a laser beam tuned slightly lower in frequency than a strongly allowed resonance transition is as follows: when the velocity of the ion is directed against the laser beam, the light frequency in the ion's frame is Doppler shifted closer to resonance so that the light scattering takes place at a higher rate than when the velocity is along the laser beam. Since the photons are reemitted in random directions, the net effect, over a motional cycle, is to damp the ion's velocity, due to absorption of photon momentum. If the laser frequency is tuned above resonance, it causes heating. In certain cases laser cooling can reduce the ion temperature below 1 K. Because of rf heating, it may be more difficult to do significant laser cooling on a cloud of many ions in an rf trap than in a Penning trap. [2] Consequently laser cooling experiments with a cloud of many ions have primarily been done in Penning traps.

Laser cooling of Mg^+ [4,22-24] and Be^+ [25,26] ions in a Penning trap has been achieved. For both types of ions, the light sources were the second harmonics, generated in nonlinear crystals, of cw dye lasers. The ions were optically detected by monitoring the cooling laser light scattered by the ions. Because the photon scatter rates can be very large ($> 10^6$ s^{-1} per ion), the optical detection provides a very sensitive detection technique where the noise in the system can be limited to the statistical fluctuations in the number of ions that made the clock transition. [27]

As a step towards realizing a frequency standard based on laser cooled stored ions, a clock based on a hyperfine transition in $^9Be^+$ has been constructed [26]. The average frequency of an rf oscillator was locked to the (M_I, M_J) = (-3/2, 1/2) to (-1/2, 1/2) nuclear spin flip transition in the ground state of $^9Be^+$, near the magnetic field (0.8194 T) at which the first derivative of the frequency with respect to field goes to zero. The ions were cooled to less than 2K. The 303 MHz resonance was observed with 25 mHz linewidth by rf-optical double resonance (see Fig. 2). The frequency stability of the locked oscillator ($\sigma_y(\tau) \cong 2 \times 10^{-11} \tau^{-1/2}$) was comparable to that of commercial Cs atomic beam frequency standards. The frequency accuracy was on the order of 10^{-13}, limited primarily by the uncertainty of the second-order Doppler shift due to heating of the ions during the rf resonance period, when the cooling radiation was shut off in order to avoid light shifts. At the end of the 20 s Ramsey interrogation period, the ion temperature had increased to ~ 30 K. The dominant heating mechanism may be due to axial asymmetries in the trap. [28,29] Reduction of the heating (and consequently the second order Doppler shift) by an order of magnitude should be possible by constructing a trap with better axial symmetry or by the use of a second type of ion (e.g. $^{24}Mg^+$) to "sympathetically" cool the $^9Be^+$ ions. [22,23] Primary cesium standards are slightly better than this first frequency standard based on a laser cooled ion, but future improvements with the $^9Be^+$ standard are anticipated.

Because $^9Be^+$ is experimentally easy to cool with a laser, it was used to investigate the generic problems of a laser cooled stored ion frequency standard. As a microwave frequency standard, $^9Be^+$ is limited because of the low 303 MHz frequency of the clock transition. Clock transition linewidths are probably independent of the species of the trapped ion used. Therefore an ion with as high a clock transition frequency as possible should be used in order to increase the line Q and reduce the measurement imprecision. For this reason a better ion for a laser cooled microwave clock is Hg^+. Unfortunately laser cooling is much harder to achieve with Hg^+ than with Be^+ (partly because the 194 nm cooling radiation is difficult to produce), and has not yet been demonstrated. A proposal for a frequency standard based on a 25.9 GHz magnetic field independent transition in $^{201}Hg^+$ has the potential of achieving absolute accuracies of better than one part in 10^{15} and frequency stabilities of less than 10^{-16}. [27]

OPTICAL FREQUENCY STANDARDS

In order to increase the Q even further, one could go to a much higher frequency; for example, use a narrow optical transition. The anticipated Q in this case can be extremely high, 10^{15} or more. A number of transitions in various ions have been proposed [2]; Dehmelt [30] was the first to suggest that such extremely high resolution spectroscopy could be carried out using one photon transitions in, for example, single group IIIA ions. For instance the $^1S_0 \leftrightarrow ^3P_0$ transition in Tl^+ ($\lambda = 202$ nm) has as $Q \approx 5 \times 10^{14}$. [30] For such optical one photon transitions, it is desirable to approximately satisfy the Dicke criterion; this is most easily accomplished with single trapped ions [2,30]. Others [31] have proposed using Doppler free two photon transitions, for example the $^2S_{1/2} \to ^2D_{5/2}$ transition in Hg^+ ($\lambda = 563$ nm, $Q \approx 7 \times 10^{14}$). Optical two photon transitions using equal frequency photons have the potential of completely eliminating the first order Doppler effect for a cloud of many ions where it is impossible to satisfy the Dicke criterion. They ultimately have the disadvantage that the rather large optical fields necessary to drive the transition cause undesirable ac Stark shifts [27,31].

The projected accuracy for optical frequency standards using single ions is extremely high. Second order Doppler shifts of 10^{-19} or lower are possible. [2] Other systematic shifts can occur [1,2,7,27,30,31] but it is possible that they can be controllable to this level. These extreme accuracies make important the problem of measurement imprecision since the signal-to-noise ratio on a single ion will at best be about one for each measurement cycle. Practically speaking, this means that a long averaging time will be required to reach a measurement precision equal to these accuracies. In fact, for a while, the accuracy and resolution may be limited by laser linewidth characteristics (linewidth and linewidth symmetry). However, the potential for extremely narrow lasers also exists [32].

Unfortunately, to use such laser devices as clocks one must count cycles of the radiation, that is, measure its phase. At microwave frequencies this is straightforward. At optical frequencies it is technically feasible but very hard [33]. In any case, the potential accuracy for stored ion spectroscopy in all spectral regions seems extremely high. Frequency standards and clocks with inaccuracy of one part in 10^{15} appear very reasonable, eventually they could be orders of magnitude better than this.

ACKNOWLEDGEMENTS

REFERENCES

1. H. G. Dehmelt, Advan. At. Mol. Phys. 3, 53 (1967) and 5, 109 (1969).
2. D. J. Wineland, W. M. Itano, and R. S. Van Dyck, Jr., Advan. At. Mol. Phys. 19, 135 (1983).
3. D. J. Wineland, W. M. Itano, J. C. Bergquist, J. J. Bollinger and J. D. Prestage, Proc. 9th Int. Conf. At. Phys.; Seattle, Washington, 1984, in press.
4. W. M. Itano and D. J. Wineland, Phys. Rev. A 24, 1364 (1981).
5. D. J. Wineland, Science, 226, 395 (1984).
6. R. M. Dicke, Phys. Rev. 89, 472 (1953).
7. W. M. Itano, L. L. Lewis, and D. J. Wineland, Phys. Rev. A 25, 1233 (1982).
8. D. J. Wineland, Proc. 13th Ann. Precise Time and Time Interval Appl. and Planning Meeting, Washington, DC 1981 (NASA Conf. Publ. 2220, Scientific and Tech. Info. Branch, 1982) p. 579.
9. E. Fischer, Z. Physik 156, 1 (1959); R. F. Wuerker, H. Shelton, and R. V. Langmuir, J. Appl. Phys. 30, 342 (1959).
10. F. M. Penning, Physica 3, 873 (1936).
11. F. G. Major and G. Werth, Phys. Rev. Lett. 30, 1155 (1973).
12. M. D. McGuire, R. Petsch, and G. Werth, Phys. Rev. A 17, 1999 (1978).
13. M. Jardino, M. Desaintfuscien, R. Barillet, J. Viennet, P. Petit, and C. Audoin, in Proc. 34th Ann. Symp. on Freq. Control, 1980 (Electronic Industries Assoc., 2001 Eye St., NW, Washington, DC 20006) p. 353 and Appl. Phys. 24, 107 (1981).
14. L. S. Cutler, R. P. Giffard, and M. D. McGuire, in Proc. 37th Ann. Symp. on Freq. Control, 1983 (Systematics General Corp., Wall Township, NJ 07719) p. 32.
15. M. Jardino, F. Plumelle, M. Desaintfuscien, and J. L. Duchene, in Proc. 38th Ann. Symp. on Freq. Control, 1984 (Inst. of Electrical and Electronics Eng., 445 Hoes Lane, Piscataway, NJ 08854) p. 431.
16. R. Blatt and G. Werth, Phys. Rev. A25, 1476 (1982).
17. W. Becker, and G. Werth, Z. Phys. A 311, 41 (1983).
18. R. Blatt, H. Schnatz, and G. Werth, Phys. Rev. Lett. 48, 1601 (1982) and Z. Phys. A 312, 143 (1983).
19. W. Ruster, J. Bonn, P. Peuser, and N. Trautmann, Appl. Phys. B30, 83 (1983).
20. T. W. Hänsch and A. L. Schawlow, Opt. Commun. 13, 68 (1975).
21. D. J. Wineland and H. G. Dehmelt, Bull. Am. Phys. Soc. 20, 637 (1975).
22. D. J. Wineland, R. E. Drullinger, and F. L. Walls, Phys. Rev. Lett. 40, 1639 (1978).
23. R. E. Drullinger, D. J. Wineland, and J. C. Bergquist, Appl. Phys. 22, 365 (1980).
24. D. J. Wineland, J. C. Bergquist, W. M. Itano, and R. E. Drullinger, Opt. Lett. 5, 245 (1980).
25. J. J. Bollinger and D. J. Wineland, Phys. Rev. Lett. 53, 348 (1984).

26. J. J. Bollinger, W. M. Itano, and D. J. Wineland, in Proc. 37th Ann. Symp. on Freq. Control, 1983 (Systematics General Corp., Wall Township, NJ 07719) p. 37.

27. D. J. Wineland, W. M. Itano, J. C. Bergquist, and F. L. Walls, in Proc. 35th Ann. Symp. on Freq. Control, 1981 (Electronic Industries Assoc., 2001 Eye St. NW, Washington DC 20006) p. 602.

28. J. J. Bollinger, J. D. Prestage, W. M. Itano, and D. J. Wineland, to be published.

29. C. F. Driscoll and J. H. Malmberg, Phys. Rev. Lett. 50, 167 (1983); D. L. Eggleston, T. M. O'Neil, and J. H. Malmberg, Phys. Rev. Lett. 53, 982 (1984).

30. H. Dehmelt, IEEE Trans. Instrum. Meas. IM-31, 83 (1982).

31. P. L. Bender, J. L. Hall, R. M. Garstang, F. M. J. Pichanick, W. W. Smith, R. L. Barger and J. B. West, Bull. Am. Phys. Soc. 21, 599 (1976).

32. J. L. Hall, L. Hollberg, Ma Long-Shen, T. Baer and H. G. Robinson, J. Phys. (Orsay, Fr.) 42, C8-59 (1981); A. Yariv and K. Vahala, IEEE J. Quant. Electronics, vol. QE-19, 889 (1983); R. W. P. Drever, J. L. Hall, F. V. Kowalski, J. Hough, G. M. Ford, A. J. Manley and H. Ward, Appl. Phys. B 31, 97 (1983); J. Hough, D. Hils, M. D. Rayman, Ma L. S., L. Hollberg, and J. L. Hall, Appl. Phys. B 33, 179 (1984).

33. See: Proc. Third Symp. Freq. Standards and Metrology, J. Physique 42, Colloque C-8, Dec., 1981; V. P. Chebotayev, V. G. Goldort, V. M. Klementyev, M. V. Nikitin, B. A. Timchenko, and V. F. Zakharyash, Appl. Phys. B 29, 63 (1982); D. A. Jennings, C. R. Pollock, F. R. Petersen, R. E. Drullinger, K. M. Evenson, J. S. Wells, J. L. Hall, H. P. Layer, Opt. Lett. 8, 136 (1983); K. M. Baird, Physics Today 36, no. 1, p. 52 (1983). B. Whitford, Conf. Precision Electromagnetic Measurements Digest, Amsterdam, 1984.
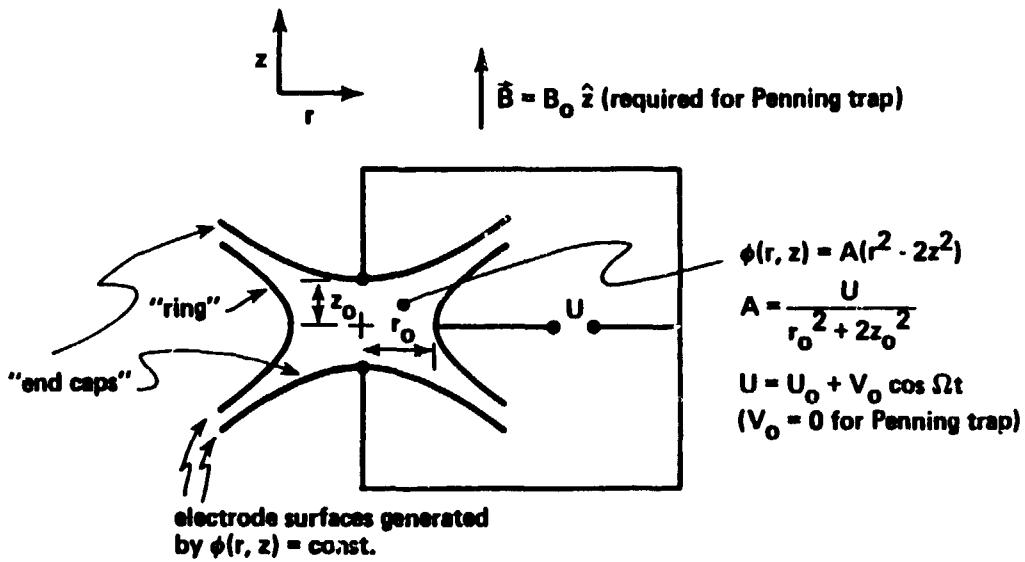
FIG. 1 Schematic representation of the electrode configuration for the "ideal" Paul (rf) or Penning trap. Electrode surfaces are figures of revolution about the z axis and are equipotentials of $\phi(r,z) = A(r^2 - 2z^2)$. (Cylindrical coordinates are used with the origin at the center of the trap.) Typical dimensions are $\sqrt{2}\, z_0 = r_0 \approx 1$ cm. Typical operating parameters are: for the Paul trap, $V_0 = 300$ V/cm, $\Omega/2\pi \approx 1$ MHz; for the Penning trap, $U_0 \approx 1$V, $B \approx 1$T.
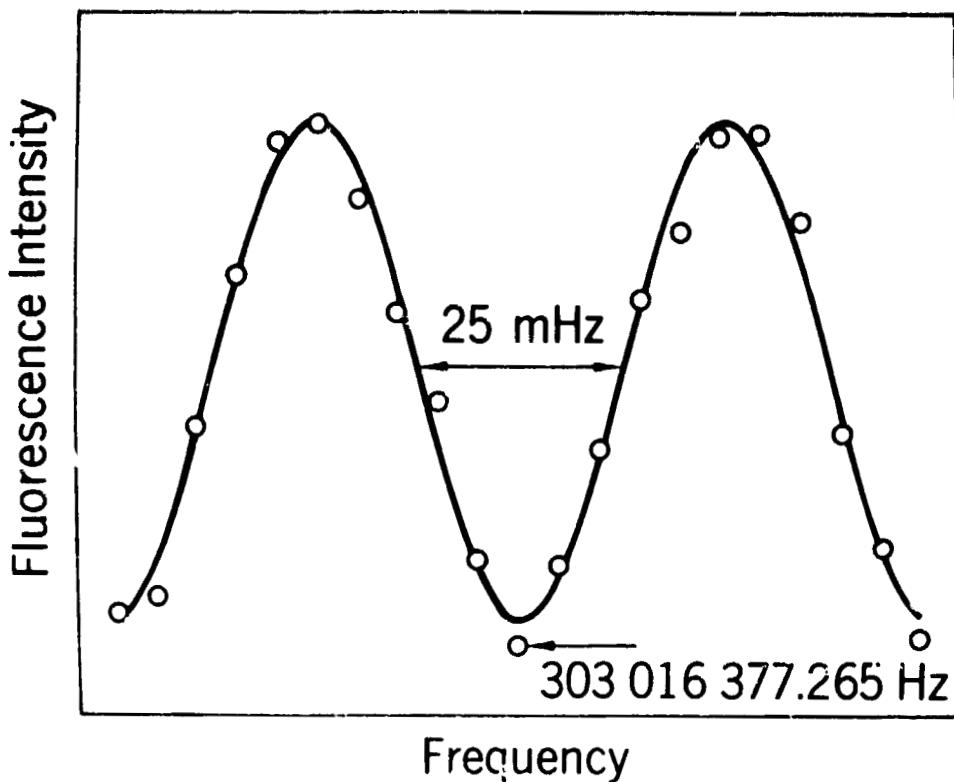
FIG. 2. Signal obtained with two 0.5s Ramsey pulses separated by a 19 s free precision inteival on the clock transition in $^9Be^+$ (see text). The sweep width was 100 mHz and the frequency interval between points was 5 mHz. The dots are experimental and are the average of 10 sweeps; the curve is a least squares fit.

QUESTIONS AND ANSWERS

MR. HELLWIG: What is the difference between mercury 199 and mercury 201? It has to do with the F numbers, right?

MR. BOLLINGER: Since we wanted to do an experiment in the Penning trap, because the laser cooling appears easier, we have to find a field independent transition at a large magnetic field, and one exists in mercury 201 at around 29.5 GHz. That's the reason the proposal is made for mercury 201 as opposed to mercury 199.

ON THE ACCURACY OF Cs BEAM PRIMARY FREQUENCY STANDARDS

J-S Boulanger, R.J. Douglas, J. Vanier,
A.G. Mungall, Y.S. Li, C. Jacques

Electrical and Time Standards Section
Physics Division
National Research Council
Ottawa, Ontario, Canada

ABSTRACT

Two effects which influence the accuracy of cesium beam primary frequency standards are examined: (A) second order Doppler shift, and (B) apparent frequency shift upon reversal of the static C-field (~ 60 mGauss) in which the hyperfine transitions occur.

(A) A new technique for evaluating the velocity distribution of the Cs beam is presented. Using this method, the second order Doppler shift ($\frac{\Delta f}{f} \simeq 4 \times 10^{-13}$ for our primary standards) can be evaluated to an uncertainty of $\frac{\Delta f}{f} \simeq 10^{-15}$, an improvement on our previous uncertainty of 2×10^{-14}.

(B) Progress in understanding the origins of the frequency shift of our primary standards as the static C-field is reversed in direction is reported. This effect has been eliminated in our evaluations of CsV, but not for the CsVI's.

Application of these methods in evaluating NRC clocks gives no frequency shift outside previously published error budgets.

INTRODUCTION

A major problem with primary cesium clocks is determining the velocity distribution of the Cs atoms, which is necessary to evaluate the second order Doppler shift. Previous approaches either simulated the Ramsey pattern with truncated velocity distributions (Mungall[1]); used the Ramsey pattern itself (Daams[2] and Jarvis[3]); or used pulse excitation (Hellwig[4]). The first two methods suffer from the approximations made either to the form of the velocity distribution or in its calculation from the Ramsey pattern. The third method requires major modification of the microwave excitation system. We haved found another method using the relation between the transition probability at the center of the Ramsey pattern and the (microwave) excitation level. We have shown that this function is a simple

cosine transform of the time of flight distribution. The new method is more accurate and is easier to use than the old methods.

Another problem which was thought to exist in cesium beam clocks is the so-called "Millman effect"[5]. It has been proven by Vanier et al[6] that the Millman effect does not exist for a $\Delta m_F = 0$ transition but only for a $\Delta m_F = \pm 1$ transition. The frequency shift resulting from reversal of the C-field reported earlier by Mungall[5] for CsV, was a consequence of the method used to measure and set the C-field in the normal and reversed field directions (using (4,-4) to (4,-3) transitions). It is not an offset in frequency due to the direction of the C-field. This was demonstrated in CsV, using field dependent transitions with $\Delta m_F = 0$ to measure and set the C-field. However, in the case of CsVI's there is an apparent shift in frequency upon field reversal using either of these two methods.

A - Determination of the velocity distribution

a) The excitation level method
In cesium frequency standards, the transition probability at the resonant frequency of an atom between states p and q is given by[7]:

$$P_{p,q} = 4\sin^2 b\tau \cos^2 b\tau, \tag{1}$$

where b is the excitation level and τ the time of flight through one of the two cavities. It can be shown that this relation is true within a part in 10^6 for typical primary cesium standards with currently attainable uniformity of the C-field, microwave excitation level and microwave phase*.

Using simple trigonometric manipulation this equation can be rewritten:

$$P_{p,q} = \frac{1}{2} - \frac{1}{2} \cos 4b\tau . \tag{2}$$

On the other hand, the measured signal amplitude is the integral over all possible times of flight

$$I(b) = \frac{1}{2} \int_0^\infty (1 - \cos 4b\tau) f(\tau) d\tau, \tag{3}$$

which can be rewritten as:

$$I(b) = \text{Constant} - \frac{1}{2} \int_0^\infty f(\tau) \cos 4b\tau \, d\tau . \tag{4}$$

---

* J-S Boulanger, to be published.

60

The second term is a cosine transform of the time of flight distribution. The reverse operation gives (for $\tau \neq 0$):

$$f(\tau) = \frac{-16}{\pi} \int_0^\infty I(b) \cos 4b\tau \, db \,. \qquad (5)$$

Since $v\tau = \ell$, the length of one cavity, it follows that the velocity distribution is:

$$f(v) = \tau^2 f(\tau) \times constant \qquad (6)$$

Consequently it is possible to calculate the time of flight distribution, and hence the velocity distribution, from measurments of the amplitude of the signal at the center of the resonance as function of the excitation level.

Once the velocity distribution is known it can be used in the general Ramsey equation[7] to retrieve the Ramsey pattern of Cs beam intensity vs microwave frequency. This pattern can also be measured and the agreement between the calculated and the measured patterns serves as a check for the accuracy of the velocity distribution. The second order Doppler shift can be evaluated from the velocity distribution in a straightforward manner.

(b) Experimental and computational technique
We used the clocks without modifications although for CsV, the 2-meter clock, we had to change the microwave source in order to obtain sufficient power. These clocks[8] are of the flop-in type with a single cavity providing two excitation regions. The excitation is normally provided by a Gunn oscillator and a calibrated variable attenuator. For the CsVI's, 10 mW of microwave power is available, and the attenuator covers a range of 70 dB. For the present experiment the Gunn oscillator was locked to a separate Cs reference and set at the center frequency of the Ramsey pattern.

The excitation level in the cavity is not known exactly. It can be calculated within a few percent from a knowledge of the cavity Q (loaded $Q \sim 4000$ for our clocks) and the power available. Greater accuracy can be obtained by fitting the calculated Ramsey pattern to the Ramsey pattern measured on the clock. This pattern can be characterized by its shape (the relative amplitude of secondary peaks and valleys to the central peak, the number of peaks, etc.) and by its scale in Hertz (the distance between peaks, or the width at half the height of the central peak, etc).

From the Ramsey equation, it can be seen that, apart from the dependence on b, the shape of the Ramsey pattern is dependent only on the shape of the velocity distribution, if the second order Doppler shifts and the cavity phase differences are neglected (valid for a first approximation). The frequency scale of the Ramsey pattern (or its width) is determined only by the velocity scale (or the average velocity of the distribution), and the clock length.

We adjust a scale factor and recompute the Fourier transform of the excitation level data until the theoretical and experimental widths of the Ramsey patterns are equal. The adjustment is a few percent of the power. This fitting is required once for each clock. The Gunn oscillators are sufficiently stable in power for the same scale factor to be adequate two months after the first measurement, including a reversal of the beam direction.

In order to resolve the Rabi resonances and minimize the effect of the overlapping of the field dependent transitions on the $(3,0) \leftrightarrow (4,0)$ transition at high power levels, the C-field was raised temporarily. As is seen in Figure 1, at 20 dB above the optimum power level for the Ramsey resonance, this effect is quite serious at a C-field of 67 mGauss which is the normal operating field. A magnetic field of 260 mGauss is enough to reduce this problem to acceptable levels as seen in the same figure.

(c) Processing of data
A Fast Fourier Transform (FFT) program was used. It requires data equally spaced in excitation level. Because of the difficulty in satisfying this condition with our attenuator, we used a spline interpolation to extract about 200 points from the 75 experimental points (see Figure 2). We hope in the near future to be able to take more points, improving the accuracy of the data fed to the FFT.

We have also added a "tail" of constant value equal to that of the highest power data point beyond the last measured point to fill the 1024 points needed by the program. This approach is justified by the fact that at high excitation level the detector response tends towards a constant. If the excitation is sufficiently great, even the high velocity atoms make many transitions in passing through the cavities. If we average a large number of atoms at different velocities, the average transition probability is then exactly one half. The effects of adding this "tail" are discussed below.

(d) Effects of experimental difficulties
In order to evaluate the influence of potential sources of error in this method, we have exaggerated four separate error sources and examined the consequences of each. In each case, following the method detailed above, a velocity distribution was obtained, and the scale factor was checked using the widths of the experimental and calculated central Ramsey peaks.

Each time, the quality of the agreement in terms of the shape of the two Ramsey curves could be observed, and changes in the calculated velocity distribution could be noted. For the curves presented in Figures 3 to 6, the agreement between the two Ramsey curves is approximately 1% of the central Ramsey peak. The four sources of errors we have investigated in this manner are:

1) Effect of $m_F \neq 0$ transitions
If the magnetic field is too low, an extraneous signal from neighbouring transitions is added to the true signal for high excitation levels. Comparing Figure 3 with Figure 7-a shows the difference between two sets of data at low (67 mGauss) and high (260 mGauss) magnetic fields. At a low field the effect causes an error at the high velocity end of the spectrum, creating small false velocity peaks. These arise since the signal from the

neighbouring transitions makes I(b) increase as the excitation level is raised. This increase adds peaks in the short time of flight (or high velocity) region.

2) Inadequate microwave excitation level

If the experiment is limited to low values of excitation power, the integral appears to be truncated. The resolution in the time-of-flight distribution is limited, and the velocity distribution is distorted with the addition of an "oscillation" along the velocity axis. The distortion looks much the same as for the first source of error at high velocity and adds some noise at low velocity as can been seen by comparing Figure 4 with Figure 7-a. The peaks at high velocity are due to the offset generated by the "tail" added at the wrong level.

3) Noise in the measured signal

Since the Cs beam noise is much the same at any excitation level, its effect after FFT should be visible in the regions of long times of flight or at low velocities. This effect is simulated in Figure 5 which represents the data of Figure 4 to which a noise equivalent to 5% of the signal maximum has been added before the interpolation. A Ramsey pattern calculated from such a noisy set of data would still give an estimate of the second order Doppler shift within 10 µHz of the noise-free set of data. In practice the noise is below 0.2%.

4) Density of points

As expected, an increase in the density of points gives better results. As can be seen in Figure 6, when compared to Figure 7-c, an increase from 45 to 75 points reduces the noise at low velocities by at least a factor of 4. We expect that doubling the number of points should reduce it even further.

e) Results for each clock: second order Doppler shift

Figures 7-a, 7-b and 7-c show the results obtained on CsVI-A, CsVI-B and CsVI-C respectively. Figures 8-a, 8-b, and 8-c show the Ramsey patterns calculated for each clock from the velocity distribution found by the FFT. For comparison with Figure 8-a, the experimental Ramsey pattern of CsVI-A is also shown in Figure 8. We have suppressed the noise at low velocity, since the geometry of the clock would eliminate all atoms with velocities below a certain value.

It is remarkable how well these curves fit the experimental Ramsey patterns up to a thousand hertz away from the center of resonance (see Figure 8-a). The agreement is better than 1% everywhere. If the deliberately distorted velocity distribution of Figure 3 or Figure 4 is used the agreement is reduced to a region of about 500 Hz around the center of resonance.

Despite this reduction in quality of fit, the second order Doppler shifts, as calculated from these theoretical Ramsey patterns for any one clock, all agree within 10 µHz for a particular clock or one part in 10^{15} of the frequency of the clock. The previous method used for the CsVI's, which assumed a truncated Maxwellian distribution, is in agreement with the present method to within its stated (1 σ) error of 2×10^{-14} of the clock frequency.

Unfortunately, the results to date are not as good on CsV. At the time of measurement, the calibrated attenuator used in CsV had a much narrower range (20 dB) than the ones on the CsVI's (70 dB). The use of an uncalibrated attenuator in series with it made the measurements more difficult and the reproducibility was adversely affected. To obtain sufficient microwave power, the Gunn oscillator was temporarily replaced by a 100 mW klystron (also phase locked). The results are shown in Figure 9.

In Figure 9-b the hump at around 150 m/s is false; and, possibly, also the long tail at high velocities (> 500 m/s). A Ramsey pattern calculated from it would be significantly in error. If we used the other sets of data, at low magnetic field or low maximum power, the hump would be displaced and the main peak would also be slightly affected.

Despite that, the Ramsey pattern calculated in Figure 10-b is good to better than 1% up to 500 Hz from the center of resonance. The evaluation of the second order Doppler shift may not be quite as accurate as for the CsVI's. The maximum variation (50 μHz) is 6 parts in 10^{15} of the frequency of the clock using the different sets of data and will likely be improved by using a better attenuator.

It seems that for each NRC clock (CsV and the CsVI's) the second order Doppler shift has been overestimated in the past by the same amount. This error is still within the error limits of the old method that used truncated velocity distributions[1]. Adoption of the new method will reduce the NRC primary clock frequency by 1.7×10^{-14}.

B - The Millman effect revisited

Another source of error in our clocks is the evaluation of the magnetic field needed to operate the clock at zero offset in frequency. It was reported some years ago by A.G. Mungall[5] (1976) that there was a difference in frequency between the two orientations of the magnetic orienting field (C-field) in CsV. An explanation based on the Millman effect was then thought to be the solution, but now proves to be incorrect. A change of method in setting the C-field has eliminated the frequency shift on C-field reversal for CsV.

In the old method, the magnetic field was evaluated with low frequency coils inducing (4,-4) to (4,-3) transitions at 8 points along the beam trajectory. In the new method, the field dependent microwave transitions ($m_F = 1$ or $m_F = -1$; $\Delta m_F = 0$) are used to evaluate the average field between the exciting cavities. Both methods have been used in the evaluation of the C-field of the four primary Cs clocks in operation at NRC.

For CsV there was typically a fractional frequency shift of 1×10^{-13} when the low frequency method was used to set the C-field in the reversed, compared to the normal direction. If the microwave method was used to set the field, no significant shift was observed. The average of the two methods agreed, and since the averaged C-field has always been used for setting CsV, the effect and the change of method for C-field evaluation has had no influence on the CsV time scale. The explanation of the C-field

reversal effect using the old method, in terms of the Millman effect on the clock frequency[5], is wrong. Theoretically, the Millman effect can exist only for $\Delta m_F = \pm 1$ transitions (eg. the old method's low frequency transitions) and not for $\Delta m_F = 0$ transitions (such as the clock transition and the transitions used for the new method)[6]. The results for CsV can be explained completely as a Millman effect acting only on the low frequency transition used for the old method of setting the C-field.

For the CsVI clocks, it was found that the clock frequencies showed frequency shifts with either method for setting the C-field. Furthermore, the frequency determined, using the average of normal and reversed C-field direction, differs for the two methods by up to 1×10^{-13}. The average of normal and reversed C-field determined by the microwave method has always been used for the CsVI clocks, and after evaluation they have agreed with the CsV frequency within a few parts in 10^{14}.

In the case of the CsVI clocks, it seems that the uniformity of the C-field is the source of the problem. In CsV, the magnetic shields are larger than on the CsVI clocks, and any residual magnetic domains affect the uniformity of the field to a lesser extent. Simulating the microwave method, our calculations have shown that if the excitation level is not identical in the two excitation regions, the C-field inhomogeneities (in the excitation regions or in the drift space) can cause Ramsey pattern distortions which make the average frequency differ from the true frequency. Empirically this effect is likely to be small in our clocks since the rates of all four of them are within a few parts in 10^{14} of each other immediately following evaluation.

CONCLUSION

We have presented a new and much more exact method for evaluation of the velocity distribution and the second order Doppler shift in cesium beam frequency standards. This method can evaluate the shift to an accuracy better than a few parts in 10^{15} of the frequency of the clock. It seems feasible to improve the accuracy even further with better measurements. The evaluation of the C-field however is still limited to a few parts in 10^{14} because of the uncertainties linked to the method used, and this uncertainty remains one of the major limitations of NRC's primary clocks.

REFERENCES

1 A.G. Mungall, "The Second Order Doppler Shift in Cesium Beam Atomic Frequency Standards", Metrologia, vol. 7, 49-56, April 1971.

2 H. Daams, "Corrections for Second-Order Doppler Shift and Cavity Phase Error in Cesium Atomic Beam Frequency Standards", IEEE Trans. Instrum. Meas., vol. IM-23, No. 4, December 1974.

3 S. Jarvis, "Determination of Velocity Distributions in Molecular Beam Frequency Standards From Measured Resonance Curves", Metrologia 10, 87-98, 1974.

4 H. Hellwig, S. Jarvis, Jr., D. Halford and H.E. Bell, "Evaluation and Operation of Atomic Beam Tube Frequency Standards Using Time Domain Velocity Selection Modulation", Metrologia 9, 107-112, (1973.)

5 A.G. Mungall, "The Millman Effect in Cesium Beam Atomic Frequency Standards", Metrologia 12, 151-158, (1976).

6 J. Vanier, A.G. Mungall and J-S Boulanger, "The Millman Effect in Cesium Beam Atomic Frequency Standards: Further Considerations", Metrologia 20, 1984.

7 N. Ramsey, "Molecular Beams", Clarendon Press, Oxford, p. 86 (1956).

8 A.G. Mungall, H. Daams and J-S Boulanger, "Design, Construction and Performance of the NRC CsVI Primary Clocks", Metrologia 17, 123-145, (1981).

0.3 MHz

1.0 MHz
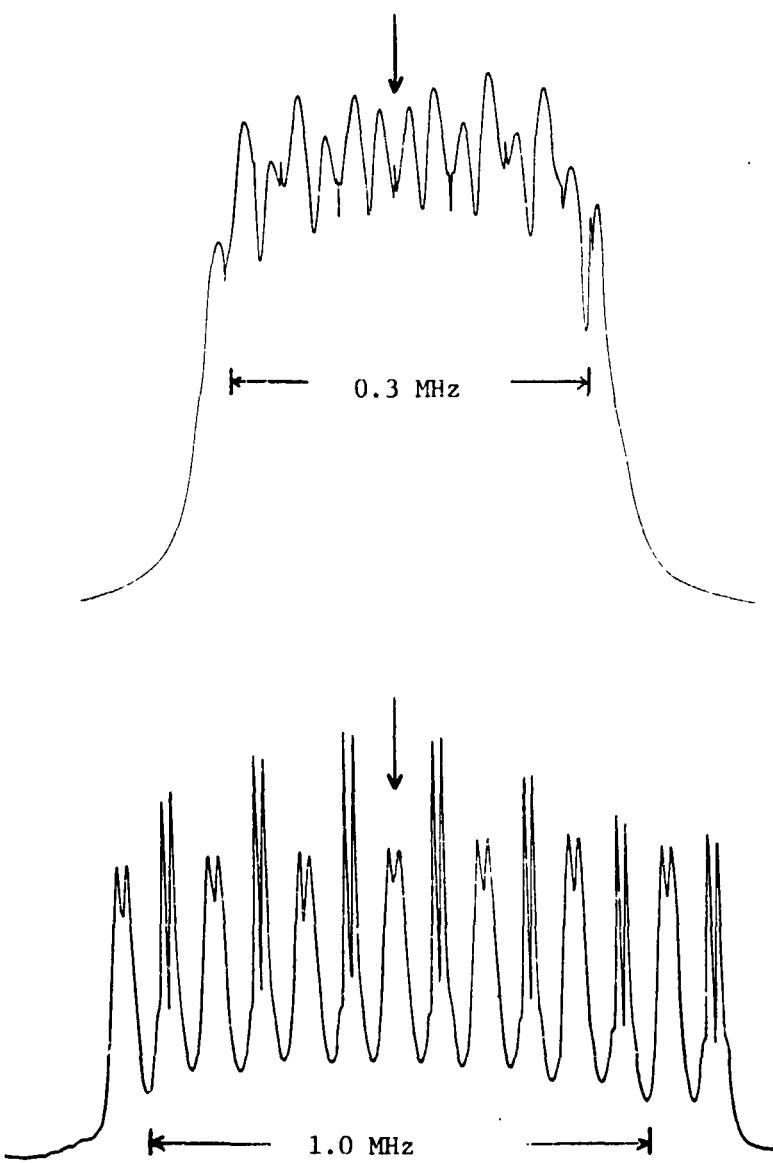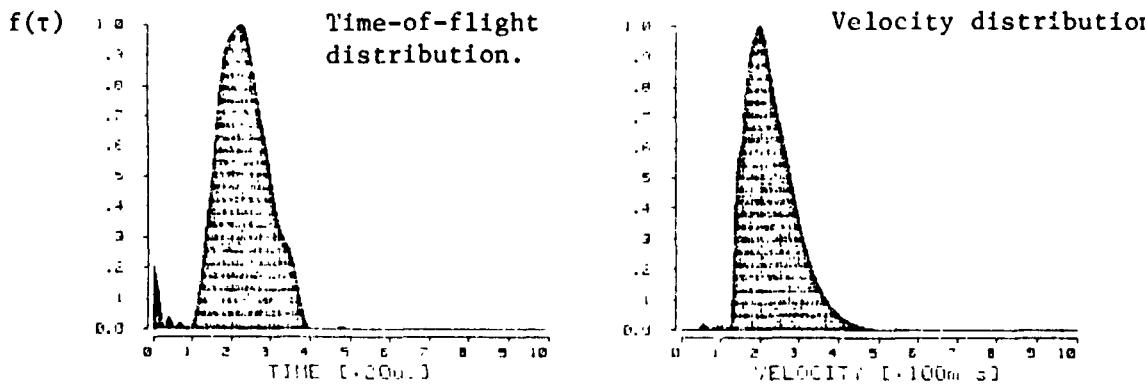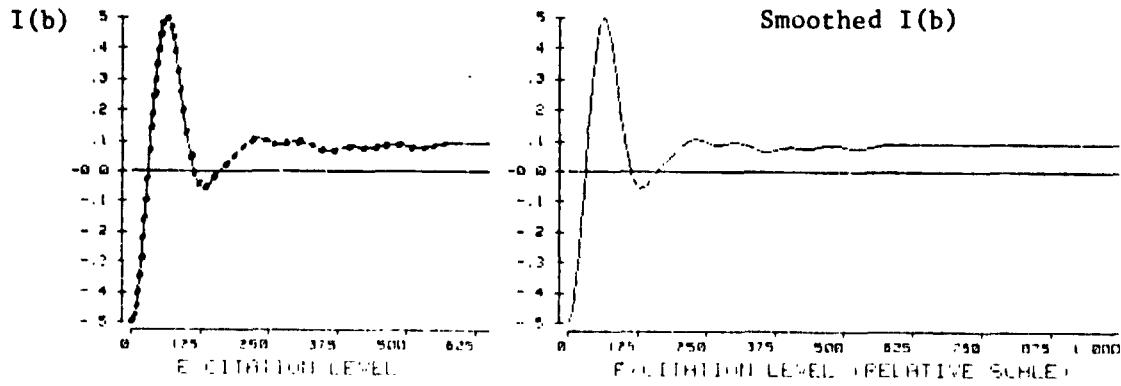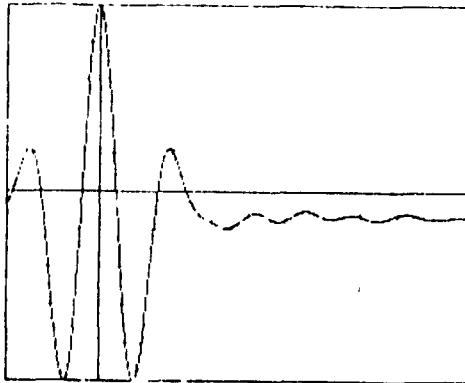
Figure 1. High Power hyperfine resonances as observed in NRC primary cesium clocks. The power level is 20 dB above that for normal clock operation. The seven σ and seven π Rabi pedestals are not resolved at the normal C-field of 67 mGauss (upper curve). At a higher C-field of 260 mGauss the Rabi pedestals are resolved (lower curve), and the $(3,0 \leftrightarrow (4,0)$ Ramsey resonance (vertical arrow) is not greatly contaminated by the neighbouring Rabi pedestals.

67

I(b)

Smoothed I(b)

EXCITATION LEVEL

EXCITATION LEVEL (RELATIVE SCALE)

f(τ)

Time-of-flight
distribution.

Velocity distribution

TIME [·200u.]

VELOCITY [·100m·s]

Ramsey pattern vs frequency
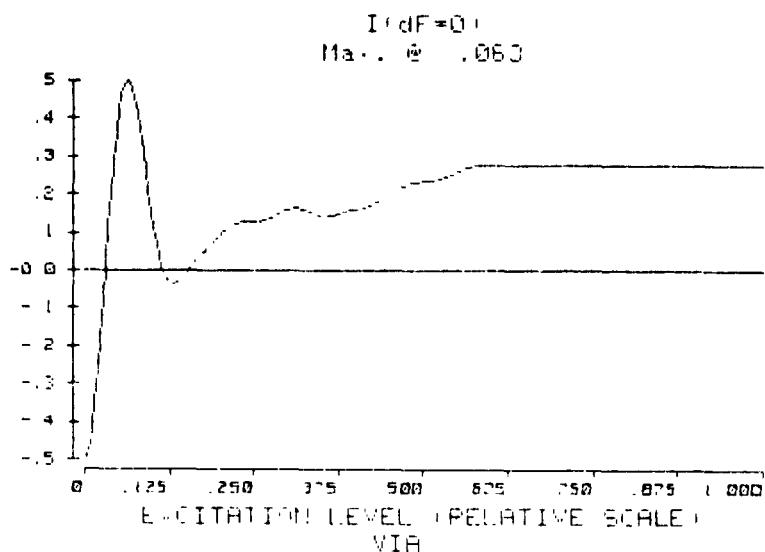
Figure 2. Processing data for CsVI-A.
The Cs beam intensity vs (microwave power)$^{\frac{1}{2}}$ at the centre of the $(3,0) \leftrightarrow (4,0)$ Ramsey resonance is the measured I(b) (upper left). Interpolation is used to create a set of equally spaced points, to which a "tail" is added (upper right). This curve is Fourier transformed to obtain the time-of-flight distribution (middle left) through one $\sim$ 1 cm microwave interaction region. The time scale factor is only approximate at this stage. Using $f(\tau)$, the $\sim$ 1 cm distance and Eq. 6, a velocity distribution is obtained (middle right). The velocity scale factor is only approximate at this stage. The scale factor is accurately determined by fitting the width of the calculated Ramsey pattern (bottom) to experiment: this width depends on the mean time of flight between the two interaction regions (2.090 m for CsV, 1.006 m for the CsVI's).

I(dF=0)
Ma... @ .063

EXCITATION LEVEL (RELATIVE SCALE)
VIA

VELOCITY DISTRIBUTION

VELOCITY [.100m/s]
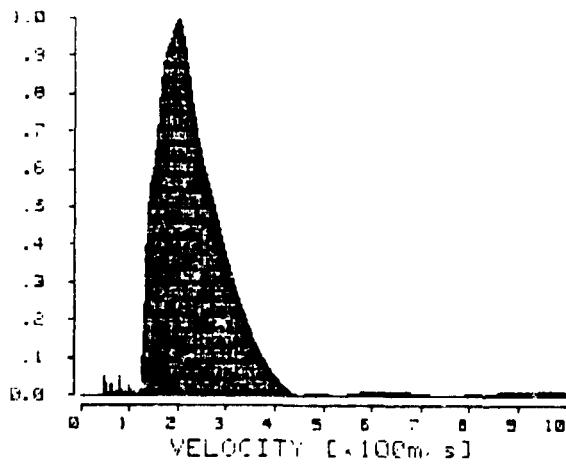
Figure 3. I(b) (after interpolation) and the velocity distribution determined for CsVI-A at low C-field (67 mGauss). Compared with Figure 7-a, neighbouring transitions have changed I(b), yet the mean velocity (over the range 118 m/s to 457 m/s) is 230 m/s, and the second order Doppler shift for the clock is -23.2×10^{-14} of the clock frequency, vs -23.1×10^{-14} for Figure 7-a.

I(dF=0)
Max. @ .063

EXCITATION LEVEL (RELATIVE SCALE)
VIA

VELOCITY DISTRIBUTION

VELOCITY [·100m/s]
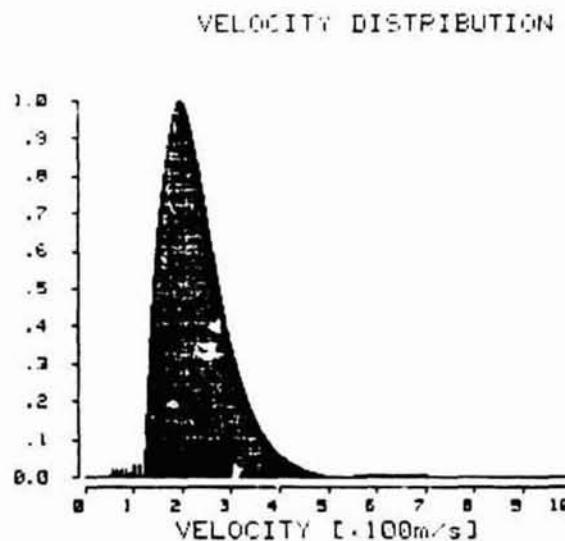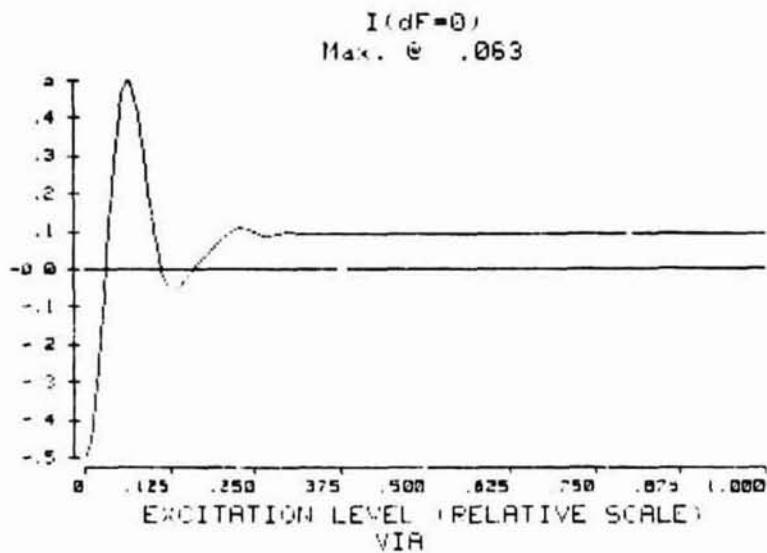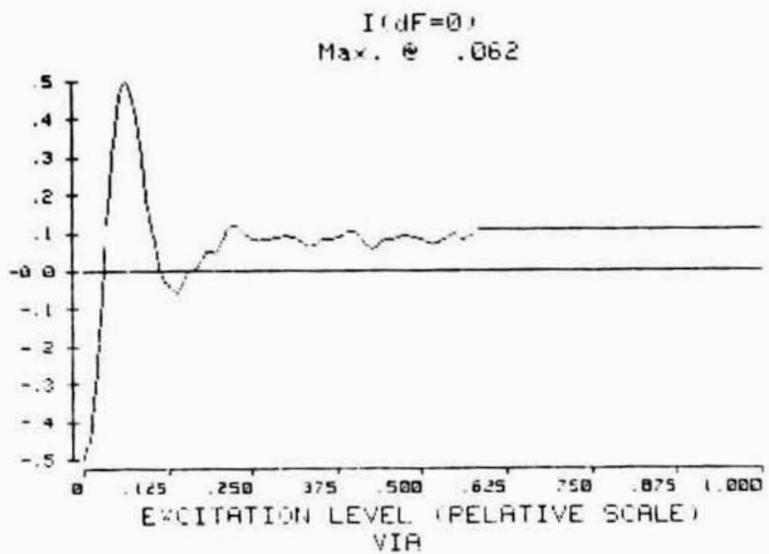
Figure 4. I(b) (after interpolation) and the velocity distribution determined at low maximum microwave power (3 mW) for CsVI-A. Compared with Figure 7-a, in the velocity distribution (10 mW maximum power) there are changes in the velocity distribution (lower resolution and "oscillations"), yet the mean velocity (over the range 121 m/s to 522 m/s) is 230 m/s, and the second order Doppler shift for the clock is -23.1×10^{-14} of the clock frequency, vs -23.1×10^{-14} for Figure 7-a.

I(dF=0)
Max. @ .062

EXCITATION LEVEL (RELATIVE SCALE)
VIA

VELOCITY DISTRIBUTION

VELOCITY [×100m/s]
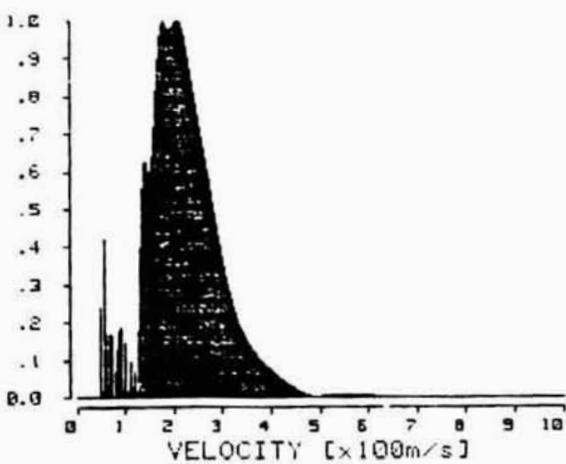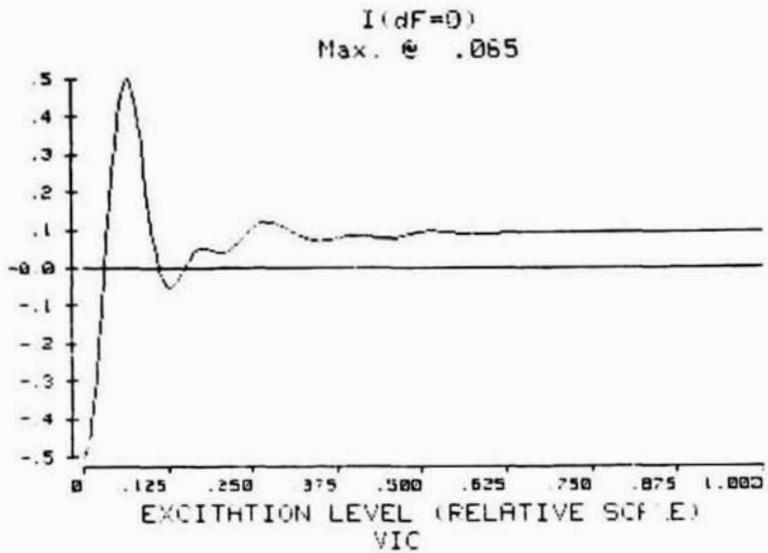
Figure 5. I(b) (after interpolation) and the velocity distribution determined for CsVI-A with excess noise added (rms noise is 5% of the maximum). This should be compared to Figure 7-A. The mean velocity (over the range 122 m/s to 984 m/s) is 232 m/s, and the second Doppler shift for the clock is -23.1×10^{-14} of the clock frequency, vs -23.1×10^{-14} for Figure 7-a.

I(dF=0)
Max. @ .065

EXCITHTION LEVEL (RELATIVE SCALE)
VIC

VELOCITY DISTRIBUTION
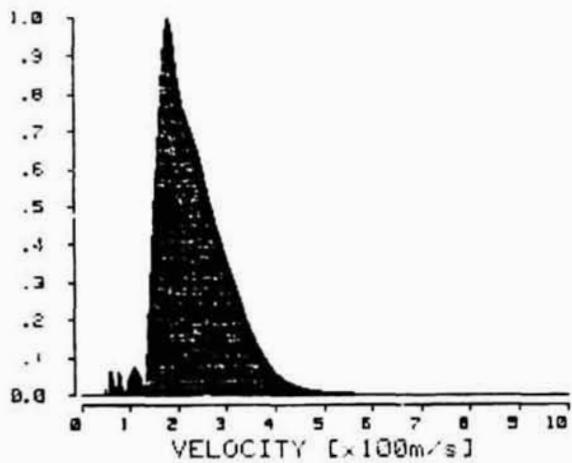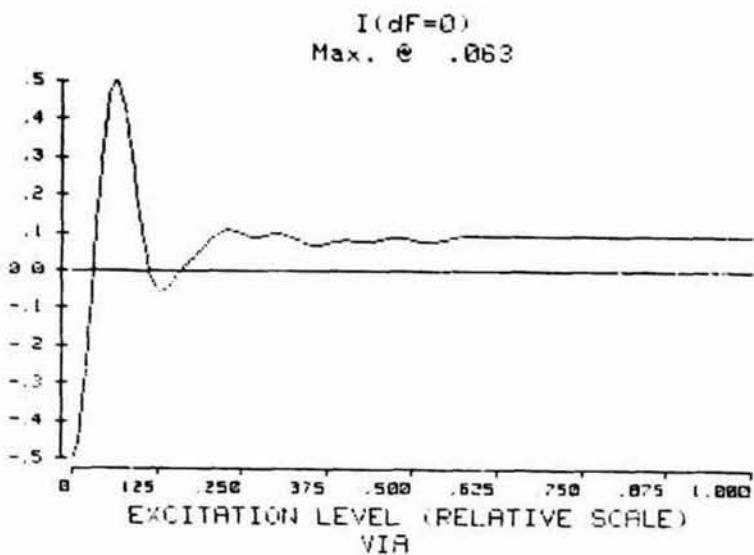
VELOCITY [×100m/s]

Figure 6. I(b) (after interpolation) and the velocity distribution determined using 45 points of data for CsVI-C. This should be compared to Figure 7-c for which 75 data points were used. The mean velocity (over the range 131 m/s to 700 m/s) is 238 m/s, and the second order Doppler shift for the clock is -24.1×10^{-14} of the clock frequency vs -24.1×10^{-14} for Figure 7-c.

72

I(dF=0)
Max. @ .063

EXCITATION LEVEL (RELATIVE SCALE)
VIA

VELOCITY DISTRIBUTION

VELOCITY [x100m/s]
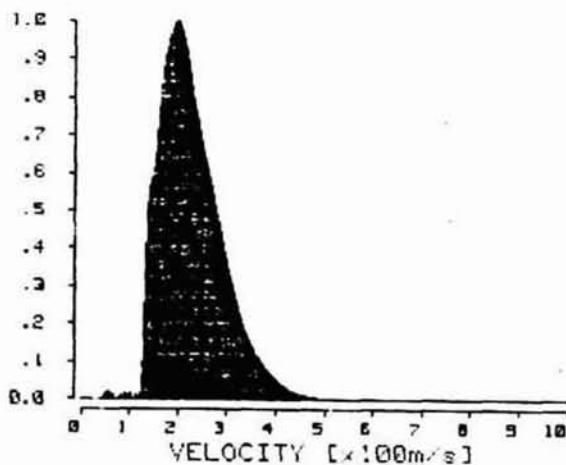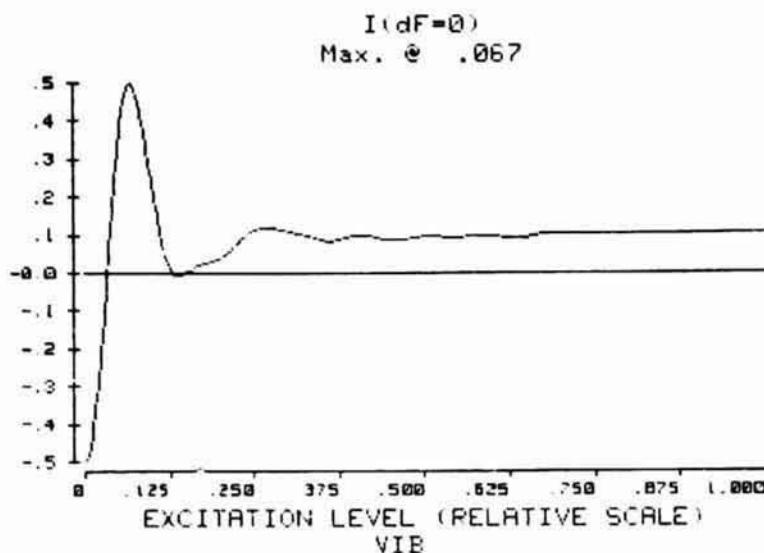
Figure 7-a. I(b) (after interpolation) and the velocity distribution for CsVI-A. The mean velocity (over the range 113 m/s to 522 m/s) is 230 m/s, and the second order Doppler shift for the clock is -23.1×10^{-14} of the clock frequency.

73

I(dF=0)
Max. @ .067

EXCITATION LEVEL (RELATIVE SCALE)
VIB

VELOCITY DISTRIBUTION

VELOCITY [x100m/s]
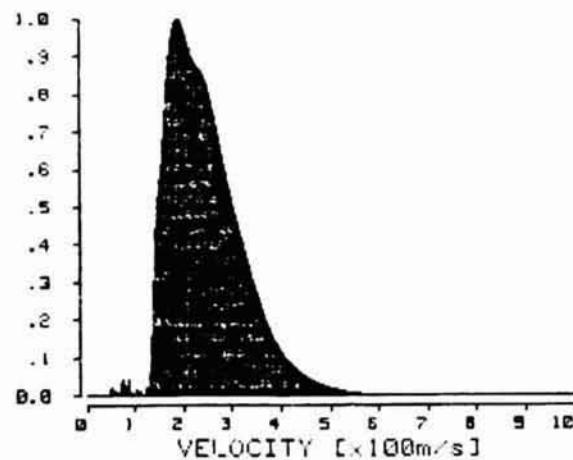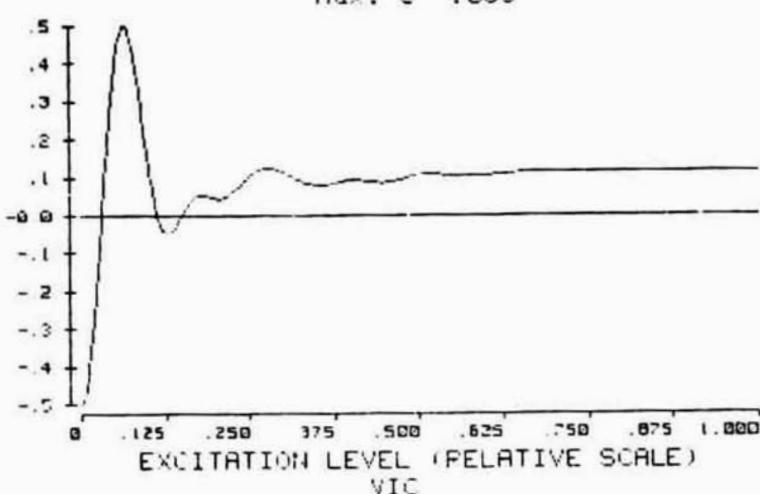
Figure 7-b. I(b) (after interpolation) and the velocity distribution for CsVI-B. The mean velocity (over the range 121 m/s to 610 m/s) is 248 m/s, and the second order Doppler shift for the clock is -25.7×10^{-14} of the clock frequency.

74

I (dF=0)
Max. @ .065

EXCITATION LEVEL (RELATIVE SCALE)
VIC

VELOCITY DISTRIBUTION

VELOCITY [×100m/s]
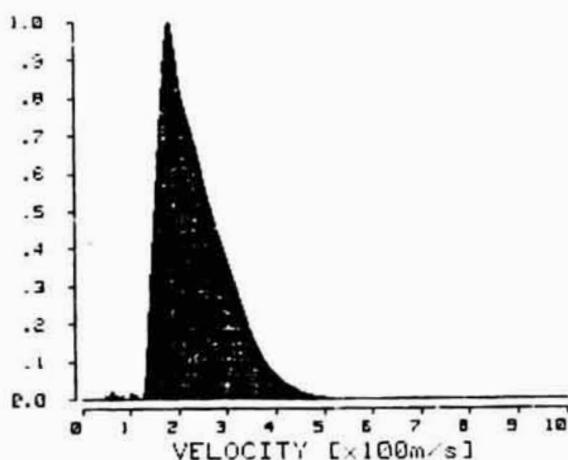
Figure 7-c. I(b) (after interpolation) and the velocity distribution for CsVI-C. The mean velocity over the range 123 m/s to 552 m/s is 236 m/s, and the second order Doppler shift of the clock is -24.1×10^{-14} of the clock frequency.

100 Hz/division →
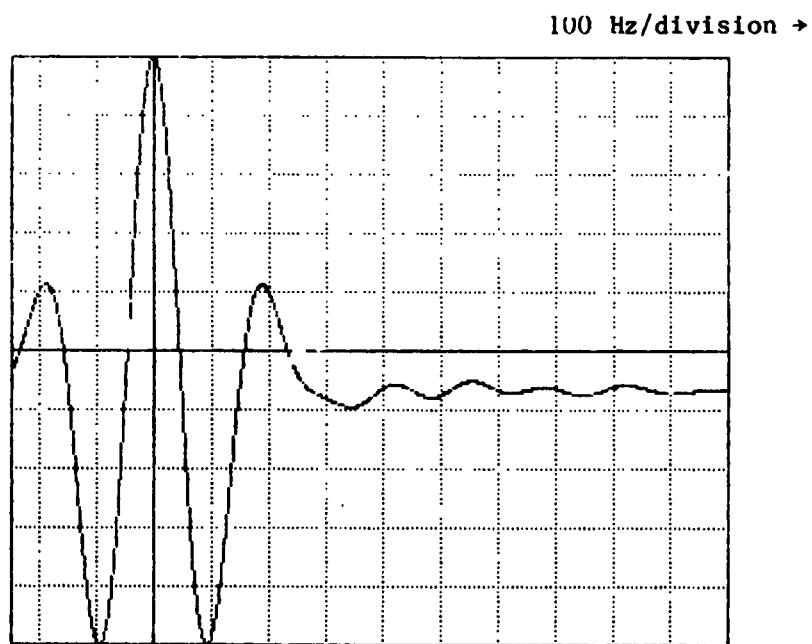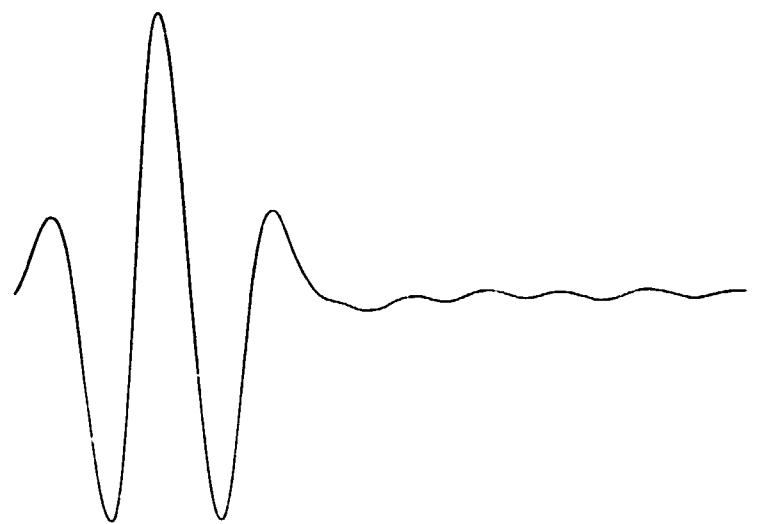
Figure 8-a. Upper: Experimental Ramsey pattern for CsVI-A.

Lower: Calculated Ramsey pattern for CsVI-A.

100 Hz/division →
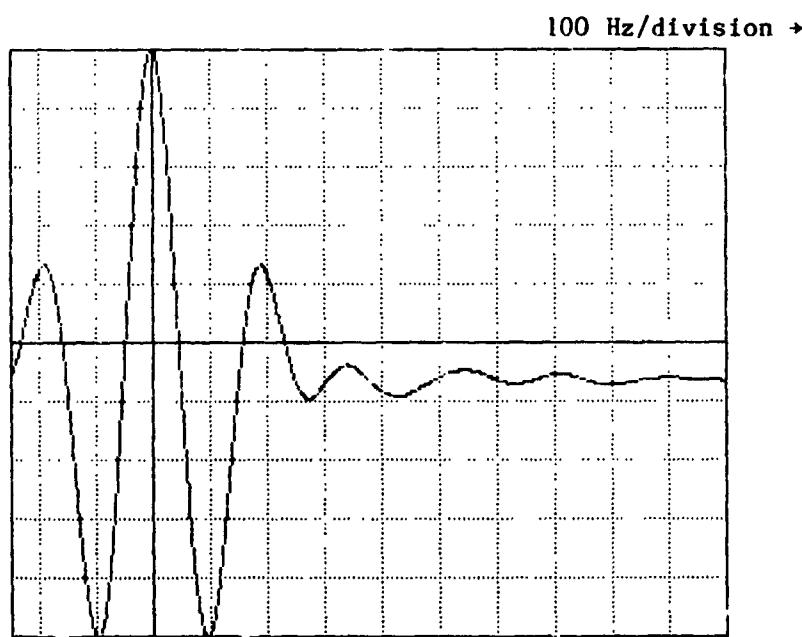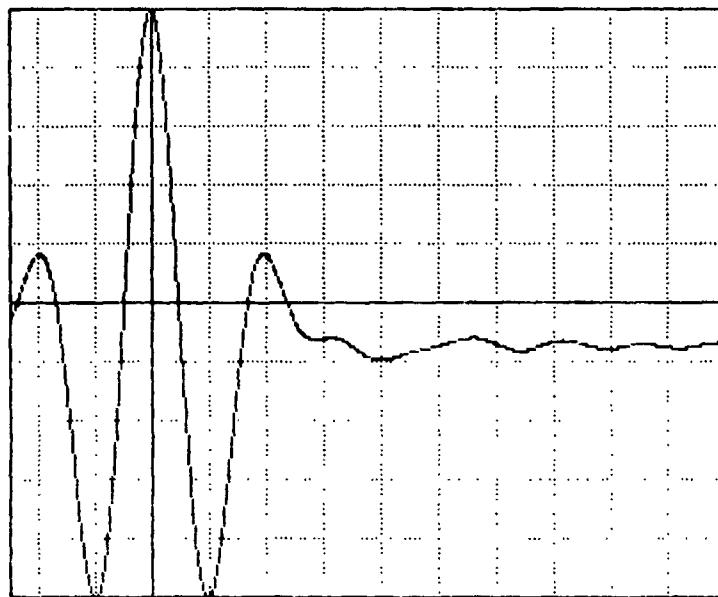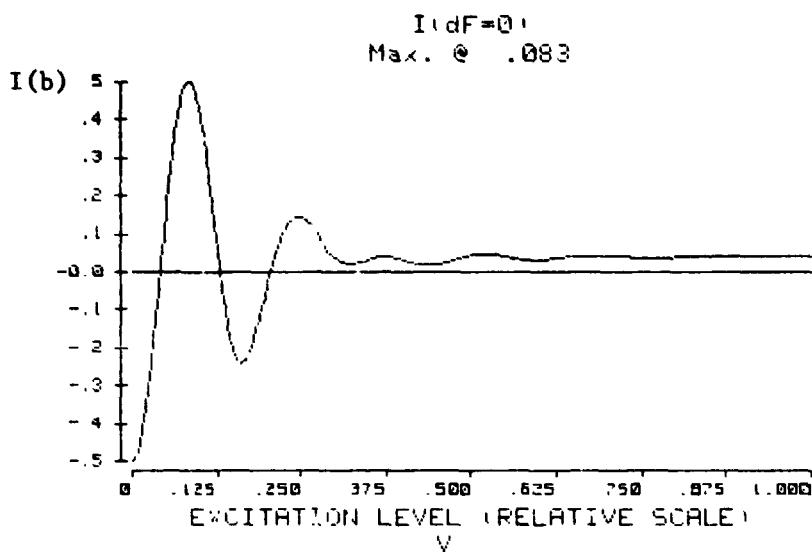
Figure 8-b. Calculated Ramsey pattern for CsVI-B. It differs by less than 1% from the experimental pattern.

Figure 8-c. Calculated Ramsey pattern for CsVI-C. It differs by less than 1% from the experimental pattern.

I(dF=0)
Max. @ .083

VELOCITY DISTRIBUTION
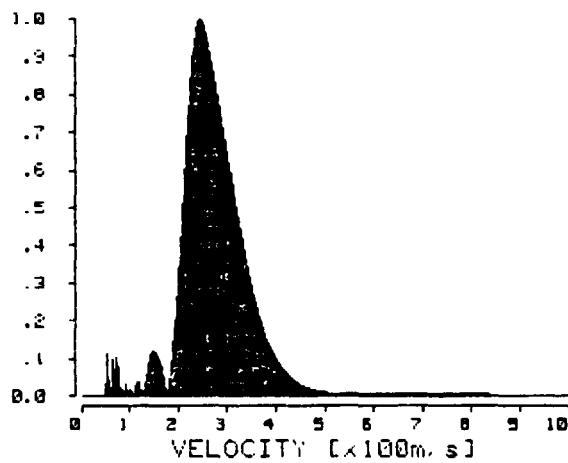
Figure 9-a. Upper: I(b) (after interpolation) for CsV.
The maximum power level 's 28 mW. Three sections of I(b) have been matched
to extend the 20dB ra. of the calibrated attenuator in CsV.

Figure 9-b. Lower: The velocity distribution determined for CsV. The
mean velocity (over the range 178 m/s to 700 m/s) is 283 m/s, and the second
order Doppler shift for the clock is -39.5×10^{-14} for the clock frequency.
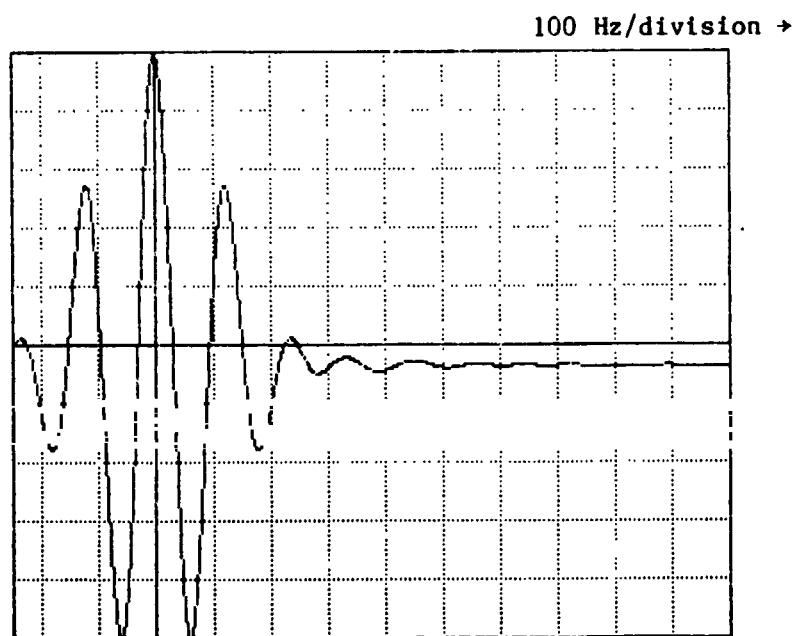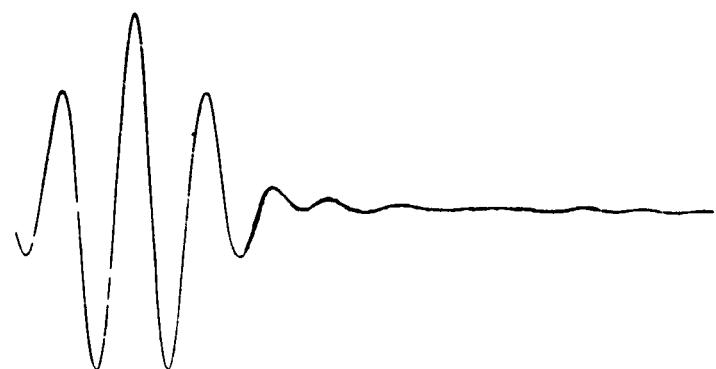
Figure 10-a. Experimental Ramsey pattern for CsV.

Figure 10-b. Calculated Ramsey pattern for CsV. It differs by less than 1% from the experimental pattern above.

QUESTIONS AND ANSWERS

DAVID ALLAN, NATIONAL BUREAU OF STANDARDS: The accuracy numbers you quote, are they one sigma, or two sigma, or three sigma numbers?

MR. JACQUES: They are one sigma.

MR. HELLWIG: What is the N. R. C.'s official claim for the realization of the second?

MR. JACQUES: We think that we can safely claim a part in ten to the thirteenth, because, despite all of the problems that we have in the magnetic shields, the frequencies are within one to two parts in ten to the fourteenth, one from the other. But on the other hand, we are not sure how long we can go. Because of those problems in the magnetic shields, we can't evaluate them as well as we would like. We have only Cesium V for which the magnetic shields are very stable. This leaves us with only one clock, which we can't compare to itself.

MR. HELLWIG: You cannot compare using GPS?

MR. JACQUES: We just got the GPS receiver, but the problem is that we need to do these comparisons within twenty-four hours, or possibly forty-eight hours to be sure that they are accurate, especially for the reversal of the beam, which we have to do as fast as possible.

METHODS TO RECOVER THE NARROW DICKE SUB-DOPPLER FEATURE
IN EVACUATED WALL-COATED CELLS WITHOUT RESTRICTIONS ON CELL SIZE

H. G. Robinson
Duke University
Durham, North Carolina 27706

ABSTRACT

The hyperfine resonance observed in evacuated wall-coated cells
with dimensions < $\lambda/2$ (λ is the hyperfine resonance wavelength)
consists of a narrow Dicke sub-Doppler linewidth feature, the
'spike', superimposed on a broad pedestal. The hydrogen maser
provides a classic example of this lineshape. As cell size is
increased, an effect unique to evacuated wall-coated cells
occurs. Certain combinations of microwave field distribution and
cell size result in a lineshape having a pedestal with a small
spike feature or only the broad pedestal with no spike. Such
conditions are not appropriate for atomic frequency standard
applications. This paper reviews the cause of the evacuated
wall-coated cell lineshape and discusses methods to recover the
narrow spike feature without restrictions on cell size. One
example will be a cell with dimensions having equal volumes of
exposure to opposite phases of the microwave magnetic field. The
typical signal recovery technique would have no spike in this
case. Potential application is especially appropriate for Rb or
Cs evacuated wall-coated cells.

INTRODUCTION

The hydrogen maser provides a practical example of the use of the evacuated
wall-coated cell in an atomic clock application. The high Q, narrow line
width, homogeneous lineshape afforded by this technique provides one of
technology's best clocks. In this use, the cell is designed to have
dimensions < $\lambda(H)/2$ where λ is the cavity wavelength of the hyperfine
transition (free-space $\lambda \sim 21$ cm). The recent demonstration [1-3] of
narrow, 87Rb hyperfine transitions in an evacuated wall-coated sealed cell
(EWSC) raises the possibility of taking advantage of the homogeneous
lineshape for a superior 87Rb atomic frequency standard. Here the free-
space wavelength, $\lambda \sim 4.4$ cm, is considerably smaller than that for
hydrogen. Thus relatively small Rb cells compared to those used for
hydrogen still may have dimensions > $\lambda(Rb)/2$. In addition, both hyperfine
resonance linewidth and wall shift are inversely proportional to the cell
size: signal is proportional to cell size. Such considerations alone would
lead to use of larger cells for improvement in these important parameters.

The understanding of the effects of cell size on lineshape then becomes an
important design consideration. In this paper, we review the basic cause of
the EWSC lineshape with a simple one-dimensional model and discuss
techniques to take advantage of the large relaxation times available in such
cells even if cell dimensions are > $\lambda/2$.

DISCUSSION
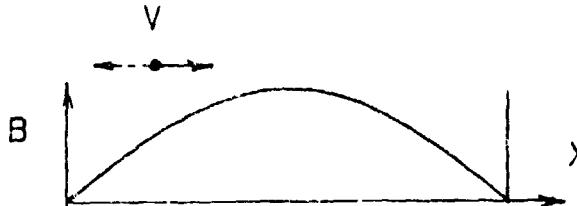
A number of theoretical treatments have been made which address the

lineshape of motionally averaging systems. Dicke's is well-known for the Doppler-linewidth reduction as applied to an atom diffusing in an inert buffer gas.[4] The theory for the hydrogen maser lineshape was particularly applicable to cells with dimensions $< \lambda/2$ where only a small microwave phase variation exists across the cell.[5] A theoretical statistical treatment of the lineshape for TE111 and TE011 mode cavities has been made with some simplifying assumptions.[6] A two-dimensional model Monte Carlo trajectory calculation has given results for both wall-coated and gas filled cells.[7] Three dimensional Monte Carlo trajectory calculations have been used to explore the lineshape of a Zeeman transition in the spherical evacuated wall-coated cell in the presence of magnetic field inhomogenetfes.[8] Experiment and theory were compared with good agreement. The code developed was later employed in studies on systematic effects of magnetic field gradients on the hydrogen maser.[9] The reader will find these papers informative.

The lineshape characteristic of the evacuated wall-coated cell is a narrow sub-Doppler spike centered on a broad pedestal having approximately the full Doppler width (~ 9kHz) of the hyperfine transition . The width of the spike is limited by the relaxation time of the atom-wall interaction. The narrowest width attained for 87Rb has been ~ 10Hz FWHM -- the observed lineshape was Lorentzian.[1] The interest in this paper is in understanding basic phenomena of the averaging process leading to the relative heights of the spike and pedestal in order to maximize the former and minimize the latter. This not only moves the signal toward an optimum but also minimizes systematic effects associated with the pedestal.

First we recall Dicke's one-dimensional model. A radiating oscillator is permitted to bounce between two confining walls. The moving oscillator as seen in the laboratory frame emits a constant amplitude, square-wave frequency modulated wave. Thus the oscillator is periodically Doppler-shifted either up or down from the resting oscillator's frequency due to its rattling motion. The resulting frequency spectrum is found by Fourier analyzing the time-dependent oscillation frequency. The result is the 'lineshape' for the motionally averaged radiating system.

The simple model chosen for discussion in the case of the evacuated wall-coated cell is very similar to Dicke's. It consists of an ensemble able to move in one-dimension in an evacuated cell with walls which permit bouncing without perturbing the quantum state. A given atom is acted on by a standing-wave field applied to cause a transition from one hyperfine state to another [e.g.(2,0) <--> (1,0)]. In the frame of the atom, an oscillating field is seen which is amplitude modulated due to motion through the standing-wave field. Two special cases are considered: in the first, the cell has dimension $D = \lambda/2$.
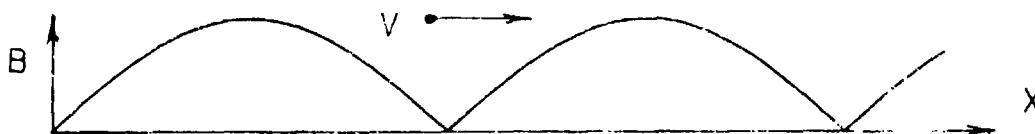
The first sketch shows the cell with atom moving to right with speed v in the standing-wave field. After collision with the right-hand wall, the atom

moves with the same speed to the left through the same standing field. The field $B_1(x)$ seen by the atom at position x is

$$B_1(x) = \sin\frac{2\pi x}{\lambda} \cos\omega_o t = \sin\frac{2\pi vt}{\lambda} \cos\omega_o t = \sin\omega_D t \cos\omega_o t \; : \; 0 < t < T/2$$

$$= \sin\frac{2\pi v(T - t)}{\lambda} \cos\omega_o \tau = \sin\omega_D(T - t) \cos\omega_o t \; : \; T/2 < t < T$$

where $\omega_D = 2\pi v/\lambda$.

Apparently this system can be replaced by one in which the atom moves only to the right in the field amplitude arranged to mimic that actually seen by the atom. See sketch below. Fourier analysis of the periodic waveform $B_1(x)$ gives the frequency spectrum seen by the atom.

This spectrum consists of symmetric sidebands on either s of the applied frequency ω_o and a central non-shifted component at ω_o. Fourier analysis gives this central amplitude simply as $\langle B_1(x)\rangle$, the spatial average of the field over the cell. The transition probability, proportional to the square of this perturbation, gives a spike signal proportional to $\langle B_1\rangle^2$.

The presence of well-defined sidebands is an artifact of the assumption of a constant speed for a given member of the ensemble. A non-coherent superposition of signals from an ensemble with a Maxwell-Boltzmann distribution of speeds produces the pedestal-spike lineshape. The pedestal height is taken proportional to $\langle B_1^2\rangle$ as a result of the incoherent addition of sidebands. Note that the width of the pedestal is expected to be related to that of the non-narrowed Doppler width. Other considerations are involved in attaining the relative heights of the spike and pedestal signals, e.g., the linewidths of the respective features. This will be discussed shortly. No doubt our assumptions are too simplified -- but some of the basic physics generating the lineshape becomes clearer.

The second case treated in the same spirit is that of a cell with $D = \lambda$. The equivalent periodic field seen by an atom traveling always to the right is sketched below.

Fourier analysis of this periodic waveform obviously will give $\langle B_1(x)\rangle = 0$ since the average value of the waveform is zero by symmetry. Thus no spike would be seen under these conditions of excitation no matter how strong the applied B_1 is. However the broad pedestal with its characteristic Doppler width will appear since $\langle B_1^2\rangle$ is not zero.

Another explanation for the absence of the spike follows by considering an arbitrary atom which begins a transition from state 1 to state 2 under stimulation of the oscillating microwave magnetic field. Since the atom is not constrained to remain fixed in space, it moves through the cell bouncing from wall to wall in straight line paths. As long as it moves through a region of the cell having the same spatial phase as it experienced at the beginning of its transition, it will continue making the transition from state 1 to state 2. However, when it crosses a microwave spatial phase boundary and finds itself in a region of the cell having the opposite spatial phase from that which it first experienced, the transition process will reverse and move from 2 back to state 1. On the average then, it is possible for the atoms bouncing from the walls of the cell to have a net zero transition probability for the spike component of the lineshape.

Thus, then with a more detailed theory of the motionally averaged lineshape in evacuated wall-coated cells, we know what conditions will maximize the spike. In the limit of no microwave saturation, the transition probability for the spike is found by considering the case of a δ-function of stimulating radiation interacting with a Lorentzian lineshape of width δv_{spike}. Thus the spike height will be proportional to $\langle B_1 \rangle^2 / \delta v_{spike}$. On the other hand, the transition probability for the pedestal requires a broad stimulating spectral width interacting with a narrow intrinsic Lorentzian lineshape. The pedestal height then is proportional to the energy density in the field per unit frequency, $\propto \langle B_1^2 \rangle / \delta v_{ped}$. Therefore the ratio of heights S_s/S_p will be proportional to

$$\frac{S_s}{S_p} \propto \frac{\langle B_1 \rangle^2 \times \delta v_p}{\langle B_1^2 \rangle \times \delta v_s}$$

The δv_i are the spike and pedestal linewidths. The spike linewidth is a delta-function in the one-dimensional model -- there is zero Doppler shift and zero Doppler width. In a real cell, the intrinsic linewidth is then determined principally by the actual wall-relaxation mechanism which is limited mainly by dispersion in the phase shift due to the atom-wall interaction.

The three dimensional Monte Carlo calculations[8] clearly showed that the atom statistically prefers to bounce 'back and forth' revisiting the region from which it came before the last wall bounce. This is a consequence of the boundary condition that $\underline{R} \cdot \underline{v} < 0$ where $\underline{R}$ is the vector from the cell center to the moving atom and $\underline{v}$ is the atom's velocity. The wall allows access only to a 2π solid angle after a collision while in an atom-gas collision, access to 4π solid angle is available. These physical constraints separate atom-wall collisions in evacuated cells from atom-gas collisions in gas cells. Thus one can expect different consequences to follow from collisions in wall-coated evacuated cells and those in gas cells.[10] Motional averaging effects are dramatically different.

An important issue regarding possible use of the EWSC in atomic frequency standards is the attainable figure of merit, M (signal-to-noise/linewidth), relative to that, say, of the Rb gas cell device. Consider a Lorentzian line with width 500Hz and height S_o attained in a cell with Rb density ρ_o. Thus $M \propto S_o/500$. If it were possible to reduce linewidth by a factor of 10 at constant Rb density, the height of the resonance would increase to $10S_o$. [Since the spike has a Lorentzian lineshape to a good approximation, the

product of signal height and linewidth is constant under conditions of no (or weak) saturation.] Now $M \propto S_o/5$, a factor of 100 improvement over M_o. Thus a quadratic gain in M results from a decrease in linewidth.

If we reduce the Rb density by a factor of 100, the signal drops by this same factor to $S_o/10$, assuming constant linewidth. But now $M = M_o \propto S_o/500$. Thus the same M is achieved with 1/100 the original Rb density. In gas cells as used in Rb frequency standards, 500-700 Hz are typical linewidths. A sizable fraction of this linewidth is due to Rb - Rb spin exchange collisions due to the high required Rb density. The simple argument presented above shows that operation of the EWSC is feasible at Rb densities far less than those used in gas cells. Hence, Rb-Rb collisional broadening due to spin exchange need not be a major component in the linewidth of evacuated wall-coated cells even when operated at a figure of merit comparable to or exceeding that of gas cells.

EXPERIMENTAL TECHNIQUE
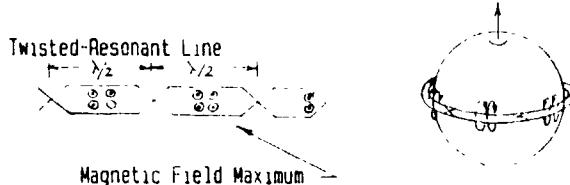
The attainment of a large spike-to-pedestal signal ratio can proceed in two stages: minimizing the spike linewidth and maximizing the $\langle B_1 \rangle^2/\langle B_1^2 \rangle$ ratio. Among the factors determining the spike linewidth are dispersion in phase shift at wall (dominant cause of intrinsic width): light intensity broadening: microwave power broadening: geometric lifetime: etc. The phase shift component of width is proportional to 1/R where R is a measure of cell size. In [1], using a cell with a diameter to $\lambda/2$ ratio of 3.3, a 12:1 spike-to-pedestal height ratio was attained by judicious adjustment of a microwave horn's location/orientation with respect to the cell. A second method was also used to achieve the $\langle B_1 \rangle \neq 0$ condition.

In this case a small microwave loop whose dimensions were comparable to $\lambda/20$ was positioned close to the cell wall with appropriate orientation to provide a sizable fraction of its field with proper orientation to drive the desired hyperfine transition. The spatial phase of the near-zone field does indeed change phase at a $\lambda/2$ distance from the loop: but the spatial gradient in the microwave field due to the small loop size reduces the amplitude of the unwanted phase so that $\langle B_1 \rangle \neq 0$ as desired. See sketch.

The result is that an atom samples the field at random times but remains phased with the inducing field's phase even when so far away as to see no field. On each entrance into the field it continues making a transition. Thus the spike feature is large. The pedestal is also present although its lineshape is altered from Gaussian. One linewidth contribution to the pedestal is now due to the lifetime the atom spends in one pass through the localized field. (Lineshape due solely to the lifetime effect would be Lorentzian.) Since the ensemble has a velocity distribution, this width is weighted by this distribution. Deviations from Gaussian pedestal lineshape were observed. Effects of the far and intermediate zone fields have been calculated for $\langle B_1 \rangle^2$ and $\langle B_1^2 \rangle$ as a function of cell size.

A symmetric array of dipoles can also be used. A pair are sketched above. An extension of the array is a resonant-line structure constructed in principle of twisted sections each of length $\lambda/2$.

Quadrupole loops have been used to create even stronger spatial gradient field falloffs. Unwanted microwave fields can be controlled by appropriately placed absorptive material.

Larger cell size is advantageous in providing smaller linewidth and increasing the signal at constant Rb density. Not only is signal increased because linewidth is decreased, but also since a larger number of Rb atoms are being interrogated (assuming constant Rb density). However, it may then become more difficult to attain a reasonable $\langle B_1 \rangle^2 / \langle B_1^2 \rangle$ ratio. Likewise, in using smaller cells of interest in miniaturization, a microwave cavity mode may be selected in which $\langle B_1 \rangle = 0$, thus producing no spike signature at all. An example of this is the wall-coated cell which fills a TE111 mode cavity.[6] Use of such modes is still possible by physically dividing the cell with a septum placed along the region where the spatial phase changes, although the smaller effective cell size will increase spike linewidth. In fact for the hydrogen maser, this has been proposed.[11]

PRACTICAL CONSIDERATIONS

Consider use of an EWSC in a TE011 mode cavity. In a right-circular non-loaded cavity, the spatial average of the z-component of the cavity magnetic field over a spherical cell is given by

$$\langle B_z \rangle / B_{center} = 3 \left[\frac{\sin \Omega}{\Omega^3} - \frac{\cos \Omega}{\Omega^2} \right]$$

with $\Omega = (R_{cell}/D_{cavity}) \times [(kD)^2 + \pi^2]^{1/2}$: $kD = 2 \times 3.832$
In the hydrogen maser, the filling factor given below is a relevant parameter.

$$\eta_H = \langle B_z \rangle^2_{cell} / \langle B_{tot}^2 \rangle_{cavity}$$

with $\langle B_{tot}^2 \rangle_{cavity} / B_{center}^2 = J_o^2(kR_{cav}) \times [1 + (\pi/kL)^2]/2$

where L = cavity length and R_{cav} = cavity radius. A closed form expression for η_H is thus found. This is plotted in Fig. 1. This result does not agree with KGR's[5] Fig. 3 (corrected by a factor of two) when the cell radius is large. It appears that KGR may have plotted $\langle B_z^2 \rangle_{cell} / \langle B_{tot}^2 \rangle_{cav}$.

A plot of the 'filling factor' for the EWSC, $\langle B_z \rangle^2_{cell} / \langle B_z^2 \rangle_{cell}$, is given in Fig. 2. This is the relevant quantity for field averages when driving the (2,0) - (1,0) hyperfine transition. Rho, ρ, is the cell radius/cavity diameter. First results on a cell ~ 30 cc give an intrinsic linewidth of ~

86

20 Hz at 6.8 GHz with 1.5 µA light intensity. The hfs resonance in this cell is shown in Fig. 3.

CONCLUSIONS

As a practical matter, it appears that large EWSC, $D > \lambda$, are not necessary to attain significant figures of merit. A cell which fits in TE011 mode cavity is a good example. The EWSC appears to remain an excellent candidate for atomic frequency standard use.

ACKNOWLEDGEMENT
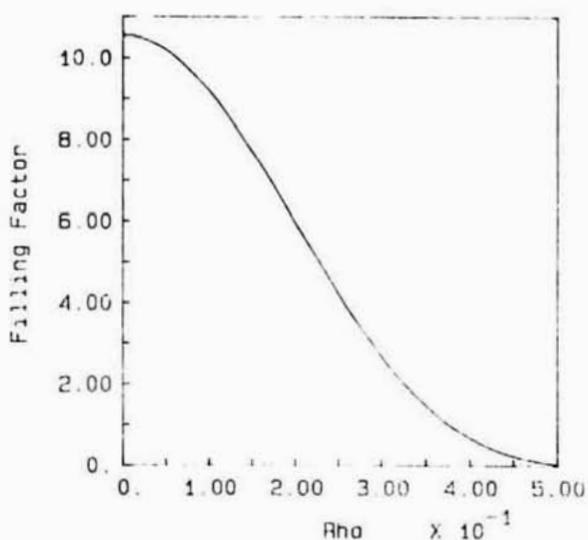
REFERENCES
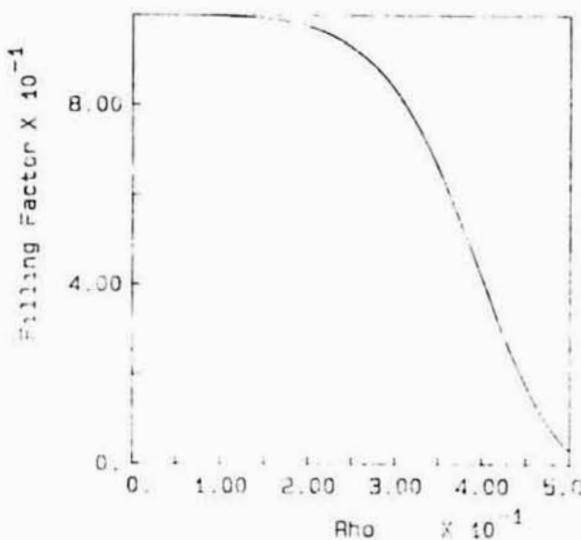
1. H.G. Robinson and C.E. Johnson, Appl. Phys. Lett. 40, 771(1982).
2. H.G. Robinson and C.E. Johnson, Proc. 14th PTTI, 307(1982).
3. H.G. Robinson and C.E. Johnson, IEEE Trans. Inst. Meas. IM-32, 198(1983).
4. R.H. Dicke, Phys. Rev. 89, 472(1953) R.H. Romer and R.H. Dicke, Phys. Rev. 99, 532(1955).
5. D. Kleppner, H.M. Goldenberg, and N.F. Ramsey, Phys. Rev. 126, 603(1962).
6. R.P. Frueholz, C.H. Volk, and J.C. Camparo, J. Appl. Phys. 54,5613(1983).
7. R.P. Frueholz and C.H. Volk, Proc. 38th Annual Freq. Control Symp., 401(1984).
8. S.F. Watanabe and H.G. Robinson, J. Phys. B: Atom. Molec. Phys., 10, 931(1977).
   S.F. Watanabe, G.S. Hayne, and H.G. Robinson, ibid., 941.
   S.F. Watanabe and H.G. Robinson, ibid., 959.
   J. Sykes , ibid., 1151.
   S.F. Watanabe and H.G. Robinson, ibid., 1167.
9. S.B. Crampton, E.C. Fleri, and H.T.M. Wang, Metrologia 13, 131(1977).
10. Compare with reference 7 in which the authors attribute to Vanier et. al. [J. Vanier, J.F. Simard, and J.S. Boulanger, Phys. Rev. A9, 1031(1974)] the idea that the mechanism of wall collisions and gas collisions are identical insofaras concerns the colliding Rb atom.
11. E.M. Mattison, M.W. Levine, R.F.C. Vessot, Proc. 8th PTTI Meeting, 355(1976).

H Maser   EWSC

Figures 1 & 2. The filling factors for the H-maser, $\langle B_z\rangle^2_{cell} / \langle B^2_{tot}\rangle_{cavity}$, and for the EWSC used with optical pumping, $\langle B_z\rangle^2_{cell} / \langle B^2_z\rangle_{cell}$, in an unloaded cylindrical right-circular TE011 mode cavity. Rho is R_{cell}/D_{cavity}.
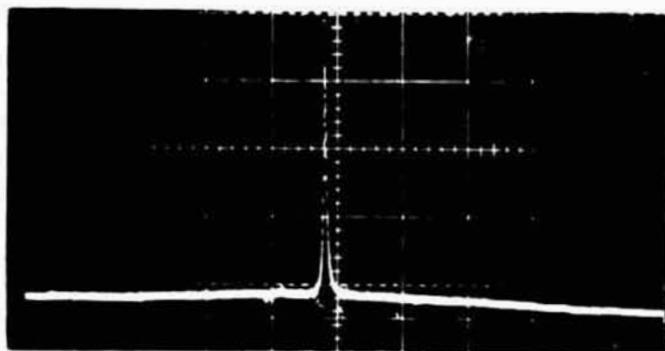
Figure 3. The 0-0 hyperfine transition resonance in a   30 cc cell shown with a wide sweep.

QUESTIONS AND ANSWERS

HARRY PETERS, SIGMA TAU CORPORATION: I was curious as to what your wall coating was, and what the stability of frequency, or linewidth would be.

MR. ROBINSON: This particular coating is the same coating we used originally. It's Tetracontane. Time is the main thing that prevents us from trying other coatings. We would give the same answer to your second question. We really haven't explored in detail how stable the frequency is, or the linewidth and so forth. Those are things that clearly need to be done. The talk this afternoon right after lunch details some of the parameters that are important in deciding whether you can use this for atomic frequency standards. That particular issue is not addressed, though, this afternoon.

DIODE LASER 87Rb OPTICAL PUMPING IN AN EVACUATED WALL-COATED CELL

Wah-Keat Lee and H.G. Robinson
Physics Department, Duke University
Durham, North Carolina 27706

C.E. Johnson
Physics Department, North Carolina State University
Raleigh, North Carolina 27650

ABSTRACT

The evacuated wall-coated sealed cell coupled with diode laser optical pumping offers a number of attractive potential advantages for use in Rb or Cs atomic frequency standards. An investigation of systematic effects is required to explore possible limitations of the technique. We report on the use of diode laser optical pumping of 87Rb in an evacuated wall-coated sealed cell. Experimental results/discussion to be presented include the signal strength and line broadening of the 0 – 0 hyperfine resonance as a function of light intensity for the D1 optical transitions 'F -> F') = (2 ->1') and (2 -> 2') : shift of the 0 – 0 hyperfine frequency as a function of laser intensity and de-tuning from optical resonance : and diode laser frequency stabilization techniques.

INTRODUCTION

Previously we have observed 87Rb and 133Cs $\Delta m = 0, + 1$ hyperfine transitions in an evacuated wall-coated sealed cell (EWSC) of 200cc volume using conventional Rb or Cs rf-excited plasma lamps.[1-3] The use of diode lasers in optical pumping has been reported by other researchers for both Cs and Rb using gas cell or atomic beam apparatus.[4-9] High efficiency optical pumping with diode lasers has been studied theoretically for the EWSC.[10] In this paper, we report on the use of diode lasers in hyperfine pumping an evacuated wall-coated sealed cell of ~ 30cc volume. The frequency of the ground state hyperfine transition $(F,m_F) = (2,0) <-> (1,0)$ was monitored permitting a determination of a number of parameters useful in criticizing such wall-coated cells coupled with diode laser signal acquisition as a candidate for use in atomic frequency standards.

APPARATUS

The basic apparatus is shown in Fig. 1. It consists of a diode laser, objective lens, attenuator, evacuated wall-coated cell inside a thermal enclosure, and a photodetector which monitors transmitted light intensity. A Rb side-arm on the cell was maintained at a temperature below that of the enclosure to control the Rb density in the cell. The diode laser is tuned to one of the four resolved D1 (F <-> F') optical hyperfine transitions at 794.7 nm. Figure 2 shows the optical transitions available. We report here only on simple pumping with either the (2 <-> 2') or the (2 <-> 1') optical transition using linearly polarized light propagated along the direction of the applied magnetic field.

Light intensity was monitored by measuring the photocurrent resulting from light transmitted through the cell. The conversion factor between current and power is ~ 640μA/mw (or 1.67μw/μA) at 795 nm for unit quantum efficiency at the detector. Typical photocurrents used are 10 μA which implies < 17 μw. The estimated intensity incident on the cell for a 10μA detected current is ~ 100μw/cm^2.

Instead of an inhomogeneous lineshape characteristic of the gas cell, the homogeneous lineshape which results from use of an EWSC is one of its chief advantages. Thus even though light intensity does not uniformly illuminate the EWSC, all atoms interact in the same way with the light due to the averaging which a given atom performs in bouncing against the cell walls. Indeed, it is this averaging which generates the homogeneous Lorentzian lineshape.

RESULTS

The EWSC was maintained at 40°C while the Rb side-arm was kept at ~ 22°C. With the Rb density attained under these conditions and using 10 μA on the (2 <-> 1') transition, the fractional absorption of light with no microwave power was ~ 7.5 x 10^{-2}. This was determined by a rapid sweep of the laser through the optical resonance - optical pumping effects were present to some degree. The fractional 0-0 signal under a high saturation condition by microwave power was 1.5 x 10^{-2}. This is taken as evidence of good optical pumping/detection efficiency even at the low light levels used. The long T1 relaxation time available in wall-coated cells implies relatively low light intensity will produce significant level population differences.

The optical hyperfine pumping light which establishes population differences between the F = 2 and 1 levels in the ground electronic state and which provides the means for detecting the 0-0 hyperfine transition in the presence of a resonant microwave field also causes a broadening of the 0-0 resonance. The intrinsic linewidth attained in this cell at ~ 1.5 μA light intensity was ~ 20 Hz. The following increases in the 0-0 width due to light intensity were determined:

$$(2 <-> 2') \quad => \quad \sim 4 \text{ Hz}/\mu A$$
$$(2 <-> 1') \quad => \quad \sim 2 \text{ Hz}/\mu A .$$

The 0-0 signal amplitude vs. light intensity is shown in Fig. 3. The Hitachi laser was used in this case. The microwave power was kept at an arbitrary but constant level and was weakly saturating. The klystron signal source was locked to the 0-0 resonance. Note the relatively low light intensities used. The data for the (2 <-> 2') and (2 <-> 1') transitions were taken individually. Both sets of data are plotted on Fig. 3 for convenience.

Two parameters are used for the light-induced frequency shift.[11] The parameter $a(I)$ gives the shift of the 0-0 frequency per unit optical intensity when the optical frequency is tuned to resonance.

$$a(I) = \partial \nu_{0-0} / \partial I$$

Thus the 0-0 frequency shift $\delta \nu_{0-0}$ caused by the resonant light intensity I is given by

$$\delta \nu_{0-0} = a(I) \times I .$$

Another parameter β describes the shift of the 0-0 frequency when the optical radiation is de-tuned from resonance.

$$\beta(I) = \partial\nu_{0-0} / \partial\nu_{opt}.$$

The frequency shift due to this effect for a small de-tuning is

$$\delta\nu_{0-0} = \beta \times \Delta\nu_{opt}.$$

A discriminator-like frequency shift of the 0-0 transition is produced for larger de-tuning of the optical resonance.

In Fig. 4 are shown the results of the measurement of the 0-0 frequency vs. light intensity for both Hitachi and Mitsubishi lasers. The slope of this data gives the light shift parameter $\alpha(I)$. Here the klystron was locked to the 0-0 resonance and the laser was locked to the optical absorption resonance in the EWSC itself. Using on-resonance (2 <-> 1') light at ~ 10 µA intensity, a 0-0 shift of ~ - 4.5 Hz was found. Thus a fractional intensity stability of 1.5×10^{-3} will produce a 0-0 fractional shift of 1×10^{-12} at 6.8 GHz under conditions used. The Hitachi laser linewidth was ~ 30 MHZ whereas the Mitsubishi laser linewidth was ~ 100 MHz. Both of these widths were determined for free-running lasers (not locked to an atomic resonance). In spite of the factor of three difference in linewidths, both lasers have almost identical α coefficients, as seen from Fig. 4. Because the lasers were locked to the atomic absorption, narrowing of the spectral width occurs. We have not yet measured the laser linewidths in the locked condition.

Measurements on the second light-shift parameter β were more difficult. In this case neither the laser nor the klystron was locked to the 0-0 transition. The laser was detuned from optical resonance typically by ~ 150 MHz. This is small compared to the optical Doppler width and therefore implies remaining in the linear region of the discriminator shaped 0-0 shift curve. Figure 5 shows results for the (2 <-> 2') and (2 <-> 1') transitions where β is found at a given light intensity by dividing the observed 0-0 frequency shift by the laser detuning from optical resonance. The β-coefficient has also been reported for Rb gas cell devices.[5,7] Table I compares data obtained from the indicated sources.

Table I. Comparison of β-coefficient for gas cells and the EWSC.

Reference	Cell Type	Optical Transition F -> F'	Incident Intensity µw/cm^2	$|\beta|$ Hz/MHz	$|\beta|/I$ mHz-cm^2/MHz-µw
5	gas	2->1',D2	280	0.63	2.25
7	gas	1->2',D1	300	0.41	1.37
This paper	EWSC	2->1',D1	100	0.025	0.25

Using this data a comparison between the gas cell and the EWSC is difficult since different conditions were used in each case. Nevertheless, a β normalized to unit intensity is calculated in the last column. In this Table, our transmitted intensity of ~ 85 µw/cm^2 (as inferred by ~ 10µA photocurrent) was taken to imply ~ 100µw/cm^2 intensity incident on the glass cell.

DIODE LASER STABILIZATION

A description has been given by Lewis and Feldman[5] on the use of diode lasers in atomic frequency standards. They reported long-term locking of the

laser to an atomic absorption line. Other researchers have also reported locking diode lasers.[12,13] For the initial determinations reported in this paper of various parameters characterizing the 0-0 hyperfine transition in the EWSC, it was convenient to stabilize the diode laser to the Rb optical absorption of interest. Methods useful for this purpose are presented briefly.

Two diode laser stabilization schemes have been implemented. For app. tus simplicity, the first scheme uses the normal Doppler broadend opt. 1 absorption in the EWSC itself. (A separate non-wall-coated cell ould ha been used.) The other cheme uses Doppler free saturated absorption in separate cell. Both of these methods require that the laser be frequency modulated in order to interrogate the optical line center.[14] Long-term drift is tuned out by a temperature servo and short-term noise is removed by feedback to the laser current.

The block diagram for the basic scheme to observe saturated absorption[15] is shown in Fig. 6. To suppress the non saturation features, the saturating beam can be chopped. This selectively modulates the saturation effect. Subsequent lock-in detection produces the sub-Doppler features shown in Fig. 7c. Also shown is the normal Doppler broadened absorption signature (Fig. 7a) and the absorption-saturation signature without suppression of background (Fig. 7b). All of these traces are shown using wide-band (5 kHz) signal recovery channels. Either the 7b or 7c signature can be used to lock the laser. With the β-coefficient measured for the 2 -> 1' optical transition at 10 μA intensity, a signal-to-noise ratio of ~ 145 would be required to stabilize the laser so that the 0-0 frequency would be stable to 1 part in 10^{-12}. Adequate S/N appears to be present.

Figure 8a shows the block diagram of the system used in acquiring most of the data presented in this report. Both the laser and the klystron were locked to the Rb atoms. Figure 8b shows the saturated absorption laser lock diagram.

CONCLUSIONS

Several parameters have been determined relating to the potential for use of the evacuated wall-coated sealed cell coupled with diode laser signal acquisition in an atomic frequency standard. This work may be regarded as preliminary -- measurements need to be repeated, refined, and expanded. The encouraging results on the 30cc cell provide excellent motivation for continued research.

ACKNOWLEDGEMENTS

REFERENCES

1. H.G. Robinson and C.E. Johnson, Appl. Phys. Lett. 40, 771(1982).
2. H.G. Robinson and C.E. Johnson, Proc. 14th PTTI, 307(1982).
3. H.G. Robinson and C.E. Johnson, IEEE Trans. Instr. Meas., IM-32, 198(1983).
4. M. Arditi and J.L. Picque, J. de Phys. Lett. 41, L370(1980).

5. L.L. Lewis and M. Feldman, Proc. 35th Annual Freq. Control Symposium, 612(1981).

6. M. Feldman, J.C. Bergquist, L.L. Lewis, and F. Walls, Proc. 35th Annual Freq. Control Symposium, 625(1981).

7. C.H. Volk, J.C. Camparo, and R.R. Frueholz, Proc. 13th PTTI, 631(1981).

8. J.C. Camparo, R.P. Frueholz, and C.H. Volk, Proc. 14th PTTI, 113(1982).

9. J.C. Camparo and C.M. Klimcak, Am. J. Phys. 51, 1077(1983).

10. C.L.J. Newton and H.G. Robinson, Proc. 14th PTTI, 133(1982).

11. These parameters are defined for continuous optical pumping. Detection by pulsed optical pumping would apparently eliminate light shifts.

11. H. Tsuchida, M.Ohtsu, T. Tako, N. Kuramochi, and N. Oura, Jap. J. Appl. Phys. 21, L561(1982).
These authors locked the laser to a normal absorption in ^{85}Rb on a D_2 line. They reported an abnormal saturation absorption signature.

13. T. Yabuzaki, A. Ibaragi, H. Hori, M. Kitano, and T. Ogawa, Jap. J. Appl Phys. 20, L451(1981).
Authors used a saturated absorption feature in Cs to lock to a D_2 line.

14. Optical heterodyne saturation is another method available if FM on the laser is objectionable. Unmodulated laser output is produced. See for example J.L. Hall, L. Hollberg, Ma Long-sheng. T. Baer, and H.G. Robinson, J. de Phys., Colloque C8, 59(1981).

15. For example see F.T. Arecchi, F. Strumia, and H. Walther, Advances in Laser Spectroscopy, Plenum Press (1983):
    or Wolfgang Demtroder, Laser Spectroscopy, Springer-Verlag (1981).
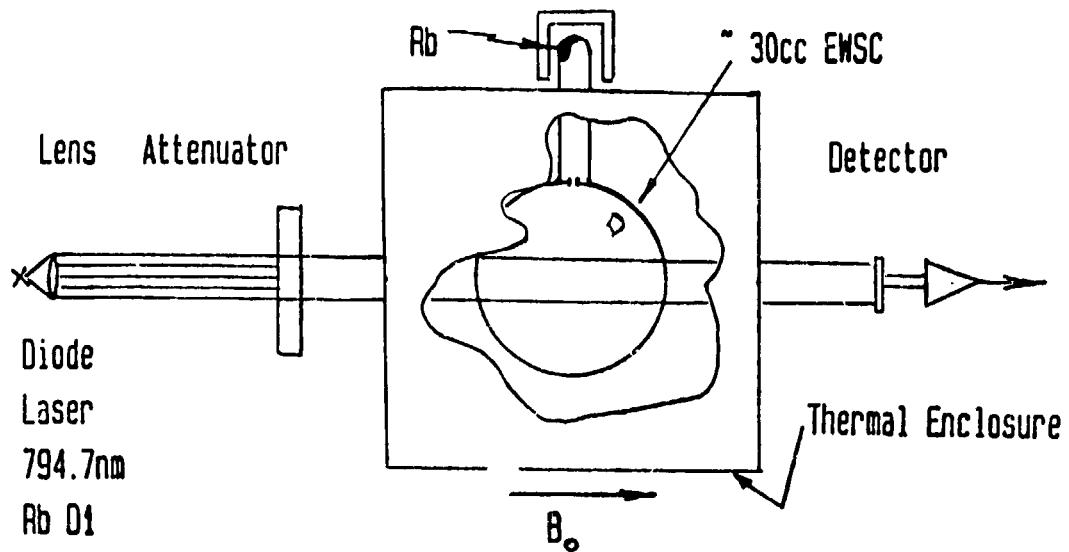
Figure 1. Schematic of basic optical pumping apparatus used with the EWSC. The thermal enclosure was operated at 40C while the Rb was maintained at 22C.
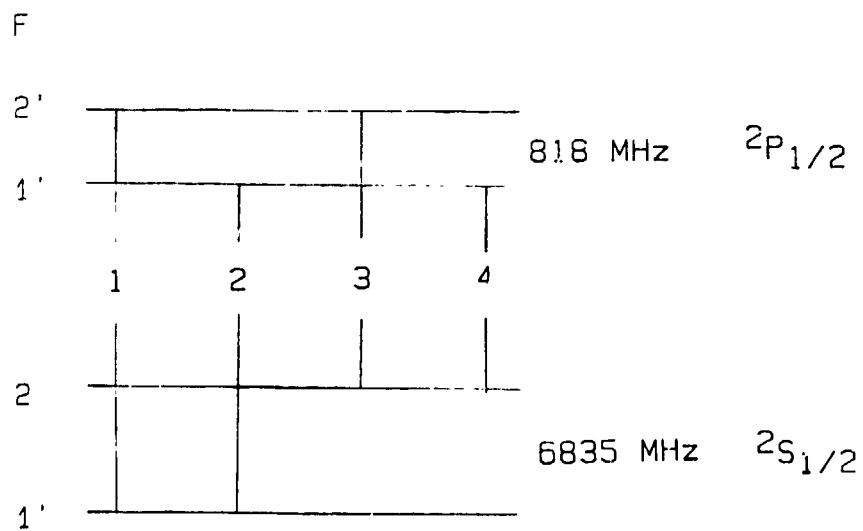
Figure 2. Rb D1 optical transitions available. The (F - F') = (2 - 2') and (2 - 1') transitions were used for this work.

96
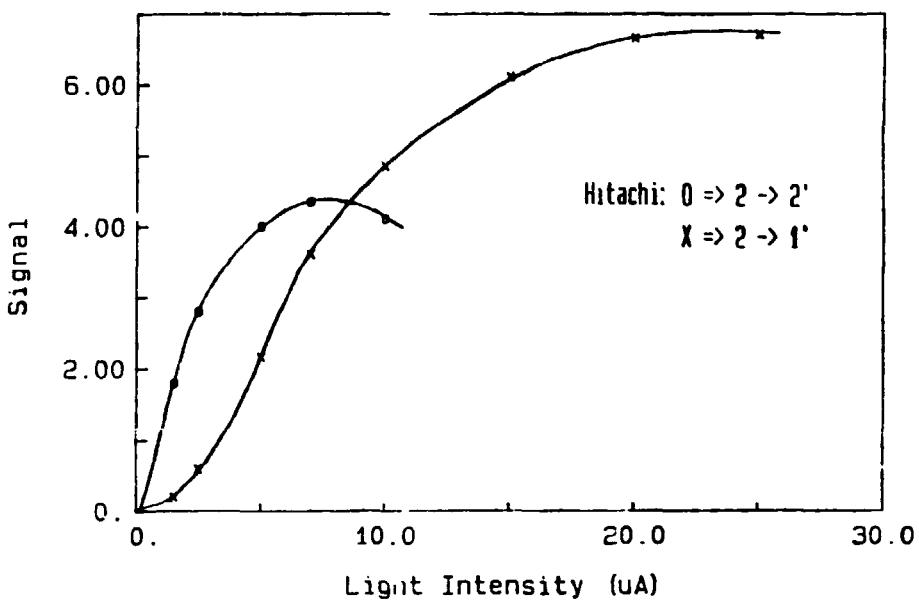
Figure 3. The 0-0 hyperfine signal vs. light intensity at a weakly
saturating microwave power.
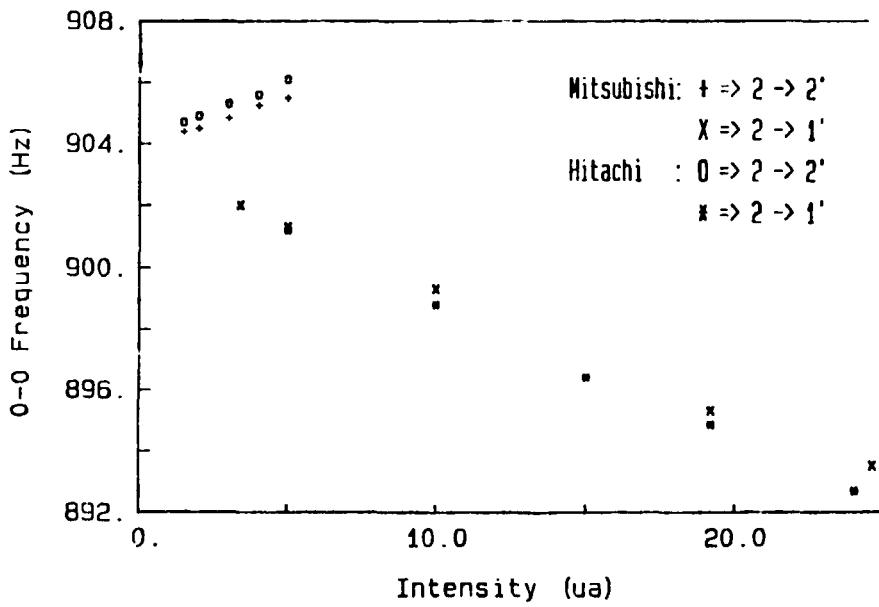
Figure 4. The 0-0 frequency vs. light intensity as a function of optical
transition and type of laser used. The slope of this data gives the light
shift parameter α(I). This data was taken with the laser locked to the Rb
optical absorption and the klystron locked to the 0-0 hyperfine transition.
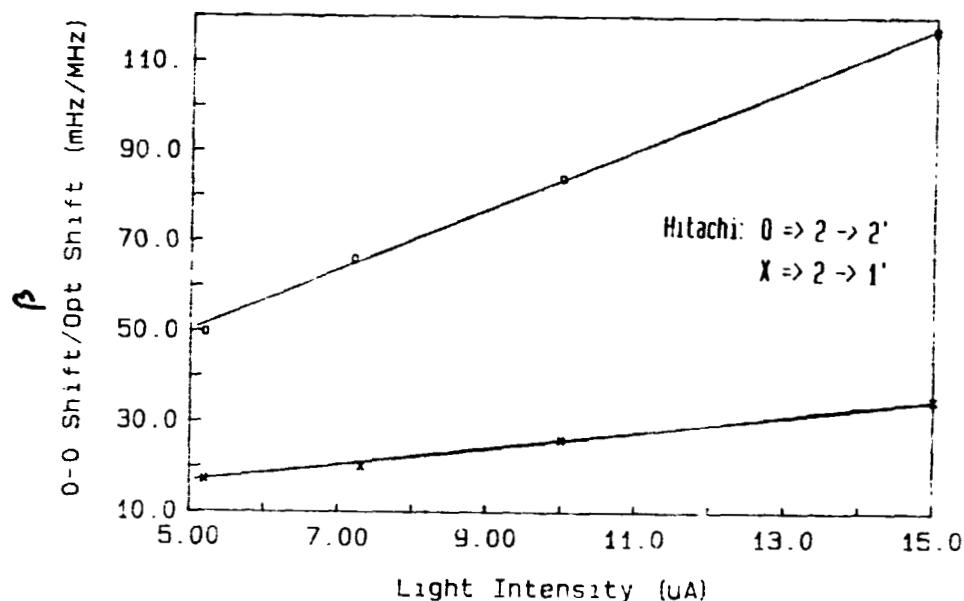
Figure 5. Light shift parameter $\beta = \partial\nu/\partial\nu_{opt}$ as a function of light intensity. Data used optical detuning of ~ 150MHz, small relative to the optical Doppler width.
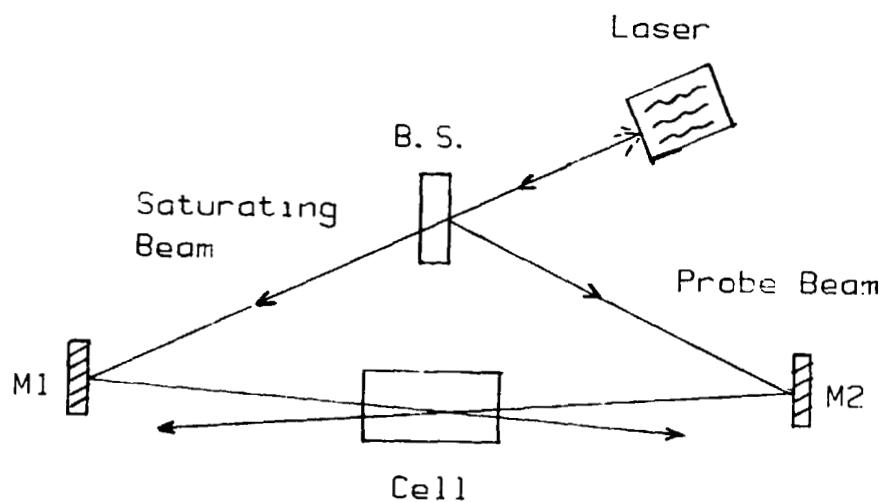
Figure 6. Block diagram for observation of saturated absorption features.
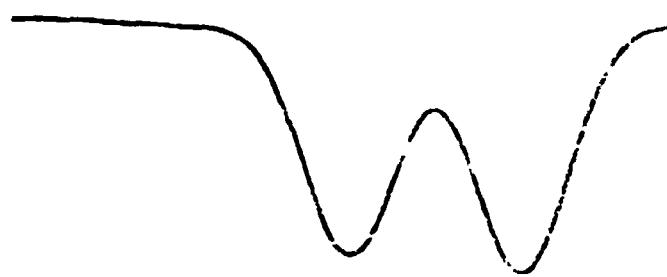
Figure 7a. Normal Doppler broadened absorption.
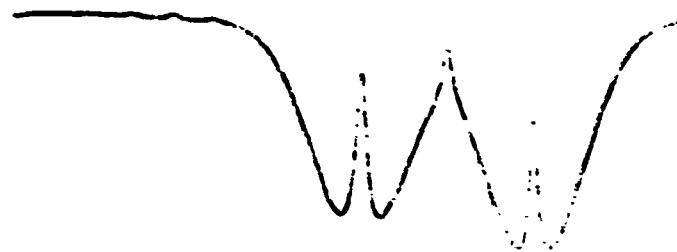
Figure 7b. Absorption-saturation signal.

Rb(85) |— 818MHz —|
         2 – 2'   2 – 1'
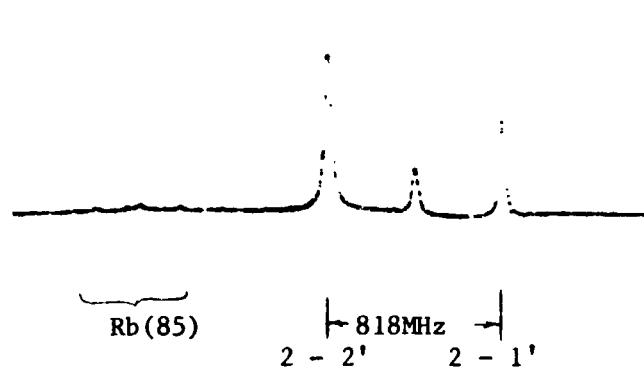
Figure 7c. Saturation feature observed with 5kHz bandwidth.
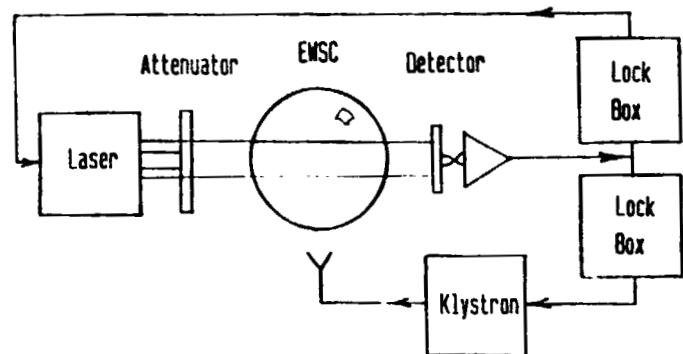
Figure 8a. Block diagram of system used to lock both laser and klystron to Rb.
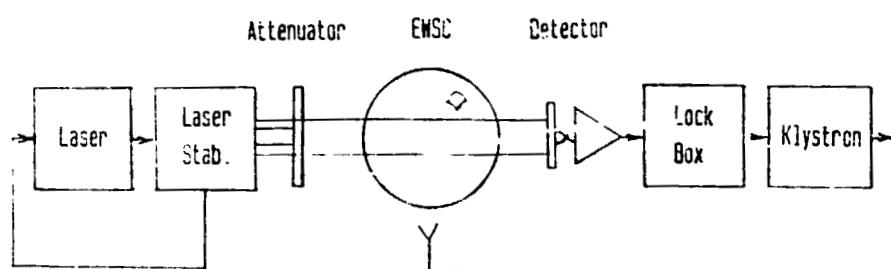
Figure 8b. Block diagram showing saturated absorption laser lock.

QUESTIONS AND ANSWERS

JACQUES VANIER, NATIONAL RESEARCH COUNCIL: Your alpha coefficient, could it be due to distortion of the spectrum of the laser diode?

MR. ROBINSON: I would have to go back to Will Happer who has worked out the theory for light shifts. He has worked out a theory using operator formalism which is an easier thing to grab hold of, and they are relatively complicated. The thing that Happer actually worked out was for light that was very broad compared to the hyperfine separation, and here we have exactly the opposite case. We have light that's narrow compared to the hyperfine separation. The theory is right. There is no question that the theory is going to work if you actually try and calculate it, I think.

There are several different effects that shift the thing. One is a second order Stark effect. You actually have applied an AC field to this ground, and you are actually tickling levels up and down, and you see then the average result of that. That's one of the ways you can get a light shift. There are virtual transitions, there are tensor shifts, there are all sorts of shifts that come in. Usually the tensor shifts have been neglected, but apparently in this case they may not be able to be.

The point is that you can get around them if you need to by using pulsed light, but they certainly are in all of these other systems. The gas cell has these things in there. It's just that you don't see them. They are masked by other things.

It just explores an explicit parameter that needs to be looked at in an evacuated wall-coated cell.

CARROLL ALLEY, UNIVERSITY OF MARYLAND: Did I hear you say a twenty Hertz linewidth?

MR. ROBINSON: Yes.

MR. ALLEY: That's for 6835?

MR. ROBINSON: That's for the 6835 line. You heard right.

MR. ALLEY: That sounded very good.

MR. ROBINSON: This stuff works.

MR. ALLEY: Oh yes, we know. What wall coating were you using?

MR. ROBINSON: This is still the same old wall-coating, Tetracontane, and I don't have any idea that that is the best wall-coating. It's just that we are moving relatively slowly, doing one thing at a time, and we had gotten that to work before, so that's what we tried again.

So this is the first one -- we had a 200 cubic centimeter cell that's about fifteen years old that is sealed off. These cells are absolutely sealed. There is no vacuum system associated

with them. You can carry them around in your fingers. That's the cell that we have talked about here.

So they apparently have longevity. There are a lot of questions -- Harry Peters asked one today about what happens in the time history of these things. We don't know that yet. We haven't gotten there yet. That's still to come, clearly. But everything we do seems to be very attractive so far in getting the system to work.

MR. ALLEY: I will give you a thirty year old cell and see if it will work.

MR. ROBINSON: I should say that Carrol Alley tried pumping with lasers, diode lasers, and what we have done here is certainly not unique. There are several Japanese authors that have locked lasers to saturated absorption things. I know people at N. B. S. have done that. Lyndon Louis has done that, we are just following in the track.

I think that we may have some really gorgeous curves. I am not sure that anybody else has anything comparable to this sort of beautiful saturated absorption curve. I haven't seen it anyway. But the stuff just works. It's just gorgeous.

MR AUDOIN: There is a third resonant feature on your curve. Is that a level crossing?

MR. ROBINSON: The third resonant feature? Oh, in the saturated absorption curve. That's called a cross-over resonance, and it's nothing particularly unusual. I would like to explain that to you. The saturated feature, or curves are only for certain atoms. Since the two beams are shot through in opposite directions, the only atoms they both talk to are those which are moving perpendicular to both beams. In other words, the non-doppler shifted thing. That's the reason you get the main saturated absorption feature, which doesn't have any Doppler width to speak of.

The other resonance occurs when two opposite curves cross over, and those tails can be made to do the same thing. That's an artifact, it's not really a resonance. You don't want to lock on that, you want to lock on the two central ones.

ON-ORBIT FREQUENCY STABILITY ANALYSIS
OF THE GPS NAVSTAR-1 QUARTZ CLOCK AND
THE NAVSTARs-6 AND -8 RUBIDIUM CLOCKS

by

Thomas B. McCaskill
James A. Buisson
Marie M. Largay
Wilson G. Reid
Naval Research Laboratory
Washington, D.C. 20375-5000

ABSTRACT

This paper presents an cn-orbit frequency stability performance analysis of the GPS NAVSTAR-1 quartz clock and the NAVSTARs-6 and -8 rubidium clocks. The clock offsets were obtained from measurements taken at the GPS monitor stations which use high performance cesium standards as a reference.

Clock performance is characterized through the use of the Allan variance, which is evaluated for sample times of 15 minutes to two hours, and from one day to 10 days. The quartz and rubidium clocks' offsets were corrected for aging rate before computing the frequency stability. The effect of small errors in aging rate is presented for the NAVSTAR-8 rubidium clock's stability analysis.

The analysis includes presentation of time and frequency residuals with respect to linear and quadratic models, which aid in obtaining aging rate values and identifying systematic and random effects. The frequency stability values were further processed with a time domain noise process analysis, which is used to classify random noise process and modulation type.

NAVSTAR-1 results indicate good performance for a quartz clock. Comparison of the quartz clock's stability with the best on-orbit cesium clock results indicates that the cesium standard is more stable by at least a factor of two for a 900 second sample, and increases to two orders of magnitude for a one day sample time.

The NAVSTAR-8 rubidium clock differed from the NAVSTAR-6 rubidium clock in its improved thermal environment. This rubidium clock exhibited an effect that lasted for nearly five months. Following this transient, the rubidium clock performed with better-

than-expected stability. A final discussion of quartz, rubidium, and cesium on-orbit will be presented.

INTRODUCTION

The NAVSTAR Global Positioning System (GPS) is a space-based navigation satellite system, which when operational in the late 1980's, will provide accurate navigation and time information to users anywhere in the world, or in near-Earth orbit. A constellation (1) of 18 to 24 satellites will be tracked and controlled by a network of Monitor Stations (MS).

GPS will provide a near-instantaneous navigation capability because each NAVSTAR Spacecraft Vehicle (SV) clock is synchronized to a common GPS time. The NAVSTAR clock offsets, orbital elements, and spacecraft health are periodically determined by the Master Control Station (MCS). These updated parameters are then uploaded to each NAVSTAR SV. Each NAVSTAR clock must then maintain GPS time until the next update by the MCS. Current system performance requires three updates per day to meet navigational requirements.

The Naval Research Laboratory (NRL) has recognized the importance of clock performance to the GPS mission (2,3), and is conducting the NRL GPS Clock Development Program. The on-orbit clock performance (4,5) was determined through the procedure depicted in Figure 1, and described in detail in reference 6. Key features of this technique are (1) use of a high-performance ground reference clock at each MS, and (2) use of a Naval Surface Weapons Center (NSWC) smoothed reference orbit to separate the orbital and clock signals from the pseudo-range and pseudo-range- rate measurements.

CLOCK PERFORMANCE MODELS

GPS on-orbit clock performance is characterized for both systematic and random effects. Systematic parameters include clock time and frequency offsets, and aging rate, all as function of time. The clock's random behavior, in the time domain, is characterized through use of the Allan variance (7,8). A typical frequency stability profile(9) is presented in Figure 2.

A time domain noise process analysis is performed to determine random noise process type. These time domain parameters may then be transformed to the frequency domain using conversion formulas detailed in reference (10).

Once a clock has been characterized through a frequency stability analysis, the frequency profile may then be used to estimate a clock's time prediction performance. Figure 3 presents a set of time prediction curves, as a function of frequency stability and clock update time, using optimal two point prediction (10,11). Other models for time prediction are

presented in reference (7). Each of these optimal time prediction models has one thing in common -- namely that the long-term clock prediction performance is driven by the product of the clock update time and the frequency stability. The clock update time is determined by GPS requirements, hence improved clock stability is the parameter that will directly influence GPS time prediction. This analysis represents total system errors super-imposed on the clock results. GPS system influences either enhance or detract from actual clock performance. Therefore the apparent indication of slight deviations from normal clock behavior could be expected.

NAVSTAR-1 QUARTZ RESULTS

NAVSTAR-1 was launched on Feb 22, 1978, and the quartz clock was activated only after all on-board rubidium clocks failed. This quartz clock is still working as of this date, however its status is listed as "unhealthy" because more stable atomic clocks are now available in other NAVSTAR SVs. Of interest is the determination of the short- and long-term frequency stability of the NAVSTAR-1 quartz clock and its comparison with the NAVSTAR atomic clocks.

The clock offsets between the NAVSTAR-1 quartz clock and the Vandenberg Monitor Station (VMS) are presented in Figure 4. The data indicates a sequence of smooth quadratic curves, with occasional adjustments by the Master Control Station, to keep the quartz clock's time and frequency within prescribed limits. The concave shape of the quadratic curves is due to the negative aging rate of the NAVSTAR-1 quartz clock. The relative maximum clock offsets occur as the quartz clock's frequency offset passes through zero. The cusps in the quadratic curves occur because of step frequency adjustments, which keep the frequency offset between (+/-)1PP10(9). In addition to the frequency adjustments, several clock phase adjustments were made to align the clock offsets with respect to GPS time.

Frequency offsets for the NAVSTAR-1 quartz clock were computed, using clock offsets separated one day in time, and are presented in Figure 5. The time axis is labelled in units of Modified Julian Day (MJD), day-of-year, and calendar date. The frequency offsets decrease with time, with adjustments in frequency occuring as the frequency offset approaches (+/-)1PP10(9). Visual inspection of Figure 5 indicates small departures from a linear change in frequency, which are of primary interest in the on-orbit stability analysis.

Using the times of the frequency adjustments made by the GPS Master Control Station, the quartz frequency data was corrected to remove the effect of the frequency adjustments. These corrected frequency offsets are presented in Figure 6. These data were further analyzed to determine if the quartz clock aged at a constant rate. A constant aging rate is part of the clock model used by the GPS MCS for the quartz and rubidium clocks.

105

Assuming a constant aging rate for all of 1982, a linear frequency model was fitted to the data, and the frequency linear residuals are presented in Figure 7. The residuals indicate a change in aging rate near day 150, 1982. The data was segmented into two subsets, with a linear frequency model used for the first segment, and a quadratic model for the remainder of the year. The residuals for these two segments are presented in Figures 8 and 9.

Clock stability during a pass is determined by evaluating the Allan variance for sample times of 15-minutes to 2-hours. Stability results for 900-second and 2-hour sample times are presented by Figures 10 and 11. Note that the frequency stability values are plotted as a function of running time, rather than the sample time. The most interesting result evident in Figure 10 is a change that occurs near day 150, 1982. Inspection of the stability values indicates a small increase in the correlated noise after day 150. This decrease in stability is further supported by the prior results on aging rate, which indicate a change that occured near day 150, from a constant aging rate to a linear change in aging rate. This change can be seen by inspection of Figures 6, 7, and 9.

Long term frequency stability results for the NAVSTAR-1 quartz clock are computed after estimating and correcting the clock offsets for a constant aging rate. The effect of the aging rate errors on frequency stability will be explictly addressed later in this report.

A composite of short- and long-term frequency stability results for the NAVSTAR-1 quartz clock are presented by Figure 12. Uncharacteristic of a typical clock is the transition from random walk FM to flicker noise FM, which occurs at a sample time of about 3 days. Further conclusions will be made after comparing the quartz stability results with previous (6) on-orbit results for the NAVSTAR-6 cesium clock.

Parameteric frequency stability results are obtained by comparing the NAVSTAR-1 quartz stability with the NAVSTAR-6 cesium stability, which is presented by Figure 13. The results of this comparison are summarized in Table 1.

Table 1

NAVSTAR-1 QUARTZ CLOCK
COMPARISON WITH NAVSTAR-6 CESIUM CLOCK PERFORMANCE

SAMPLE TIME		IMPROVEMENT WITH CESIUM
900	seconds	FACTOR OF 2
2	hours	1 ORDER OF MAGNITUDE
1	day	2 ORDERS OF MAGNITUDE
10	days	FACTOR OF 300

106

NAVSTAR-6 RUBIDIUM RESULTS

On-orbit frequency stability results will be presented for one of the three rubidium clocks onboard the NAVSTAR-6 SV. The fourth clock, a cesium, was first activated, and operated from May, 1980 until early in 1984. The rubidium clock was activated in Feburary, 1984, and was operated for six months. This rubidium clock was deactivated because of degraded performance.

Frequency offsets for the NAVSTAR-6 rubidium clock are presented in Figure 14. Inspection of these data indicates an initial positive aging rate, which lasted for about 1-week, followed by a long trend with a negative aging rate. It is postulated that the initial positive aging rate is due to a transient.

The frequency data was edited to remove the transient and other outliers. The remaining data (Figure 15) was fitted with a linear frequency model. The residuals to this linear frequency model are presented in Figure 16. The aging rate value obtained was -8.2PP10(14)/day, which is lower than expected for the rubidium clocks. The RMS frequency noise was 1.4PP10(12), which is higher than expected.

Short- and long-term stability results are presented in Figure 17. The best after-the-fact aging term has been removed from the data for the long-term frequency stability determination. For the short-term analysis, the effect of the aging rate correction is small enough to be neglected. The short term stability results indicate 1.8PP10(12) for a 900-second sample time. For a 2-hour sample time, the stability was 1.3PP10(12). The long-term stability results indicate a 4.2PP10(13) stability for a 1-day sample time, which remains essentially constant for sample times from 2 to 10 days.

NAVSTAR-8 RUBIDIUM RESULTS

The NAVSTAR-8 spacecraft (SC) was launched on July 14, 1983, as part of the GPS Phase I constellation. NAVSTAR-8 is equipped with three rubidium clocks and one cesium clock. One of the three rubidium clocks was activated shortly after launch and has been the operational clock for NAVSTAR-8 from launch to the present time.

The rubidium clock currently in use onboard NAVSTAR-8 has additional temperature control which is provided by a Thermo Electric Device (TED). Preliminary analysis of temperature correlations for other NAVSTAR rubidium clocks has indicated a temperature coefficient on the order of 1.96PP10(12)/degree C.

The NAVSTAR-8 rubidium clock offset data analyzed is presented by Figure 18. Four adjustments in offset or clock frequency are present in the NAVSTAR-8 data. The first is a change in frequency which was a result of a C-field adjustment (September,1983). The second change was in clock offset as a

result of a phase adjustment (Feburary, 1984). The third change (July, 1984) is another frequency adjustment with the fourth change (August, 1984) being a phase adjustment after the on-board cesium clock was cycled on and off for a period of hours.

By correcting for the adjustments in time and frequency, a continuous frequency is obtained as presented by Figure 19. A linear frequency model was fitted to the entire data span. This fit resulted in an average aging rate of -3.2PP10(13)/day for the entire span. Inspection of the residuals indicates the presence of a systematic behavior in the frequency. Careful analysis of the residuals indicated a change in aging rate near January, 1984. Because of this apparent change, a linear frequency model was fit to the data from January, 1984 until June, 1984. Then this model was back-dated to the beginning of the NAVSTAR-8 clock data. The residuals to the entire span of current data were computed and are presented to Figure 20.

The residuals to the data span from August, 1983 until June, 1984 indicate a possible long-term effect which lasted from August through December 1983. On July 12, 1984 an adjustment in TED temperature of three degrees was performed. Shortly thereafter a change in aging rate of the NAVSTAR-8 rubidium clock was measured.

NAVSTAR-8 rubidium frequency stability during a pass was evaluated using data from January, 1984 until September, 1984. The database was partitioned into 5-day sets for the stability calculations. This procedure is fully described in reference 6. The stability calculations were made for sample times of 900-seconds to 2-hours, in 900-second increments.

Frequency stability results for 900- and 2700-second sample times are presented in Figure 21 and 22. Analysis of these results indicates that an unexpected phenomena is occuring for the NAVSTAR-8 rubidium clock. The results indicate a two-state stability. This result is more evident for the 2700-second sample time than for the 900-second sample time. All checks to date have not produced a satisfactory explanation to this observed phenomena.

A short-term frequency stability profile for the NAVSTAR-8 rubidium clock is presented by Figure 23. This curve shows an uncharacteristic peak for a typical clock, at a 1-hour sample time.

Long-term frequency stability results for the NAVSTAR-8 rubidium clock are presented by Figure 24. A 280-day set was used for these stability results, which is more than a factor of 10 longer than the longest sample time. These results indicate a stability of 7PP10(14) for a 1-day sample time, which decreases to 5.5PP10(14) for a 3-day sample time, followed by an increase to 8PP10(14) for a 10-day sample time. These stability results

were achieved assuming an accurate knowledge (after-the-fact) of the aging rate of the NAVSTAR-8 rubidium clock. In addition the assumption that the aging rate was constant is necessary. Occasional unpredictable changes in aging rate can occur, which will degrade long- and short-term rubidium clock performance.

A sensitivity analysis of the NAVSTAR-8 long-term frequency stability to aging rate was computed using a 95-day subset, and is presented by Figure 25. The stability analysis was computed with an increment of aging rate of 2 nanoseconds/day/day. The best stability was obtained using an aging rate of -28 nsec/day/day. Analysis of these results indicates a low sensitivity to aging rate errors for a 1-day sample time, with dramatically increasing sensitivity as the sample time increases to 10 days. The importance of this analysis is readily seen when GPS is used in a prediction mode. An aging rate value of some fashion must be assumed during the predicted span of time.

NAVSTAR 1/3/4/5/6/8 RESULTS

A composite of the NAVSTARs 1,3,4,5,6, and 8 results is presented in Figure 26, using previously presented results (6) in addition to those presented in this paper.

These results indicate that GPS NAVSTAR atomic clocks are stable to 2PP10(12) for a 900-second sample time, and improve with longer sample times, with better than 2PP10(13) for a 1-day sample time. For sample times longer than 1-day, the cesium clocks show a spread in stabilities from 8 to 10PP10(14). The rubidium clocks show a spread in stabilities from 5 to 25PP10(14). The long-term stability presentation has the best after-the-fact aging effect removed for all the rubidium clocks analyzed. This was not necessary for the cesium clocks since the aging term for cesium clocks is essentially zero.

REFERENCES

1. Buisson, J.A., and McCaskill, T.B., "TIMATION Navigation Satellite System Constellation Study", NRL Report 7389, June 27, 1972.

2. Easton, R.L., et al, "The Contribution of Navigation Technology Satellite to the Global Positioning System", NRL Report 8360, December 28, 1979.

3. Bartholomew, C.A., "Satellite Frequency Standards", Navigation: Journal of the Institute of Navigation, 25(2), 113-120 (Summer, 1978).

4. McCaskill, T.B., and Buisson, J.A., "NTS-1 (TIMATION-III) Quartz- and Rubidium-Oscillator Frequency Stability Results", NRL Report 7932, December 12, 1975.

5. Buisson, J.A., et al, "GPS NAVSTAR-4 and NTS-2 Long Term Frequency Stability and Time Transfer Analysis", NRL Report 8419, June 30, 1980.

6. McCaskill, T.B., Buisson, J.A., and Stebbins, S.B., "On-Orbit Frequency Stability Analysis of the GPS NAVSTARs 3 and 4 Rubidium Clocks and NAVSTARs 5 and 6 Cesium Clocks", Proceedings of the Fifteenth Annual Precise Time and Time Interval (PTTI) Applications and Planning Meeting, December 6-8, 1983.

7. Allan, D.W., "Clock Characterization Tutorial", Proceedings of the Fifteenth Annual Precise Time and Time Interval (PTTI) Applications and Planning Meeting", December 6-8, 1983.

8. ..rnes, J.A., et al, "Characterization of Frequency Stability", IEEE Transactions on Instrumentation and Measurement", Volume IM-20, No. 2, May, 1971.

9. Luck, J.Mc., "Construction and Comparison of Atomic Time Scale Algorithms", TR#32, Division of National Mapping, Canberra, Australia, 1983.

10. Allan, D.W., et al, "Statistics of Time and Frequency Data Analysis", TIME AND FREQUENCY: Theory and Fundamentals, National Bureau of Standards Monograph 140, Boulder, Colorado, 80302.

11. McCaski l, T.B., "Two Point Time Prediction Error", NRL Space Applications Branch Internal Memorandum #153, 19 April 1979.

NAVAL RESEARCH LAB (NRL)

CLOCK ANALYSIS FLOW CHART
FOR NAVSTAR GPS
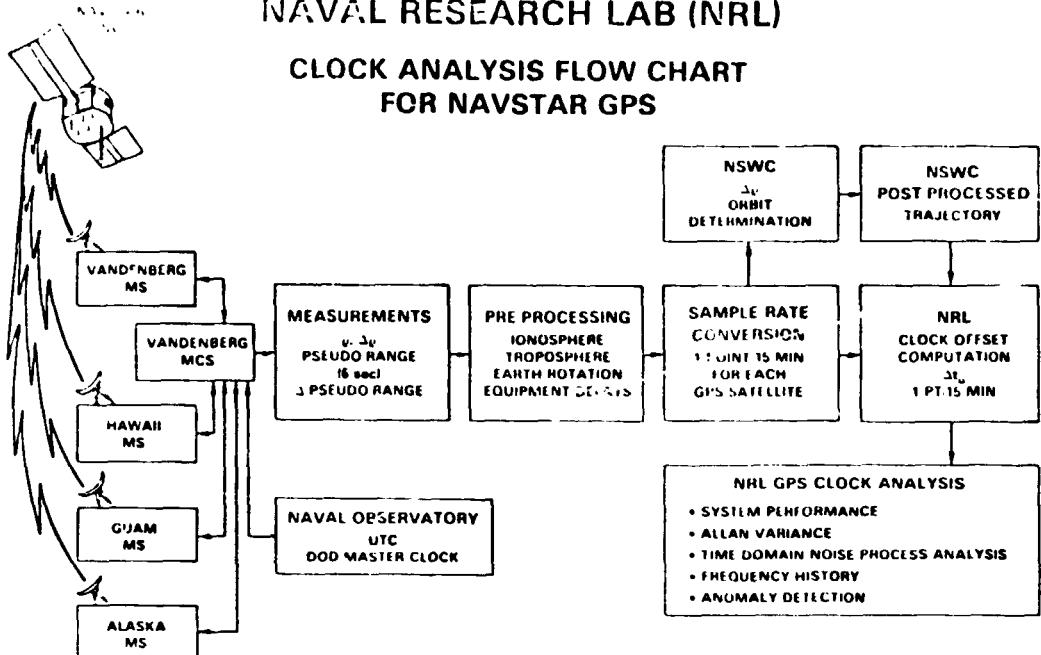
Figure 1

TIME DOMAIN
FREQUENCY STABILITY PROFILE

Figure 2

111

CLOCK

FREQUENCY STABILITY

Figure 3

CLOCK PREDICTION ERROR (METERS)

FREQUENCY STABILITY
$\sigma_y (\tau)$

$\tau =$ CLOCK PREDICTION TIME

$\tau =$ SAMPLE TIME

CLOCK PREDICTION ERROR (NANOSECONDS)
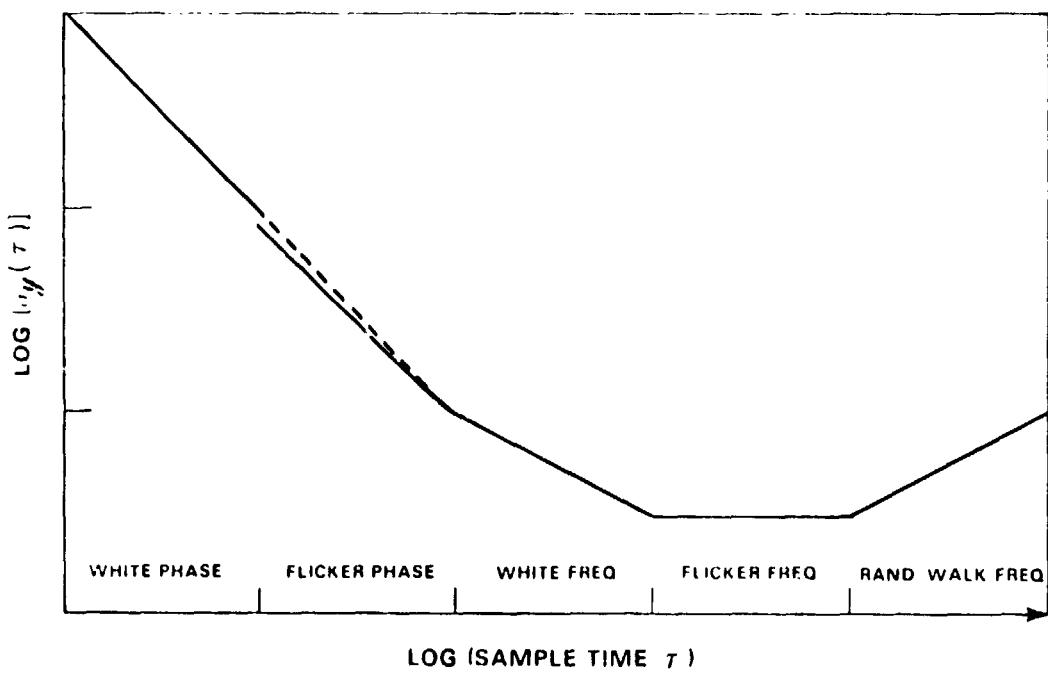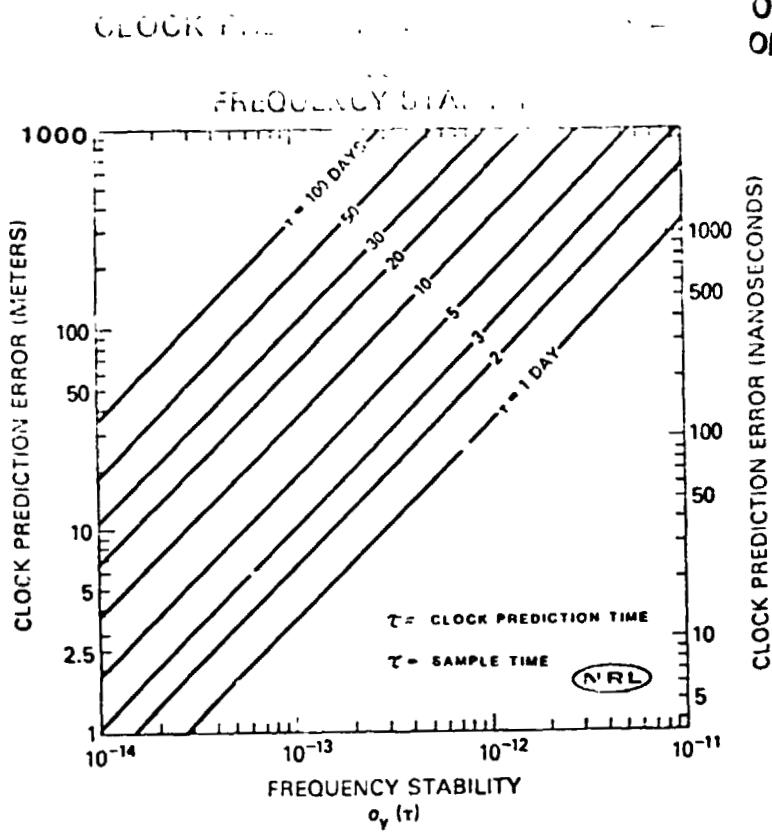
Figure 3

FN 4

CLOCK DIFFERENCE BETWEEN
GPS MS VANDENBERG
AND NAVSTAR #1

MICROSECONDS

DAYS 1982

NRL

Figure 4

112
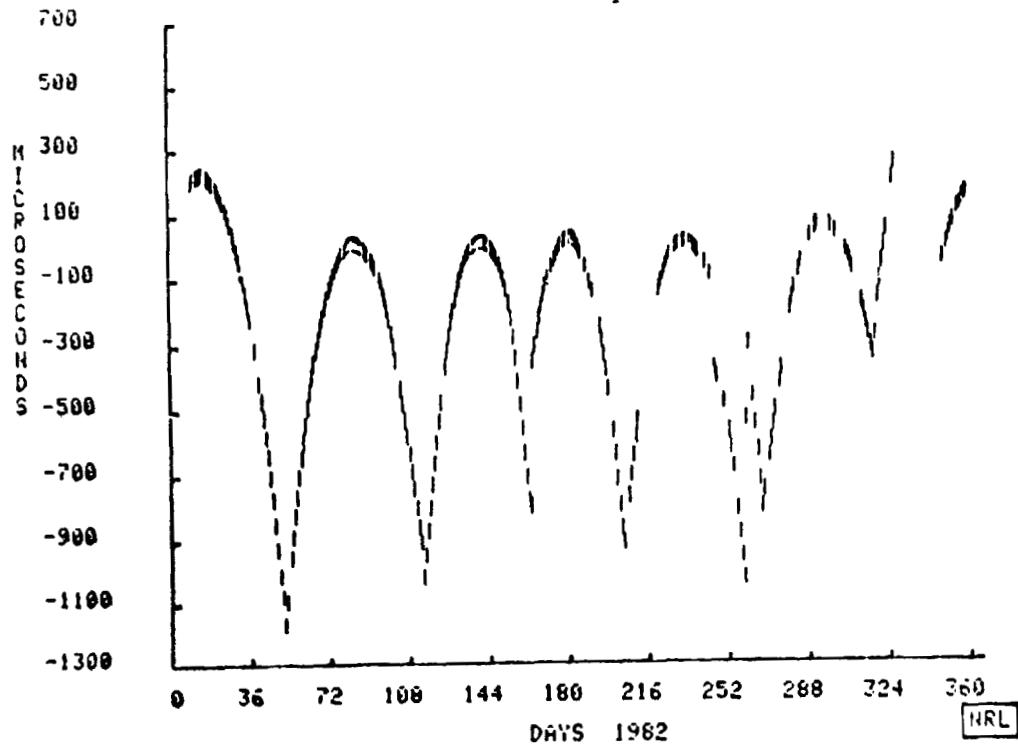
GPS QUARTZ FREQUENCY OFFSET
NAVSTAR 1
Vandenberg Monitor Station

MODIFIED JULIAN DAYS
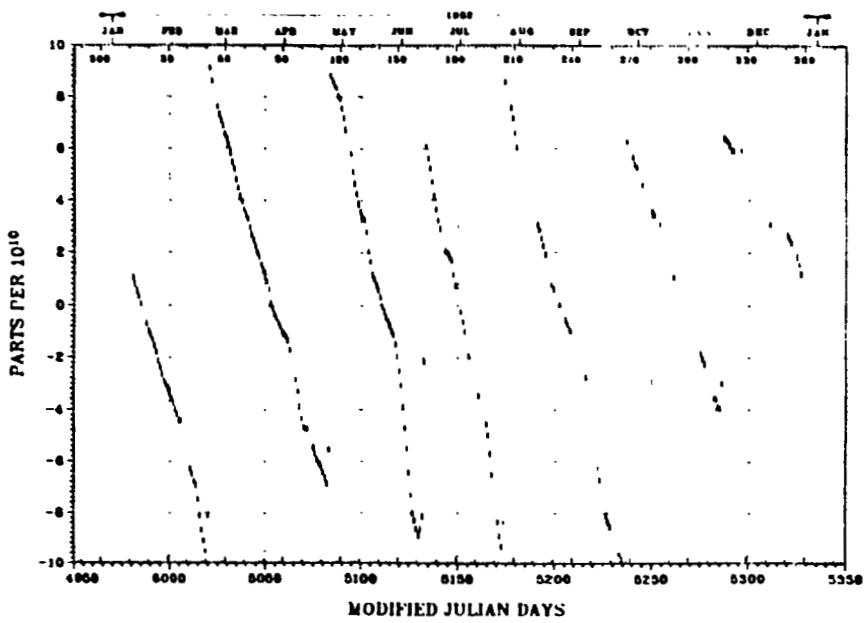
Figure 5

GPS QUARTZ FREQUENCY PURGED AND CORRECTED OFFSET
NAVSTAR 1
Vandenberg Monitor Station
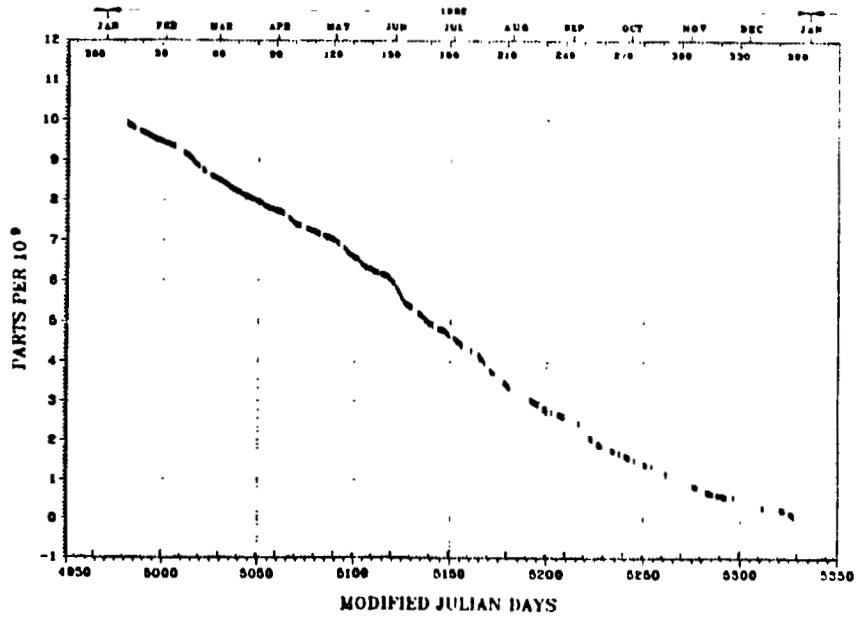
MODIFIED JULIAN DAYS

Figure 6

113

GPS QUARTZ FREQUENCY LINEAR RESIDUALS
NAVSTAR 1
Vandenberg Monitor Station
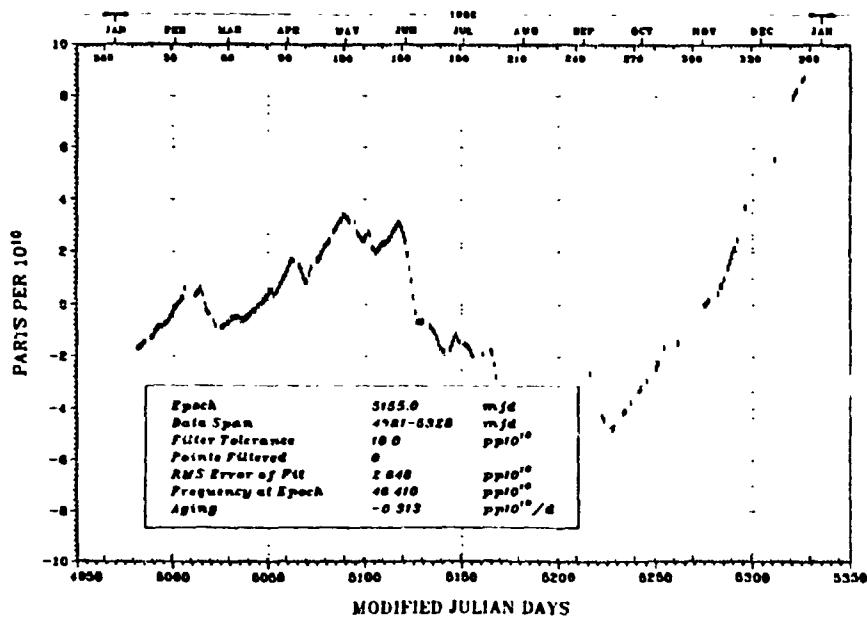
Figure 7

GPS QUARTZ FREQUENCY LINEAR RESIDUALS
NAVSTAR 1
Vandenberg Monitor Station

Figure 8

114
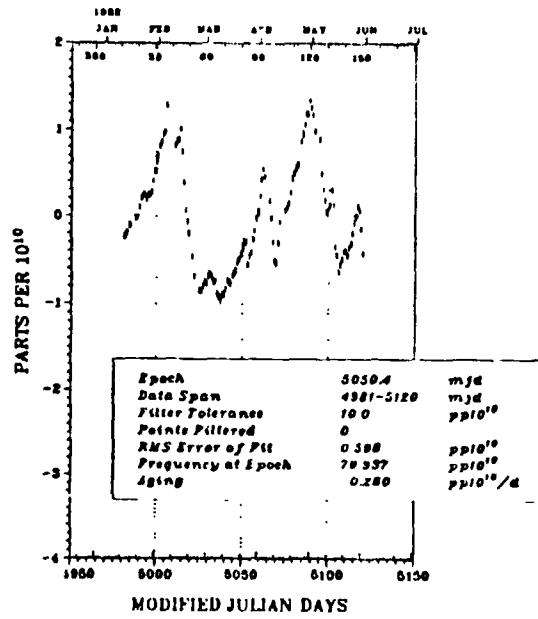
GE - QUARTZ FREQUENCY QUADRATIC RESIDUALS
NAVSTAR 1
Vandenberg Monitor Station

Epoch	5224.4	mjd
Data Span	5120-5329	mjd
Filter Tolerance	10.0	pp10^10
Points Filtered	0	
RMS Error of Fit	0.604	pp10^10
Frequency at Epoch	20.633	pp10^10
Aging	-0.276	pp10^10/d
Aging Rate	0.001	pp10^10/d²

MODIFIED JULIAN DAYS
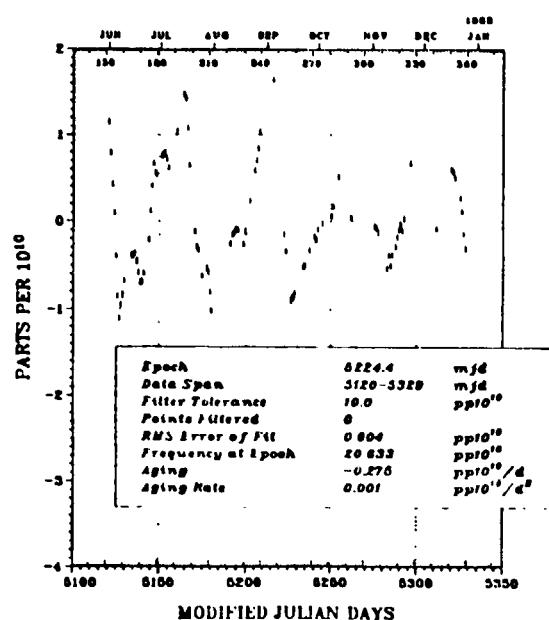
Figure 9

GPS
CLOCK ANALYSIS
VANDENBERG VS NAVSTAR 1

TIME IN DAYS 1982
SAMPLE TIME   900 SEC
5-DAY DATA SETS

Figure 10

NRL

31-MAY-84

115

GPS
CLOCK ANALYSIS
VANDENBERG VS NAVSTAR 1
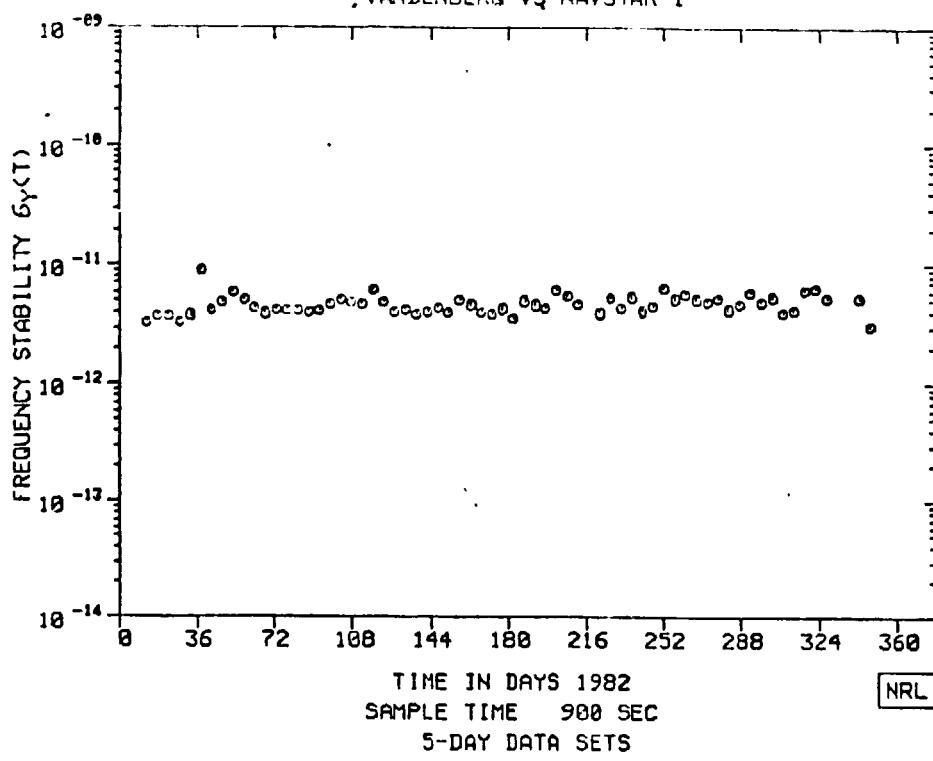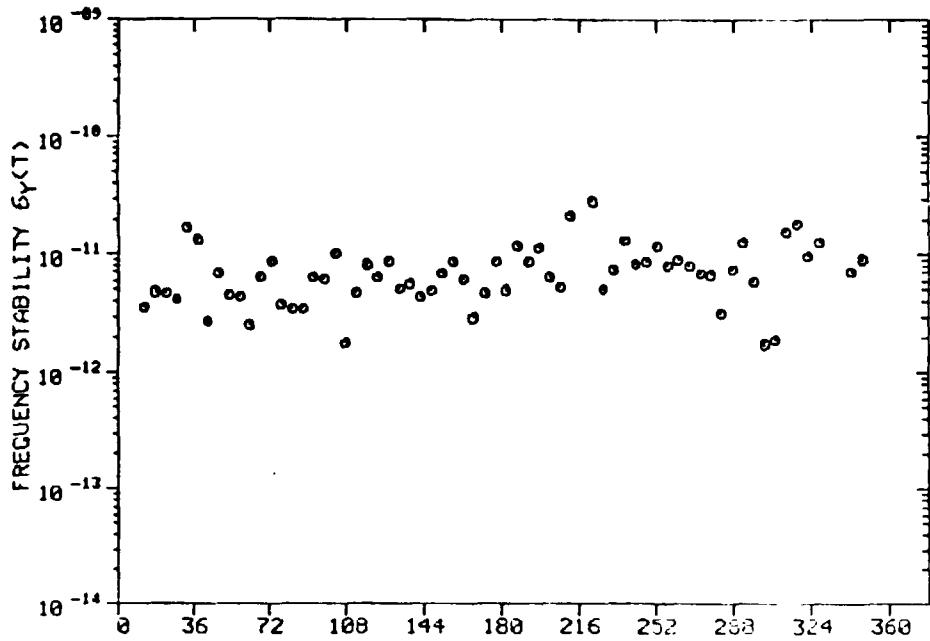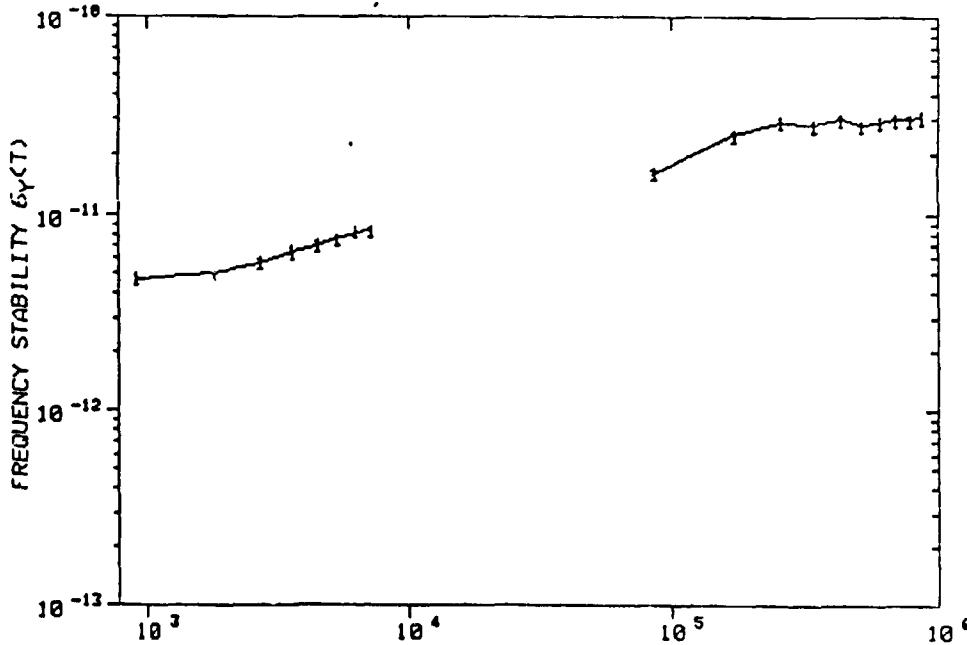
TIME IN DAYS 1982
SAMPLE TIME 7200 SEC
5-DAY DATA SETS

Figure 11

31-MAY-84

GPS
CLOCK ANALYSIS
VANDENBERG VS NAVSTAR 1
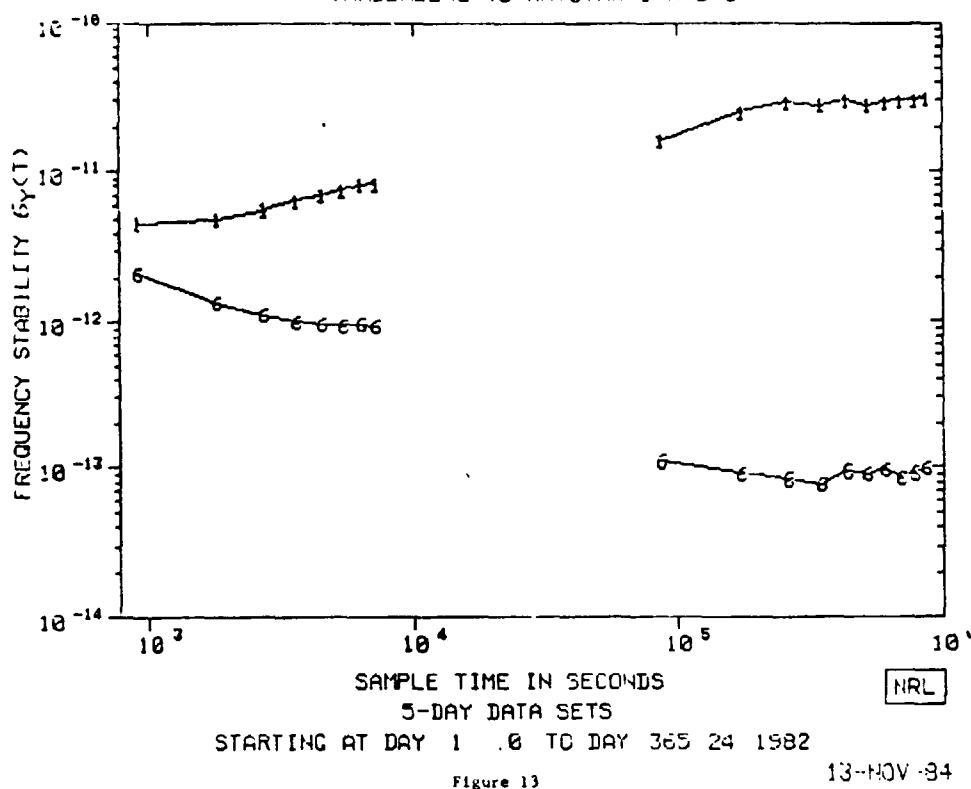
SAMPLE TIME IN SECONDS
5-DAY DATA SETS
STARTING AT DAY 11 .14 TO DAY 361 .14 1982

116

CLOCK ANALYSIS
VANDENBERG VS NAVSTAR 1 AND 6

SAMPLE TIME IN SECONDS
5-DAY DATA SETS
STARTING AT DAY 1 .0 TO DAY 365 24 1982

Figure 13

13-NOV-84

NRL

GPS RUBIDIUM FREQUENCY FILTERED OFFSET
NAVSTAR 6
Vandenberg Monitor Station

Epoch	5849.0	mjd
Data Span	5703-5994	mjd
Filter Tolerance	2.00	pp10¹²
Points Filtered	3	
RMS Error of Fit	1.847	pp10¹²
Frequency at Epoch	-39.522	pp10¹²
Aging	-0.077	pp10¹²/d

MODIFIED JULIAN DAYS

Figure 14

117
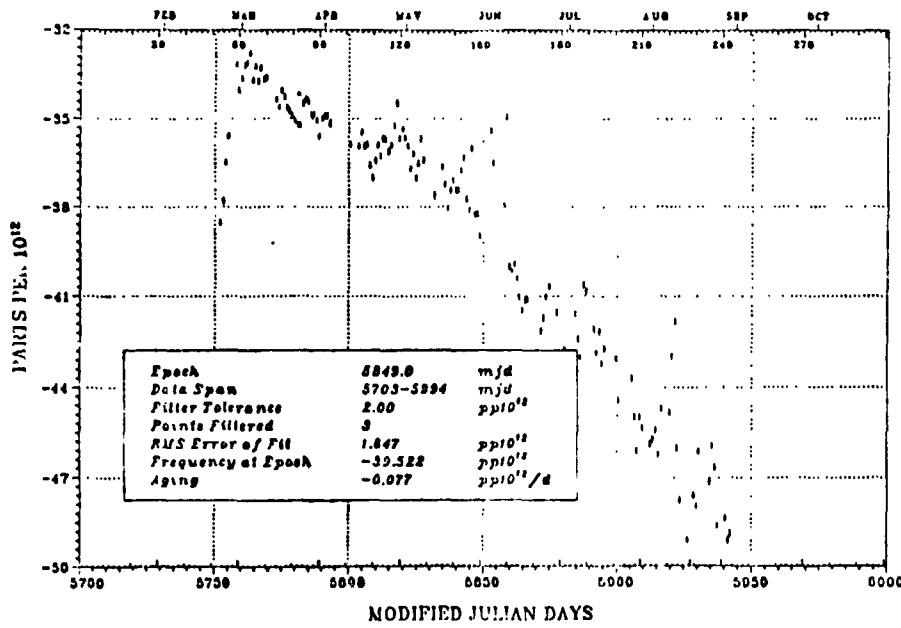
GPS RUBIDIUM FREQUENCY FILTERED OFFSET
NAVSTAR 6
Vandenberg Monitor Station
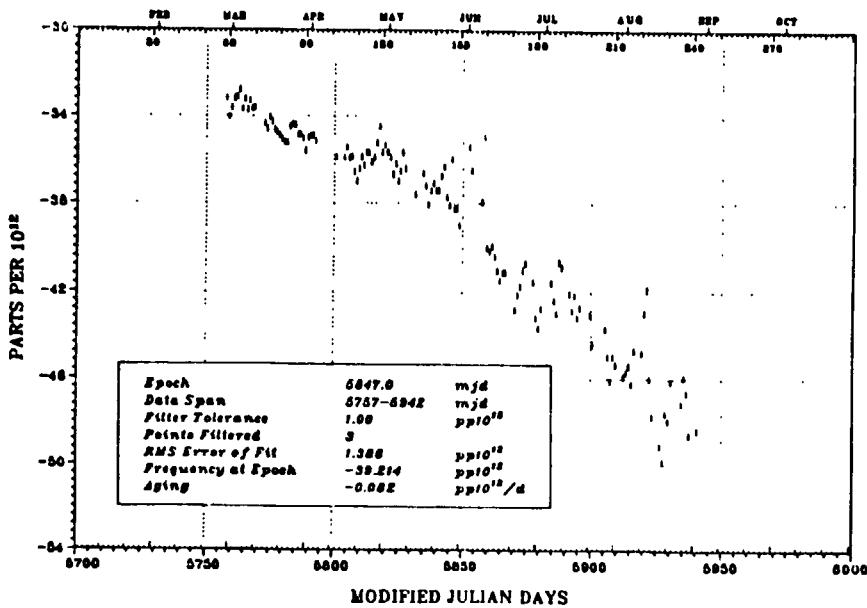
Figure 15

GPS RUBIDIUM FREQUENCY LINEAR RESIDUALS
NAVSTAR 6
Vandenberg Monitor Station

Figure 16

118
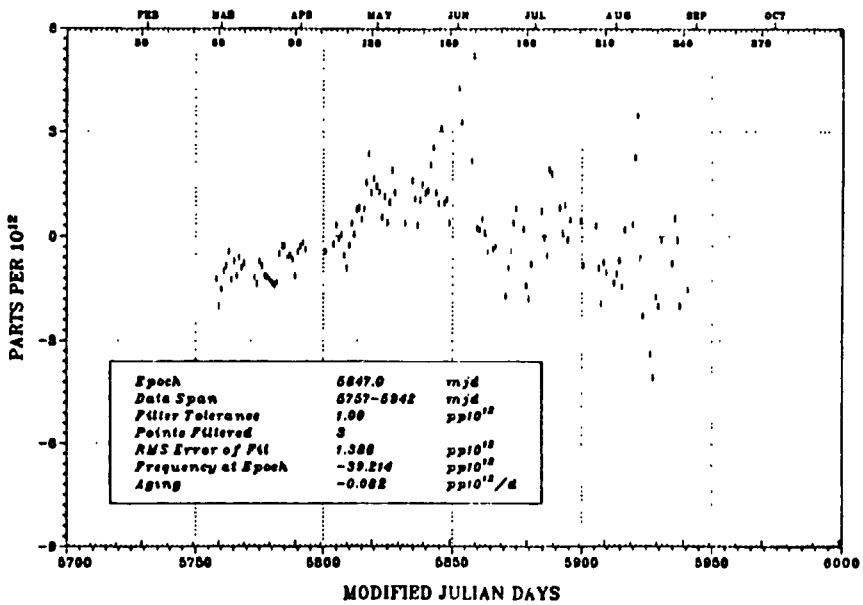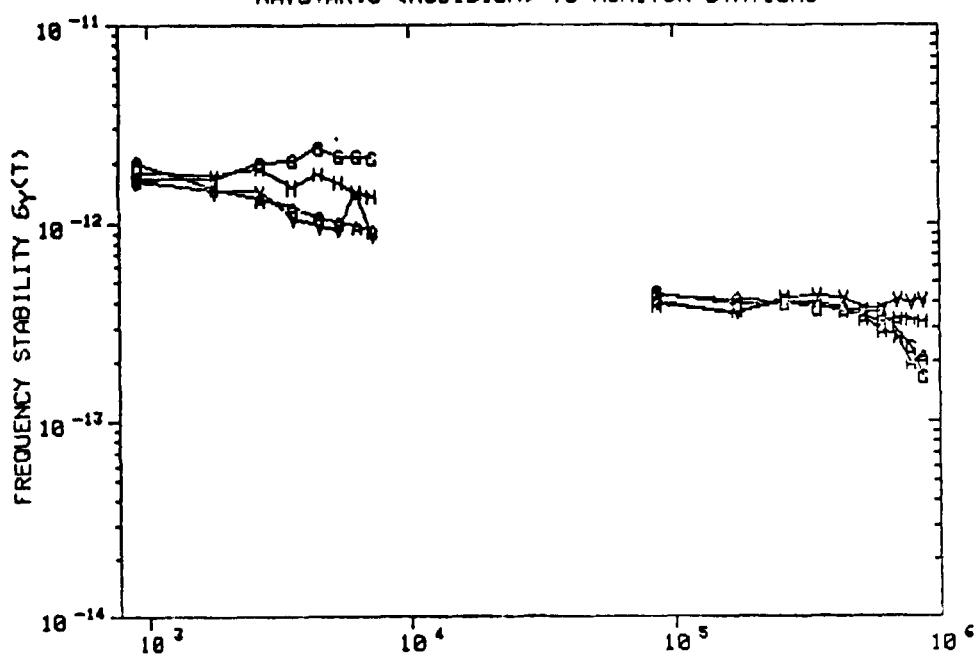
GPS
CLOCK ANALYSIS
NAVSTAR.6 (RUBIDIUM) VS MONITOR STATIONS

SAMPLE TIME IN SECONDS
5-DAY DATA SETS
STARTING AT DAY 52 .7 TO DAY 217.19 1984

NRL

09-NOV-84

Figure 17

GPS RUBIDIUM PHASE OFFSET
NAVSTAR 8
Vandenberg Monitor Station

MODIFIED JULIAN DAYS

Figure 18

119
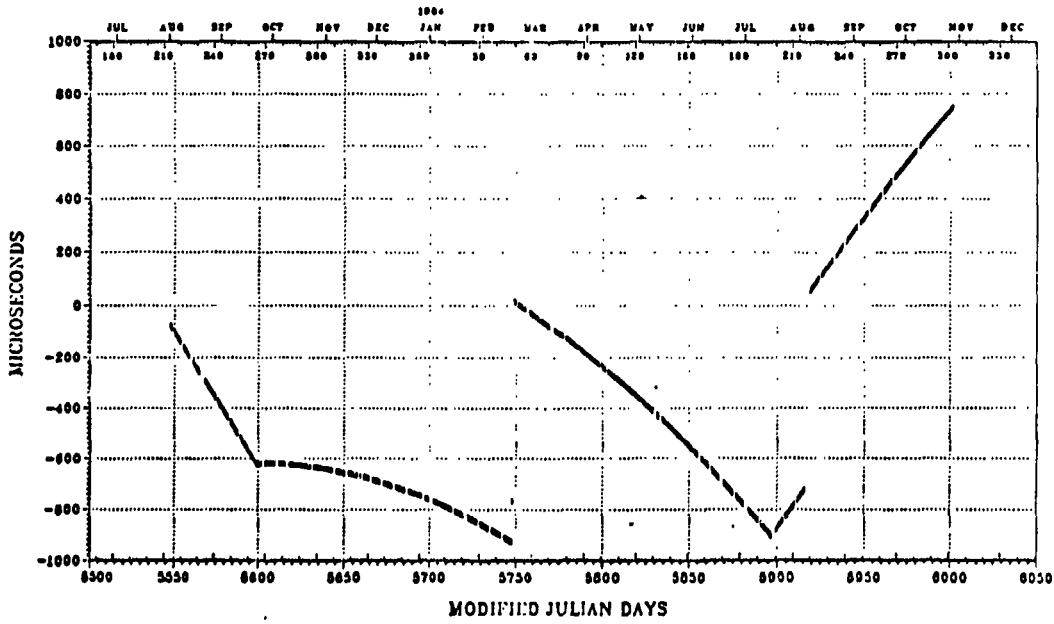
GPS RUDIDIUM FREQUENCY CORRECTED AND PURGED OFFSET
NAVSTAR 8
Vandenberg Monitor Station
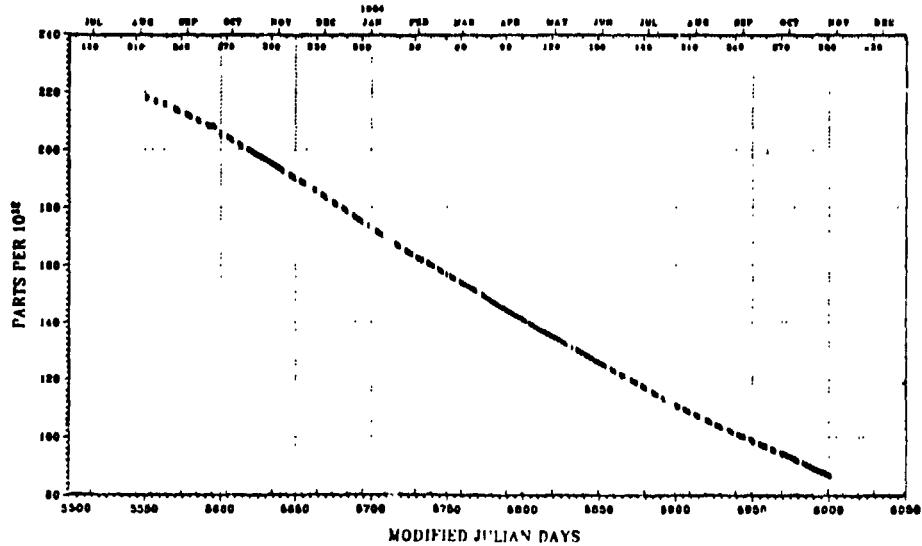
Figure 19

GPS RUBIDIUM FREQUENCY ASYMPTOTIC LINEAR RESIDUALS
NAVSTAR 8
Vandenberg Monitor Station

Figure 20

Figure 21

TIME IN DAYS 1984
SAMPLE TIME   900 SEC
5-DAY DATA SETS

NRL
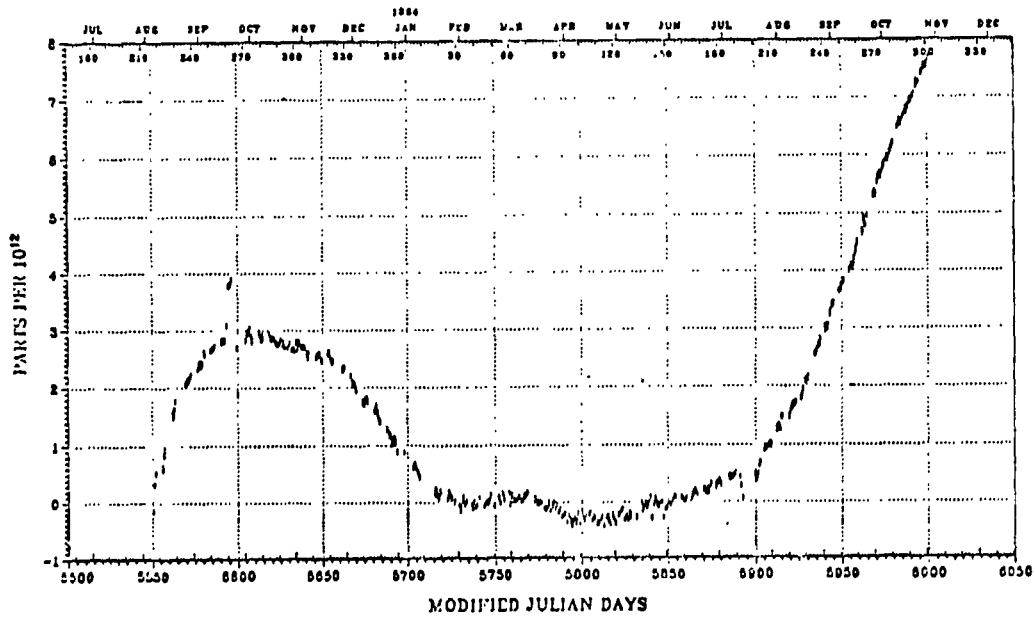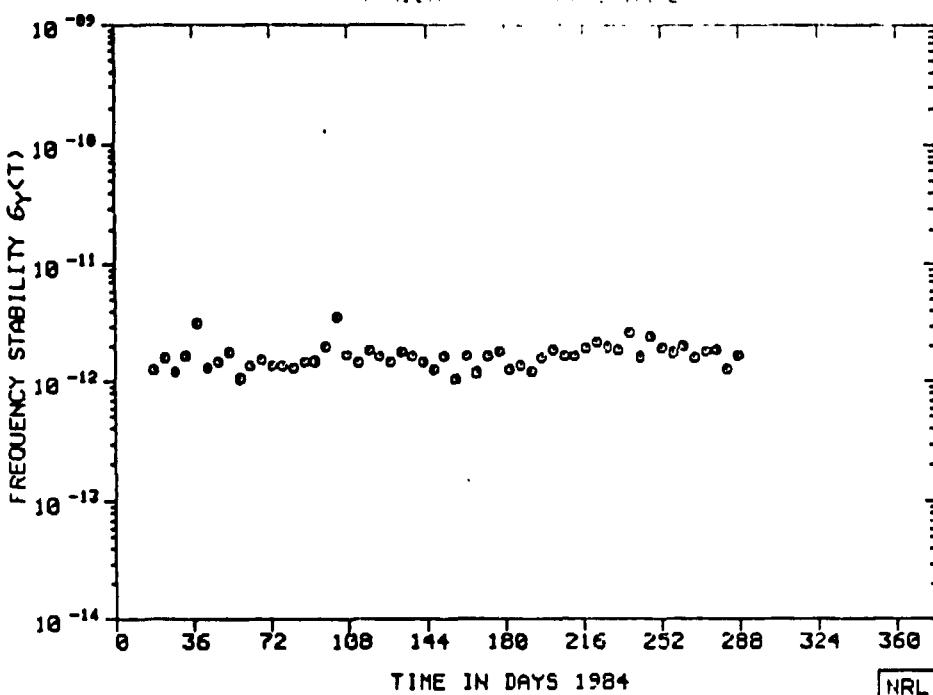
02-NOV-84

GPS
CLOCK ANALYSIS
VANDENBERG VS NAVSTAR 8

Figure 22

TIME IN DAYS 1984
SAMPLE TIME   2700 SEC
5-DAY DATA SETS

NRL

02-NOV-84

121

GPS
CLOCK ANALYSIS
NAVSTAR 8 VS MONITOR STATIONS (MS)

FREQUENCY STABILITY ($\sigma_y(\tau)$)

SAMPLE TIME IN SECONDS
5-DAY DATA SETS

Figure 23

GPS
CLOCK ANALYSIS
NAVSTAR 8 VS MONITOR STATIONS (MS)

FREQUENCY STABILITY ($\sigma_y(\tau)$)

SAMPLE TIME IN SECONDS
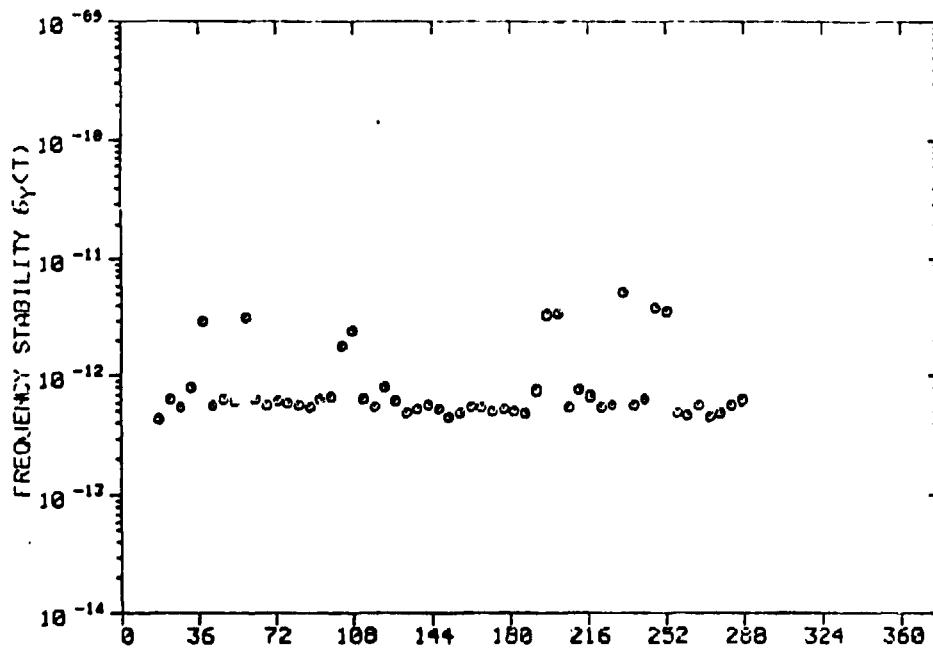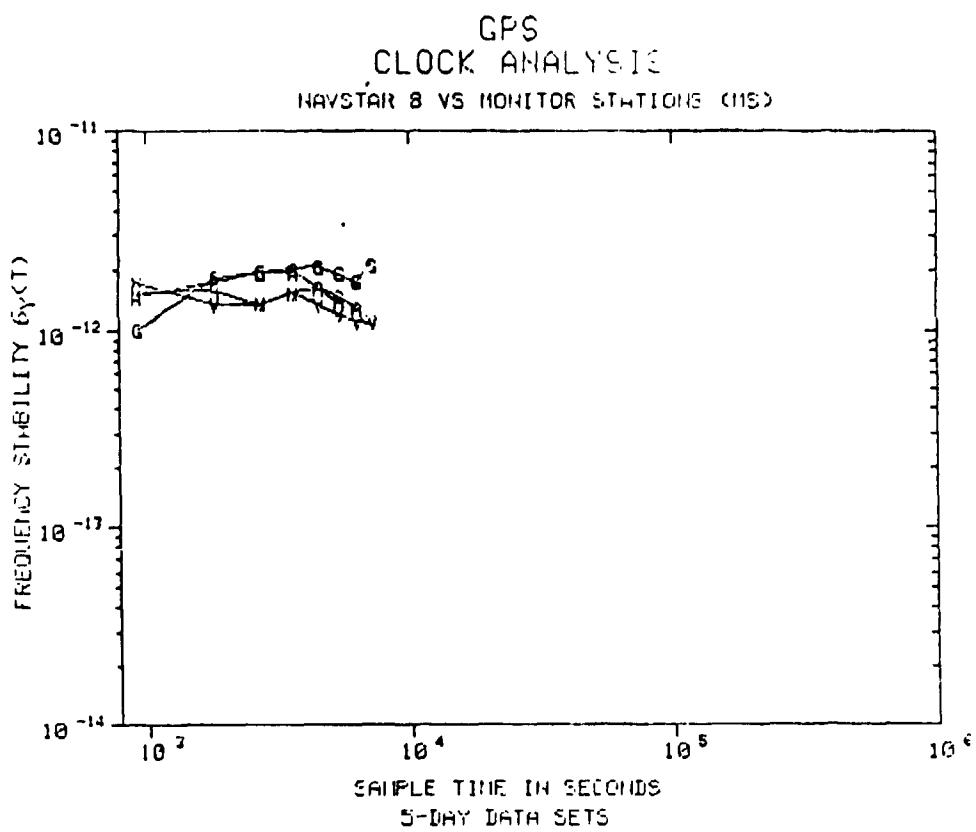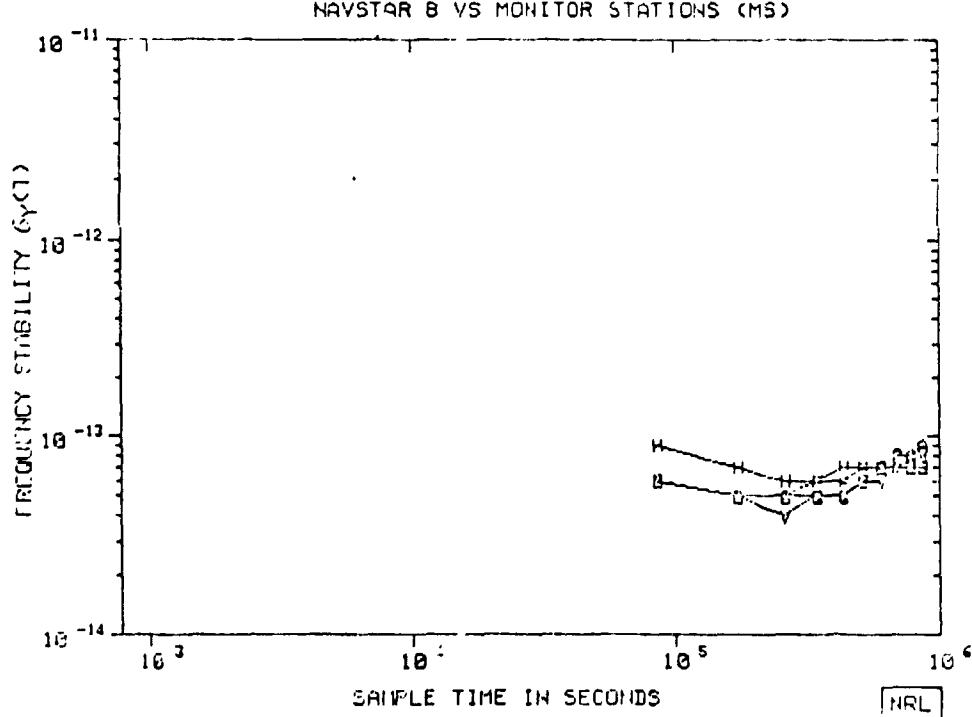
NRL

STARTING AT DAY 16.4 TO DAY 295.9 1984

07-NOV-84

Figure 24

122

NAVSTAR 8 RUBIDIUM - VANDENBERG MS
DAY 270-365 1983

Figure 25

**GPS
CLOCK ANALYSIS**

STATION ENSEMBLE VS NAVSTAR 1/3/4/5/6/8
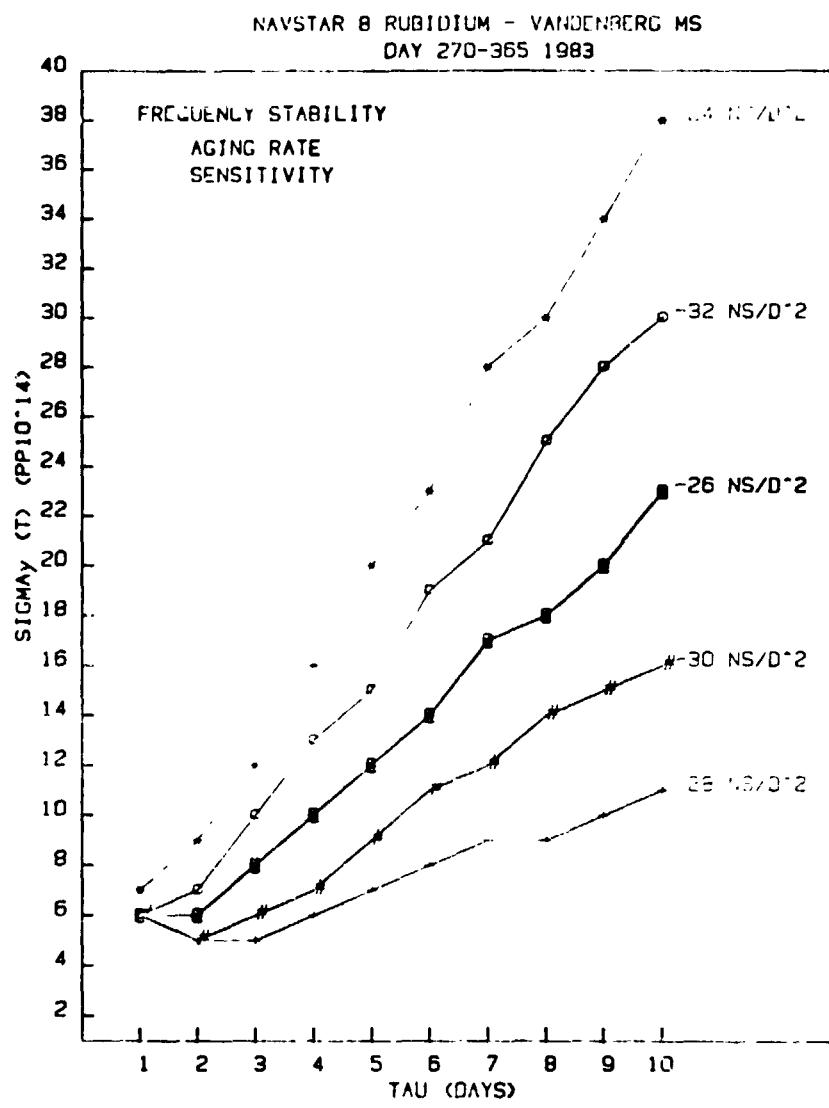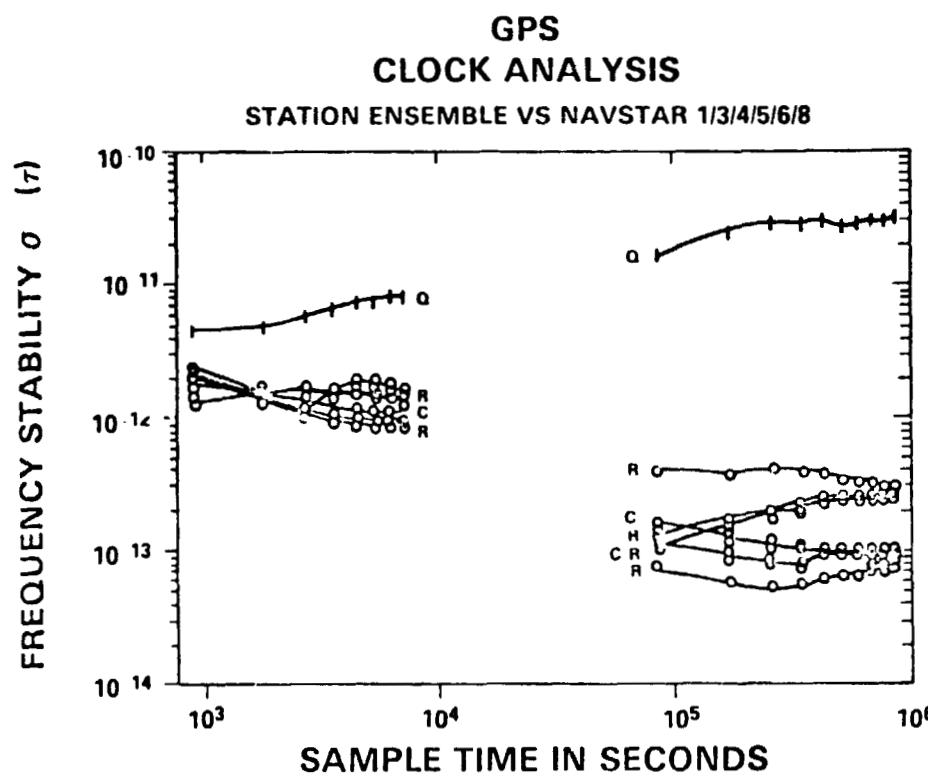
Figure 26

QUESTIONS AND ANSWERS

PHIL TALLEY, AEROSPACE CORPORATION: I would like to comment that there is a post-correlation for those variations in the frequency that you can see with solar activity, and I have looked at that in some depth, and every time there is a significant case that's being noted, there will be, within the next twenty-four hours, a significant change in the aging rate, and they correlate very closely with the changes in aging rate that you showed in your curve. I mentioned it to Jim Buisson earlier, but we can discuss that in some depth later. That is not an inherent quartz characteristic. It is induced, and we think we know to what extent.

MR. McCASKILL: Thank you for your comments, Phil.

DAVID ALLAN, NATIONAL BUREAU OF STANDARDS: There was a question earlier in my mind with regard to the deviations in sigma at 900 seconds. I wondered if those could be induced by a deviation in one of the other spacecrafts, since the Kalman filter forces the error somewhere in the system. If you have a problem in another part of the system, it can show up on another spacecraft, and not be on that spacecraft. It might be worth looking at the correlations of some bad performance on other spacecrafts at those times when those events occurred.

MR. McCASKILL: That would, of course, be true if we were using the orbital elements that were generated by the GPS master control station. We are not. We are using an after-the-fact smoothed orbit, which is determined for each of the spacecraft, the NAVSTAR 8 Rubidium in this case.

The fluctuations on NAV 8 showed up first at about 900 seconds, and they seem to increase as you go out to around 2,700 seconds sample time. We have looked, but at the moment we have still not been able to isolate the cause.

GERNOT WINKLER, NAVAL OBSERVATORY: Would you repeat the performance concerning one day and ten days? It appears that the Rubidium clock is better than the Cesium clock. Is that correct?

MR. McCASKILL: The NAVSTAR 8 Rubidium clock with the additional thermal control does give a better stability at a one day sample time. That's assuming that you know what the aging rate is going to be. We have determined the aging rate after the fact. If you do not know what the aging rate is, you can get results that don't look like this, but they follow an apparent random walk FM process.

Please keep in mind that we are determining, on the rubidium clocks, and on the quartz, the aging rate after the fact. On the cesium clocks, the stability measurements were made without any aging correction at all. Cesiums don't age.

RUBIDIUM AND CESIUM FREQUENCY STANDARDS
STATUS AND PERFORMANCE ON THE GPS PROGRAM
HARRY BETHKE, DALE RINGER AND M. VAN MELLE

Rockwell International
Satellite System Division
Seal Beach, California

ABSTRACT

This paper describes the on-orbit operational performance of the frequency standards on the GPS 1-10 Navstar satellites. The history of the Rb frequency standards showing the improvements incorporated at various stages of the program and the corresponding results are presented. Also presented is the operational history of the Navstar Cesium Frequency Standards. The frequency standards configuration data presented will cover the chronology of events from the concept validation satellites, Navstars 1-10, starting in 1978 to the present, including the configurations of clocks to be used on the GPS Production Program.

Data will be presented additionally showing the results of long-term laboratory testing of a production Rb frequency standard with the necessary data taken to calculate Delta F, drift, time error, and Allan variance.

INTRODUCTION

The evolution of the Rb frequency standards (RFS) on the GPS program started with the Block I concept validation program beginning with a proposal program in 1973, followed by the (GPS 1-8) prototype space vehicle contract in 1974. The full scale developmental (GPS 9-11) models, contracted in 1978, provided both navigation and nuclear detection capability. The production qual vehicle (GPS-12) was contracted in 1980, and the production vehicles (GPS 13-40) in 1982. During the proposal phase of this program, the on-board frequency standards were considered the most critical item within the GPS navigational system for achieving user position accuracy. Therefore, a considerable amount of effort was devoted to the frequency standards. To minimize the risk to the GPS program on this critical item, the initial GPS vehicles (GPS 1 through 3) incorporated three Rb frequency standards, each with a backup mode. This was achieved by operating a high performance VCXO without Rb reference. This design concept resulted in the redundancy potential of six frequency standards per vehicle. Later space vehicles, starting with GPS 4, included an additional cesium frequency standard, also with a backup VCXO mode. This extended redundancy was deemed necessary in lieu of the more conventional dual redundancy. The actual on-orbit GPS frequency standard operating history, shown in Figure 1, illustrates the results of this hardware implementation.

As of mid-1973, no space-borne suppliers of atomic frequency standards existed. Therefore, Rockwell pursued a plan to review all credible candidates for conversion from commercial to aerospace units. The plan to develop a Rb frequency standard was to select the best available voltage-controlled crystal oscillator (VCXO) and phase lock it to a small Rb standard. The design was to be such that if the Rb atomic physics package failed, the VCXO could be utilized as a backup device. This condition would still maintain frequency stability for a specific period of time to maintain navigation accuracy over the test area. The development of this Rb frequency standard started during the GPS proposal phase. Efratom commercial units were procured and underwent the following modifications and tests:

1. Commercial parts were replaced with high reliability parts.

2. One unit was repackaged to allow thermal dissipation in a vacuum.

3. Fabrication of special Rb components with multiple buffer gases were designed to reduce temperature sensitivity.

4. The unit was repackaged to accommodate the GPS boost vibration environment.

5. One unit was subjected to radiation tests to verify operation to GPS requirements.

6. The National Bureau of Standards was contracted to perform both ambient and vacuum stability tests.

128

This plan has resulted in the development of very stable, high-reliability Rb frequency standards, but not without the normal development problems associated with new hardware. As this program progressed, ten different models of the Rb standards have evolved. The part numbers of the different models of each frequency standard are shown in Figure 1. The first Rb standards on Navstar's 1 and 2 accumulated a total of 44 months of operation with six failures, which necessitated switching to the backup mode (1978-1980). The last 42 months of GPS Rb clock operation on Navstar's 5, 6, and 8 have been failure free. This vast improvement can be mostly attributed to the clock improvements as the program progressed.

Although Rockwell was not directly involved in the early stages of development of the cesium frequency standards, the on-orbit chronology of events were very similar to the Rb clocks. The first engineering development model failed a few hours after turn-on. The problem was corrected in the pre-production models (PPM) as verified by a total of 77 months of operation for two units with only one failure. This failure will be addressed in the subsequent paragraphs as well as a description of the corrective actions taken to eliminate the problem.

RFS ORBITAL ANOMALIES

On-orbit operation data of GPS Rb frequency standards started with Navstar 1 in March, 1978, followed by Navstar 2 in May, 1978. The original Dash 001 part number clocks were used in Positions 1, 2, and 3 on Navstar 1 and in Positions 3 on Navstar 2. Dash 002 clocks were used in Positions 1 and 2 and Navstar 2. The only difference in the Dash 002 from the Dash 001 clocks was a time constant change in the servo control loop. As shown in Figure 1, three types of problems were experienced:

1. Power supply transformer failures

2. Lamp failures

3. Low frequency oscillation of the VXCO heater control

The operating summary of GPS standards is shown in Table 1. The following paragraphs will address each type of problem, corrective actions taken, and results.

Transformer problems were experienced on both the Dash 001 and Dash 002 standards. The transformer problem was isolated to be a short circuit between the primary and secondary windings, which took time to materialize. After extensive analysis and testing, the cause of the problem was isolated to a number of factors in the transformer design and fabrication processes:

1. The potting compound, used in the transformer, softened the wire insulation.

2. The transformer core, around which the wire was would, had sharp edges and gradually wore through the insulation which has thinned when stretched over the sharp edges on the core.

3. There was an insufficient amount of detail in the transformer assembly and process instructions.

4. The transformer level screening test were inadequate to identify or screen out this type of problem.

The primary corrective actions taken to alleviate this problem are:

1. A new potting resin, compatible with the wire insulation coating, was selected.

2. A very stringent inspection criteria was initiated on all transformer cores.

3. A parylene/RTV coating was applied to the cores.

4. Very detailed fabrication and process instruction procedures were prepared.

5. Each transformer was exposed to a very detailed Acceptance Test Procedure which included post-potting test, thermal cycling, and burn-in testing.

6. Extensive quality inspection controls were instituted.

The new transformer was installed in all Dash 003 and subsequent clocks. Results of this change are very apparent from the data shown on Table 1. A total of 186 months (15.6 years) of on-orbit operation have accumulated with no transformer failures. Referring to Figure 1, note that Frequency Standard 1 on Navstar 3 nas been operating continuously for 70 months (approximately six years); this provides a very high degree of confidence that the transformer problem has been corrected.

The Rb lamp failures were perhaps the most critical on-orbit problem encountered on the early space vehicles. To investigate the problem, a team was assembled that consisted of representatives from Rockwell, the National Bureau of Standards, Duke University, the USAF, Aerospace Corporation, and Efratom. Once the clock failure was established to be the lamp, a plan was initiated to duplicate the on-orbit failures in the laboratory. Lamps were prepared with an intentionally low Rb fill, installed into the physics packages, and subsequently installed into several frequency standards. Laboratory testing on these standards duplicated the on-orbit lamp failures. All units exhibited the same lamp voltage decay characteristics symbolic of the suspected lamp failures as illustrated in Figure 2.

To determine the amount of Rb in the lamps, a three-fold corrective plan of action was instituted:

1. For Rb lamps already built, the fill would be determined by neutron activation.

2. The fill of newly fabricated lamps would be determined by sampled destructive analysis.

3. A calorimetric measurement utilizing a differential scanning calorimeter is now used.

NEUTRON ACTIVATION ANALYSIS OF Rb LAMPS

Neutron activation analysis was one of the methods used to determine the quantity of Rb-87 in the lamps. The procedure is as follows: Lamps are inserted into a nuclear reactor and irradiated with thermal neutrons for about an hour. In addition to the lamps being tested, a special lamp with no Rb, and another lamp with a precisely weighed milligram quantity of Rb metal also are irradiated. The thermal neutrons are absorbed into the Rb in the lamps, producing one or more short-lived radioactive species. The resultant radioactivity is measured by counting with a lithium-drifted germanium gamma ray spectrometer the intensity of certain gamma rays emitted by the activated Rb. The empty bulb provides the background counting rate, and the bulb with a known milligram quantity of rubidium is used to determine the number of counts per second (less background) per milligram of Rb. The amount of rubidium in each lamp then is obtained from the single ratios of counts less background to the known standard. This technique is no longer used due to cost.

DESTRUCTIVE ANALYSIS

Destructive analysis is a method by which the Rb fill of a sample of lamps was made from the same production manifold. Since all of the lamps on the manifold are filled at the same time, it was assumed that the remainder of the lamps had the same fill as the sample. Good results were achieved using this technique. However, the production yield was small. With a manifold of five lamps, three were used to determine the Rb fill and only two remained for clock usage.

The frequency standard dash numbers were changed to identify the types of lamps. Dash 4, 5, 6, and 7 clocks had the lamp fill measured by neutron activation, and the Dash 8, 11, and 12 clocks had the fill measured by destructive analysis. The usage of these dash numbers on the GPS satellites starting with Navstar 5 is shown on Figure 1. Table 1 summarizes the operating history of these frequency standards thorough November 1984. Note that 44 months of failure-free, on-orbit operation has accumulated.

CALORIMETRIC MEASUREMENT

The newest technique that is used to determine the amount of Rb fill is making use of a differential scanning calorimeter, Perkin-Elmer DSC-2C. This instrument is used to measure the heat energy required to melt the Rb in a lamp. This allows (using the known heat of fusion of Rb)(6.2 cal/gram) the amount of Rb to be determined with a resolution of a few micrograms. Life test data shows that the Rb consumption (due to Rb diffusion into the glass) closely obeys a power law model and thus allows an estimate of lamp life to be made. The key variable is the initial Rb fill and its measurements.

VCXO ON-ORBIT PROBLEM

Rb Frequency Standard 2 on Navstar 2 was turned on May 2, 1978. At turn-on, the Kalman filter residuals indicated a cyclic error with a period of 54 seconds. The trouble shooting plan to determine which part of the frequency standard was at fault, was to switch the standard to the backup mode, record range data, and process this data to determine the delta range residuals. This data was processed by the Aerospace Corporation. The residual errors showed the same cyclic period as the primary mode except the range error magnitude had increased by a factor of the servo loop gain This increase in short-term error clearly showed the problem to be associated with the 10.23 MHz VCXO.

Laboratory testing was initiated at both Rockwell and Frequency Electronics Inc., (FEI) the VCXO manufacturer. The initial hypothesis was that the oscillation was caused by either the inner or outer oven heaters. To verify this hypothesis, the outer heater was forced to oscillate with a 30-second period. No effect was observed on the VCXO output frequency. This test verified the problem was not caused by the outer oven.

The investigation of the probable causes of the inner oven oscillation was isolated to two areas:

1. A mechanical bond separation at the thermistor, heater winding, or heater transistor

2. A short across the inner oven feed back resistor.

FEI, after extensive testing including aging, vibration, x-ray, and neutron radiography, could not detect any thermistor bond defects. The conclusion reached was that the oscillation was not related to a bond separation.

A computer simulation of the inner heater circuitry showed that a short across R8 would cause an oscillation with a 53-second period. Laboratory test with a short across this resistor duplicated the spacecraft anomaly. Further investigation of the Autonetics test data indicated that the anomaly was not present prior to launch and therefore was caused by the launch environment. The final conclusion was that the short across R8 was caused by an isolated workmanship defect in the routing of jumper wires in the assembly. This conclusion is substantiated by that fact that the oscillation has not re-occurred on any space vehicle Rb clocks.

A very significant fact about the effectiveness of these changes and the improved reliability can be seen by noting the total operating history of the Dash 3 and subsequent standards. Clock 1 on Navstar 3, has been operating for 73 months; Clock 3 on Navstar 4 for 35 months; and the 44 months accumulated on Navstar's 5 through 8 yield a total of 152 months (approximately 13 years) of failure-free operation.

CFS ORBITAL ANOMALIES

As previously stated, the first GPS satellite to have a cesium frequency standard (CFS), in addition to three Rb standard, was Navstar 4. A government-furnished engineering development model (EDM-002), built by Frequency and Time Systems (FTS), was installed into GPS-004 on February 17, 1978; successfully completed all ground space vehicles testing; and was launched on December 11, 1978. A total of 493 space vehicle operating hours were accumulated prior to launch. On February 23, 1979, it was turned on, operated correctly for approximately 12 hours, and failed. The results of an Air Force anomaly team concluded that the spacecraft telemetry indications were not conclusive to isolate the exact cause of the problem. The frequency standard had switched to the backup mode of operation because the cesium-half of the power supply was off. There are two possible failures that would cause this condition: (1) the relay that feeds the second inverter could have failed, and (2) the high-voltage power supply could have failed. The conclusion reached was that the cesium-half of the power supply had apparently failed. The results of the team's investigation verified that, if required, the backup VCXO mode of this clock was still operational.

Numerous design changes were incorporated into the pre-production model power supplies. Table 2 is a summary of the operating history of clocks with modified power supplies. PPM-2 operated on Navstar 5 for 31 months with no problems. The unit was turned off because of a space vehicle attitude control problem. PPM-11 operated on Navstar 6 for 44 months. This unit was turned off because of a depletion of cesium. The two dash 0001 Rockwell units on Navstar's 9 and 10 have a total of 7 months operating time. A resultant total of 84 months of operating time has accumulated on all CFS's with no power supply related problems. This record clearly shows that the problem has been corrected.

As stated in the previous paragraph, PPM-11 was turned off because of the depletion of cesium. Under normal operating conditions, the one gram of cesium in these units was considered to be more than adequate to satisfy the specified 5-year operating life of the PPM units. After reviewing the on-orbit operating data, it became apparent that a cesium leak developed in the cesium oven assembly after 8 months of operation. This additional loss of cesium over a 36-month period caused the earlier than expected depletion of cesium. This same problem developed on another PPM unit (S/N 10) during space vehicle testing. The unit was returned to FTS and a failure analysis was performed. The results of this analysis showed that there was a microscopic tunnel in a braze joint in the oven assembly. Because of the suppliers proprietary nature of this information, no additional details are presented.

As a result of this analysis, the following corrective actions were instituted by FTS in both their commercial and high-reliability tube fabrications:

1. A new brazing procedure was developed.

2. Helium leak testing is performed on all brazed joints.

3. Stricter quality control and inspection points were instituted during the fabrication process.

In addition to these actions, FTS also has increased the amount of cesium fill to 1.5 grams to provide an additional safety margin for the production tubes that have 7-1/2 year specification requirement.

The only corrective measure, in effect at the time the tubes were fabricated for the standards on Navstar's 8, 9, and 10, was the stricter quality control and the institution of inspection points. Therefore, the effectiveness of all of these changes will not be fully verified by on-orbit data of the present satellite constellation. However, the Naval Research Laboratory (NRL) has life testing in progress on two tubes that were fabricated with all improvements. Twenty-four months of continuous operating time have been accumulated on each tube with no failures.

Another significant data point demonstrating the reliability of the cesium frequency standards is the testing of PPM-14 at NRL. This unit has the same tube configuration as the units operating on Navstar's 9 and 10. The test started at NRL on November 17, 1982, and is still in progress. Adding to this, the 6-month operating time of PPM-14 at Rockwell yields 30 months of operation with no problems.

RFS LONG-TERM LABORATORY TEST

An unmodeled deviation of a GPS vehicle clock from GPS time, leads to errors in navigational accuracy. These errors may be minimized by the periodic recharacterization of the clocks in terms of the time difference or phase offset, frequency offset, and the frequency drift with respect to GPS time. In the event the vehicle is not uploaded with this data, the rate at which time error is accumulated depends on the validity of the previously uploaded characterization data.

In order to predict precise user time errors for systems such as GPS, David Allan of the National Bureau of Standards (NBS) has published a model (References 1, 2) for the prediction of time error based on the previous performance of the clock in terms of the Allan variance, $\sigma_y(t)$, and the length of test data. This model has set GPS autonomous operation standards and prediction of available navigational accuracy versus time from upload.

An internal project was initiated in an effort to better characterize the Rb frequency standards developed for GPS associated with the autonomous operational goals. In order to perform this task, an 140-day stability test was completed from February to June 1983, with the necessary data taken to calculate drift, time error, and Allan variance. During this test, the phase accumulation between the test RFS and the reference cesium clock, frequency performance, and test telemetry were recorded to determine the actual time prediction error accumulated during the test (Reference 3).

This time prediction error is the difference in the actual phase accumulation and the predicted phase. The time error is sensitive to external and internal environmental influences on the clock.

The beat frequency, $\Delta f/f$, is shown in Figure 3. The frequency was calculated from 1,000-second period average data, which was then averaged over 10 data points to conform to computer storage requirements. Examination of the entire 140-day period shows an initial "warmup" period of about 50 days, during which the drift changes from about minus 6 x 10^{-14} $\Delta f/f/day$ to minus 2 x 10^{13} $\Delta f/f/day$. The frequency drift is relatively constant from Day 50 to Day 140, except for a dip from Day 70 to Day 86. This dip correlates to a drop the clock baseplate temperature of about $0.8^{\circ}C$. This points out the critical role that temperature stability plays with frequency and time prediction error.

The Allan variance, σ_y, can be calculated both with and without the warmup period data. It can be seen in Figure 4 that the main effect of the behavior is on the long-term values or the "random walk." The total data σ_y represents the usual RFS Allan variance signature; whereas, the day 50-150σ_y values are better in terms of random walk. If μ is the slope of the random walk portion of the Allan variance plot where $\sigma_y \sim t\mu$ for large t, then $\mu = 0.7$ for Day 0 to Day 140 data, and $\mu \simeq 0.1$ for Day 50 to Day 140 data.

Excluding the data which was affected by the warmup or temperature change, the time prediction error is found to be very small. This points out the importance to the time error of small temperature changes to the RFS. Since the on-orbit Rb standards now have a baseplate temperature controller that controls the clock temperature to within +$0.1^{\circ}C$, excellent time error values on orbit are expected as evidenced in Navstar 8.

This test has shown that time prediction error is very sensitive to environmental influences, both external and internal to the RFS. Specifically, the apparent aging of the Rb lamp represents an internal, systematic change and correlates with the clock frequenc characteristics This characteristic influences both the clock warmup time and the apparent random walk portion of the Allan variance. Measuring the long-term Allan variance during this warmup period gives a random walk slope in the $t = 10^5 - 10^7$ region. However, this does not represent random walk behavior of the clock that has warmed up, but a systematic change. Once the RFS has been on for 50 to 60 days, the lamp voltage curve begins to straighten out and the RFS random walk values decrease dramatically. Data beyond this 60-day warmup period best characterizes the frequency standard if the temperature is held within $\pm 0.1^{\circ}C$.

It was seen from the baseplate temperature that a $0.8^{\circ}C$ temperature plateau resulted in a small frequency shift. For a 15-day period, this gave a 600 to 700-nanosecond offset. This period influenced longer data length prediction intervals before, during, and after the occurrence of the plateau. All subsequent RFS's now are being controlled to $\pm 0.1^{\circ}C$ by a temperature controller.

The final test period (beyond the lamp warmup and the $0.8^{\circ}C$ temperature variation) data resulted in excellent time prediction error values with the longer period plots, satisfying the 131-meter, 14-day user range error requirement. This is significant in the view of the GPS autonomous operation requirements, which were previously thought optimized by only the cesium standard.

CONCLUSION

Considering there were no space qualified Rb or cesium frequency standards available 11 years ago at the start of the GPS program, the development and on-orbit performance of both types of standards has been outstanding. This is not to say that this program has not experienced the normal types of problems associated with new hardware. As substantiated by on-orbit performance data, the corrective actions taken to eliminate the problems have been very effective. No transformer or VCXO oven oscillation problems have occurred since the implementation of corrective actions in the Dash 0003 Rb frequency standards. No lamp problems have occurred since the corrective action implementation in the Dash 0004 standards. The same results are apparent in the cesium frequency standards. The corrective actions taken associated with the power supply problem have not re-occurred in any of the PPM or Dash 0001 units. Although there is not sufficient on-orbit data to verify the corrective measures taken to eliminate early depletion of the cesium, more than 24 months of laboratory data have accumulated at NRL that demonstrates the effectiveness of this change.

The validation of the approach taken on the GPS program to have frequency standards with both a primary and secondary mode of operation is very apparent. If this approach had not been taken, both Navstar's 1 and 2 would have been inoperative in less than 3 years. Both Navstar 1 and 2 have been operating in the backup mode for approximately 4 years. The backup mode of operation is still available on all other Navstar space vehicles, if required at some later time to illustrate the effectiveness of this approach. A total (all clocks) of 312 months (26 years) of on-orbit time have accumulated in the primary mode of operation and 428 months (35.7 years) including the backup mode of operation.

REFERENCES

1. Allan, Dave and Helmut Hellwig. Time Deviation and Time Prediction Error for Clock Specification.

2. Allan, Dave. Addendum to Paper, Time Deviation and Time Prediction Error for Clock Specification Characterization and Application.

3. Bryan, E.T. Time Prediction Error Measurements During a Long-Term Stability Test, Rockwell IR&D Report (1983).

ACKNOWLEDGEMENTS
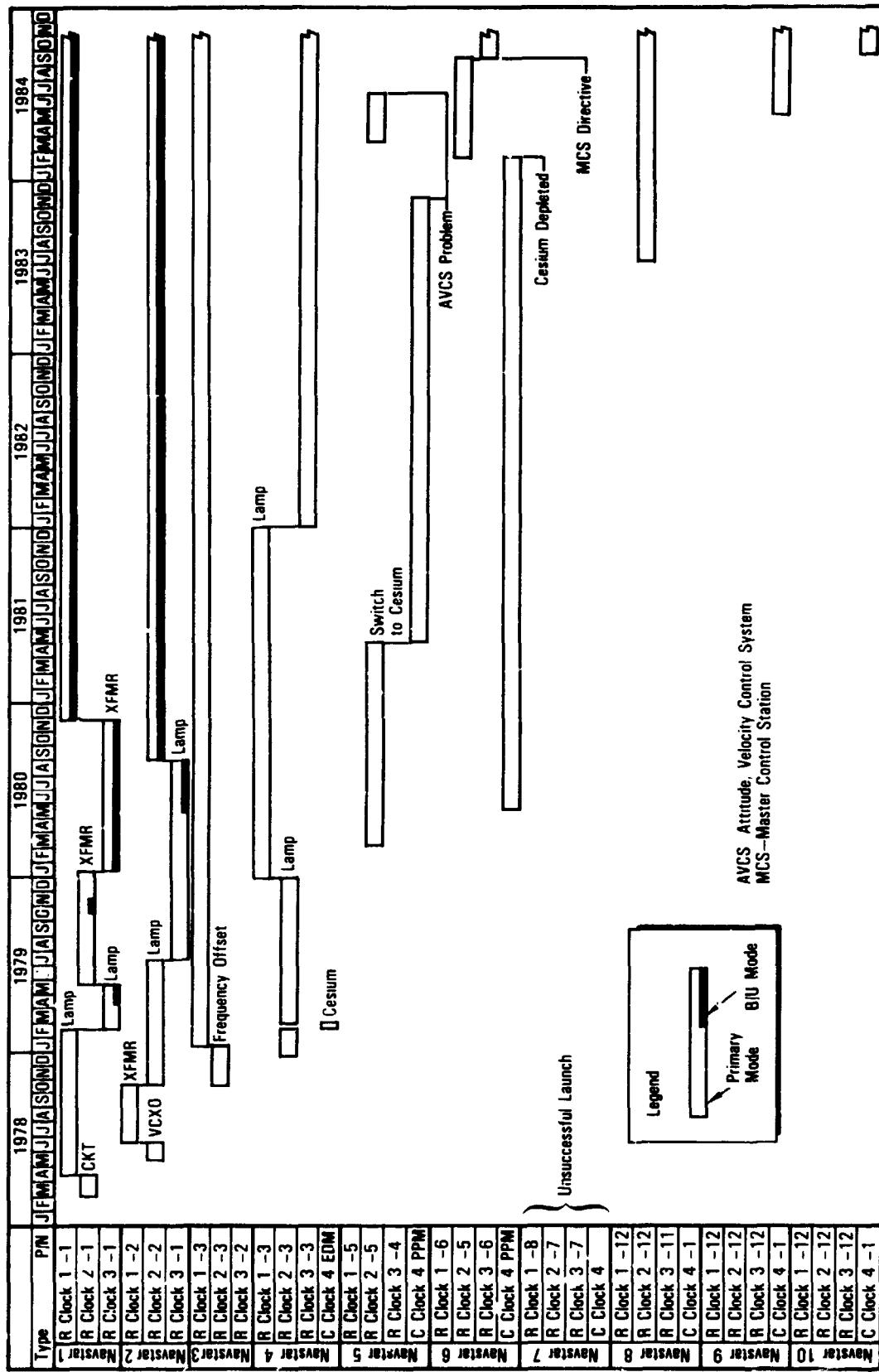
Figure 1. Navstar Clock Operating History

138
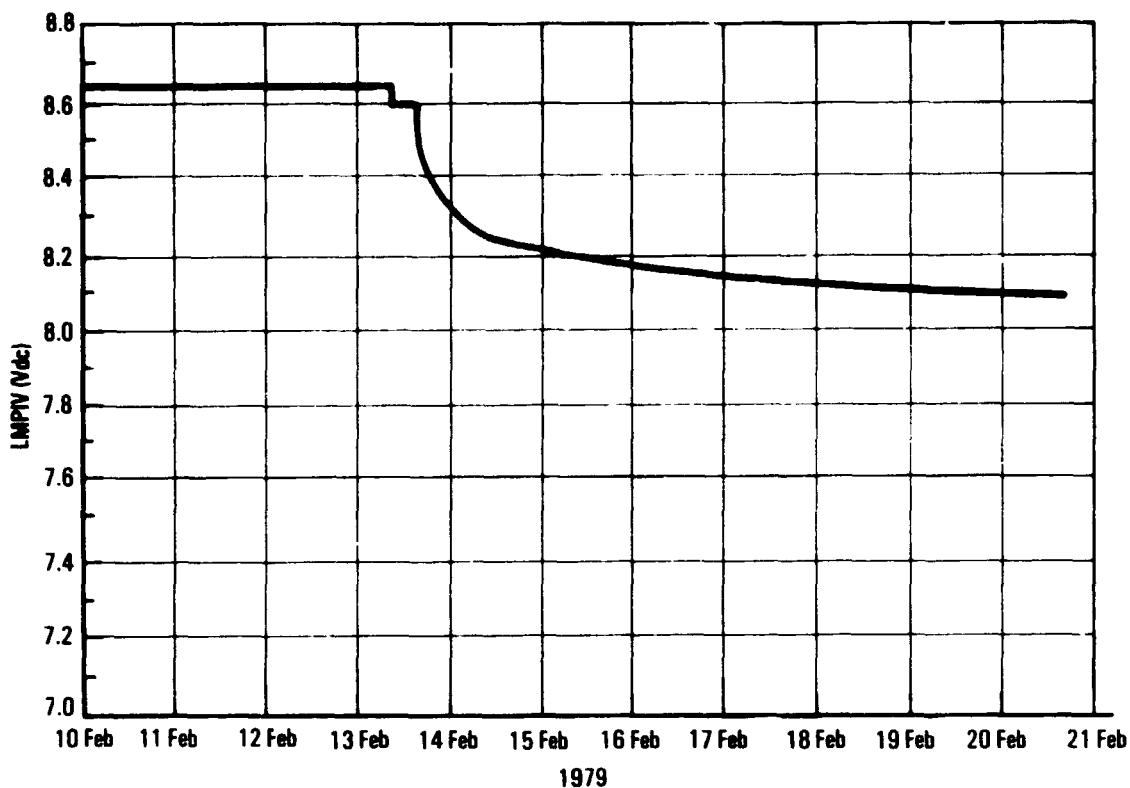
Figure 2. Navstar 1 Frequency Standard No. 1 LMPIV Anomaly
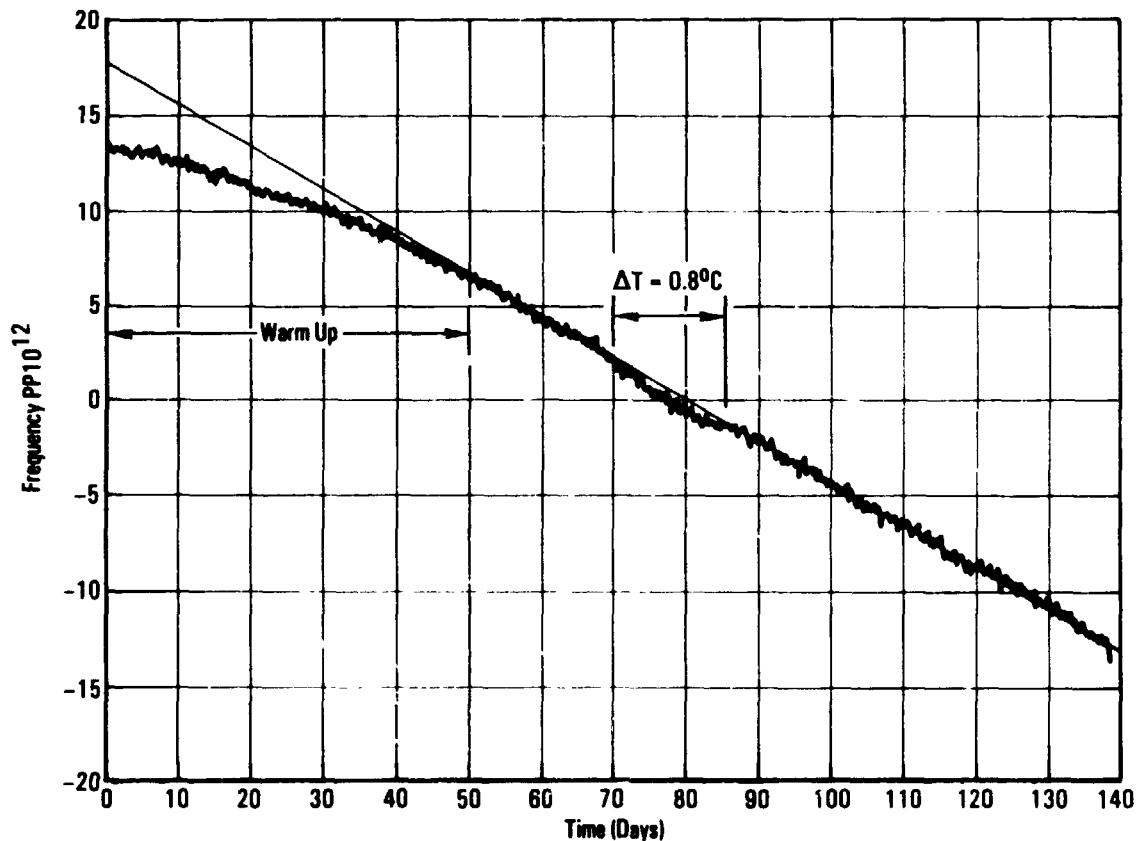
Figure 3. GPS 140-day Rb Stability Test
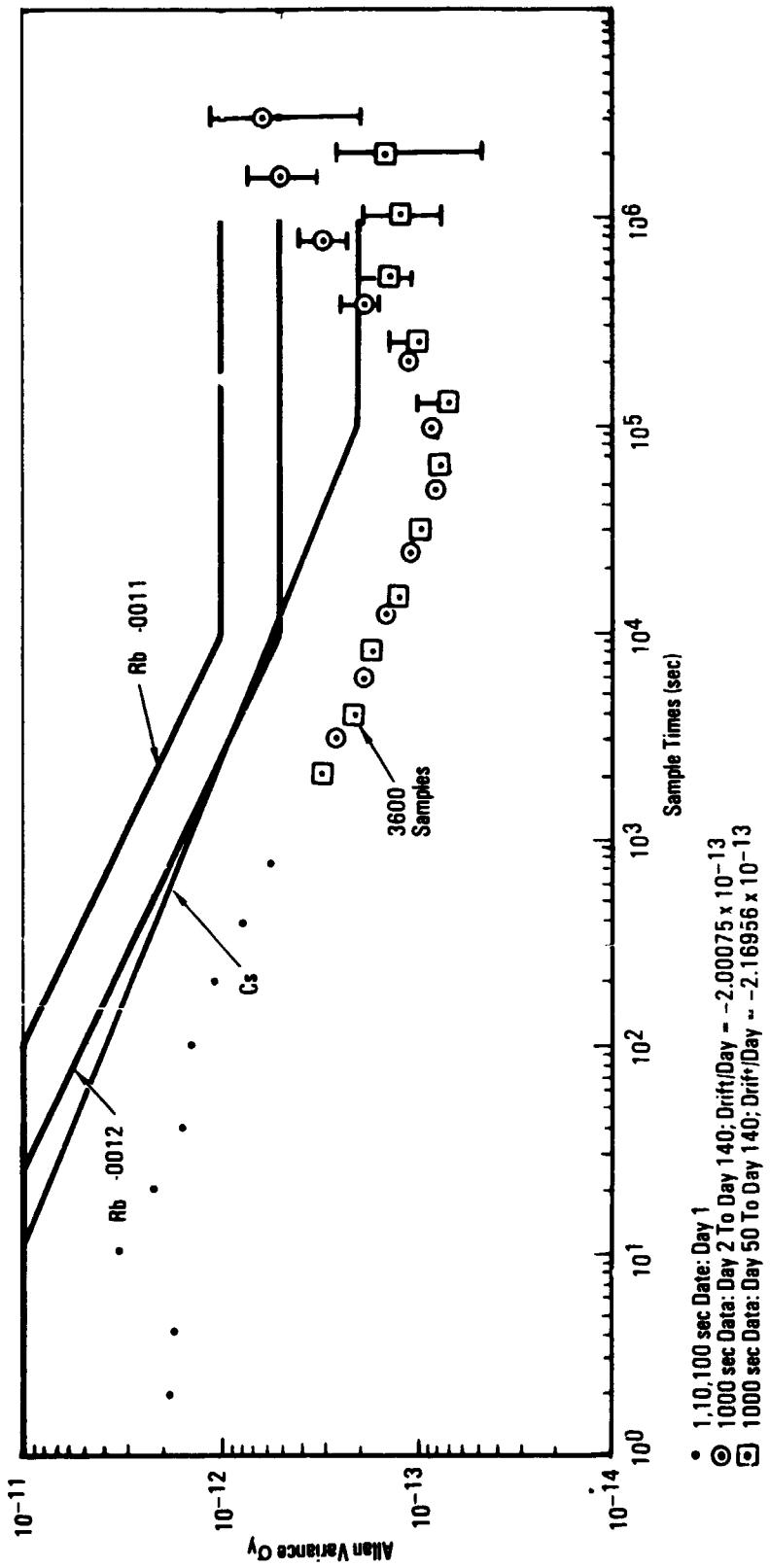
Figure 4. IR&D Time Error 140-day Stability Test Rb Frequency
Standard No. LQX0001

Table 1. GPS Rubidium Frequency Standard Operating Summary (Primary Mode)

Navstar	P/N	Months of Operation							Total (months)	Failures	Failure Mode	Comments
		1978	1979	1980	1981	1982	1983	1984				
1	-0001	10	12	B/U	B/U	B/U	B/U	B/U	22	3	Lamps, XFMR	B/U--backup mode Must update every orbit
2	-0001 -0002	6	12	4	B/U	B/U	B/U	B/U	22	3	Lamps, XFMR	Low frequency oscillation Nonoperational
Total		16	24	4	0	0	0	0	44	6		Months of operation/ failure 44/6 = 7.3
New Power Supply XFMR Design (-0003 and subsequent)												
3	-0003	2	12	12	12	12	12	11	73	1	Frequency offset	Second Rb clock on for 70 months (5.8 years)
4	-0003	0	12	12	12	12	12	11	71	2	Lamps	
Total		2	24	24	24	24	24	22	144	3		Months of operation/ 144/3 = 48
Rubidium Lamp Change (-0004 and subsequent)												
5	-0004 -0005	0	0	10	4	Cs Op	Cs Op	3	17	0	None	AVCS problem Cs--Cesium clock
6	-0005 -0006	0	0	Cs Op	Cs Op	Cs Op	Cs Op	10	10	0	None	Cs--Cesium clock
8	-0011 -0012	0	0	0	0	0	4	11	15	0	None	
9	-0012	0	0	0	0	0	0	Cs Op	0	0	None	
Total		0	0	10	4	0	4	24	42	0	None	No failures--42 months of operation

Table 2. GPS Cesium Frequency Standard Operating Summary

Navstar	P/N	Months of Operation							Total (months)	Failures	Failure Mode	Comments
		1978	1979	1980	1981	1982	1983	1984				
4	EDM	0	0	0	0	0	0	0	0	1	High voltage power supply	Backup (VCXO) mode still operational
5	PPM	0	0	0		12	11	0	31	0	None	
6	PPM	0	0	7	12	12	12	1	44	1	Depletion of Cs	Backup (VCXO) mode still operational
9	-0001	0	0	0	0	0	0	5	5	0	None	
10	-0001	0	0	0	0	0	0	2	2	0	None	
Total		0	0	7	20	24	23	8	82	2		Months of operation/ failure 82/2 = 41
	PPM 14											Additional testing: 24 months at NRL, 6 months at Rockwell

141

A MINIATURE TACTICAL Rb FREQUENCY STANDARD

T. M. Kwon, R. Dagle, W. Debley,
H. Dellamano, T. Hahn, J. Horste,
L. K. Lam, R. Magnuson and T. McClelland*

Litton Guidance and Control Systems
5500 Canoga Ave., Woodland Hills, CA 91364

ABSTRACT

Work on an innovative design for miniature rubidium frequency standards has reached the pre-production demonstration stage at Litton Guidance and Control Systems. Pre-production units have been built and tested under contract to the Rome Air Development Center of the U.S. Air Force Systems Command. The units, which are designed for use in tactical military applications, feature fast warm-up, low power consumption, and vibration insensitivity. The output stability under vibration is maintained without the need for external shock-mounts. The design objectives and test results are discussed.

INTRODUCTION

Reported herein are design considerations and preliminary test result of the pre-production model Tactical Rubidium Frequency Standard (TRFS) developed by the Guidance and Control Systems Division, Litton Systems, Inc., under contract with the Rome Air Development Center of the U.S. Air Force Systems Command.[1]

The TRFS must be capable of operating under severe environmental conditions, specifically extreme operating temperatures and vibrations. An innovative design of a rubidium frequency standard was necessary in order to meet these requirements and to realize small size, fast warm-up, and low power consumption. Several design features are considered unique to the Litton TRFS and are discussed briefly. The Litton TRFS development program has reached the pre-production demonstration stage, and further developmental efforts are continuing. Presented in this paper are preliminary test results available from the Litton pre-pro duction model TRFS at the demonstration stage. The Litton TRFS is shown in Figure 1, and measures 3-1/4" W x 4-1/2" L x 3-1/4" H excluding connectors.

---

*Presently Manager of Rb Freq. Std. at Frequency Electronics Inc., Mitchel Field, N.Y.
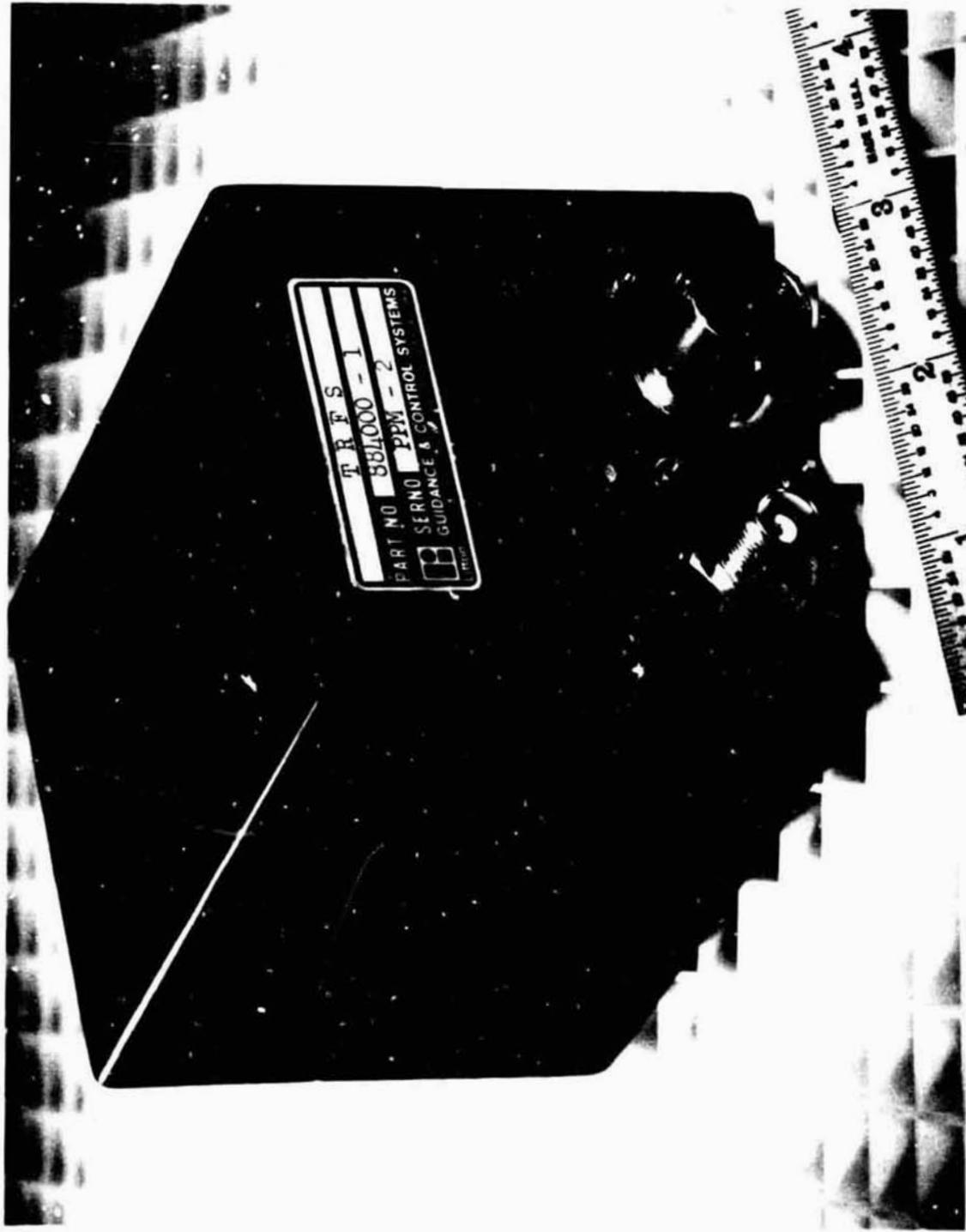
Figure 1   Litton Preproduction Model TRFS

DESIGN CONSIDERATIONS

Rubidium Physics Package

Shown in Figure 2 is the Litton TRFS physics package module. The module contains a Rb^{87} electrodeless discharge lamp and lamp driver circuitry, a 6.8 GHz microwave cavity, and a pair of coils generating a uniform magnetic field. A separate Rb^{85} filter cell and a Rb^{87} resonance cell are located inside the microwave cavity. Both cells are of cylindrical shape, 12 mm dia x 8 mm length. The rubidium light from the lamp is directed through optical lenses to the filter cell, the resonance cell, and finally to the photodetector mounted on the outside of the microwave cavity.

The glass envelope of the lamp is designed to allow strong adhesion of liquid rubidium onto the glass wall, a desired feature for a lamp to be vibration resistant. The lamp driver circuitry is of the conventional type, modified for fast lamp start-up. The lamp starts within 10 sec and 30 sec at room temperature and at -55°C, respectively. Lamp start up in a "wrong discharge mode" is prevented through an electronic control under all power off-on conditions.

Both the lamp housing and the cavity are maintained at elevated temperatures by strip heaters. The strip heaters represent an extended uniform heat source, rather than a point source, and tend to reduce the temperature gradient across the heated block. Unique design of the strip heater temperature control circuitry minimizes stray magnetic fields, which would cause an excessive frequency shift when heater current changes, for example, as a function of environmental temperatures.

The microwave cavity is of rectangular shape as described previously.[2,3] The extremely small size of the cavity has resulted in rapid warm-up, as it will be shown later, with low peak warm-up power.

The entire physics elements are enclosed within two layers of magnetic shields. The outer shield, which is seen in Figure 2, measures 1-3/8" x 1-3/8" x 3". Its performance characteristics are similar to those described previously.[4]

VCXO

The VCXO is a self-contained module (1.2" x 1.2" x 2.4") complete with heaters and oscillator electronic circuitry.[5] The quartz crystal in the VCXO is a SC-cut 10 MHz crystal having an acceleration sensitivity of $Y \approx 4 \times 10^{-10}$/g. The VCXO module is mounted on a set of wire-suspended vibration isolators inside the TRFS package.

The wire-suspended isolators were chosen instead of the conventional rubber-type primarily due to their consistent
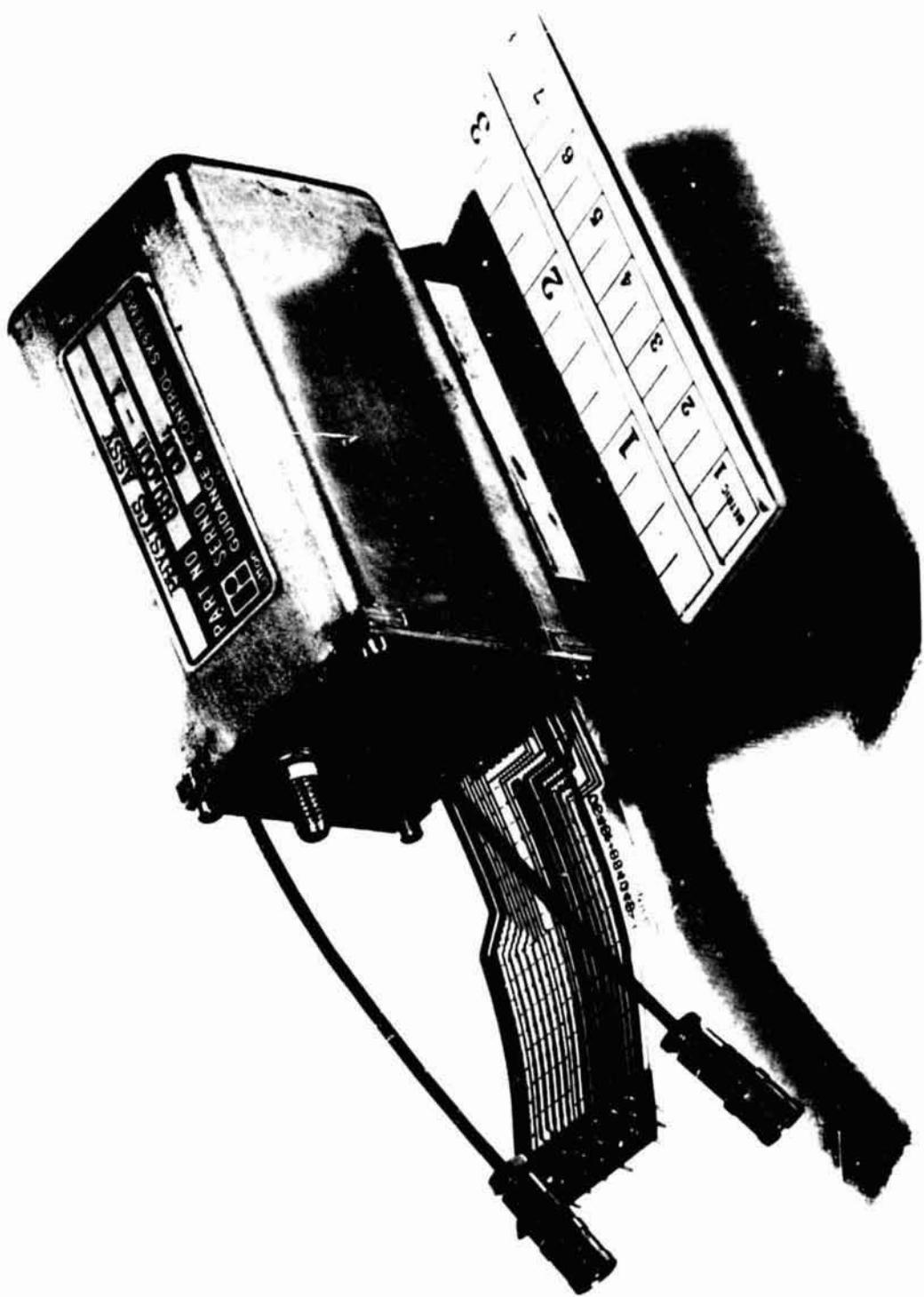
Figure 2   Physics Package Module of the Litton TRFS
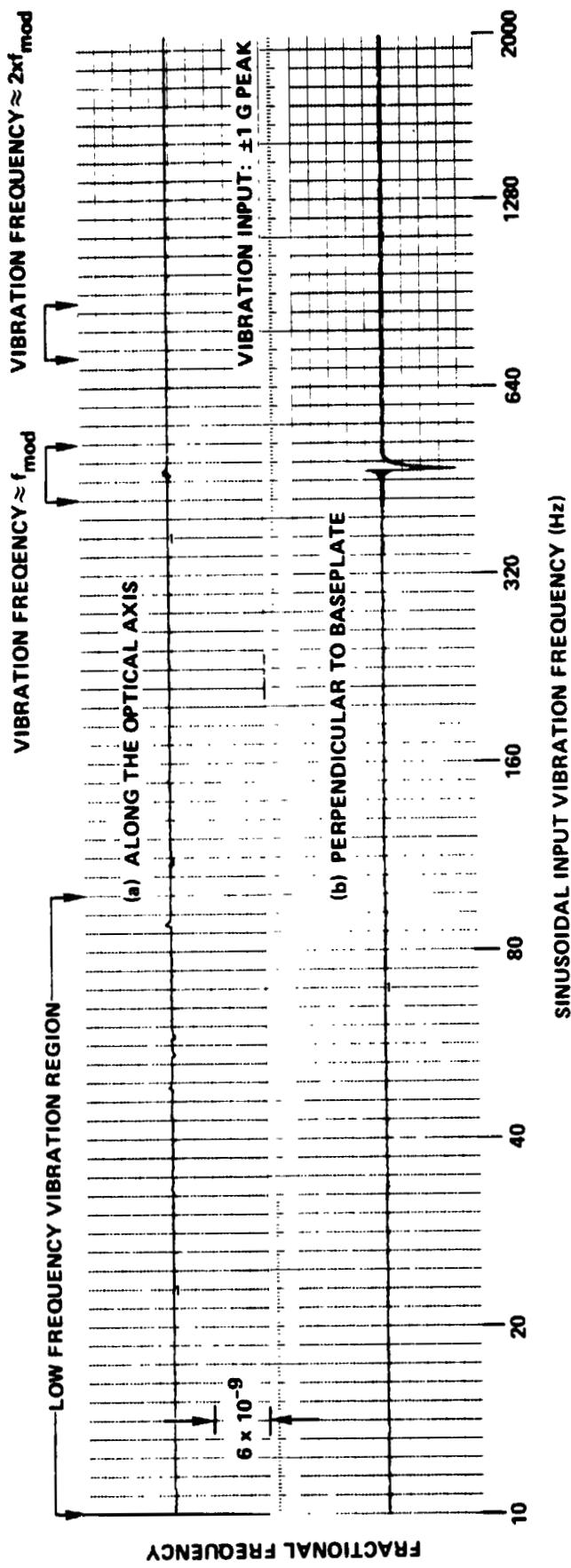
Figure 3   Fractional Frequency Shift versus Vibration Frequency
for Vibration Input (a) along the Optical Axis, and
(b) along the Axis Perpendicular to the Baseplate

147
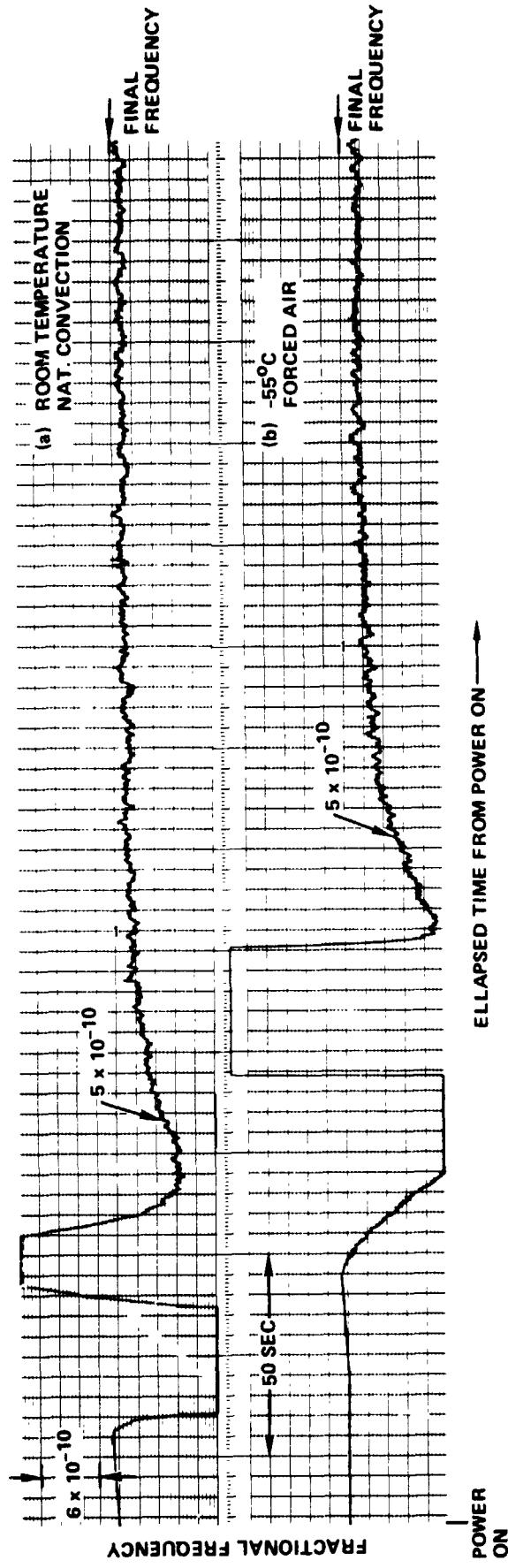
Figure 4   Fractional Frequency versus Time from Turn-on (a) at
Room Temperature with Natural Convection, and (b) at
-55°C with Forced Air

148

characteristics under all temperatures. (The rubber mounts tend to harden at low temperatures.) The isolator transmissibility is designed to have a minimal resonance rise while providing a high attenuation of vibration inputs at high frequencies.

Vibration-induced sidebands of the VCXO output, including those at the isolator resonance rise, are minimized by a fast VCXO control servo loop (bandwidth $\approx$100 Hz).[6]

Vibration Sensitivity Design Considerations

Sources of vibration sensitivity in a conventional rubidium frequency standard have shown to be both the VCXO and the physics package.[7] Since the output of a rubidium frequency standard is essentially that of a VCXO, vibration-induced sidebands of the VCXO appear directly in the frequency standard output at all vibration frequencies. In most frequency standard applications, either as a clock or as a stable, low-noise frequency source, the vibration-induced sidebands do not appear to be a serious drawback at high vibration frequencies. In order to improve the low frequency vibration sensitivity of the Litton TRFS over that of a conventional rubidium frequency standard, a large bandwidth ($\approx$100 Hz) is implemented in the VCXO control servo loop.[6]

Unlike a VCXO, the physics package is not intrinsically vibration sensitive. Vibration sensitivity of the physics package is generally considered as an engineering design challenge. In a typical mechanization of a rubidium frequency standard such as the Litton TRFS, rubidium atomic resonance signal is in the form of a modulated (ac) light intensity riding on top of a large dc light background. The ac portion of the light, i.e., the resonance signal, is an extremely small fraction of the total light intensity detected by the photodetector. The ac signal is demodulated in a conventional phase sensitive detector, and processed further to generate dc control voltage for the VCXO.

Any spurious modulation in the detected dc light intensity in addition to the resonance signal, generates an erroneous control voltage. Such an effect is most significant when the spurious modulation frequency is close to the modulation frequency (f_{mod}) of the phase sensitive detector. The spurious modulation may be a result of, for example, periodic displacement of the lamp with respect to the photodetector under vibration. The TRFS physics package is designed for maximal mechanical integrity of the whole while allowing for adequate thermal isolation of the different components operated at different temperatures.

Vibration-induced sidebands of the VCXO also cause spurious light intensity modulation. The VCXO control servo loop is upset when the vibration frequency is close to $2 \times f_{mod}$. In order to reduce the vibration input at this frequency, the Litton TRFS incorporates a shock-mounted VCXO.

149

Electrical Design

One important aspect of the electrical design is to mini-
mize spurious signals which may upset the VCXO control
servo loop resulting in an erroneous output frequency. Any
spurious signal at frequencies close to f upsets the
VCXO control loop as a spurious light intensity modulation
does. The interference effects observed[8] in a rubidium
frequency standard operating in the vicinity of others
demonstrates the effect of the spurious signal pick-up.
Spurious signals may be picked up from the voltage ripple
present in the input power line, if not regulated
adequately.

The Litton TRFS accepts two separate power inputs: one for
all heaters and the other for all electronics. Both power
inputs may be 22V to 33VDC with ripples as large as 3Vrms
at audio frequencies, and may contain high voltage
transients.

Voltage regulation for electronics is accomplished by a
switching DC/DC converter followed by a linear regulation
stage. This combination provides adequate ripple regula-
tion and constant power dissipation at all input voltage
conditions. The feature of constant power dissipation
minimizes input voltage dependent frequency shift (via
temperature dependence of output frequency).

The 6.8 GHz resonance interrogation frequency is generated
by a step recovery diode (SRD), which is driven by ~40 MHz.
Direct frequency synthesis technique is used to generate 40
MHz from the VCXO 10 MHz.

The rubidium resonance signal is detected in a conventional
way with sinusoidal modulation technique. The modulation
waveshape is generated piecewise digitally through dividing
the VCXO 10 MHz and adding the resultant square waves with
proper amplitudes.

Temperature control circuitry, which maintains the lamp and
the cavity at elevated temperatures, is of high gain, and
utilizes both proportional and integral gain. Combination
of unique circuit design and the strip heater minimize the
stray magnetic field generated by heater current.

The entire circuitry is contained in five circuit cards,
each having the size of ~3"x3". Each card contains more
than one layer of ground plane which acts also as heat
paths for electronic components. Neither hybrids nor LSI's
are used in the entire design; all components are discrete
devices.

All material, components, processes and construction
methods are in accordance with the governing military
specifications and/or with the accepted military practice.

Mechanical Design

The Litton TRFS package is designed with a modular concept: five circuit cards, EMI filter-multipin connector module, physics package, and VCXO module. One of the five circuit cards is a mother board into which all modules are plugged. No hard-wiring is necessary between the modules; miniature RF connectors are used for all coaxial cable connections.

The package bonding is per the governing military specification. The case may be sealed by laser-weld, if necessary, for water immersibility. Heat dissipation is accomplished primarily by conduction through chassis structure to the baseplate.

Vibrational characteristics of the entire structure was studied by finite element method, and was determined to be satisfactory.

PRELIMINARY TEST RESULTS

The TRFS development program has reached a demonstration stage at Litton. As a part of planned design verification tests, the TRFS unit has been subjected to a number of functional and environmental tests. Design modifications are planned if the test results warrant them. Such modifications, if necessary, are expected to be minor in nature. When completed, the TRFS unit will be subjected to rigorous military qualification testing. Discussed in this section are the test results available to date. Design verification tests are continuing.

Sinusoidal Vibration

Figure 3a and 3b are the plots of fractional frequency shift versus vibration frequency under sinusoidal vibration of ±1g peak acceleration for vibration inputs along the optical axis and along the axis perpendicular to the baseplate, respectively.

The optical axis is parallel to the baseplate. Bandwidth of the frequency measurement system including the strip-chart recorder is a few Hz, while the vibration input is swept from 10 Hz to 2KHz at a rate of one octave/min. (The horizontal axis of Figures 3a and 3b is, however, linear in time.)

Referring to Figure 3a, the observed frequency shift is less than $\pm 3 \times 10^{-10}$ from the nominal under all vibration frequencies including those of f_{mod} and at $2 \times f_{mod}$.

Figure 3b is for vibration input applied along the axis perpendicular to the baseplate, and shows no observable frequency shift within $\leq 2 \times 10^{-10}$ under all vibration frequencies except as noted below.

151

A large unexpected frequency shift was observed in Figure 3b, when vibration frequency is close to f_{mod}. Investigation revealed that a fastening screw was loose during the test causing the microwave cavity rock excessively within the physics package.

We note that no measurable frequency shift was observed at vibration frequencies close to $2xf_{mod}$, and that output frequencies are well behaved at low vibration frequencies. No loss of resonance lock were seen during the measurement.

Audio Susceptibility

Audio susceptibility refers to the TRFS output frequency dependence on the audio frequency voltage ripple present in the input power. Test was conducted with a 3Vrms ripple added to the nominal dc voltages applied to the power input for electronics. The ripple frequency was varied slowly from 5 Hz to 2K Hz dwelling for an extended period of time at ripple frequencies equal to $1/2f_{mod}$, f_{mod}, and $2f_{mod}$. No frequency shift was observed beyond the measurement precision ($\leq 2x10^{-10}$).

Warm-up and Power Consumption

Figures 4a and 4b are typical output frequency behavior during warm-up after temperature soak at room temperature (natural convection) and at -55°C (forced air), respectively. Warm-up test results are summarized in Table I.

Table I - Litton TRFS Warm-Up Characteristics

	Time After Power-On	
	Room Temp	-55°C
o Lamp Start	8 sec	28 sec
o Resonance Lock	1 min 12 sec	2 min 22 sec
o Warm-up to $5x10^{-10}$ from the final freq.	1 min 39 sec	2 min 49 sec
o Total Steady State Power	10.4 watts	19.5 watts
o Total peak power during warm-	84 watts for 20 sec	84 watts for 42 sec

Temperature

No measurable frequency shift was observed beyond the measurement precision ($\leq 2\times 10^{-10}$) when the TRFS was subjected to environmental temperature steps ranging from -55°C to +71°C.

Orientation

A rubidium resonance frequency may be orientation dependent under the influence of earth magnetic field. Displacement of physics elements with respect to each other under gravitation may also be a source of orientation dependency. In a properly designed physics package, both of these effects are considered to be negligible. Perhaps the most significant orientation dependence of the TRFS output frequency arises from its temperature sensitivity. This is because the rate of heat dissipation, and therefore the baseplate temperature of the TRFS, depend on the orientation. Such a temperature-related frequency shift was reported by others[9] while measuring static g-sensitivity of an oven-controlled crystal oscillator.

The TRFS unit was positioned at various orientations while its output frequency was monitored continuously. The unit was held fixed at each orientation for an extended period of time in order to observe any temperature-related frequency shift. No measurable frequency shift was observed above the measurement precision ($\leq 2\times 10^{-10}$).

Input Voltage Variation

Similar argument presented for the orientation dependence applies to the input voltage dependence. If a unit depends solely on a linear voltage regulator whose heat dissipation depends greatly on the input voltage level, temperature dependence of the output frequency may be manifested as if it were the voltage dependence. As discussed earlier, the Litton TRFS incorporates a switching DC/DC converter followed by a linear regulator.

The Litton unit was powered at +22 Vdc and then the input voltage was varied to 33 Vdc by steps of a few volts. At each voltage, the unit was operated for an extended period of time to observe temperature-related frequency shift. No measurable frequency shift was observed with measurement precision of $\leq 2\times 10^{-10}$.

Short-Term Stability

Short-term stability of $\leq 4\times 10^{-11}$ at 1 sec averaging time was measured with phase noise $\leq -70\text{dB/Hz}$ at 1 Hz away from the 10 MHz carrier. Note that the measured stabilities are those of physics resonance signal, not those of VCXO. Physics stability of $\leq 2\times 10^{-11}$ is obtainable, if desired, with a minor modification.

153

SUMMARY AND ACKNOWLEDGEMENT

Design features unique to the Litton TRFS are presented briefly.
Preliminary test results are reported. Demonstrated performance
characteristics of the unit under vibration, excellent warm-up
time and temperature sensitivity break new grounds for the
rubidium frequency standard technology to be beneficial to many
tactical military applications. We wish to express our appreci-
ation for encouragements from Mr. Richmond (Dick) Terrell, Dr.
Emery Moore, Mr. Harry Daubert, Mr. Alex Hertzberg, and Mr. Dave
Deuser. Much of our work has received technical support from Mr.
Chong C. Lee and Mr. Carl Davidson. Technical advices of Mr.
Bruce Grover, Mr. Howard Williams and Mr. Jim Steele are
acknowledged.

REFERENCES

1. Rome Air Development Center of the Air Force Systems
    Command, Contract No. F19628-83-C-0174.

2. T. M. Kwon, H. Williams and T. McClelland, Proc. 37th Ann.
    Freq. Control Symp. (1983) p. 12

3. M. Tetu, et.al., Proc. 38th Ann. Freq. Control Symp.
    (1984); in print

4. B. Grover and T. Kwon, Proc. 15th PTTI Meeting (1953), p.
    677

5. Purchased from Frequency Electronics Inc., Mitchel Field,
    N.Y.

6. T. M. Kwon and T. Hahn, Proc. 37th Ann. Freq. Control Symp.
    (1983), p. 18

7. T. Kwon, B. Grover and H. Williams, Final Technical Report
    prepared for RADC/USAF Systems Command under Contract No.
    F19628-82-C-0042 (RADC-TR-83-230 March, 1983); Will be
    available through NTIS

8. Norman Houlding, Proc. 13th PTTI Meeting (1981), p. 505

9. Private communication with Dr. J. Vig and Dr. E. Filler, US
    Army ERADCOM, N.J.

QUESTIONS AND ANSWERS

ALAN JENDLY, OSCILLOQUARTZ: I have a question regarding the g-sensitivity, the static g-sensitivity.

MR. KWON: All right.

MR. JENDLY: You mentioned that you are using an oscillator which typically has a static g-sensitivity of four parts in ten to the minus ten per g.

MR. KWON: That's correct.

MR.JENDLY: You also mentioned that you are using it at a bandwidth of about 100 Hz, I believe. Then you say that this device, the complete device, is totally insensitive to orientation.
My question is: If you take this device and slowly rotate it by 180 degrees, and 90 degrees within the three axes, don't you measure those four parts in ten to the ten?

MR. KWON: The answer to that question is no, because we have a very fast servo loop. So, the orientation dependence of the VCXO is servoed out by the physics package.

THE RUBIDIUM-CRYSTAL OSCILLATOR HYBRID DEVELOPMENT PROGRAM

by

John R. Vig and Vincent J. Rosati

US Army Electronics Technology and Devices Laboratory (ERADCOM)
Fort Monmouth, New Jersey 07703-5302

ABSTRACT

The rubidium-crystal oscillator hybrid (RbXO) will make precise time available to systems that lack the power required by atomic frequency standards. The RbXO consists of two subassemblies in separate enclosures. One contains a small rubidium frequency standard (RFS) without its internal oven-controlled crystal oscillator (OCXO), plus interface circuits. The second contains a low-power OCXO, and additional interface circuits. The OCXO is ON continuously. Periodically, e.g., once a week, the user system applies power to the RFS. After the few minutes necessary for the warmup of the RFS, the interface circuits adjust the frequency of the OCXO to the RFS reference, then shut off the RFS. The OCXO enclosure is separable from the RFS enclosure so that manpacks will be able to operate with minimum size, weight, and power consumption, while having the accuracy of the RFS for the duration of a mission.

A prototype RbXO's RFS has operated successfully for 4200 ON-OFF cycles. Parallel efforts on a Phase II RbXO development are in progress. Two sources for the RbXO are scheduled to be available during 1986.

INTRODUCTION

The rubidium-crystal oscillator hybrid (RbXO for short) is intended to satisfy the requirements of systems that need frequency (or clock) accuracies that are currently beyond the capabilities of crystal oscillators, but which cannot tolerate the high power consumption of atomic frequency standards.

Rubidium frequency standards (RFS) typically have about 100 times better long-term stability than the best oven-controlled crystal oscillators (OCXO's). RFS's, however, also consume about 100 times more power than the lowest-power-consuming OCXO. The RbXO will provide the best qualities of both types of oscillators, i.e., it will have the long-term stability of a RFS with only slightly more power consumption than the OCXO.

PRINCIPLE OF OPERATION OF THE RbXO

A RFS normally consists of an atomic (Rb) resonator, an oven controlled crystal oscillator (OCXO), plus multiplier and feedback circuits, in a single enclosure. The RbXO consists of two subassemblies in separate

157

enclosures. One contains a small RFS, without the OCXO, plus interface circuits. The second contains a low-power OCXO and additional interface circuits. The OCXO is ON continuously. Periodically, the user system applies power to the RFS. After the few minutes necessary for the warmup of the RFS, the interface circuits adjust the frequency of ("syntonize") the OCXO to the RFS reference, then shuts off the RFS. For manpack applications, the OCXO subassembly will be separable from the rest of the RbXO so that the manpack can operate with minimum size, weight, and power consumption, while having nearly the accuracy of the RFS for the duration of a mission.

The following will illustrate how the RbXO is expected to operate. The RFS is expected to be able to maintain a frequency accuracy of $\pm 1 \times 10^{-9}$ for a period of ten years when operated in a duty-cycling mode (e.g., 5 minutes ON time per week). The OCXO can be expected to have an aging (or "drift") rate of better than 1×10^{-10} per day when operated for extended periods, and a maximum frequency offset, due to all other factors, of $\pm 1 \times 10^{-9}$. One can then determine the worst-case time errors for various scenarios. For example, if the RbXO syntonizes the OCXO once a week, then, for any period of a month after synchronization, the RbXO will be able to maintain a time accuracy of better than ten milliseconds (i.e., under this scenario the worst-case offset would be 2.7×10^{-9}).

For comparison, the same OCXO without the RbXO would accumulate an offset, due to aging alone, of about 3×10^{-8} one year after its calibration. At that time, it would be able to maintain an accuracy of only 100 msec for a one month resynchronization interval. If the user needed 100 msec per month or better accuracy, then the OCXO would have to be returned to depot for recalibration at intervals of one year or less.

POTENTIAL RbXO APPLICATIONS

One can envision several potential military applications for the RbXO. Examples are:

1. Manpacks and teampacks
2. Vehicles - where, although sufficient power is available for a RFS while the vehicle generator is ON, precise time must be maintained even when the generator is OFF.
3. Troop transport vehicles - after the vehicle transports the troops into the field, the RFS stays with the vehicle, the OCXO's in the manpack(s) are disconnected from the RFS at the start of a mission, and are reconnected at the conclusion of the mission,
4. Missiles and remotely piloted vehicles (RPV) - the RFS stays with the launcher, the OCXO goes with the missile or RPV.

THE OCXO

A miniature, low-power OCXO is a key part of the RbXO. The main candidate for this is the Tactical Miniature Crystal Oscillator (TMXO),[1] which is currently the subject of a Manufacturing Methods and Technology contract with Bendix, Inc. Since the TMXO is not yet available in production quantities, and in order to minimize the risk associated with this task, the RbXO technical requirements specify that "The RbXO interface shall

be capable of interfacing with either a 10 MHz TMXO, or any 10 MHz Hewlett-Packard 10811 equivalent OCXO, or any comparable stability OCXO." If, for whatever reason, the TMXO is not available, the power consumption of the RbXO would be higher because other OCXO candidates consume several times more power.

RbXO ENERGY CONSUMPTION AND TIME AND FREQUENCY UNIT

Significantly lower energy consumption is one of the major advantages of the RbXO over continuously operated RFS's. A comparison of the expected RbXO performance with: the performance of a RFS; the expected performance of production TMXO's; and an HP 10811 type OCXO (e.g. the Piezo Crystal model no. 007) is shown in Table 1. The comparison is based upon the Efratom M1000 specifications for the RFS, the use of the TMXO for the OCXO of the RbXO, and assumes that a pair of lithium batteries[2] (BA-5590/U) are available for powering the oscillators. The RbXO increases the battery life from less than a day with a continuously operated RFS, to 52 days.

Each BA-5590 has a capacity of about 6.5 Ah, and a volume of 883 cm^3. Therefore, a "time and frequency unit" consisting of an RbXO, two BA 5590's, a time code generator and a frequency distribution system could operate continuously without battery replacement for over a month while occupying a volume on the order of 3200 cm^3 (195 in^3), e.g., a box of size 14 cm X 15 cm X 15 cm (5½" X 6" X 6").

PHASE I RbXO DEVELOPMENT

During Phase I of the RbXO Development effort (under an FY-83 contract with Efratom, Inc.), a breadboard RbXO was designed and constructed. The breadboard consists of an Efratom M1000 RFS, and an interface box that contains the interface circuits, a government furnished miniature OCXO (the "TMXO"), a time-of-day clock, and a timer with which the ON-OFF intervals of the RFS can be set. The dimensions of the interface box are about 17" X 16.5" X 6". A copy of the Phase I final report is available to qualified requesters from tne Defense Technical Information Center.[3]

RbXO PROTOTYPE TEST RESULTS

As the reliability under intermittent operation is a major uncertainty about the RbXO approach, as soon as the RbXO prototype was received in April 1984, it was placed on test at laboratory ambient temperature. The interface box was set to turn on the RFS once an hour for 5 minutes each time. The time error was measured by comparing the RbXO's 1 pps output with that of a Hewlett-Packard 5601 cesium standard.

During the first 700 hours (i.e., 700 on-off cycles), the average time error was about 8 microseconds per day. Changing the ON time changed the slope of the accumulated time error curve; e.g., increasing the ON time to 6 minutes resulted in a slope of about 10 microseconds per day (which corresponds to an average frequency offset of 1.2 X 10^{-10}). The variation of time error with ON time was the result of the variation of the RFS's frequency offset with warmup time.

	RFS alone	RbXO with TMXO	TMXO alone	HP 10811-type OCXO's alone
Power consumption at -55°C	20W	0.35W	0.25W	4W
Power consumption at 0°C	17W	0.25W	0.15W	2.5W
Battery life, at 0°C, with two BA-5590/U's	18 hours	52 days	86 days	5 days
Size	790 cm^3	<1300 cm^3	17 cm^3	230 cm^3
Aging per year (1st year)	2 X 10^{-10}	6 X 10^{-10}	3 X 10^{-8}	3 X 10^{-8}
Short term stability $\sigma_y(\tau)$ 1 sec $\leq \tau \leq$ 10 sec	3 X 10^{-11} (τ ½)	5 X 10^{-12}	5 X 10^{-12}	5 X 10^{-12}
Temperature stability	3 X 10^{-10} -55°C to +68°C	1 X 10^{-9} -55°C to +68°C (RFS) -55°C to +90°C (TMXO)	1 X 10^{-9} -55°C to +90°C	1 X 10^{-8} -55°C to +71°C

Table 1. Oscillator comparisons

160

After about 1500 on-off cycles, the RFS was cooled to -45°C, while the interface box remained at laboratory ambient. The slope of the time error vs. elapsed time changed to -25 microseconds per day. After about 90 on-off cycles at -45°C, the RFS's internal crystal oscillator failed to hold lock; i.e., it would lock for a few seconds, then unlock, then lock, etc. When the temperature was increased gradually, reliable locking started to occur at about +10°C. After cooling again, the failure to lock was reproduced.

The RFS was returned to Efratom for failure analysis. Efratom confirmed the failure at low temperatures and determined that the cause of failure was insufficient gain in the crystal oscillator circuit. Replacement of the crystal oscillator and resetting the crystal oscillator gain corrected the problem. Since the RFS in the Phase II and production RbXO's will not contain an internal crystal oscillator, this failure is not significant.

After receipt of the repaired RFS, the on-off cycling was continued at room ambient for 1176 cycles. The RFS was then temperature-cycled daily for 38 days between -55°C and +70°C, and on-off cycled about hourly during this 38 day period, for a total of 840 on-off cycles. The time error was measured each day after stabilizing the temperature at 60°C. The accumulated time error vs. elapsed time had a slope of -51 μsec per day, as shown in Figure 1, indicating a constant frequency offset of -5.9 X 10^{-10}.
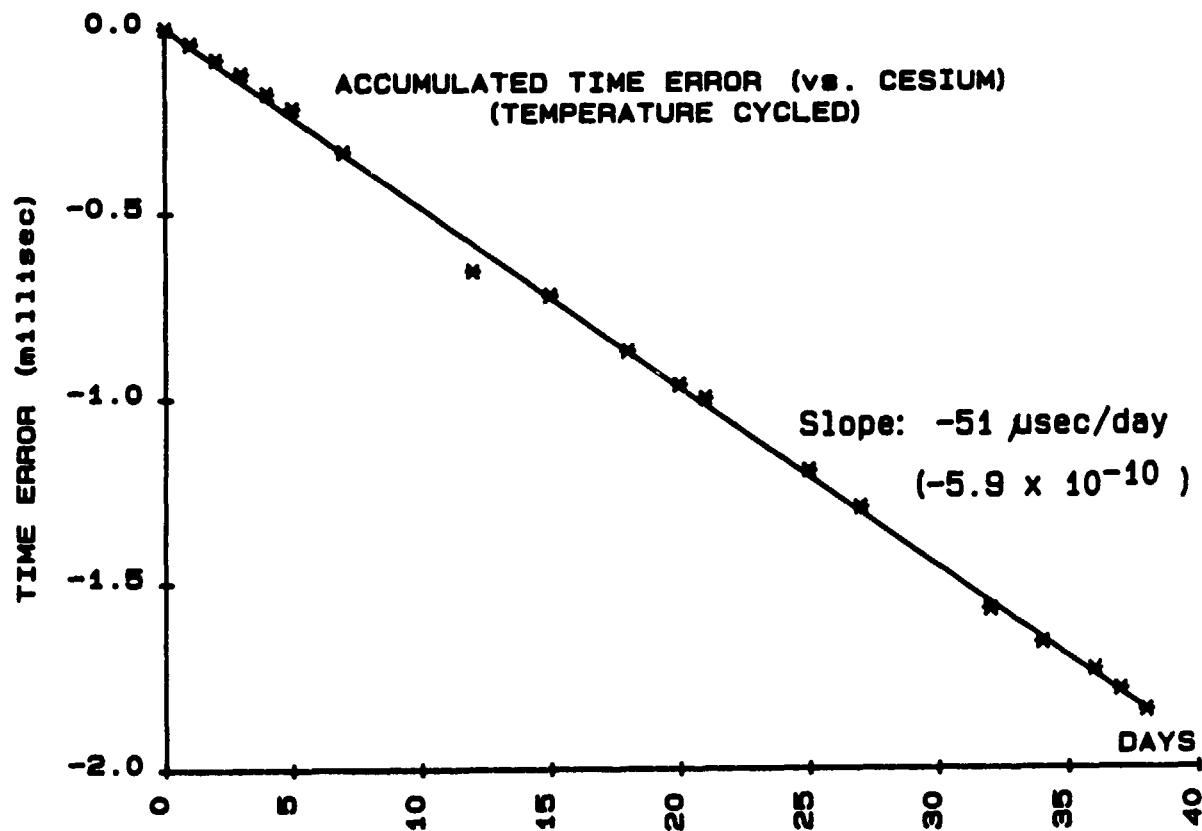
Figure 1. Time error vs. elapsed time

During the temperature cycling, frequency vs. temperature data was collected once a week during a cycle from -55°C to +70°C to -55°C. The RFS was ON continuously during the frequency vs. temperature run. The result of one such run is shown in Figure 2. The frequency excursion was within the M-1000's 3×10^{-10} specification.
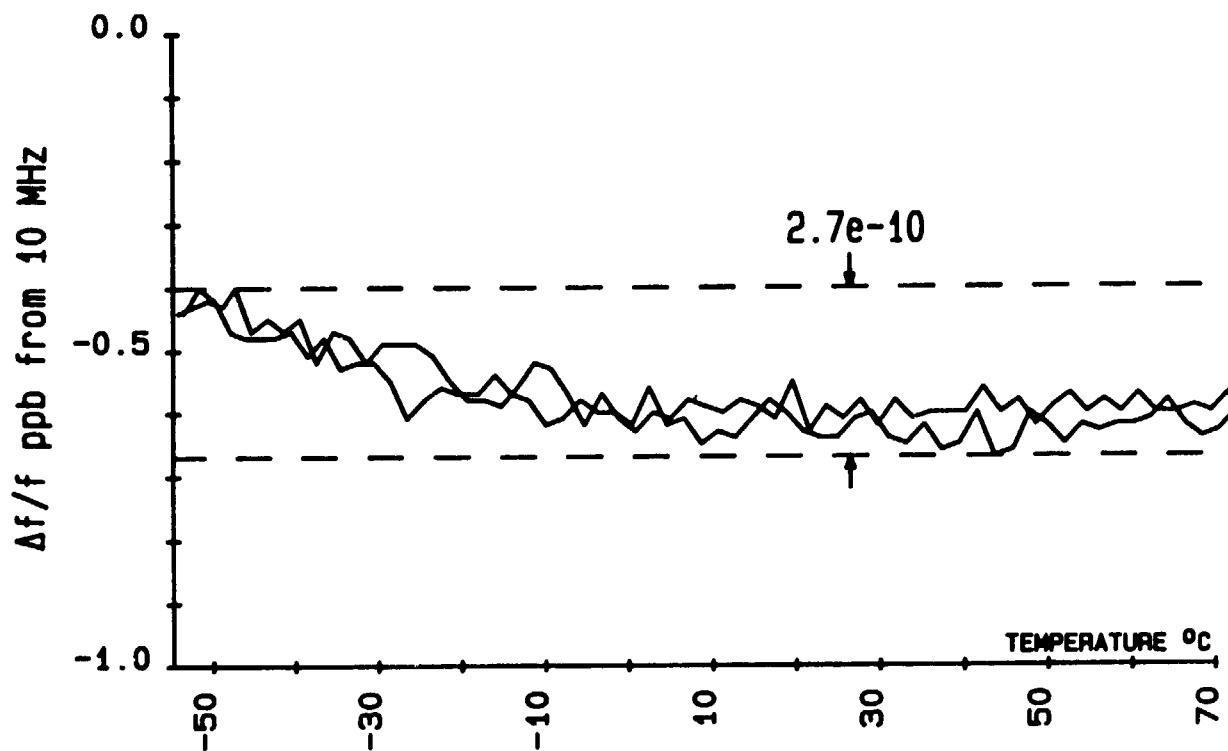
Figure 2. RFS frequency vs. temperature characteristic.

The on-off cycling history of the RbXO prototype RFS is summarized in Table II. The summary includes 600 cycles the RFS experienced at Efratom prior to shipment. That the RFS stayed within specifications for over 4200 on-off cycles (aside from the failure of the RFS's internal crystal oscillator) is very encouraging because it indicates that inherent failure mechanisms due to on-off cycling do not exist. Of course, additional units need to be tested. Sixteen additional units are scheduled to be tested during the Phase II RbXO development, as is described below.

Upon completion of the 4206 on-off cycles, the RbXO prototype RFS was placed on long-term aging while continuously ON, initially at 23°C. The results for the first 44 days at 23°C are shown in Figure 3. (Straight lines in the curve indicate that no data was collected during the period.) On day 12, a momentary power interruption resulted in a frequency offset of -4 $\times 10^{-11}$ and an increased aging rate. On day 25, an intentional 10-second power interruption returned the frequency to its previous value. The cause of this "glitch" has not yet been determined. However, if we ignore the offsets, the total aging is 7×10^{-12} in 44 days, and the aging rate at day 44 is about 1×10^{-13} per day.

RbXO BREADBOARD RFS HISTORY

(APRIL 1984 TO NOVEMBER 1984)

# ON/OFF CYCLES	TEMP	TIME ERROR/DAY	REMARKS
600	23	– – –	AT EFRATOM
1500	23	8 μSEC AVG	
90	–45	ERRATIC	INTERNAL XO FAILED
1176	23	– – –	NO DATA TAKEN
840	T CYCLED	51 μSEC AVG	–55 TO 70 DEG. C
4206	VARIOUS	– – –	TOTAL NUMBER OF CYCLES.

TABLE II
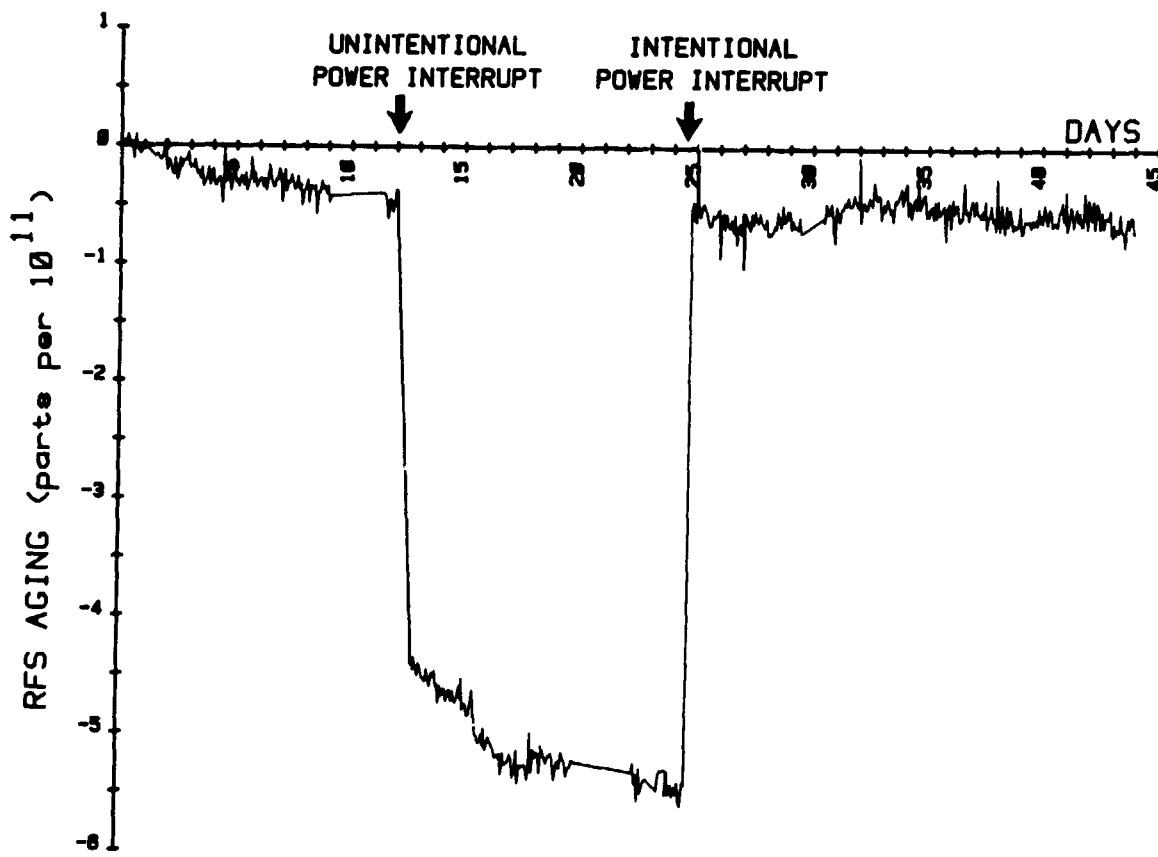
Figure 3.   RFS aging after 4200 on-off cycles

PHASE II RbXO DEVELOPMENT

On 26 June 1984, two firm fixed price contracts were signed for Phase II of the RbXO program, one with the Efratom Division of Ball Corp., the other with E.G.& G., Inc. The total cost of the two contracts is $668,000. Both companies are to meet the same requirements and both programs are of 18 months duration. Salient features of the requirements are:

1) Size: 80 cu. in. (517 cm^3) plus the size of the OCXO
2) Operating temperature range: -55°C to +68°C
3) RFS thermal retrace/hysteresis: 5 X 10^{-11} at all operating temperatures
4) RFS frequency vs. temperature: ±4 X 10^{-10}
5) RFS aging after 30 days at 60°C ambient: 1 X 10^{-12} per day
6) Power consumption at -55° (after warmup): 23W for the RFS, 80mW for the interface circuits
7) Hardened to tactical radiation levels,
8) Usable with 5MHz and 10MHz OCXO's
9) Deliverable hardware from each contractor: 8 RbXO's, four of which have passed the design verification test, plus four which are to be tested by the government, and 3 RbXO demonstrators that include a digital clock and timer for turning the RFS ON periodically.

THE DESIGN VERIFICATION TEST

This requirement of the Phase II RbXO development calls for the RbXO to be temperature-cycled from -55°C to +68°C to -55°C once a day, and for the RFS be turned ON and OFF twenty times a day for a total of 3600 on-off cycles, according to a specified schedule. This test is intended to uncover failure mechanisms and stability changes due to the duty cycling mode of operation.

Prior to this program, there had been only hearsay type of information on the stability and reliability of RFS's operating intermittently. A major goal of the Phase II RbXO program is to determine the degree of risk due to the intermittent operation and to minimize the risk through proper RbXO design. A second goal is to determine the stability of RFS's under intermittent operation.

RbXO SCHEDULE

The RbXO program schedule of major milestones is as follows:

1. Breadboard phase: complete
2. Design and build: August 1984 to March 1985
3. Design verification test by contractors: March 1985 to September 1985
4. Delivery of the 16 RbXO's to government: Oct - Nov 1985
5. Design verification tests by government: December 1985 to June 1986
6. Government long-term tests start: July 1986.

Milestones 3 to 6 assume that the contractors' design verification tests

are successful on the initial attempts. If failures occur, contractors will have to correct the problem and repeat the tests. The schedules will then slip.

CONCLUSIONS

The RbXO will make precise time available in systems that lack the power required by atomic frequency standards. The feasibility of the RbXO has been demonstrated. That the prototype RFS has operated properly for 4200 on-off cycles is encouraging. (If the RFS is on-off cycled once a week, the 4200 cycles correspond to an 80 year life!)

Parallel efforts on the Phase II RbXO development are in progress. Two sources for the RbXO are scheduled to be available during 1986.

ACKNOWLEDGEMENTS

The authors wish to acknowledge Dr. Raymond L. Filler and Mr. Dennis Bowman for their contributions to the collection and analysis of the data.

REFERENCES

1. D. Brown, et al., "Manufacturing Methods and Technology for Tactical Miniature Crystal Oscillator," Proc. 38th Annual Frequency Control Symposium, pp. 380-386, 1984.

2. US Army Battery Applications Manual, June 1984; copies can be requested from Power Sources Div., ATTN: DELET-PB, US Army Electronics Technology and Devices Laboratory, Ft. Monmouth, NJ 07703-5302.

3. R.D. Paul, "Rubidium Oscillator and Time-of-Day-Clock," Research and Development Technical Report DELET-TR-83-0412-F, April 1984, AD-B086125L.

NEW FEATURES OF DIFFERENT FREQUENCY GENERATING SYSTEMS DUE TO THE USE OF ELECTRODELESS RIGIDLY MOUNTED BVA QUARTZ CRYSTAL RESONATOR

A. Jendly/E. Graf/G. Busca
OSCILLOQUARTZ S.A.
Brévards 16
2002 NEUCHATEL - Switzerland

D.A. Brownsea
PLESSEY ELECTRONIC SYSTEMS LTD.
Grange Road
CHRISTCHURCH - England

ABSTRACT

Design and production data of BVA quartz crystal resonators and oscillators have been presented in the past at the Frequency Control Symposium. [1,2,3,4]

The BVA 5 MHz crystal equipped frequency sources exhibit a new blend of remarkable performances such as 10^{-11} daily stability, 5×10^{-13} short term stability (1 to 30 s time intervals) and close to the carrier low phase noise (1 Hz : -120 dBc, 10 Hz : -140 dBc), whereby retaining the customary crystal oscillator benefits of small volume, high reliability and low price, as opposed to more sophisticated frequency generators which would be required to achieve comparable performances.

Examples illustrating the impact of the Oscilloquartz BVA OCXO in different frequency generating systems will be presented :

- in cesium frequency standards
- in a hydrogen frequency standard
- in a precision distribution sub-system for satellite ground stations
- in high hierarchy exchanges of digital networks, synchronized by the master-slave method

INTRODUCTION

Over the past 4 years, OSCILLOQUARTZ S.A. went through the various and challenging steps of turning the basic "BVA CONCEPT" into an industrial product, then to put that product into the field.
This paper intends to focus on the last portion of the programm, namely to describe where and why BVA oscillators have been chosen for various frequency generating devices, and how such devices benefit from the BVA technology.

PRODUCT DESCRIPTION : BVA RESONATOR

The BVA unit we are discussing here, consists of an "electrodeless" resonator at 5 MHz, 5th overtone, AT-cut, which is decoupled from his mounting structure by 4 bridges. These bridges are precisely made (width : 0.4 mm) and located and serve the purpose of keeping the mounting stress away from the active center part (resonator) as much as possible.
The electrodes are evaporated on two counterpieces, like condensors, also made of AT quartz blanks with the same cutangle as the resonator blank (see fig. 1).
The 3 parts are rigidly held together with stainless steel clips, and the whole sandwich is spring-mounted into a rigid cage consisting of a base plate and a cover plate which are fixed to four columns.
The BVA assembly is mounted in a cold-weld enclosure with a chimney which enables to bake out the finished resonator at 250°C while pumping it to 10^{-8} mbar with a cryo pumping system and sealing the enclosure by a pinch-off process (see fig. 2).

This fairly complex structure offers many advantages, namely :
- the "electrodeless design" eliminates most of the problems linked to surface perturbations and ion migrations
- the use of a crystal resonator mounting made out of quartz material eliminates the problems linked to discontinuities, relaxation and stresses in the mounting points
- the reduction of space surrounding the active part eliminates the problem linked to contamination

Typically, the BVA resonator provides the following characteristics (5 MHz AT 5th overtone unit) :
$$Q = 2.5 \times 10^{6}$$
$$R1 = 80 \ \Omega$$
$$C1 = 1.02 \times 10^{-4} \ pf$$
$$CO = 4.1 \ pf$$
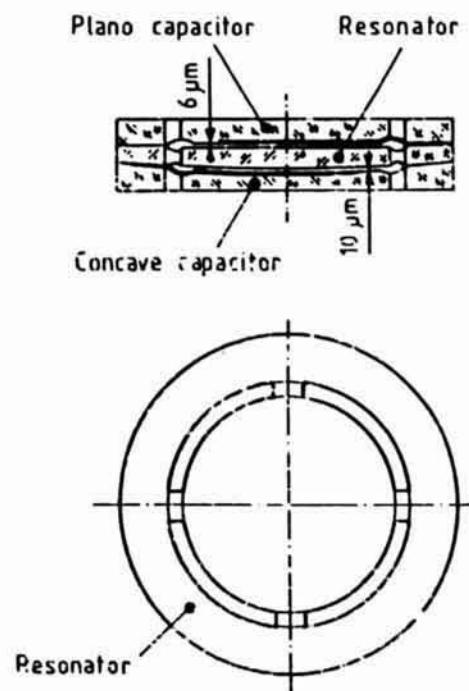
FIGURE 1 : BVA INNER ASSEMBLY
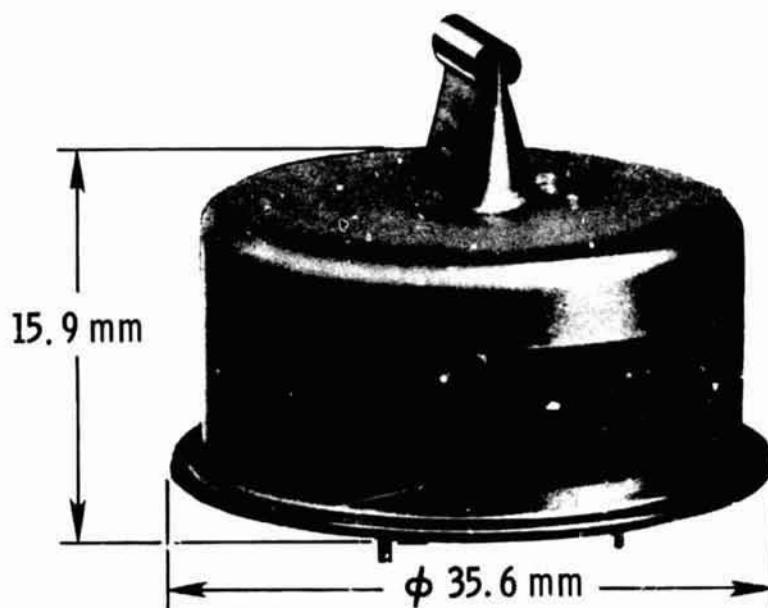
FIGURE 2 : BVA RESONATOR (COMPLETE)

169
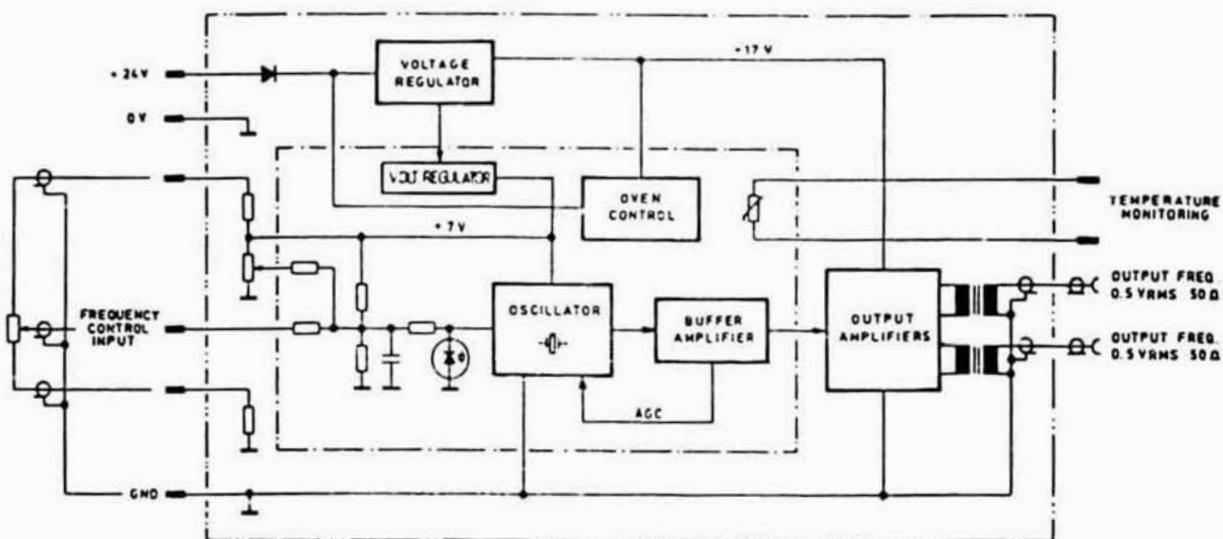
FIGURE 3 : OSCILLATOR BLOCK DIAGRAM (MODEL 8600/8601)
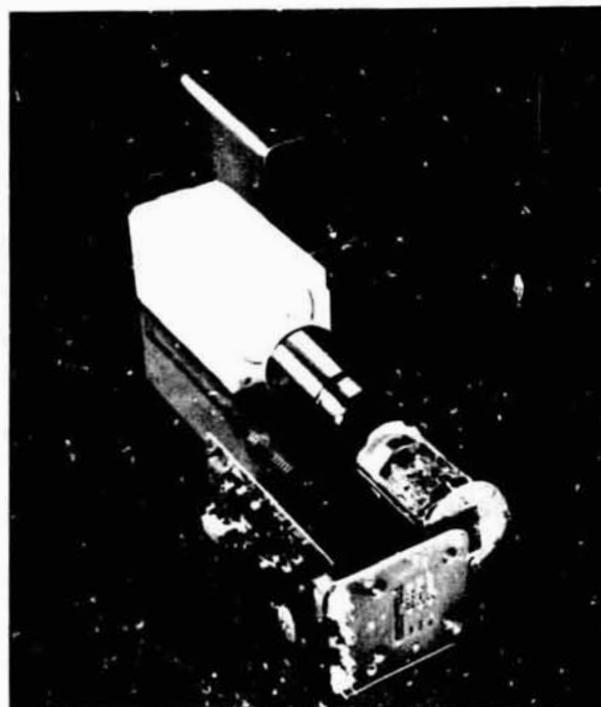
FIGURE 4 : BVA OSCILLATOR (MODEL 8600/8601)

PRODUCT DESCRIPTION : BVA OSCILLATOR

To match the outstanding performances of the resonator, the electronics of our best OCXO B-5400 has been redesigned, with high emphasize on low noise and high stability at all levels of the package. Basically, the BVA oscillator (so-called 8600 or 8601) includes the following sub-sections (see fig. 3 and 4).

Inside the oven assembly : - BVA resonator
- 5 MHz oscillator and automatic gain control
- frequency pulling network
- oven control circuit
- 17 V/7 V voltage regulator

Outside the oven assembly : - thermal isolation
- 24 V/17 V voltage regulator
- dual output buffers
- mechnical frequency adjustment

The most significant features and performances of the BVA oscillator can be outlined as follows (typical values) :

long term stability : $\leq$ 1x10-10/month

short term stability ($\sigma\tau$) : $\leq$ 5x10-13 for τ = 0.2 to 30 sec

phase noise ($S\psi$) : at 1 Hz = -120 dB / at 100 Hz = -150 dB

static "g" sensitivity : 5x10-10/g

In these areas, the BVA oscillator has considerably improved the performances obtained with commercially available OCXOs, and has set new standards to this category of frequency sources. This further, closes the gap between the best OCXOs and the Rb sources offered on the market.
It should also be noted that due to its relative simplicity, the BVA oscillator compares very advantageously to its nearest atomic competitor (rubidium standards) both in terms of prices and reliability.
We shall now take a closer look at the various possibilities offered with this device, when integrating it into various frequency generating systems.

APPLICATION IN CESIUM FREQUENCY STANDARDS

Combined requirements for high accuracy and good spectral purity of the output signal can be found in Doppler Radar Networks, where many observation sites must operate in perfect synchronization.

A cesium standard with BVA oscillator offers the ideal solution to fulfill these requirements :

the cesium accuracy enables plesiosynchronization of the network while
the BVA oscillator guarantees the spectral purity of the distributed output

The crystal oscillator in a cesium frequency standard loop (see fig. 5) serves the following purposes :

- provides a 5 MHz output to the user and to the multiplier chain
- contributes to the determination of the loop time constant
- contributes to the phase performances of the output signal ($S\psi$)
  for Fourier frequencies located above the loop band-width
- contributes to the short term stability performances of the output signal
  ($\sigma\tau$) for the time intervals (τ) shorter than the loop time constant

For a given device (in our example, the cesium oscillator OSA 3000), the replacement of the flywheel oscillator (conventional AT-P5 OCXO) by a BVA oscillator results in the following advantages :

POSSIBILITY TO INCREASE THE LOOP TIME CONSTANT FROM 1 TO 3 sec (SHORT)
AND/OR 10 TO 30 sec (LONG)

A conventional AT-cut, 5th overtone crystal oscillator has a typical static g-sensitivity of $2\times10^{-9}/g$ while the BVA oscillator improves that figure by a factor of 4 (typically $5\times10^{-10}/g$). In the cesium loop, the BVA oscillator can therefore be more losely locked to the cesium beam tube, thus allowing a better exploitation of its superior short term stability and spectral purity.

IMPACT ON THE PHASE NOISE PERFORMANCES

With a time constant set to either 3 or 30 sec, the cesium standard now exhibits the following characteristics (see fig. 6) :

Frequency offset from carrier	$S\psi$ τ = 3 sec	$S\psi$ τ = 30 sec
1 Hz	- 90 dB	-105 dB
10 Hz	-132 dB	-136 dB
100 Hz	-145 dB	-145 dB
1'000 Hz	-145 dB	-145 dB
10'000 Hz	-145 dB	-145 dB
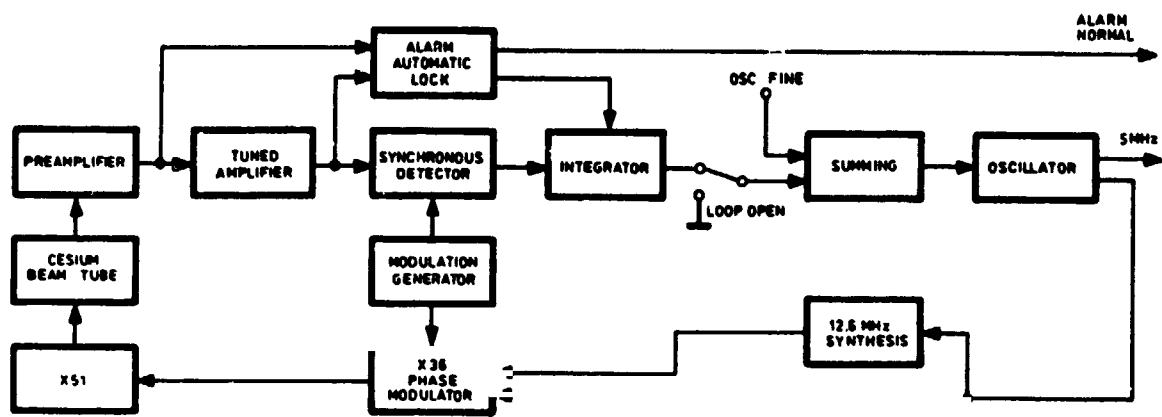
FIGURE 5 : <u>CESIUM FREQUENCY OSCILLATOR BLOCK DIAGRAM</u>
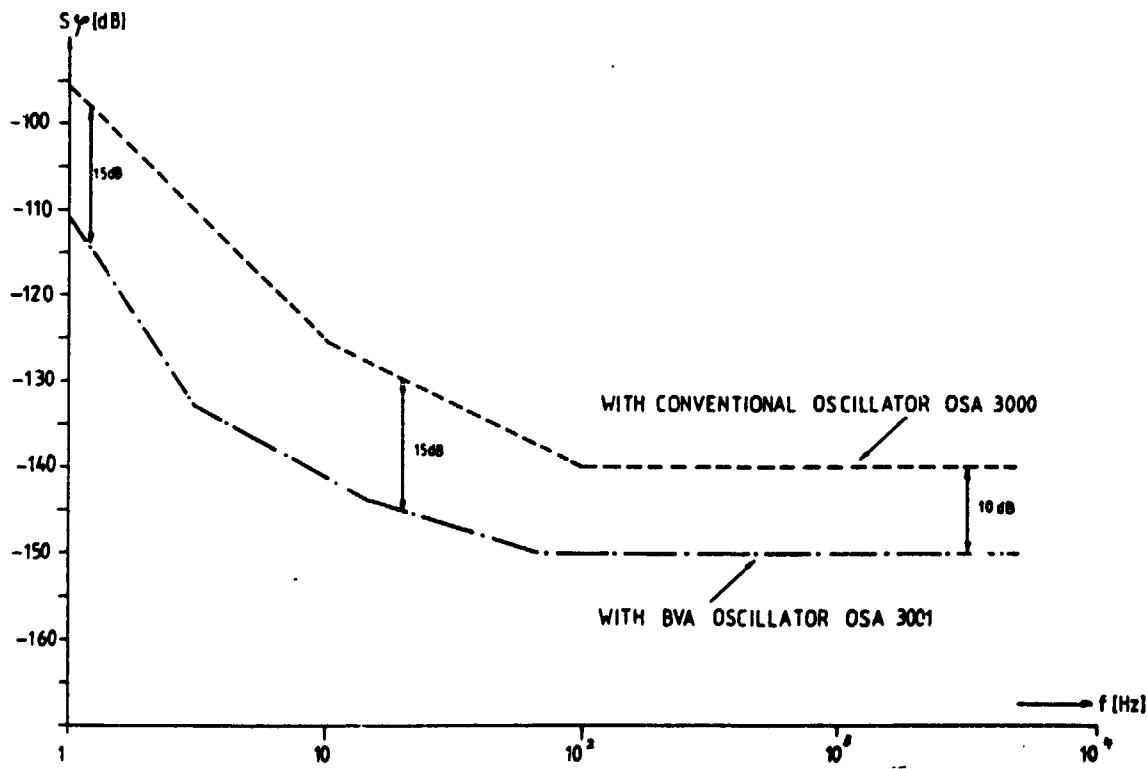
FIGURE 6 : <u>3000/3001 - PHASE NOISE DATA PLOT (10^0 ÷ 10^4 Hz)</u>

173

IMPACT ON THE SHORT TERM STABILITY PERFORMANCES

With a time constant set to either 3 or 30 sec, the cesium standard now exhibits the following characteristics (see fig. 7) :

Time interval (τ)	σ ($\tau = 3$ sec)	σ ($\tau = 30$ sec)
0.1 sec	5x10-12	1x10-12
1 sec	2x10-11	2x10-12
10 sec	9x10-12	4x10-12
100 sec	3x10-12	3x10-12

Figure 6B provides the same data, looking at Fourier frequencies very close-in to the carrier. Assuming that the equipment could operate in a very stable environment, the loop time constant could even be increased to 100 sec, providing even better results.
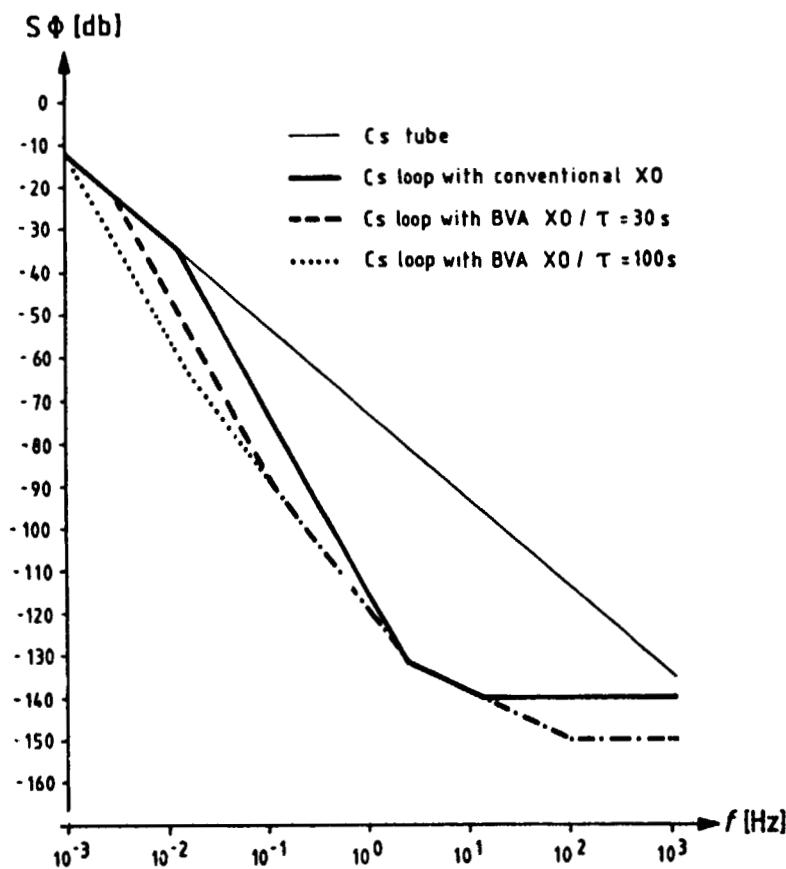
FIGURE 6B : <u>300G/2001 PHASE NOISE DATA PLOT (10^{-3} - 10^{3} Hz)</u>

174
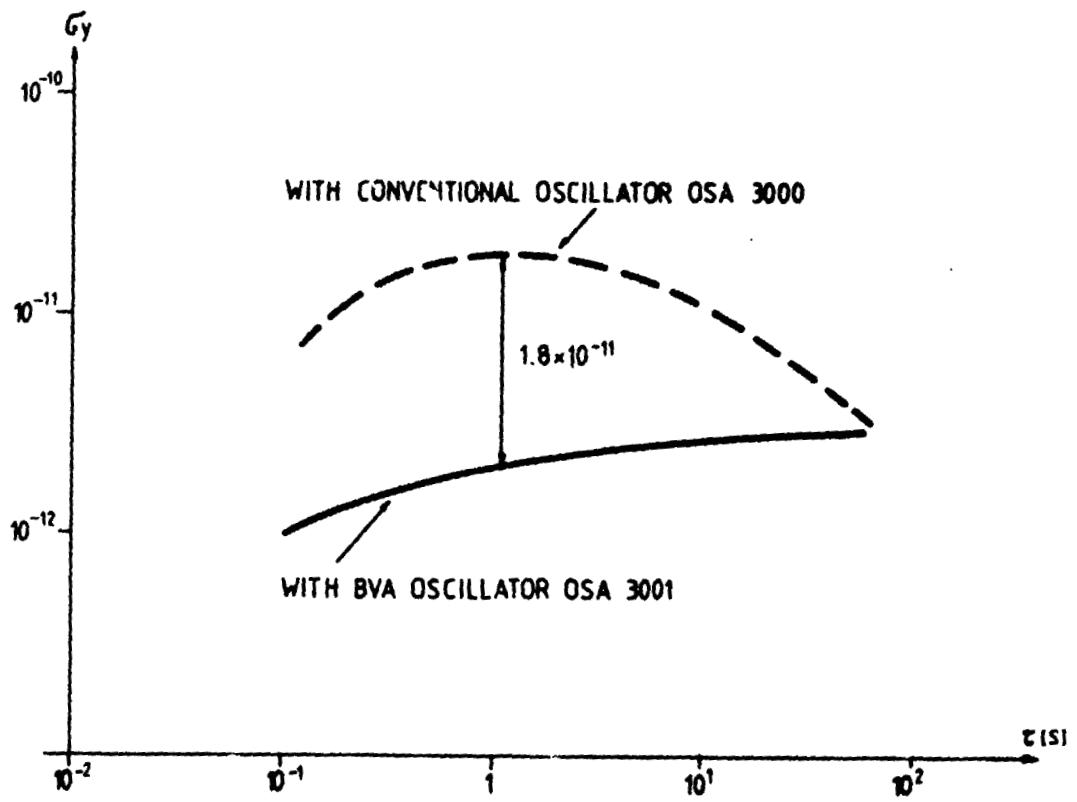
FIGURE 7 : 3000/3001 SHORT TERM STABILITY DATA PLOT (10^{-2} - 10^{2} s)

APPLICATION IN A HYDROGEN MASER

The use in radioastronomy and VLBI (Very Long Baseline Interferometry) of increasingly higher observation frequencies creates a unique requirement for an oscillator having the lowest spectral density of phase fluctuations ($S\psi$) obtainable for both high Fourier frequencies (i.e. from 1 Hz up to a few MHz) and low Fourier frequencies (i.e. down to 10^{-5} Hz). The LO (Local Oscillator) signal needed for a radioastronomy receiver is normally derived from an H-maser atomic signal through at least 2 phase lock loops (see fig. 8). A VCXO (Voltage Controlled Crystal Oscillator) having normally a 5 MHz output frequency is phase locked to the atomic signal with a typical loop bandwidth of a few Hz, and the microwave oscillator is phase locked to the VCXO signal. The bandwith of this last PLL (Phase Locke Loop) depends on the phase noise characteristics of the microwave oscillator and is typically of the order of 10^5 Hz. The reason behind that design resides in the fact that the atomic signal has the lowest phase noise for Fourier frequencies below 1 Hz, the VCXO multiplied to the LO frequency has normally the lowest phase noise in the Fourier frequency range between 1 and 10^5 Hz and the microwave oscillator has the lowest phase noise for Fourier frequencies above 10^5 Hz. Here we are concerned mostly with the phase locking of the VCXO on the atomic signal.
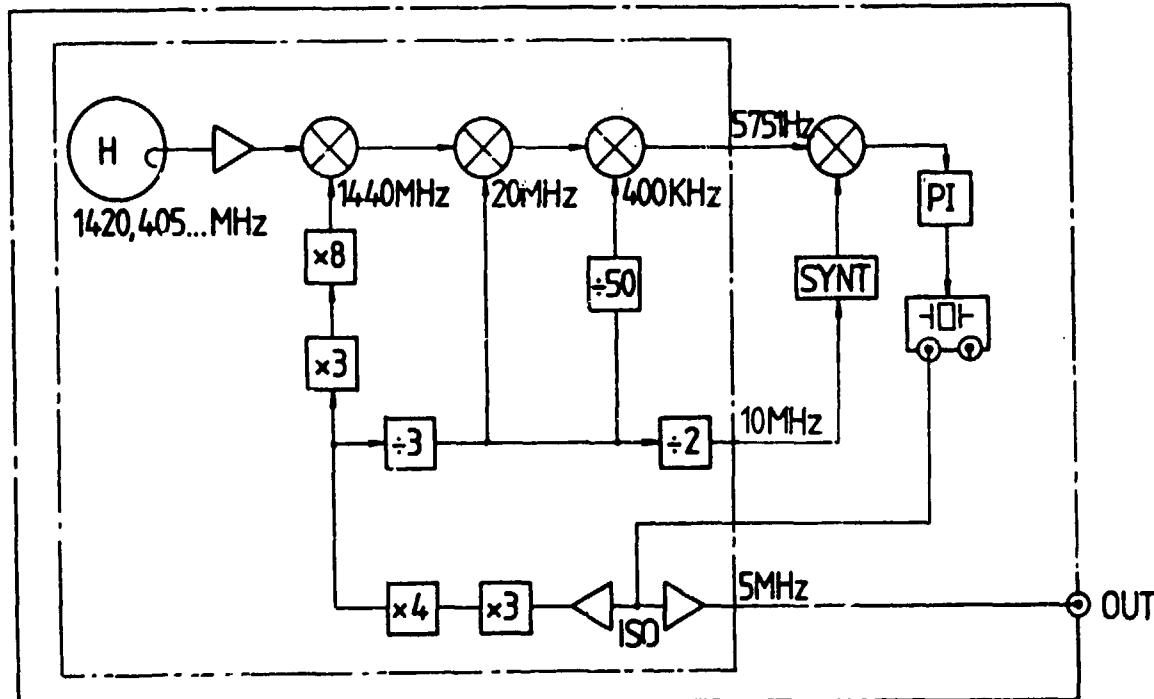
FIGURE 8 : MASER PHASE-LOCK SYSTEM

REALISATION OF AN "OPTIMUM" PLL

The state-of-che-art 5 MHz BVA quartz crystal oscillators (4) has a spectral density, at 5 MHz, given by

$$S_{\psi Q} = 10^{12.2} x f^{-3} + 10^{-13.2} x f^{-1} + 10^{-15.7} x f^{-0} \quad [6]$$

A maser oscillator typical phase noise referred to 5 MHz is given by [4]

$$S_{\psi A} = 10^{12.9} x f^{-2} + 10^{-11.1} x f^{0} \quad [4]$$

An "optimum" PLL similar to the one described in ref. 7 has been designed and realized according to the criterion of minimum integrated rms phase noise. The experimental results are in good agreement with the theoretical calculation and are represented, at che 5 MHz output frequency, in fig. 9, 10 and 11, for Fourier frequencies above 1 Hz. The result derived from the final setting (fig. 11) is believed to be one of the best available today and is still susceptible to an improvement of 15 dB in the white phase noise region. The previous results give a total rms time jitter of 0.32 ps in the 1 Hz-100 kHz bandwidth, this means that this maser could be conveniently used up to 200 GHz interferometer frequency with a negligible 10% coherence loss. For the details of the calculation we refer to ref. 5

SPECIFICATIONS DETERMINATION - FREQUENCY STABILITY

In addition to the previous discussion t the requirement of the shcrt term/long term frequency stability the following comment is in order. The optimum PLL previously described can be used conveniently only in vibration free environments, because the loop bandwidth is approximately 0.5 Hz and the BVA oscillator g-sensitivity 5x10-10/g the slow coherence requirement normally is translated in the following specification for the Allan Variance :

$$\text{and } \sigma_y(\tau) = 7x10^{-13} \tau^{-1} \quad 1 \leq \tau \leq 100 \text{ sec}$$

$$\sigma_y(\tau) = 2x10^{-15} \tau^{0} \quad 1'000 \leq \tau \leq 10'000 \text{ sec}$$

which appears fully satisfactory in consideration of the 1x10-14 Allan "ariance limitation imposed by the atmosphere itself. The 5 EFOS H-masers [8] constructed and tested in our laboratory have shown consistently stabilities within the previous specs (see fig. 9),
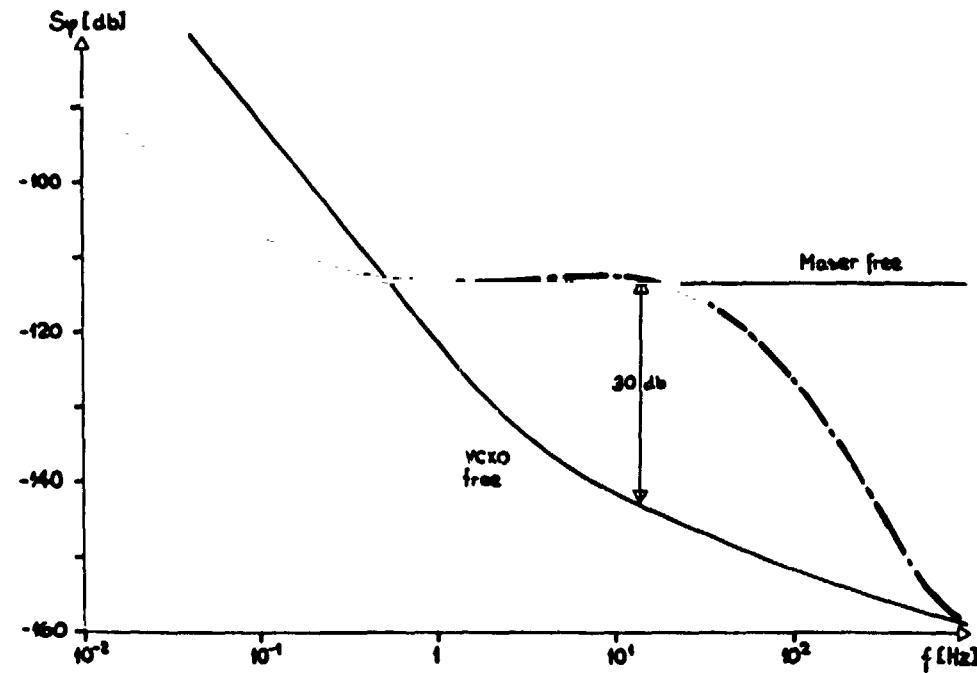
FIGURE 9 : <u>MASER PLL & VCXO TYPE BVA 8601/5 MHz</u>
Fn = 10.6 Hz
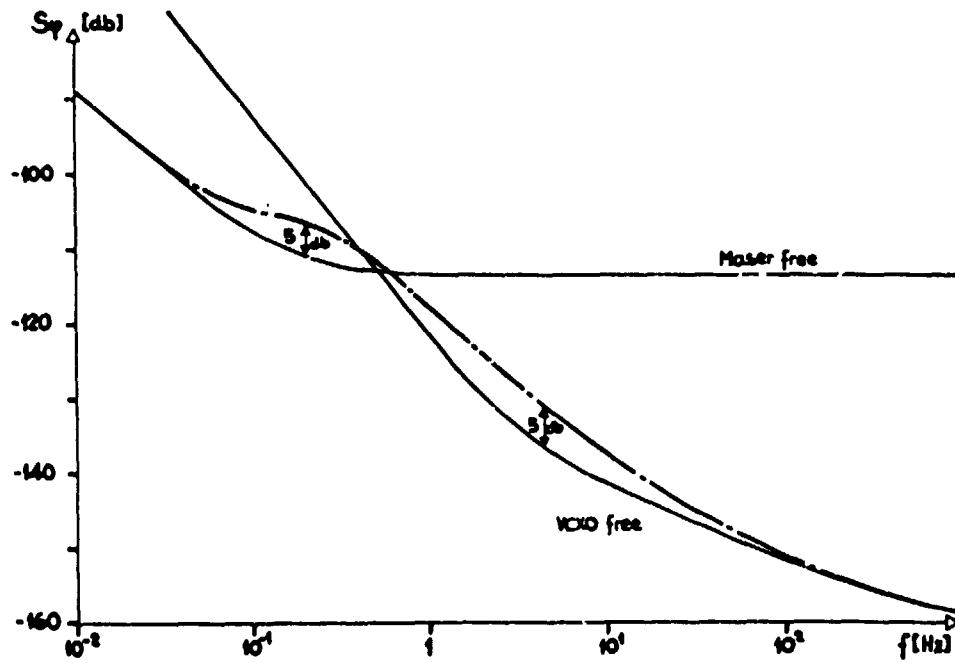
FIGURE 10 : <u>MASER PLL & VCXO TYPE BVA 8601/5 MHz</u>
Fn = 0.2 Hz

178
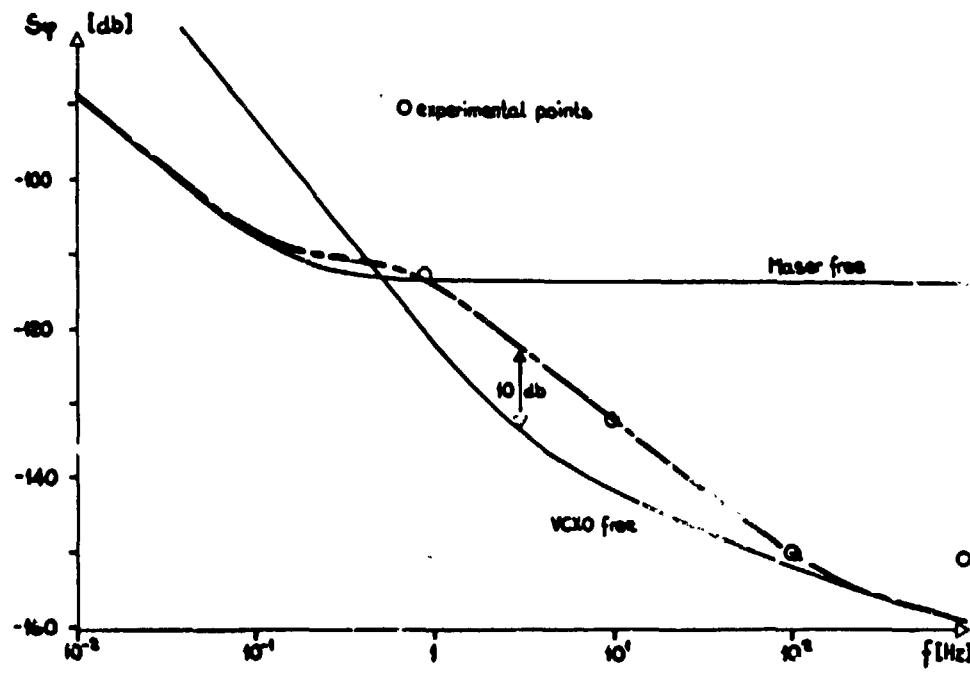
FIGURE 11 : MASER PLL & VCXO TYPE BVA 8601/5 MHz (FINAL SETTING)
Fn = 0.55 Hz
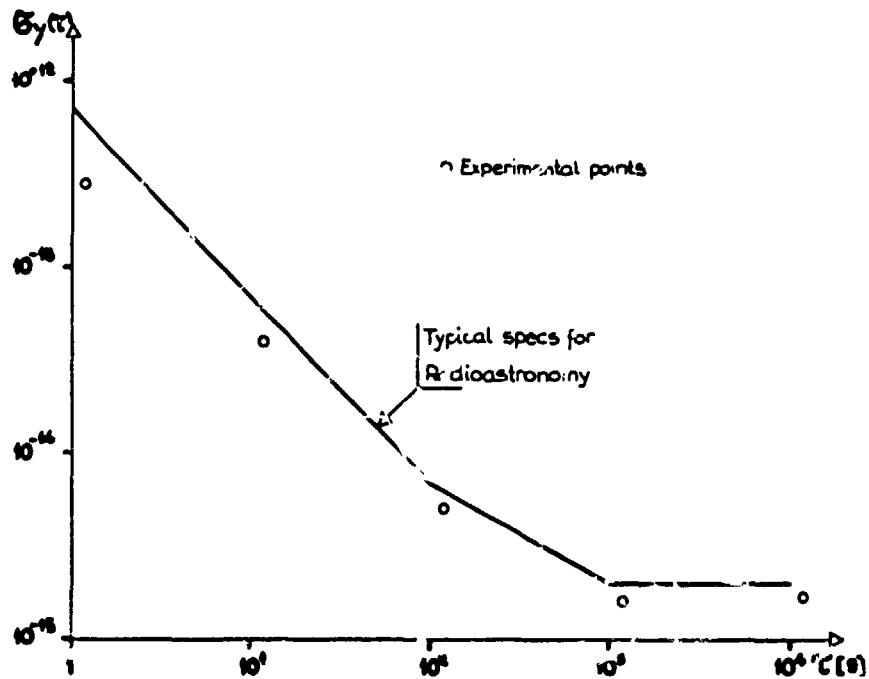
FIGURE 12 : EFOS MASER FREQUENCY STABILITY

179

APPLICATION IN PRECISION DISTRIBUTION SUB-SYSTEM FOR SATELLITE GROUND STATION

DESIGN PHILOSOPHY

With the requirements in satellite communication systems to make maximum usage of the frequency spectrum, coupled with the reliability and availability requirements of a state-of-the-art communications system, the technical specification of a frequency distribution sub-system is extremely stringent, especially since the operation of the station is totally dependent on that sub-system.

In order to meet this high technical specification within a relatively short development timescale, a design was evolved making the maximum use of state-of-the-art proprietary equipment modules.

The main frequency references for the sub-system are provided by two crystal frequency standards, each including BVA oscillators.

Crystal oscillators although not as stable, long term wise, than rubidium standards, were used because of their extremely low phase noise and high MTBF.

Longer term trends in stability are determined by comparing the oscillator outputs with a rubidium standard. Considering the typical aging of the oscillator below 10-11/day, the number of periodic recalibration can be set to a minimum.

IMPLEMENTATION

The sub-system may be conveniently divided into five main areas for consideration :

<div align="center">

THE FREQUENCY GENERATION

INTERMEDIATE CABLING

REMOTELY SITUATED AMPLIFIERS

THE POWER SUPPLY

</div>

The relationship between these areas can be seen in fig. 13.
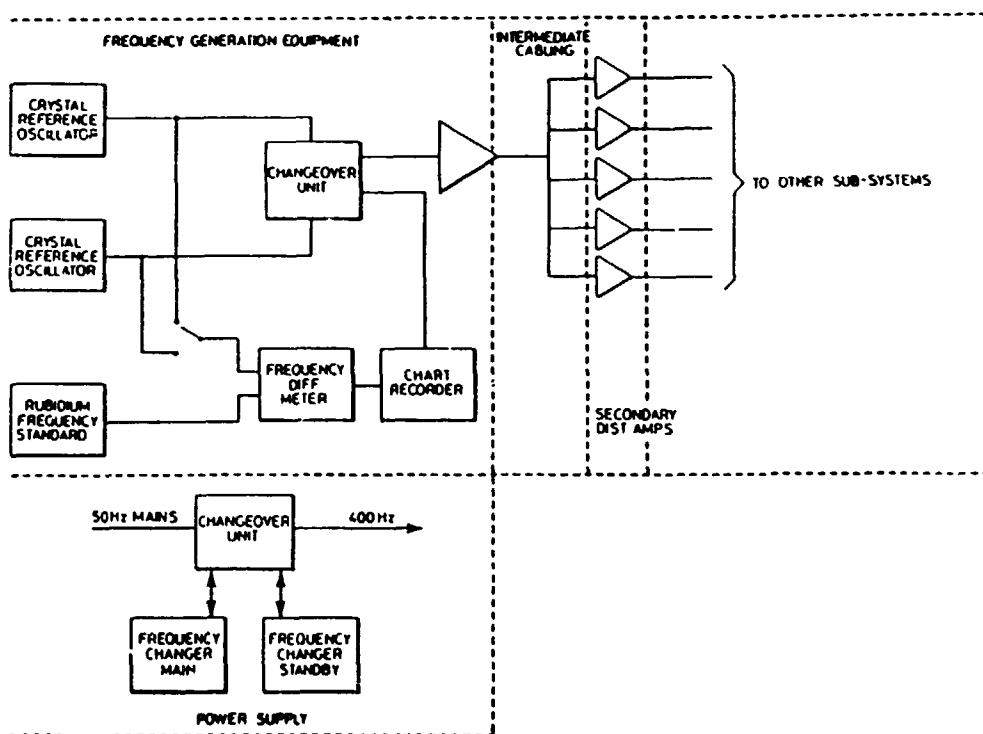
FIGURE 13 : FREQUENCY DISTRIBUTION SUB-SYSTEM -BLOCK DIAGRAM-

C - 3

FREQUENCY GENERATION EQUIPEMENT (see fig. 14)

Two frequency references are provided in the frequency generation equipment. These sources, each of which is provided with its own internal backup battery supply, contain a unique type of crystal oscillator which provides an output signal with a long term stability of better than $\pm$ 2 parts in 10^{11} per day, ie approaching that of a rubidium standard. The outputs of these two reference sources are fed to an automatic changeover unit in order to increase the reliability and availability of the output. The output from the automatic changeover unit is in turn fed to a main distribution amplifier which provides the main feeds for the various areas. The output frequencies from the reference sources are compared to the output from a rubidium standard using a frequency difference meter, coupled with a chart recorder, enabling appropriate fractional changes to be effected manually. To further increase the availability, battery backup is provided for the whole rack of equipment and comprehensive monitoring is provided to enable faults to be quickly rectified.

INTERMEDIATE CABLING
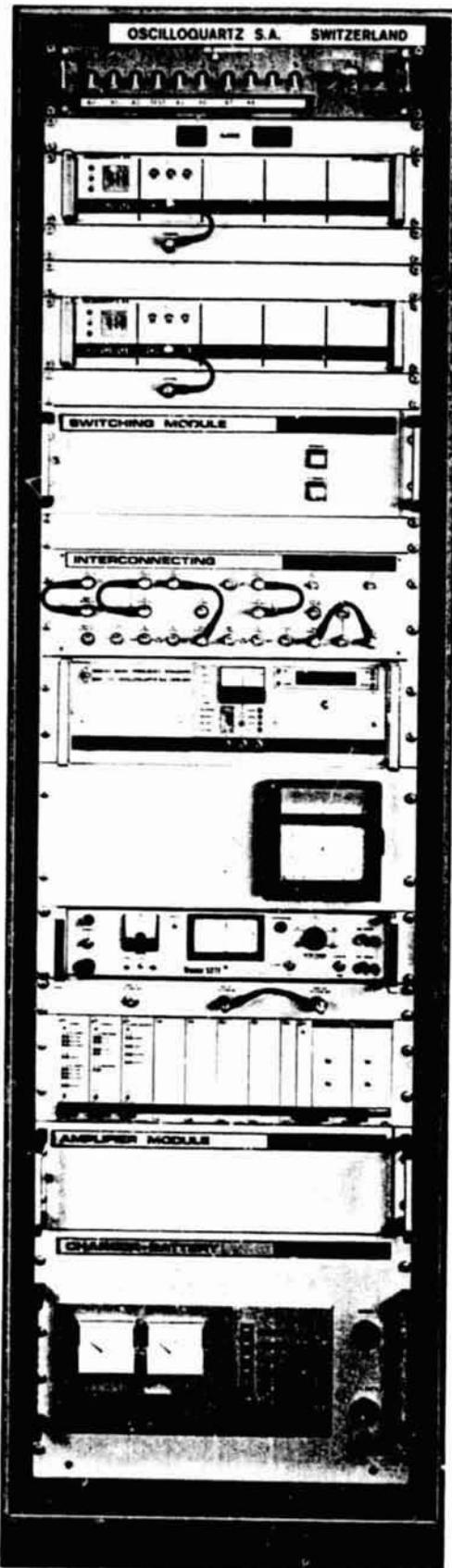
Having obtained a very high signal, it is essential that it is not degraded to any extent during transmission to other sub-systems. For this reason, a coaxial cable originally designed for electro-magnetic protection in nuclear reactors is used. It consists of three braids and two spirally wound mu-metal tapes. This provides greater protection against electro-magnetic interference than semi-rigid coaxial cables, whilst retaining a flexibility similar to that of standard coaxial cable. Special connectors are used with this cable in order to preserve its high shielding properties.

REMOTELY SITUATED AMPLIFIERS

As many more outputs are required than can be supplied by one amplifier, further amplifiers are situated in the sub-systems that they serve. These amplifiers are of the same type as the main distribution amplifier and are once again of a very low noise design. Situating them in the same area as the equipments they serve keeps interference to a minimum and reduces cable costs. Each amplifier is coupled to an alarm unit to display power or frequency failure faults.

POWER SUPPLY

Due to the requirements for extremely low phase noise outputs, it is also vitally important to avoid components in the phase noise that are derived from the power supply. Whilst it is not possible to eliminate 50 Hz mains components completely in an unshielded environment they are reduced by providing a 50 to 400 Hz power convertor. Most of the sub-system is run off 400 Hz, thus reducing the effect of the components produced. Generally, the 400 Hz components in the phase noise will fall outside the loop bandwidth of the RF convertors and the RF system is subsequently more tolerant of such components. The convertors are provided in duplicate together with automatic changeover to maintain the overall availability of the system.

FIGURE 14 : FREQUENCY GENERATION EQUIPMENT

182

SUMMARY

The frequency sub-system meets the stringent technical requirements with a phase noise performance that represents the best available, using today's technology.

The phase noise figures obtained are equal to, or better than, the following :

Frequency offset from carrier (Hz)	SSB phase noise in 1 Hz bandwidth (dBc/Hz)
1	-110
10	-130
100	-140
1'000	-141
10'000	-141
100'000	-141

Now harmonically related and power supply related spurious phase noise components (spurs) are better than

and
-144 dBc in the range of   1 Hz to 395 Hz from carrier
- 94 dBc in the range of 395 Hz to 10 kHz from carrier

The achievable system stability is : short term, ± 1 part in 10" per second
long term, ± 2 parts in 10" per day

An available figure of 99.9995% ensures almost continuous on-line operation of the station.
The modularity of the sub-system makes simple provision for future expansion to meet new requirements. The sub-system can be either compressed or expanded in size, or modified to suit different physical constraints without affecting its essentially high technical specification.

APPLICATION IN A SYNCHRONIZED DIGITAL NETWORK

The needs and characteristics of reference clocks for digital communications systems are extensively described in ref. 10 and 11. From these information, we can summarize trends, facts and requirements as follows :

- Data transmissions by means of time division multiplex (TDMA) are becoming increasingly popular in modern telecommunication networks.
- International data communication are r. ed by ITU (International Telecommunication Union), by means of CCITT recommendations.
- CCITT recommendation G-811 calls for a maximum frequency offset of $\cong$ 1x10-11 between two international exchanges. This value is based on the maximum error rate (or slip rate) allowable between two nodes to ensure proper data transmission.

To comply with this recommendation, trends are nowadays to achieve "frequency synchronization" :

- At an INTERNATIONAL LEVEL in a plesiosynchronous way, using master clock systems including cesium standards.
- At a NATIONAL LEVEL in a synchronous way, using synchronizing modules at each nodes connected directly or indirectly to the master clock.

A typical network configuration is given in fig. 15.
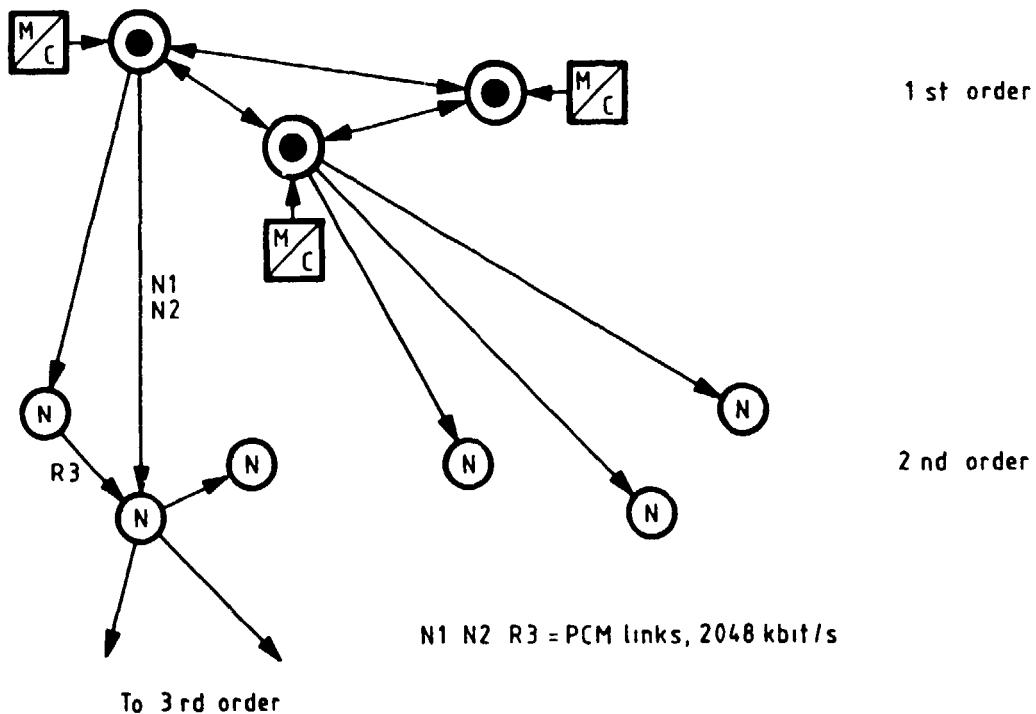
FIGURE 15 : TYPICAL NETWORK CONFIGURATION (MASTER SLAVE MODE)

TERMS AND DEFINITION

It should be mentioned at this stage that the requirements and concerns of the "telecommunications people" in terms of frequency sources are expressed in a very specific manner.

- "Oscillators people" like to define and characterize their product in terms of ACCURACY, STABILITY per unit of time or over a given environment, REPRODUCIBILITY, AGING, etc.

- "Telecommunication people" on the other hand specify their needs by using the following terms :

JITTER : RMS phase deviation in a given bandwidth

WANDER : systematic and/or random phase or time fluctuation, linked to cable delay, seasonal temperature variations, transmission effects, etc.

TIE : "TIME INTERVAL ERROR"; definition of the clock performances limits given by the relation

$$TIE \ (t) = \Delta T \ (t + \tau) - \Delta T \ (t)$$

AVAILABILITY : time during which the system will remain within the CCITT G-811 limits, in case of degradation or absence of synchronizing reference

The latter is of particular interest to us since directly related to the long term stability (aging), of the fly-wheel oscillator in the synchronizing module. A low aging oscillator will indeed give more time to the operator for servicing the nodes in case of reference failure.
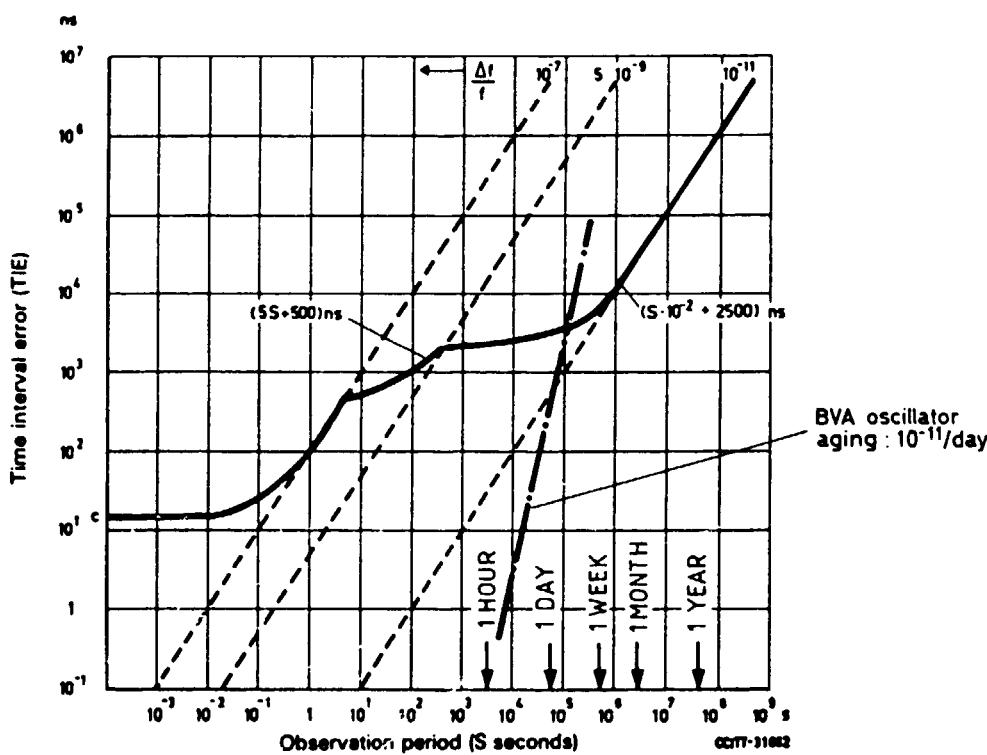
FIGURE 16 : **TIME INTERNAL ERROR LIMITS, CCITT REC. G-811 (DRAFT REVISION 1980)**

SYNCHRONIZING MODULE

As previously shown (fig. 15), each node located at a secondary level is connected to one or several lines carrying the synchronization and reference signal (in our example, at 2048 kHz).

Each line also carries messages which, combined with the effects of distance and the nature of transmission, require special precaution to extract and use the reference frequency.

The main purpose of the synchronizing module is to extract, filter and regenerate, from this signal a clean reference frequency which is compatible to the CCITT recommendation G-811.

This frequency will be used for driving the frequency converter and distribution amplifiers intended for local use.

A typical 2nd level node configuration would consist of 3 synchronizing modules each driven by one or preferably several reference input lines (see fig. 17).
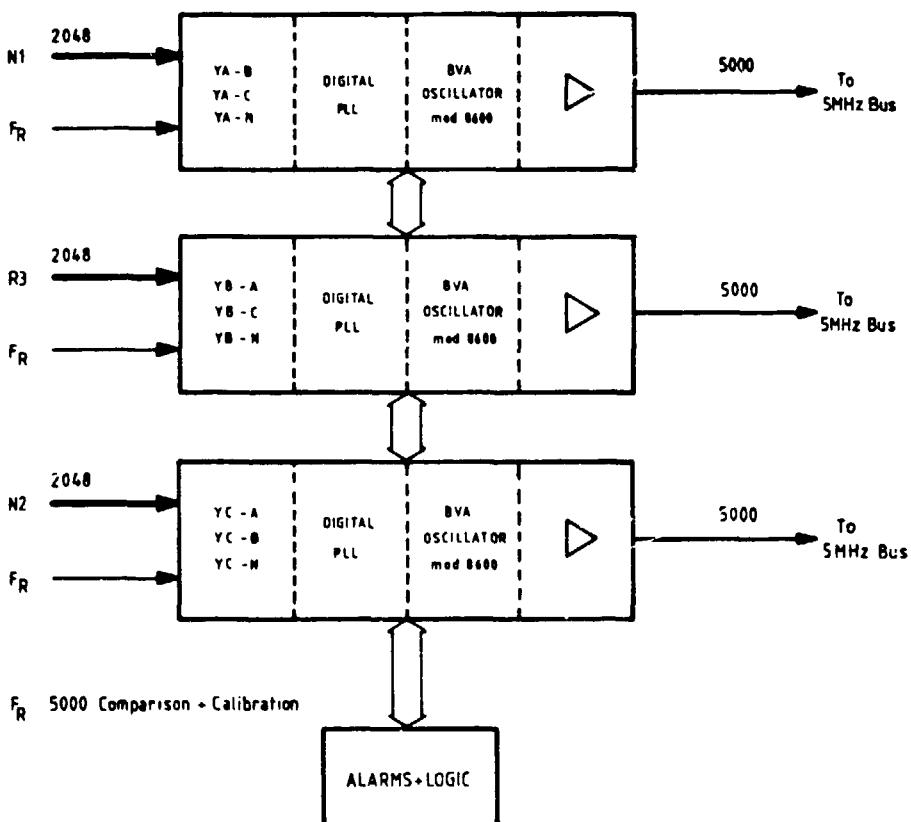
FIGURE 17 : TRIPLICATE SYNCHRONIZING MODULE

ROLE OF THE OSCILLATOR

In view of these different constraints, many features only offered with the BVA oscilla-
tor can be exploited to the benefit of the system performances :

OSCILLATOR FEATURES	SYSTEM BENEFITS
Very low aging rate (< 10^{-11}/day)	24 hours autonomy (availability in case of loss of reference)
Excellent short/medium term stability ($\leq 5 \times 10^{-13}$ from 0.1 to 30 s) and low sensitivity to environmental changes	Possibility to use high PLL time constant, thus to improve the jitter rejection
High MTBF	Improves system's availability figure. Decreases servicing and operating costs
Linearized frequency control function	No variation of loop time constant with time (following compensation of XO aging)

The data plots provided in fig. 18 and 19 exhibit the performances of the synchronization
module we realized for this application, based on the use of a BVA oscillator in a loop
bandwidth of $\sim$ 1x10-4 Hz.
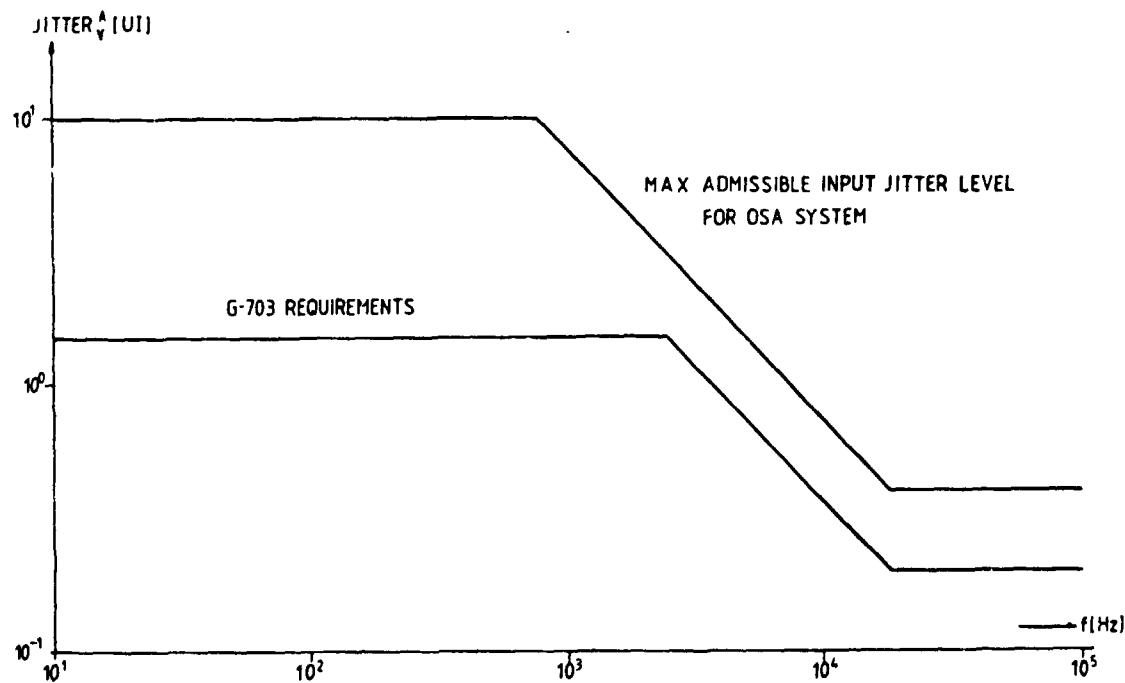
FIGURE 18 : **MAX. JITTER LEVEL VS G-703 RECOMMENDATION**
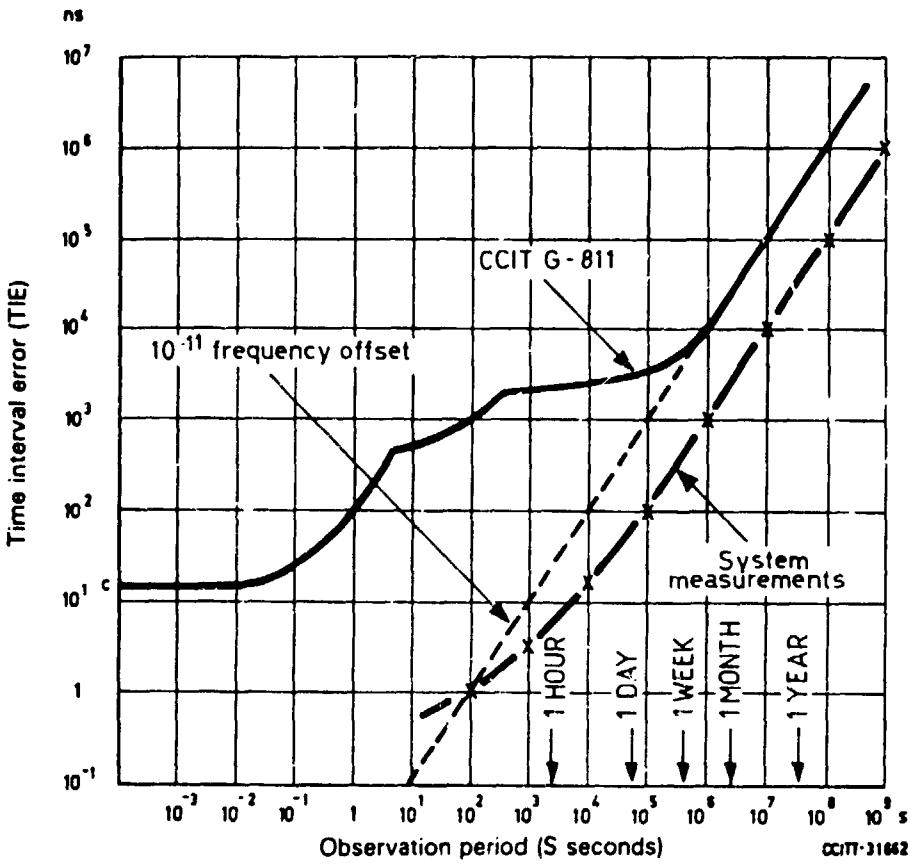
FIGURE 19 : PERMISSIBLE TIE (G-703) AND TYPICAL SYSTEM'S PERFORMANCES

CONCLUSIONS

- BVA oscillators have now reached industrial maturity both in terms of their production and applications.

- Substantial performances improvements have been demonstrated in various frequency generating devices, following the replacement of the conventional OCXO with a BVA oscillator.

- Developments based on the BVA technology are being conducted in the areas of HF OCXO and low g-sensitivity oscillators. These efforts, combined with the growing number of applications calling for very high performances frequency sources, are contributing to further improve the state-of-the-art in quartz crystal oscillators.

188

REFERENCES

1) R. Besson, "A New Piezoelectric Resonator Design",

   Proc. 30th AFCS (1976), p. 78-83

2) R. Besson and U. Peier, "Further Advances on BVA Quartz Resonators",

   Proc. 34th AFCS (1980), p. 175-182

3) E.P. Graf, D.A. Emmons, et al., "Performance of New Oscillators Designed for 'Electrodeless' Crystals",

   Proc. 34th AFCS (1980), p. 457-462

4) E.P. Graf, U. Peier "BVA Quartz Crystal Resonator and Oscillator Production. A Statistical Review",

   Proc. 37th AFCS (1983), p. 492-500

5) S. Weinreb, National Radio Astronomy Observatory Charlottesville, Virginia, Electronics Division, Internal Report No 223 "Short Term Phase Stability Requirements for Interferometer Coherence", June 1983

6) A.E. Rogers and J.M. Moran, IEE Transactions and Means, Vol 17 30, No 4, p. 283-286, December 1981

7) L. Probst, G. Busca and F.E. Gardiol, IEEE Trans. on Inst. and Measur., June 1984, Vol 33, No 2, p. 116

8) G. Busca et al., Proc. of the 36th Annual Frequency Control Symposium Philadelphia, 1982, p. 260-264

9) B. Vessot, Proc. of the 15th Annual Precise Time and Time Interval (PTT) Appl. and Planning Meet., Washington 1983, in publication

10) P. Kartaschoff "Reference Clock Parameters for Digital Communications Systems Application"

11) P. Kartaschoff "Frequency Control and Timing Requirements for Communications Systems"

QUESTIONS AND ANSWERS

ALBERT BENJAMINSON, S. T. RESEARCH: Can you tell us more about the BVA resonator?

MR. JENDLY: Do you mean specifications?

MR. BENJAMINSON: Yes.

MR. JENDLY: Yes, they are in the paper. I can give you the paper right away, if you wish. The Q factor is 2.5 million, and the resistance is 280 ohms, and C1 and C_p I can give you right away.

The System Design of a Rubidium Maser Frequency Standard

Cheng-Xi Xiong
Beijing Institute of Radio
Metrology and Measurement
Beijing, China

ABSTRACT

The Rubidium Maser Frequency Standard is a precision frequency source with excellent short-term stability. A type PBR-II Rb maser frequency standard has been developed by the Beijing Institute of Radio Metrology and Measurement (BIRMM). The time-domain frequency stability (two-sample variance) of this frequency standard is less than $1.5 \times 10^{-13} \tau^{-1}$ for $\tau = 10ms \to 1.0s$, $f_h = 1.0$ kHz.

Two PBR-II frequency standards have been used as reference frequency sources in a frequency stability measurement system.

In this paper some important system characteristics for the PBR-II Rb maser frequency standard such as phase noise and frequency stability transfer characteristics will be discussed. Furthermore, the following topics will be included as well:

1. Design of the frequency standard for optimum frequency stability of the output signal.

2. The choice of a VCXO for the frequency standard.

3. The design of the phase-locked loop.

The frequency stability test results on the PBR-II show the achievement of the system design goals given above.

INTRODUCTION

The Rubidium maser is an active atomic frequency standard. One of its characteristics is that of very good short-term stability. In atomic frequency standards, the Rubidium maser frequency standard has the best frequency stability for averaging times between milliseconds and seconds. Thus, the Rubidium maser is a precision frequency source which can be used in frequency stability measurement systems.

This paper presents the design considerations for the PBR-II rubidium maser frequency standard developed by the Beijing Institute of Radio Metrology and Measurement (BIRMM). The main

problem that will be discussed is the frequency stability of the
output signal of the rubidium maser frequency standard. We will
first discuss the basic design equations of the frequency
standard system and give a description of different phase noise
spectral densities occurring in these components so that the
relationship between the phase-noise and the frequency stability
of the output signal of the frequency standard can be determined.
We then discuss the optimization of the design of the low-noise
receiver, the VCXO and the phase-locked loop that are used in the
PBR-II. Finally we present the methods used and the experimental
results for measuring residual frequency instability of the
phase-locked receiver. The design values and the experimental
values are in basic agreement, demonstrating the validity of the
design considerations. A description of the time-domain frequency
stability of the complete PBR-II frequency standard and of the
Rubidium maser are given.

The Rb maser and the transfer of its frequency stability to an
output signal have been discussed extensively (1 through 10). The
development of the Rb maser frequency standard began in the BIRMM
in 1971. An earlier model of the Rb maser frequency standard
which was developed by the Wuhan Institute of Physics and BIRMM
has been described before (10). The PBR-II Rb maser frequency
standard presented in this paper is a new model. Its frequency
stability is now $1.5 \times 10^{-13} \tau^{-1}$ for averaging times between milli-
seconds and seconds, and exhibits better operational reliability
than the earlier model.

BASIC SYSTEM DESIGN PRINCIPLES

The system design for the PBR-II was directed toward the achieve-
ment of optimum system performance and gives requirements on the
various components of the system.

1. General Description of the Rb Maser Frequency Standard

The Rubidium maser frequency standard, like other maser atomic
frequency standards, consists of a Rb maser and a phase-locked
receiver, as shown in Figure 1. The Rb maser is a frequency
source with excellent frequency stability. The operating
frequency, V, of the maser is 6834 MHz and its power output is on
the order of 10^{-10} W. The phase-locked receiver shown in Figure 2
plays a major role in the transfer of the frequency stability to
the output signal, conversion to a standard frequency and in-
crease in the power level. A typical system of the Rb maser
frequency standard with the relevant components and their contri-
butions are shown in Figure 3. The preamplifier shown in Figure 3
is not used in the PBR-II Rb maser frequency standard. It is
included in the diagram for the purpose of analysis and
comparison.

The voltage controlled crystal oscillator (VCXO) has a mean
output frequency V, a phase spectral density S_{ϕ_0} in the locked
case and a tuning sensitivity K_u expressed in radians/volt-
second. Its frequency is multiplied by an integer M to yield a

signal with frequency ν_{LO1} close to the maser frequency. The phase noise contribution of the multiplier referred to the input frequency is given by $S_{\phi Mu}(f)$. The microwave mixer is fed by the amplified maser signal (or the maser signal) and the frequency multiplied VCXO signal to yield an intermediate frequency (IF) signal with a frequency ν_{IF1} much smaller than ν_M. The if contains both the phase instability of the maser and of the multiplied VCXO. The VCXO signal is also the reference of a frequency of a synthesizer which yields an output frequency ν_{LO3} equal to ν_{IF2}. The maser frequency, and consequently, the intermediate frequency ν_{IF} and the VCXO frequency are not related by a simple rational number. The frequency synthesizer acts as a third fractional multiplication factor M3. The frequency synthesizer also exhibits its own phase noise, but since the multiplication factor is so small it can be neglected when compared to the phase noise added by the first multiplier. The signals with frequencies ν_{IF2} and ν_{LO3} feed the phase detector having a phase sensitivity K_d expressed in volts/radian. That part of the receiver comprising the multiplier synthesizer, mixer, IF amplifier and phase detector is designated as the down converter.

The low-frequency output signal of the phase detector is a measure of the phase error between the signals at frequencies ν_M and ν_{LO1}. The error signal is passed through the loop filter with the transfer function $F(j\omega)$. Usually the loop filter is of the low-pass type, and the transfer function is chosen to yield optimal PLL performance. Finally the filtered error signal is fed to the tuning input of the VCXO, which is then locked to the frequency of the maser signal.

2. Basic Equations

The basic block diagram of the phase-locked system is shown in Figure 2. As stated in (8), the phase noise spectral density of the output of a VCXO which is phase-locked to a reference signal can be written:

$$S_{\phi o}(f) = S_{\phi x}(f) \cdot |H_1(f)|^2 + S_{\phi r}(f) \cdot |H_2(f)|^2. \qquad (1)$$

The power spectral density of the relative frequency fluctuations can be calculated from:

$$S_{yo}(f) = (f/\nu_o)^2 \cdot S_{\phi o}(f) = S_{yx}(f) \cdot |H_1(f)|^2 + S_{yr}(f) \cdot |H_2(f)|^2, \qquad (2)$$

where

$$H_1(f) = \frac{j2\pi f}{j2\pi f + Kd \cdot Kv \cdot F(j2\pi f)}, \qquad (3)$$

$$H_2(f) = \frac{Kd \cdot Kv \cdot F(j2\pi f)}{j2\pi f + Kd \cdot Kv \cdot F(j2\pi f)}, \qquad (4)$$

$H_1(f)$ and $H_2(f)$ are the transfer functions of the phase locked loop, $F(j2\pi f)$ is the transfer function of the loop filter, Kd is

the phase sensitivity of the phase detector. Kv is the voltage controlled oscillator tuning sensitivity. $S_{\phi rx}(f)$ and $S_{\phi r}(f)$ are the phase noise power spectral density of the the free-running VCXO and the reference source respectively.

The above basic relationships can be applied to the Rb maser frequency standard, shown in Figure 3 [11]. The relations for this figure can be expressed:

$$S_{\phi r}(f)=S_{\phi MU}(f)+(S_{\phi M}(f)+S_{\phi i}(f)+S_{\phi A}(f)+S_{\phi R}(f)+S_{\phi IF1}(f)+S_{\phi R2}(f) \quad (5)$$
$$+S_{\phi 2}(f)+S_{\phi L}(f))/M^2+(M_2/M)S_{\phi MU2}(f)+(M_3/M)S_{\phi s}(f)$$

$$S_{yr}(f)=S_{yM}(f)+S_{yi}(f)+S_{yA}(f)+S_{yR}(f)+S_{yIF1}(f)+S_{yR2}(f)+S_{yIF2}(f)+ \quad (6)$$
$$S_{yl}(f)+S_{yMU}(f)+S_{ys}(f)$$

$$H_1(f)=\frac{j2\pi f}{j2\pi f+Kd \cdot Kv \cdot M \cdot F(j2\pi f)} \quad (7)$$

$$H_2(f)=\frac{Kd \cdot Kv \cdot M \cdot F(j2\pi f)}{j2\pi f+KdKv \cdot M \cdot F(j2\pi f)} \quad (8)$$

$$S_{\phi o}(f)=S_{\phi x}(f) \cdot |H_1(f)|^2+S_{\phi r}(f) \cdot H_2(f)|^2 \quad (9)$$

$$S_{vo}(f)=S_{yx}(f) \cdot |H_1(f)|^2+S_{tr}(f) \cdot |H_2(f)|^2 \quad (10)$$

The time domain frequency stability of the VCXO output signal than then be expressed (12) by:

$$\sigma^2_{yo}(\tau)=2 \int_o^\infty S_{yo}(f) \cdot \frac{\sin^4(\pi\tau f)}{(\pi\tau f)^2 \cdot (1+(f/f_c)^2)} \quad df \quad (11)$$

or

$$\sigma^2_{yo}(\tau)=\frac{8}{(2\pi\nu_o\tau)^2} \int_o^\infty S_{\phi o}(f) \cdot \sin^4(\pi\tau f) \cdot \frac{1}{1+(f/f_c)^2} \quad df \quad (12)$$

where f_c is the cutoff frequency of the first-order low pass filter used in the measurement system. From equation (10) we see that the first term represents the contribution from the VCXO. The loop acts as a high pass filter with a limiting value of one for very high Fourier frequencies. The second term is the contribution from the reference sources which include the maser, the preamplifier, the mixer the multiplier, etc. In that case, the loop acts as a low pass filter with a limiting value of one for very low Fourier frequencies. The overall performance of the system will then give the high frequency fluctuations of the VCXO plus the low frequency fluctuations of the reference sources. This is an important consideration for the designer of the system.

194

From the above we can conclude:

1. The reference system consisting of the Rb maser, preamplifier, mixer and multiplier must have low phase noise at low Fourier frequencies. The flicker of phase and flicker of frequency noise must be controlled as low as possible.

2. The VCxO used in the Rubidium maser frequency standard must exhibit very low white phase noise. The long term frequency and drift are not too important.

3. The transfer function $F(j\omega)$ of the loop filter plays an important role in the frequency standard. The choice of the loop parameters must be made to optimize the frequency stability of the output frequency.

CHARACTERIZATION OF THE NOISE IN THE COMPONENTS

1. Rubidium maser

Several authors [9] [11] have shown that the one-sided-spectral density of the fractional frequency fluctuations can be approximated by:

$$S_{yM1}(f) = \frac{4kT}{P_{at}} \cdot (f/\nu_M)^2 + \frac{4kT}{P_{at}} \cdot (1/2Q_1)^2 \cdot G_c(f) \qquad (13)$$

where K is Bolzmann's constant, T is the absolute temperature of the system. P_{at} is the power generated inside the active medium, Q_1 is the atomic line quality factor, M is the atomic resonant frequency and $G_c(f)$ is the power transfer function of the microwave cavity. The first term represents the white phase noise contribution and the second term is the white frequency noise contribution resulting from stimulated emission of radiation within the atomic linewidth. According to the experimental results of at BIRMM and the reference [7] there is random walk of frequency in the rubidium maser, but the source of the noise is still unknown. According to the preliminary analysis [3] [6] it is believed to come mainly from cavity temperature fluctuations or light fluctuations. The time domain frequency stability goes as $\tau^{1/2}$ for averaging time $\tau > 3s$. From experimental results, shown in Figure 15, we can obtain $\sigma^2_y(\tau) = 4.7 \times 10^{-14} \tau^{1/2}$ for $\tau = 3-100s$. The power spectral density of the relative frequency fluctuations can be calculated from (12)

$$S_y(f) = \frac{6}{(2\pi)^2 \tau f^2} \sigma^2_y(\tau) \qquad (14)$$

From (14) we obtain then

$$S_{yM2}(f) = 3.4 \times 10^{-28} f^{-2} \qquad (15)$$

The spectral density of fractional frequency fluctuations of the Rb maser PBR-II can be written:

$$S_{yM}(f)=S_{yM1}(f)+S_{yM2}(f)=3.4\times10^{-28}\,f^{-2}+2.5\times10^{-27}+2\times10^{-30}\,f^2 \quad (16)$$

Thus, the power spectral density of the phase noise can be expressed:

$$S_{\phi M}(f)=(\nu_M f)^2\,S_{yM}(f)=10^{-7.8}f^{-4}+10^{-6.9}f^{-2}+10^{-10} \quad (17)$$

2. VCXO

VCXO's which are commonly used with atomic frequency standards are 5MHz, 10 MHz and 100MHz quartz crystal oscillators. The power spectral density of the phase noise of the VCXO's which have been developed at BIRMM can be expressed as:

$$S_{\phi 1}(f)=10^{-10}f^{-3}+10^{-11}f^{-1}+10^{-15} \qquad (5MHz\ VCXO) \quad (18)$$

$$S_{\phi 2}(f)=10^{-9}f^{-3}+10^{-10.2}f^{-1}+10^{-15} \qquad (10MHz\ VCXO) \quad (19)$$

$$S_{\phi 3}(f)=10^{-5}f^{-3}+10^{-15} \qquad (100MHz\ VCXO) \quad (20)$$

The power spectral density of the fractional frequency fluctuations can then be written:

$$S_{y1}(f)=4\times10^{-24}f^{-1}+4\times10^{-25}+4\times10^{-29}f^2 \qquad (5MHz\ VCXO) \quad (21)$$

$$S_{yx2}(f)=10^{-23}f^{-1}+5.3\times10^{-25}+10^{-29}f^2 \qquad (10MHz\ VCXO) \quad (22)$$

$$S_{yx3}(f)=10^{-21}f^{-1}+10^{-31}f^2 \qquad (100MHz\ VCXO) \quad (23)$$

3. Microwave preamplifier

Microwave preamplifiers find wide use in low-noise receivers, so we have been trying to find a suitable unit for Rubidium maser use. We have only been able to find FET microwave amplifiers. The phase noise of several of these amplifiers were tested. Models CX511A and CX511C are being used in the Rb maser. They have a gain of 17.2 to 17.5 dB and a noise figure of 4 to 6 dB over an input power range of -20 to -60 dBm. The phase noise spectral density was found to be:

$$S_{\phi A}(f)=(10^{-7}.1\tilde{}6.1)f^{-3}+(10^{-8.3}\tilde{}9.3)f^{-1}+(10^{-19.7}\tilde{}20.1)P_i^{-1} \quad (24)$$

where P_i is the input power level, expressed in watts. Equation (24) shows that the FET amplifier has not only white phase noise, but also flicker FM and PM noise. The first term represents the flicker FM noise, the second term represents the flicker PM noise. They are independent of the input signal power level for an typical amplifier. The noise level varies with the FET model and the operational conditions of the amplifier. The third term represents white phase noise. This noise is independent of the input signal power level and amplifier noise figure.

From (24), the spectral density of fractional frequency fluctuation can be written:

$$S_{Ya}(f)=(1.7\sim17)\times10^{-26}f^{-1}+(1\sim10)\times10^{-29}f+(1.7\sim4.3)\times10^{-40}f^2P_i^{-1} \quad (25)$$

Data on flicker PM and flicker FM noise levels of such an amplifier are not available from any source to our knowledge. We will make a further effort to develop low noise preamplifiers in the future.

4. Microwave mixer

The microwave mixer is an important component in the PBR-II frequency standard. The white phase noise of a mixer which operates at low signal level is available from the noise figure specification. Data on flicker PM noise at low signal levels are not available and must be measured. The phase noise of several microwave low level balanced mixers have been measured. The model WH32 Schottky diodes are used in the mixer.

The mixer has a noise figure of 6-10 dB, a LO power P_1 of 3 dBm and signal power level of 0 dBm to -20 dBm.

The phase noise spectral density is found to be:

$$S_{\phi R}(f)=(10^{-15.2\sim16.2})f^{-1}P_s^{-1}+(10^{-18.2\sim19.2})P_s^{-1} \quad (26)$$

where P_s is the signal power level expressed in watts.

The local oscillator power to the mixer is constant, so that the operating condition of the mixer is invariant. We can deduce a conclusion from the above statements that expression (26) will be valid for lower signal levels. From (26), the spectral density of fractional frequency fluctuations of the mixer can be written as:

$$S_{yR}(f) = \sim13.5)\times10^{-36}fP_s^{-1} + (1.35\sim13.5)\times10^{-39}f^2P_s^{-1} \quad (27)$$

According to (27), the phase noise of the mixer is in inverse proportion to the signal power level for the case of low signal levels. The first term represents flicker PM noise which was neglected in general. The second term represents white phase noise which is dependent on the noise figure of the mixer. The phase noise varies with the diode and the microwave circuit of the mixer.

5. Microwave frequency multiplier

The frequency multiplier consists of a transistor power amplifier, a 100 MHz frequency doubler and a high order multiplier with a step recovery diode. The input power is 0 dBm and the output power is +13 dBm at 6.8 GHZ. The measured phase noise spectral density referred to 100 MHz is:

$$S_{\phi MU}(f)=10^{-11}f^{-1}+10^{-15}.$$

The spectral density of the fractional frequency fluctuations can be given:

$$S_{yMU}(f)=10^{-17}f+10^{-31}f^2 \tag{28}$$

6. Microwave isolator and attenuator

The isolator and attenuator are passive dissipative non-reciprocal components and contribute only white phase noise:

$$S_{\phi i}(f)=\frac{(1-\alpha)KT}{\alpha P_i} \tag{29}$$

where α is the insertion loss of the isolator and attenuator and P_i is the available signal power at the input of the components. The actual values are: $P_i=1\times10^{-10}W$, $\alpha=0.8$ (1 dB). From (27) it follows that:

$$S_{\phi i}(f)=10^{-10.28} \tag{30}$$

and

$$S_{y i}(f)=10^{-30}f^2 \tag{31}$$

7. Other components in receiver

The influence of the other components in the receiver on the performance of the frequency standard is theoretically smaller than that of the above components. In order to improve the performance of the frequency standard, we measure phase noise and frequency stability of these components to acquire the following results:

a. 5 MHz x 7 frequency multiplier

$$S_{\phi MU2}(f)=10^{-12}f^{-1}+10^{-15} \tag{32}$$

b. Phase detector

$$S_{\phi p}(f)=10^{-12.5}f^{-1}+10^{-15.5} \tag{33}$$

c. Second mixer

$$S_{\phi R2}(f)=10^{-12.5}f^{-1}+10^{-15.7} \tag{34}$$

d. Frequency synthesizer

$$\sigma_{ys}(\tau)\leq1\times10^{-9}f^{-1} \quad \text{for } f_h=1 \text{ kHz} \tag{35}$$

Therefore:

$$S_{yMU2}(f)\approx4\times10^{-26}f+4\times10^{-30}f^2 \tag{36}$$
$$S_{yo}(f)=6.8\times10^{-33}f+6.8\times10^{-36}f^2 \tag{37}$$
$$S_{yR2}(f)=6.8\times10^{-33}f+4.3\times10^{-36}f^2 \tag{38}$$

8. Summary of the noise contributions

In order to compare the noise contributions of the different components, the power spectral density of fractional frequency fluctuation of the various components are given in Figure 4.

CONSIDERATIONS OF THE SYSTEM DESIGN

By system design we mean the optimization of the system frequency stability. In this section we will present design considerations of the main components in the PBR-II frequency standard.

1. Consideration of the Rubidium maser design

From (16), the output signal of the Rb maser exhibits three main noise components. Because the Rb maser is included in the reference source of the frequency standard, the noise contribution of the low Fourier frequencies is the main contribution to the output frequency of the frequency standard. We see from Figure (4) that the main noise component is random walk FM. Other noise components can be neglected compared to the flicker phase noise of the microwave mixer of the reference source system.

In order to reduce the random walk FM noise, a high precision DC power supply and high stability oven are used in the PBR-II. Even then a good method has not been found to reduce this noise component.

According to (27), it is very important to increase the output power of the Rb maser to reduce the noise contribution of the microwave mixer. With this end in view, the microwave cavity and the maser bulb operate at a temperature of $60^{\circ}C-62^{\circ}C$. The lamp oscillator can give an output power of about 10 W. Thus, the output power of the Rb maser is on the order of 2×10^{-10} W. A detailed design of the maser will not be given in this paper.

2. Low noise receiver

Generally a low noise microwave receiver is characterized by the noise figure, but only the white phase noise can be determined by this value.

As stated above, the FET preamplifier and the microwave mixer exhibit flicker FM or FM noise in addition to white phase noise. They will contribute to the overall noise of the frequency standard and degrade the performance.

There two methods which could be used to receive the low power level output of the Rb maser. One of these uses a FET preamplifier and the other goes directly into the microwave mixer. The noise contribution of each method is given in Figures 5a and 5b, where $S_{yRe1}(f)$, $S_{yRe2}(f)$, $\sigma_{yRE1}(\tau)$ and $\sigma_{yRe2}(\tau)$ represent the frequency domain and time domain noise contribution of the first and second method.

Assuming that other noise contributions can be neglected compared to the preamplifier and microwave mixer, the noise contribution of each method can be expressed:

$$S_{yRe1}(f)=S_{ya}(f) \tag{39}$$

$$S_{yRe2}(f)=S_{yR}(f) \tag{40}$$

and consequently

$$\sigma_{yRe1}(\tau)= 2 \int_0^\infty S_{ya}(f)\frac{\sin^4(\pi\tau f)}{(\pi\tau f)^2(1+(f/f_c)^2)} \, df \tag{41}$$

$$\sigma_{yRe2}(\tau)= 2 \int_0^\infty S_{yR}(f)\frac{\sin^4(\pi\tau f)}{(\pi\tau f)^2(1+(f/f_c)^2)} \, df \tag{42}$$

From Figures 5a and 5b, we see that: the second method is better than the first, that is, the noise contribution of the microwave mixer is less than the FET amplifier. In view of operational reliability, noise contribution, cost and volume of the system, we have decided to choose the system with the microwave mixer as the input stage of the phase-locked receiver.

3. Choice of VCXO

The VCXO is an important component in the active frequency standard. It must be locked to the resonant frequency of the atomic line and exhibit excellent spectral purity and low white phase noise.

The 100 MHz VCXO has been chosen as the basic oscillator in the PRB-II Rb maser frequency standard. The reasons are summarized below:

(1) In view of the noise contribution for frequency stability of the system, the white phase noise of the VCXO is most important. From Figure 4, we can see that the white phase noise of the 100 MHz VCXO is less than the 10 MHz VCXO and the 5 MHz VCXO.

The Rb maser frequency standard using the 5 MHz VCXO has been discussed extensively in references [7] and [8]. It has been shown that the 5 MHz VCXO is not the best choice for the Rb maser frequency standard.

(2) The order of the frequency multiplier will b reduced with respect to the 5 MHz VCXO and 10 MHz VCXO. The noise contribution of the frequency multipliers will be thus reduced and the stability of the multiplier chain can be improved.

The frequency multiplier has an input frequency of 5 MHz and an output frequency of 6800 MHz. The measured phase noise spectral density, referred to 5 MHz is

$$S_{\phi MU}(f)=10^{-12}f^{-1}+10^{-15.7} \tag{43}$$

200

and

$$S_{yMU}(f)=4\times10^{-26}f+8\times10^{-30}f^2 \qquad (44)$$

The noise contribution of the frequency multiplier chain with an input of 5 MHz will become a major factor in degrading the frequency stability of the reference source system in the Rb maser frequency standard.

(3) The PBR-II frequency standard is mainly used as a reference frequency source with excellent frequency stability in the measurement of short-term frequency stability. The high stability precision frequency sources, such as 5 MHz and 10 MHz standards must be multiplied to 100 MHz to achieve sufficient measurement resolution. The PBR-II output need not be multiplied, thereby improving the performance of the measuring system.

(4) Design of the phase-locked loop

The main task of the loop is to correct the frequency drift of the VCXO and to transfer the frequency stability of the Rb maser to the output. Doubly balanced mixers using Schottky diodes are used as the phase detector which has to be very sensitive and contribute very little noise. In order that no frequency error exists when the free-running VCXO is drifting, a second order loop type 2 [13] is chosen. An integrator with phase-lead correction gives rather good loop stability performance and is used as a filter following the phase detector. Its transfer function is:

$$F(j\omega)=\frac{1+j\omega\tau_2}{j\omega\tau_1} \qquad (45)$$

After substitution of (45) into (7) and (8), the two loop transfer functions become

$$H_1(s)=\frac{s^2}{s^2+2\zeta\omega_n^2+\omega_n^2} \qquad (46)$$

$$H_2(s)=\frac{2\zeta\omega_n s+\omega_n^2}{s^2+2\zeta\omega_n^2+\omega_n^2} \qquad (47)$$

where $s=j\omega$, ω_n is the natural frequency of the loop and is defined by $\omega_n=2\pi f_n=(K_dK_\upsilon M/\tau_1)^{1/2}$ (48) and ζ is the damping factor defined by:

$$\zeta=\frac{\omega_n\tau_2}{2} = \frac{\tau_2}{2}\cdot\frac{(K_dK_\upsilon M)^{1/2}}{\tau_1^{1/2}} \qquad (49)$$

With this loop design these two parameters ζ and ω_n can be selected independently by setting the values of τ_1 and τ

201

is important when one is concerned with the conditions for optimum transfer of frequency stability.

The capture and locking range are not critical parameters in the active atomic frequency standard, because the two frequencies are already very close to each other and stable.

From the expressions (46) and (47), the transfer functions of the frequency standard system can be written:

$$|H_1(f)|^2 = \frac{f^4}{f^4 + 2f_n^2(2\zeta^2 - 1)f^2 + f_n^4} \tag{50}$$

$$|H_2(f)|^2 = \frac{f_n^2(4\zeta^2 f^2 + f_n^2)}{f^4 + 2f_n^2(2\zeta^2 - 1)f^2 + f_n^4} \tag{51}$$

When $\zeta = 0.707$, that is the critical damping. (50) and (51) can be written:

$$|H_1(f)|^2 = \frac{f^4}{f^4 + f_n^4} \tag{52}$$

$$|H_2(f)|^2 = \frac{f_n^4 + 2f_n^2 f^2}{f^4 + f_n^4} \tag{53}$$

When $f/f_n = 1.55$, these two transfer functions are equal. The first method of loop design for the PBR-II is a method of rough approximation of f_n and calculation of the values of τ_1 and τ_2 according to the equations:

$$\tau_1 = \frac{k_d k_v M}{w_n^2} \tag{54}$$

$$\tau_2 = \frac{2\zeta}{w_n} \tag{55}$$

If the cross-over point of power spectral density of fractional frequency fluctuation between the 100 MHz VCXO and the reference source can be found, such as point O in Figure 4, denote the frequency of the cross-over point by f_o and the natural frequency of the loop can be expressed as:

$$f_n = \frac{f_o}{1.55} \tag{56}$$

Another method of loop design which has been applied to the PBR-II frequency standard is the calculation of f_n from the optimum frequency stability of the output signal. A microcomputer was

202

used to calculate the optimum value of f_n according to the expression (11) or (12). For example, according to the first method, we find $f_o = 170$ Hz from Figure 4. Then, f_n is obtained:

$$f_n = \frac{f_o}{1.55} = 110 \text{ Hz}$$

The values of τ_1 and τ_2 can be evaluated from (54) and (55)

$$\tau_1 = \frac{k_d k_v M}{W_n^2} = 15 \text{ ms}$$

$$\tau_2 = \frac{2\varsigma}{W_n} = 2.2 \text{ ms}$$

where $k_d = 0.5$ v/rad, $k_v = 30 \times 2\pi$ rad/v, $M = 68$, $\varsigma = 0.707$ and $W_n = 2 \times 110\pi$ rad/s. The actual values of τ_1 and τ_2 will be determined by setting the value of R while measuring the frequency stability of the PBR-II frequency standard.

DESCRIPTION OF THE SYSTEM BLOCK DIAGRAM

The system block diagram of the PBR-II frequency standard is shown in Figure 17. The microwave mixer is used as the first stage of the phase-locked receiver and a 100 MHz VCXO is used as the basic oscillator. The second LO signal of 35 MHz is delivered from a 5 MHz VCXO used as a reference signal for the 311 kHz frequency synthesizer. The 5 MHz signal is a non-standard output signal Its noise contribution can be neglected compared to the 100 MHz VCXO. We can show that the time-domain frequency stability which is added by the 5 MHz VCXO can be expressed as:

$$\sigma_{yo}^1(\tau) = (35/6800)\sigma_{y5}(\tau) \tag{57}$$

where $\sigma_{yo}^1(\tau)$ is the time domain frequency stability added by the 5 MHz VCXO and $\sigma_{y5}(\tau)$ is the time-domain frequency stability of the 5 MHz VCXO. From (57) $\sigma_{yo}^1(\tau) = 5 \times 10^{-14}\tau^{-1}$ for $\sigma_{y5}(\tau) = 1 \times 10^{-11}\tau^{-1}$. The 5 MHz VCXO is readily available from our own laboratory. It can also be operated open loop if the frequency stability of the free-running VCXO is good enough for the system. The 311 kHz frequency synthesizer has a frequency range of 1 kHZ and a resolution of 1 Hz. I has a time-domain frequency stability better than $1 \times 10^{-9}\tau^{-1}$. A 311 kHz quartz crystal oscillator may be substituted for the synthesizer for less demanding uses.

PERFORMANCE EVALUATION

The time-domain frequency stability is a most important specification of the PBR-II frequency standard. The basic equations for evaluating the time-domain frequency stability of the output signal of the frequency standard can be written as:

203

$$\sigma_{yo}^2(\tau)=2 \int_0^\infty S_{yo}(f)\frac{\sin^4(\pi\tau f)}{(\pi\tau f)^2 \ (1+(f/f_c)^2)} \, df \qquad (58)$$

$$S_{yo}(f)=S_{yx}(f)|H_1(f)|^2 + S_{yr}|H_2(f)|^2 \qquad (59)$$

$$S_{yr}(f)=S_{ym}(f)+S_{yr}(f)+S_{yMU}(f) \qquad (60)$$

$$|H_1(f)|^2= \frac{f^4}{f^4+f_n^4} \qquad (61)$$

$$|H_2(f)|^2 = \frac{f^4+2f_n^2f^2}{f^4 +f_n^4} \qquad (62)$$

The spectral density of fractional frequency fluctuati(the main components in the PBR-II is found to be

$$S_{ym}(f)=3.34\times10^{-28}f^{-2}+2.5\times10^{-27}+2\times10^{-10}f^2 \qquad (63)$$

$$S_{yR}(f)=2.1\times10^{-26}f+1.0\times10^{-28}f^2 \qquad (64)$$

$$S_{yMU}(f)=1.0\times10^{-27}f+1.0\times10^{-31}f^2 \qquad (65)$$

$$S_{yx}(f)=1.0\times10^{-21}f+1.0\times10^{-31}f^2 \qquad (66)$$

After subst tion of (63)-(59)-(60), the numerical evaluation of $\sigma_{yo}(\tau)$ from (58) can be obtained. It is shown in Figure 6 for cutoff frequency f_c = 1 kHz and a loop natural frequency of $f_n=200$ Hz. We see that $\sigma_{yo}(\tau)$ shows a τ^{-1} dependence over the range of averaging times from 2 ms to 1 s and a $\tau^{1/2}$ dependence for averaging times $\tau > 3s$. According to Figure 6, the time domain frequency stability $\sigma_{yo}(\tau)$ can be expressed approximately as

$$\sigma_{yo}(\tau)=[(1.4\times10^{-13}\tau^{-1})^2+(4.7\times10^{-14}\tau^{0.5})^2]^{0.5} \qquad (67)$$

From the second design method, we evaluated the optimum value of f_n. The relationship bet een the numerical evaluation of $\sigma_{yo}(0.1 \ s)$ and the natural frequency of the loop is shown in Figure 7. It is seen that the optimum value of f_n is about 180 Hz.

EXPERIMENTAL RESULTS

1. Time domain frequency stability

The time domain frequency stability (two-sample variance) of the PBR-II frequency standard was measured using the configuration shown in Figures 8 and 9. The results are given in Figure 10.

The beat frequency method is used as the basic frequency stability measurement method. For averaging times between 2 ms and

100 ms, the reference oscillator is a low-noise frequency synthesizer. The beat frequency is approximately 10 Hz-500 Hz. For averaging times from 100 ms -100s, the reference oscillator is another PBR-II frequency standard. The beat frequency is about 10 Hz. The noise bandwidth is about 1 kHz for averaging times between 2 ms and 100 s.

2. Frequency instability added by the phase-locked receiver

The frequency instability added by the phase-locked receiver is defined as the frequency stability of the output signal of the Rb maser frequency standard when the Rb maser is an ideal oscillator, that is, $S_{yM}(f)=0$. A detailed block diagram of the measurement system is shown in Figure 11a and 11b. The measurement principle is shown in Figure 12a and 12b.

The noise spectral density shown in Figure 12a can be written as:

$$S_{yo}(f)=S_{yx}(f)|H_1(f)|_L^2+S_{yR}(f)|H_2(f)|_L^2+$$

$$S_{yux}(f)|H_1(f)|_s^2|H_2(f)|^2+$$

$$S_{yol}[1-|H_2(f)|_s^2|H_2(f)|^2]+$$

$$S_{ys}(f)|H_2(f)|_s^2|H_2(f)|_L^2 \tag{68}$$

where $|H(f)|_s^2$ and $|H(f)|_L^2$ are respectively the system transfer functions of the microwave synthesizer and the phase-locked receiver. $S_{yux}(f)$ and $S_{yuo}(f)$ represent the noise spectral density of the VCXO in free oscillation and locked condition respectively, $S_{yx}(f)$ represents the noise spectral density of the 100 MHz VCXO of the receiver in free oscillation, $S_{yol}(f)$ represents the noise spectral density of the 100 MHz VCXO in the microwave synthesizer. $S_{ys}(f)$ and $S_{yR}(f)$ represent the noise contributions of the synthesizer and the phase-locked receiver reference system respectively and $S_{yp1}(f)$ is the noise contribution of the phase-locked receiver. Because the phase lock bandwidth of the synthesizer is wider than the receiver's, the fourth term in (51) can be neglected. The third and fifth terms can be measured by the method shown in Figure 11b. The first and second terms in (68) can be evaluated by

$$S_{yp1}(f)=S_{yx}|H_1(f)|_L^2+S_{yR}(f)|H_2(f)|_L^2.$$

The time domain frequency instability added by the phase-locked receiver is measured actually by the beat frequency method. The beat frequency signal between two 100 MHz VCXO's is about 10 Hz to 100 Hz, which can be obtained by varying the output frequency of the microwave synthesizer. The measurement results are shown in Figure 13.

3. Rubidium maser

The block diagram of the measurement setup is shown in Figure 13. Shown in Figure 15 is the measurement result which includes the

noise contribution of the receiver. We have not found a good method to precisely measure the noise contribution of the Rb maser.

The beat frequency signal between the two Rb masers is about 500 Hz. The twin-T tuned amplifier is used to control the noise bandwidth from 3 Hz to 3 kHz.

4. Discussion

From the measurement results in Figures 10 through 15, we see that the noise contribution of the phase-locked receiver predominates for 2 ms $\leq \tau \leq$ 1 s. For longer averaging times the random walk FM noise of the Rb maser predominates and degrades the frequency stability of the PBR-II frequency standard.

The measurement results of Figure 16 basically agrees with the calculated values.

The frequency instability added by the phase-locked receiver can be used to characterize the performance of the receiver. It is very useful for developing a low-noise phase-locked receiver. From the measurement results in Figure 15, we see that $\sigma_y(\tau)$ shows a $[1.038+3Ln(2\pi f_n \tau)]^{\frac{1}{2}}$ dependence over the range of averaging times from 10 ms to 1 s for noise bandwidths, f_h, from 10 Hz to 1 kHz. This dependence shows clearly that the noise contribution of $1/f$ PM noise of the microwave mixer predominates for 10 ms $\leq \tau \leq$ 1 s.

Conclusion

We have shown that the system design method adopted for the PBR-II maser frequency standard is a useful one for choosing components and parameter design. Precision characterization of the noise spectral density is the basis of the system design. The main noise contribution from the PBR-II frequency standard is the flicker phase noise of the microwave mixer, random walk FM noise of the the Rb maser and white phase noise of the 100 MHz VCXO.

Acknowledgment

REFERENCES

(1) P. Davidovits and R. Novick., "The optically pumped rubidium maser" Proc IEEE. Vol.54   pp.155-170   1966.

(2) J. Vanier., "Relaxation in Rb^{87} and the rubidium maser"Phys Rev. Vol.168 pp.129-149   1968.

(3) E.N. Bazarov. V.P. Goubin., "Short-term frequency stability of Rb maser". Trans IEEE IM-19 No4   pp.417-419   1970

(4) M. Tetu, G. Busca and J. Vanier., "Short-term frequency stability of the Rb^{87} maser" IEEE Trans Instrum. Meas. Vol. IM-22 pp.250-257   1973.

(5) G. Busca. R. Brousseau and J. Vanier "Long-term frequency stability of the Rb^{87} maser". IEEE Trans Instrum. Meas Vol. IM-24   pp.291-296   1975.

(6) J. Vanier. M. Tetu and L. G. Bernier. "Transfer of frequency stability from an atomic frequency reference to a quartz crystal oscillator" IEEE Trans. Instrum. Meas.   Vol. IM-28 pp.188-193   1979.

(7) M. Tetu. R. Brousseau and J. Vanier. "Frequency domain measurements of the frequency stability of a maser oscilltor" IEEE Trans. Instrum. Meas. Vol. IM-29.   pp.94-   1980.

(8) J. Vanier and M. Tetu., "Phase-locked loops used with masers: atomic frequency standards". IEEE Trans. Communications. Vol. COM-30 No.10 pp.2355-2361   1982.

(9) M. Tetu. P. Tremblay. D. Bonnier. and J. Vanier. "Short-term frequency stability and systematic effects on the rubidium 87 maser oscillator frequency". Proc of the 36th Annual Symposium

on Frequency Control   1982.   pp.340-347.

(10) H. T. Wang. "The frequency and time standard and activities
at the Beijing Institute of Radio Metrology and Measurements"
Proc 11th Annual PTTI   1979.   pp.657.

(11) L. S. Cutler and C.L. Searle., "Some aspects of the theory
and measurements of frequency fluctuations in frequency standards"
Proc IEEE Vol. 54 pp.136-154   1966.

(12) J. A. Barnes. et al., "Characterization of frequency
stability" IEEE Trans. Instrum. Meas. Vol. IM-20.   pp.105-120.
1971.

(13) F. M. Gardner., Phaselock Technigues JOHN WILEY & SONS. 1979.
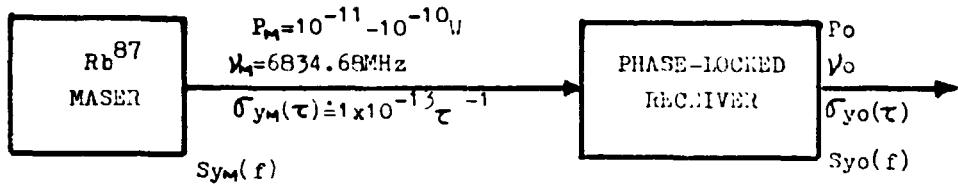
Fig.1. Basic configuration of Rb maser frequency standard
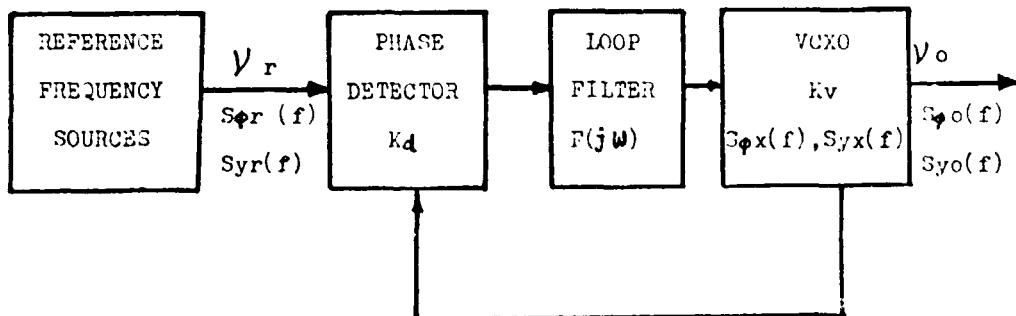
Fig.2. Basic block diagram of phase-locked system
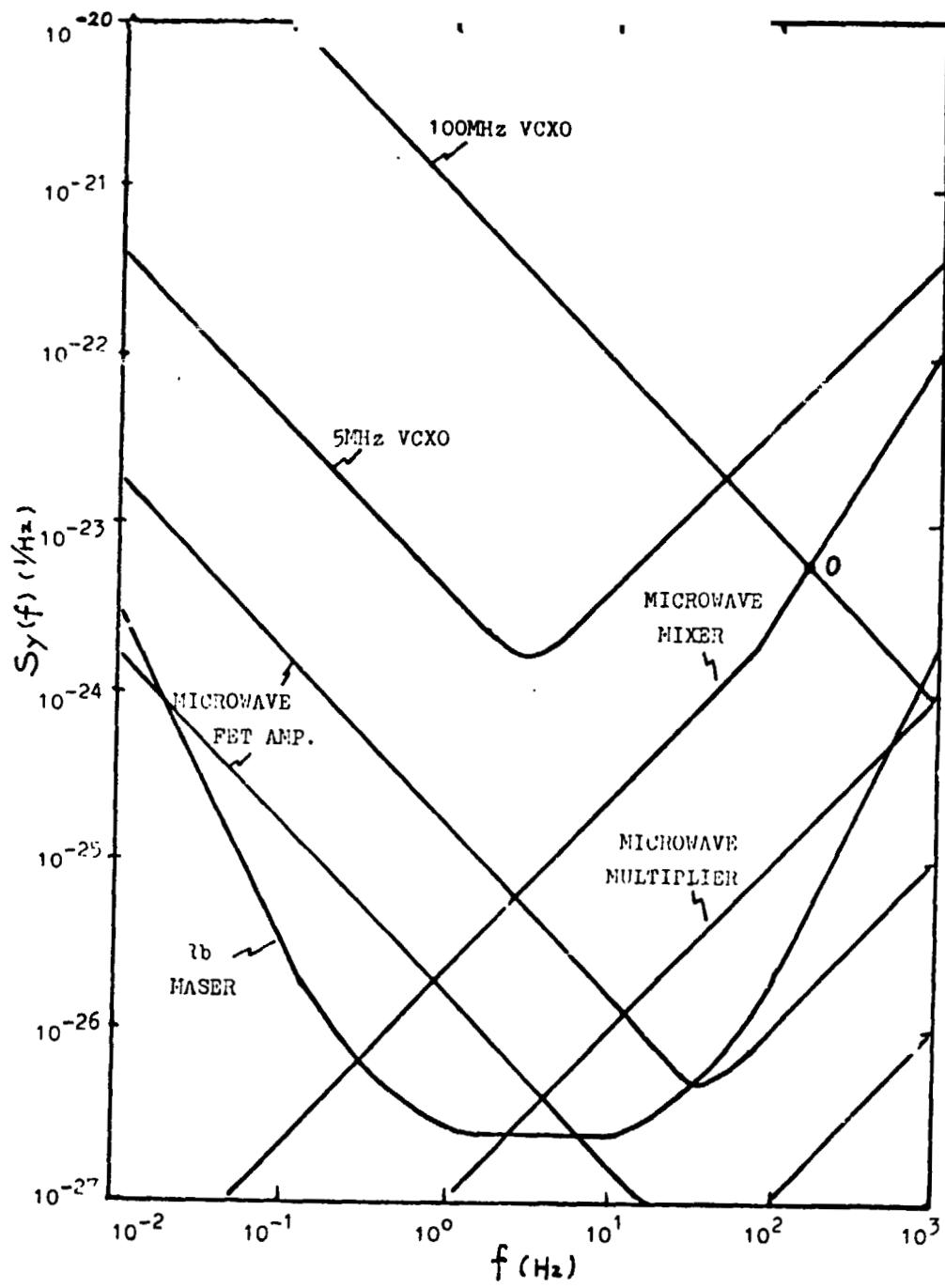
Fig.4. Frequency-domain stability of main components
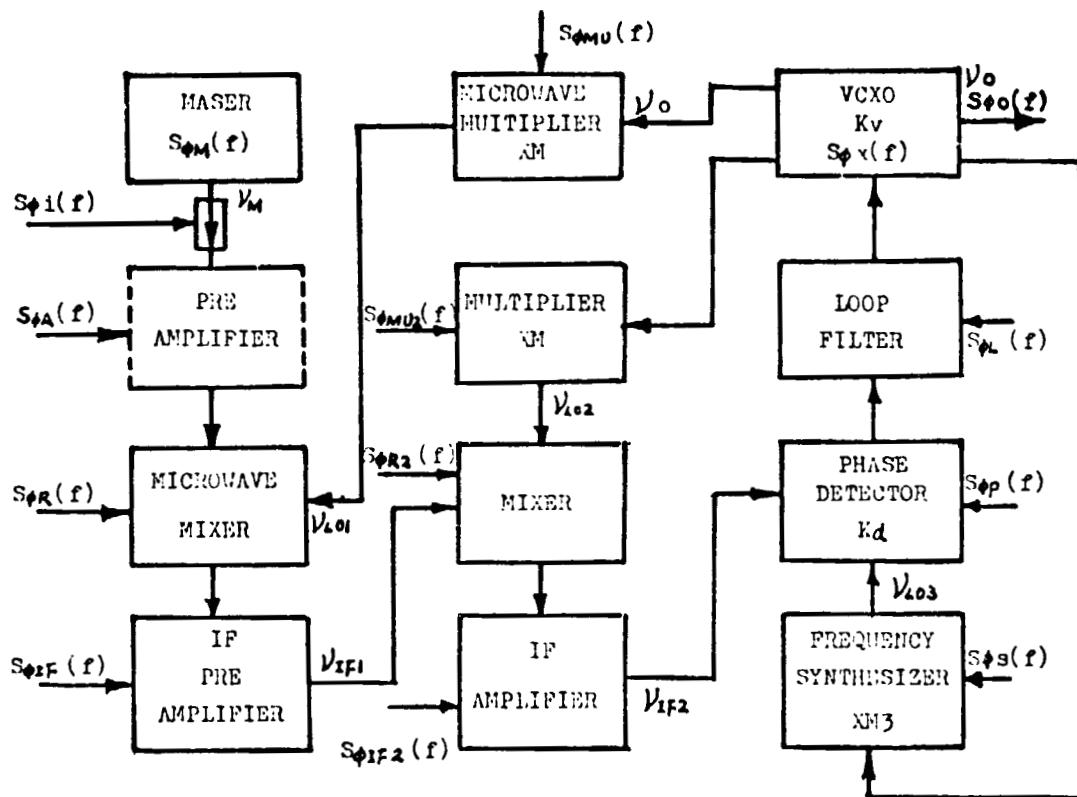
Fig.3. General block diagram of a maser receiver and main

noise contribution
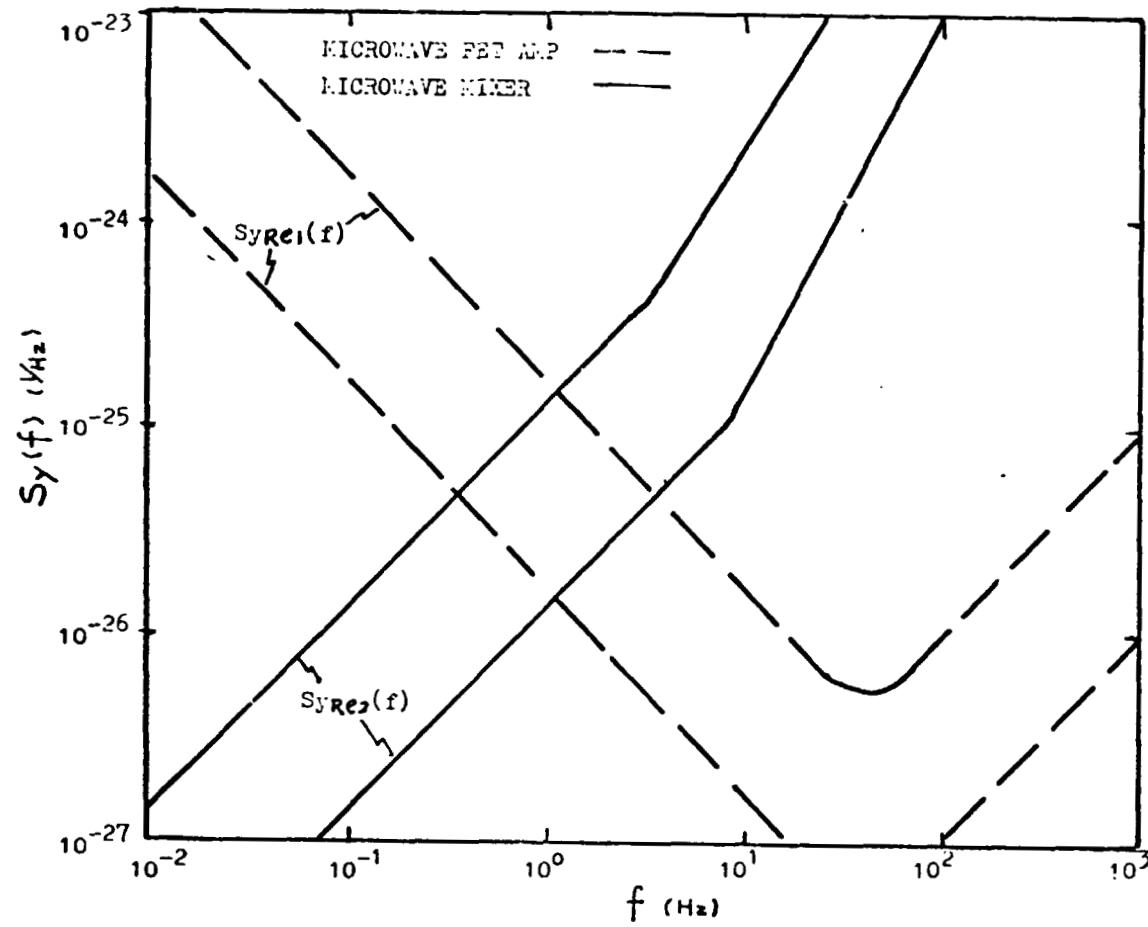
Fig.5. a Frequency-domain frequency stability of two low-noise receives.
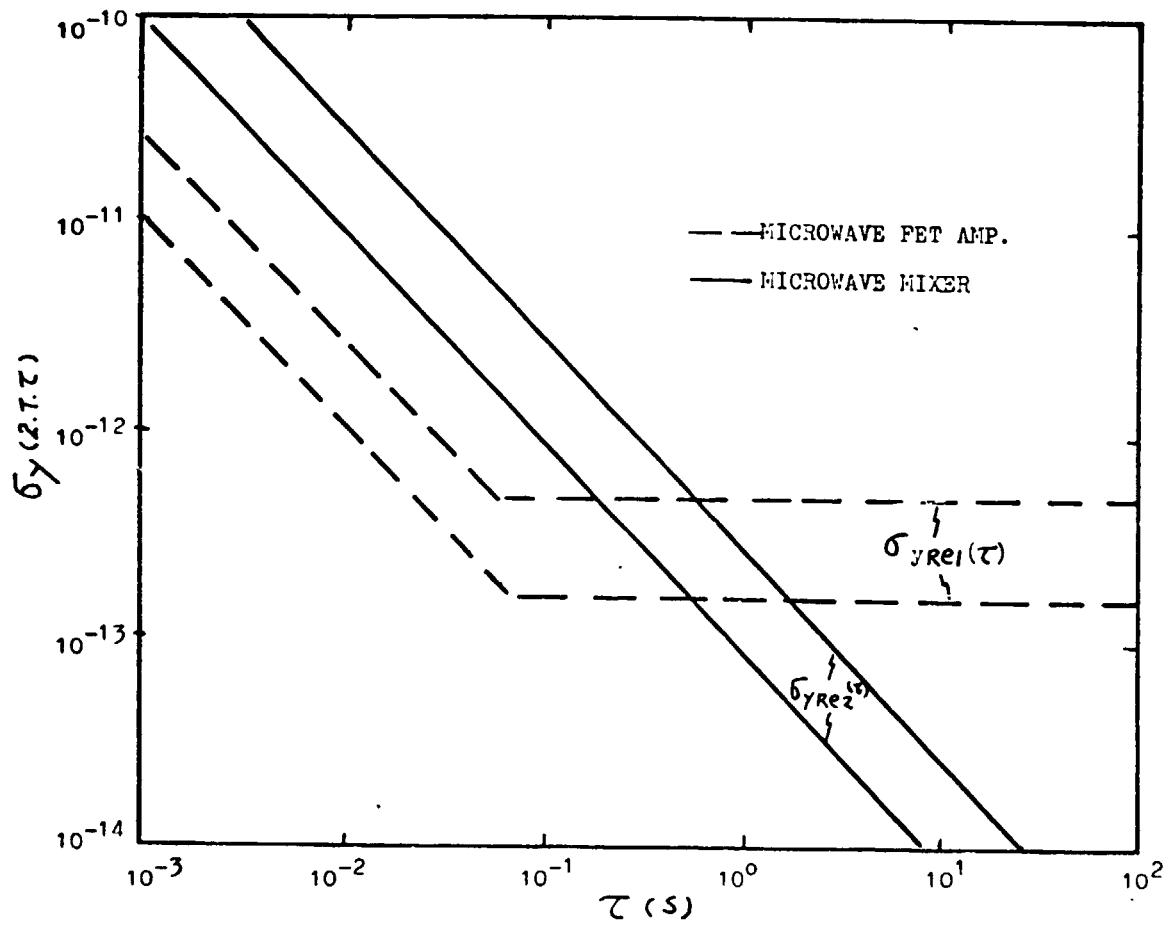
Fig.5.b Time-domain frequency stability of two low-noise receives.
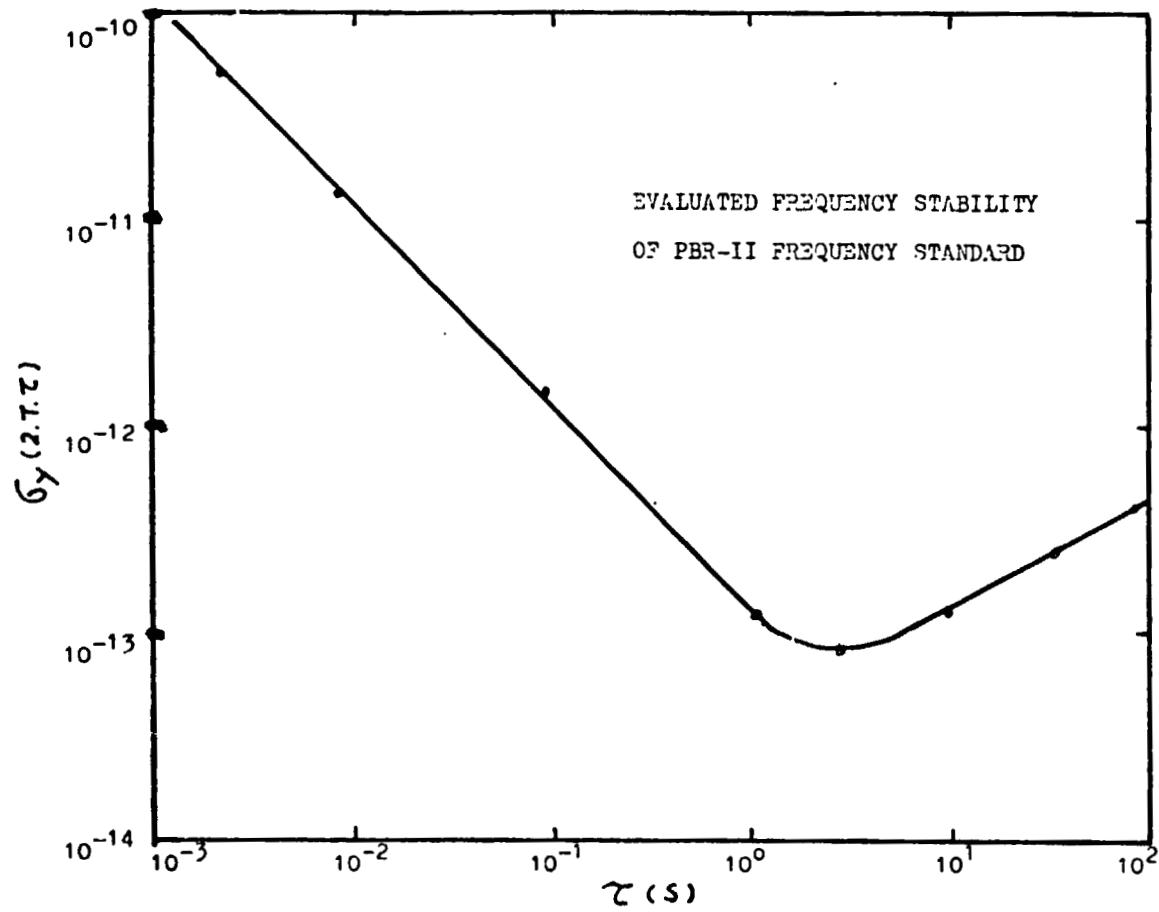
Fig.6. Evaluated time-domain frequency stability of PBR-II
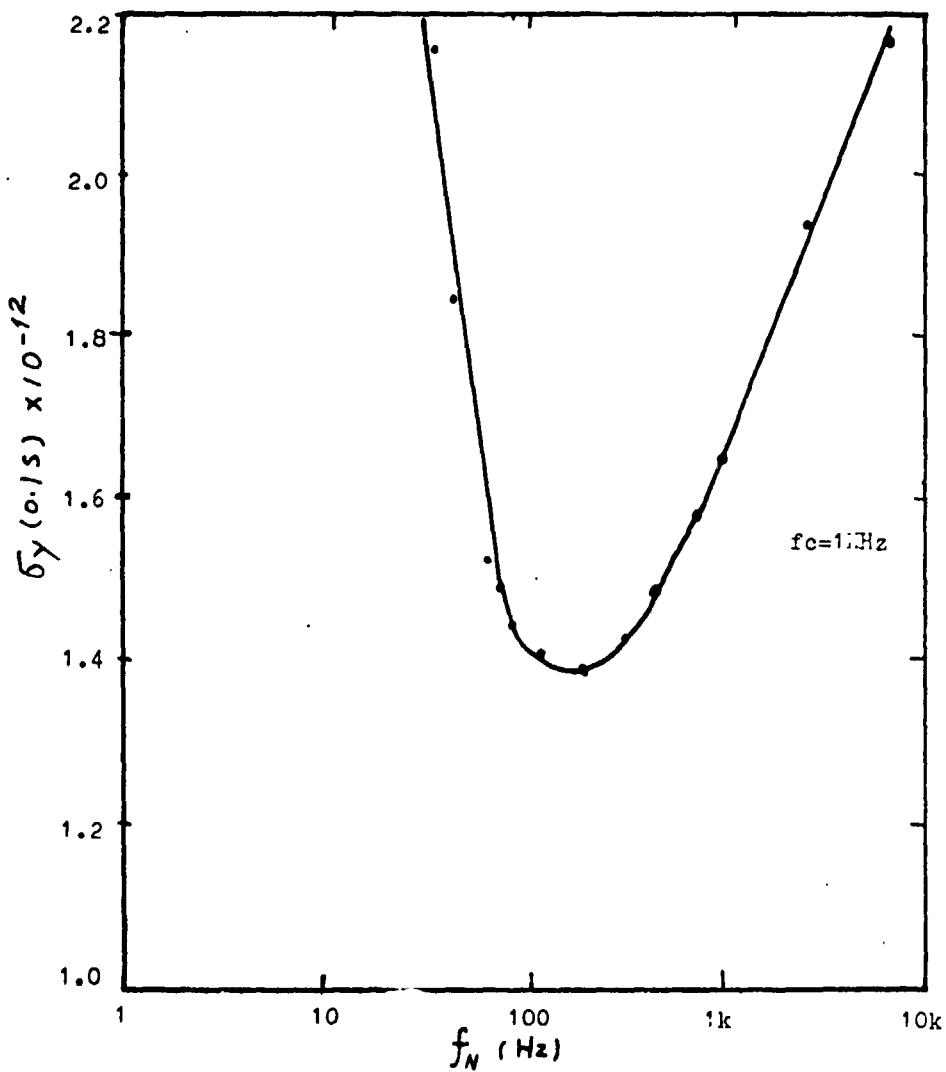
Fig.7. Evaluated value of the time-domain frequency stability $\sigma_{y(\Delta\theta)}$ versus loop nature frequency f_N for $\tau = 0.1^S$, fc=1KHz.
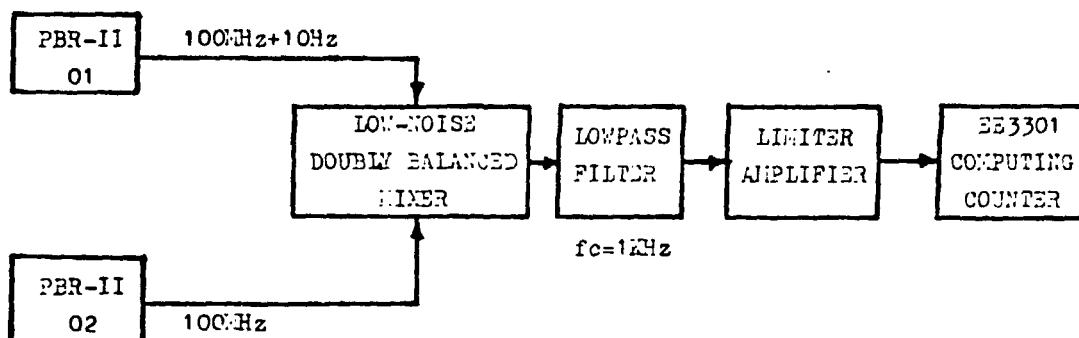
Fig.8. Experimental setup used in measurement of PBR-II frequency stability for averaging time $\tau = 100^{mS} - 100^{S}$.
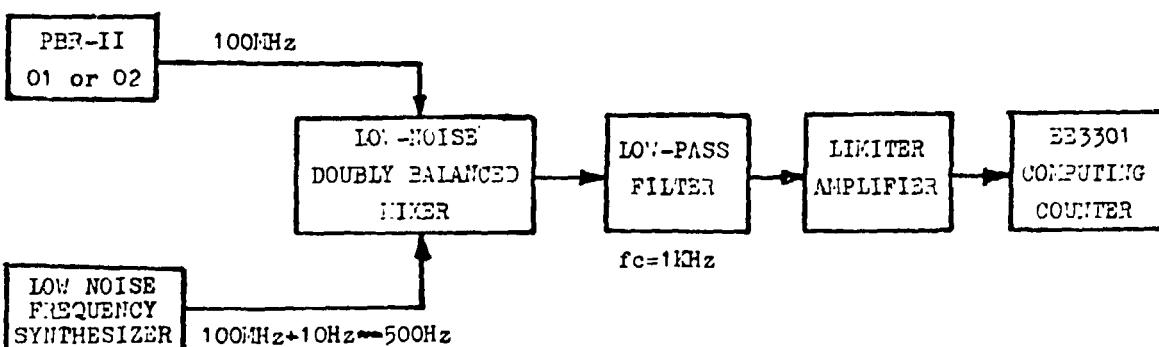
Fig.9. Experimental setup used in measurement of PBR-II frequency stability for averaging time $\tau = 2^{mS} - 100^{mS}$.

MEASURED FREQUENCY STABILITY OF
PBR-II FREQUENCY STANDARD.

$f_h = 1KH_z$
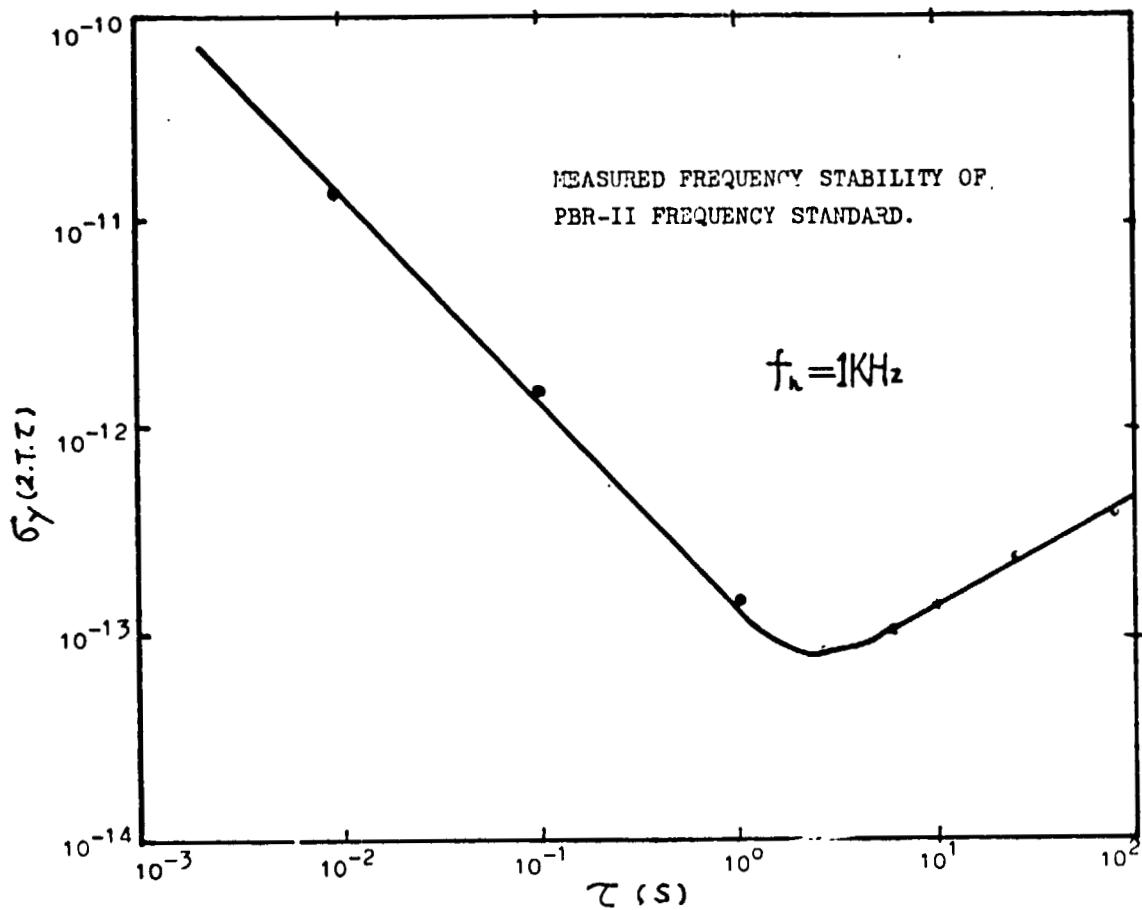
Fig.10. Actual tested time-domain frequency stability of PBR-II

217
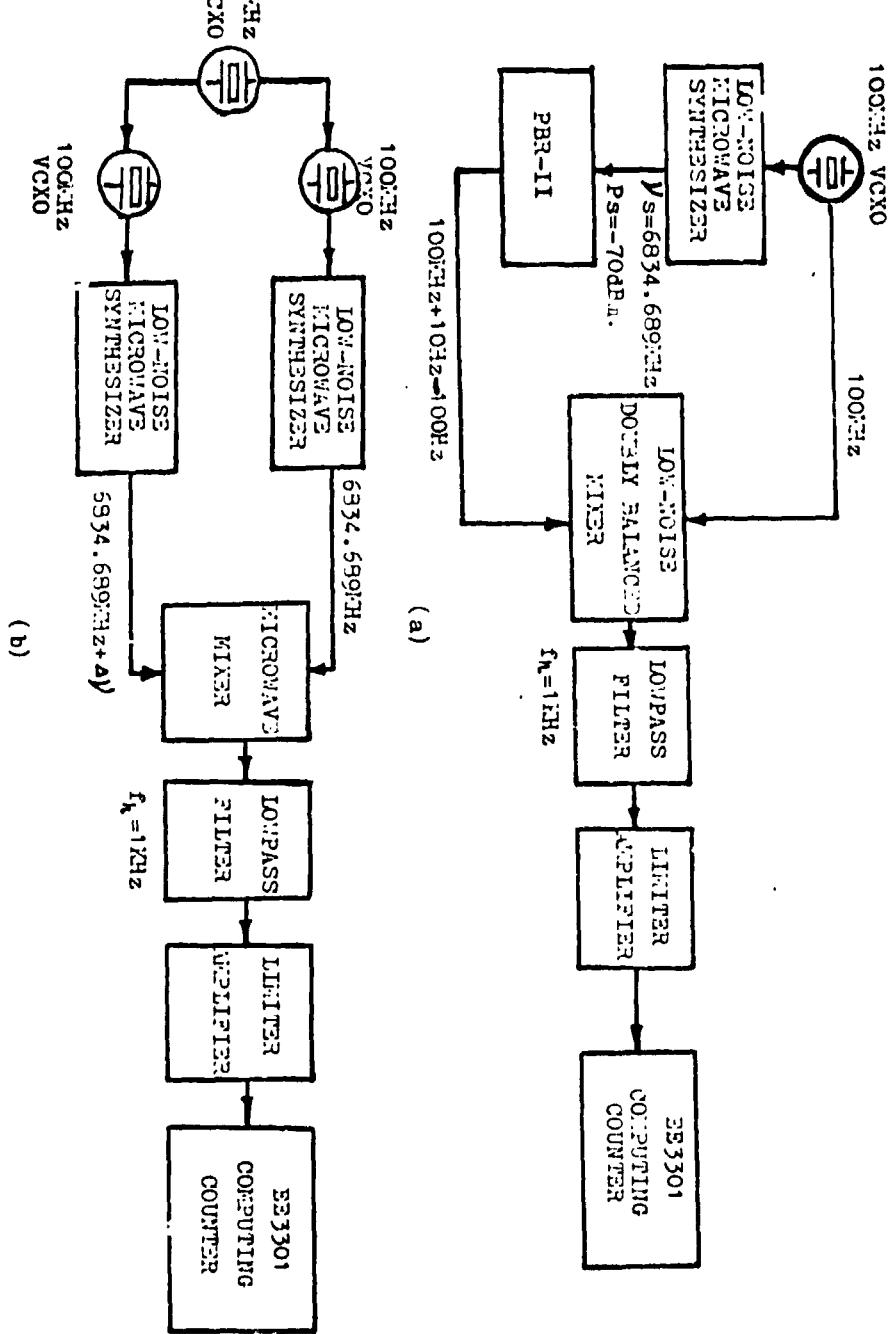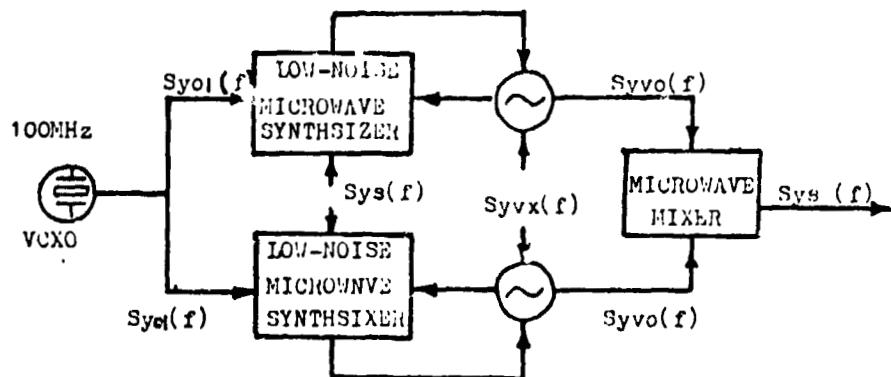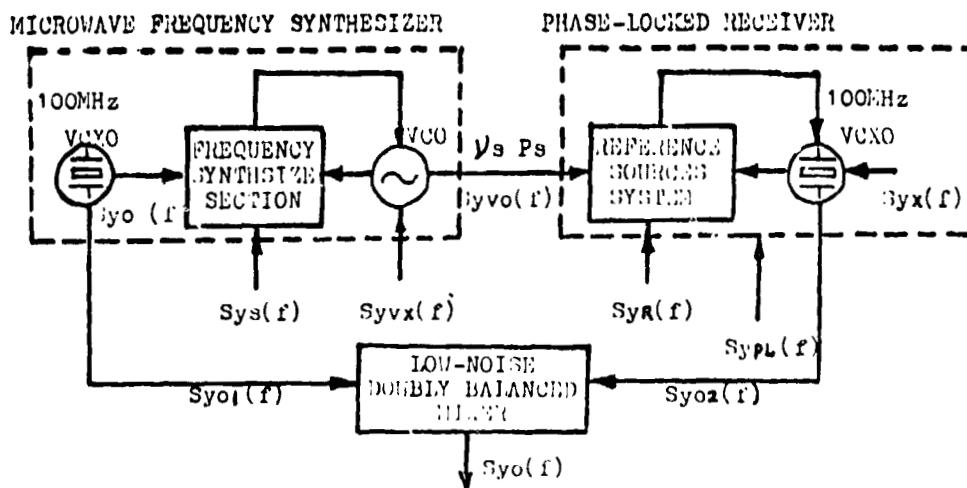
Fig.11. Experimental setup used in measurements noise contribution of phase-locked
receiver (a) and Microwave synthesizer (b)

MICROWAVE FREQUENCY SYNTHESIZER   PHASE-LOCKED RECEIVER

Fig.12. Principle block diagram of Fig.11a, and Fig.11b.

(b)
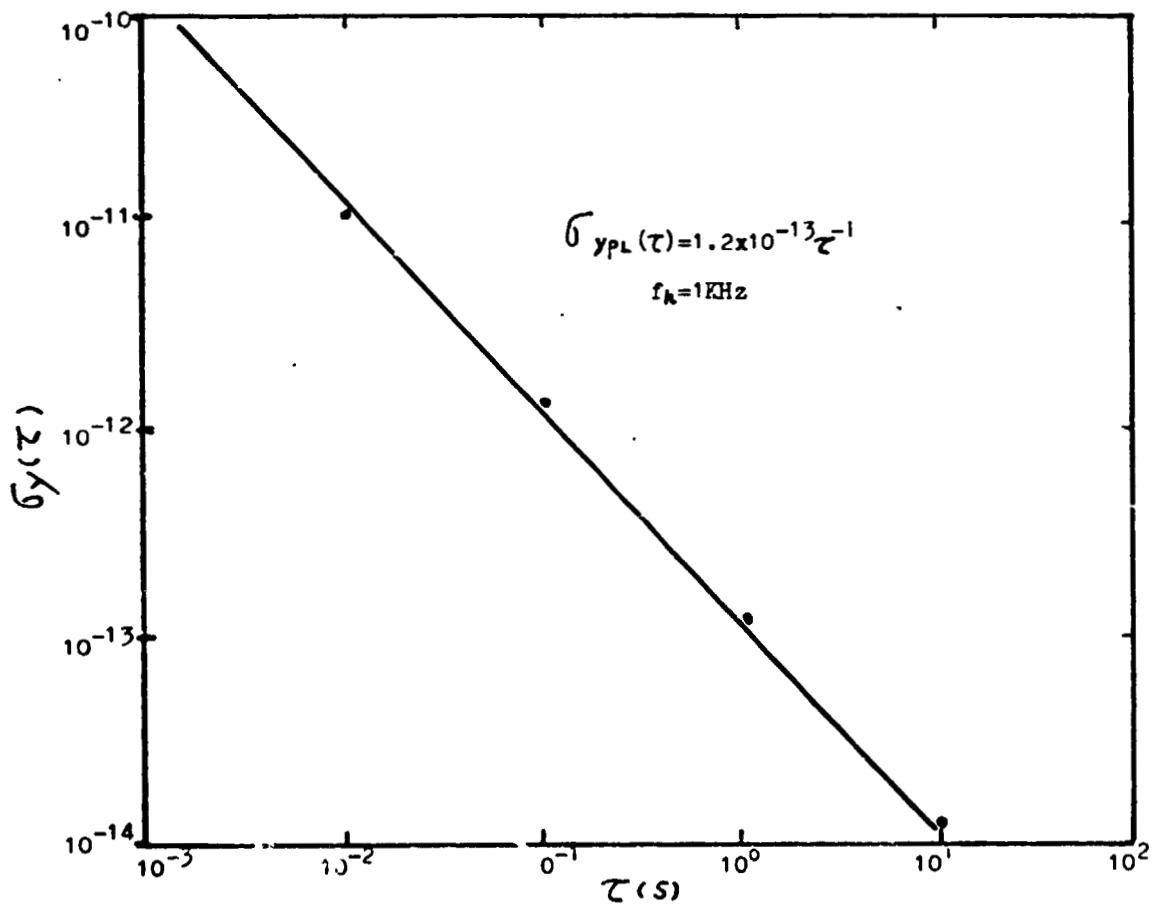
Fig.13. Phase-locked receiver noise contributions measured in
the time-domain for f_h=1KHz.
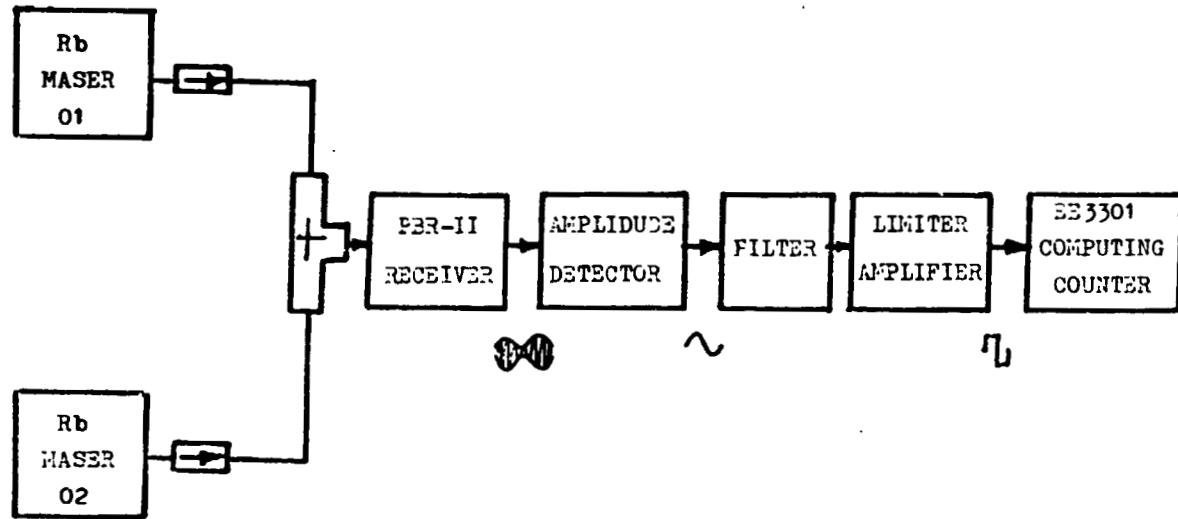
Fig.14. Block diagram of measurements Rb maser frequency stability.
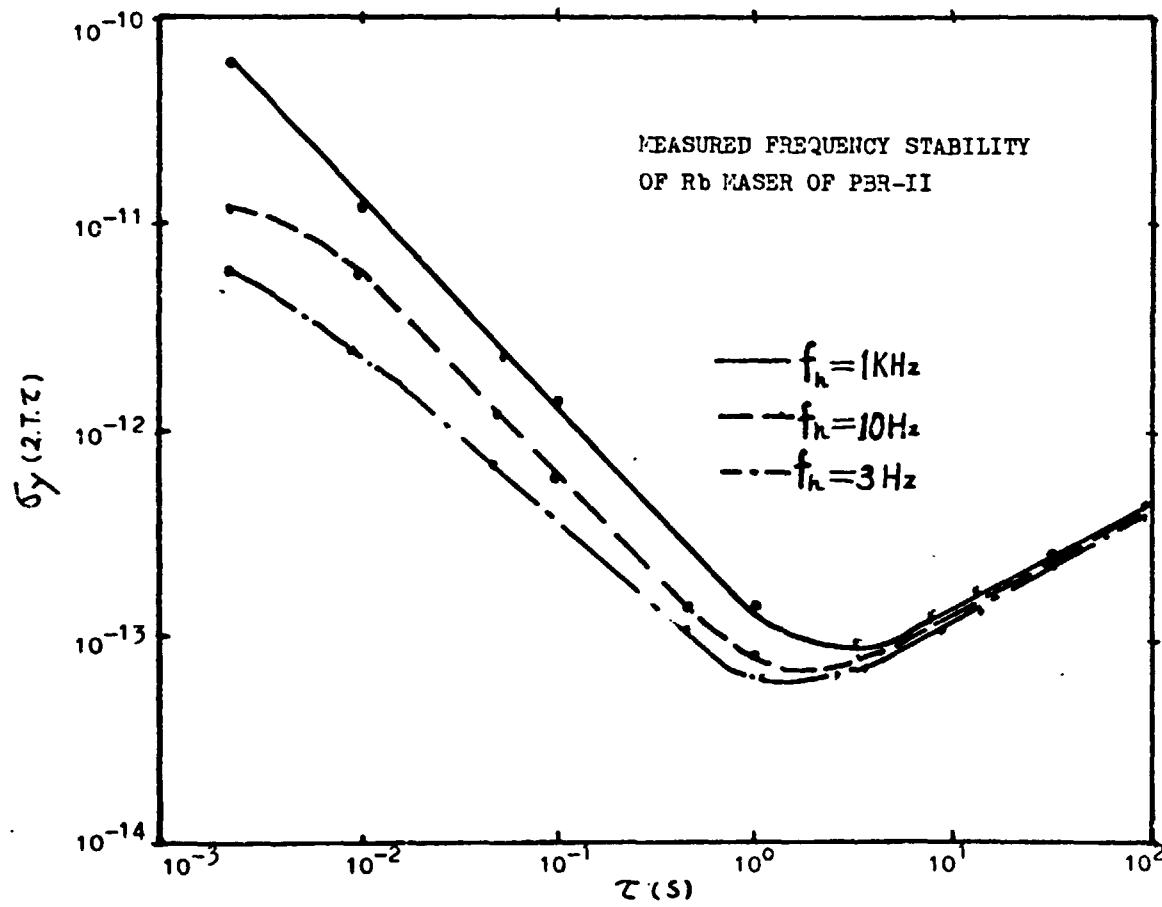
Fig.15. Time-domain frequency stability of Rb maser.
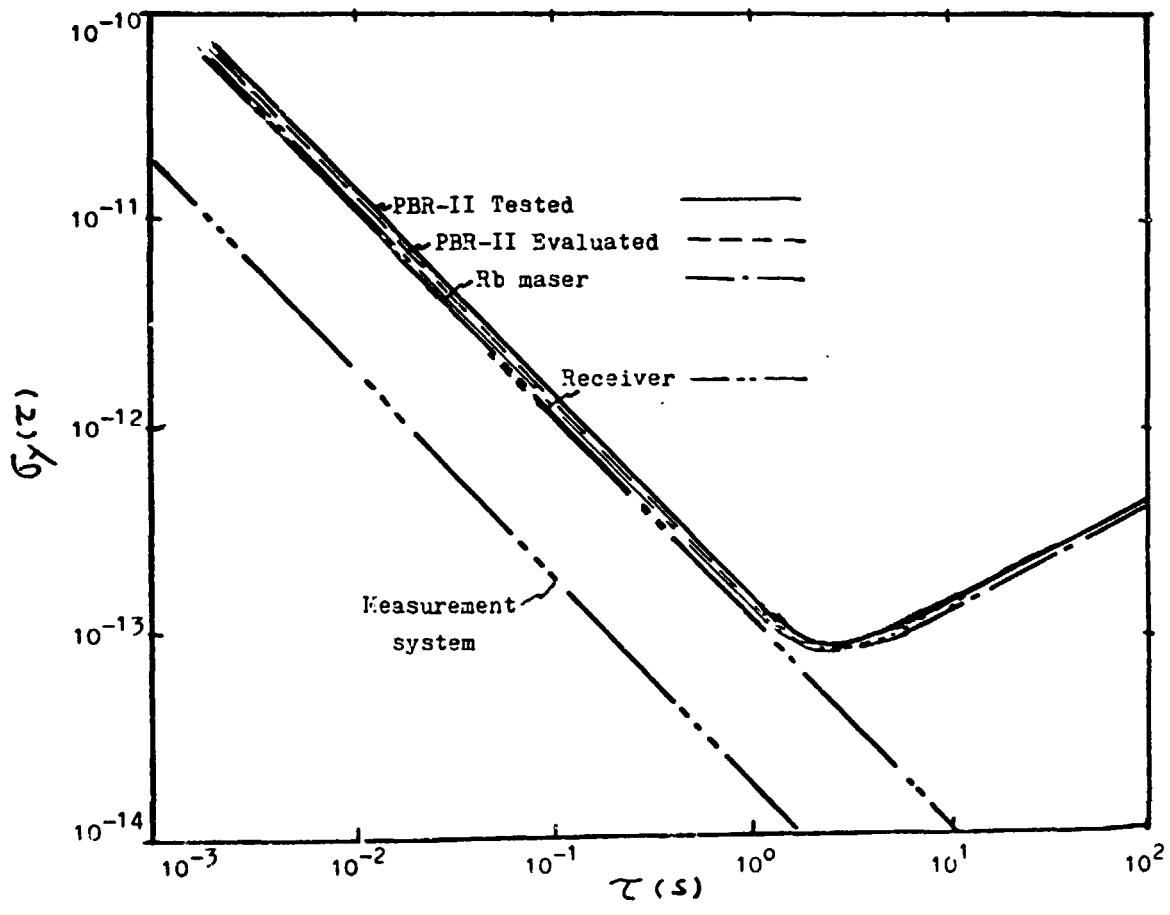
Fig. 16. Time-domain frequency stability
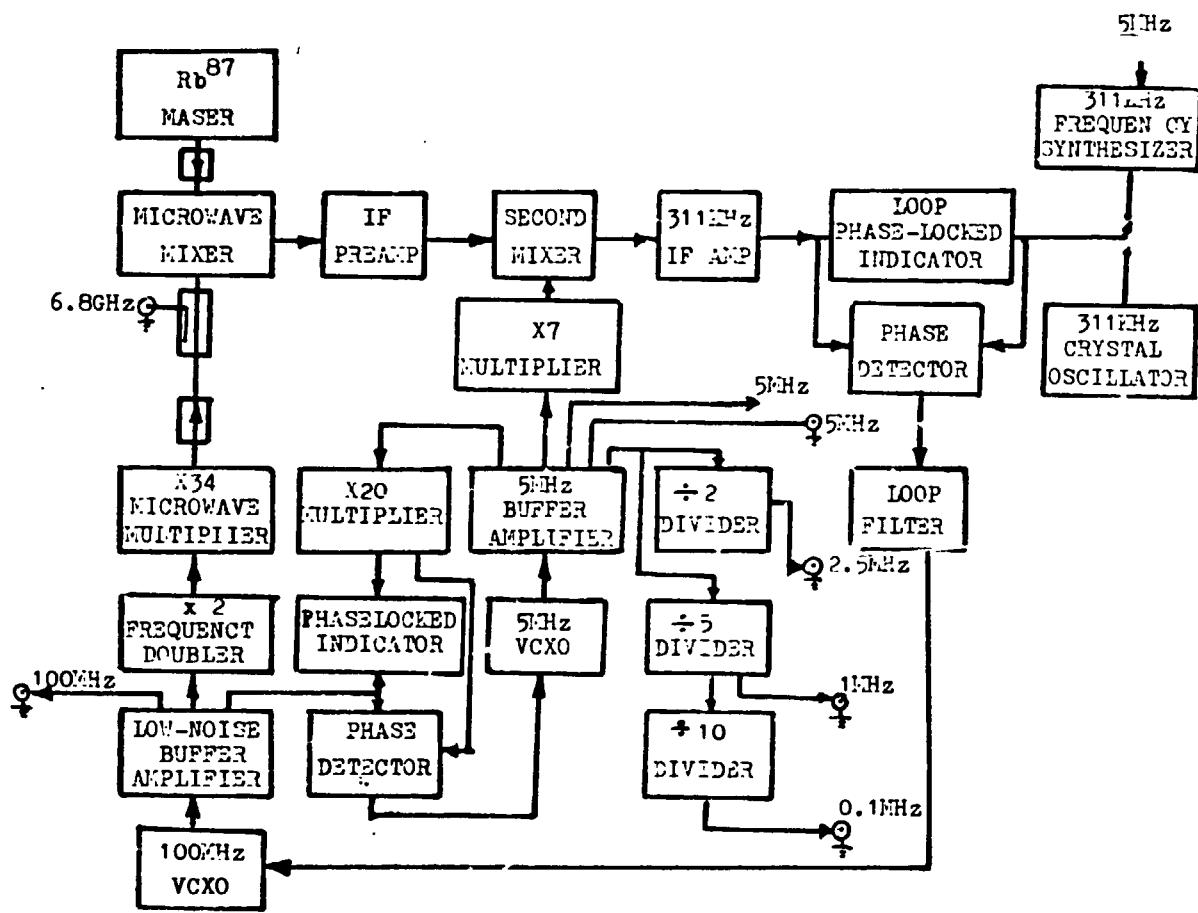
Fig.17. Detailtd block diagram of PBR-II Rb maser frequency standard

A REVIEW OF IONOSPHERIC EFFECTS ON EARTH-SPACE PROPAGATION

John A. Klobuchar
Ionospheric Physics Division
Air Forace Geophysics Laboratory
Hanscom AFB, MA 01731

ABSTRACT

Radio waves undergo several effects when they pass through the earth's ionosphere. One of the most important of these effects is a retardation, or group delay, on the modulation or information carried on the radio wave that is due to its encounter with the free, thermal electrons in the earth's ionosphere. Other effects the ionosphere has on radio waves include: (1) RF carrier phase advance; (2) Doppler shift of the RF carrier of the radio wave; (3) Faraday rotation of the plane of polarization of linearly polarized waves; (4) angular refraction or bending of the radio wave path as it travels through the ionosphere; and (6) amplitude and phase scintillations. With the exception of scintillation, all the other effects listed here are proportional, at least to first order, to the total number of electrons encountered by the wave on its passage through the ionosphere or to their time rate of change. In fact, phase scintillation also is merely the short term time rate of change of total electron content (TEC) after the longer term variations have been removed.

In this review, a short description will be given of each ionospheric TEC effect upon radio waves, along with a representative value of the magnitude of each of these effects under normal ionospheric conditions. This will be followed by a discussion of the important characteristics of average ionospheric TEC behavior and the temporal and spatial variability of TEC.

This paper was not received for publication.

JULES SCHLESINGER, HAZELTINE CORPORATION: Obviously, to get a high confidence level, I can't use every reading that's coming down from a group of satellites. Is that correct?

MR. KLOBUCHAR: Yes, I would assume so.

MR SCHLESINGER: Going from that, in your best judgment, how many readings would I probably have to take to make sure that I am in good shape?

MR. KLOBUCHAR: Do you have to have this time continuously? You must have some sort of an oscillator there that's fairly stable that you can rely upon for seconds, or tens of seconds, of time.

MR. SCHLESINGER: Yes, that's correct. However, we are planning -- and this is in the planning stage -- some sort of an algorithm to use the GPS system as a master to keep updating the ground station flywheel.

Now, if I were to use every measurement in my algorithm, on occasion, during fading, my algorithm would indicate a failure. So, somewhere in my algorithm, judging from your information, I must put in some coefficient which says I have to use "x" number of readings rather than a single reading. What would this number "x" be in your best estimate?

MR. KLOBUCHAR: Well, I don't know whether I brought any with me, but we have various power spectra of the simulation fading. I guess that's really what you are asking.

Does must of it occur within the first tenth of a second, or one second? The answer is yes, a second let's say. None of the deep fades have occurred with any length of time, duration, longer than something on the order of half a second to a second.

Now the question is: How are you going to know when you have a bad reading? Just by the AGC on your receiver channel? Because that's what we are measuring, in effect.

MR. SCHLESINGER: What will happen in this proposed system is that there will be an error generated because the signal coming down from the satellite will be probably markedly different from that originating, or being kept in the flywheel system. From what you just said, it appears that if I were to do two measurements every two seconds I wouldn't see an error, because the fading would be less than a second long. Isn't that correct?

MR. KLOBUCHAR: That's right. You can measure that by just using the AGC on your receiver, and know whether you have that sort of problem or not.

MR. SCHLESINGER: Would that be indicated in this "quality" signal that comes from the GPS?

MR. KLOBUCHAR: Nothing in the telemetry coming down from the GPS is going to tell you that there is anything in the intervening

atmosphere. It's the ionosphere itself, from your particular direction, that you will have to measure in one way or another to tell you whether you have a problem.

MR. SCHLESINGER: I think that you have answered the question. If I use not every reading, but perhaps every two, I will probably be safe anywhere in the world most of the time. Is that a correct assumption?

MR. KLOBUCHAR: If you can integrate for a second, I think that you will be in good shape.

DAVID ALLAN, NATIONAL BUREAU OF STANDARDS: When you have a large deviation, 1 to 3 sigma, what is the extent of that? Is it worldwide?

MR. KLOBUCHAR: No. In fact, from Colorado, back in the early or mid-seventies, we were making measurements -- "we" meaning not me, but some ionospheric people -- were making measurements in two directions; one station near Boulder, and one near Fort Collins, and we were looking at two different sateliites. One of them saw a big increase, and one of them didn't. That happened to be the demarcation line, because all of the east coast stations did see a big increase, and all of the west coast stations, from the one looking westward in Boulder, to the ones at Stanford and other places in the west, only saw a decrease.

No, it's not a worldwide phenomenon, and it will be later in time, generally, the lower in latitude you go, because these things propagate from the higher latitudes.

MEL BUCHWALD, LOS ALAMOS NATIONAL LABORATORY: Ionospheric people have been looking at simulations and the effects of simulations on the disturbing radio transmissions for localizing electromagnetic pulses using the W sensors on these GPS satellites, and we wonder where the body of data on simulations exist, and is it measured only through this Rayleigh fading data?

MR. KLOBUCHAR: We can probably talk privately in more detail about this, but I can answer that. There is a lot of empirical data, that is, fading data of the occurrences of different depths of fade versus time for different stations.

There is at least one group that is trying to make a model based partially on this empirical data, and partially on some theoretical work. They are making good progress in that. This is all for the background natural ionosphere, however.

There are also groups who are making extrapolations to the nuclear disturbed ionosphere. We probably deal with the bulk of the statistics on the natural ionosphere in our group, on the naturally occurring ionosphere measurements, at least.

MR. BUCHWALD: All we are interested in is the range of naturally occurring simulation.

MR. KLOBUCHAR: Well, the worst is Rayleigh fading. You can't get worse than that. Everything gets better from there, but I don't

know what percentage of the time you have Rayleigh fading at different locations. That's a function of a lot of things: time of day, season, solar geodetic activity, where you are located, an those kinds of factors.

MR. BUCHWALD: Thank you.

MR. KLOBUCHAR: On that general subject, I have one more view graph, and that is to show you about the solar cycle. This is the last of twenty-some odd solar cycles. It is a bit out of date now, because we are well down on this present solar cycle. If you look carefully, the highest solar cycle recorded according to sunspot number. was recorded in 1958.

The second highest was the one that we have just completed. It hadn't passed that point at the time this graph was made. The third highest was the one back in the forties. The one that peaked in 1968 or 1969 was a good average cycle.

We have been on a roll, then, during the last four cycles, if I may use that expression. We have have had either an average, or well above average cycles. We have been well above the average for the last four cycles.

Who is to say what we are going to get in the future? We are now nearing the minimum of the present cycle. Those of you who are going to try to make measurements tomorrow, or for the next few years, here is a curve and we are about here on the curve (indicating). The first seven cycles are left off this curve because the optics and the quality of the data are suspect. You see that we have been at the mean or higher for the last several cycles. In the next few years, we are going to be down in the minimum, and who knows what will be the maximum for the next cycle. If I had to bet today, I would bet on the average, not above or below it. I attended, in June, a meeting in Paris of solar forecasters, among other ionospheric forecasters, and you can flip a coin and come up with a better approximation.

This is what they predicted for the present cycle (indicating). The prediction, the guy's name and the date of the prediction. You can see from the actual maximum and the range of the guesses that they are all over the ballpark. Things are improving, but it's really empirical.

If anyone has any predictions they want to add to this, it was done by Jerry Brown. I grabbed it from him just to show the futility in trying to look a few years in advance for solar cycles.

IONOSPHERIC LIMITATIONS TO TIME TRANSFER BY SATELLITE

by

S. H. Knowles

Naval Research Laboratory
E.O. Hulburt Center for Space Research
Space Science Division, Ionospheric Effects Branch

ABSTRACT

The ionosphere can contribute appreciable group
delay and phase change to radio signals traversing
it; this can constitute a fundamental limitation
to the accuracy of time and frequency measurements
using satellites. Because of the dispersive nature
of the ionosphere, the amount of delay is strongly
frequency-dependent $(1/f^2)$. At the 1.5 GHz
frequency band used in the GPS systems the
vertical-incidence ionospheric excess delay is
typically 5 nanoseconds during the daytime (based
on a total electron content of $10^{17}/m^2$), and
20% of that at night. Even at X-band, the total
daytime ionospheric delay of about 1 nanosecond
is enough to make compensation necessary for
implementation of extremely precise time transfer
schemes such as the coherent satellite link
proposed by Knowles. Calibration using models is an
unreliable procedure because of the variable nature of
the ionosphere. It is possible in principle to provide
a self-calibration by observing at two frequencies
simultaneously. While this technique has on
occasion proven successful in reducing ionospheric
errors, a fuller understanding of the underlying
phenomenon is necessary in order to understand
the basic limitations it mandates in time transfer
techniques.

The ionosphere is known to be highly variable,
both in terms of large-scale changes and in
terms of smaller-scale irregularities. Much
work in recent years has focused on
'pathological' irregularities in the polar
regions and equatorial region that amount to
variations of 10% to several hundred percent
in the total electron content. Recent

efforts to investigate ionospheric disturbances
using radio astronomy interferomters have shown
that the mid-latitude region, where most time
transfer experiments take place, also has a
prevalent irregularity distribution. This work
has been undertaken by our NRL group using
interferometers at Green Bank, W. VA, and
Magdalena, NM, and also by a Dutch group using
the Westerbork interferometer (3). These
experiments measure the differential electron
content between two or more antenna locations,
and relate more closely to the ionospheric effect
seen by a time transfer experiment than most
other techniques. Easily measurable ionospheric
irregularities have been seen in mid-latitude
regions. Our group has observed a typical
differential electron content of about $10^{15}/m^2$
over a baseline of 35 km. A day-night correlation
with TEC values is observed; the night-time
ionosphere is more irregular during periods of
high geomagnetic activity. By combining results
from our work with that of the Dutch group, who
used a baseline that was considerably shorter,
it is possible to obtain information about the
size distribution of the irregularities. The
irregularity amplitude is approximately
proportional to the baseline over the range
studied. Only limited information is available
about another parameter of interest, the time
scale distribution of these irregularites.
Irregularities have been observed on all time
scale from seconds to hours, as illustrated by
data samples. The typical irregularity in the
mid-latitude region is about 1% of the total
electron content. While this is less than
the extreme variations seen in polar regions,
calibration of these anomalies must also take
place to achieve full accuracy in time transfer
and its associated use for position location.

INTRODUCTION

The ionosphere can contribute appreciable group delay to signals traversing
it. This delay depends on both the frequency and the state of the ionosphere.
The equation for the refractive index of the ionosphere can be expressed as:

$$n = 1 - K_1 \frac{n_e}{f^2} \pm K_2 \frac{n_e B \cos\theta}{f^3} + O(1/f^4).$$
(1)

where n_e is the electron density

    B is the earth's magnetic field

    Θ is the angle between the wave normal and the magnetic field, and

    K_1, K_2 are numerical constants (Mathur et al., 1970).

If n_e is replaced by a typical total electron content along a vertical column (TEC), an estimate can be obtained of the additional group delay due to the ionosphere. Such a curve is plotted in figure 1 for a typical daytime TEC of $2 \times 10^{17}/m^2$. The curve is for a vertical path and is multiplied by the secant of the zenith distance of the line-of-sight. The dominant term from equation (1) has a shape inversely proportional to frequency squared, and a total magnitude of about 5 nanoseconds at the Global Positioning System (GPS) frequency. The typical night-time delay is about 25% of this. Klobuchar (1984) discusses the limitations in attempting to correct for the delay with a model due to the variations in TEC. Such a model can be expected to be accurate to about $\pm$ 25%.

A method often mentioned for correcting accurately for the ionospheric group delay is dual-frequency measurements. Because of the dispersive nature of the ionospheric delay, measurements at two frequencies can be used to determine what the delay constant is and correct for it. In principle this method can be very accurate, because it measures the TEC along the same line of sight that is to be used for the observation. Although the dual-frequency method has been used in a number of experiments, and is to be implemented for GPS, its accuracy has not been critically examined. Possible inaccuracies in this method include error multiplication caused by a finite frequency difference, and the effect of higher-order terms in equation (1). Figure 1 contains an estimate of the residual component if this correction is accurate to 1%. One residual component of concern is the $1/f^3$ component in equation (1). This component gives rise to two possible phase and group velocities in a wave propagating through the ionosphere. The difference in velocities depends on the angle of the propagation direction to the earth's magnetic field. This effect gives rise to Faraday polarization rotation, but it also causes a difference in group delay between the two modes. Figure 1 shows the "worst-case" magnitude of this effect. While the net time delay change caused is zero, a propagation bifurcation results that causes a dual arrival time measurement. This can be a serious limitation on lower-frequency timing measurements.

When considering the limitations provided by the ionosphere to time transfer measurements, it is important to consider the complete temporal and spatial spectrum of ionospheric irregularities. Klobuchar (1984) discusses the large-scale (global) component of TEC variations. Recent experimental information has been accumulating about medium-scale (100 m - 1000 km) irregularities in TEC that are important in contributing to time measurement inaccuracies. It has been deduced from in-situ satellite measurements that medium-scale irregularities of 1-10 % of TEC exist commonly at all times in

the arctic, and during nighttime in equatorial regions (Szuszczewicz et al, 1983). Although it has been commonly assumed that medium-scale irregularities in the "normal" mid-latitude ionosphere are insignificant, recent research using radio astronomy interferometers have shown that this is not the case.

In a radio interferometer, two or more large radio antennas are pointed at the same distant natural radio source. The outputs of these antennas are combined coherently, after correction for differential delay, to make a Michaelson interferometer. The output of this interferometer measures any source of differential phase delay. Since the ionosphere is the dominant dispersive effect, it is possible to measure the difference in total electron content by combining measurements at two frequencies in an appropriate manner. To this end, the Naval Observatory's Green Bank, West Virginia interferometer and the newer Very Large Array facility in New Mexico have been used to conduct preliminary investigations into the feasibility and usefulness of such a tool. The radio interferometer system at Green Bank, whose primary mission is to measure geodetic parameters, observes contimously a succession of radio sources at quasi-random points n the local sky. (Klepczynski et al., 1979). Simultaneous observations at 2695 MHz (11.1 cm. wavelength) and 8085 MHz (3.7 cm. wavelength) provide a measurement of the differential electron content between the ionospheric paths of any of the possible antenna pairs. The continuous availabililty of data from this array makes its use attractive for ionospheric monitoring. At the time the present data was recorded, the array consisted of 3 antennas of 85-foot diameter located along a 2.5 kilometer track that is oriented at an azimuth of 62.05 degrees, and one remote station with a 45-foot diameter antenna located about 55 km away. An additional remote station has since been added. The Very Large Array, described in detail by Thompson et al (1980), is an array of 27 antennas located near Socorro, NM, and designed with maximum flexibility for a variety of astrophysical experiments. Its 27 antennas allow significantly more complete spatial sampling of ionospheric phase differences than the Green Bank array. The maximum baseline available is approximately the same as the Green Bank array.

The differential phase path between two antennas due to the ionosphere is:

$$\Delta L = \delta L_{2T} - \delta L_{1I} = K_1 \frac{\int^2 n_e dl - \int^1 n_e dl}{f^2} = K_1 \frac{(D.E.C.)}{f^2} \qquad (2)$$

so that the differential phase delay is proportional to the difference in total electron content along the two parallel paths. In the context of this article, D.E.C. will be used to refer to the experimentally determined difference in ionospheric path length as between the locations of different antennas. It may be due to a number of different mechanisms; e.g., ionospheric gradients (Komesaroff, 1960), irregularities, diurnal effects on TEC, etc. This quantity $(\int^2 n_e dl - \int^1 n_e dl)$ will henceforth be called differential electron content = D.E.C. Converting from measurement units of delay to units of phase, a power of frequency is cancelled, so that:

$$\Delta\phi_I = \frac{K \ (D.E.C.)}{f} \tag{3}$$

where $K = \frac{2\pi k_1}{C}$

and $\Delta\phi_I$ is the measured phase change due to the ionosphere.

Another important parameter to consider is the effective area intercepted by each antenna primary beam as it transits the ionosphere, as well as the overlap between beams. The differential phase effects on an interferometer from the ionosphere are described by a special case of scintillation-scattering-diffraction theory; in particular one may expect thin-screen diffraction theory to serve as a basis. This type of theory is complex and has been discussed by a number of authors (Crane, 1977; Rufenach, 1975), although relatively few (Whale and Gardiner, 1966) discuss the expected phase perturbations. While it is beyond the scope of this article to develop a complete theory for this phenomenon, the basic remark can be made that if the two antenna beams do not overlap the phase fluctuations will be fully developed, while for beams that largely overlap the phase fluctuations will be largely cancelled. With the 27 antennas of the VLA, it is possible to do a more complete reconstruction of the ionosphere. If the antenna beams do not intersect while passing through the ionosphere, 27 independent points in the ionosphere, located along a Y-configuration at distances from each other of up to 35 km, will be sampled by the VLA.

The differential electron content measured by an interferometer pair is a sum of the true difference in the free electron density between the paths over each antenna, and a second order difference in between the paths over each antenna, and a second order difference in the path length caused by the curvature of the earth. The formula for the curvature effect may be shown to be in phase units

$$\Delta\phi = 4.85 \times 10^{-11} \ \frac{(TEC)}{f} \cdot \left(\frac{1}{\sin\theta_2} - \frac{1}{\sin\theta_1} \right) \tag{4}$$

where θ_1, θ_2 are the elevation of the source at each antenna, f is the frequency in MHz, and $\Delta\phi$ is the differential phase in units of degrees. The difference $(1/\sin\theta_2 - 1/\sin\theta_1)$ can be either positive or negative, depending on the source geometry, but is always less than d/r where d is the distance between antennas, and r is the earth's radius. Since this is a refraction effect due to the sphericity of the earth, it does not depend on the height of the electron layers doing the refracting. The total measured differential electron content is thus the sum of the differential electron content due to variations in total electron content between the two locations and that due to the sphericity of the earth.

For the baselines used in our data sample, both effects are of comparable magnitude and must be considered. To measure the irregularity component, the

other must be subtracted. In order to do this, some estimate must be made of the TEC. In analyzing the Green Bank data TEC values obtained from satellite Faraday rotation data by the Air Force Global Weather Control (1981) were used for this purpose. Values obtained at Sagamore Hill, MA were used as the closest approximation available to the Green Bank, WV site. A time correction was made in the TEC data to compensate for the difference in longitude. In order to simplify the date analyses only phases from two baselines, one of 35 km and one of 1.5 km, were considered. Data taken with the U.S.N.O.'s Greenbank interferometer during November 1983 together with smaller samples from 1980-81, was analyzed to isolate ionospheric effects. The periods include a wide range of geomagnetic activity.

Figure 2 shows the estimates of variance of estimates of k for the long and short Green Bank baseline for the month of November 1983. Data has been grouped into periods of morning twilight, day, evening twilight, and night to emphasize diurnal effects. Occasional data points have been bridged. Both the higher absolute value of the variance on the long baseline and its increased variability are evident. Figure 3 shows a weighted average of the variance for the four time periods for the entire month. The day variance for the long baseline is clearly greater during the daytime, while this effect is not present for the short baseline. An obvious interpretation of this is that D.E.C.'s of $5 \times 10^{14}/m^2$ are consistently present during the daytime over a 35 km baseline, while irregularities over a 1.5 km baseline are consistently less than $1.5 \times 10^{14}/m^2$. The phase of the effect agrees with that of TEC measurements, which is normally four times higher during daylight hours. Although the constant portion of the long baseline variance may be due to the ionosphere, it is more reasonable to ascribe this to equipment effects.

Although the variance correlates well with the diurnal TEC effect, it would be expected to correlate more directly with an index that would predict irregularities in the ionosphere. In Figure 4 the daytime long baseline variance is plotted on the same graph as the geomagnetic index A_p. A general correlation is evident. No noticeable correlation of the daytime variance with the daytime maximum TEC was evident. This is an indication that irregularities are being measured, rather than some differential of the normal daily gradient.

Another method of displaying the results of the experiment is to follow the tracks of one or more sources and compare the measured differential ionospheric effect with that predicted from independent total electron content data. This is done in Figures 5 and 6 for the radio source 0355+508, which was observed at night, and the radio source 1749+701, which was observed during the day. Also plotted on these figures is the differential path length ionospheric effect predicted from the total electron content data. The data from the nighttime source is seen to be generally smoother, although variable from night to night. That from the daytime source always, and that from the nighttime source sometimes, has fluctuations of $1-2 \times 10^{15}$ in differential electron content. The data is too sparsely sampled to enable a detailed Fourier analysis of the time scale of the fluctuations, but it appears that a typical time scale is of the order of 1-2 hours. For the baseline of 35 km, the observed 1-2 hour time scale means that the ionospheric irregularities

observed are typically either changing with that time scale or moving with a velocity of at least 20 km/hr (7m/sec) with respect to the earth's surface. This estimated speed is much lower than currently accepted values for the ionospheric superrotation rate of 50-150 m/sec.

A sample detection of an ionospheric irregularity using the VLA is shown in Figure 7. A method similar to that described above has been used to separate phase excursions at frequencies of 1.4 GHz and 5 GHz into dispersive, or ionospheric, and non-dispersive, or tropospheric terms. The data shown includes spacings of 17 km., 9 km., 3 km., and 0.4 km., during a period of 24 hours beginning at 08 hours local time on 21 January 1979. The figure snows observed phase in units of degrees at 1.4 GHz (100 degrees = 2.5×10^{15} D.E.C.). During this period, the source 1311+678, which is circumpolar, was observed until about 14.7 hours local time; then source 0552+398 was observed until the first source was again visible at about 0.7 hours. Source-change times are indicated by the long, vertical bars extending through the figure.

The deep protrusion in the 17 km. and 9 km. ionospheric outputs may be interpreted as a gradient in TEC which lasted for a duration of about 7 hours, with a mean epoch of about 16 hours local time. Its apparent intensity is magnified by the fact that the observations at that time were low in the sky. After correcting for a secant effect multiplication of about 3, an irregularity of 6×10^{14} in D.E.C. is indicated; this is consistent with the Green bank results.

The 9 km spacing is generally similar to the 17 km spacing, but is decreased in amplitude by about 50%, as would be expected for an ionospheric gradient. Thus, the total D.E.C. may be larger depending on the size of the irregularity. A consistency check is provided by the tropospheric output, which snows no significant change during this period.

DISCUSSION

The radio astronomy technique, can measure ionospheric structure on a variety of scales, and provides a measure of an effect integrated through the ionosphere, rather than the marginal electron content measurement made by either bottomside or topside (Reinisch and Xuegin, 1982) sounders. During the observational periods described here, irregularities of the order of from 2×10^{14} to 2.5×10^{15} in differential electron content were observed. This amounts to about 0.5 to 5 % of the measured TEC, and indicates the frequent presence of significant irregular structure in the ionosphere on this scale.

A Dutch group (Spoelstra and Kelder, 1984) have recently used the Westerbork interferometer to measure ionospheric disturbances. Although their longest baseline available was only 2.7 km., they were able to easily measure ionospheric irregularities. They found the typical size to be consistently greater than their maximum baseline, which is in agreement with the present size estimates. Their conclusions about the greater prevalence of disturbances during the daytime are in general accord with ours, although the Dutch group did not provide numerical estimates of differential electron content.

Both the Green Bank results and the sample of data from the VLA show clear evidence of horizontal ionospheric gradients in TEC persisting for periods of several hours, while the Dutch group observed periods of less than fifty minutes. The mid-latitude radio interferometer observations clearly are not related to the ionospheric wind, which is known to have velocities of 50-150 kilometers per second (Regan and Rodriquez, 1981; Rino and Livingston, 1982). They are most easily accounted for by the phenomenon of traveling ionospheric disturbances, or TID's. This class of disturbances, as pointed out by Evans et al (1983), includes fluctuations with a wide variety of periods, which, in spite of many observations with various techniques, are not well-defined.

From the limited observations undertaken by our group and the Dutch group, it is possible to make a rough estimate of the approximate amplitude vs. distance relationship of these medium-scale irregularities. This is shown in figure 8. A similar graph that gives typical time scales is not yet possible due to inadequate data.

SUMMARY

Ionospheric compensation is necessary for the most precise time transfer and frequency measurements, with a group delay accuracy better than 10 nanoseconds. A priori modeling is not accurate to better than 25%. The dual-frequency compensation method holds promise, but has not been rigorously experimentally tested. Irregularities in the ionosphere must be included in the compensation process.

REFERENCES

1. Air Force Global Weather Central, Omana, Neb., suppliers of data base for T.E.C. Measurements.

2. Aarons, J.H., E. Whitney and R.S. Allen, "Global Morphology of Ionospheric Scintillation", Proc. IEEE 59, 159-172 (1971).

3. Coffey, H.E. (ed.), "Geomagnetic and Solar Data", J.G.R. 89, 241¹ (1984).

4. Hamaker, J.P., "Atmospheric Delay Fluctuations with Scale Sizes Greater than One Kilometer, Observed with a Radio Interferometer Array", Radio Science 13, p 873, 1978.

5. Klepczynski, W.J., G.H. Kaplan, D.D. McCarthy, F.J. Josties, R.L. Branham, K.J. Johnston and J.S. Spencer, "Progress Report of the USNO/NRL Green Bank Interferometer Program", NASA Conference Publication 2115, Radio Interferometry Techniques for Geodesy", Proceedings of a conference held at M.I.T., Cambridge, MA., June 19-21, 1979, p. 63.

6. Klobuchar, J.A., "A Review of Ionospheric Effects in Earth-Space Propagation", submitted to Proceedings of the Sixteenth PTTI Meeting.

7. Knowles, S.H., W.B. Waltman, F.J. Kelly and S. Odenwald, "Observations of the Radio Noise Background in the Frequency Range 150-180 kHz", in press for Radio Science (1985).

8. Mathur, N.C., M.D. Grossi and M.R. Pearlman, "Atmospheric Effects in Very Long Baseline Interferometry", Radio Sci. 5, 1253 (1970).

9. Regan, R.D. and P. Rodriguez, "An Overview of the External Magnetic Field with Regard to Magnetic Surveys", Geophys. Surveys 4, 256 (1981).

10. Reinisch, B.W. and H. Xueqin, "Automatic Calculation of Electron Density Profiles from Digital Ionograms I. Automatic O and X Trace Identification for Topside Ionograms", Radio Sci. 17, 421 (1982).

11. Rino, C.L. and R.C. Livingston, "On the Analysis and Interpretation of Space-Receiver Measurements of Transionospheric Radio Waves", Radio Sci. 17, 845 (1982).

12. Spoelstra, T.A.T., and H. Kelder, "Effects Produced by the Ionosphere on Radio Interferometry", Radio Sci., 19, 779, 1984.

13. Szuszczewicz, E.D., R.T. Tsunoda, R. Narcisi, and J.C. Holmes, "Coincident Radar and Rocket Observations of Equatorial Spread-F", Geophys. Res L. 7, 537 (1980).

14. Szuszczewicz, E.D., M. Singh, P. Rodriquez, and S. Mango, "Ionospheric Irregularities and their Potential Impact on Synthetic Aperture Radars", Radio Science 18, p. 765 (1983).

15. Thompson, A.R., B.G. Clark, C. Wade and P.J. Napier, "The Very Large Array", Ap. J. Supp. 44, 151 (1980).

16. Whale, H.A. and C.W. Gardiner, "The Effect of a Specular Component on the Correlation Between the Signals Received on Spaced Antennas", Radio Sci. 1, 557, 1966.
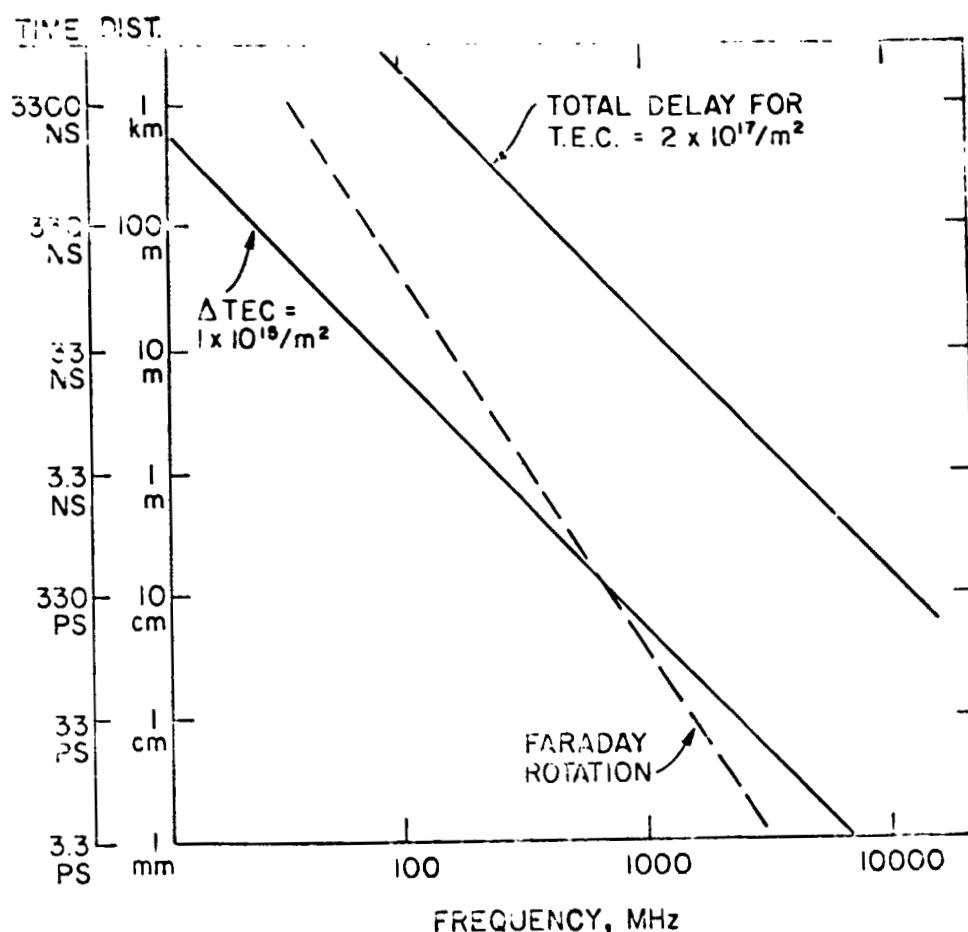
Fig. 1   Ionospheric effects on group delay.
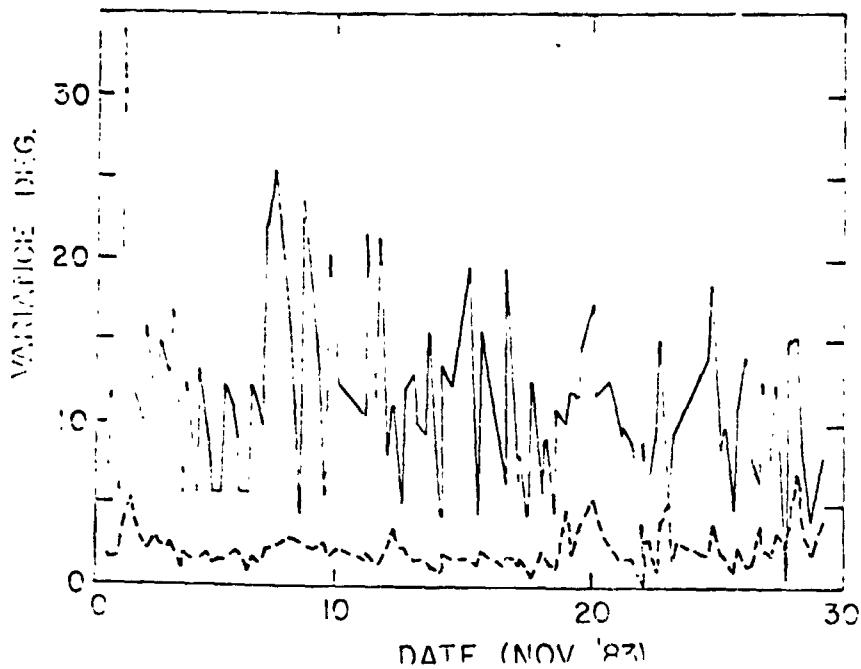
Fig. 2. Scatter in ionospheric phase measurments for Green Bank
interferometer for the month of November, 1983. Dotted line marks
short baseline; solid line marks long baseline. Data is grouped into
morning twilight, day, evening twilight and night.
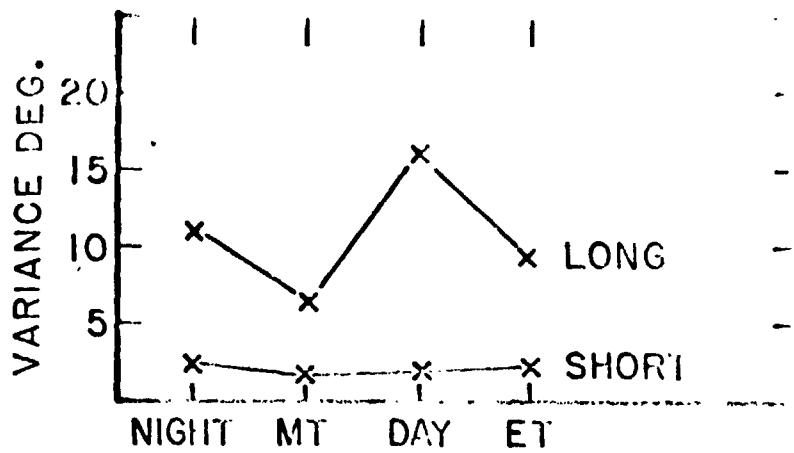
Fig. 3 All data of Figure 2 grouped to show behavior of variance as a
function of time of day.

239
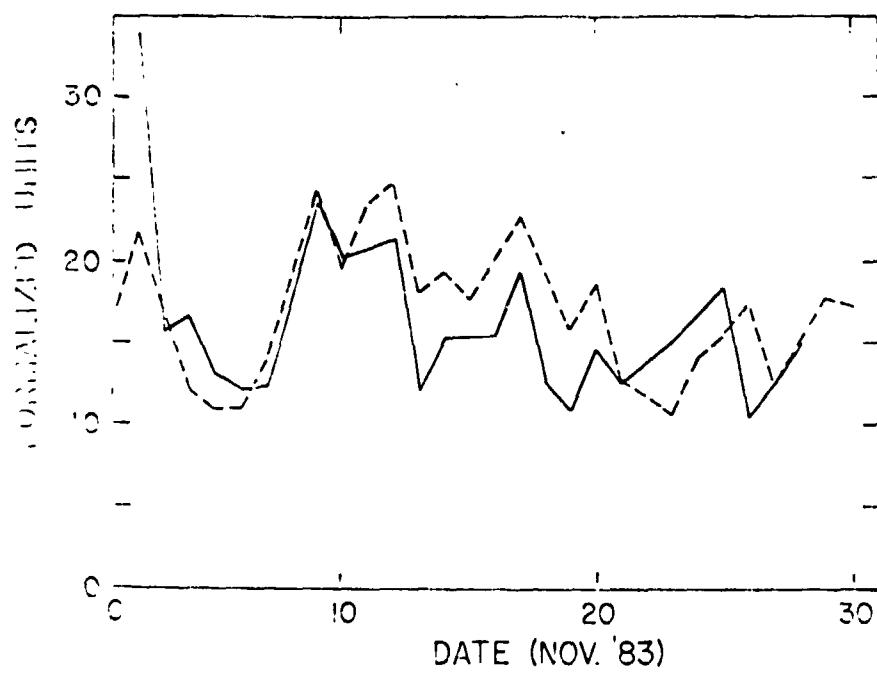
Fig. 4   Comparison of Green Bank long baseline variance for daytime with geomagnetic index A_p.   Normalized units used on ordinate.
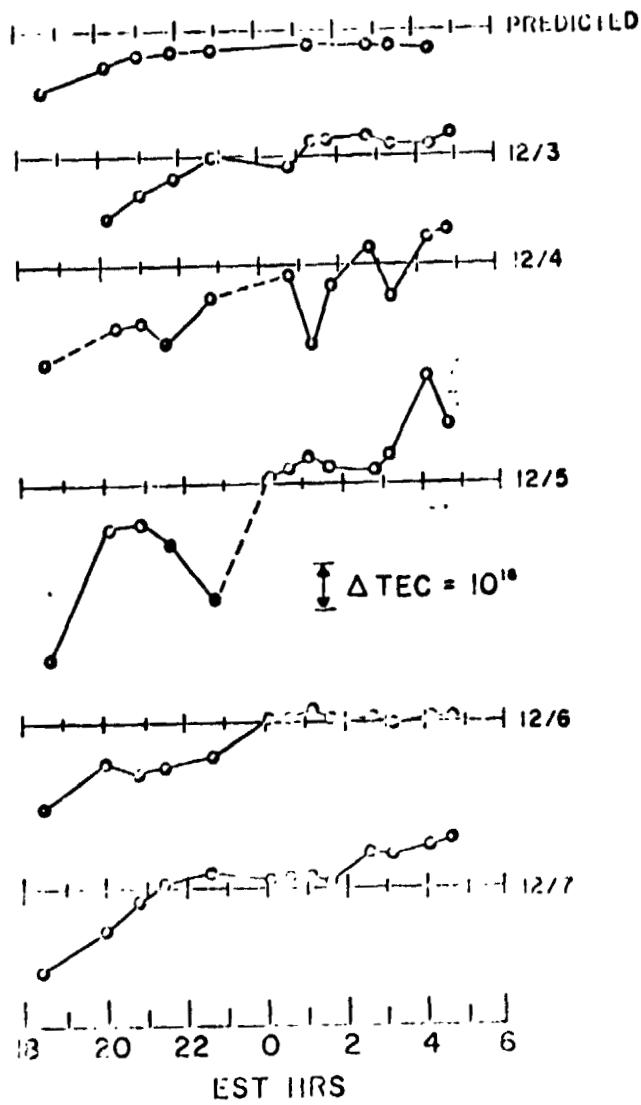
Fig. 5 Differential electron content measurement as a function of time for
0355+308, a nighttime source. Observations taken during early
December, 1981.
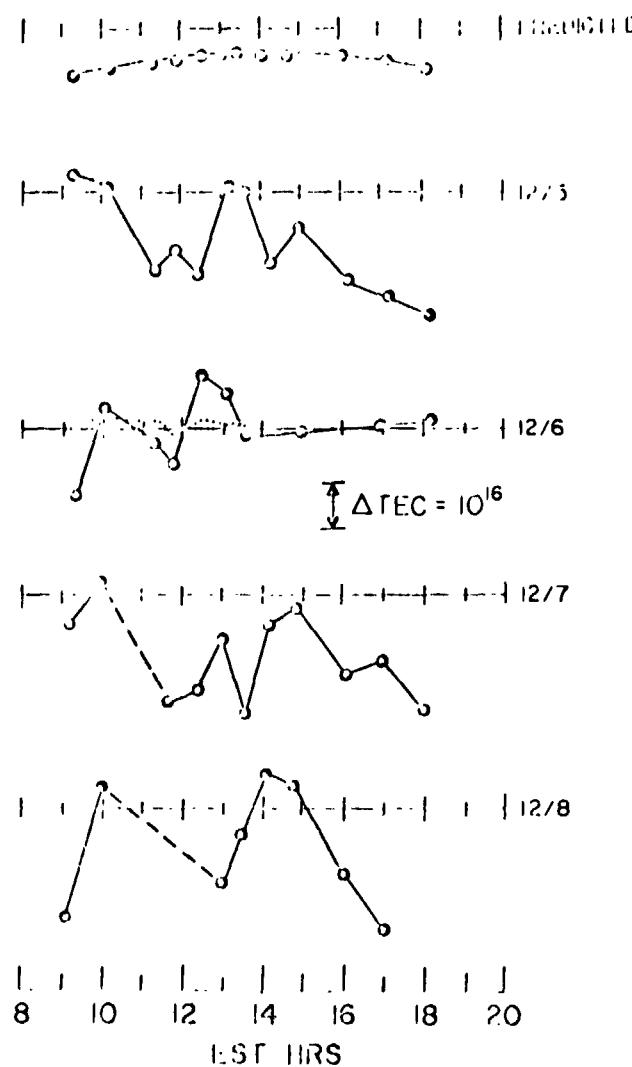
Fig. 6 Differential electron content measurement as a function of time for
1749+701, a daytime source. Period ot observations same as Fig. 5.
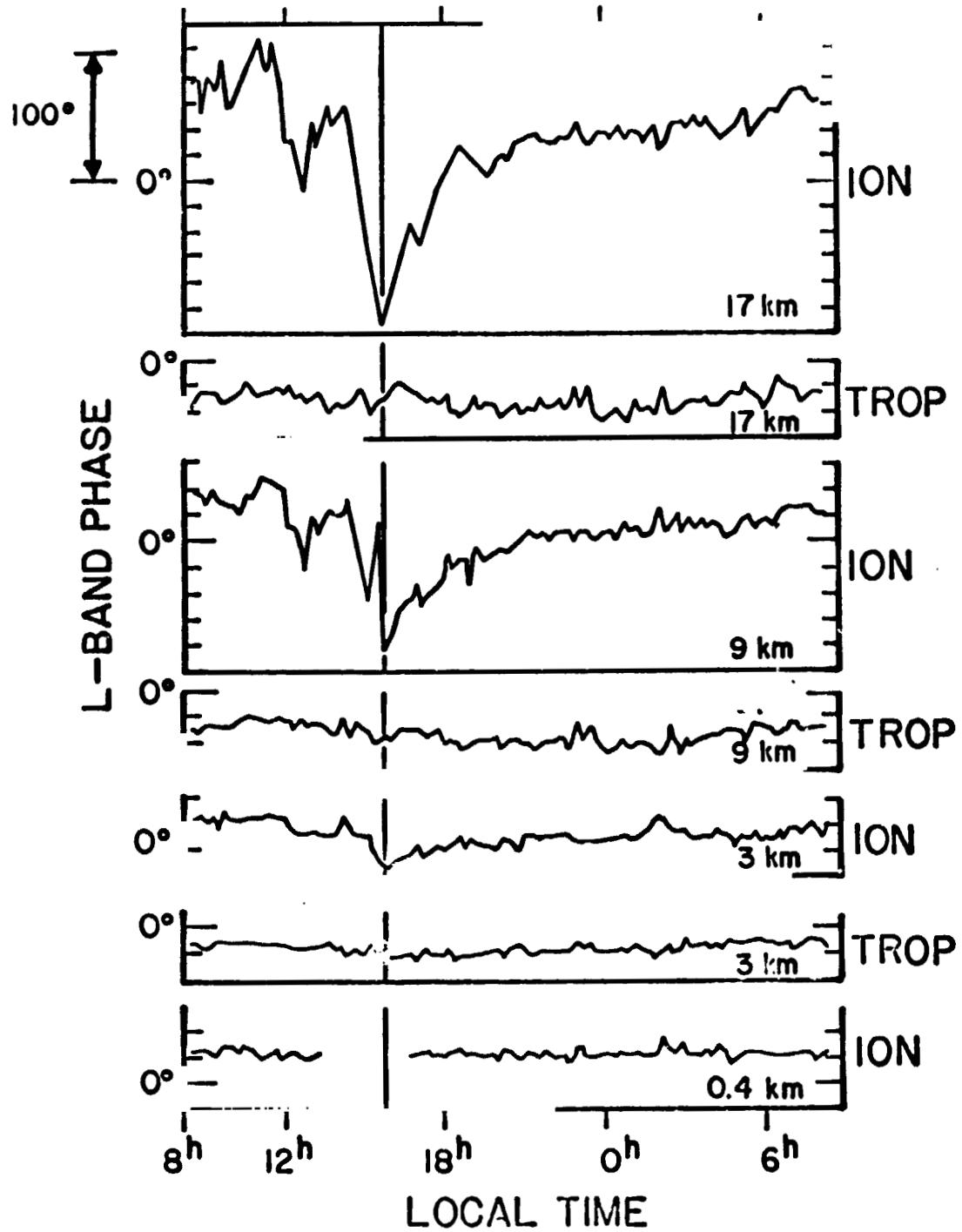
Fig. 7   Sample ionospheric measurements made using a series of baselines with
          the Very Large Array, illustrating the detection of an ionospheric
          disturbance. The graph shows both non-dispersive, or tropospheric
          and dispersive or ionospheric differential phases. Long vertical
          bars mark source changes.
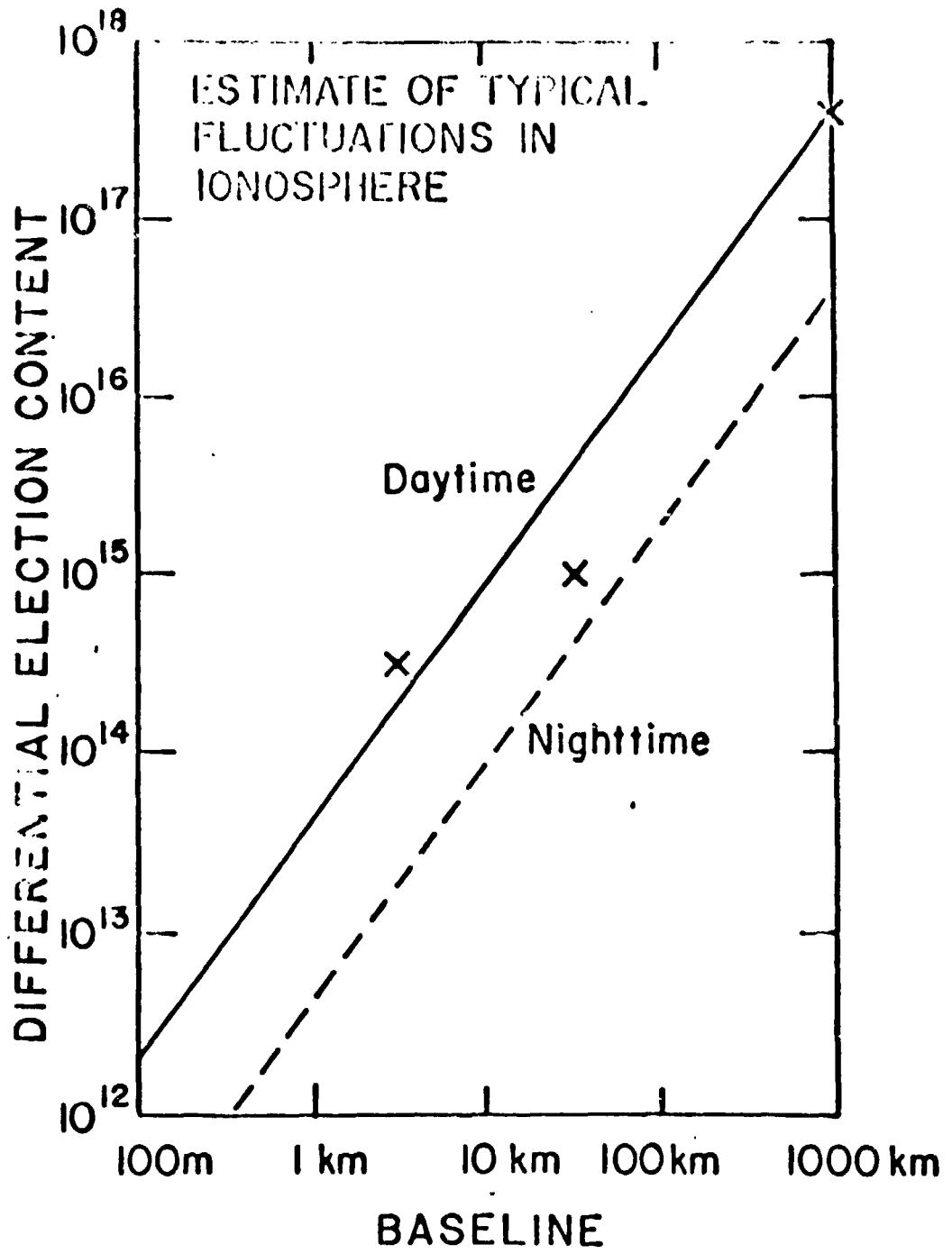
Fig. 8 Amplitude vs. size parameters of ionospheric irregularities.

QUESTIONS AND ANSWERS

LARRY D'ADDARIO, NATIONAL RADIO ASTRONOMY OBSERVATORY: This information about the variations between stations on relatively short baselines would also suggest that, for a single station, there would be a lot of variation in direction if you are looking at the sky. Thus, knowledge of the zenith total electron content would not be a good predictor of the path delay in other directions where you are usually looking. Is that right?

MR. KNOWLES: I would agree with that statement.

MR. KLOBUCHAR: If I could interject a comment here, that's certainly true, but you have to look at what detail is true. If Steve would show the 1 st view graph.... (the view graph was shown here). You will notice that the two real points that you said were actually observed, were down around ten to the fifteenth. The point way up at the top here at around a thousand kilometers above ten to the seventeenth is actually a difference in the diurnal curve between two points. The total time delay might be on the order of ten to the seventeenth, and you are seeing effects here on the order of ten to the fifteenth, one or two percent. Ten to the sixteenth is half a nanosecond at L-band, so we are talking about much less than a nanosecond, differential. If that's a problem for your time transfer, then you are in trouble, because you always get fluctuations of this order. For the VLBI folks, it is a serious problem, and Steve's work is very important in this regard, because this size of irregularity is one that really hasn't been measured before. It is very important to continue that kind of work, because there are irregularities at all levels, and no one up until this work has done anything in that distance range that I am aware of. The Dutch work and this work are the only ones.

A REVIEW OF TROPOSPHERIC REFRACTION EFFECTS ON EARTH-TO-SATELLITE SYSTEMS

Edward E. Althsuler
Electromagnetic Sciences Division
Rome Air Development Center
Hanscom AFB, MA 01731

ABSTRACT

Tropospheric refraction effects may seriously limit the performance of communication, navigation and radar systems that operate at low elevation angles. The lower atmosphere has an index of refraction which is slightly larger than unity at the earth's surface and which decreases approximately exponentially with height. As a result, radio waves travel at slower velocity than in free space and as they traverse layers of decreasing index of refraction, they are bent downward. Thus, targets observed from the ground appear to be at higher elevation angle than the true angle and if the range of the target is based on a time delay measurement, the target will appear farther away. In addition, abnormal refractivity gradients may cause radio waves to be trapped within tropospheric layers, thus producing regions through which the waves do not pass: these are called "radio holes".

For some locations and for many applications, refractive corrections based on the surface refractivity are adequate for elevation angles above a few degrees. However, new systems which operate at elevation angles near the horizon often require improved accuracies. In this paper, techniques for obtaining these improved corrections are reviewed.

This paper was not received for publication.

PRECEDING PAGE BLANK NOT FILMED

QUESTIONS AND ANSWERS

VICTOR REINHARDT, HUGHES AIRCRAFT COMPANY: Those error figures you had for the range, is that the one way range, or the two way range?

MR.ALTHSULER: One way.

MEL BUCHWALD, LOS ALAMOS NATIONAL LABORATORY: You said that ducting was very unusual except in certain locations where it's common. I think a lot of us are wondering if we live in one of those places.

MR.ALTHSULER: As I understand it, the ducting very often takes place over water. There is a region off of San Diego where they say that ducting occurs on a very regular basis. The ducting is very serious over the Persian Gulf. It is, I think, one of the hottest bodies of water on the earth, and, as you know, there have been all kinds of problems as to whether to put radars on the ground, or up in the mountains. If you put them on the ground, then you have usually serious ducting conditions. If you put them up in the mountains, you have less ducting, but you have other problems. It's a real nightmare.

It is something which is obviously very difficult to measure, but the data that are available indicate that it occurs mostly over water, and there are locations where you can expect it.

MR. REINHARDT: Is there a simple cosecant law that you can use to get the average delay for correction?

MR. ALTHSULER: Thank you for bringing that up. It turns out the distance of the slant path through the atmosphere is a function of the cosecant of the elevation angle, or the secant of the zenith angle, whichever you choose.

For angles typically around four or five degrees you know how the secant behaves. It eventually goes to infinity. But depending upon how much of an error you are willing to absorb, you can get down to eight or ten degrees without any problem. Once you get below eight or ten degrees, you are starting to compromise a little. Of course, I certainly wouldn't try it below four degrees.

ATMOSPHERIC LIMITATIONS TO CLOCK SYNCHRONIZATION AT MICROWAVE FREQUENCIES

George M. Resch
Jet Propulsion Laboratory
California Institute of Technology
Pasadena, CA. 91109, USA

ABSTRACT

Clock synchronization schemes utilizing microwave signals that pass through the earth's atmosphere are ultimately limited by our ability to correct for the variable delay imposed by the atmosphere. The atmosphere is non-dispersive at microwave frequencies and imposes a delay of roughly 8 nanosec times the cosecant of the elevation angle. This delay is composed of two parts, the delay due to water vapor molecules (i.e. the "wet" delay), and the delay due to all other atmospheric constituents (i.e. the "dry" delay). Water vapor contributes approximately 5 to 10% of the total atmospheric delay but is highly variable, not well mixed, and difficult to estimate from surface air measurements. However, the techniques of passive remote sensing using microwave radiometry can be used to estimate the line of sight delay due to water vapor with potential accuracies of 10 to 20 picosec. The devices that are used are called water vapor radiometers and simply measure the power emitted by the water vapor molecule at the 22.2 GHz spectral line. An additional power measurement is usually included at 31.4 GHz in order to compensate for the effect of liquid water (e.g. clouds). The dry atmosphere is generally in something close to hydrostatic equilibrium and its delay contribution at zenith can be estimated quite well from a simple barometric measurement. At low elevation angles one must compensate for refractive bending and possible variations in the vertical refractivity profile. With care these effects can be estimated with accuracies on the order of 30 picosec down to elevation angles of 10 degree.

I. INTRODUCTION

During the past decade we have witnessed a steady improvement in our ability to synchronize clocks on a global basis. Techniques such as Very Long Baseline Interferometry (VLBI) or any of several schemes that utilize earth orbiting satellites such as the Global Positioning System (GPS) offer the prospect of sub-nanosecond clock and frequency comparison. Atmospheric errors have not been a major contributor to the error budget in these techniques but as we approach the nanosecond (ns) level of accuracy, as our instrumentation and experimental technique improves, the atmospheric delay effects begin to take on the aspect of a limiting error source (Resch,1980). This paper is intended to quantify the magnitude of these atmospheric effects at microwave frequencies and review the extent to which they can be reduced with technology that is currently available.

II. ATMOSPHERIC DELAY

At microwave frequencies it is a good approximation to consider the atmosphere to be non-dispersive. An elemental volume of air is characterized by its index of refraction n(s), so that the total delay experienced by a signal from an extraterrestrial source (neglecting bending) is;

$$\tau_{ATM} = \int_L n(l)/c \, dl \tag{1}$$

Where c is the vacuum speed of light and the integral is evaluated along the ray path L whose line element is dl. It is convenient to define a parameter N, called the refractivity, that is a measure of the departure of the index of refraction from unity.

$$N = (n - 1)10^6 \tag{2}$$

We can now write the "extra" delay imposed by the atmosphere (i.e. over and above the geometric delay) as,

$$\Delta \tau = 10^{-6} \int_L N(l) \, dl/c \tag{3}$$

If we are trying to synchronize clocks by observing an extraterrestrial source then the entire problem of accounting for atmospheric effects reduces to estimating this simple integral.

Using the molecular properties of atmospheric constituents it is possible to derive an analytic expression for the refractivity (Bean and Dutton, 1968). A simple formulation for the refractivity has been given by Smith and Weintraub (1953) as,

$$N = 77.6(P/T + 4810e/T^2)$$

$$N = N_D + N_W \tag{4}$$

Where, T is the temperature in Kelvin (K), P the total pressure in millibar (mb), and e is the partial pressure of water vapor in mb. This expression is accurate to 0.5% over the range of temperature, pressure, and vapor content normally found in the atmosphere. Note that the refractivity can be decomposed into two components. One component we call the "wet" component because it depends primarily on the density of water vapor (i.e. a polar molecule), and the other we call the "dry" component in which we lump the effects of all atmospheric gases (including water vapor) but is dominated by the most abundant molecules of oxygen and nitrogen.

Hence, the atmospheric delay correction is simply decomposed into two separable problems. Using elementary definitions, the dry and wet atmospheric delay corrections can be written as;

$$\Delta\tau_D = \int_L \rho_D(l)dl/c \tag{5}$$

$$\Delta\tau_W = \int_L \rho_v(l)/T\,dl/c \tag{6}$$

where ρ_D is the density of dry air, ρ_v is the vapor density, and T is the temperature. Estimating the dry delay is equivalent to evaluating the integral of the dry air density along the ray path. Estimating the wet delay is equivalent to evaluating the integral that contains the vapor density divided by the temperature, again along the entire ray path.

III. ZENITH DELAY VALUES AND MAPPING FUNCTIONS

At sea level under average conditions the total atmospheric delay at the zenith is approximately 8 ns. The dry atmospheric delay at the zenith is just a bit less than 8 ns and is dominated by the gaseous form of oxygen and nitrogen. These components are well mixed throughout the atmosphere and hydrostatic equilibrium is a reasonable approximation. The wet delay is highly variable and can range from practically zero up to 1 ns at the zenith. Although the wet delay contributes less than 10% of the total atmospheric delay it dominates the variability and will take 99% of your effort should you require its accurate calibration.

The reason that the wet delay is such a problem lies in the fact that water is not a well mixed atmospheric constituent, it occurs in all three phases (solid, liquid, and gas). The mixing ratio is driven primarily by thermal processes in the lower atmosphere which means that it is difficult to estimate the wet zenith delay using only surface meteorological measurements. Nevertheless, one can model the water vapor and estimate a zenith delay. The problem with a water vapor model is the accuracy of the resulting estimate which must be judged in the context of the goals for a particular experiment. Depending on how a set of observations is constructed, it may be possible to solve for the zenith values of atmospheric delay with higher confidence th an is afforded by a model.

If you have ever tried to synchronize clocks with VLBI or by using satellites you will have noticed that the sources are never at the zenith. Zenith values of the delay correction must be mapped to the line of sight to the radio source. If we assume that the atmosphere is homogeneous and plane-layered, then the delay along an arbitrary line of sight (LOS) is simply,

$$\Delta\tau_{LOS} = \Delta\tau_z \csc E \tag{7}$$

where $\Delta\tau_z$ is the zenith delay and E is the elevation angle (azimuthal symmetry is implied in the assumption of homogenieity). This simple cosecant mapping function is generally quite adequate for elevation angles greater than 20 degrees Of course the error in the zenith delay is also multiplied by the cosecant of the elevation angle, hence the premium on obtaining an accurate value of the zenith delay. For clocks that are separated by large distances it is not practical to restrict elevation angles to greater than 20 degrees.

If equation (5) is evaluated along a zenith ray path we see that it is simply the mass of air in a vertical column and can be measured with a barometer. If the total zenith delay at sea level is roughly 8 ns then an error of 1 mb in the barometric measurement corresponds to a delay error of 8 picosecond (ps). If we assume an elevation angle cutoff of 6 degrees, the line of sight atmospheric delay is approximately 80 ns (corresponding to 10 airmasses) and a 2 mb barometric measurement accuracy would map to 160 ps of line of sight delay error. Thus, with reasonable care of our barometer we can neglect measurement errors.

Much larger line of sight delay errors arise from three effects; 1) both the atmosphere and the ray path is curved, 2) errors in estimating the zenith vapor delay, and 3) the real atmosphere is not homogeneous.

If we use the simple mapping function we will make a 6 or 7 ns error at a 6 degree elevation because we did not account for earth curvature or ray bending. Variations in the real atmosphere and mis-modeling water vapor will account for another 1 or 2 ns error independent of the mapping function. Using a function only slightly more complicated than the cosecant we can take into account earth curvature and ray bending and reduce that portion of the error to less than 1 ns. There are long-term variations in the atmosphere (seasonal effects) that can be modeled, included with the mapping function and can remove perhaps 0.5 ns from the variable portion of the atmosphere. Finally, we are left with roughly 1 ns of variations that cannot be modeled but can be estimated using remote sensing to the 0.1 ns level down to 10 degree elevation.

There are at least a half-dozen mapping functions from various authors that account for atmospheric and ray path curvature at low elevation angles. In general they are semi-empirical formulas. In order to derive an improved mapping function one typically starts with some average profile of the refractivity, assumes horizontal homogeniety, performs ray-trace calculations at various elevation angles, and then notes that the delay as a function of elevation angle can be approximated by an analytic function containing a few parameters. Figure 1 compares some of the most popular mapping functions with actual ray trace calculations down to an elevation angle of 6 degrees. Shown are mapping functions from Lanyi (1984), Black (1978), Black and Eisner (1984), Chao (1974), Marini and Murray (1973), and Saastamoinen (1972).

The ray trace calculations that are used in Figure 1 as the "truth" are in fact based on the assumption of homogenieity. Bending of the ray path will depend upon the vertical density profile. Water vapor variations dominate the variations in the density profile and will exhibit variations on several timescales and may even exhibit horizontal gradients that are driven either by local topography or mesoscale weather patterns. If vertical soundings of temperature and relative humidity are available for a particular observing site then it is possible to identify the low frequency fluctuating components (e.g. seasonal variations) and incorporate them into the mapping function.

All of these mapping functions shown in Figure 1 offer significant improvement over the simple cosecant mapping. The most recent, by Gabor Lanyi at JPL has the distinct advantage of agreeing with ray trace calculations to better than 10 ps down to elevation angles of 6 degree. Lanyi's mapping function together with improved estimates of seasonal variability is now being tested on 7 years of VLBI data taken between the stations of the Deep Space Network. Preliminary indications are that this new mapping function exhibits one of the sought after qualities of accurate atmospheric delay correction - it improves the repeatability between experiments.

As mentioned earlier, the wet delay can also be modeled. Modeling is of course the least expensive method to account for atmospheric effects so there is a great deal of fiscal motivation to use them whenever possible and there is a plethora of models that can be used with varying degrees of statistical success to estimate the wet atmospheric delay. Berman (1976) has discussed several of these models. In general, one starts with the assumption that the vertical profile of vapor density is described by an analytic function, measure the surface value of vapor density, and use the model to estimate the zenith delay. The typical accuracy that is achievable is on the order of 100 ps at the zenith which translates to a 1 ns error at an elevation angle of 6 degree.

It is sometimes possible to structure an experiment so that it is possible to solve for the zenith delay. In this case, if one uses a good mapping function it is only the departures from homogenieity and temporal variations of the atmosphere that are error sources. If it is not possible to solve for the zenith delay and high accuracy is a requirement then one must directly estimate the line of sight vapor content. The technique that can be used falls in the category of passive remote sensing and is based on the fact that the water vapor molecule radiates weakly at the microwave frequency of 22.2 GHz. If the molecule is locked in the solid or liquid state the transition is inhibited so the spectral line is a direct indicator of water vapor. The technique has been reviewed by Hogg *et al.* (1983) and by Resch (1984) and will only be outlined here.

Figure 2 shows what an ideal radiometer would measure if it observed the zenith through a standard atmosphere between the frequencies of 10 to 300 GHz. The intensity or power level of the received radiation is shown along the vertical scale and is given in units of Kelvin which is a measure of the brightness temperature - the temperature that a black body would have if the black body were to replace the atmosphere and to deliver an equivalent amount of power to the radiometer. The lower curve shows the spectrum when there is no water vapor in the atmosphere and the upper curve is drawn for the case of a precipitable vapor of 2 gm/cm^2. You see several spectral feature between 10 and 300 GHz, one of which is the 22.2 GHz line from water vapor that was just mentioned. Under the assumption of low total absorption (i.e. less than 3 db) the strength of the line is proportional to the total amount of water vapor along the line of sight. In equation (6) we saw that the wet path delay can be cast into a form that very much resembles the integral of the vapor density along the line of sight. This means that we can use a radiometer operating at a frequency near 22.2 GHz to measure the intensity of radiation and develop an algorithm to then use the measurement in order to estimate the wet path delay. Unfortunately, nature does not let us off quite that easily.

Figure 3 shows the effects on the brightness temperature of liquid water assumed to exist as very small droplets similar to what exists in a cloud. This shows the brightness spectrum of the atmosphere for three cases: 1) no vapor and no liquid, 2) 2 gm/cm^2 of vapor and no liquid, and 3) 2 gm/cm^2 of vapor and 0.1 gm/cm^2 of precipitable liquid. This amount of liquid water has negligible effect on the delay but you can see that it has a very large effect on the measurement of the brightness temperature. We can either be content with a single channel radiometer that will operate only under clear sky conditions or we can add a second radiometer operating at a frequency off the water vapor line and use the second measurement along with the first to simultaneously estimate both the water vapor and liquid in the atmosphere. One can look at the second channel as the price you must pay in order to operate in both clear and cloudy conditions.

Instruments that are capable of estimating the line of sight delay have been described by Giraud et al. (1979) and by Resch et al. (1982). The absolute accuracy of the technique over the dynamic range that is experienced in the real atmosphere is addressed in Figure 4 (Resch, 1984) by comparing the amount of atmospheric water determined by two independent techniques. Along the vertical axis is plotted the wet delay that was inferred from an instrumented aircraft measurement. The aircraft carried a package of instruments that measured temperature, pressure, and relative humidity and flew predetermined flight paths that approximated various lines-of-sight through the atmosphere. The measurements were recorded and later converted to vapor density and integrated to obtain wet delay. The horizontal axis shows the vapor delay as determined by a water vapor radiometer (WVR) operated during the aircraft flight pointing along the flight path. The rms scatter of roughly 50 ps is the quadratic sum of the errors in both measurement techniques. If we rather generously assume that the errors in the aircraft measurement were on the order of 10% of the total delay then we can infer that the accuracy of the WVR is about 30 ps in the delay domain. Simulation calculations suggests that the theoretical limit of performance for the WVR is approximately 10 ps.

Figure 5, taken from Resch et al. illustrates the precision of two WVRs operating along with an interferometer in the Very Large Array located in New Mexico. The experiment was unusual in two respects. First, the baseline is only 7 km long and we would normally expect the atmosphere to be well correlated over that kind of separation however the data was taken during the summer when there was thunderstorm activity in the area and the atmosphere was very dynamic. Secondly, this is not a VLBI experiment, we were comparing the WVRs with a connected element interferometer whose phase stability is on the order of a few ps over a several hour period. The dotted line shows the interferometer phase in delay units as a function of time and the solid line shows the resulting phase after corrections were applied from the two WVRs. The rms of the corrected phase is approximately 20 ps and corresponds to the expected noise level of the WVRs in this observing mode. Although this is an unusual event on a 7 km we can speculate that it my not be quite so unusual in the uncorrelated atmospheres that one would find using 1000 or 10,000 km baselines. The data indicates that large delay changes are possible in relatively short time periods, and the delay changes are indeed dominated by water vapor. Used properly the WVR is capable of tracking the vapor delay changes with a precision of a few ps.

IV. SUMMARY

Using a simple barometer to measure the surface pressure, a thermometer, something to measure surface water vapor density, and a model, we can estimate the zenith delay and then use any of a half-dozen mapping functions to estimate the delay along the line of sight. If we use a model for the atmosphere that can remove a portion of the dynamics we can achieve a 1 ns delay accuracy at elevation angles of 6 degree. If the experiment is structured properly it is possible to solve for the zenith delay and reduce the atmospheric delay error to less than 1 ns.

If we wish to improve on this capability we must estimate the line of sight vapor delay. An instrument to make accurate measurements of atmospheric brightness temperature at two frequencies near the 22.2 GHz spectral line is called a water vapor radiometer and will cost about $150K. Someone will have to maintain and operate it, and someone will have to analyze the data it produces. For the effort one can anticipate roughly an order of magnitude improvement over models.
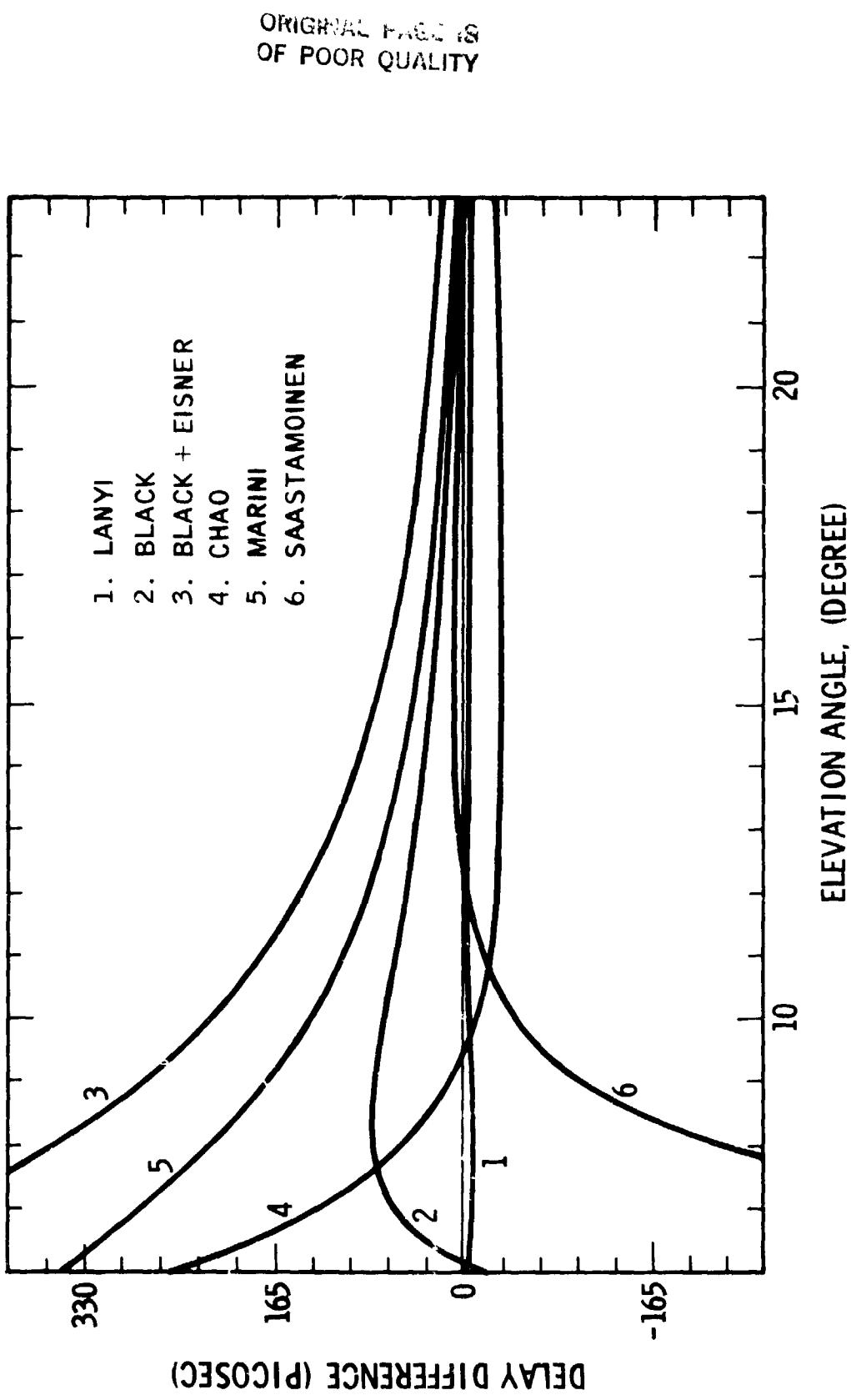
Figure 1 -Difference between the mapping functions and ray tracing
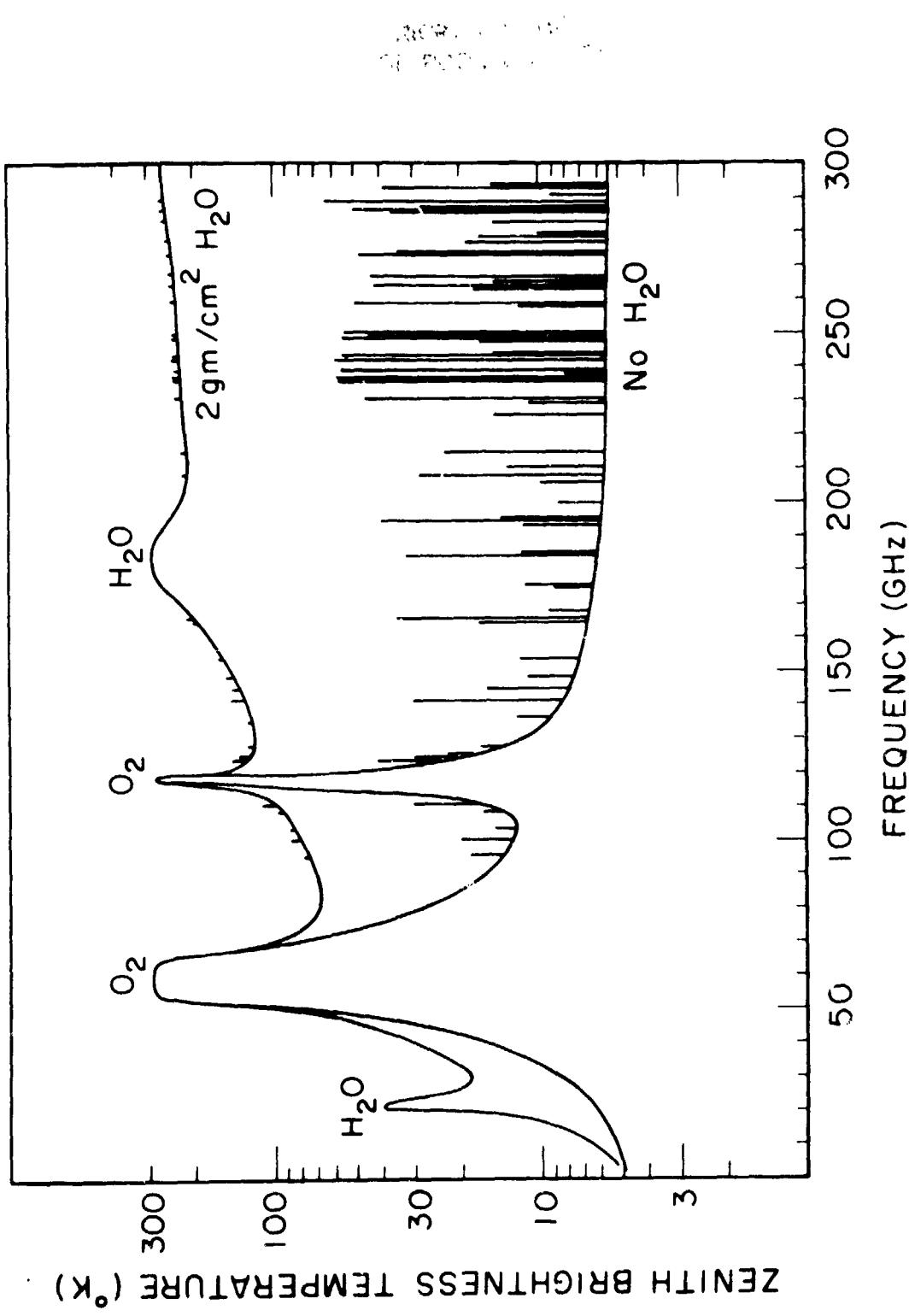
Figure 2 -Brightness Spectrum of the atmosphere
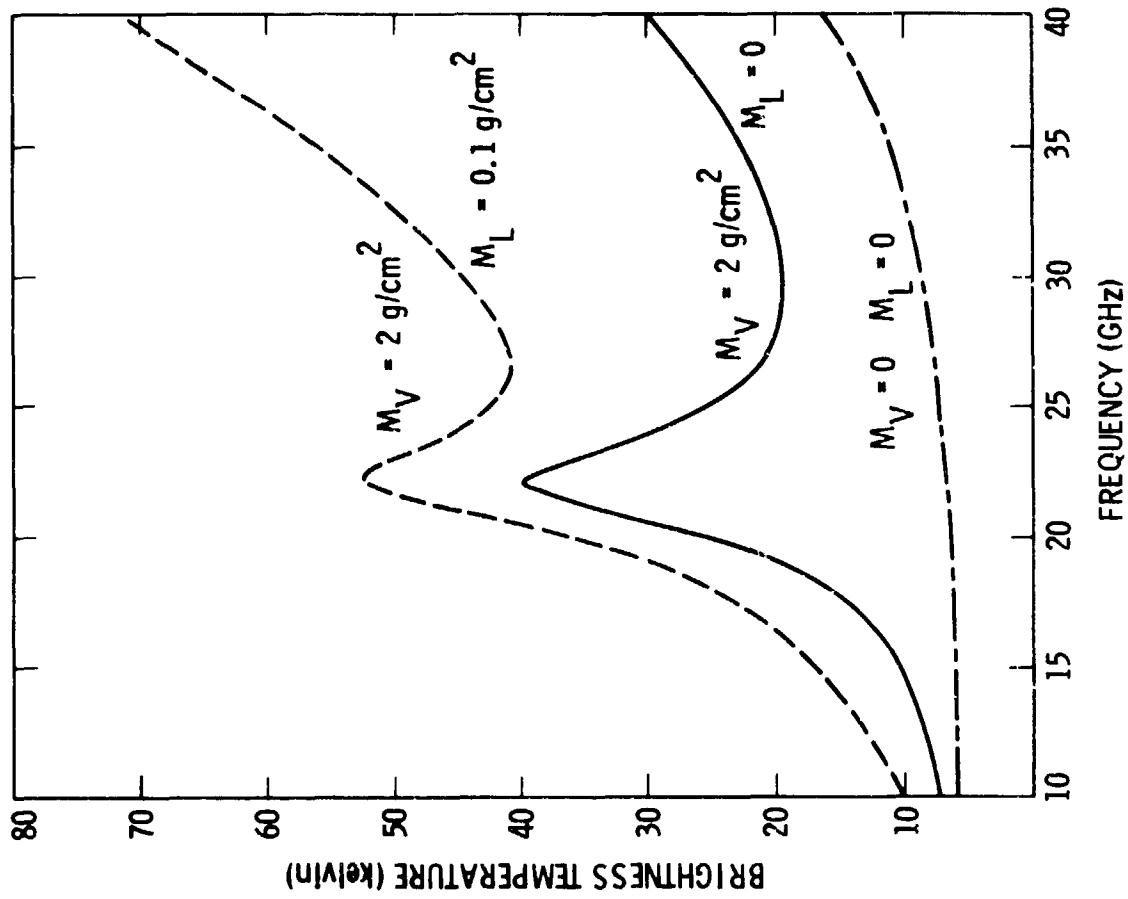
Figure 8 - Effect of liquid water on the brightness temperature
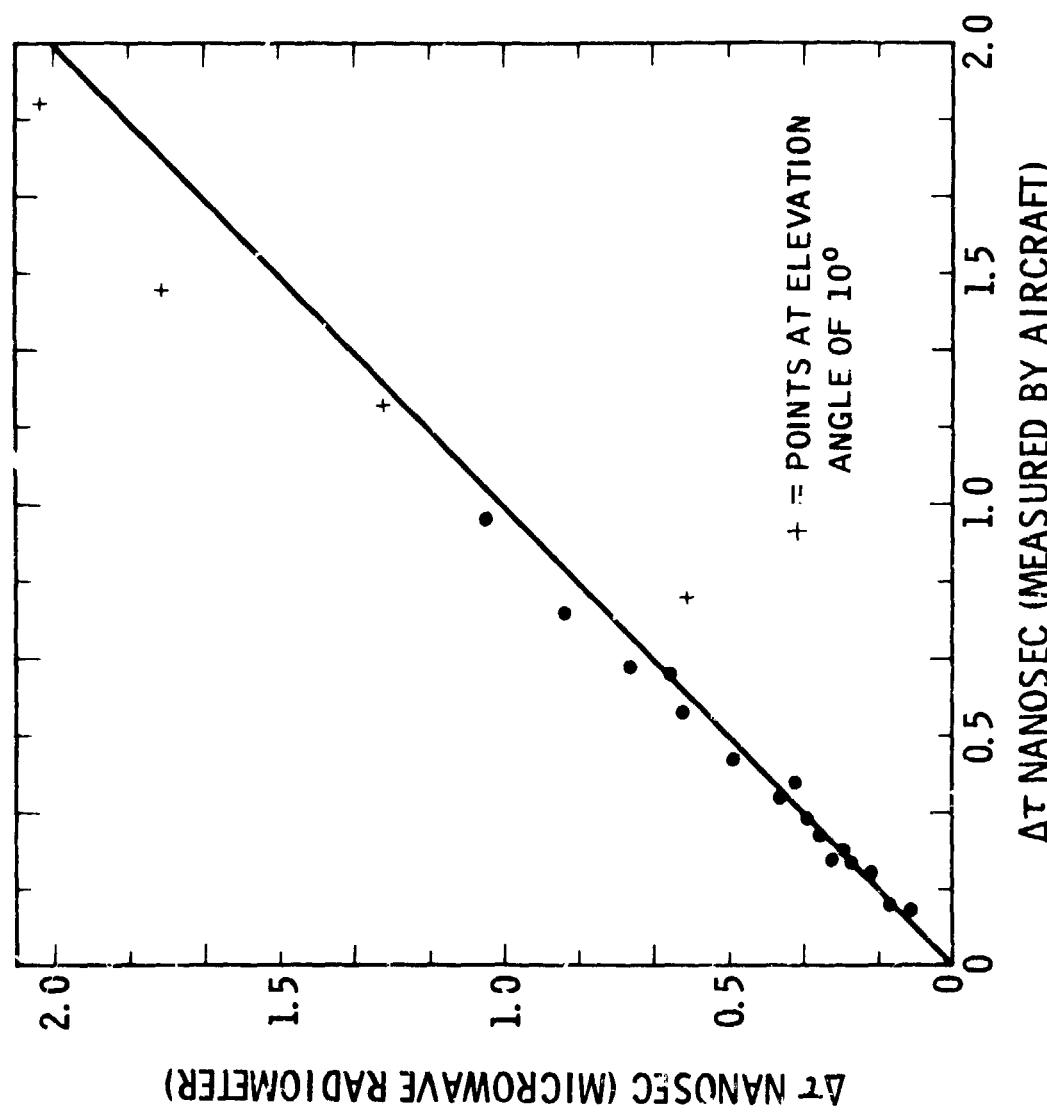
Figure 4 -Accuracy of a water vapor radiometer

+ = POINTS AT ELEVATION ANGLE OF 10°

$\Delta\tau$ NANOSEC (MEASURED BY AIRCRAFT)

$\Delta\tau$ NANOSEC (MICROWAVE RADIOMETER)
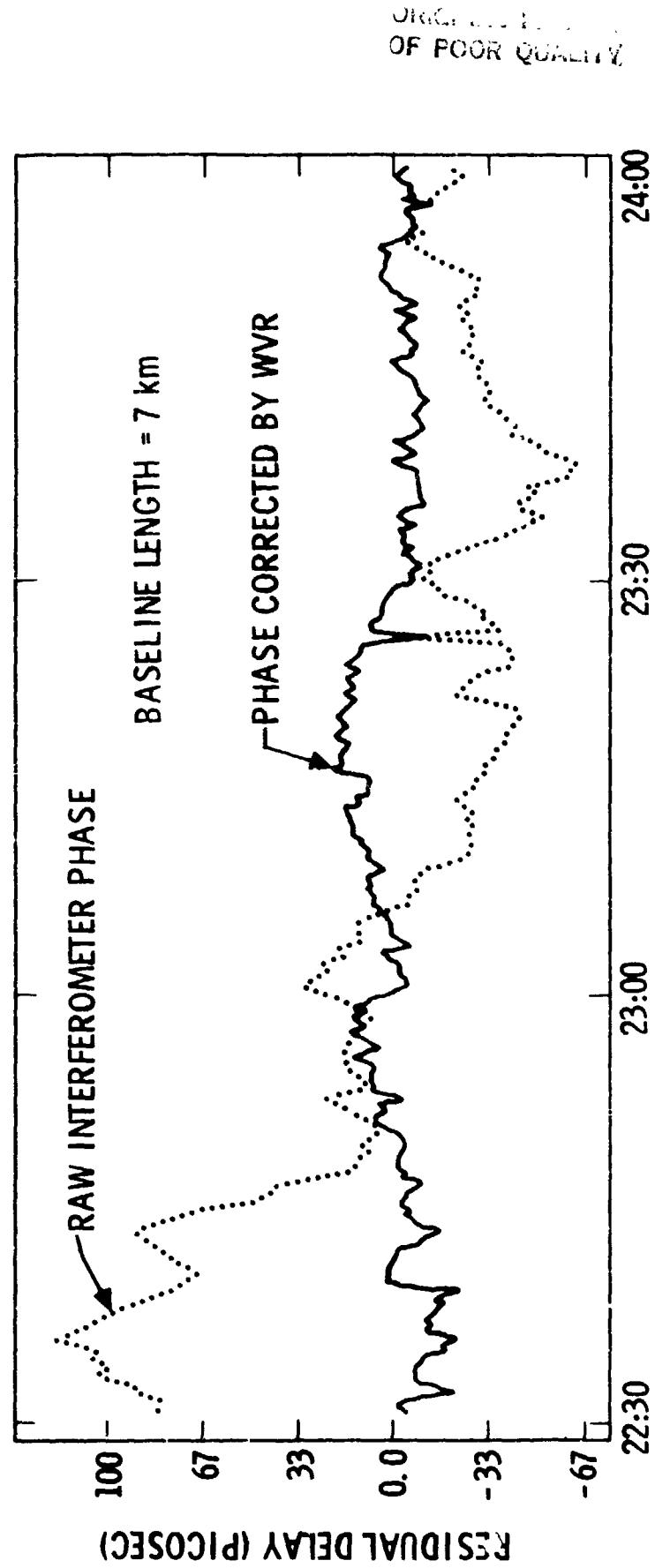
Figure 5 - VLA residual delay before and after correction by WVRs

QUESTIONS AND ANSWERS

NICHOLAS YANNONI: This particular question might be answered best by you, Jack, or perhaps by the speaker. I would like to have a quick comparative statement of the domains of correction that has been addressed by the speakers. These altitude domains, or lines of demarcation where tropospheric effects dominate ionospheric effects. I know that these exist, and would like to have a ballpark statement about them.

MR. KLOBUCHAR: Let me say a few words about the ionosphere. I think that the GPS L-1 frequency is probably a reasonable demarcation line. There are times when the total zenith time delay, due to the ionosphere, might be of the order of a few nanoseconds, say five to ten nanoseconds.

Let me ask, either George or Ed, the zenith time delay due to the atmosphere would be how much?

VOICE FROM AUDIENCE: Nine total.

MR. KLOBUCHAR: About the same. However, they can model theirs. The variability of the troposphere is what, a few percent?

VOICE FROM THE AUDIENCE: Ten percent.

MR. KLOBUCHAR: Is ten percent the highest?

VOICE: That's maximum.

MR. KLOBUCHAR: Whereas the variability of the ionosphere, during the nighttime, when the total delay is five to ten nanoseconds, is very high. It may be 40 or 50 percent. It depends on the region of the world you are in.

That is still about where they become equal. There are times when the ionosphere is several or many tens of nanoseconds at L-1, for instance, and the troposphere never gets to many tens of nanoseconds, does it? I think that you had something like 100 nanoseconds, didn't you, or 100 feet of error?

MR. ALTHSULER: The largest error, right on the horizon, is like 100 meters, but when you get up to four or five degrees, it's more like 100 feet. You are talking about a maximum of 100 nanoseconds, at four or five degrees.

MR. RESCH: It's also strongly frequency dependent. With GPS you have two frequencies, so you have a handle on calibrating the ionosphere to some level, perhaps as good as a few centimeters of equivalent path delay. With the atmosphere, you are left with a model, or a water vapor radiometer as an independent way of coping with the error.

MR. KLOBUCHAR: I guess that the answer is that GPS L-1 is a good ballpark to start arguing. If you get down to a couple of hundred megahertz, the Transit frequencies, then the ionospheric errors probably predominate.

When we get to a few gigahertz, the ionosphere is not so important, although the VLBI people use S and X band to get rid of the ionosphere because it's a relatively easy thing to do. I can't see $150,000 for a dual frequency ionospheric scheme. Certainly around ten gigahertz you start not worrying about the ionosphere, but it's all relative, because a few years ago if you guys could transfer time within a microsecond, everybody was happy. Now you are talking about nanoseconds, and in a few years we will be talking about picoseconds. come back and see us then. The ionosphere won't go away, and I don't think the water vapor and the dry component of the atmosphere will go away either.

MR. KNOWLES: I have just a minor quibble. I think your estimate of 150K for that water vapor radiometer is a bit high. That would certainly decrease when they were made on a production line.

MR. RESCH: I am not so sure about that, at least the quantities. There is at least one company that is making these devices as a commercial product, and in a conversation with one of their representatives a few weeks ago, that was the price that was quoted to me.

MR. PONSONBY, JODRELL BANK, ENGLAND: I would like to ask whether the delays that have been discussed are reciprocal delays? Can we assume that the io⌐ ᵇheric delay in particular is the same for the down path as it ᶠor the up path?

MR. KLOBUCHAR: Yes, period, and also for Faraday rotation. It's very interesting that back when people first started measuring it, some people thought that you would get rotation in one direction for the up-going signal and rotation in the other direction for the down-going signal and thus get cancellation of the rotation. You folks at Jodrell Bank did some of the earl work in that and know that you get twice the amount. The paths are essentially identical, at least for the frequencies that we are talking about.

KALMAN FILTER MODELING

R. Grover Brown
Electrical and Computer Engineering Department
Iowa State University
Ames, Iowa   50010

ABSTRACT

The main emphasis of this tutorial paper is on the formulation of
appropriate   state-space   models   for   Kalman   filtering
applications.   The so-called "model" is completely specified by
four   matrix   parameters   and   the   initial   conditions   of   the
recursive equations.   Once these are determined, the die is cast,
and the way in which the measurements are weighted is determined
foreverafter.   Thus, finding a model that fits the physical
situation at hand is all important.   Also, it is often the most
difficult aspect of designing a Kalman filter.   Formulation of
discrete state models from the spectral density and ARMA random
process descriptions is discussed.   Finally, it is pointed out
that many common processes encountered in applied work (such as
band-limited white noise) simply do not lend themselves very well
to Kalman filter modeling.

INTRODUCTION

Kalman filtering is now well known, and tutorial discussions of the tech-
nique are given in a number of standard references [1,2,3].   The filter
recursive equations are summarized in Figure 1 for ref erence purposes here.
It should be noted that once the initial conditions and the ϕ_k, H_k, R_k, Q_k,
parameters are specified, the die is cast and the way in which the
measurement sequence is processed is completely determined.   Thus, the
specification of these parameters is especially important -- they are, in
effect, the filter "model".   The emphasis in this tutorial paper will be on
the modeling aspect of Kalman filtering.   To see where these parameters come
from, we will now review the basic process and measurement equations.
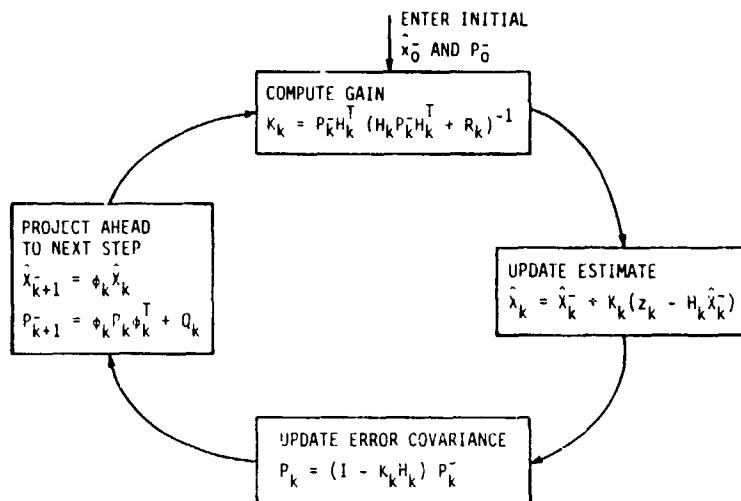
Figure 1 Kalman filter loop

THE DISCRETE PROCESS AND MEASUREMENT EQUATIONS

The starting point for discrete Kalman filter theory begins with the process and measurement equations. The random process under consideration is assumed to satisfy the following recursive equation

$$x_{k+1} = \phi_k x_k + w_k \tag{1}$$

where k refers to the k-th step in time, x_k is a vector random process, ϕ_k is the transition matrix, and w_k is a Gaussian white sequence with a covariance structure given by

$$E[x_k x_k^T] = Q_k \tag{2}$$

The measurement relationship is assumed to be of the form

$$z_k = H_k x_k + v_k \tag{3}$$

where v_k is also a Gaussian white sequence, uncorrelated with w_k, and described by the covariance

$$E[v_k v_k^T] = R_k \tag{4}$$

In words, then, the key parameters of a Kalman filter model can be described as follows:

(1) ϕ_k is the transition matrix that describes the natural dynamics of the process in going from step k to k+1.

(2) H_k is the linear connection matrix that gives the ideal (noiseless) relationship between the measurement z_k and the process to be estimated x_k.

(3) Q_k describes the additional noise that comes into the x_k process in the Δt interval between step k and k+1.

(4) R_k describes additive measurement noise.

It is important to note that the discrete model described by Eqs. (1) through (4) stands in its own right. It is not an approximation of some continuous system, nor does it have to be related to another continuous linear dynamical system in any way. Once the discrete model is assumed, the recursive estimation process given in Fig. 1 follows directly.

IMPORTANCE OF THE GAUSSIAN ASSUMPTION

We will digress for a moment and look at the Gaussian assumption used in Eqs. (1) through (4). If w_k and v_k are Gaussian white sequences, then x_k and z_k will be Gaussian processes. Even though the Gaussian assumption is often omitted in discussions of least-squares filtering, we make here with no apology. The reason for this is that minimizing the mean square error really does not make very good sense for non-Gaussian processes. To illustrate this, consider the two processes shown in Fig. 2. The first is a scalar Gauss-Markov process which has the general appearance of typical noise. The second process is the random telegraph wave which switches between +1 and -1 at random points in time. If the parameters of the two processes are adjusted appropriately, they can be made to have identical power spectral density functions. Yet, they are radically different processes! The least-squares prediction far out into the future is zero for both cases. This makes good sense in the Gauss-Markov case because zero is the mean and most likely value. On the other hand, it is ridiculous to predict zero in the random telegraph wave case. We know a priori that this waveform is never zero. We would be better off to predict either +1 or -1 and be correct half the time than to predict zero and be wrong all the time! Thus, the Gaussian assumption is a reasonable one in the least squares estimation theory, and to stray from it leads us into dangerous territory.
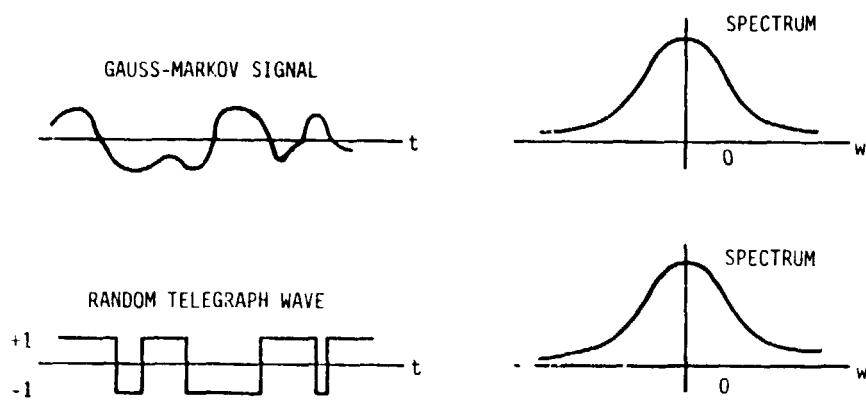
Figure 2 Gauss-Markov and random telegraph waves

TRANSITION FROM A SPECTRAL DESCRIPTION TO A DISCRETE STATE MODEL

In Kalman filter applications, we frequently begin with a spectral description of the various random processes involved. The problem then is to convert this information to a model of the form specified by Eqs. (1) through (4). The general procedure for making the transition to the discrete model is as follows

(1) Look for a continuous dynamical system that yields the desired process when driven by white noise. (The white noise input assures that w_k will be a white sequence.)

(2) Then write the dynamical equations in state-space form:

$$\dot{x} = Ax + Bu \qquad (5)$$

(3) Solve the state equations for step size Δt and obtain

$$x_{k+1} = \phi_k x_k + w_k \qquad (6)$$

(4) Determine the measurement equation from the particular situation at hand.

To illustrate the procedure further, suppose the y process power spectral density function $S_y(s)$ can be written as a ratio of polynomials in s^2 (or ω^2, where $\omega^2 = -s^2$). The spectral function can then always be factored into two symmetric parts, one with its poles and zeros in the left-half s plane, the other with mirror-image poles and zeros in the right-half plane. This is called spectral factorization and is represented mathematically as

264

$$S_y(s) = S_y^+(s) \cdot S_y^-(s) \tag{7}$$

where S_y^+ and S_y^- are the left- and right-half plane parts respectively. $S_y^+(s)$ then becomes the shaping filter that will shape unity white noise into a process $y(t)$ with a spectral function $S_y(s)$. (See Ref. [1] for further details.)

Now suppose that the shaping filter is of the form shown in Fig. 3. We seek a state-space model for that dynamical system. One way of achieving this is

$$w(t) \longrightarrow \boxed{\dfrac{b_m s^m + b_{m-1}s^{m-1} + \cdots b_o}{s^n + a_{n-1}s^{n-1} + \cdots a_o}} \longrightarrow y(t)$$

(Unity White Noise)
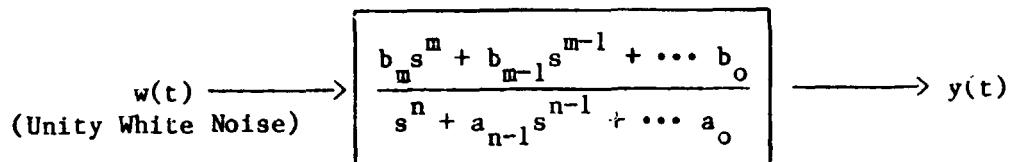
Figure 3   Shaping filter

shown in block diagram form in Fig. 4. The state-space equations are then

Define state variables as
$r, \dot{r}, \ddot{r}, \cdots$ where r is an
intermediate variable.
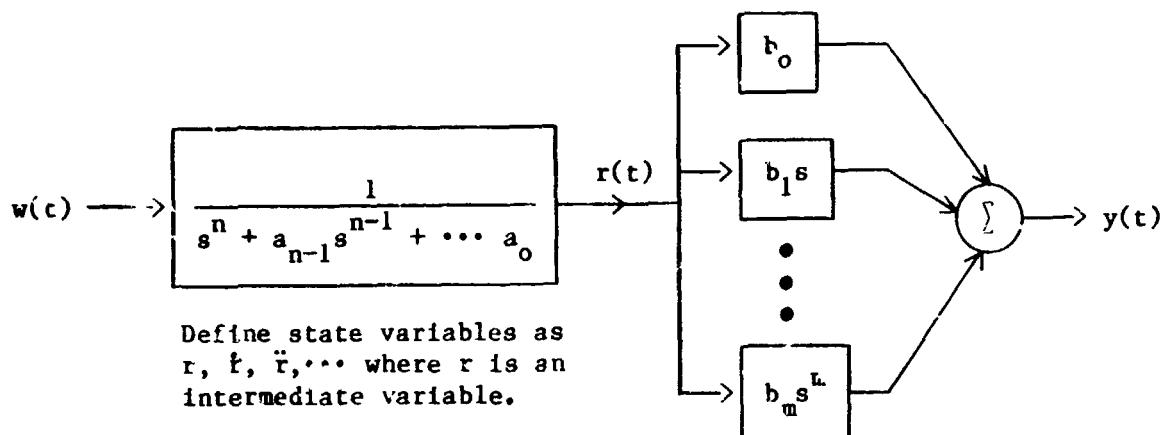
Figure 4   Shaping filter redrawn

$$
\begin{bmatrix} \dot{x}_1 \\ \dot{x}_2 \\ \cdot \\ \cdot \\ \cdot \\ \dot{x}_n \end{bmatrix}
=
\begin{bmatrix}
0 & 1 & 0 & 0 & \cdot & \cdot & \cdot \\
0 & 0 & 1 & 0 & \cdot & \cdot & \cdot \\
0 & 0 & 0 & 1 & \cdot & \cdot & \cdot \\
& & & \cdot & & & \\
& & & \cdot & & & \\
-a_o & -a_1 & \cdot & \cdot & \cdot & & -a_{n-1}
\end{bmatrix}
\begin{bmatrix} x_1 \\ x_2 \\ \cdot \\ \cdot \\ \cdot \\ x_n \end{bmatrix}
+
\begin{bmatrix} 0 \\ 0 \\ \cdot \\ \cdot \\ \cdot \\ 1 \end{bmatrix} w(t) \tag{8}
$$

$$y = [b_0 \quad b_1 \quad \cdots \quad b_{n-1}] \begin{bmatrix} x_1 \\ x_2 \\ \cdot \\ \cdot \\ \cdot \\ x_n \end{bmatrix} \qquad (9)$$

Control system engineers refer to this as the controllable canonical form, and it can always be achieved for the dynamical system as shown in Fig. 3. If y is the process that is actually measured, then the H matrix is just the row matrix of b's given in Eq. (9).

EXAMPLE

Suppose we have a scalar Gauss-Markov process $y(t)$ whose power spectral density function is

$$S_y(s) = \frac{2\sigma^2\beta}{? + \beta^2} \quad \left(\text{or} \quad \frac{2\sigma^2\beta}{\omega^2 + \beta^2} \right) \qquad (10)$$

We first factor S_y as follows:

$$S_y(s) = \frac{\sqrt{2\sigma^2\beta}}{s + \beta} \cdot \frac{\sqrt{2\sigma^2\beta}}{-s + \beta} \qquad (11)$$

The shaping filter is then $\sqrt{2\sigma^2\beta}/(s+\beta)$ which corresponds to the dynamical equation

$$\dot{y} + \beta y = \sqrt{2\sigma^2\beta} \, w(t) \qquad (12)$$

This is a simple first order differential equation, so we only have one state variable. Call it x_1. Our state equation is then

$$\dot{x}_1 = -\beta x_1 + \sqrt{2\sigma^2\beta} \, w(t) \qquad (13)$$

The solution of this equation for a step size Δt is

$$x_{k+1} = e^{-\beta\Delta t} x_k + w_k \qquad (14)$$

and $e^{-\beta\Delta t}$ can be seen to be the transition matrix ϕ_k. The mean square value of w_k can be determined from random process theory [1], and it works out to be

$$Q_k = E[w_k^2] = \sigma^2(1-e^{-2\beta\Delta t}) \qquad (15)$$

The process model is now complete.

UNIQUENESS

We might pose a question at this point:

Are Kalman filter models unique?

The answer is an _emphatic_ NO. We know from linear system theory that any nonsingular linear transformation on the state vector leads to another equally legitimate state vector. The choice of coordinate frame for performing the estimation process is purely a matter of convenience. Optimal estimates can be transformed freely from one coordinate frame to another (through a _linear_ transformation) and still remain optimal estimates in the new frame of reference.

ARMA MODEL

Sometimes the random process model comes to us in the form of a difference equation rather than a continuous differential equation. For example, consider the auto-regressive moving average (ARMA) model that relates a discrete process $y(k)$ to an input white sequence $u(k)$.

$$y(k+n) + \alpha_1 y(k+n-1) + \cdots \alpha_n y(k) = \beta_1 u(k+n-1) + \cdots \beta_n u(k) \qquad (16)$$

There is a close analogy between difference and differential equations, and it works out that this nth-order difference equation can be converted to vector form in much the same manner as for a differential equation. If we define an intermediate variable $y'(k)$ as the solution to Eq. (16) with just $u(k)$ as the driving function, and then define our state variables as

$$x_1(k) = y'(k), \quad x_2(k) = y'(k+1), \quad \text{etc.} \qquad (17)$$

then the system of Eq. (16) translates into state-space form as

$$\begin{bmatrix} x_1(k+1) \\ x_2(k+1) \\ \cdot \\ \cdot \\ \cdot \\ x_n(k+1) \end{bmatrix} = \begin{bmatrix} 0 & 1 & 0 & 0 & \cdot & \cdot & \cdot \\ 0 & 0 & 1 & 0 & \cdot & \cdot & \cdot \\ & & \cdot & & & & \\ & & \cdot & & & & \\ & & \cdot & & & & \\ -\alpha_n & -\alpha_{n-1} & \cdot & \cdot & \cdot & & -\alpha_1 \end{bmatrix} \begin{bmatrix} x_1(k) \\ x_2(k) \\ \cdot \\ \cdot \\ \cdot \\ x_n(k) \end{bmatrix} + \begin{bmatrix} 0 \\ 0 \\ \cdot \\ \cdot \\ \cdot \\ 1 \end{bmatrix} u(k) \tag{18}$$

$$y(k) = [\beta_n \;\; \beta_{n-1} \;\; \cdots \;\; \beta_1] \begin{bmatrix} x_1(k) \\ x_2(k) \\ \cdot \\ \cdot \\ \cdot \\ x_n(k) \end{bmatrix} \tag{19}$$

Note that our choice of state variables leads to the controllable canonical form, just as in the continuous dynamical case. Of course, we could have defined our state variables differently and arrived at a form different from Eqs. (18) and (19). We will not pursue this further other than to say the choice of state variables is (within limits) a matter of convenience for the situation at hand.

PROCESSES DERIVED FROM IRRATIONAL SHAPING FILTERS

The random process modeling procedures discussed thus far have been straightforward. They may be tedious for higher-order processes, but they do not call for much imagination. There exists, however, a whole class of processes where this is not the case. These are the processes that cannot be thought of as the result of passing vector white noise through a linear dynamical system of finite order. Such processes are commonplace in engineering literature. For example, bandlimited Gaussian white noise is a very useful abstraction in communication theory. It is Gaussian noise that has a flat spectrum in the baseband and then is zero out beyond the cutoff frequency. It can be thought of as the result of passing pure white noise through an idealized lowpass filter, but no such filter can be represented as a ratio of polynomials in s of finite order. (Note that a Butterworth filter can be made to approximate the ideal case, but not equal it.) The

idealizations of bandlimited white noise are often a convenience in communication theory; however, they are an obstruction in Kalman filter theory.

There is a theorem from linear systems theory that is useful at this point. Chen [4] gives us the following criterion for the realization of linear dynamical models.

A linear dynamical model of the form

$$\dot{x} = Ax + Bu$$
$$y = Cx + Du \tag{20}$$

will exist for a system with an input-output impulsive response $G(t,\tau)$, if and only if, $G(t,\tau)$ is factorable in the form

$$G(t,\tau) = M(t)N(\tau) \tag{21}$$

M and N are finite-order matrices, so if $G(t,\tau)$ is scalar (i.e., single-input, single-output), $M(t)$ is a row vector and $N(t)$ is a column vector. This theorem can then be used as a test to see if a dynamical system will exist for a corresponding impulsive response function. Furthermore, the factorization provides the necessary information for realization of the model. (See Chen [4] for further details.) We will use flicker noise to illustrate the use of Chen's theorem. Flicker noise is of special interest to the PTTI community because of its presence in precision frequency standards. It is characterized by a power spectral density function of the form of $1/f$ at the frequency level, or $1/f^3$ when referred to the phase level [5,6]. A block diagram showing the relationship between flicker noise and white noise is given in Fig. 5.

White
Noise ─────────⟶ | $\dfrac{1}{s^{1/2}}$ | ─────────⟶ | $\dfrac{1}{s}$ | ─────⟶ phase (time)
w(t)   Frequency
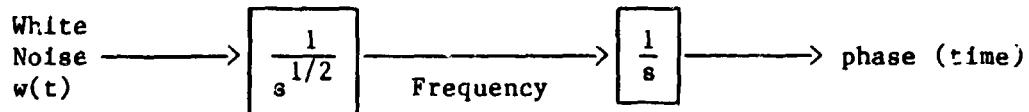
Figure 5   Block diagrams relating flicker noise to white noise

Clearly, the transfer function relating input white noise to the output phase $x(t)$ is $1/s^{3/2}$. The inverse transform of $1/s^{3/2}$ gives the impulsive response to an impulse applied at $t=0$. This is $2\sqrt{t}/\sqrt{\pi}$. Thus, for an impulse applied at $t=\tau$, we have (in Chen's notation)

$$G(t,\tau) = \frac{2}{\sqrt{\pi}} \sqrt{t-\tau} \ , \quad t > \tau \tag{22}$$

The question is, "Is $G(t,\tau)$ factorable in the form $M(t)N(\tau)$?" It appears that it is not, although this is difficult to show in a rigorous sense. This being the case, Chen's theorem says that no linear dynamical system will exist that corresponds to the $G(t,\tau)$ of Eq. (22). This is to say that no finite-order state model will exactly represent flicker noise! Of course, the state model is essential for Kalman filtering, so this leads to a dilema when one attempts to include flicker noise in a Kalman filter clock model. This is the subject of a companion paper in these Proceedings [6], so we will not pursue this further here.

SUMMARY

Various aspects of Kalman filtering modeling have been discussed briefly in this paper. Perhaps the most important thing to remember is that the random processes under consideration must be modeled in vector state-space form. This can often be done with exact methods. If the exact methods discussed here cannot be used, as in the case of flicker noise, then one must seek approximate finite-order vector models in order to form a workable Kalman filter. The measurement model usually does not cause difficulty, because it simply depends on what state variables are being observed.

REFERENCES

[1] R. Grover Brown, Introduction to Random Signal Analysis and Kalman Filtering, John Wiley, Inc., 1983.

[2] P. S. Maybeck, Stochastic Models, Estimation and Control, (Vol. 1), Academic Press, 1979.

[3] A. Gelb (Ed.), Applied Optimal Estimation, MIT Press, 1974.

[4] C. T. Chen, Introduction to Linear System Theory, Holt, Rinehart and Winston, 1970.

[5] J. A. Barnes and D. W. Allan, "A Statistical Model of Flicker Noise", Proc. of the IEEE, Vol. 54, No. 2, February 1966.

[6] A. J. Van Dierendanck, J. B. McGraw and R. Grover Brown, "Relationship Between Allan Variances and Kalman Filter Parameters", Proceedings of this Conference (1984).

VICTOR REINHARDT, HUGHES AIRCRAFT COMPANY: I think you are right about that not being able to be factored, and I think that I have a reason for that. You can show that flicker noise can be mathematically generated by the sum of an infinite number of gaussian processes where the beta term goes from zero to infinity. Therefore, there are infinite time constants in the process. So, you can't give a state vector at any one time, because the beta term goes from zero to infinity.

MR. BROWN: I agree with what you say. I think that it fits my intuition to think the same thing, and I have read that paper that you wrote on it. I think that it's a very nice paper, and a nice way to look at it.

Other people have also approximated flicker noise with a cascaded sequence of what we, in control system engineering, call lead or lag networks, which gives kind of a staircase sort of frequency response function, which, to a certain degree of approximation, drops off at ten dB per decade rather than twenty dB.

If you take any rational transfer function, or one that is written out in integer powers, and look at the Bode plot, the slopes go in multiples of twenty dB per decade, There are no thirty dB per decade, or fifty dB per decade slopes.

In the case of flicker noise, and consider the filter that shapes white noise into flicker noise, it requires an s to the negative one-half power in the transfer function. That would give a Bode plot that drops off at ten dB per decade instead of twenty. What you would do is approximate that ten dB per decade slope with a whole sequence of filters with alternating zeros and poles. You then end up with a staircase shape response which, on the average, has a ten dB per decade slope.

Incidentally, I think that this is a very good way to model flicker noise. The difficulty is that every time you put a new pole in the system you have a new state model. If you want get a reasonably accurate approximation of flicker noise that way, it s involve escalating the order of the Kalman filter considerably. There is nothing wrong with doing it off-line for analysis purposes. I think that there are some on-line cases where it would not be accepted.

MR. REINHARDT: I think that some people have reported on a similar method where they used a finite number of filters and it worked very well in an operational case. If you try to limit that process though, what happens is that all the poles run together, and you end up with a branch line.

MR. BROWN: I guess my answer to that would be that, in any of these processes, in the case of flicker noise for example, at zero frequency and out at infinity, there are singular conditions for either case. If it drops off as one over f, the area under the curve out at infinity is not finite. You are talking about a process with infinite variance, which is physically ridiculous.

The same thing happens at the other end of the spectrum, the

area under the curve doesn't converge there, either. Physically it makes sense, if you want to be careful and talk about processes of finite variance, that you have to bound the power spectral density at the low frequency end and at the high frequency end. It has to roll off at least twenty dB per decade in order to have a process of finite variance.

It doesn't bother me to think of putting in a filter at the origin which will bound the frequency content at zero frequency, and also put one in at the high end and make it roll off at least twenty dB per decade.

Incidentally, that impulse response function is not original with me. Other people have written about that before, including yourself, I think.

JIM BARNES, AUSTRON, INC.: I have done a fair amount of simulation of flicker noise with polynomials, the lead-lag networks you mentioned, and have one comment in their defense: Three or four stages can do an amazing amount. You can cover as much as three to four decades of frequency with only three or four stages.

MR. BROWN: Oh, is that right? It isn't as bad as it m . w appear at first glance then. I haven't used it, but would have imagined that you would need a fairly large number.

MR. REINHARDT: As another comment, even a single filter, which generates a random telegraph, will generate a flat Allan variance of about two orders of magnitude in tau, right around the peak. Then you really have to put a pole every order of magnitude or even every two orders of magnitude.

MR. BROWN: All of these are, of course, approximate models for the reasons which I just cited.

MR. ALLAN: I think, in practice, the problem with flicker noise is not a serious one, because it's only at the extremes, as you pointed out, at zero and at infinity that you have difficulties with one over f integration. In practice, that's not where the Fourier frequencies are. In reality, a few stages of the filter will work very nicely in describing, predicting or simulating a flicker process.

MR. BROWN: You need something like that though as far as the Kalman filter is concerned. You can't afford to have these fractional powers of s is you are going to do the state model. You have to have something where you only need to worry about integer powers of s, and if you can do that by only adding two or three poles, that would be a very feasible way to approximate it certainly.

RELATIONSHIP BETWEEN ALLAN VARIANCES AND KALMAN FILTER PARAMETERS

A. J. Van Dierendonck
J. B. McGraw

Stanford Telecommunications, Inc.
Santa Clara, CA 95054

and

R. Grover Brown

Electrical Engineering and Computer Engineering Department
Iowa State University
Ames, Iowa 50011

ABSTRACT

In this paper we construct a relationship between the Allan variance parameters (h_2, h_1, h_0, h_{-1} and h_{-2}) and a Kalman Filter model that would be used to estimate and predict clock phase, frequency and frequency drift. To start with we review the meaning of those Allan Variance parameters and how they are arrived at for a given frequency source. Although a subset of these parameters is arrived at by measuring phase as a function of time rather than as a spectral density, they all represent phase noise spectral density coefficients, though not necessarily that of a rational spectral density.

The phase noise spectral density is then transformed into a time domain covariance model which can then be used to derive the Kalman Filter model parameters. Simulation results of that covariance model are presented and compared to clock uncertainties predicted by Allan variance parameters. A two state Kalman Filter model is then derived and the significance of each state is explained.

$C-4$

INTRODUCTION

The NAVSTAR Global Positioning System (GPS) has brought about a challenge -- the challenge of modeling clocks for estimation processes. The system is very reliant on clocks, since its navigation accuracy is directly related to clock performance and the ability to estimate and predict time.

The estimation processes are usually in the form of Kalman Filters, or variations thereof such as Square Root Information Filters. These filters range from the large Ephemeris Determination Filter in the Control Segment, to Navigation Filters in the User Equipment, to Positioning Filters for stationary positioning or for merely solving for time and frequency in a Time Transfer system. In all of these applications, clock states and thus clock models exist. Not all of the models are necessarily proper.

It is the purpose of this paper to shed some light on how to model clocks for Kalman Filters. The presentation of clock statistics as Allan Variances has frustrated systems engineers for some time now because they don't know how to interpret them or how they can be used to predict system performance. The problem is even compounded because flicker noise is not a rational process.

In the past, Dr James Barnes [1,2] and Dave Allan [1] had shed some light on the clock modeling problem, although some of it was well in the past (1966)[1]. For some young modern day engineers, this work is hidden in old IEEE proceedings and NBS Technical Notes. Here, we are going to resurrect some of that work and form it into Kalman Filter models, but not without problems because of the flicker noise phenomenon.

Review of the Allan Variance Parameters

The Allan Variance parameters of an oscillator or atomic frequency standard are based on measurements of phase differences between that oscillator or atomic standard and a reference standard (which may be a low phase noise crystal oscillator for short term - high frequency measurements). These measurements are processed in two ways -- spectral analysis for higher frequency phase noise and time domain analysis for the relatively low

frequency variations. The single sided phase noise spectral density is converted to a single-sided spectral density of fractional frequency fluctuation of the form [3]

$$S_y(f) = h_2 f^2 + h_1 f + h_0 + h_{-1}/f + h_{-2}/f^2 \; ; \; f_1 \leq f \leq f_h \qquad 1)$$

where f_1 and f_h define the measurement system noise bandwidth, and where the h_α coefficients represent the following processes:

h_2 - white phase noise
h_1 - flicker phase noise
h_0 - white frequency noise
h_{-1} - flicker frequency noise
h_{-2} - random walk frequency noise

Normally the spectral density of equation 1 is obtained from a combination of the measured single-sided phase noise spectral density in radians/squared/Hz by

$$S_y(f) = \frac{f^2}{f_0^2} S_\phi(f) \qquad 2)$$

for a nominal frequency f_0, and from the square root of the Allan two-sample variances, $\sigma_y(\tau)$, which are computed as [3]

$$\sigma_y^2(\tau) = \frac{(\bar{y}_{k+1} - \bar{y}_k)^2}{2} \qquad 3)$$

$$\approx \frac{1}{2(M-1)} \sum_{k=1}^{M-1} (\bar{y}_{k+1} - \bar{y}_k)^2 \qquad 4)$$

where < > is the expected value operator and

$$\bar{y}_k = \frac{1}{\tau} \int_{t_k}^{t_k+\tau} y(t)dt = \frac{\phi(t_k + \tau) - \phi(t_k)}{2\pi f_0 \tau} \qquad 5)$$

where $\phi(t_k)$ are the measurements of the phase differences mentioned earlier.

When plotted, $\sigma_y(\tau)$, as shown in Figure 1, has the form [3]

$$\sigma_y^2(\tau) = \frac{h_0}{2}\tau^{-1} \qquad\qquad\qquad 6)$$

$$\sigma_y^2(\tau) = (2\ln 2)h_{-1} \qquad\qquad\qquad 7)$$

$$\sigma_y^2(\tau) = \frac{(2\pi)^2}{6}h_{-2}\tau \qquad\qquad\qquad 8)$$

for white, flicker and random frequency noises, respectively. In this paper we will only consider those three processes in the time domain for the Kalman Filter model. However, the white and flicker phase noises will be considered later in the model of the Kalman Filter measurement noise.

As can be seen, the h_α parameters can be obtained from two sources -- the single-side band (SSB) phase noise plot of a specification of an oscillator or frequency standard and its stability specification, which is given in terms of the Allan two-sample standard deviation. The SSB phase noise spectrum is usually given in dBc/Hz, or

$$S_\phi(f) = 20\log f_0 + 10\log[h_2 + h_1/f + h_0/f^2 + h_{-1}/f^3 + h_{-2}/f^4] \qquad 9)$$

Also of interest in later discussions is the spectral density of time fluctuation $x(t)$ in seconds, where

$$x(t) = \phi(t)/2\pi f_0 \qquad\qquad\qquad 10)$$

so that

$$S_x(f) = \frac{1}{(2\pi f_0)^2} S_\phi(f)$$

$$= \frac{1}{(2\pi)^2}[h_2 + h_1/f + h_0/f^2 + h_{-1}/f^3 + h_{-2}/f^4] \qquad 11)$$

in seconds squared per Hz.
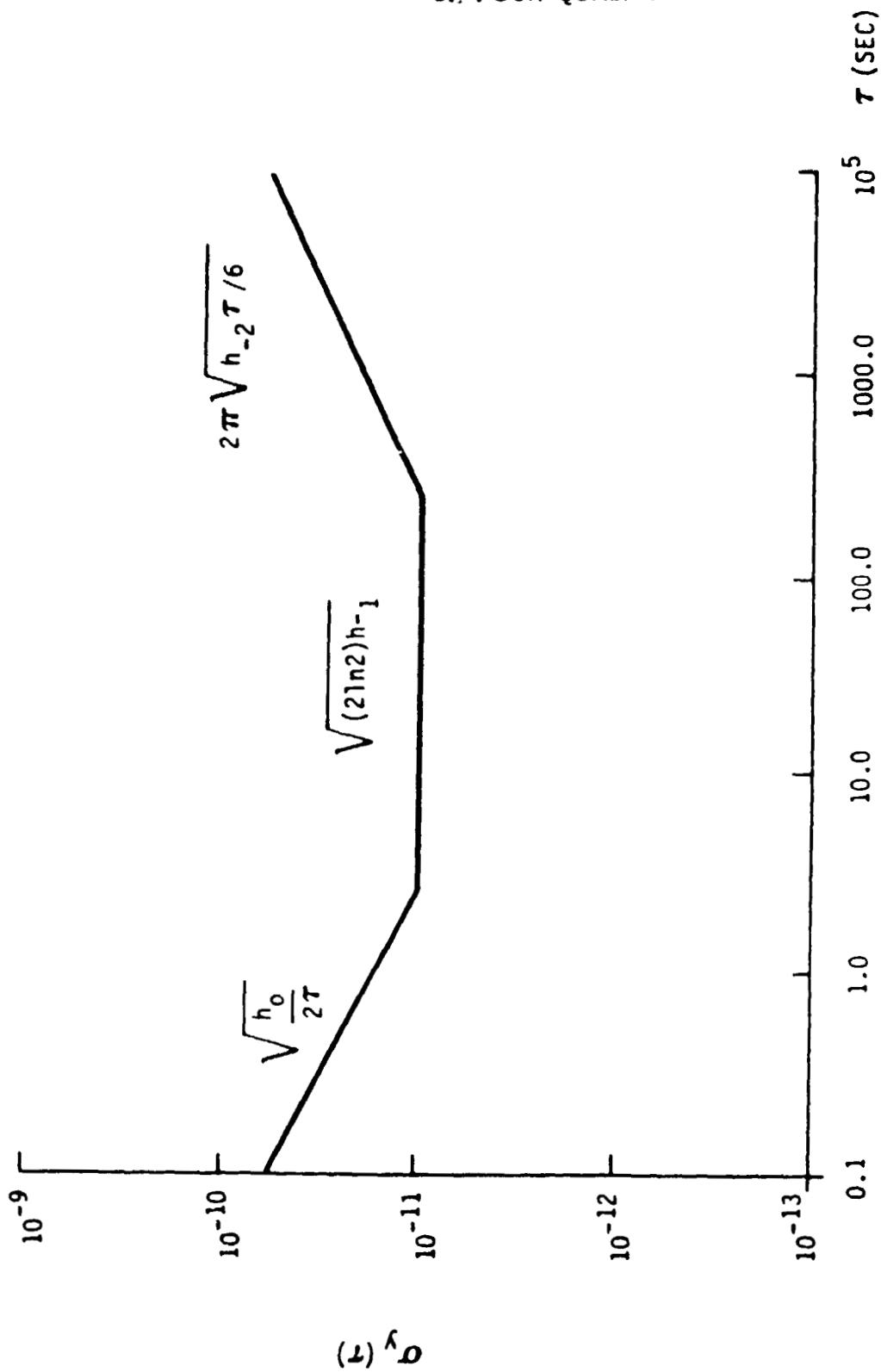
FIGURE 1 $\sigma_y(\tau)$ OF A TYPICAL FREQUENCY SOURCE

Transformation to a Statistical Covariance Model

Here, the work of Barnes and Allan [1] is expanded a bit to develop a co-
variance model that at least provides an "uncertainty" model one might use in
a Kalman Filter.* An "uncertainty" model is defined here as one that has the
variance propagation characteristics of a process, although the time auto-
correlation properties may be wanting. This is not unusual in modeling for a
Kalman Filter where large size state models are not feasible or when the
process is not truly a definable stochastic process. For example, if we were
to model position and velocity of a navigator in 6 states, where any acceler-
ation excursions are considered an uncertainty in the change in position and
velocity, that uncertainty is certainly not a "white noise" process by any
means.

Barnes and Allan only addressed the statistical model of flicker frequency
noise. However, the models for white and random walk frequency noise are
straightforward. Just in brief, they derived a convolution integral that
related the phase fluctuation due to flicker frequency noise to white noise,

where

$$z(t) = \int_{0}^{t} h(t-u)\eta(u)du \qquad \qquad 12)$$

where $h(t)$ is an impulse response of a transfer function and $\eta(t)$ is a white
noise process. The secret is in the derivation of that impulse response,
which they did for the flicker noise. To provide a more general derivation of
that impulse response, let us back up a bit.

A theoretical definition of a white noise spectral density is a constant, such
as the h_0 in equation 1. If it is possible, another spectral density can be
related to a white noise spectral density as

---

*For a tutorial on Kalman Filter Models, refer to Reference 4 by R. G. Brown,
which is the previously presented paper in this meeting.

278

$$S_z(\omega) = |H(j\omega)|^2 S_w(\omega)$$

$$= |H(j\omega)|^2 \qquad\qquad\qquad 13)$$

where we define the white noise density to be unity. Let us do that for the h_0, h_{-1} and h_{-2} processes defined in equations 1 and 11, converting first to fractional frequency squared/radians/second and seconds squared/radians/-second, and then to a two sided spectral density S'. Then,

$$S'_{y_0}(\omega) = h_0/2 \qquad \text{(white frequency noise)} \qquad 14)$$

$$S'_{y_{-1}}(\omega) = \pi h_{-1}/\omega \qquad \text{(flicker frequency noise)} \qquad 15)$$

$$S'_{y_{-2}}(\omega) = 2\pi^2 h_{-2}/\omega^2 \quad \text{(random walk frequency noise)} \qquad 16)$$

and correspondingly, and respectively

$$S'_{x_0}(\omega) = h_0/2\omega^2 \qquad\qquad\qquad 17)$$

$$S'_{x_{-1}}(\omega) = \pi h_{-1}/\omega^3 \qquad\qquad\qquad 18)$$

$$S'_{x_{-2}}{}^1(\omega) = 2\pi^2 h_{-2}/\omega^4 \qquad\qquad\qquad 19)$$

These can all be factored into the Fourier Transform of the impulse response h(t), where respectively,

$$H_{y_0}(j\omega) = \sqrt{h_0/2} \qquad\qquad\qquad 20)$$

$$H_{y_{-1}}(j\omega) = \sqrt{\pi h_{-1}}/\sqrt{j\omega} \qquad\qquad\qquad 21)$$

$$H_{y_{-2}}(j\omega) = \sqrt{2\pi^2 h_{-2}}/j\omega \qquad\qquad\qquad 22)$$

$$H_{x_0}(j\omega) = \sqrt{h_0/2}/\omega \qquad\qquad\qquad 23)$$

$$H_{x_{-1}}(j\omega) = \sqrt{\pi h_{-1}}/(j\omega)^{3/2} \qquad\qquad\qquad 24)$$

$$H_{x_{-2}}(j\omega) = \sqrt{2\pi^2 h_{-2}}/(j\omega)^2 \qquad\qquad\qquad 25)$$

Converting these to La Place Transforms (s=jω) and using tables from Reference 5, we have the respective impulse responses

$$h_{y_0}(t) = \sqrt{h_0/2}\ \delta(t) \tag{26}$$

$$h_{y_{-1}}(t) = \sqrt{h_{-1}/t}\ ;\ t > 0 \tag{27}$$

$$h_{y_{-2}}(t) = \pi\ \sqrt{2h_{-2}}1(t)\ ;\ t \geq 0 \tag{28}$$

$$h_{x_0}(t) = \sqrt{h_0/2}\ 1(t)\ ;\ t \geq 0 \tag{29}$$

$$h_{x_{-1}}(t) = 2\sqrt{h_{-1}t}\ ;\ t \geq 0 \tag{30}$$

$$h_{x_{-2}}(t) = \pi\ \sqrt{2h_{-2}}t\ ;\ t \geq 0 \tag{31}$$

Where $\delta(t)$ is the Dirac delta function and $1(t)$ is the unit response function.

We can now derive the autocorrelation, variance and cross-correlation functions of these processes from the following:

The autocorrelation function is

$$R(t,\tau) = \int_0^t \int_0^{t+\tau} h(t-u)h(t+\tau-v)\ E[\eta(u)\eta(v)]dvdu \tag{32}$$

$$= \int_0^t h(u)h(u+\tau)du\ ;\ \tau \geq 0 \tag{33}$$

Using the property that

$$E[\eta(u)\eta(v)] = \delta(u-v) \tag{34}$$

and that

$$\int_0^{t+\tau} f(v)\delta(u-v)dv = f(u) \tag{35}$$

provided that $0 \leq u \leq t+\tau$, which it is if we restrict τ to be greater than zero. The variance of a process is then

$$\sigma^2(t) = R(t,0)$$

$$= \int_0^t h^2(u)du \qquad \qquad 36)$$

Similarly, the cross-correlation function between two processes is

$$R_{xy}(t,\tau) = \int_0^t h_x(u)h_y(u+\tau)du \; ; \; \tau \geq 0 \qquad \qquad 37)$$

provided that they are driven by the same white noise process. (Otherwise $R_{xy}(t,\tau)$ is zero.)

For each process then

$$R_{y_0}(t,\tau) = \frac{h_0}{2}\delta(\tau)$$

$$\qquad \qquad 38)$$

$$R_{y_{-1}}(t,\tau) \text{ is undefined}$$

$$R_{y_{-2}}(t,\tau) = 2\pi^2 h_{-2}t \; ; \; \tau \geq 0 \qquad \qquad 39)$$

$$R_{x_0}(t,\tau) = \frac{h_0}{2}t \; ; \; \tau \geq 0 \qquad \qquad 40)$$

$$R_{x_{-1}}(t,\tau) = h_{-1}\left\{(2t+\tau)\sqrt{t^2+t\tau} - \frac{\tau^2}{2}\ln\left[\frac{2t+\tau+2\sqrt{t^2+t\tau}}{\tau}\right]\right\} \qquad 41)$$

$$R_{x_{-2}}(t,\tau) = 2\pi^2 h_{-2}\left(\frac{1}{3}t^3 + \frac{1}{2}t^2\tau\right) \qquad \qquad 42)$$

$R_{y_{-1}}(t,\tau)$ does not exist because its impulse response (equation 27) is infinite at t=0. However, if one bounds the flicker noise spectral density to a frequency region of $f_1 \leq f \leq f_h$, such as suggested in Reference 2, a stationary process is defined and an autocorrelation function can be defined as the inverse Fourier Transfer of the spectral density as

$$R_{y_{-1}}(\tau) = h_{-1} \int_{2\pi f_1}^{2\pi f_h} \frac{\cos\omega\tau}{\omega} \, d\omega$$

$$= h_{-1}\ln\frac{f_h}{f_1} + h_{-1} \sum_{n=1}^{\infty} (-1)^n \frac{(2\pi f_h\tau)^{2n}-(2\pi f_1\tau)^{2n}}{2n(2n)!} \qquad 43)$$

which is a well defined function of τ.

Then, the variances can be derived as

$$\sigma_{y_0}^2 = h_0 f_{h_0} \qquad 44)$$

$$\sigma_{y_{-1}}^2 = h_{-1}\ln\frac{f_h}{f_1} \qquad 45)$$

$$\sigma_{y_{-2}}^2(t) = 2\pi^2 h_{-2}t \qquad 46)$$

$$\sigma_{x_0}^2(t) = \frac{h_0}{2} t \qquad 47)$$

$$\sigma_{x_{-1}}^2(t) = 2h_{-1}t^2 \qquad 48)$$

$$\sigma_{x_{-2}}^2(t) = \frac{2}{3} \pi^2 h_{-2}t^3 \qquad 49)$$

Here, $\sigma_{y_0}^2$ is defined for a limited bandwidth f_{h_0} and $\sigma_{x_{-1}}^2$ is derived from equation 36. Cross correlations between frequency and time of like processes are then

$$R_{xy_0}(t,\tau) = \frac{h_0}{2} \; ; \; \tau = 0 \qquad 50)$$

$$= 0 \; ; \; \tau > 0$$

$$R_{xy_{-1}}(t,\tau) = 2h_{-1}\sqrt{t^2+t\tau} - h_{-1}\tau\ln\left[\frac{2\sqrt{t^2+t\tau} + 2t+\tau}{\tau}\right] \qquad 51)$$

$$R_{xy_{-2}}(t,\tau) = \pi^2 h_{-2}(t^2+2t\tau) \qquad 52)$$

or, for zero correlation time (cross-covariances).

$$R_{xy_0} = \frac{h_0}{2} \tag{53}$$

$$R_{xy_{-1}} = 2h_{-1}t \tag{54}$$

$$R_{xy_{-2}} = \pi^2 h_{-2} t^2 \tag{55}$$

Equations 44 through 49 and 53 through 55 could be used to define a covariance matrix at any time t describing the combined uncertainty in instantaneous time and fractional frequency. That is

$$\text{COV}[x(t),y(t)] = \begin{bmatrix} \dfrac{h_0}{2}t + 2h_{-1}t^2 + \dfrac{2}{3}\pi^2 h_{-2}t^3 & \dfrac{h_0}{2} + 2h_{-1}t - \pi h^2 t_{-2}^2 \\[4mm] \dfrac{h_0}{2} + 2h_{-1}t + \pi^2 h_{-2}t^2 & h_0 f_{h_0} + h_{-1}\ln\dfrac{f_h}{f_1} + 2\pi^2 h_{-2}t \end{bmatrix} \tag{56}$$

However, discrete Kalman filters do not estimate instantaneous frequency, but an average fractional frequency over a Kalman filter time interval Δt. Let that average fractional frequency be

$$\bar{y}(t) = \frac{x(t+\Delta t) - x(t)}{\Delta t} \tag{57}$$

Then, using equations 40 through 42 with $\tau = \Delta t$, but first simplifying equation 41 to a steady state value (large t/τ) of

$$R_{x_{-1}}(t,\tau) \approx 2h_{-1}(t^2 + t\tau) \tag{58}$$

and equations 47 through 49, a new covariance can be computed, where

$$\text{COV}[x(t),\bar{y}(t)] = \begin{bmatrix} \dfrac{h_0}{2}t + 2h_{-1}t^2 + \dfrac{2}{3}\pi^2 h_{-2}t^3 & 2h_{-1}t + \pi^2 h_{-2}t^2 \\[4mm] 2h_{-1}t + \pi^2 h_2 t^2 & \dfrac{h_0}{2\Delta t} + 2h_{-1} + \dfrac{2}{3}\pi^2 h_{-2}\Delta t \\[4mm] & \quad + 2\pi^2 h_{-2}t \end{bmatrix} \tag{59}$$

all of which is a well-balanced function of t, except the 2,2 term that has terms as a function of Δt that basically describe the Allan standard deviation (within ln2).

Transformation to a 2-state Kalman Filter Covariance Model

It should be noted that both x and $\bar{y}$ are nonstationary random processes that grow with time. If we wish to obtain a measure of this growth over a Δt interval, we simply let $t = \Delta t$ in equation ⁓ and obtain

$$\text{Cov}[x(\Delta t), \bar{y}(\Delta t)] = \begin{bmatrix} \frac{h_0}{2}\Delta t + 2h_{-1}\Delta t^2 + \frac{2}{3}\pi^2 h_{-2}\Delta t^3 & 2h_{-1}\Delta t + \pi^2 h_{-2}\Delta t^2 \\ & \\ 2h_{-1}\Delta t + \pi^2 h_{-2}\Delta t^2 & \frac{h_0}{2\Delta t} + 2h_{-1} + \frac{8}{3}\pi^2 h_{-2}\Delta t \end{bmatrix} \qquad 60)$$

We now propose the following 2-state Kalman filter model. Let the state variables be defined as

$$x_1 = x \text{ (i.e., time as before)}$$

$$61)$$

$$x_2 = \text{"Noisy" average frequency}$$

The precise meaning of x_2 will be made apparent presently. Now, following the usual notat'⁓n of Kalman filter theory [4], we let the transition matrix for a Δt interval be

$$\Phi = \begin{bmatrix} 1 & \Delta t \\ 0 & 1 \end{bmatrix} \qquad 62)$$

and we let the Q matrix be

$$Q = \text{Cov}[x(\Delta t), \bar{y}(\Delta t)] \qquad 63)$$

as given by equation 60.

We also postulate that we will step the estimate of the state vector and its error covariance ahead via the usual projection equations.

$$\hat{x}^-(t+\Delta t) = \Phi\hat{x}(t) \qquad\qquad 64)$$

$$P^-(t+\Delta t) = \Phi P(t)\Phi^T+Q \qquad\qquad 65)$$

We will now have a proper Kalman filter model except for the measurement equation. This portion of the model depends on the situation at hand, so we will omit further discussion of this here. (For example, the clock model might be imbedded in a larger state model as in the GPS application [6].)

We now need to explore more carefully the connection between our postulated state model and the x and $\bar{y}$ statistics as dictated by equation 60. First, by choosing our Q matrix as exactly that of equation 60, we are assured of having the proper growth of uncertainty in our time and average frequency estimates in the Δt interval. This is necessary in order to generate appropriate filter gains with each step of the estimation process. However, we cannot have x_2 in our state model represent true average frequency, and at the same moment require the 1,1 term of the Q matrix to be nonzero. This is not compatible with the defining equation for average frequency. That is, equation 57 states

$$x(t+\Delta t) = x(t)+\Delta t\cdot\bar{y} \qquad\qquad 66)$$

Whereas, our state model says

$$x_1(t+\Delta t) = x_1(t)+\Delta t\cdot x(t)+w_k \qquad\qquad 67)$$

We have defined x_1 to be x, and thus x_2 must differ from $\bar{y}$ by the additive discrete white noise term $w_k/\Delta t$. We are comforted, though, with the fact that the average x_2 in the state model is equal to the usual average frequency.

It should be noted that the Kalman filter model proposed here is entirely self-consistent in terms of state-space theory. The transition matrix is legitimate in that it reduces to the identity matrix for $\Delta t=0$; and Q is positive-definite for all Δt as it must be to be a legitimate covariance

285

matrix. The only inconsistency lies in the state model's connection to the $x, \bar{y}$ processes are described by equation 59. In view of the remarks about flicker noise in the companion paper in these Proceedings [4], we should not expect to be able to make this connection exact. No finite-order state model will fit flicker noise perfectly! Thus, something has to give. We intentionally kept the identity of time exact in our model, i.e., $x_1 = x$. We then circumvented inconsistency in the state model by letting x_2 be a noisy version of $\bar{y}$. The filter's estimate of x_2 is still a valid estimate of frequency, though, because the mean of x_2 is $\bar{y}$.

An Example

Standard deviation plots of the time state $x(t)$ of typical crystal oscillators are plotted in Figures 2 and 3, whose Allan variance characteristics are represented in Figure 4. Also shown in Figure 4 are plots of the standard deviation of time $\sqrt{Q_{11}(\tau)}$ divided by τ for comparison to the two-sample standard deviation. It has been suggested in the past that a procedure to estimate the standard deviation of time is to simply multiply the two-sample standard deviation by the elapsed time. These plots either verify that estimate or verify the validity of the derivation provided earlier.

Kalman Filter Measurement Noise

Suppose one uses a phase lock loop to track the phase difference between an oscillator and a reference frequency source as shown in Figure 5. The variance of the tracking error $\delta\phi$ in radians due to phase noise of the oscillator is given as

$$\sigma_{\delta\phi}^2 = \int_0^{f_h} S_\phi(f) \cdot |1 - H_{PLL}(j2\pi f)|^2 df \qquad 68)$$

where

$$|1 - H_{PLL}(j2\pi f)|^2 = \frac{f^4}{f^4 + f_N^4} \qquad 69)$$
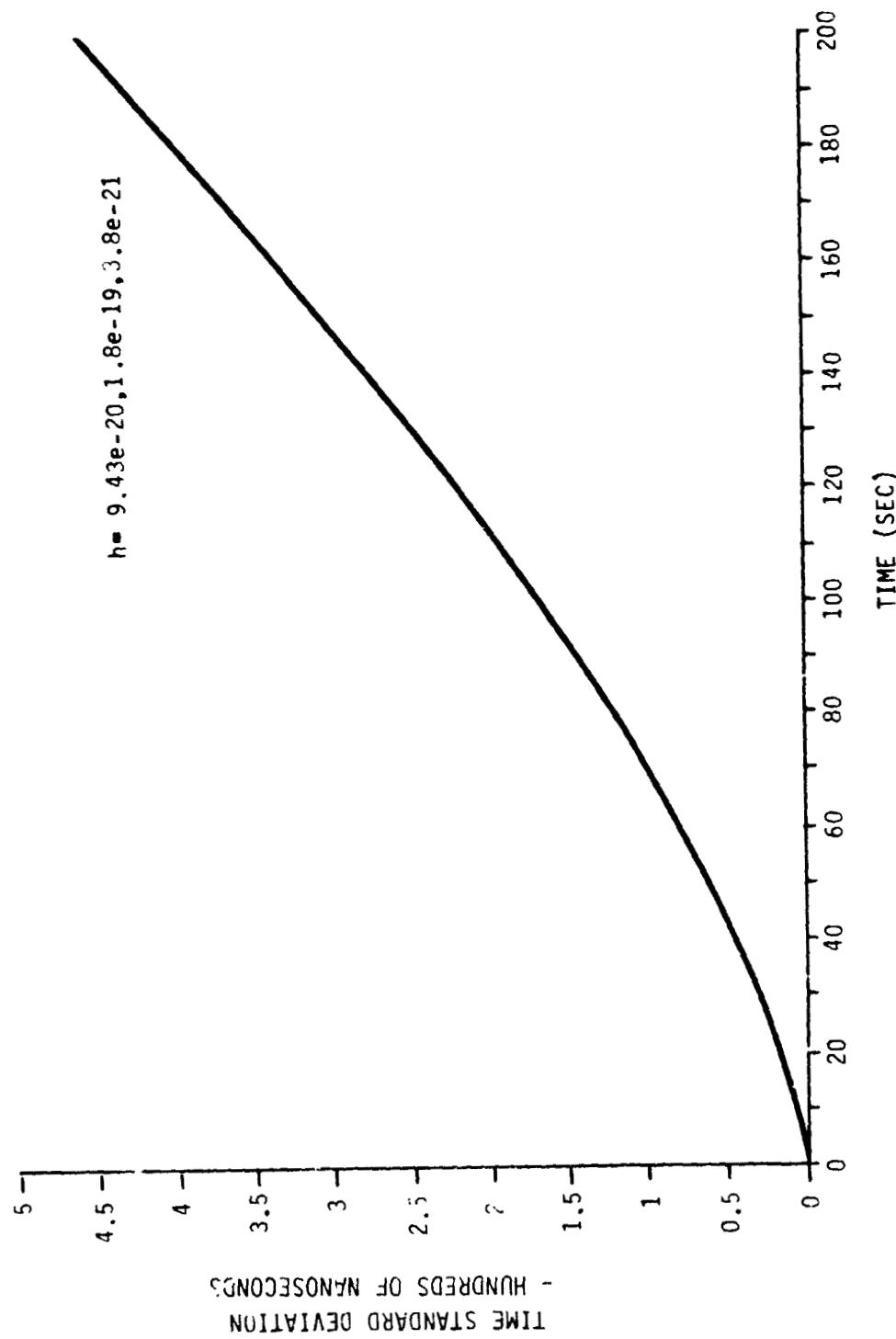
FIGURE 2 STANDARD DEVIATION OF TIME FOR A 5 PARTS IN 10^{10} CRYSTAL OSCILLATOR

h = 9.43e-20,1.8e-19,3.8e-21
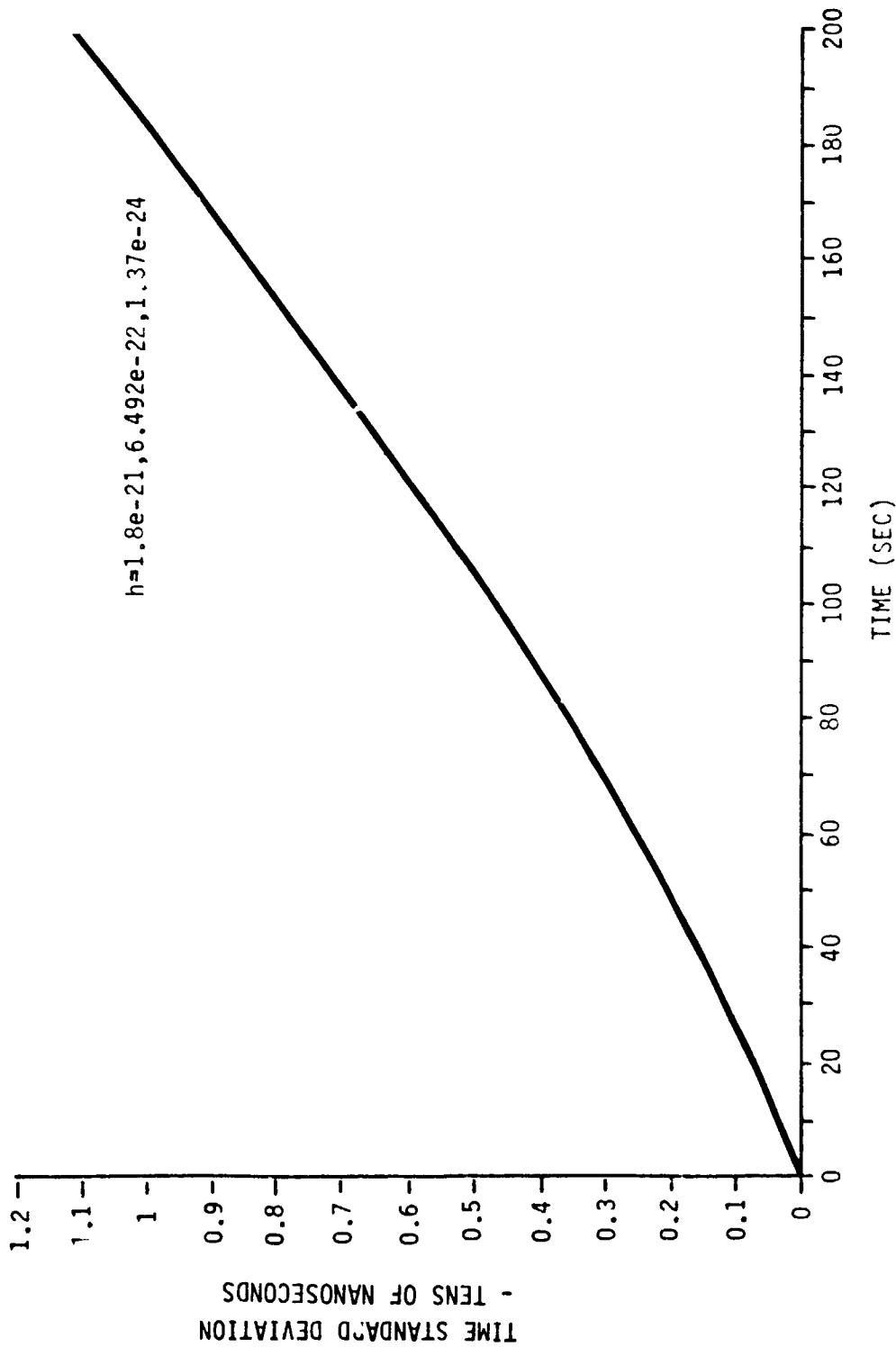
FIGURE 3   STANDARD DEVIATION OF TIME FOR A 3 PARTS IN 10^{11} CRYSTAL OSCILLATOR

h=1.8e-21,6.492e-22,1.37e-24
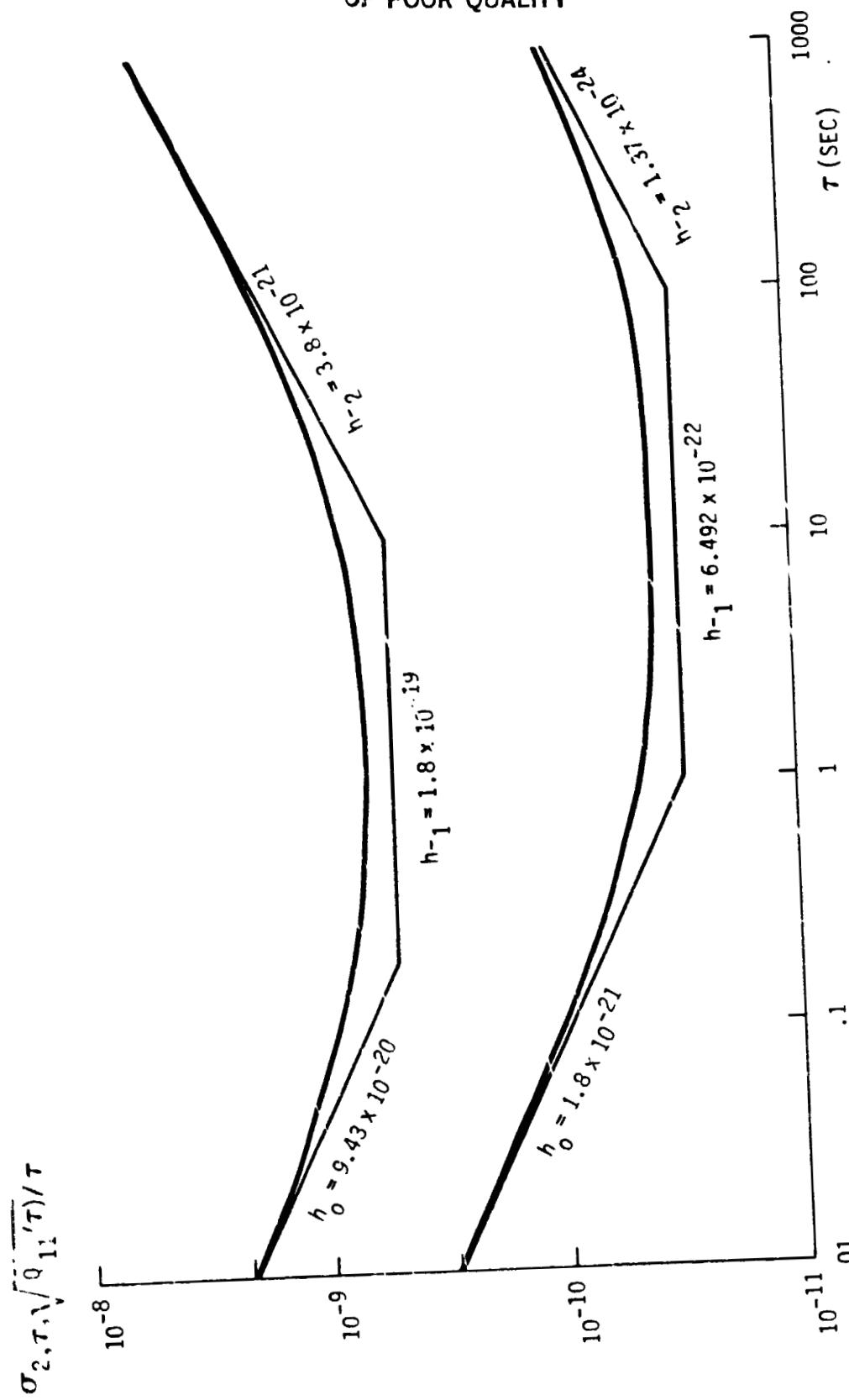
FIGURE 4 $\sigma_{2,\tau}$ AND $\sqrt{Q_{11}(\tau)}/\tau$ FOR TWO TYPICAL CRYSTAL OSCILLATORS
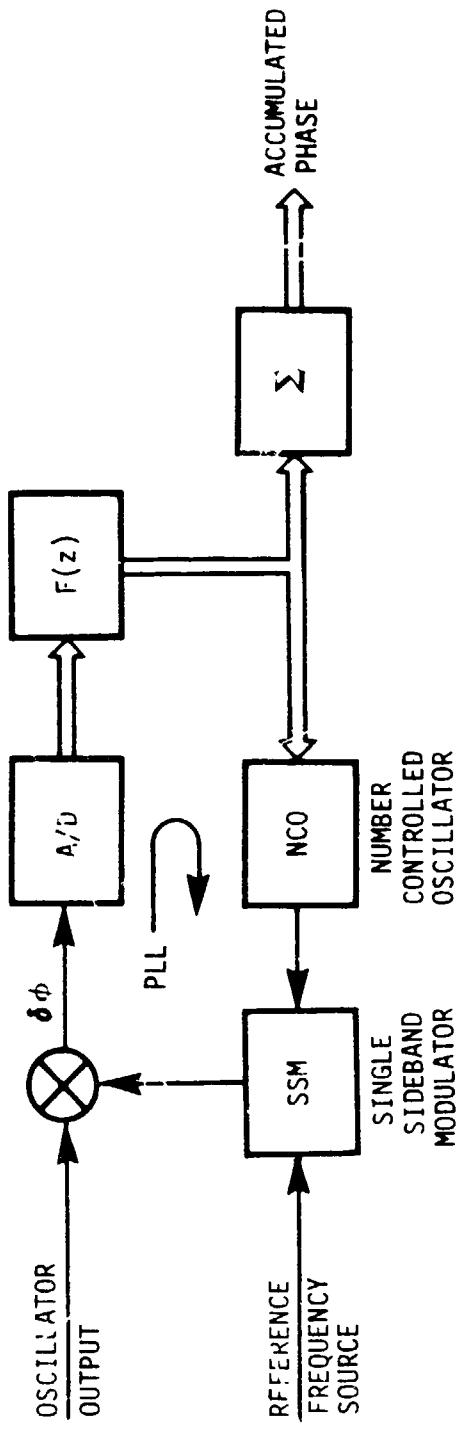
FIGURE 5   PHASE LOOP MEASURING OSCILLATOR PHASE

of a phase lock loop with corner frequency f_N and damping ratio of $\sqrt{2}/2$, and $S_\phi(f)$ is the phase noise spectral density represented in equation 9. $\sigma_{\delta\phi}^2$ represents that part of the measurement error introduced into the Kalman Filter. It is usually affected mostly by the h_2, h_1 and h_0 terms of $S_\phi(f)$, depending upon the loop bandwidth.

In a laboratory environment, the measurement error whose variance is depicted in equation 69 may be the only measurement error of significance. However, in such systems as GPS, it is usually dominated by thermal noise and other system effects.

SUMMARY AND CONCLUSIONS

Because of flicker noise, good models of clocks for Kalman Filters can be elusive. In this paper we derived a two state model of clock characteristics that can be used in a Kalman Filter. It represents the characteristics of a clock described in terms of Allan variance parameters. We believe the models presented within this paper are a vast improvement over those used in most applications of the NAVSTAR GPS system, and that they could also be used in many other applications of time and frequency where real-time estimates and predictions of time and frequency are required.

ACKNOWLEDGMENT

The authors are indebted to Dr. James A. Barnes for his suggestion that the second state variable in our model should not be referred to as average frequency, which already has precise meaning in the PTTI community.

REFERENCES

[1] Barnes, J.A. and Allan, D.W., "A Statistical Model of Flicker Noise," Proceedings of the IEEE, Vol. 54, No. 2, February, 1966.

[2] Barnes, James A., "Models for the Interpretation of Frequency Stability Measurements," NBS Technical Note 683, August 1976.

[3] Time and Frequency: Theory and Fundamentals, Byron E. Blair, Editor, NBS Monograph 140, May 1974.

[4] Brown, R. Grover, "Kalman Filter Modeling," paper presented at this conference.

[5] Brown, R.G., and Nilsson, J.W. Introduction to Linear Systems Analysis, John Wiley, 1962.

[6] Van Dierendonck, A.J. and Hua, Q.D., "Enhancements to the TTS-502 Time Transfer System," Proceedings of the Fifteenth Annual Precise Time and Time Interval (PTTI) Applications and Planning Meeting, December, 1983.

QUESTIONS AND ANSWERS

VICTOR REINHARDT, HUGHES AIRCRAFT CO.: I have a comment on f sub h and f sub l. They are not really arbitrary, but real physical parameters that have to be set by the experiment. Just as with the white noise process, you have to set the bandwith before you can define the amount of noise that's going to enter the system. The white noise process is another process that requires the definition of the high frequency limit, and flicker noise, a low frequency limit. I think that's real effect, because the Allan variance goes to infinity. So, those are real things that you have to define, they are not arbitrary. I do think that you can leave those parameters as things to be defined by the person using the model.

MR. BROWN: There was something that you said that I didn't understand. What is it that goes to infinity? The second difference is stationary, that is the reason that it is used.

MR. REINHARDT: I am talking about the effect of having a dead time in the Allan variance, when the dead time between samples goes to infinity. The variance does go to infinity then. Or, if you have N samples, the process goes to infinity as log N.
  What this means is that there is definitely a low frequency cut-off parameter which has to be considered in your measurement process, which may not necessarily be associated with tau.

MR. ALLAN. I think that one can make a general statement about this whole argument. The Kalman filter concept is strongly model dependent, and no model is perfect. The fact that, in the case of flicker noise, we may need to approximate the state matrix with a few terms doesn't bother me at all, because the model is approximate anyway.
  Whether you are talking about white noise or other noise, it's approximate at every leg of the trip, and you have to approximate for flicker noise or anything else. You have a finite measuring system bandwidth in the real world. You have low frequency and a high frequency cut-off, so these are only approximations to the ideal. I think that everything fits together rather well.

MR. BROWN: I certainly agree with that. In this particular model that Al and I have come up with, we were working especially hard to come up with a two state model, and there have to be serious approximations in that.
  I do plan to have a student working on this through the winter doing some simulations to see which of the two state models, or which of these options will work out to be the best. Of course, we are not absolutely limited to a two state model. We thought that it would be nice, with all the other approximations that go into the thing, to just keep it a two state model.

DEVELOPMENT OF HYDROGEN MASERS FOR K-3 VLBI SYSTEM

Takao Morikawa,Yasusada Ohta,and Hitoshi Kiuchi
Radio Research Laboratories
Ministry of Posts and Telecommunications
Tokyo 184 Japan

ABSTRACT

The Radio Research Laboratories of Japan (RRL) has developed two field operable hydrogen masers for the VLBI joint experiment conducted by the cooperation between RRL and NASA. They are now playing an important role as the time and frequency standard of the K-3 VLBI system,which has also been developed by RRL.

The masers consist of a physics package and an electronics package. The physics package is 84cm wide,94cm deep and 160cm high. Four permalloy magnetic shields are set in a vacuum chamber and function also as thermal radiation shields. The standoffs which support the magnetic shields,the C-coil and the cavity are made of polyimide with low thermal conductivity. Thus the thermal isolation is greatly improved. Also set in the vacuum chamber are two aluminium cylinder ovens, and the cavity temperature stability of 1mK has been achieved without thermal isolators. The cavity cylinder is made of glass ceramics (NEOCERAM) with a thermal expansion coefficient of -5.0×10^{-7}. Change of the mechanical stress on the cavity is absorbed by a Belleville spring. As the result, the temperature coefficient of the cavity frequency is reduced to 500Hz/K.

The electronics package consists of a receiver,a cavity auto tuner,and environment control circuits such as temperature controllers. The receiver uses a low noise preamplifier and an image rejection mixer ,and has an overall noise figure of 4.5dB. The receiver front end and the phase locked frequency multiplier for the first local oscillator are temperature-stabilized within 5mK by a peltier module. The frequency of the standard signal is adjustable by a synthesizer with a resolution of 7×10^{-13}.

The frequency stability has been measured between the masers. The measured stability is 2×10^{-13} at 1 second, 2.4×10^{-15} at 830 seconds,and 1.4×10^{-14} at 10^5 seconds. The external magnetic field sensitivity is 2.5×10^{-13}/G,which has been measured by adding a vertical magnetic field with a Helmholtz coil. The temperature sensitivity is 2.3×10^{-14}/K,which has been obtained by changing the room temperature.

1. Introduction

The Radio Research Laboratories (RRL) has developed the K-3 VLBI system [1],[2], which is compatible with the Mark III VLBI system of NASA, for the VLBI joint experiment between RRL and NASA [3]. As a part of this project two field operable hydrogen masers have been developed as the time and frequency standard of the K-3 system.

In a VLBI system a signal from a radio star should be down-converted to the video frequency without the loss of the coherence. Therefore the phase noise of the local oscillator of the VLBI system must be small enough. The phase stability required of the local oscillator, which is phase-locked to a hydrogen maser, depends on the noise temperature of the VLBI system and the signal source, and the sample time. In the K-3 system the phase fluctuation below $\pi/8$ radian for the sample time of 600sec and the observation frequency of 8GHz was projected.

In a VLBI experiment several radio stars are observed and the delay time must be measured for each observation. Therefore the fluctuation of the system clock during the experiment must be smaller than the precision of the delay time measurement. In the Japan-USA VLBI experiment the precision of subnanosecond was required.

In order to satisfy the above requirements of the K-3 system the following frequency stability of the masers was projected as the minimum requirement.

$$\sigma_y(\tau) < 1.0 \times 10^{-14} \qquad \tau = 600sec$$
$$\sigma_y(\tau) < 2.8 \times 10^{-14} \qquad \tau = 18000sec$$

This paper presents the design and the performance of the developed masers and some discussion on the external magnetic field disturbance on the maser which has been observed at Kashima Branch where the K-3 system is located.

2. Design of the masers

The masers consist of a physics package and an electronics package. The physics package is 84cm wide, 94cm deep, and 160cm high. It weighs 550kg. The electronics package is mounted in a rack, which is 175cm high and 57cm wide. In Fig. 1 the physics packages and the electronics packages are shown.

2.1 Physics package

In Fig. 2 the structure of the physics package is shown.

2.1.1 Magnetic shielding

The maser has four permalloy magnetic shields, all of which are 2mm thick and set in a vacuum chamber. This structure has two advantages.

One is that the conduit pipe which connects the ion pump and the resonant cavity can be eliminated. This enables us to make the aperture of the magnetic shields for the hydrogen beam path smaller, which results in better magnetic shielding. The diameter of the aperture is 40mm, while that of the laboratory type maser ⌐ RRL which has a conduit pipe is 80mm. The magnetic shields also small holes for the standoffs, which fix the shields, and the driving axis of the cavity tuning post. The diameters of ⌐ ⌐les are 16mm and 10mm, respectively. This structure has also enabled us to eliminate the heat-flow through the conduit pipe, and the thermal insulation can be improved.

The other advantage is that the magnetic shields function also as the thermal radiation shields, which contribute to improving the thermal isolation. The magnetic shields are degaussed by applying directly AC current of 50A [4].

2.1.2 Resonant cavity

As well known, the fluctuation of the resonance frequency of the cavity disturbs the oscillation frequency of the maser. The main causes of the fluctuation are the thermal expansion of the cavity material, the mechanical distortion of the cavity material, and the thermal fluctuation of the dielectric constant of the storage bulb. The last cause can be reduced by using a light storage bulb [5]. Fig. 3 shows the cavity structure.

The cavity cylinder and the upper end plate are made of glass ceramics (NEOCERAM) with a low thermal expansion coefficient of -5×10^{-7}. Silver conductive composition is painted on the inner surface of the glass ceramics. The measured loaded quality factor is 50000. The coarse tuning is carried out by moving the upper end plate. The screwed axis for adjusting the upper end plate is made of molybdenum which has relatively low thermal expansion coefficient of 5×10^{-6} [6]. The resolution of the coarse tuning is 1kHz.

In order to fix the cavity cylinder, a stress is given to the ceiling plate, which holds the coarse tuning axis. This stress distorts the ceiling plate and the distance between the cavity end plates is changed. In order to achieve the maser frequency stability of 1×10^{-14}, the fluctuation of the distance should be below 0.3nm. Therefore the cavity material should be highly rigid and the stress should be stable. The flexural rigidity of a plate depends on its

Young's modulus and the third power of its thickness [7]. The ceiling plate is made of alumina which has high Young's modulus of 3×10^6 kg/cm^2. The base plate is 29mm thick and made of aluminium. The fluctuation of the stress is mainly caused by the thermal expansion of the cavity hold-down can. This stress change is absorbed by a Belleville spring [8], which is made of titanium. The characteristic of a Belleville spring is given by the following equations,

$$P=\frac{C_1 CEh^4}{r_2^2}$$

$$C=\pi\left(\frac{\alpha+1}{\alpha-1} - \frac{2}{\ln\alpha}\right)\left(\frac{\alpha}{\alpha-1}\right)^2$$

$$C_1=\frac{1}{(1-\nu^2)h}\left(\left(\frac{H}{h} - \frac{\delta}{h}\right)\left(\frac{H}{h} - \frac{\delta}{2h}\right)+1\right)$$

$$\alpha=\frac{r_2}{r_1}$$

where E and ν are the Young's modulus and the Poisson's ratio of the spring material, respectively. δ is the distortion of the spring and H is the free height of the spring. P is the load given to the spring. Other parameters are given in Fig. 4. The load of the spring of which H equals $\sqrt{2}h$ becomes constant if δ is H. Using this constant-load characteristic the stress on the ceiling plate can be stabilized. As shown in Fig. 5 the change in the cavity frequency becomes very small when the spring distortion is between 1 and 2mm. The cavity can be stabilized by setting the spring in this region.

The storage bulb is spherical and made of quartz glass. Its diameter is 180mm and the weight is 260g. The overall thermal coefficient of the cavity frequency is 500Hz/K.

2.1.3 Thermal control

The stability of the cavity temperature should be better than 1mK to achieve the maser frequency change of less than 1×10^{-14}. The thermal control is carried out by double ovens. The cavity hold-down can on which heaters and thermistor control sensors are attached is used as the inner oven. The heaters are divided into two zones, each of which is independently controlled to minimize the thermal gradient. The outer oven is made of a thick aluminium cylinder with heaters and sensors and placed on the outside of the innermost magnetic shield. It is also divided into the cylinder zone and the base zone, each of which is independently controlled. Since the heat-flow through the conduit pipe is eliminated and the thermal radiation is shielded by the magnetic shields, the residual heat-flow paths are the cables and the standoffs which support the

298

cavity, C-coil, magnetic shields, and the ovens. The standoffs are made of polyimide (VESPEL) with low thermal conductivity of 0.28kcal/m.hr.°C. They are outgassed in a vacuum environment by being baked at 200°C for several hours before the assemble of the maser. This process is needed to achieve high vacuum. The cables are thermally connected to the base of the outer oven to prevent the heat from flowing directly into the cavity. Thus the cavity temperature stability of 1mK is achieved without any other thermal insulators.

2.2 Electronics package

2.2.1 Phase-lock receiver

Fig. 6 shows the block diagram of the phase-lock receiver. The output signal of the maser is amplified by the low noise amplifier, which is preceded by the varactor diode for the cavity auto-tuning and the 60dB isolator. The noise figure of the low noise amplifier is 2.2dB and, the overall noise figure of the receiver is 4.5dB. The signal is then mixed with the 1.40GHz local signal from the phase-locked multiplier in the image rejection mixer. The resultant 1st IF signal (20.405MHz) is again down-converted to 405kHz. The 2nd IF signal is phase-compared with the reference signal from the synthesizer (hp3336A). The resultant error signal is filtered by the low-pass amplifier and used to tune electronically the 10MHz voltage-controlled crystal oscillator (VCXO) to the maser frequency. The 10MHz output signal of the VCXO is distributed to the multipliers, the synthesizer, the second pulse generator, the cavity auto-tuner and the VLBI system, via the distribution amplifier with 120dB isolation.

The temperature fluctuation will cause the phase fluctuation of the receiver front end. Therefore the front end, which is enclosed by the broken line in Fig. 6, is thermally controlled by the peltier module to improve the phase stability. The stability of the temperature is 5mK. The front end is mounted in the physics package.

In the VLBI experiment the frequency difference between the local oscillators of the VLBI stations should be less than 1×10^{-12} in order to suppress the phase rotation of the cross-correlation spectrum. Therefore the frequency of the 10MHz output signal is required to be finely adjusted. This can be carried out by the synthesizer of which the setting resolution is 7×10^{-13}.

2.2.2 Cavity auto-tuner

The maser is equipped with the cavity auto-tuner [9], of which the block diagram is shown in Fig. 7. The output signal of the low noise amplifier of #1 maser (1.42GHz) and the output signal of the

phase-locked multiplier of #2 maser (1.40GHz) are mixed in the image rejection mixer. The resultant IF signal (20.405MHz) is mixed with the IF signal of #2 maser and the beat signal between the masers is obtained. The beat signal is then divided and its period is measured by the counter. The hydrogen beam is modulated by the mechanical shutter, which is driven by the pulse motor. The CPU (Z80) calculates the difference between the beat periods at Hi beam and Lo beam, and generates the varactor control signals and the shutter control signals. The CPU also controls the loop gain, the measurement mode, and the other measuring parameters of the cavity auto-tuning.

If a miscount of the beat period happens, the varactor control voltage and, hence, the cavity frequency may be changed by a large amount. To avoid this miscount the CPU monitors the difference between the newly and last generated varactor control voltages. If the difference exceeds the preset limit, the CPU rejects the new value as abnormal and holds the varactor control voltage at the last value. Then the measurement is repeated again.

3. Frequency stability of the masers

The frequency stability of the free running masers was measured. The period of the beat signal from the cavity auto-tuner was measured by the counter (hp5300B) and $\sigma_y(\tau)$ was calculated. The bandwidth of the measuring system was 2Hz. A C-field of 20mOe was added to one of the masers to offset the maser frequency by 1.2Hz. During the frequency stability measurement both masers were placed in the same thermal and magnetic environment. The room temperature was controlled within $\pm 1°$ C and the control cycle was about 1000 to 2000sec.

Fig. 8 shows the frequency stability obtained. It shows the τ^{-1} characteristic between 1 and 20 sec and $\tau^{-1/2}$ characteristic between 20 and 1000sec. In the VLBI experiment the observation period of a radio star is between about 10 and 20min. and the frequency stability in this region is the most important. The frequency stability obtained is better than 3×10^{-15} for the averaging period between 500 and 5000sec and is 2.4×10^{-15} for 830sec, which is enough for a VLBI experiment.

The long term frequency stability gradually deteriorates for the averaging period of more than 3000sec, and is 1.4×10^{-14} for 10^5 sec. The main reason for the deterioration may be the relatively high C-field of 20mOe, which is added to one of the masers, and the inadequate stability of the C-field current source. The specification of stability of the current source is 5×10^{-5}/day. This corresponds to the maser frequency stability of 7.8×10^{-14}/day for the C-field of 20mOe, though the measured stability is 1.0×10^{-14} for

one day. The real performance of the current source may be better than the specification, which explains the discrepancy between the values. However it is very probable that the long term frequency stability is restricted by the stability of the current source. In VLBI experiments the maser which distributes the standard frequency and time signal to the K-3 system is operated under the C-field of 0.2mOe and the fluctuation of the current source can be neglected. Fig. 9 shows the monitor record of the beat period between the masers and the 1CMHz phase comparison among the masers and a commercial Cs clock.

4. Sensitivity to the environment

The frequency of a maser is disturbed by several environmental factors. They are the room temperature, the external magnetic field, the barometric pressure, and the mechanical vibration. The influence of the last two factors could not been evaluated because the measurement facilities were not available.

As stated above, the temperature of the room where the masers are placed is controlled within ·1°C and the control cycle is about 1000 to 2000sec. The maser frequency is not significantly disturbed by this temperature control, but is disturbed by a slower temperature change. In order to evaluate this influence the room temperature was changed by 6.5°C and the change of the beat frequency was monitored. The time constant of the temperature change was 3.9hours. During the measurement the laboratory type maser of which the cavity was auto-tuned was used as the reference maser. The reference maser was placed in another room and independent of the temperature change. The change of the beat period was measured 24hours after the temperature had been changed. It was 1.5×10^{-13} and the temperature sensitivity of the maser is $2.3 \times 10^{-14}/°C$.

In order to evaluate the influence of the external magnetic field, a Helmholtz coil was wound on the vacuum bell jar and a vertical magnetic field of 1G was added. The maser was operated under the 1mOe C-field during the measurement. The measured magnetic sensitivity is $2.5 \times 10^{-13}/G$, and the magnetic shielding factor is 15000.

The above measurement was carried out at the RRL Headquarters, where the masers had been developed, and the measured value was considered to be good enough for the VLBI experiment under the usual geomagnetic circumstances. However, after the masers had been transported to Kashima Branch, where the VLBI station of RRL is located, frequency fluctuation of $4~5 \times 10^{-14}$ was observed only during the VLBI experiments. During the VLBI experiments a large parabolic antenna, 26m in diameter and 160ton in weight, was swung to track the radio stars. This movement of the antenna disturbed the

301

environmental magnetic field. The fluctuation of the magnetic field in the maser room, which is located about 20m distant from the basement of the antenna, has been measured by using a magnetic flux gate meter. The results are shown in Fig.10 and Fig.11. Fig.10 shows the variation of the magnetic field in the maser room when the azimuth of the antenna is swept. Fig.11 shows the fluctuation of the magnetic field in the maser room during the VLBI experiment which was carried out at the end of August 1984. The magnetic disturbance amounts to more than 10mG. During the VLBI experiment one maser was operated under the 0.2mOe C-field and used as the time and frequency standard of the K-3 system, while the other maser was operated under the 20mOe C-field and used as the reference maser. The magnetic variation disturbed the reference maser. Later the C-field of the reference maser was set to 6mOe and the fluctuation of the maser frequency reduced to 1×10^{-14}.

Therefore it should be recommended to check the external magnetic field variation and to operate the maser under low C-field at VLBI stations. Especially at mobile VLBI stations the magnetic disturbance of the antenna may be large because he maser is placed very close to the antenna.

5. Conclusion

Two field operable hydrogen masers have been developed as the time and frequency standard of the K-3 VLBI system. The measured performance fully satisfies the requirements of the K-3 system, and they are now playing an important role as the time and frequency standard of the K-3 system at Kashima Branch.

The magnetic disturbance by the VLBI antenna tracking, which has been observed at Kashima station, suggests that it is necessary to check the magnetic environment in the maser room and to operate the maser under low C-field for VLBI experiments.

Acknowledgements

References

[1]   Kawaguchi, N., Sugimoto, Y., Kuroiwa, H., Kondo, T., Hama, S., Amagai, J., Morikawa, T., and Imae, M.; "The K-3 Hardware System Being Developed in Japan and Its Capability", NOAA

Technical Report NOS 95 NGS 24 Proceedings of Symposium No.5: Geodetic Applications of Radio Interferometry, pp.163-176 May 1982

[2] Takahashi, F., Yoshino, T., Murakami, H., Koike, K., Kunimori ,H., and Kondo, T.; "K-3 VLBI Software Development for International Experiments", NOAA Technical Report NOS 95 NGS 24 Proceedings of Symposium No.5: Geodetic Applications of Radio Interferometry, pp.177-183, May 1982

[3] VLBI Research Development Group, RRL; "The First US-JAPAN VLBI Test Observation by Use of K-3 System of the Radio Research Laboratories", J. Radio Res. Labs. vol.31, No.132, pp.31-37 March 1984

[4] Hermannsfeld, W.D. and Salsburg, B.L.; "Demagnetization of Magnetic Shield in the Presence of the Earth's Field", Rev. Sci. Instrum., 35, 906E, 1964

[5] Levine, M.W., Vessot, R.F., and Mattison, E.F.; "Performance Evaluation of the SAO VLG-11 Atomic Hydrogen Maser", Proceedings of the 32nd Annual Symposium on Frequency Control, pp.477-485, 1978

[6] Sabisky, E.S. and Weaklin, H.A.; "An Operating Development Model Spacecraft Hydrogen Maser", Proceedings of the 32nd Annual Symposium on Frequency Control, pp.499-505, 1978

[7] Timoshenco, S.; "Strength of Materials Part II :Advanced Theory and Priblems", Third Edition 1956 D. Van Nostrand Company Inc., New York

[8] Levine, M.W., Vessot, R.F., Nystrom, G., Hoffman, T.   and Blomberg, E.; "A New Generation of SAO Hydrogen Masers", Proceedings of the 31st Annual Symposium on Frequency Control, pp.525-534, 1977

[9] Brousseau, R. and Vanier, J.; "An Electronic System for the Tuning of Masers", IEEE Trans. IM-22, 4, pp.367-375, Dec. 1973
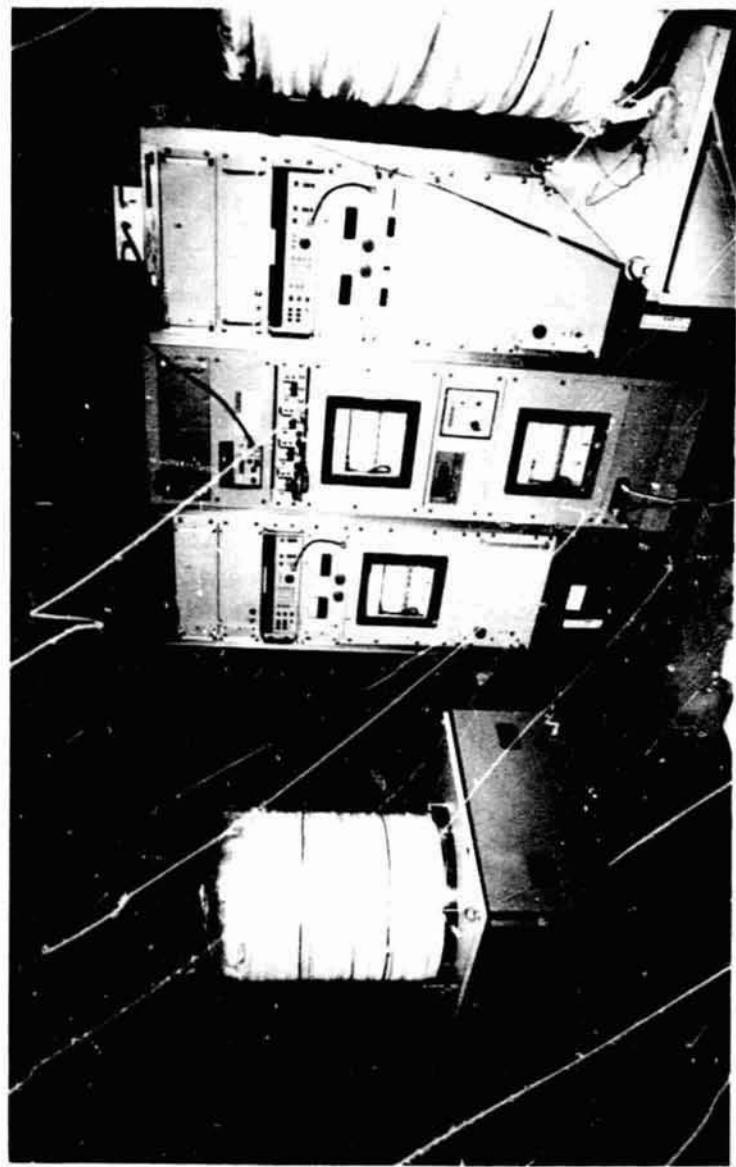
Fig.1   The hydrogen masers for K-3 VLBI system
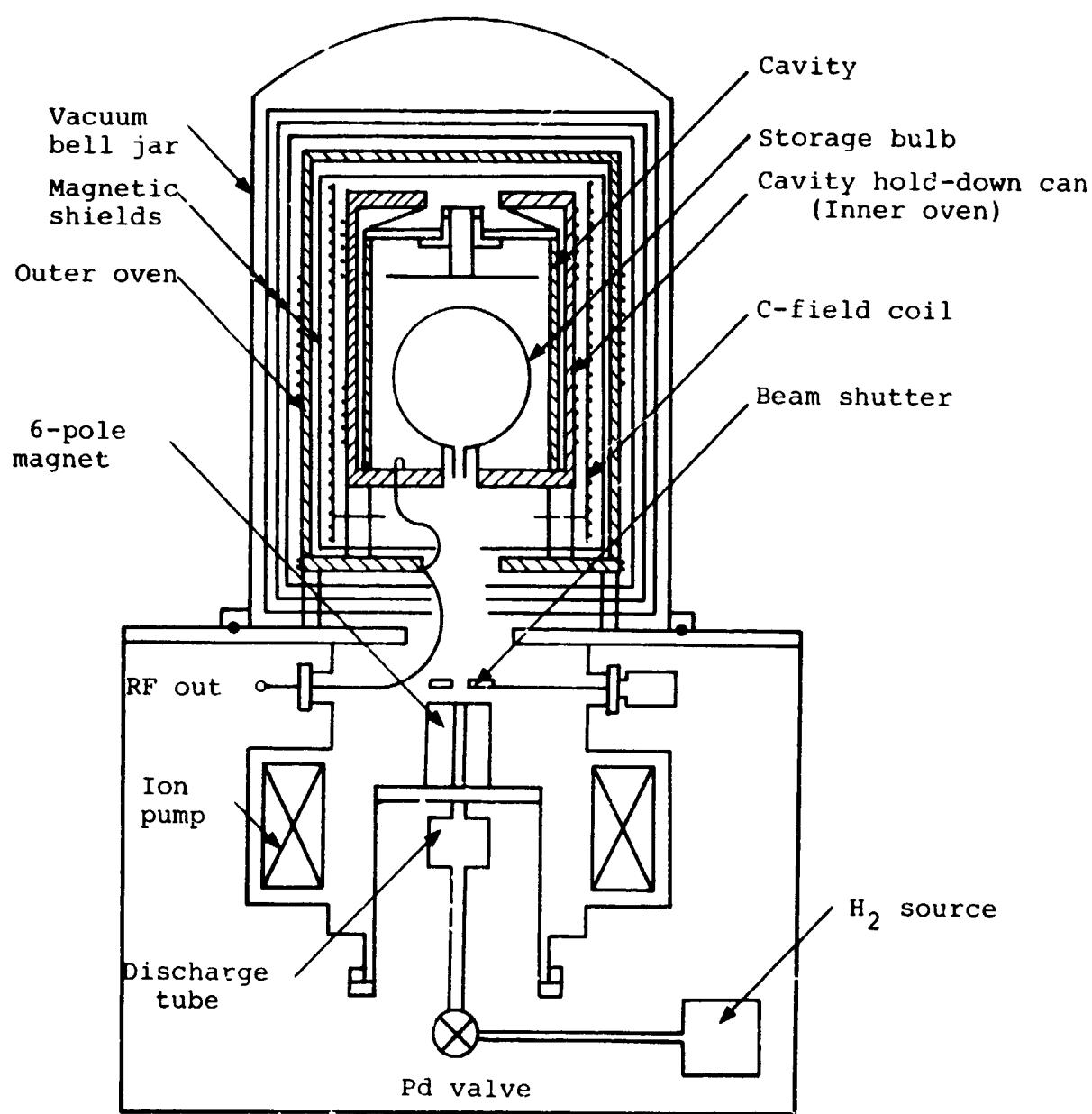
Fig.2 Structure of the maser for K-3 VLBI system
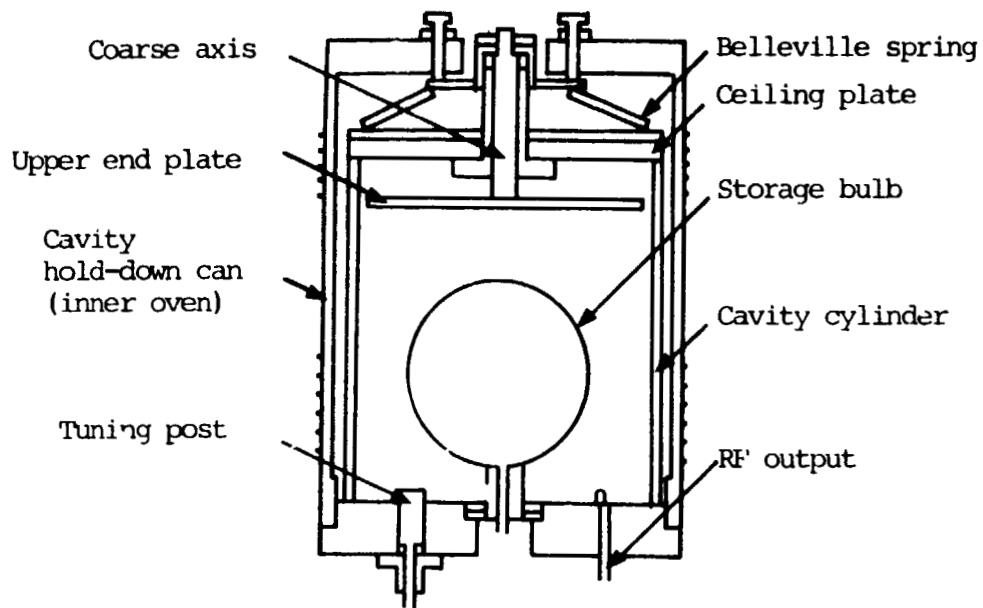
Fig.3 Structure of the cavity
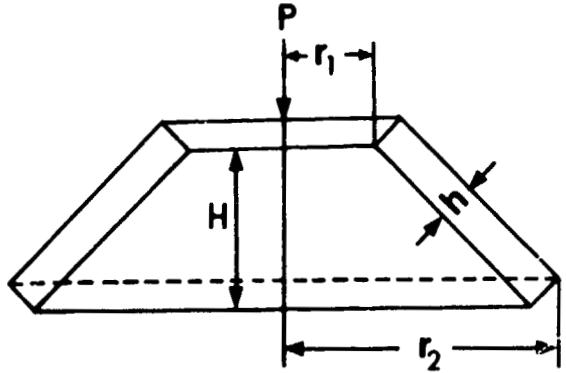
Fig.4 Belleville spring
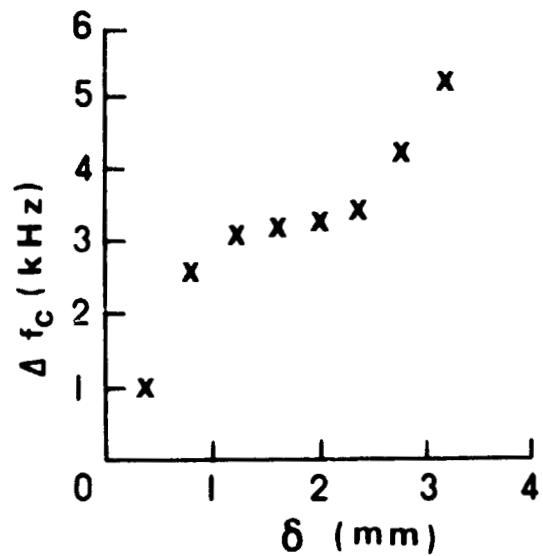
Fig.5 Stabilization of cavity
by Belleville spring

Peltier module controller

Synthe-sizer

x2

IF out

Filter

VCXO (10MHz)

Filter

20dB

Filter

60dB

60dB

x140

Distri-bution amplifier

1PPS generator

60dB

Varactor control sig.

Maser sig. in

Preamp. out (1.42GHz)

Local out (1 40GHz)

10MHz Std. out

1PPS out

Fig.6   Block diagram of the phase-lock receiver

307

#1 RF In
(1.42GHz)

10MHz Std. In

#2 IF In

#2 Local In
(1.40GHz)

Beat out

Varactor
control sig.1

Varactor
control sig.2

Shutter
control sig.1

Shutter
control sig.2
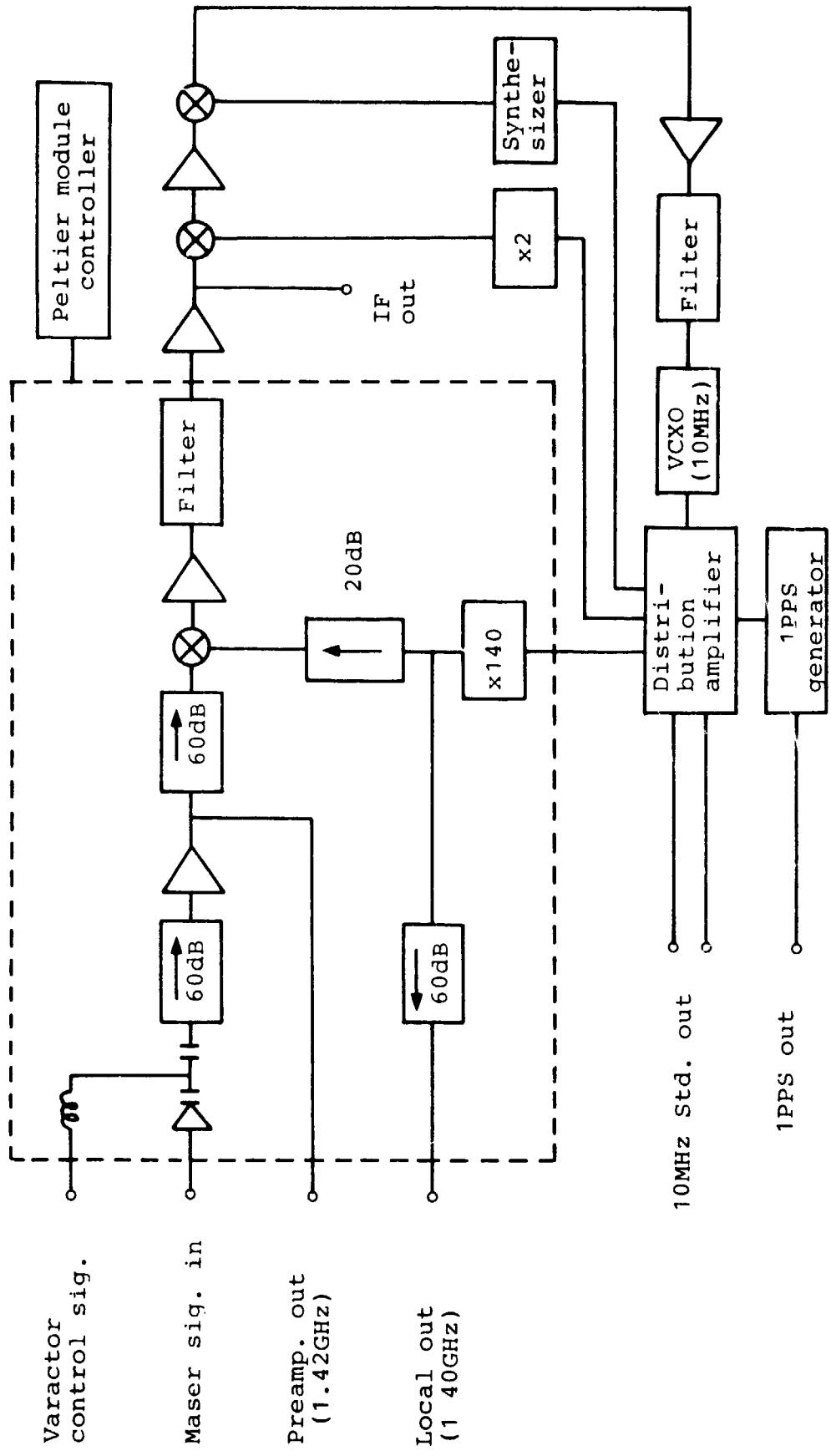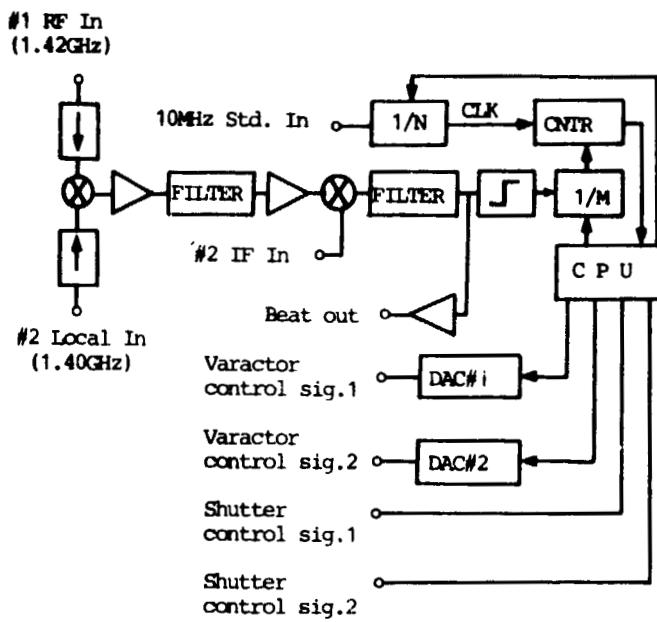
Fig.7 Block diagram of auto-tuner
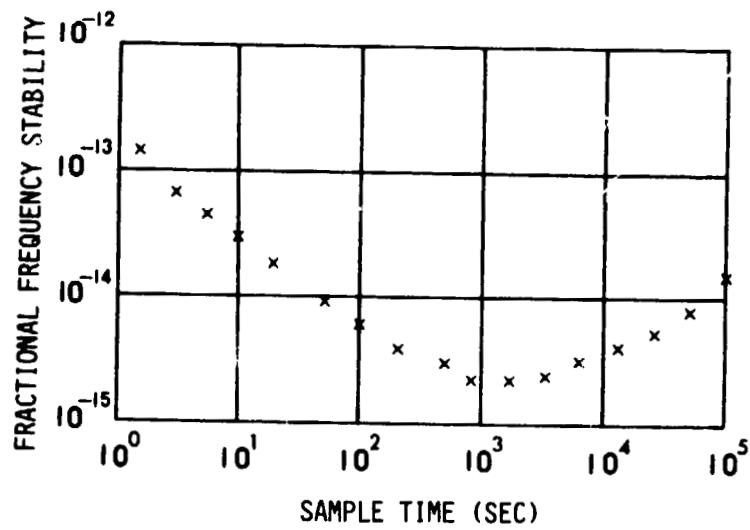
Fig.8 Frequency stability of the masers
for K-3 VLBI system
298

308
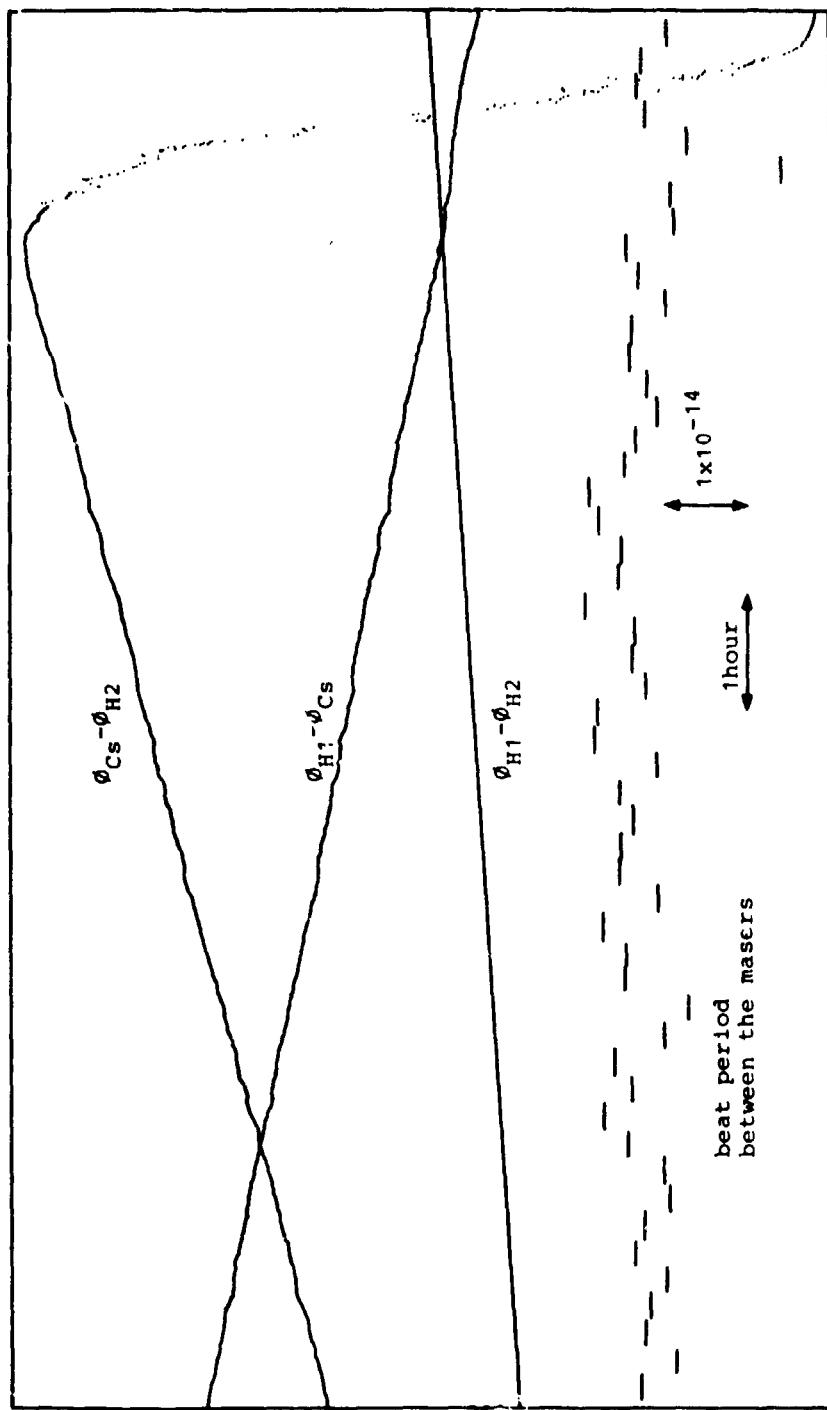
Fig.9 Chart record of the beat period and 10MHz phase
comparison between the masers and a commercial Cs
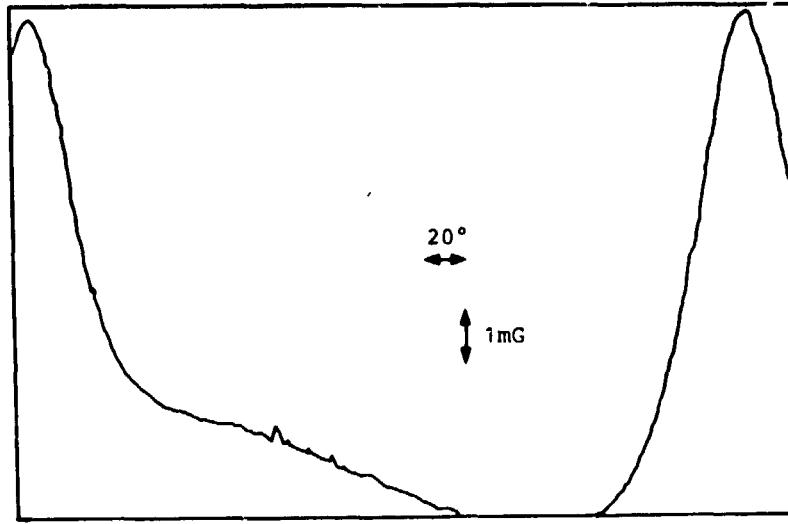
Fig.10 Change of the external magnetic field
        when azimuth of the antenna is sweeped
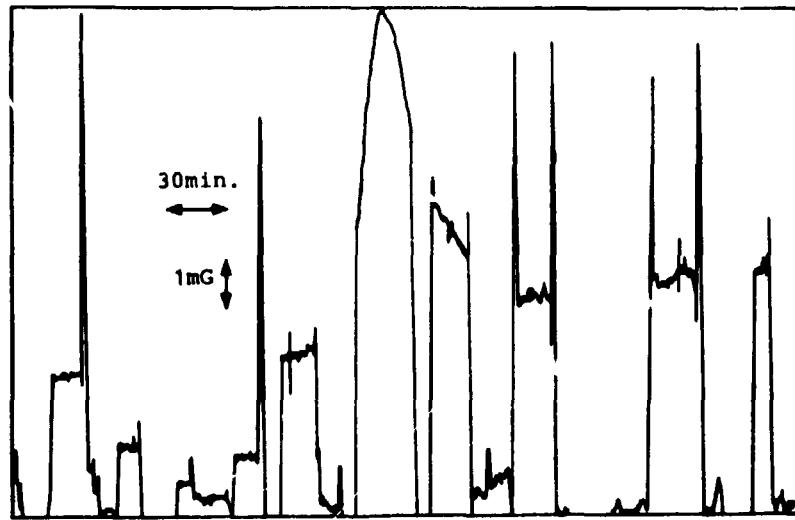
Fig.11 Change of the external magnetic field
        during the VLBI experiment

310

QUESTIONS AND ANSWERS

LAUREN RUEGER, JOHNS HOPKINS: Did you have both of the field operable masers at the site in you operating mode, or did you have only one?

MR. MORIKAWA: We have two hydrogen masers at the VLBI station. We used the first maser as the frequency source, and the other is used as a monitor, but the second maser can, of course, distribute standard signals to the system if the first maser has some trouble.

ALBERT KIRK, JET PROPULSION LABORATORY: What is the output power of the maser?

MR. MORIKAWA: It depends on the flux of the hydrogen beam. The maximum power is minus 95 dBm.

MR. KIRK: For the data that you have shown on the graph, what is the output power while that data was taken?

MR. MORIKAWA: Minus 95 dBm.

MR. KIRK: How long do you expect the ion pumps to last?

MR. MORIKAWA: About two years or more. One maser operated about two years, at which time the ion pump went down, but it recovered.

MR. MCCOUBREY: And they operated continuously during this time?

MR. MORIKAWA: Yes.

VICTOR REINHARDT, HUGHES AIRCRAFT COMPANY: In the Allan variance data you showed, was the drift removed?

MR. MORIKAWA: It was not removed.

MR. REINHARDT: What was the frequency drift per day?

MR. MORIKAWA: a few parts in ten to the minus 14.

ATOMIC HYDROGEN MASER ACTIVE OSCILLATOR
CAVITY AND BULB DESIGN OPTIMIZATION

H. E. Peters and P. J. Washburn

Sigma Tau Standards Corporation
Tuscaloosa, Alabama

ABSTRACT

The performance characteristics and reliability of the active oscillator atomic hydrogen maser depend upon "oscillation parameters" which characterize the interaction region of the maser: the resonant cavity and atom storage bulb assembly. With particular attention to use of the cavity frequency switching servo (1) to reduce cavity pulling, it is important to maintain high oscillation level, high atomic beam flux utilization efficiency, small spin exchange parameter and high cavity quality factor. It is also desirable to have a small and rigid cavity and bulb structure and to minimize the cavity temperature sensitivity. In this paper we present curves for a novel hydrogen maser cavity configuration which is partially loaded with a quartz dielectric cylinder and show the relationships between cavity length, cavity diameter, bulb size, dielectric thickness, cavity quality factor, filling factor and cavity frequency temperature coefficient. The results are discussed in terms of improvement in maser performance resulting from particular design choices.

INTRODUCTION

In an atomic hydrogen maser, hydrogen atoms are produced in an RF discharge source from which they emerge and pass in a beam through a magnetic state selector, with atoms in the proper hyperfine energy level passing to a quartz storage bulb mounted within a cavity resonant at the hydrogen frequency wherein maser action occurs, producing a CW output signal at the frequency of 1,420,405,751.689,3xx Hz. Figure 1 illustrates the major elements of the physical structure of masers currently constructed at Sigma Tau Standards Corporation. Several of the advantages of this general configuration were described in Reference 1. The optimization of the cavity assembly through computer analysis of the relevant maser oscillation parameters will be the primary subject of this paper.

CAVITY DESIGN AND ELECTROMAGNETIC FIELD DIAGRAM

The cavity configuration used in the Sigma Tau hydrogen masers is illustrated in Figure 2. A copper cylinder and copper end plates form the cavity walls. A relatively thick circular cylinder of quartz is held by spring tension between the end plates, and the quartz atom storage bulb is secured to the quartz cylinder using quartz shims and hard epoxy. The quartz cylinder provides dielectric loading to reduce the outer diameter of the cavity as well as the temperature sensitivity, and at the same time provides rigid support for the bulb and a fixed spacing of the cavity end plates. The electromagnetic field mode is the TE011 mode of the usual hydrogen maser active oscillator. Figure 2 also illustrates the orientation of the electric and magnetic field lines.

Figure 3 shows a diagram of the cavity and bulb assembly which is the model used for subsequent computations. The region within the inner diameter of the storage bulb is Region 1 with the dielectric constant of vacuum. In computing the filling factors, integrations of the z axis magnetic field were performed numerically over the inside volume of the bulb. Region 2, with the dielectric constant of fused quartz, includes the quartz wall of the bulb as well as the wall thickness of the quartz cylinder. The approximation is used that the quartz wall of the bulb ends is equivalent to the effect of the extra wall thickness at the ends of the cylinder, and this is a very adequate approximation since the cavity fields are relatively weak in the end regions and the bulb wall is relatively thin. Region 3, with the dielectric constant of vacuum, extends from the quartz cylinder to the copper side wall of the cavity.

OPERATIONAL EQUATIONS OF THE HYDROGEN MASER

Reference (2) presented the basic operational equations for the hydrogen maser oscillator, and the maser equations presented herein will either be taken from or derived from that reference. By combining equations (15) and (9) of Reference 2, the following equation is obtained for the relative power radiated by the hydrogen atomic beam:

$$P/Pa = 1 - I/Ith - 3q - 2q^2 (I/Ith).$$

In this equation, P is the radiated power, Pa = the power available from the beam if the maser were 100 percent efficient, I is the beam intensity (atoms/second), Ith is the flux required for oscillation if spin exchange could be neglected, and q is the spin exchange parameter defined in Reference (2).

Spin exchange is due to collisions between hydrogen atoms within the maser storage bulb and is the main factor which limits the possible oscillation level and line Q of the hydrogen maser. Figure 4 illustrates the severe limitation on beam utilization efficiency as the spin exchange parameter becomes large. The dependence of the spin exchange parameter on the cavity assembly configuration may be expressed (from Ref .2, Eq. 11) as:

$$q = Kl/(n'x \ Qc)$$

where K1 is a constant (approximately equal to 1,000), Qc is the loaded quality factor of the cavity, and η' is the "filling factor," which is defined as:

$$n' = \frac{V_b}{V_c} \frac{\langle H_z \rangle_b^2}{\langle H^2 \rangle_c} .$$

In the foregoing equation, Vb is the bulb volume, Vc the cavity Volume, $\langle H_z \rangle_b$ is the z axis magnetic field averaged over the bulb volume and $\langle H^2 \rangle_c$ is the average of the square of the magnetic field over the volume of the cavity.

Considering only those factors which depend on the cavity configuration, Ith may be expressed as:

$$Ith = K2 \times (bulb\ dia.)/(n' \times Qc).$$

Therefore both the spin exchange parameter and the flux required to oscillate depend upon the product of n' and Qc. The loaded quality factor of the cavity, Qc, is given by:

$$Qc = Qo/(1 + Pc/Po)$$

where Pc is the power coupled from the cavity which is available to the receiver input amplifier and Po is the power dissipated within the cavity.

In a practical hydrogen maser oscillator it is very desirable that the coupling of the receiver to the cavity be light to reduce cavity frequency dependence on receiver impedance changes or other external environmental effects, and so Pc/Po is typically a small fraction (of the order of .1 to .3). The above considerations indicate that it is highly desirable to maximize the product of n' and Qo to obtain an efficient and reliable maser oscillator.

ELECTROMAGNETIC FIELD ANALYSIS

The electromagnetic field analysis follows conventional procedures and will not be given in detail in this paper. In outline, we start from Maxwell's equations for the curl of the electric and magnetic fields in material media and use the expressions for the curl in cylindrical coordinates. The general known solution for the electric field is expressed in terms of Bessel's functions of the first and second kinds of orders 0 and 1, and by application of appropriate boundary conditions, differentiations and integrations, several simultaneous equations are obtained which describe the electric and magnetic field coordinate components in the separate cavity regions identified in Figure 3. A computer was then programmed to obtain subroutines for the fields and the subroutines were used in further calculations to obtain the data presented in the pages which follow.

Typical results for the field analysis are illustrated by Figures 5 and 6, which show the electric and z axis magnetic fields for a cavity 12 inches long with a bulb 4.13 inches in diameter having several different thicknesses of quartz cylinder.

Q x n', CAVITY SIZE AND TEMPERATURE COEFFICIENT

In the curves which follow it has been assumed that the dielectric loss factor of quartz is .000,1 and the dielectric coefficient is 3.75. Also, the electrical conductivity of copper = 2.0 microohm-cm and the expansion coefficient of copper = 1.7 x 10-5. The length of the bulb for the 12 inch long cavities is 9.0 inches, and the assumed shape is a straight central section with hemispherical ends. This shape is not quite optimum, but is a practical approximation which more detailed calculations show is very close to optimum. For cavity lengths other than 12 inches, the bulb length was made proportionately greater or smaller. In calculating the cavity frequency temperature coefficients, both the expansion coefficient of quartz and the variation of the dielectric coefficient of quartz with temperature have been ignored since these have a small effect compared to the thermal properties of copper.

It is interesting to observe the separate behavior of the quality factor and the filling factor as the thickness of the quartz dielectric is increased. The general form of the curves for all cases considered is exemplified by the case of the 12 inch long cavity and 4.13 inch diameter bulb shown in Figure 7. While the quality factor continuously decreases with increased dielectric loading, the filling factor rises to a peak in the range of .5 to 1.5 cm before decreasing. Therefore the use of thin-walled quartz bulbs in conventional oscillating hydrogen masers is not in general the optimum configuration to obtain the highest value of (n' x Q).

Figure 8 illustrates the variation of (Q x n') and cavity radius for several different lengths of cavity and one bulb diameter. This figure shows that there is a significant improvement in these parameters with longer cavities, and also that the optimum conditions occur with a relatively thick quartz cylinder. Figures 9 through 13 show the effect of use of different diameter bulbs and different thicknesses of quartz in cavity lengths of 18, 14, 12, 10 and 8 inches.

One of the motivations for adding quartz dielectric loading to the cavity is to reduce, as much as possible, the cavity frequency temperature sensitivity. Figures 14, 15, and 16 show the cavity frequency temperature coefficient as a function of dielectric thickness for several interesting cases. Figure 14 shows the temperature coefficient for a fixed cavity length of 12 inches and three different bulb radii. For reference, a copper cavity without loading would have a temperature sensitivity of approximately 24.0 KHz/Degree C. Figure 15 shows the result for a bulb radius of 5.25 cm and two different cavity lengths, and Figure 16 shows the result for a 4.25 cm bulb and three cavity lengths.

DISCUSSION OF RESULTS

The analysis and results presented in this paper were undertaken to optimize the hydrogen maser cavity and bulb design based upon the general configuration represented in Figures 1, 2 and 3. A primary consideration

has been that successful use of the cavity frequency switching servo technique requires very good maser output signal to noise ratio and the best possible efficiency in use of the power available in the state selected atomic hydrogen beam. It is evident that these goals can be achieved in masers with different application requirements.

For example, if small size and portability are not too important, and the highest possible line Q and smallest wall shift are desired, a large diameter bulb and long cavity would be the logical choice. As shown in Figure 9, with an 18 inch long cavity and a 6.75 cm radius bulb the best $(Q \times n')$ value occurs for minimum quartz thickness. The minimum practical bulb wall is approximately .15 cm, and using a relatively thin quartz cylinder of .25 cm wall, the cavity radius would be about 12.5 cm (9.85 inch diameter cavity), and $(Q \times n') = 27,000$. Using a cavity coupling coefficient of .25 one would calculate from the equations previously given that the spin exchange parameter q = .046. This would be a very efficient maser oscillator, and with the exception of the high Q copper cavity is very similar in size and bulb volume to masers constructed in the past at NASA, Goddard Space Flight Center (3).

To make somewhat smaller size masers without compromizing efficiency or stability significantly, one might choose a 12 inch long cavity. It is seen in Figure 8 that the improvement in $(Q \times n')$ is not great when increasing the length beyond 12 inches. For a 5.25 cm radius bulb (4.13 inches diameter) and .5 cm dielectric thickness, the resultant cavity radius would be about 12.2 cm (9.6 inches diameter) and the calculated spin exchange parameter with .33 cavity coupling is .039; these are the dimensions and parameters for the masers reported in Reference 1. These masers have extremely good efficiency, and are the first hydrogen masers to successfully use the cavity frequency switching servo technique to control cavity pulling. As cavities shorter than 12 inches are chosen, there is an increasing penalty in both $(Q \times n')$ and cavity diameter. For the larger bulb sizes in short cavities the maser becomes less efficient, and if the cavity wall material has a realized electrical conductivity much less than that of copper, a very borderline oscillator will result.

The use of copper as the cavity wall material has important advantages from several points of view. In addition to good electrical conductivity, giving high cavity Q, it has high specific heat which results in relatively large thermal mass. Systematic thermal perturbations are a most important consideration in attempts to improve stability for measuring intervals of about 1,000 seconds and longer, and the large thermal capacitance reduces the rate at which the cavity frequency can change, and also relaxes the required response time of thermal control systems or automatic cavity tuners.

The cavity frequency temperature coefficients illustrated in Figures 14, 15 and 16 are relatively low in comparison to an unloaded metal cavity. In practice, the average cavity frequency is controlled in our present designs by changing the temperature; this has the advantage of a relatively wide, linear and smooth cavity frequency control range, and the cavity, coupling loop, and cavity frequency switching varactor are automatically held at constant temperature by the control servo. If the cavity were made of a low expansion material such as silvered fused silica, it would be necessary

317

to control the average cavity frequency with a varactor; not only would this result in a non-linear and narrow frequency control range, it would introduce the possibility of changing the cavity Q's or receiver coupling coefficient when modulating the cavity frequency. So the use of a metal cavity with the cavity frequency switching servo is strongly indicated, and the temperature dependence shown by the figures is well suited to the requirements of cavity tuning.

CONCLUSION

The results presented in this paper provide guidelines for the design of cavity and bulb assemblies for hydrogen masers in an optimal fashion which are well adapted to use of the cavity frequency switching servo technique, as well as information which should be of more general interest for consideration of alternative maser cavity assembly design approaches. The two hydrogen masers described in Reference 1 were the first masers constructed using the new configuration. These masers also demonstrated the first use of the cavity frequency switching servo, and the stability results obtained show that unprecidented stability as well as the other advantages discussed in this paper can be realized. An example of the long term stability obtained in recent maser comparisons is illustrated in Figure 17. This figure shows the fractional frequency change for a thirty day period between the two hydrogen masers described in Reference 1. The slope of the frequency differences over this period is 5.8 x 10-16 per day, so the effect of drift on the daily frequency fluctuations is neglegible. Figure 18 shows the measured stability in a "Sigma Tau" plot using the two sample "Alan Variance" for intervals from one second to ten days. There has been no drift term removed, nor other modifications made to the data.
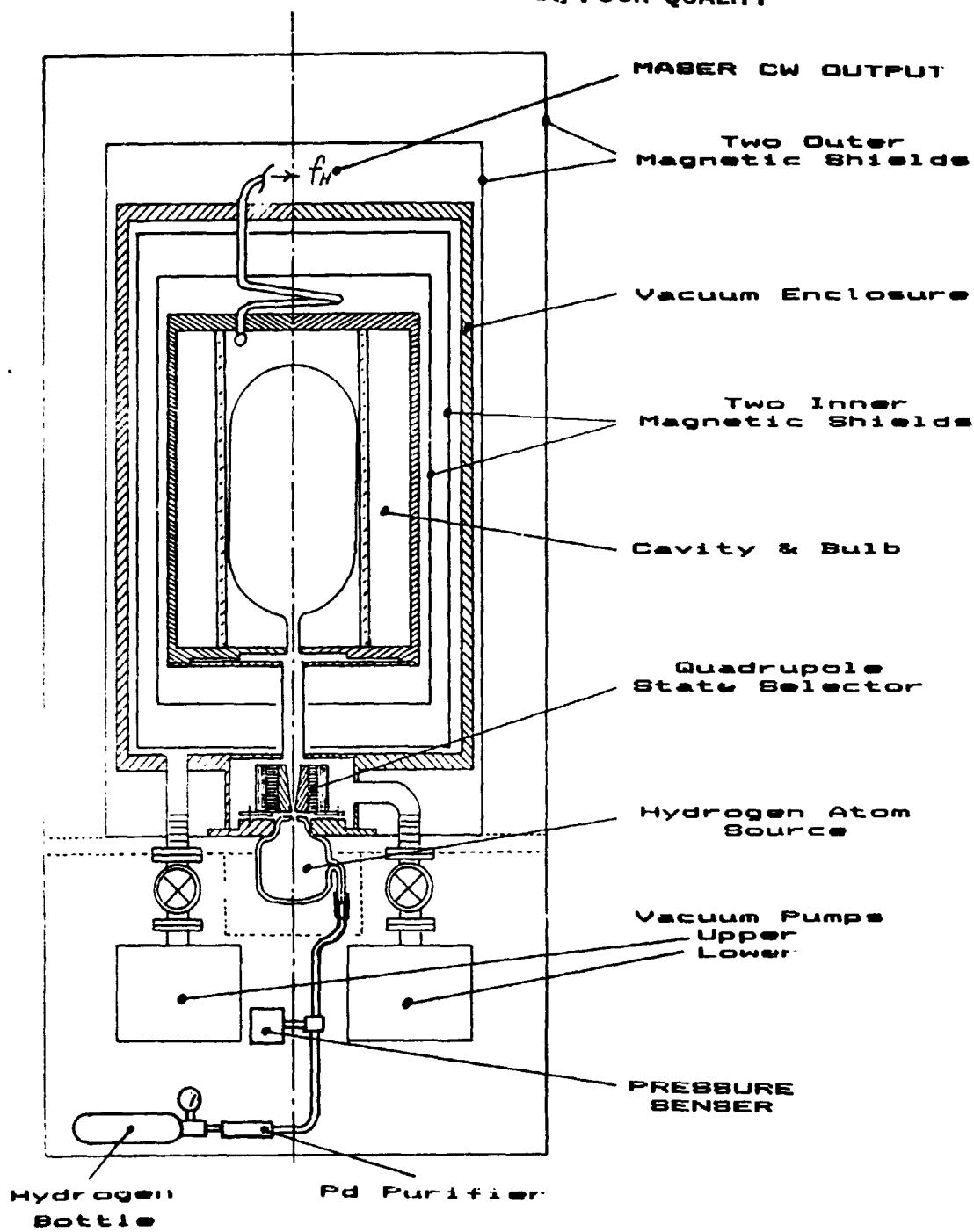
ACKNOWLEDGEMENTS

REFERENCES
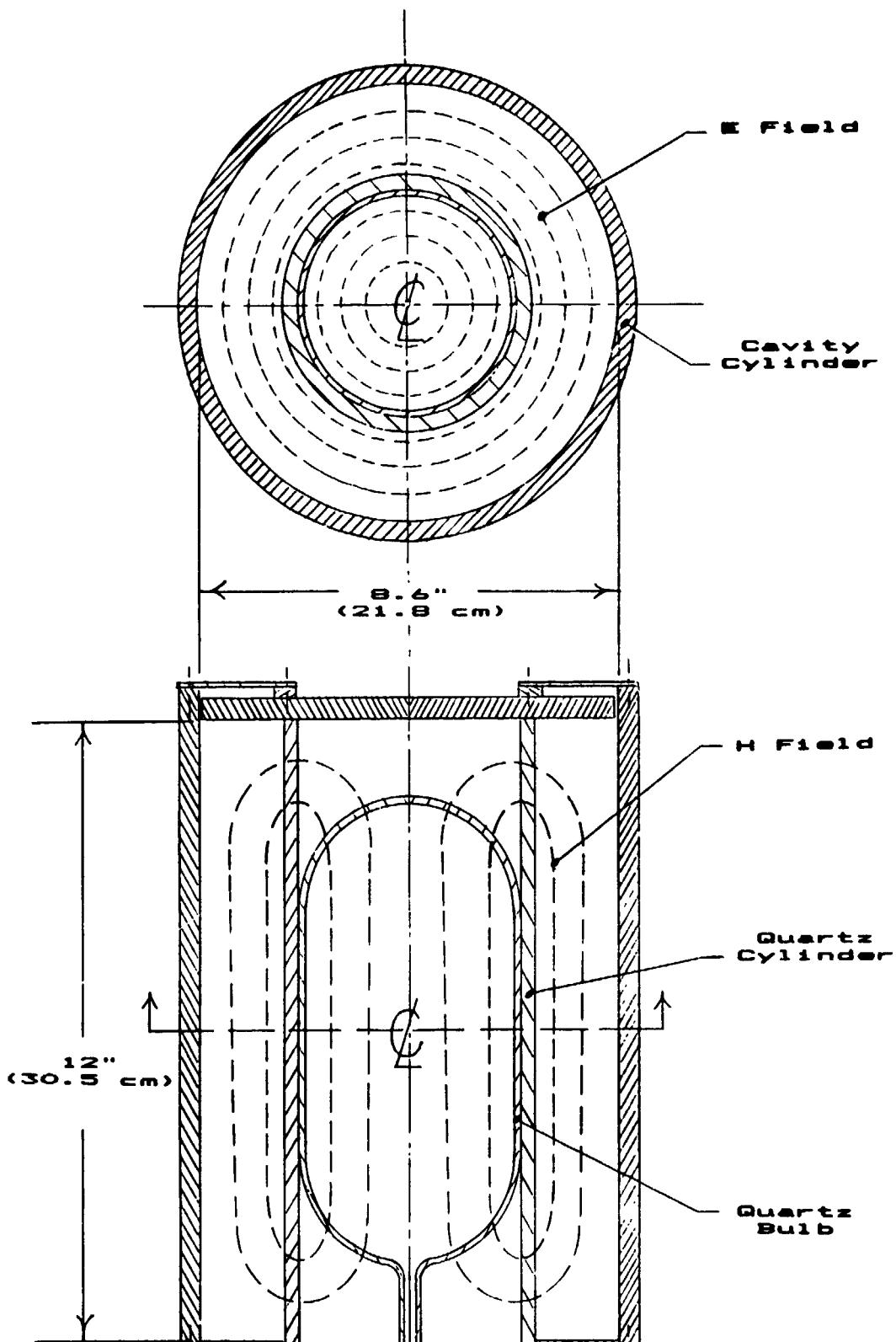
1. H. E. Peters, "Design and Performance of New Hydrogen Masers Using Cavity Frequency Switching Servos," Proceedings, 38th Annual Symposium on Frequncy Control, 1984.

2. D. Kleppner, et al. "Hydrogen Maser Principles And Techniques," Phys. Rev., Vol. 138, No. 4A, A972-A983, 17 May, 1965.

3. Victor S. Reinhardt, et al. "NASA Atomic Hydrogen Standards Program - An Update," Proceedings, 30th Annual Symposium on Frequency Control, 1976.

MASER CW OUTPUT

Two Outer Magnetic Shields

Vacuum Enclosure

Two Inner Magnetic Shields

Cavity & Bulb

Quadrupole State Selector

Hydrogen Atom Source

Vacuum Pumps Upper Lower

PRESSURE SENSER

Hydrogen Bottle

Pd Purifier

f_H
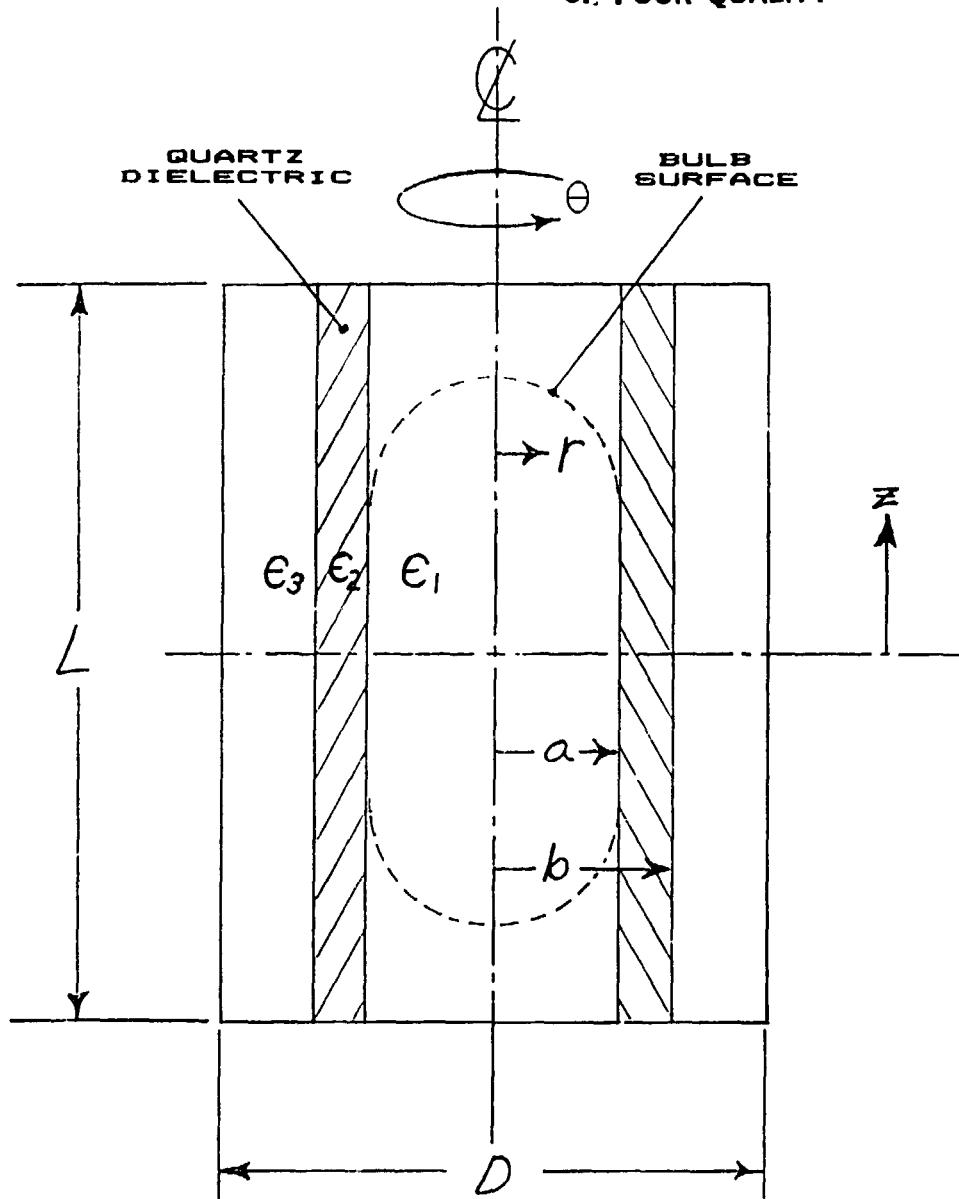
HYDROGEN MASER PHYSICAL ASSEMBLY

Figure 1.

319

E Field

Cavity
Cylinder

8.6"
(21.8 cm)

H Field

Quartz
Cylinder

12"
(30.5 cm)

Quartz
Bulb

HYDROGEN MASER CAVITY
Figure 2.

320

CAVITY ANALYSIS MODEL

Figure 3.

Figure 4.

Figure 5.

Figure 6.

324

QUALIY FACTOR (Qo)
Vs
DIELECTRIC THICKNESS

QUALITY FACTOR (X 1,000)

Cavity Length
28.48 cm
(12")

Bulb Diameter
10.5 cm
(4.13")

FILLING FACTOR (n')
Vs
DIELECTRIC THICKNESS

FILLING FACTOR - n'

$n' = \dfrac{\int_{VRS} H_R^2 \, b}{\int_{VC} H^2 \, c}$

DIELECTRIC THICKNESS - cm

Figure 7.

QUALITY FACTOR x FILLING FACTOR
Vs DIELECTRIC THICKNESS

Bulb Diameter
10.5 cm
(4.13")

CAVITY RADIUS
Vs DIELECTRIC THICKNESS

DIELECTRIC THICKNESS — cm

Figure 8.

Figure 9.

QUALITY FACTOR × FILLING FACTOR
Vs DIELECTRIC THICKNESS

Cavity Length.
35.56 cm
(14")

CAVITY RADIUS
Vs DIELECTRIC THICKNESS

Bulb radius – cm

Figure 10.

**QUALITY FACTOR × FILLING FACTOR
Vs DIELECTRIC THICKNESS**

Cavity Length
30.48 cm
(12")

CAVITY RADIUS
Vs DIELECTRIC THICKNESS

Bulb radius — cm

7.25
6.75
6.25
5.75
5.25
4.75
4.25
3.75

Bulb radius — cm

DIELECTRIC THICKNESS — cm

Figure 11.

QUALITY FACTOR x FILLING FACTOR
Vs DIELECTRIC THICKNESS

Cavity Length
24.5 cm
(10")

Q x n - Thousands

CAVITY RADIUS
Vs DIELECTRIC THICKNESS

Bulb radius - cm

7.25
6.75
6.25
5.75
5.25
4.75
4.25
3.75

Bulb radius - cm

CAVITY RADIUS - cm

DIELECTRIC THICKNESS - cm

Figure 12.

Figure 13.

Figure 14.

TEMPERATURE COEFFICIENT
Vs
DIELECTRIC THICKNESS

Bulb radius

5.25 cm

Figure 15.

333

TEMPERATURE COEFFICIENT
vs
DIELECTRIC THICKNESS

Bulb radius
4.25 cm

Cavity Length

30.48 cm (20")

25.4 cm (10")

20.32 cm (8.0")

TEMPERATURE COEFFICIENT (KHz/Deg. C)

DIELECTRIC THICKNESS — cn

Figure 16.

334

Figure 17.

335
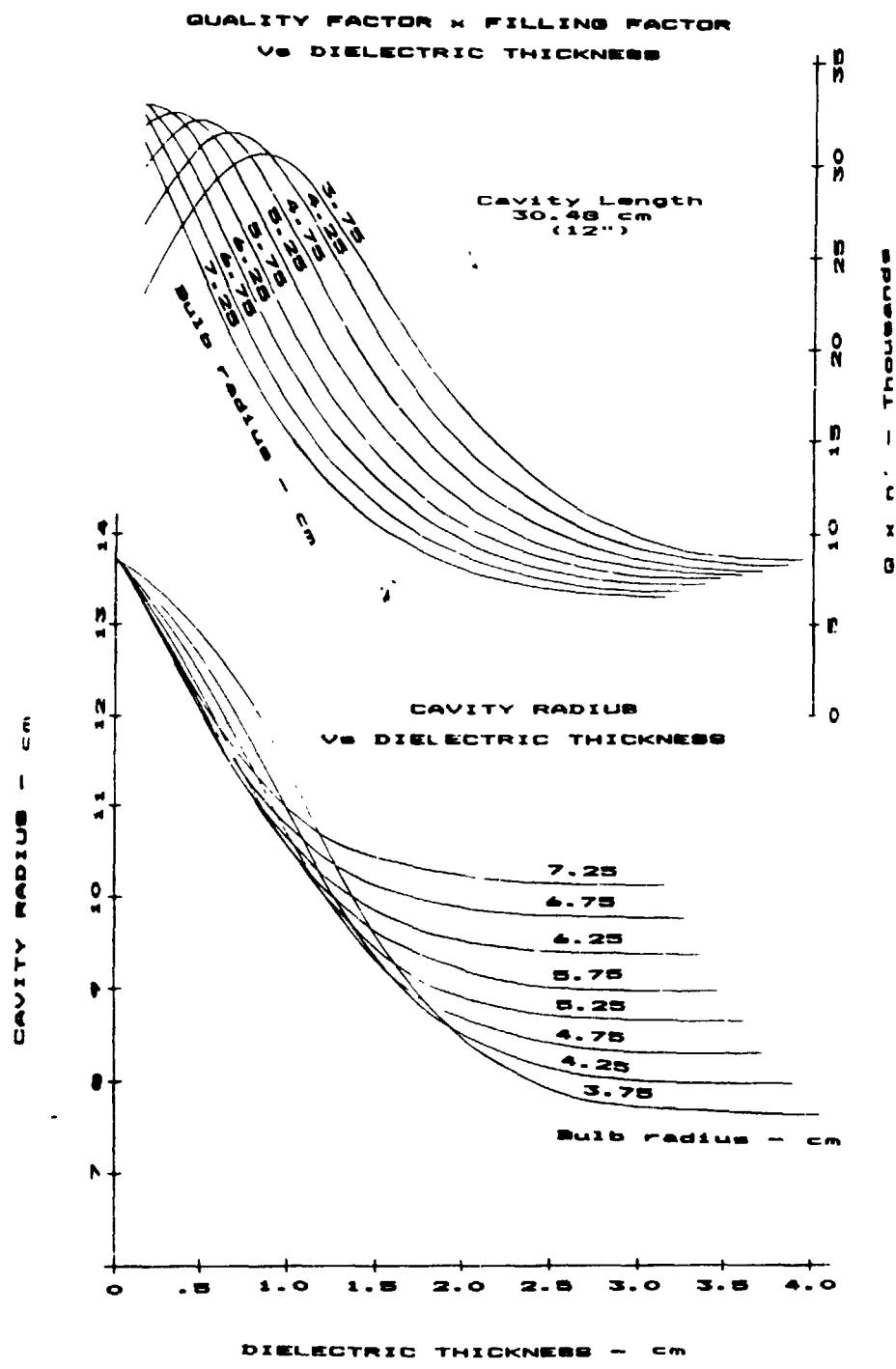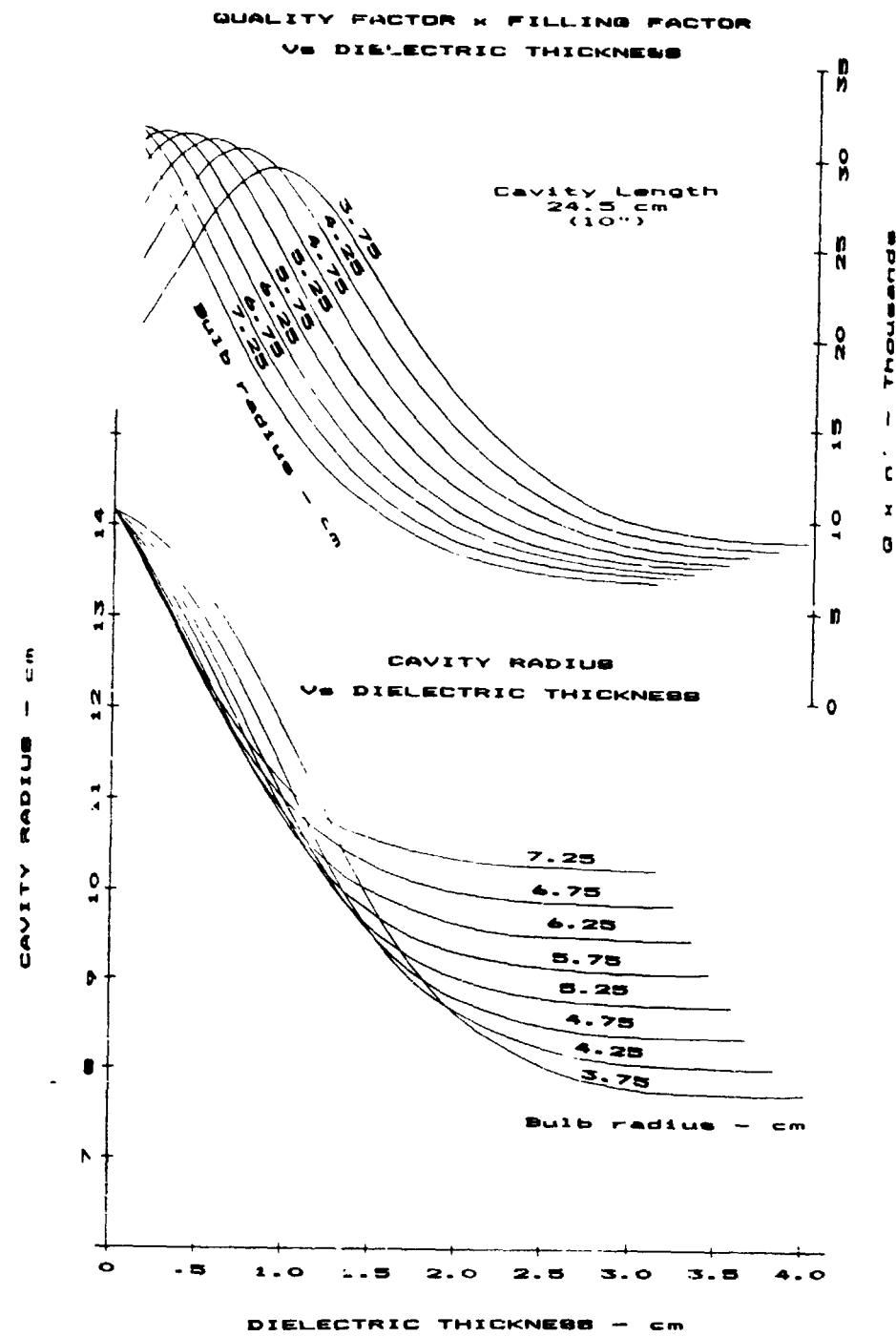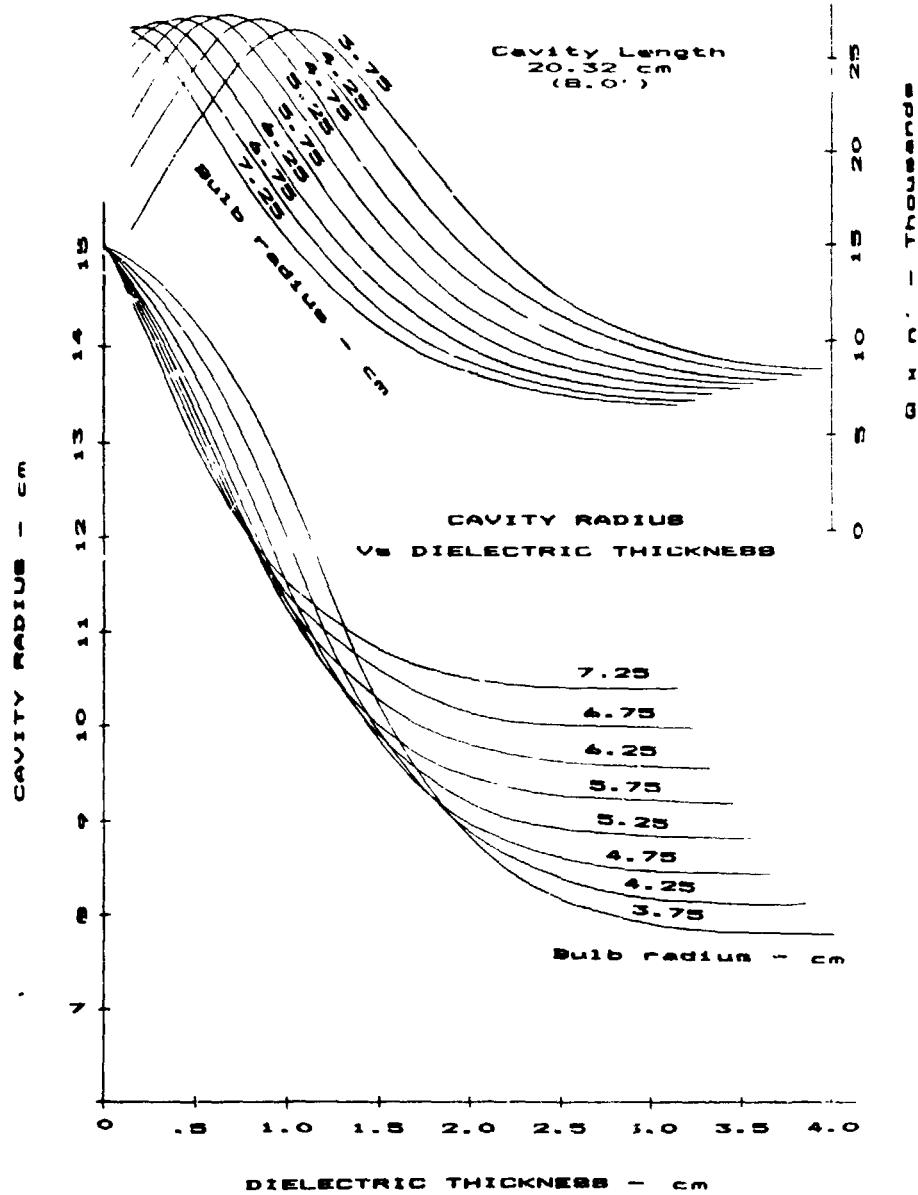
HYDROGEN MASER STABILITY

A-1 VS N-1

NO DRIFT REMOVED
Gnn Data
Oct. 14 - Nov. 18, 1984
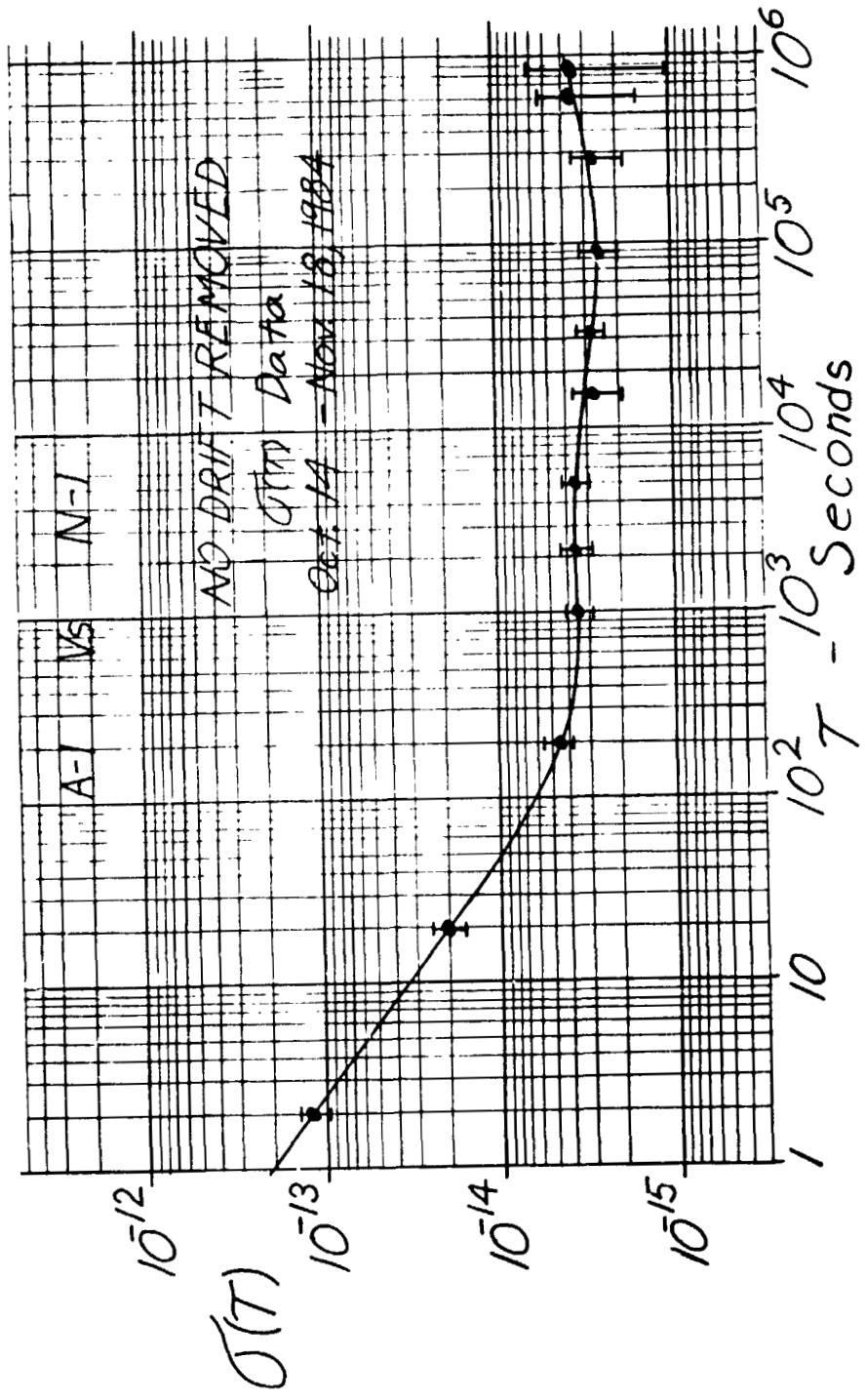
Figure 18.

JACQUES VANIER, NATIONAL RESEARCH COUNCIL: In your proposed design, would it not be simpler to remove the bulb and use the dielectric loading as a bulb itself?

MR. PETERS: Yes, that's very conceivable. I have been thinking of getting pieces of quartz ground out.

MR. VANIER: But there is no purpose for the bulb at the present time?

MR. PETERS: I haven't analyzed it completely, but I think that you need to improve the filling factor a little more by filling in the top section slightly.

STUART CRAMPTON, WILLIAMS COLLEGE: I would like to say that the last is not true when you take into account the way in which you are changing the volume of the bottle. You are better off than having those ground pieces.

MR. VANIER: You wouldn't increase the filling factor.

MR. PETERS: I think that even if you increase the bulb to the full length, that should be filled in with quartz, not make the bulb the full length of the cavity.

MR. VANIER: I see. But my question is this: You would gain in simplicity by removing the bulb completely, and use up to the end as a bulb. You would lose a little in filling factor, but so what?

MR. PETERS: You could lose something else very important though, the facility with which you could coat the bulb in a nice, clean, dependable way.

ALBERT KIRK, JET PROPULSION LABORATORY: Can you tell me the aging rate of the cavities before you apply the thermal corrections?

MR. PETERS: These are relatively unstable cavities. They are a thin wall of copper on the outside, compared to a much more thermally massive cavity. But they are still fairly respectable in that respect. One of them is going at about two to three parts in ten to the fourteen per day and the other one is about seven parts in ten to the fourteen per day.
    However, we tune continuously. All the stability data is taken with the autotuner system working, and there is no degradation in either the short term or the long term stability if you leave the cavity servo on. The cavity servo is really a thermal control system, so in that sense they don't drift.

MR. KIRK: What is the time constant of the servo system?

MR. PETERS: It's just about fast enough to come in where thermal perturbations start to become important. That is between one

thousand and ten thousand seconds.

MR. McCOUBREY: If I followed your discussion, you indicated that the long narrow cavity was advantageous with respect to the cavity Q and filling factor. Did you also consider the effect of the declining effectiveness of the magnetic shields that you put around all of this? The long narrow shields are less effective.

MR. PETERS: I think that they are more effective. The larger cavity diameter and the larger shield are shorter, and it's mostly the axial field that gives you trouble. The transverse shielding factor hardly ever gives any effect in measurement. The longer and narrower shield gives more space on the ends than wee had in the past, so you get a better shielding factor with a small diameter and also more space for thermal insulation, and vacuum and things like that.

MR. ALLAN: Is the last data point on your sigma-tau plot ten days?

MR. PETERS: I stopped it at ten days. It was only th.rty days worth of data.

HYDROGEN MASER OSCILLATION AT 10 K

S. B. Crampton, K. M. Jones, G. Nunes, and S. P. Souza

Williams College, Williamstown, Massachusetts 01267

ABSTRACT

We have developed a low temperature atomic hydrogen maser using frozen atomic neon as the storage surface. The maser has been operated in the pulsed mode at temperatures from 6 K to 11 K and as a self-excited oscillator from 9 K to 10.5 K.

INTRODUCTION

As soon as some unpolarized hydrogen atom gas had been successfully stored at 4.2 K in a bottle coated with frozen molecular hydrogen[1], it was clear that the new low temperature hydrogen storage techniques might improve atomic hydrogen maser frequency standards.[2] The most likely improvement is in the short term frequency noise, which is proportional to the radiative decay rate $1/T_2$ times the square root of the thermal noise divided by the averaging time and the power radiated by the atoms.[3] There is a dramatic decrease of the cross section for relaxation due to electron spin exchange collisions between the radiating atoms.[4] Because of collisions the radiated power is quadratic in input atomic beam flux and has maximum value proportional to the inverse of the spin exchange cross section squared. The potential improvement in radiated power is large, given sufficient beam flux. Fortunately, low temperature techniques can also provide a large gain of clean, state-selected beam flux. In addition, thermal noise power in the maser cavity and receiver first stage can be greatly reduced by cooling, and substantial improvements in radiative decay rates are anticipated. These factors should combine to produce an improvement by several orders of magnitude in the short term frequency noise of hydrogen maser standards.

Low temperature techniques may also offer substantial improvements in the long term frequency stability of hydrogen maser standards. Stability to one part in 10^{15} requires temperature stability to 7.3 mK, difficult to achieve at room temperature but routinely achieved at low temperatures. Stability to one part in 10^{15} requires stability of the cavity geometry equivalent to about $\cdot$ A in the linear dimensions; mechanical creep is literally frozen out at low temperatures. Magnetic field homogeneity and stability can be improved by using superconducting magnetic shields.

APPARATUS

Figure 1 is a schematic of the apparatus we have built to test these ideas. The apparatus is immersed in liquid helium held in a 6" ID superinsulated dewar. Molecular hydrogen is fed through a 1 cm OD pyrex tube inside a stainless steel "source dewar" separating the helium bath outside from a liquid nitrogen bath inside. The liquid nitrogen cooled 180 MHz rf discharge dissociates molecules to atoms, which pass downwards through an "accommodator" where they are cooled to 5 $^\circ$K and are then focused by a six pole state-selecting magnet to a 5 cm OD quartz storage bottle. The storage bottle is surrounded by a 4" OD 1420 MHz microwave cavity, a set of three 0.005" thick magnetic shields, and a vacuum tight can containing helium exchange gas, which allows the cavity and bottle to be heated uniformly to temperatures above the temperature of the liquid helium bath.

Figure 2 is a more detailed schematic of the hydrogen source and cavity assembly. Dissociated atoms pass from the discharge through a thin 2 mm ID orifice into the 5 mm ID by 1.5 cm long copper accommodator coated with solid molecular hydrogen. Semicircular baffles prevent atoms or impurities from getting through the accommodator without making about 100 collisions with its cold solid hydrogen surface. The accommodator is heated by recombining atoms or by an external heater, and it is cooled by a copper heat conduction path to the liquid helium bath. Slow moving H atoms are efficiently focused by a 1.3 cm bore by 10 cm long six pole permanent magnet through a 12 cm long by .75 cm ID entrance tube to the storage bottle. The cavity[5] provides a uniform rf magnetic field over the storage bottle and has unloaded Q as high as 20,000 at 4.2 K.

The inside surface of the storage bottle and its entrance tube are coated with several hundred thousand layers of solid molecular hydrogen or atomic neon, frozen out from the gas phase as the apparatus is cooled initially. Care is taken to control the gas pressure and temperature so as to form some liquid first, then the solid coating. Below the threshold for oscillation a short pulse at the $\Delta F=0$ hyperfine transiton frequency sets the atoms radiating on that transition, and the decaying cavity rf field is sampled by a coupling loop, converted to an audio frequency signal, and fed to the A/D converter and computer storage. The frequency and radiative decay rate are fitted directly from the signal, and level population recovery rates $1/T_1$ are determined from signals in response to multiple pulses. The signal amplitude, multiplied by T_1, is proportional to the input flux of $F=1$, $m_F=0$ hydrogen atoms.

Figure 3 shows the input flux of state-selected atoms plotted against the temperature of the accommodator as measured by a carbon film thermometer. The open circles represent fluxes obtained by varying the input of atoms to the accommodator. As the flux into the accommodator increases, heat due to atoms recombining on the solid hydrogen accommodator surface warms that surface. The accommodator temperature and output flux both rise with input flux and accommodator temperature until the accommodator temperature reaches about 5.3 K, where the saturated vapor pressure of H_2 over the surface becomes high enough to impede the flow. Above 5.3 K the accommodator temperature continues to rise, but the output flux actually decreases with increasing input flux. The crosses represent fluxes obtained by leaving the input flux at the level

340

FIGURE 1   SCHEMATIC OF THE APPARATUS

NITROGEN SOURCE DEWAR

PYREX TUBE

DISCHARGE COIL

ACCOMMODATOR

STATE SELECTING MAGNET

MAGNETIC SHIELDS

QUARTZ TUNING ROD

COUPLING LOOP

QUARTZ STORAGE BOTTLE

MICROWAVE CAVITY

SOLENOID

4"
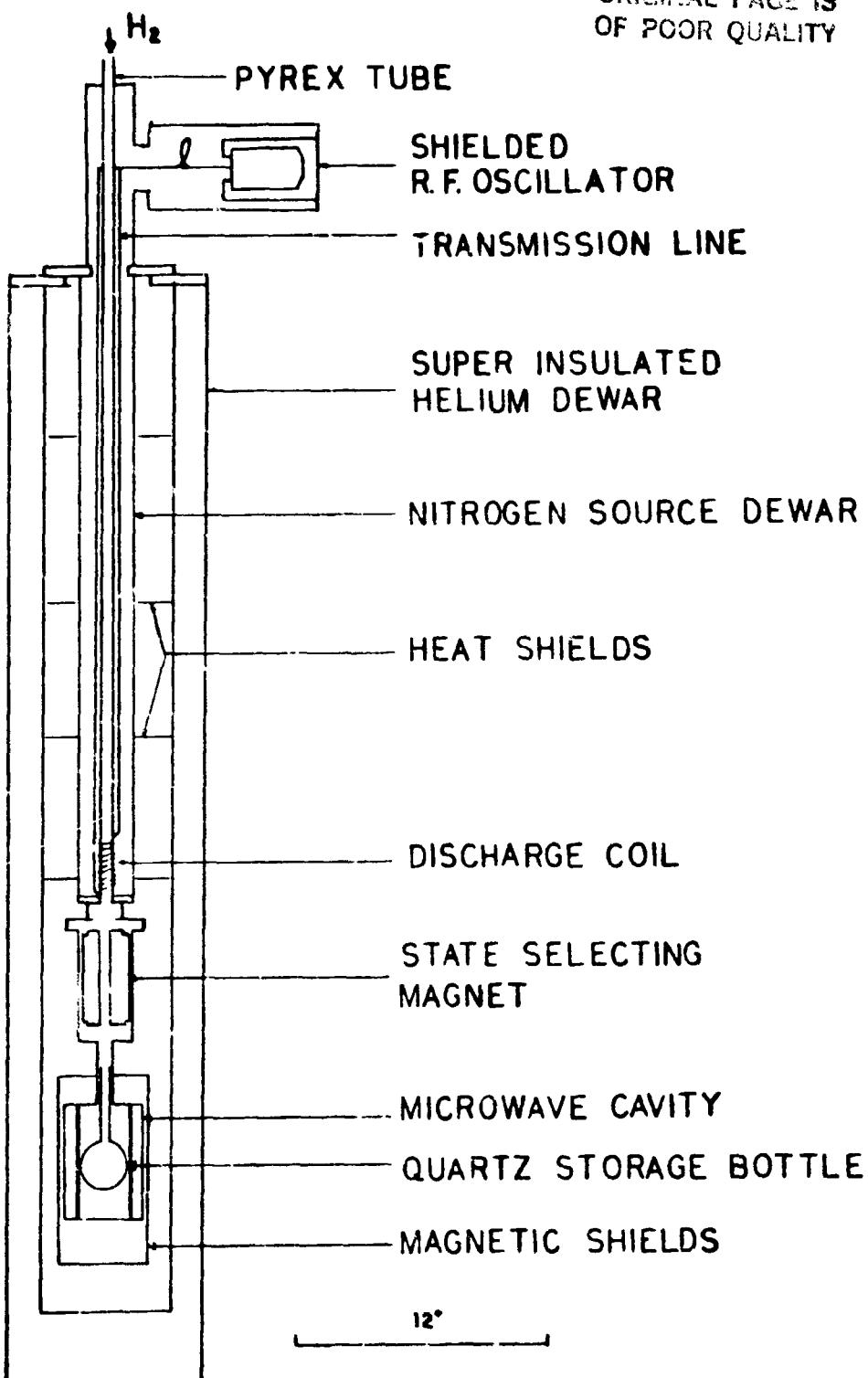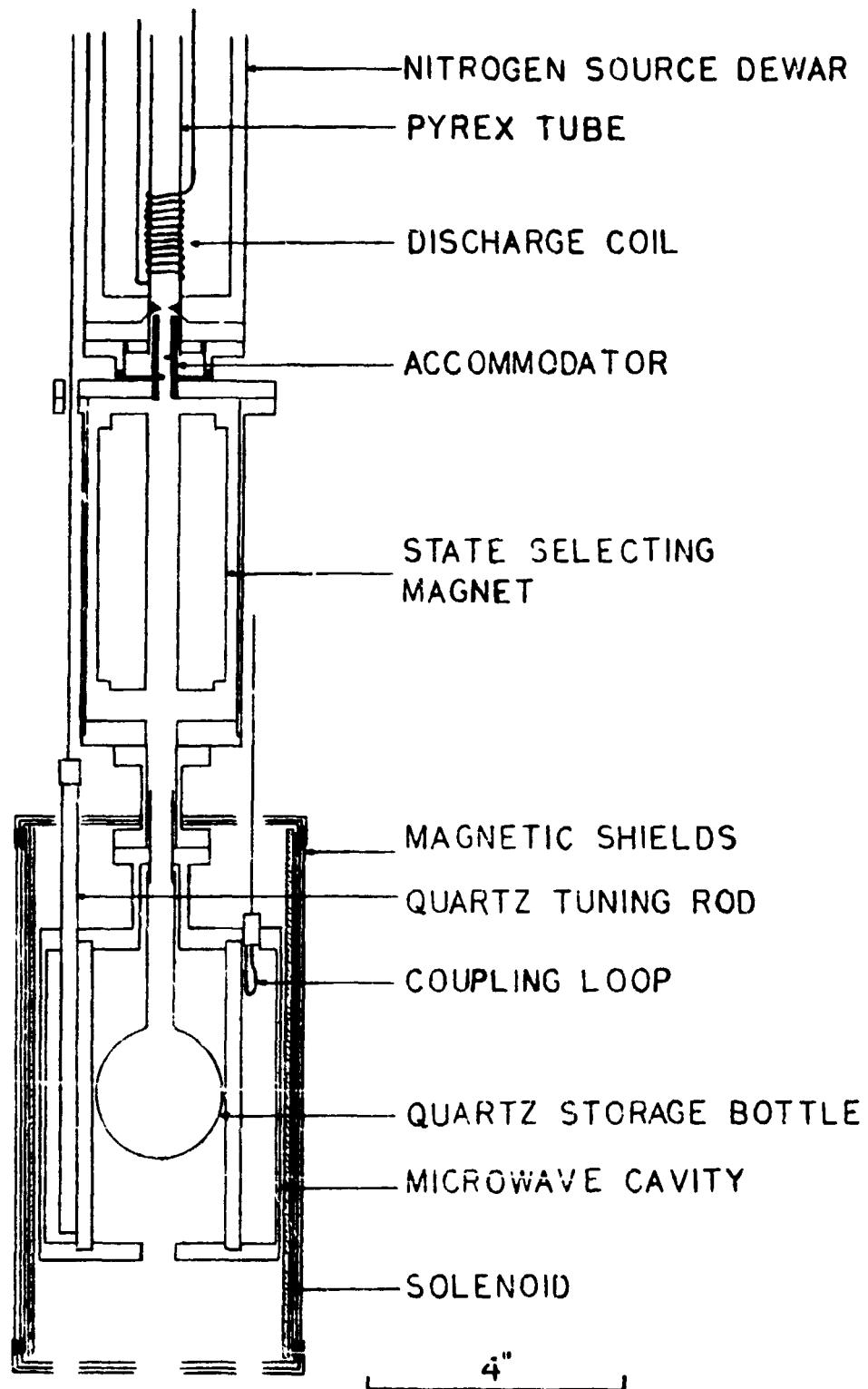
FIGURE 2   SCHEMATIC OF HYDROGEN SOURCE AND CAVITY ASSEMBLY
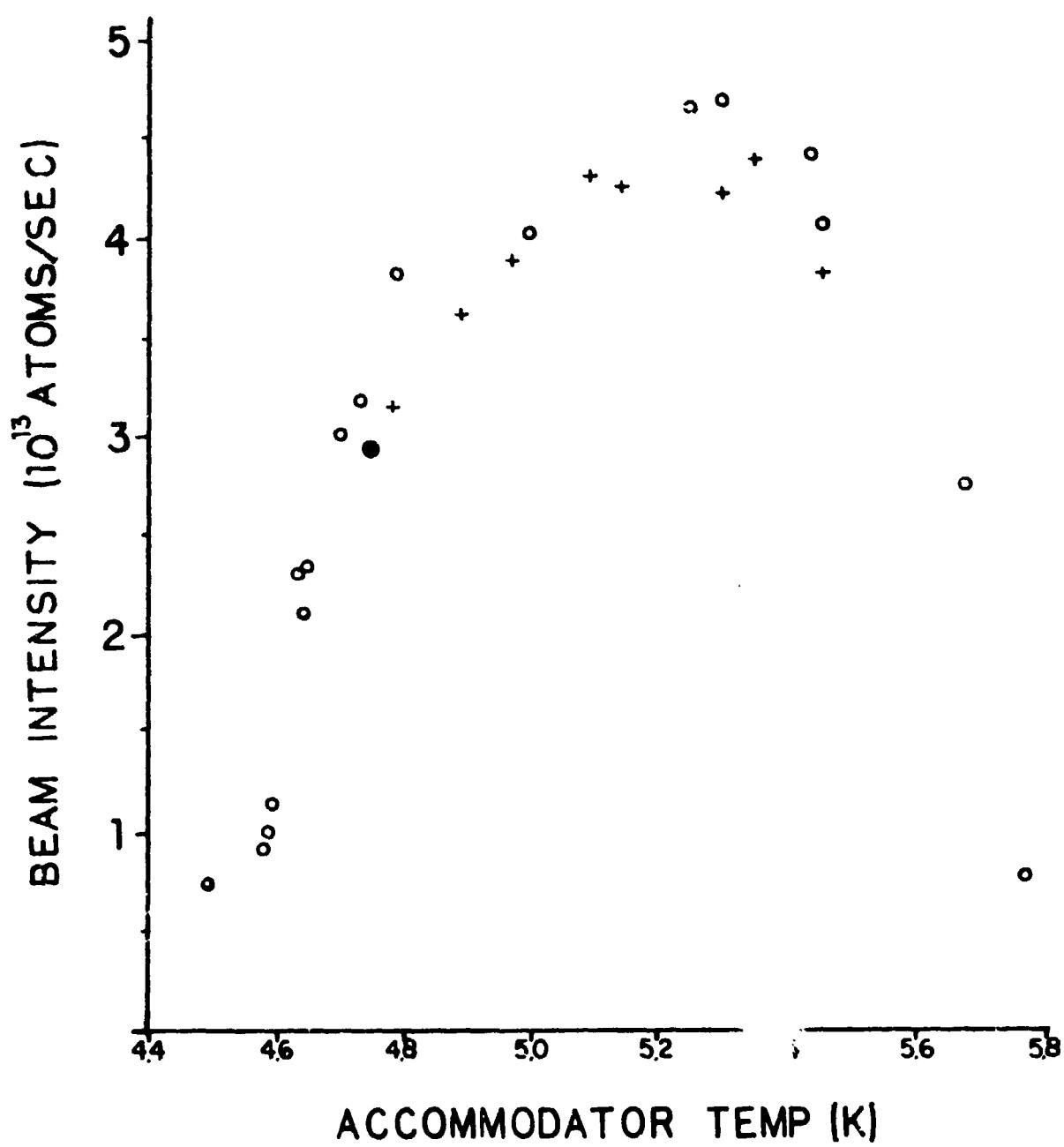
FIGURE 3   FLUX OF F=1, m_F=0 HYDROGEN ATOMS

that produced the flux at the solid circle and then increasing the accommodator temperature using an external heater. The coincidence of the output fluxes within errors suggests tnat the output flux is saturated with respect to input flux. Increasing the input flux to the accommodator will not increase output flux at the same accommodator temperature. A design requiring fewer collisions with the accommodator surface would improve output flux, but even these present fluxes compare favorably with the fluxes in room temperature hydrogen masers, and the beam is almost certainly cleaner.

SOLID MOLECULAR HYDROGEN SURFACES

We began by investigating solid molecular hydrogen wall coatings because they are the easiest coatings to make at temperatures between 4 K and 15 K and because we had already studied them over the lower temperature range from 3.5 K to 4.5 K using an earlier apparatus.[6] Figure 4 shows some results for the wall shifts for hydrogen atoms stored over these solid hydrogen surfaces at temperatures between 4.2 K and 5.5 K. The solid line has been fit by eye with slope 35.8 K equal to the value we obtained for the binding energy of H to H_2 at the somewhat lower temperatures in the earlier work. Theoretical calculations[7] of the binding of H to solid H_2 indicate that there should be a single bound state for motion perpendicular to the surface and almost complete freedom to move laterally. Theory[8] predicts that for this kind of "two dimensional gas" binding the variation of wall shift with temperature should be such as to produce a straight line in Figure 4. Within errors we find that the behavior we observed at lower temperatures extrapolates well up to the highest temperatures at which we obtain signals. The data does not go higher than about 5.5 K for the same reason that the output from the accommodator drops off to very low values at accommodator temperatures above 5.5 K: the H_2 vapor over the surface of the entrance tube prevents the state-selected H beam from entering the storage bottle. At 5.5 K the lowest wall shift observed is about 50 Hz, a factor of 1000 higher than wall shifts in room temperature hydrogen masers having Teflon wall coatings. If we could go higher in temperature, the wall shifts would be dramatically lower, but the high H_2 vapor pressure prevents that.

Relaxation processses other than the dephasing while adsorbed that produces the large wall shifts can be investigated using multiple pulses to measure the level population recovery rate $1/T_1$. These rates, less the contribution from escape through the entrance, are plotted in Figure 5. A line with slope 35 K has been drawn as a guide to the behavior that would be expected for a relaxation simply proportional to the mean surface dwell time. It appears that the relaxation rates are falling off somewhat faster than at the higher temperatures. Again, if we were able to go to higher temperatures, we would expect very low relaxation rates.

To summarize the results for H_2: This pulsed resonance experiment is an interesting probe of atom-surface interactions in a particularly simple system, but it is not a candidate for precision frequency metrology because of the high H_2 vapor pressure at temperatures where the wall shifts and relax ion rates would be low.
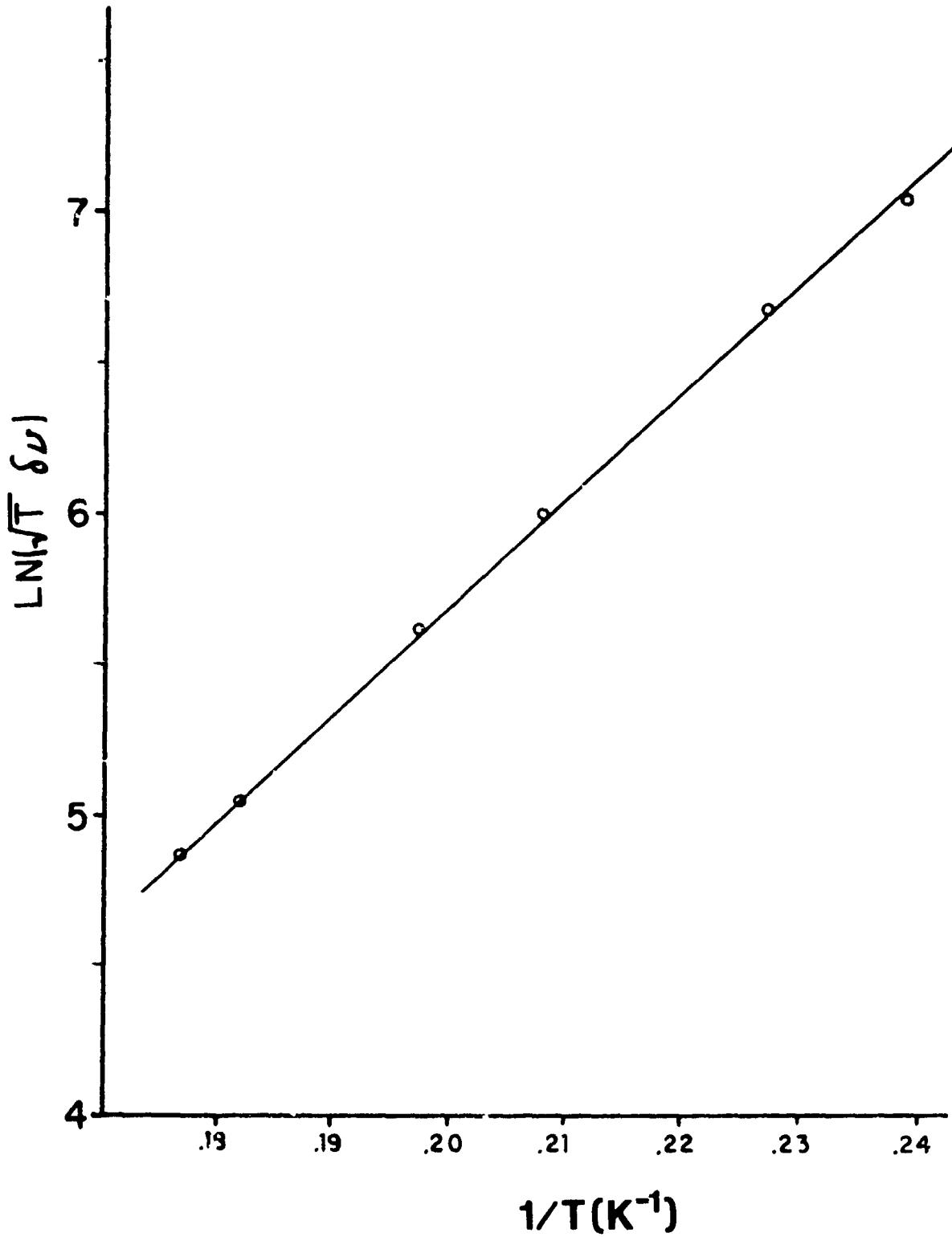
FIGURE 4   MOLECULAR HYDROGEN SURFACE WALL SHIFTS
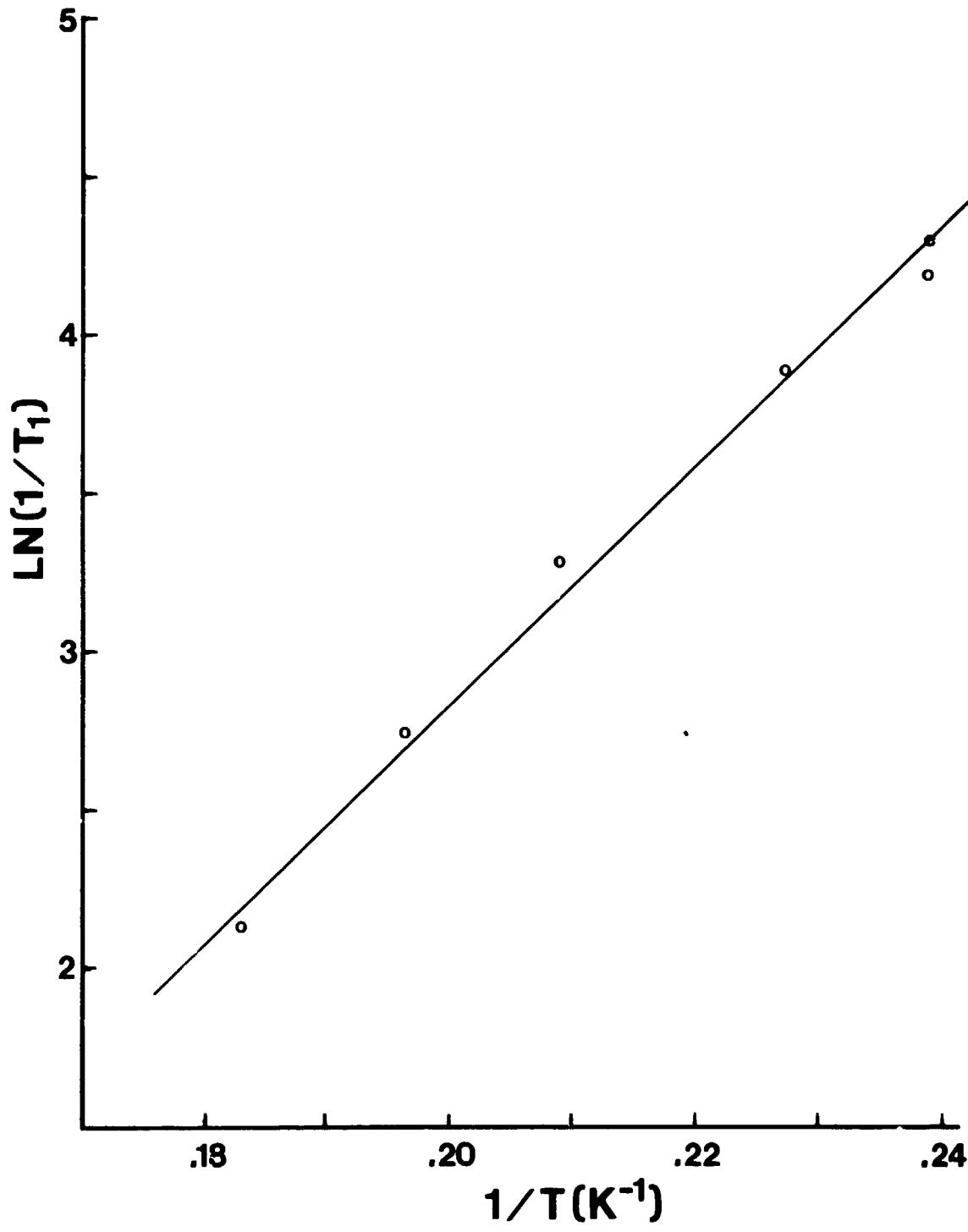
Figure 5 Molecular Hydrogen Surface Relaxation Rates

Neon atom gas has much less saturated vapor density than H_2 at the same temperature. Its electric polarizability is less than that of H_2, so that the force between a hydrogen atom and one neon atom in the surface is less than for H_2. Unfortunately, solid neon has less zero point motion than H_2 and so is more compact. The result is that the binding energy of H to a solid neon surface is predicted[7] to be about the same as the binding of H to a solid molecular hydrogen surface. Figure 6 displays wall shifts we have observed for H stored in bottles with solid neon wall coatings, plotted as in Figure 4. The slopes are the same from one surface preparation to another, indicating a consistent surface binding energy in good agreement with the theoretical predictions. The intercepts vary considerably, indicating variability of effective surface area from one surface preparation to another. These data do not show indications of thin spots or contamination by some heavy impurity; both effects would shift the slope upwards as well as the intercepts. We obtain data only up to about 11 K, where the saturated vapor pressure of neon in the entrance tube prevents atoms from getting into the bottle. The wall shift at 11 K in this 5 cm diameter bottle is about 1 Hz.

The relaxation rates vary much more than the wall shifts from one surafce preparation to another and even from one time to another for a single surface preparation as the surface evaporates. Evidently, the relaxation rates and the effective surface area are very sensitive to surface structure, but the binding energy is not. Within errors, $T_1 = T_2$, indicating that the relaxation process is predominantly one that removes atoms rather than relaxing them through some magnetic interaction. We have observed relaxation rates as low as 1 sec^{-1} greater than the rate of escape through the entrance, but we have also observed relaxation rates a hundred times higher. The fault lies with the high cohesive energy of solid neon, which tends to freeze into an open, snowy structure into which H atoms diffuse and eventually recombine. We believe that much more uniform and stable surfaces can be made by growing them very slowly at the temperature at which they are used and by maintaining over them the saturated vapor pressure of neon gas, but that will require a new apparatus.

MASER OSCILLATION AT 10 K

We have several times produced surfaces with low enough relaxation rates to support self-excited maser oscillation at temperatures ranging from 9 K to 10.5 K at fluxes of order 10^{13} state-selected atoms sec^{-1} and cavity Q's as low as 3500. The radiated power at this Q has been of order 10^{-12} watts. The linewidth of about 3 Hz has been dominated by the rate of escape through the bottle entrance. The short term frequency noise is less than that of our room temperature comparison maser, but we have not yet been able to measure the short term noise precisely. This first experimental apparatus is not optimized for temperature stability or magnetic field stability or even for surface stability. Although the wall shifts using solid neon wall coatings at 10 K are relatively high compared to the wall shifts in conventional hydrogen maser standards, the physics of the surface is much simpler. Whether the reproducibility and stability of the solid neon surfaces can be made to compensate for the higher wall shifts remains to be seen.
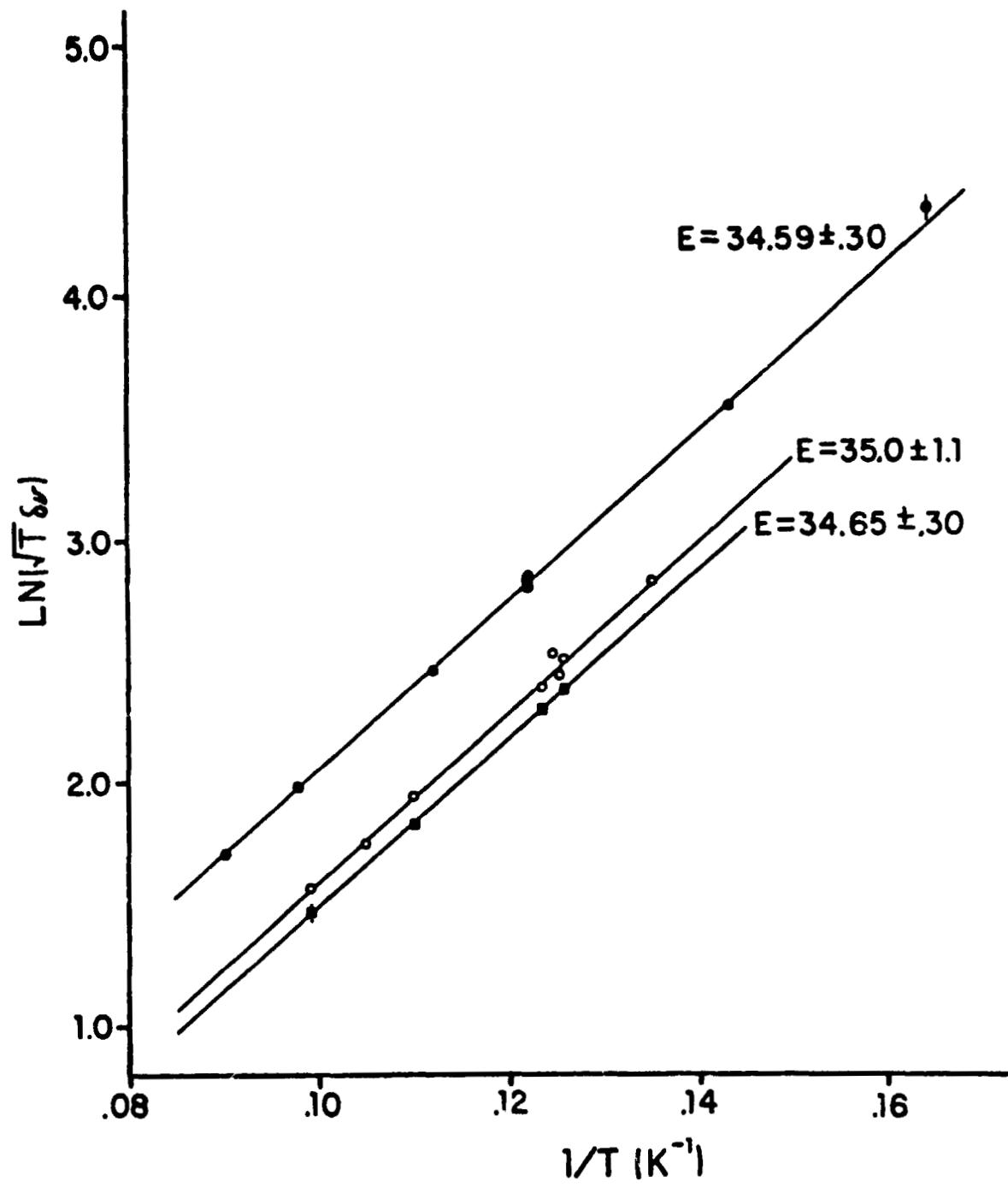
FIGURE 6   SOLID ATOMIC NEON SURFACE WALL SHIFTS

REFERENCES

1. Daniel Kleppner, Thomas J. Greytak, William D. Phillips, David A. Smith, and Abel Weinrib, Bull. Am. Phys. Soc. 23, 86 (1978).

2. Stuart B. Crampton, William D. Phillips, and Daniel Kleppner, Bull. Am. Phys. Soc. 23, 86 (1978).

3. D. Kleppner, H. M. Goldenberg, and N. F. Ramsey, Phys. Rev. 126, 603 (1962).

4. A. C. Allison, Phys. Rev. A5, 2695 (1972).

5. H. T. M. Wang, J. B. Lewis, and S. B. Crampton, in Proceedings of the 33rd Annual Symposium on Frequency Control, Atlantic City, N.J., 30 May - 1 June 1979, (Electronic Industries Association, Wsahington, D.C., 1979), p. 543.

6. S. B. Crampton, J. J. Krupczak, and S. P. Souza, Phys. Rev. B25, 4383 (1982).

7. L. Pierre, H. Guignes, and C. Lhuillier, J. Chem. Phys. (to be published).

QUESTIONS AND ANSWERS

JACQUES VANIER, NATIONAL RESEARCH COUNCIL: In view of these results, would you care to comment on the last line you had there on helium surfaces? Do you think that it's better to use helium?

MR. CRAMPTON: I would like to say two or three things about that. First, for the same geometry, that is, the same ratio of surface area to volume, the wall shift for neon surfaces are about ten times those of helium. Second, that liquid helium experiment geometries are naturally rather small. Although Hardy and Berlinsky gave their data extrapolated to a fifteen centimeter diameter storage bulb, it's not likely that someone is going to hang a fifteen centimeter diameter storage bulb from the mixing chamber of a dilution refrigerator, whereas it's no big deal to scale our bottle up from five centimeters to fifteen centimeters. So, you can get a factor of five just from the geometry. The main thing to look at is that you are talking about entirely different physics. In one case you are talking about a temperature of 10K, and a solid surface which is fairly quiet at that temperature. In the other case you are talking about a liquid helium surface at half a K. It's a factor of twenty in temperature. It's a superfluid film. That's great for temperature uniformity within the film, but liquid helium films creep towards the warmest place they can sense. Then they evaporate and reflux back. The density of helium gas is going to be proportional to the local temperature in that region. The problems are just completely different in the two cases. What should be done is that both things should be tried to see what the physics is in these two different regimes.

MR. McCOUBREY: You pointed out that the wall shifts are relatively large on the hydrogen and neon surfaces compared to the wall shifts on teflon at room temperature. I missed what you said about the model. Is the model not appropriate at room temperature?

MR. CRAMPTON: No, it is not appropriate. The binding energy is high enough so that you are going to have binding, I think, at localized sites. At least one and a half dimensional gas binding. On this model the wall shift would go to zero as you went up in temperature, whereas with teflon it goes right through zero and goes positive. The physics is very different and, of course, is very messy with teflon surfaces.

A LOW NOISE SYNTHESIZER FOR AUTOTUNING
AND PERFORMANCE TESTING OF HYDROGEN MASERS

by

James M. Cloeren
The Johns Hopkins University Applied Physics Laboratory
Laurel, Maryland

Jeffrey S. Ingold
Allied Bendix Aerospace
Columbia, Maryland

ABSTRACT

A low noise synthesizer has been developed for use in hydrogen maser autotuning and performance evaluation. This synthesizer replaces the frequency offset maser normally used for this purpose and allows the user to maintain all masers in the ensemble at the same frequency.

The synthesizer design utilizes a quartz oscillator with a B.V.A. resonator. The oscillator has a frequency offset of 5×10^{-8}. The B.V.A. oscillator is phase-locked to a hydrogen maser by means of a high gain, high stability phase-locked loop, employing low noise multipliers as phase error amplifiers. A functional block diagram of the synthesizer and performance data will be presented.

INTRODUCTION

The Johns Hopkins University Applied Physics Laboratory has been involved in the research, development and fabrication of Hydrogen Masers since 1975. The NR (NASA Research) Hydrogen Maser, developed at JHU/APL has several innovative features which greatly enhance its performance. One of these features is the ability of the NR maser to tune itself by making frequency difference measurements between itself and a reference signal, offset in frequency by 5×10^{-8}. The best autotune performance is obtained when the offset reference signal is obtained from another hydrogen maser. Unfortunately this method mandates that the reference maser be offset 5×10^{-8} thus removing a valuable maser from the on-frequency clock ensemble. Clearly it would be desirable to operate all masers on frequency and to have a synthesizer phase locked to the maser to provide the offset frequency reference signal. To be an adequate replacement for the reference maser, the synthesizer should not degrade the maser performance in autotuning, and it should be small and rugged enough for maser field repair and alignment operations.

DESIGN APPROACH

The offset generator is basically a single frequency indirect synthesizer using a multiply-mix - phase locked loop approach. (Please refer to Figure 1). For clarity of presentation, the synthesizer is divided into three parts: the fixed frequency, the phase multipliers and the phase locked loop. The fixed frequency section contains a very stable, spectrally pure VCXO which is operated at 5 MHz + 5 x 10^{-8}. The VCXO is manufactured by Oscilloquartz using a B.V.A. resonator. The VCXO has excellent short term stability below 1 second. The phase error multiplier section contains two low noise multipliers which multiply the 5 MHz outputs of the offset VCXO and the Maser to 1 GHz. The 1 GHz signals are then mixed to produce a 50 Hz signal which has 200 times the phase information as the original 5 MHz signals. The frequency of the 50 Hz signal is dependent on the fractional frequency difference between the offset VCXO (5 MHz + 5 x 10^{-8}) and the reference maser. The 50 Hz signal has a frequency sensitivity of 1 x 10^{-9} per Hz. The phase locked loop section contains a Motorola MC ..4 phase lock loop I.C., a divide by 100,000 circuit, and a mixer-low pass filter. The 50 Hz signal resulting from the two 1 GHz outputs which contains the Offset VCXO vs maser phase data is compared with a reference 50 Hz signal which is divided down from the maser input. The comparison is made using a Motorola MC 4044 digital phase detector used in the quadrature mode. The resulting error signal is translated and filtered and used to lock the offset VCXO. The 5 x 10^{-8} offset signal from the VCXO is the ^ tput of the synthesizer.

PERFORMANCE DATA

The data presented in Figure 2 was taken at JHU/APL and shows the results of comparing two masers together (NRX and NR9) in two configurations. The bottom trace is a sigma tau plot of the NRX maser compared to the NR9 maser with NR9 offset in frequency 5 x 10^{-8}. The top trace shows a sigma tau plot of the same two masers except in this instance the masers are running at the same frequency. NR9 was placed back on frequency and the offset generator was phase locked to the NRX maser thus producing the 5 x 10^{-8} offset. Note there is very little difference between the two traces and that for all practical purposes the offset generator performs as well as the maser which was intentionally offset in frequency.

The offset generator was also performance tested in the field at the Mojave Base Station, Goldstone California, in the following manner. Five NR masers were autotuned using the offset generator. Later one of the masers was offset and used to evaluate the other four masers tuned with the offset generator. The agreement was found to be within 1 x 10^{-13} tau.

CONCLUSION

The design features of a low noise single frequency synthesizer used to provide a 5 x 10^{-8} offset signal for tuning NR hydrogen masers has been presented. Test data presented indicate that there is a negligible performance penalty when using the offset generator in place of an offset maser for providing the 5 x 10^{-8} offset reference signal used for frequency difference measurements and tuning of NR masers.
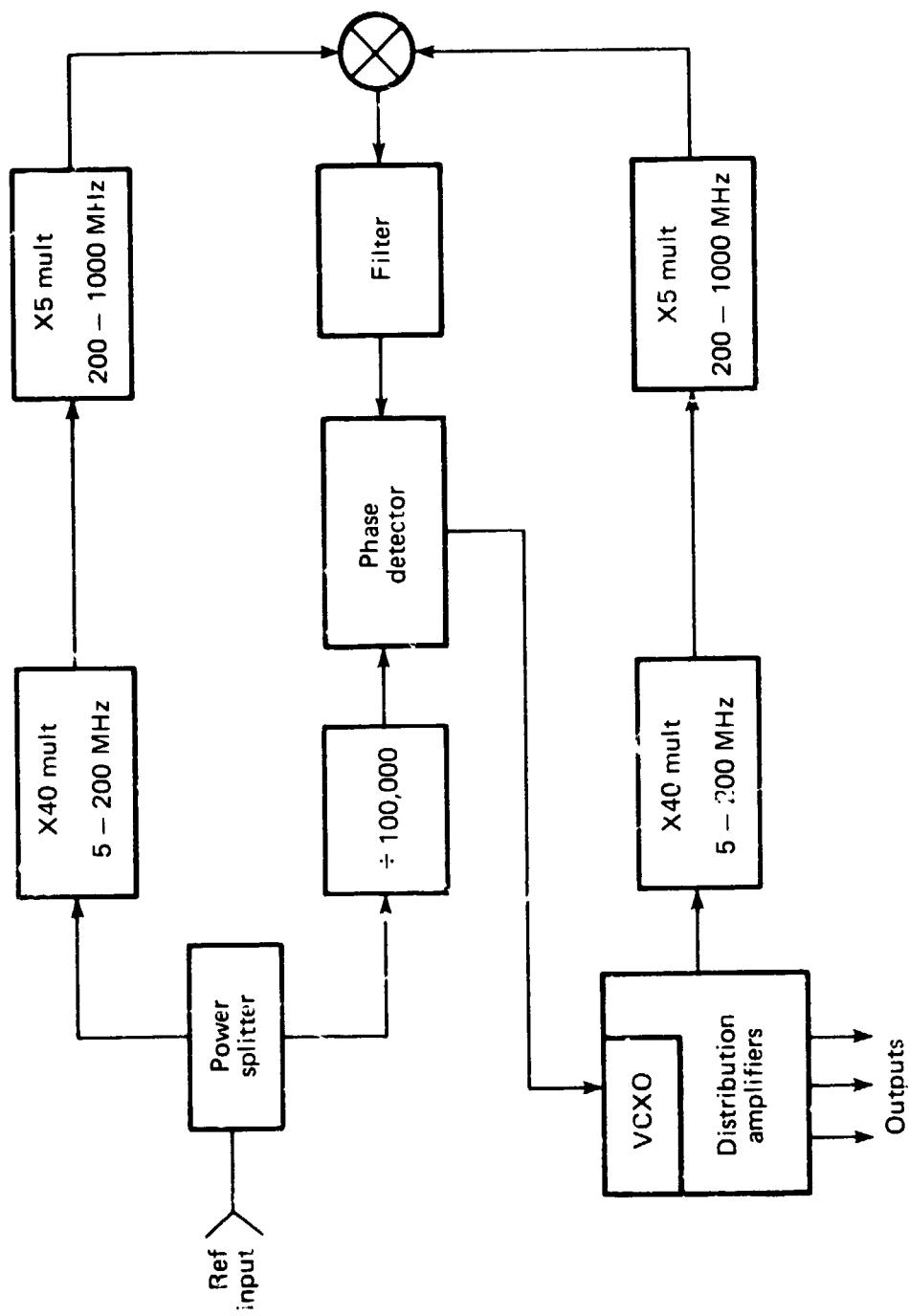
Fig. 1 Low noise synthesizer for autotuning and performance testing of hydrogen masers.

353
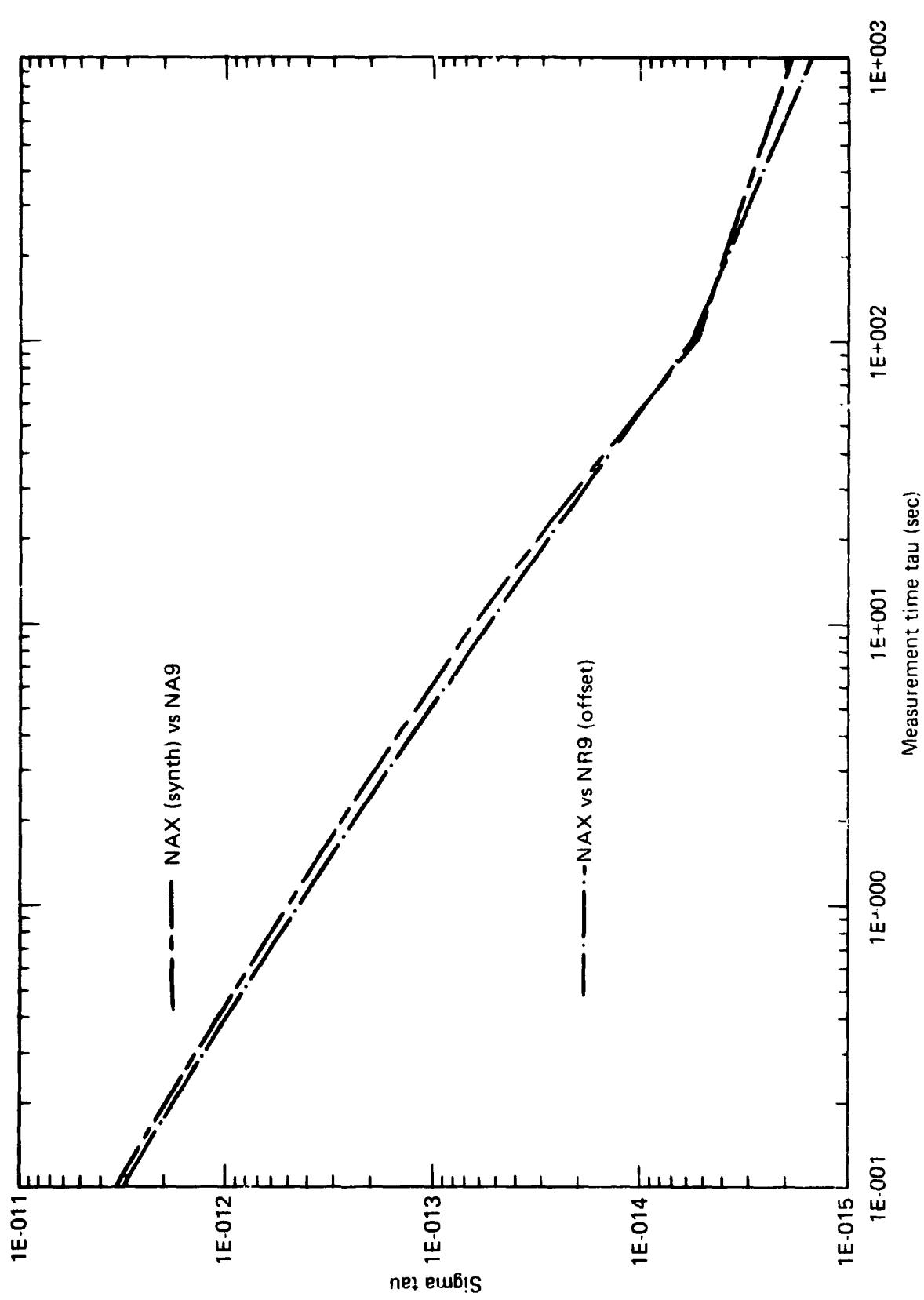
Fig. 2   Stability performance of low noise synthesizer.

QUESTIONS AND ANSWERS

MR. McCOUBREY: You point out that the use of this synthesizer permits you to operate all the masers in an assembly at the same frequency. I had always understood that when you got a number of identical oscillators close to the same frequency, they tend to pull each other and, therefore, become not all independent, which you like them to be if they are to operate in an ensemble. Is that a problem?

MR. INGOLD: I haven't seen that in the Time and Frequency lab at Johns Hopkins. Maybe Lauren Rueger could answer that.

MR. RUEGER: We have enough isolation in the instrument that we can readily see pulling if it occurred, and we do not. We look at phase plots with resolution of something on the order of one picosecond and see no evidence of pulling. We can move the C fields up and down through the resolution values and see no effect at that point.

MR. McCOUBREY: So you introduce controllable shifts and actually look for this?

MR. RUEGER: Exactly.

MR. McCOUBREY: It's very important to do that. As they get closer and closer, the difference is in the denominator, and you ultimately get them so close that even an extremely small coupling will influence the situation.

MR. RUEGER: We have isolation, in the closed loop system, of about 120 dB, and we have an additional isolation of an initial 120 dB. That's about the leakage through solid coax cables.

MR. McCOUBREY: Ultimately 200 dB.

MR. PETERS: Actually the receivers are mounted in very intimate contact with the top of the cavity, so they have enormous isolation. Besides that, we have synthesizers which have a resolution of 5 times ten to the minus seventeenth. With eleven digits, you can run the maser frequency through another one, through any frequency you wish, and you will never see any pulling phenomenon whatsoever. Unless you take the receiver apart, or put in a high power signal at or near the maser frequency, there is no signal in existence which will effect it.

MR. McCOUBREY: Apparently this has been looked at in depth.

VICTOR REINHARDT, HUGHES AIRCRAFT COMPANY: What you have to realize is that what you are doing in a hydrogen maser when you change the synthesizer is just to move the VCO, but not moving the maser frequency. You can still see effects if you are not careful. They don't effect the maser, but they do effect the VCO, and you can sometimes see interactions and beats between the crystals if you are not careful.

You have to remember that the two masers are always running at 1420 megahertz regardless of what you do with the syntnesizers.

MR. RUEGER: They are not really the same frequency.

MR. McCOUBREY: Yes. If the C fields are off, the frequencies will be slightly different.

ALBERT KIRK, JET PROPULSION LABORATORY: Have you actually measured the noise contribution of the offset generator itself?

MR. INGOLD: Yes, we have measured that. It's approximately one part in ten to the thirteenth, tau to the minus one-half. This was for a maser with the external synthesizer compared to another maser.

MR. KIRK: Yes, but have you tried taking one maser and offsetting it and then comparing it against itself?

MR. INGOLD: Yes, it's about one part in ten to the thirteen, tau to the minus one-half.

MR. ALLAN: To the minus one?

MR. REINHARDT: To the minus one-half. Why is it tau to the minus one-half?

MR. INGOLD: I can't explain it.

ATOMIC HYDROGEN MASER MEASUREMENTS

WITH WALL SURFACES OF CARBON TETRAFLUORIDE

R.F.C. Vessot, E.M. Mattison, E.A. Imbier and Z.C. Zhai

Smithsonian Astrophysical Observatory

Cambridge, Ma. 02138

1. **INTRODUCTION**

The principal objectives of the SAO cold maser research programs are:

1. To understand the behavior of the atomic hydrogen wall collision process and find better wall coating materials or processes.

2. To develop hydrogen masers of improved stability taking advantage of the following low temperature properties:

a) Lower thermal noise per unit bandwidth (kT). Both the signal-to-noise ratio of the output signal and the intrinsic stability limit vary as $T^{\frac{1}{2}}$

b) Smaller spin exchange cross section for atomic hydrogen. At 4°K this cross section 's about 200 times smaller than at room temperature. For a given rate of spin exchange quenching at room temperature we can obtain 200 times greater power output and thus reduce the signal-to-noise in the output signal.

c) Slower speed of the atoms (proportional to $T^{\frac{1}{2}}$), which reduces the wall collision rate.

d) Better mechanical and thermal stability of materials at low temperatures. Superconducting magnetic shields can also be used at sufficiently low temperatures.

The work we report here is aimed principally at understanding more about the interaction of hydrogen atoms with wall coatings of fluorinated ethylene propylene (Dupont Teflon FEP-120 co polymer) and of carbon tetrafluoride (CF_4). The principal measured quantity in these experiments is the "wall shift" of the maser's output frequency. To relate the present data to the study of cold Teflon surfaces made by Michel DeSaintfuscien,[1] we calculated the wall shift per atomic collision from the measured wall frequency shift. As will be seen later, this assumes that the wall surface area is smooth on a molecular scale.

We calculate the average phase shift $\Delta\phi_g$ per geometrical collision determined from the dimensions of the storage bulb:

$$\Delta\phi_g(T) = \frac{2\pi\Delta\nu_w(T)}{\nu_c(T)} \tag{1}$$

where ν_c is the rate of atomic collisions with the storage bulb wall and $\Delta\nu_w(T)$ is the frequency shift owing to wall collisions. ν_w is obtained by measuring the maser output frequency ν_{out} and correcting it for second-order Doppler shift, second order magnetic field dependence, and cavity resonator frequency offset pulling as follows:

$$\nu_{out} = \nu_0 + \frac{3kT\nu_0}{2mc^2} - 2752H^2 - (f_c - \nu_0)\frac{Q_c}{Q_\ell} + \Delta\nu_w(T) \tag{2}$$

Here ν_0 is the unperturbed hyperfine separation frequency of atomic hydrogen,[2] H is the static magnetic field strength in the storage volume, m is the hydrogen atom mass, f_c is the cavity resonance frequency, Q_c is the cavity Q, and Q_ℓ is the atomic line Q.

Each measurement required a determination of the output frequency at several known cavity frequency settings. The output frequency data were fit to a straight line as a function of cavity frequency f_c, and the frequency $\Delta\nu_w$ corresponding to $f_c = \nu_0$ was calculated in order to eliminate the effects of

resonator pulling. From the average velocity of the atoms, $\bar{v} = (8\frac{kT}{\pi m})^{\frac{1}{2}}$, and the geometrical surface-to-volume ratio of the storage volume A_g/V_g, we determine the average collision rate, $\bar{\nu}_c$.

$$\bar{\nu}_c = \frac{\text{average velocity}}{\text{mean free geometrical distance}} = \frac{\bar{v}}{\frac{4V_g}{A_g}} = \frac{1}{\bar{\tau}_c} \qquad (3)$$

Following Hardy and Morrow[3] we assume a model for the hydrogen wall surface interaction where some fraction of the wall collisions result in momentary binding of the atom in a potential well characterized by energy E_b. While in the well the atoms have the properties of a two-dimensional gas. The time spent in this state is very much smaller than the mean time between collisions, $\bar{\tau}_c$. The ratio of $\bar{\tau}_s$, the time spent bound to the wall, to $\bar{\tau}_b$, the time between these events, is given by[3]

$$r = \frac{\bar{\tau}_s}{\bar{\tau}_b} = \Lambda \frac{A}{V} e^{E_b/kT} \qquad (4)$$

where $\Lambda = \frac{h}{(2\pi mkT)^{\frac{1}{2}}}$ is the thermal de Broglie wavelength.

Since an atom does not bind to the wall on each impact, the time $\bar{\tau}_b$ may involve many collisions. The probability of binding per collision is represented by the fraction $\alpha = \frac{\bar{\tau}_c}{\bar{\tau}_b}$. During a binding collision the phase of the hyperfine interaction is retarded an amount

$$\overline{\Delta\phi} = 2\pi\bar{\tau}_s\Delta_s$$

where Δ_s is the frequency change of the atom while in the bound state. The wall collision frequency shift is

$$\Delta\nu_w = \frac{\nu_c\alpha}{2\pi}\overline{\Delta\phi} = \frac{h}{(2\pi mkT)^{\frac{1}{2}}}\frac{A}{V} e^{E_b/kT}\Delta_s \qquad (5)$$

and the average phase shift per collision is

$$\Delta\Phi_g(T) = \frac{V_g}{A_g} \frac{A}{V} \frac{2\pi h}{kT} e^{E_b/kT} \Delta_s \qquad (6)$$

We note in this expression that A/V is the actual area to volume ratio and A_g/V_g is the geometrically determined area to volume ratio. A is the effective surface area of the storage region coating, which may be microscopically rough, while A_g is the area of the storage region assuming perfectly smooth walls. Because the surface roughness has negligible effect on the storage volume, for practical purposes $V = V_g$.

2. EXPERIMENTAL PROCEDURE

The cryostat shown in Fig. 1 was equipped with a TE_{111}-mode cavity[4] whose interior surface was coated with FEP-120 Teflon and that had a Teflon FEP septum 0.25 mm thick. The atomic hydrogen source is cooled by contact with the copper shroud, and operates at about 80°K. Liquid helium admitted via a control valve into the sample holder cools the cavity.

The maser was operated in the range of 78°K to 50°K with the bare Teflon surface. After completing the data runs for bare Teflon, the system was stabilized at about 60°K and gaseous CF_4 was beamed toward the cavity entrance aperture by a nozzle located in the shadow of one of the pole tips of the hexapole magnet. The system pressure rose to about 10^{-3} torr and was kept there for about 4 minutes by the flow of CF_4.

The wallshift was measured and the coating process was repeated a second and third time. No further shift in frequency was observed. We conclude that we had completely and thoroughly coated the surface using this procedure.

3. EXPERIMENTAL RESULTS

Figure 2 shows the average phase shift per collision based on the geometrical surface to volume ratio of the storage volume. For Teflon we include the entire data set of 1983 and 1984 and the data point at /7.4K made by DeSaintfuscien in 1976.[1] The carbon tetrafluoride data were obtained within 30 minutes of the time of injection of CF_4. The system was then cooled at a rate of $5^{\circ}K$ per hour to $52^{\circ}K$, was allowed to equilibrate at $52^{\circ}K$ for about 40 minutes, and was then again cooled at $5^{\circ}K$ per hour until the cavity reached $45^{\circ}K$. We paused for equilibration for 20 minutes before cooling steadily to $33.6^{\circ}K$ at a rate of about $4^{\circ}K$ per hour. Frequency measurements were made with the continuously oscillating maser. Measurements at each temperature were made for three or more cavity frequency settings. Each data set was made within a two-minute time interval to minimize errors owing to the constant slow cooling of the cavity.

We found that the temperature gradient between the sample holder and the cavity caused magnetic quenching, probably due to thermoelectric currents. To keep the maser oscillating the field coil current was raised to produce a magnetic field as high as 27×10^{-3} gauss. The usual field setting was 12.8×10^{-3} gauss; when gradients were small, data were successfully taken at 2×10^{-3} gauss.

The plot of $-T\Delta\phi_g(T)$ vs $1000/T$ shown in Fig. 3 was calculated from measurements taken between noon and 7 P.M. on October 15, 1984. The straight line is a least squares fit to $-T\Delta\phi_g(T) = 0.42 \times 10^{-3}e^{154.6/T}$. Measurements made at $43^{\circ}K$, $44^{\circ}K$ and $46^{\circ}K$ on October 16 fell into the spread of the October 16 data set. Measurements made on October 17 at $53^{\circ}K$ and $55^{\circ}K$ and on October 18 at $60^{\circ}K$ lie well below expected values. We can perhaps conclude that at the higher

temperatures the CF_4 surface sublimes away. The jagged edges and prominences of this surface would disappear first, leaving a progressively smoother surface until all of the CF_4 had been pumped away. This behavior upon warming the CF_4 surfaces has been observed on at least three previous occasions. To date, we have not been able to find reliable values of the CF_4 vapor pressure for temperatures below its melting point of $89^\circ K$. From the pressure behavior observed when we warm up the system, we believe that the vapor pressure is significant, perhaps on the order of 10^{-5} torr, at temperatures around $60^\circ K$ and that at higher temperatures the surface is sufficiently volatile to change its structure significantly in an interval of several days.

We have recalculated $-T\Delta\Phi_g(T)$ vs $1000/T$ using DeSaintfuscien's data, our 1983 and 1984 Teflon data, and the October 15 data of Fig. 3. The results are plotted in Fig. 4.

From this plot we conclude that the interaction energy of atomic hydrogen on carbon tetrafluoride is $154.6^\circ K$, and that of FEP-120 Teflon is $143.4^\circ K$. These differ by only about 8 percent, and lead us to the conclusion that the surface interaction of hydrogen colliding with a fluorine atom bound to carbon does not significantly depend on the internal carbon structure. However, we observe a significant difference between the magnitudes of the phase shift per collision for Teflon and CF_4. There is about three times less phase shift per collision for frozen-in-place CF_4 than for Teflon.

From Equation 6 we see that the terms that govern this shift are the actual surface area and the hyperfine frequency shift of the hydrogen atom while in the bound state, Δ_B. Calculations of the hyperfine shift[5] have been given with reasonable agreement with experiments using the assumption that the inter-atomic hyperfine shift is proportional to the interaction potential. When the

362

hyperfine shift is calculated for collisions with an aggregate of atoms, such as a Teflon molecule, the actual structure of the surface must be modeled in the same way. This micro model of the collision process where hydrogen is considered to interact with, say, 10 fluorine atoms bound to a carbon core must be contrasted with a macro model where the surface is irregular on a much greater scale involving, say, tens of millions of atoms. The situation involving the latter scale can be represented in terms of surface area-to-volume and related to free molecular flow collision processes. In either case it is a question of the actual physical configuration of the fluorine atoms encountered by the impinging hydrogen atom.

We must remember that our plots of log $[T\Delta\Phi_g(T)]$ vs T^{-1} are normalized to a collision rate estimated from geometrical surface and volume. We have used equation 6 to show the connection between DeSaintfuscien's data and ours; we see from this equation that, in principle, $\Delta\Phi_g(t)$ is independent of A/V.

A more realistic way to plot the d- a is to use equation 5, plotting $\log[T^{\frac{1}{2}}\Delta\nu_w]$ vs T^{-1}. This has the same slope as the $T\Delta\Phi_g(T)$ data, and the prefactor contains A/V and A_s.

We conclude from the close agreement between DeSaintfuscien's data and ours that the FEP-120 Teflon dispersion has produced a fairly reproducible surface in these two applications.

From the similarity in the experimental terms shown in the FEP-120 and CF_4 data plotted in Figure 4, we see that the energy of interaction is very similar for these two surfaces. The question of the three-fold to four-fold disparity in the wall shift remains.

363

Fluorine, the most electronegative of all elements, forms extremely stable carbon compounds (fluorocarbons) whose molecular attraction (as well as repulsion) are entirely governed by fluorine. The long chains of the CF_2 (tetrafluor-ethylene) homopolymer (TFE Teflon) or the shorter branched chains of the FEP co-polymer (fluorinated ethylene-propylene) have substantially similar structure in that they can be either crystalline or largely amorphous, depending on their condition after melting, i.e. whether slowly annealed or quenched. There are substantial differences in wallshift between these two physical states[6,5,7], and these differences have been associated with the surface structure. The crystalline surface has the larger wallshift owing to the growth of platelets that produce a rougher surface on a macroscopic scale and to microscopic textural effects of the platelets when pictured as a stack of cordwood where the Teflon chains (logs) of various lengths protrude from the sides of the generally well organized stack.

The homopolymer is obtained in the form of a water dispersion of particles about 0.22 micro meters average diameter stabilized with a soap-like substance to prevent coagulation. The co-polymer has 0.1 micro meter sized particles and is also available in a water dispersion. These dispersions are cast on the surface to be coated, the water evaporated, and the particles sintered or melted together to form a film. The homopolymer has a high viscosity of about 10^{11} poises in the melted state. Its consistency is "more like a frame than a liquid".[5] The co-polymer has melt viscosity of about 10^6 poises and flows more easily. In 1978, the surface of thin films, say 0.002 inches in thickness, were found to be porous from tests made at the U.S. Naval Research Laboratory using electron scattering and low energy electron diffraction techniques.[8] This has led us to increase the coating thickness of our films from about 1 milligram per cm^3 to well over 3 milligrams per cm^3 by applying successive coatings of the

Dupont FEP-120 co-polymer. Whether or not the density of the films has been improved is open to question. What has probably happened under these multiply coated conditions is that we have piled up more and more platelets but still have a porous and, to the hydrogen atom, macroscopically rough surface.

The threefold decrease in apparent surface area by freezing CF_4 probably results from the smoothing of the Teflon surface by a build-up of CF_4 "frost" on the interior of the storage chamber. That this "frosted" CF_4 surface itself is not as smooth as it could be is strongly evidenced by the further reduction in wallshift when the surface is warmed to $60^\circ K$. Here we envir a further smoothing of the surface either by melting, or more probably, by sublimation where the pointed peaks are first to go, leaving a smoother surface that lasts as long as there is CF_4 available.

The fact that the Teflon surface is porous and that the collision rate apparently can be reduced by a factor of as much as four times leads us to reconsider the present status of wall coatings created by fusing granules of Teflon applied from a water dispersion. This is a difficult process to control and has a great deal of variability.

The importance of wall coatings is crucial to the hydrogen maser storage technique, where the linewidth of the oscillator is limited by the wall relaxation process. Remarkably little has been done to improve wall coatings since the invention of the maser by Kleppner, Goldenberg and Ramsey in 1960. With support from the Office of Naval Research included as a small part of a contract with the U.S. Naval Research Laboratory (N00011-71-A-0110-0003) an attempt was made in 1975-1976 by our group at SAO to obtain bulbs coated with Teflon polymerized in place using C_2F_4 monomer gas. The technique was developed by the Laboratoire Suisse de Recherches Hologeres (L.S.R.H.), Neuchatel,

Switzerland in 1975 and patented in the U.S.A., France, Japan and Germany. SAO engaged the L.S.R.H. to coat two quartz bulbs with a film of 1000Å to 3000Å thickness made from polymerized C_2F_4, using ultraviolet surface photo polymerization. This was to be done along with samples of glass and KB_r for analyses by pyrolysis to determine molecular weight, and other measurements to determine molecular structure and film thickness.

One bulb was received and tested in December 1975. Samples tested at L.S.R.H. by infrared spectroscopy showed proper Teflon polymer lines. The high temperature pyrolysis test showed no deterioration over $3\frac{1}{2}$ hours at 220^oC, indicating satisfactory molecular weight. As part of the contract, a complete report of the coating process from L.S.R.H. was received. Tests run at SAO on the bulbs initially showed excellent line Q results, but in less than a week the coating had failed.

While the maser was oscillating we measured the wallshift and found it to be in the range of normal values for P.T.F.E. Teflon. However, in a few days the line Q diminished steadily from a relatively high value of $1.5x10^9$ to well below $1x10^9$. We took the maser apart to examine the bulb and found that its surface had deteriorated and was very easily wetted, and that a loose powder appeared on the surface of the water drop we had introduced. We concluded that the film on the bulbs was not the same as on the test samples. L.S.R.H. agreed to recoat the bulbs after testing their system with other bulbs. This work was not done and we were forced to conclude our contract with L.S.R.H. in August of 1977.

To the best of our knowledge, no further work on Teflon-like coatings for hydrogen masers has been done since this date. The present results with frozen CF_4 suggest that another attempt at polymerizing C_2F_4 in place would be

$C-5$

worthwhile. The prospect of a possible fourfold improvement in storage time and developing a controllable means of coating hydrogen maser bulbs is a strong motivation for this renewed effort.
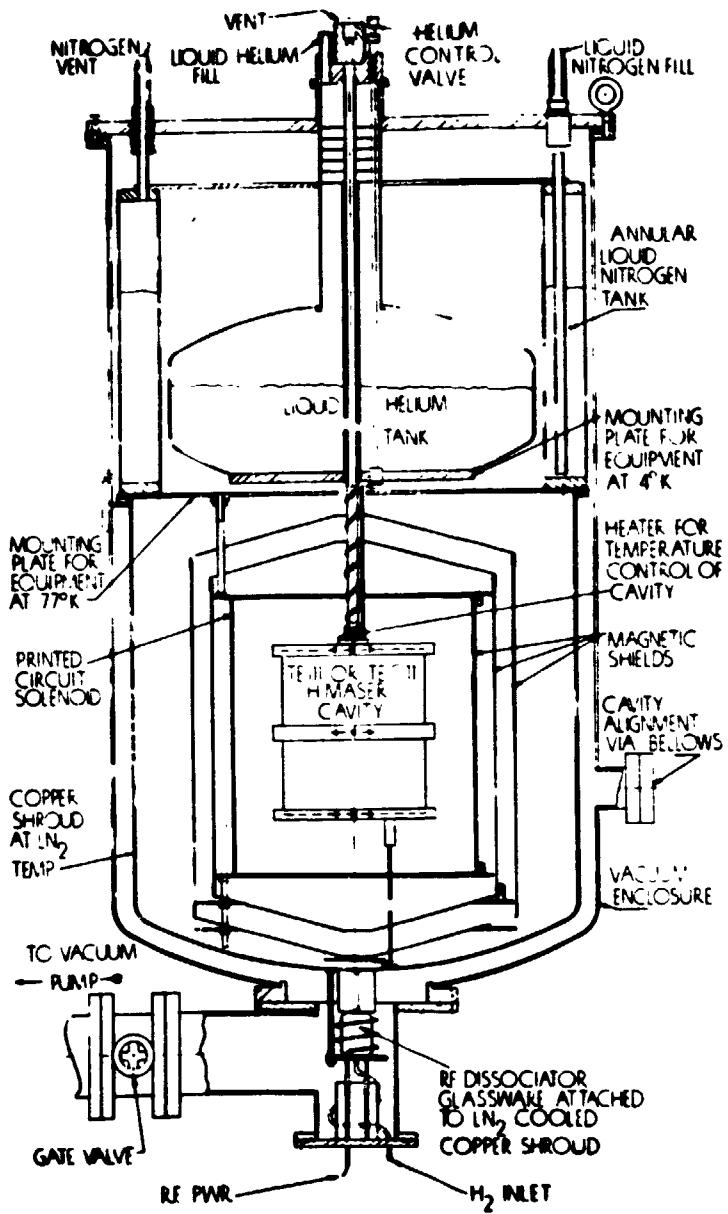
5. ACKNOWLEDGEMENTS

REFERENCES

1. DeSaintfuscien, M., "Etude des effects de paroi dans le maser a hydrogene," Thesis presented at the University of Paris XI Centre d'Orsay, 6 Nov. 1975.

2. Hellwig et.al., "Measurement of the Unperturbed Hydrogen Hyperfine Transition Frequency", IEEE Transactions on Instrumentation and Measurement, Vol. IM-19, No. 4., November 1970. Pp. 200-209.

3. Hardy, W.N., and M. Morrow, "Prospects for Low Temperature Hydrogen Masers Using Liquid Helium Coated Walls", Journal de Physique - C8 Vol. 42, December 1981. Pp. 171-179.

4. Mattison, E.M., M.W. Levine, and R.F.C. Vessot, "New TE_{111}-mode hydrogen maser," Proc. 8th Annual P.T.T.I., Nov. 30 - Dec. 2, 1976. U.S. Naval Research Laboratory, Washington, D.C., pp. 355-367.

5. Zitzewitz, P.W., "Surface Collision Frequency Shifts in the Atomic Hydrogen Maser," PhD Thesis, Harvard University, March 1970.

6. Vessot, R.F.C. and M.L. Levine, "Studies of Hydrogen Maser Wallshift for High Molecular Weight Polytetrafluoroethylene." Proc. 24th Annual Symposium on Frequency Control, USAERADCOM, Ft. Monmouth, NJ, April 27-29, 1970.

7. Zitzewitz, P.W, E.E. Uzgeris, and N.F. Ramsey, "Wallshift of FEP Teflon in the Hydrogen Maser", Rev. Sci. Instr. **41** (1970)

8. Folen, Dr. V., "U.S. Naval Research Laboratory, Washington, DC, Private Communications.

S.A.C. Cold Maser
Figure 1

FIGURE 2

CARPON TETRAFLUORIDE
DATA

● OCTOBER 15, 1984
□ DATA TAKEN LATER-DATES AND TIME SHOWN

OCT 16
(1029)

OCT 16
(1609)

OCT 17
(1018)

OCT 18
(1248)

OCT 18
(1001)

1000 / T

$-T\Delta\mathcal{S}_c^o(T)$
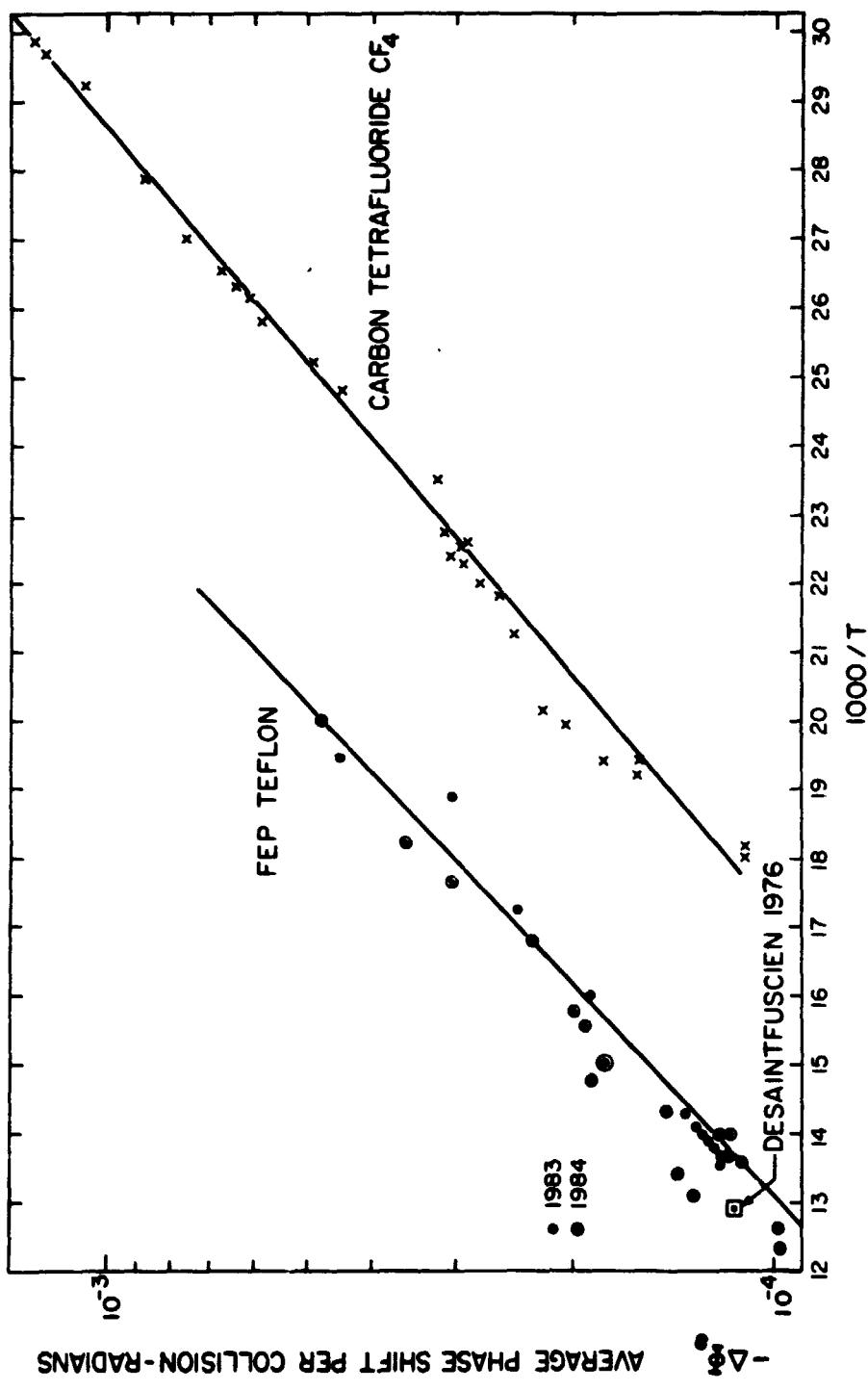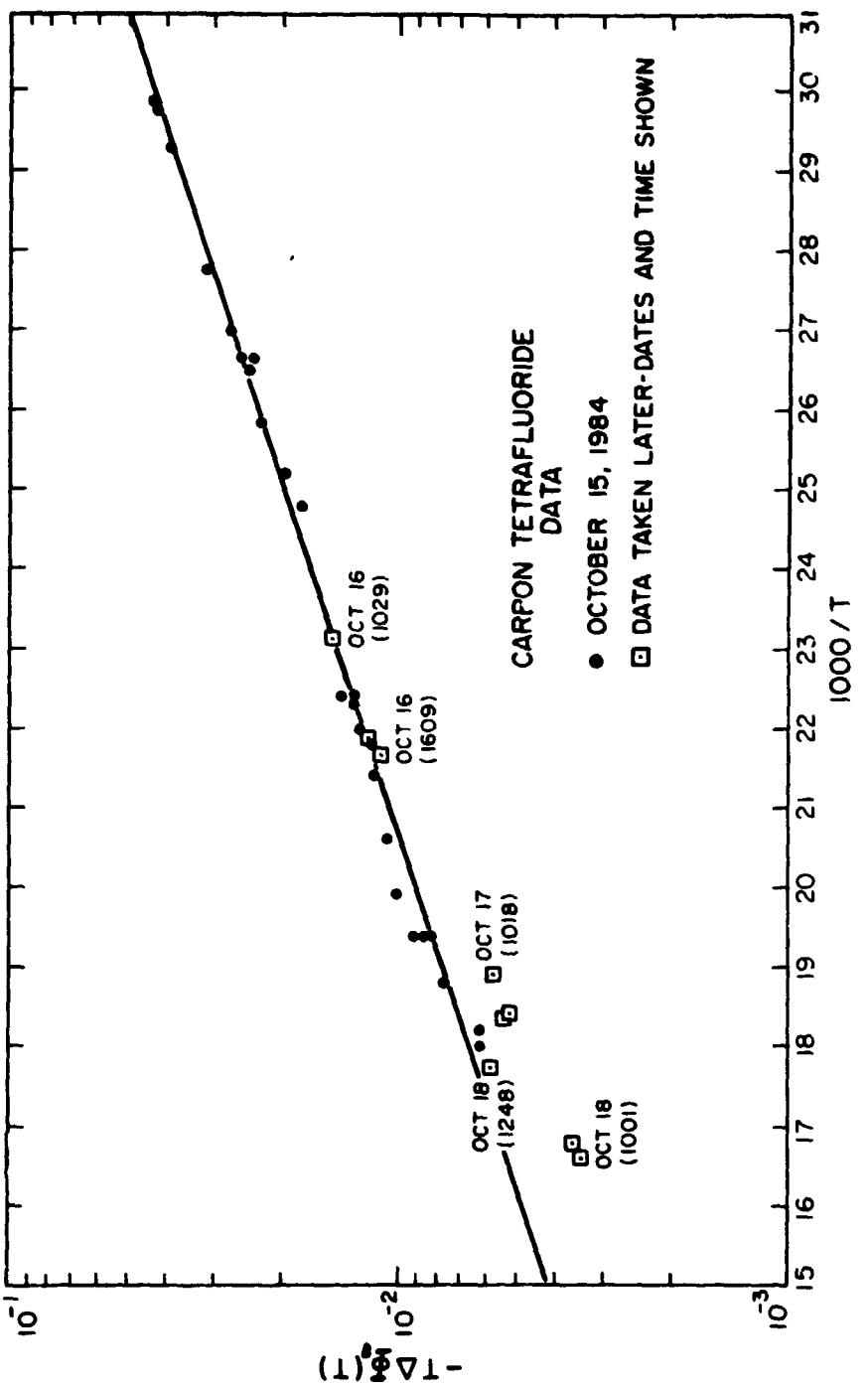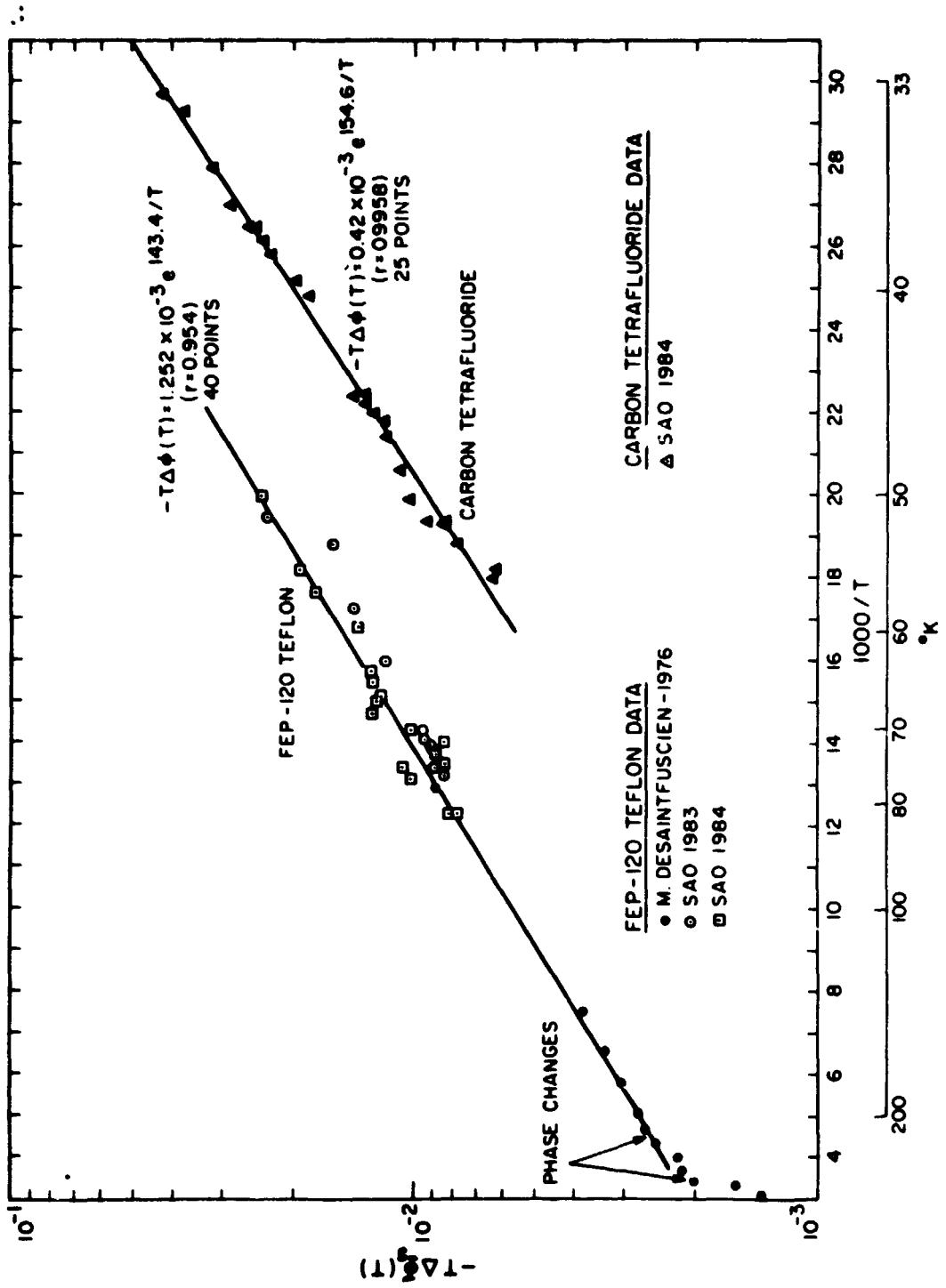
FIGURE 3

FIGURE 4

QUESTIONS AND ANSWERS

SAMUEL WARD, JET PROPULSION LABORATORY: Are you ready to make a commitment as to which of these two things is causing the pulling?

MR. MATTISON: I think that both things are going on. In the beginning of the life of the maser when you have just assembled it, the joints between the end plates and the cylinders of the cavity tend to grow together. After a while that stops, or slows down, and what you see is the shrinkage of the bulk material.

MR. WARD: My second question is: We returned a VLG-10 to you, serial number 6, last year for service, and when it came back to us -- we have had it on-line for a year now -- there has been no measurable drift. What happened?

MR. MATTISON: I am glad to hear it. I don't know what happened, but if the cavity was not disassembled, I would expect it to drift very little. The answer is that I am happy to hear it, but I can't give you a reason right off.

MICHEL TETU, LAVAL UNIVERSITY: Have you considered, as a possible influence on the change in tuning of a maser, the change in the characteristic of the tuning of the varactor with time as a possible source?

MR. MATTISON: No, but it's a possibility.

VICTOR REINHARDT, HUGHES AIRCRAFT COMPANY: This is a question really for the questioner. Have you observed that phenomenon?

MR. TETU: No, I haven't.

ALBERT KIRK, JET PROPULSION LABORATORY: What was the actual net difference in daily drift between what you measured against NBS, I guess, and what you determined by cavity tuning? I notice that they don't exactly agree. What was that disagreement?

MR. MATTISON: My rcollection is that the drift measured by cavity tuning was on the order of four in the fifteens per day, and the observed drift rate was, approximately, comparable. The difference would be a couple of parts in the fifteens per day, but the cavity tuning measured rate was an estimate, you can see the change in the slope of the curve. I can't say exactly to what extent they disagree.

MR. KIRK: Would you say that virtually all of the drift is due to the cavity, or is there a possibility that one or two parts per day drift is due to something other than the cavity?

MR. MATTISON: I think that most of it seems to be consistent with the cavity frequency change. I would expect some change in the wall properties, some long term change in the wall shift, but that doesn't show up because you can't separate the two.

MR. McCOUBREY: This initial drift, the relatively rapid drift, does it take place when the masers are first assembled? Does it start when the masers are first assemble, or when they are first turned on?

MR. MATTISON: You can't observe it until you turn them on.

MR. McCOUBREY: But they appear to start when the operation first began at the Naval Observatory, from the data you showed us.

MR. MATTISON: Those masers were built several months before that, and we had tracked that drift prior to the installation at the Observatory. We had observed it in several masers also; you have a drift that starts fairly large, and decreases over time, from the time that they are assembled.

MR. McCOUBREY: If you turn them off for a while, and then turn them back on, you would not expect to see that initial drift again?

MR. MATTISON: The drift would not go back to the original value.

PERFORMANCE DATA OF U.S. NAVAL OBSERVATORY

VLG-11 HYDROGEN MASERS SINCE SEPTEMBER 1983

R.F.C. Vessot, E.M. Mattison, E.A. Imbier and Z.C. Zhai

Smithsonian Astrophysical Observatory

Cambridge, Massachusetts 02138

W.J. Klepczynski, P.G. Wheeler, A.J. Kubik, and G.M.R. Winkler

U.S. Naval Observatory, Washington, D.C. 20390

In 1983, two VLG-11 masers were delivered to the U.S. Naval Observatory by the Smithsonian Astrophysical Observatory. Last year the short-term stability of these masers was reported and the effect of this short-term stability on timekeeping performance was discussed by G.M.R.Winkler.[1] Since the date of installation, 13 September 1983, data on the masers' long-term performance have been accumulated. Figure 1 from reference [1] shows the Allan variance, $\sigma(\tau)$, of the relative frequency between the masers. This variance reaches a minimum of about 4 parts in 10^{16} at averaging times of 5×10^3 seconds and rises at longer averaging times due, at least partly, to systematic frequency drift.

In this paper we discuss the systematic frequency drifts, expressed as $\frac{1}{f}\frac{df}{dt}$ and given in units of fractional frequency difference per day.

Figure 2 is a plot of $\frac{1}{f}\frac{df}{dT}$ in units of 10^{-15} per day versus calendar day starting in September of 1983 and continuing through October of 1984. Table 1 is a chronology of activity involving SAO VLG-11 masers P18 and P19.

TABLE 1

CHRONOLOGY OF VLG-11 MASER ACTIVITY AT U.S.N.O.

13 Sept. 1983 Power to masers turned off at SAO.
Masers shipped to the U.S.N.O. by truck.

14 Sept. 1983 Masers arrive at U.S.N.O. Power turned on
-- both masers oscillating. P19 degaussed.

22 Sept. 1983 $\Delta f/f$ (P18-UTC USNO) $= -1.13 \times 10^{12}$
$\Delta f/f$ (P19-UTC USNO) $= 0.93 \times 10^{12}$
$\Delta f/f$ (P18-P19) $= -2 \times 10^{13}$

(This, with synthesizer set at 1420405751.68700,
which was our best estimate for UTC at SAO
via Loran "C". Our probable error in UTC
is $\pm 5 \times 10^{13}$.)
Conclusion: Shipment did not alter the cavity
frequency significantly.

26 Sept. 1983 Both P18 and P19 were tuned.
After tuning $\Delta f/f$ (P19-P18) $= 0.11 \times 10^{-13}$
Maser cavity frequency shift was found to have
been as follows:

Δf_c(P18) $= +40.1$ Hz., Δf_c(P19) $= +24.68$ Hz.

27 Oct. 1983 $\Delta f/f$ (P19-P18) $= 3.03 \times 10^{-13}$
After tuning P19 $\Delta f/f$ (P19-P18) $= 2.08 \times 10^{-13}$
Δf_c(P19) $= +34.55$ Hz.

30 Jan. 1984 $\Delta f/f$ (P19-P18) $= 3.9 \times 10^{-13}$
After tuning P18 and P19 $\Delta f/f$ (P19-P18) $= 0.8 \times 10^{-13}$
Δf_c(P18) $= +28.9$ Hz, Δf_c(P19) $= +59.2$ Hz.

27 Feb. 1984 Power off P18 for several hours for installation
of U.S.N.O. Master Clock System.

24 Mar. 1984 Power off P19 for several hours for installation
of U.S.N.O. Maser Clock System.

10 May 1984 P19 automatically tuned using U.S.N.O. System.
Δf_c(P19) $= +46.4$ Hz.

16 May 1984 - $\Delta f/f$ (P19-P18) $= -0.6 \times 10^{-13}$
After tuning P18 $\Delta f/f$ (P19-P18) $= +2.4 \times 10^{-13}$
Δf_c(P18) $= +25.4$ Hz.

From the drift rate plot shown in Fig. 2, we see that tuning the masers had
no apparent effect on the drift rate. From the chronology we see that the
cavity resonator frequency of both P18 and P19 required systematic frequency

corrections to lower frequencies. The cavity frequency shifts obtained from the tuning data are shown in Fig. 3. From these data and our knowledge of the line Qs of the masers we can predict an average drift rate of the maser output frequency. For P19 we have 7×10^{-15} per day and for P18 we have 4×10^{-15} per day, between September 1983 and April 1984. This is in reasonably good agreement with drift data in February 1984, when P19 drifts $+9 \times 10^{-15}$ per day and P19 drifts 4×10^{-15} per day. The mistuning rate of the cavity, if ascribed to a change in axial length of the cylindrical cavity, requires a change of length for P18, $\frac{\Delta \ell_{18}}{\Delta T} = -1.9 \times 10^{-8}$ cm/day and for P19, $\frac{\Delta \ell_{19}}{\Delta T} = -3.8 \times 10^{-8}$ cm/day.

To relate this scale of dimensions to something very small, we note that a hydrogen atom has a diameter of about 10^{-8} cm. From the drift behavior and cavity frequency measurements we note the following:

1. The frequency change of the cavity is the dominant effect on the masers' frequency

2. The early drift rate appears more severe than the later drift and the overall drift rate seems to be asymptotically approaching zero.

The properties of ultra stable materials and the behavior of optically contacted surfaces in extremely stable materials have been described by S.F. Jacobs[2] from observations made using an iodine stabilized laser to measure length changes.

Figure 4, reproduced from reference 2, shows the settling of optically contacted surfaces in very high stability materials. The cavity cylinder and end plates of the SAO VLG-11-series masers are made of Cer-Vit C101®. After being ground to shape they are stress relieved by being etched in the surface microcracks[3] created in the grinding process. The mating surfaces are then optically polished and the cavities assembled under clean conditions so that

white light fringes are observed over the circumference of the joints between the cylinder and the endplates.

The cavities were assembled in May of 1983, and it is likely that the settling of the end plates was still in progress during late 1983, and early 1984. The settling behavior we observe with the polished surfaces of these cavities is at a much smaller rate than the previously observed settling behavior of cavity joints that were made with surfaces ground to a roughly 16 micro-inch finish. The settling rate was about 1 r.m.s. surface roughness distance in the first 40 days. The present surfaces are at least 10 times smoother and flatter, and the amount of initial mistuning after assembly has been substantially reduced.

The long-term dimensional behavior of structures made of extremely high stability material can be described in terms of $\frac{1}{\ell} \frac{\Delta \ell}{\Delta t}$, the "creep rate". Measurements of creep were made by S.F. Jacobs[2] in terms of optical path changes detected using a stabilized laser. His data give $\frac{1}{\ell} \frac{\Delta \ell}{\Delta t} \sim +5 \times 10^{-10}$ per day for Cer-Vit® (Cer-Vit C101 - Owens Illinois). Other materials, such as Zerodur® (Heraeus-Schott), Ultra Low Expansion Titanium Silicate® (Corning), Homosil® fused silica (Heraeus-Schott), and Corning® 7940 fused silica have creep rates between $+5 \times 10^{-10}$ and -5×10^{10} per day.

If we ascribe the maser frequency drift of the later months shown in Fig. 2 to cavity mistuning from material creep we obtain a rate of about -3×10^{-10} per day for Cer-Vit.

This agrees in magnitude with Jacobs' measurement on stable materials. It is opposite in sign for his creep rate for Cer-Vit, but agrees with his data for the other materials, which all have negative creep rates. This difference in sign for Cer-Vit may result from variations from sample to sample or from our

378

700°C cavity silvering process.

The performance of these masers indicates that the long-term stability of today's masers is chiefly governed by properties of the cavity materials. Electronic systems that stabilize the cavity resonance frequency beyond these levels must be capab'e of maintaining the maser frequency to better than a few parts in 10^{15} per day for long periods of time.

REFERENCES

1. Winkler, G.M.R., "Improved master-clock reference system at the U.S.N.O," Proc. 15th Ann. Precise Time and Time Interval Planning Meeting, U.S. Naval Research Laborato-/, pp 237,-248 (1983).

2. Jacobs, S.F., "Dimensional stability measurements of low thermal expansivity," Proc. 2nd Freq. Standards and Metrology Symp., U.S. National Bureau of Standards, pp. 269-278 (1976).

3. Muffoletto, C. Verne, "Reflective and refractive scattering of ultraviolet radiation caused by state-of-the-art optical grinding and polishing techniques." In Reflecting optics for synchrotron radiation. Soc. Photo-optical Instrumentation Engineers, vol. 315, pp. 85-88 (1981).
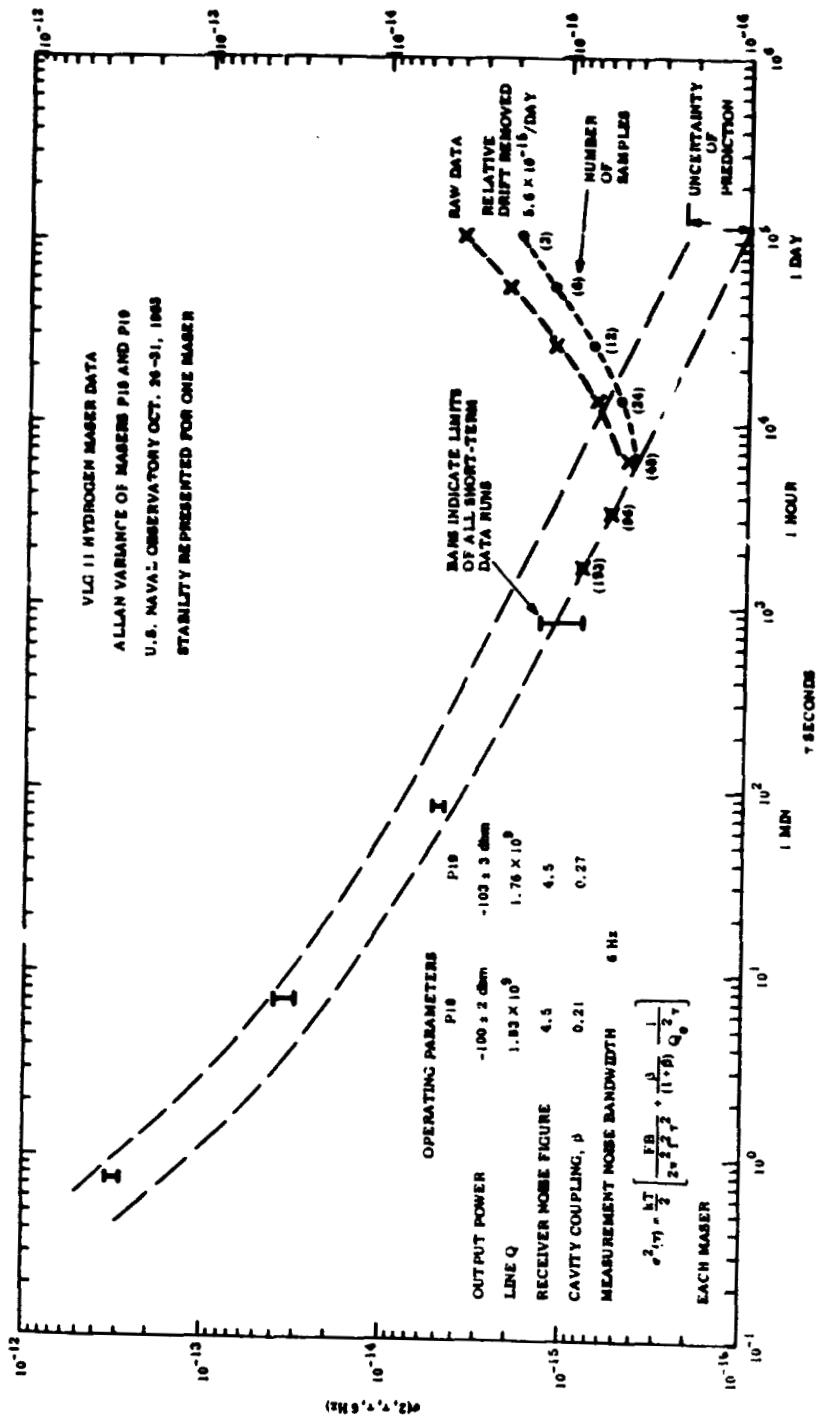
FIGURE 1

RATE OF FREQUENCY DRIFT OF
SAO P18 AND P19 AT THE
U.S. NAVAL OBSERVATORY
SEPTEMBER 1983 – OCTOBER 1984
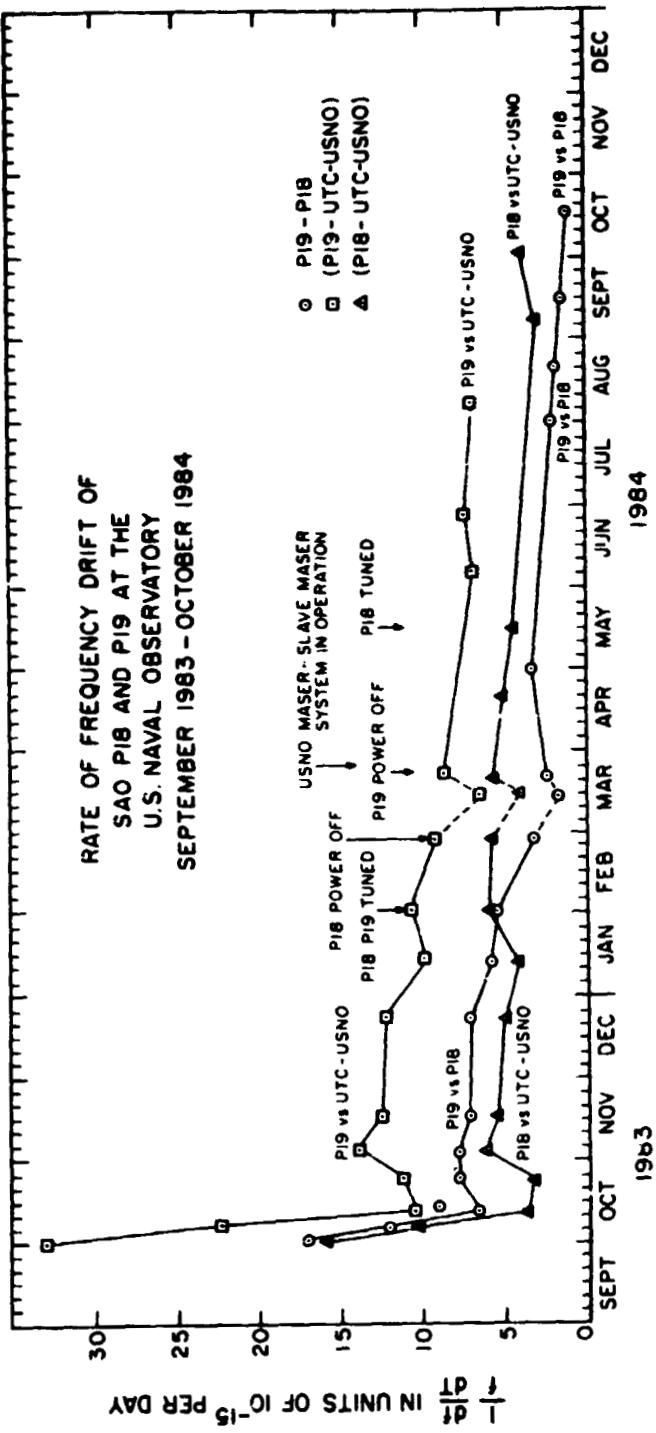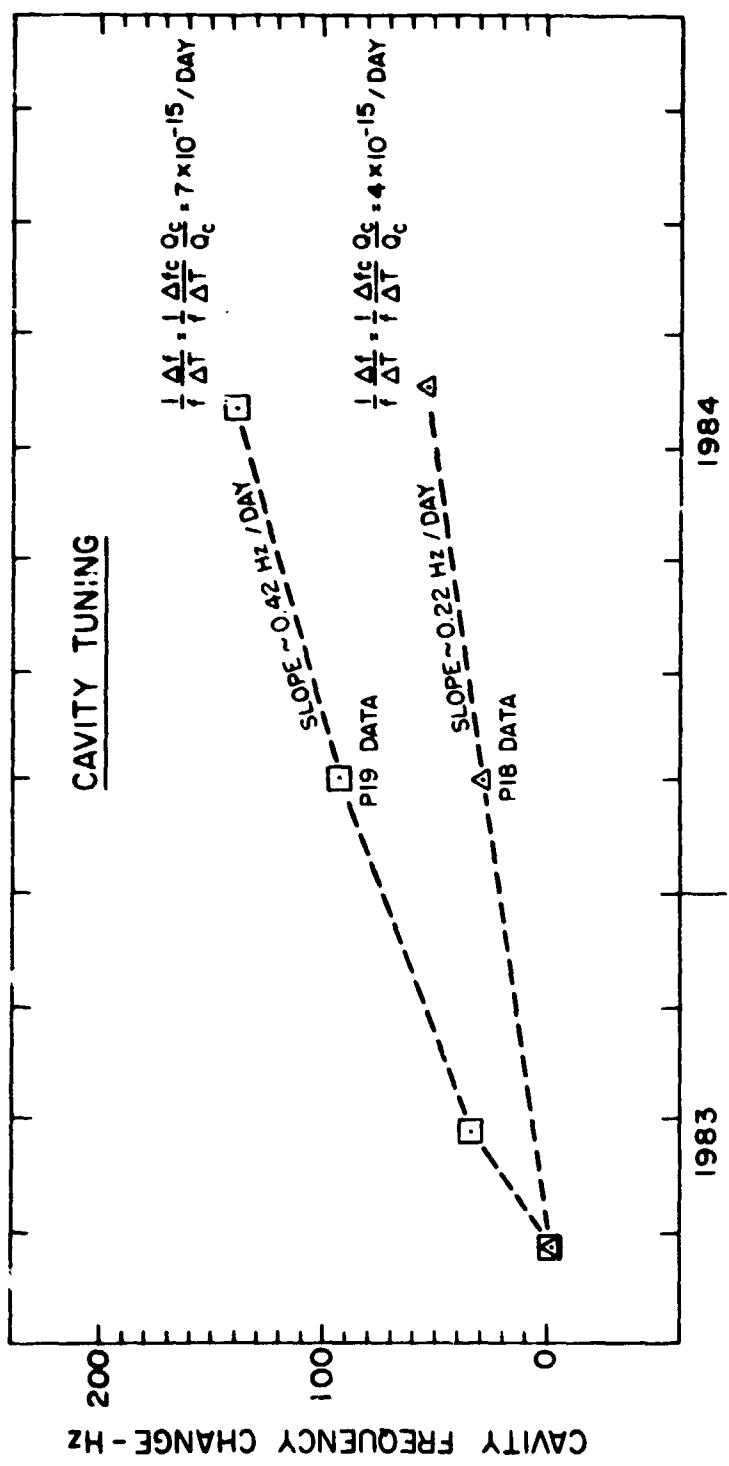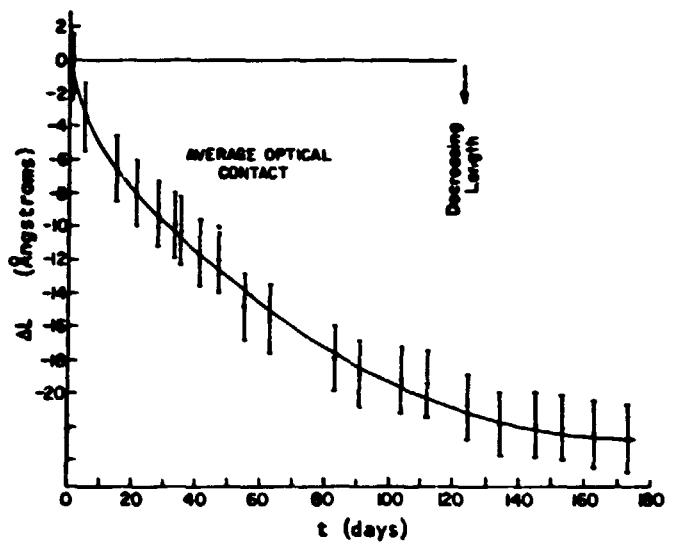
FIGURE 2

FIGURE 3

FIGURE 4

QUESTIONS AND ANSWERS

JACQUES VANIER, NATIONAL RESEARCH COUNCIL: What was the line Q that you observed in the VLG-11?

MR. MATTISON: The line Q that we used to get was on the order of 1.1 to 1.3 times ten to the ninth. More recently we have been getting values on the order of 1.8 to 1.9 times ten to the ninth.

MR. VANIER: I believe that there is a large gain to be made there. Simply a redesign of the bulb and of the collimator, so that you can increase that by a factor of three or four. Then the drift that you were talking about before, due to the creeping of the cavity, would be diminished dramatically. That would be fantastic.

MR. MATTISON: You are referring to changing the design of the collimator?

MR. VANIER: Yes. Because you can make it for a very long time constant, and it will still work very beautifully, so that you would be limited by the wall then.

MR. MATTISON: I does get limited by the wall. That increase in line Q that you observed has been due to our method of applying the teflon. We haven't changed the design at all.

MR. McCOUBREY: My impression is that with the advances you are making, there is going to be more and more interest in the actual structure and morphology of those surfaces. Maybe some of the polymer scientists would have to play a role in this, because I would expect that whatever happens with this teflon, and how it rearranges itself is something that they have looked into, and probably understand fairly well these days.

MR. MATTISON: Our method of applying teflon has changed. It is essentially a black art. All we know is that there is a recipe, and we apply it according to the recipe, and it works. If we do it a different way, it may work better.

MR. McCOUBREY: It sounds like there are some really interesting possibilities.

TIME TRANSFER TECHNIQUES: HISTORICAL OVERVIEW, CURRENT PRACTICES AND FUTURE CAPABILITIES

by

William J. Klepczynski

Time Service Department
U. S. Naval Observatory
Washington, D. C. 20390-5100

ABSTRACT

A brief historical review of time transfer techniques used during the last twenty years will be presented. Methods currently used will be discussed in terms of cost effectiveness as a function of accuracy achievable. Future trends will be discussed in terms of projected timekeeping capabilities.

INTRODUCTION

Within the last 20 years, we have seen improvements of several orders of magnitude in our ability to keep time. This has brought forth a number of sophisticated, timed navigation and communications systems and led to a dramatic improvement in the timekeeping capabilities of many laboratories and observatories. The timekeeping community has always been interested in transferring time between cooperating laboratories and in improving time transfer techniques as timekeeping capabilities improved. Obvious operational economies can be achieved through coordinated and synchronized systems.

Twenty-five years ago, timekeeping at the major observatories and laboratories of the world was between the 25-100 microsecond level. Fifteen years ago, it was at the 5-25 microsecond level. Up to about 5 years ago, it was down to the 1-10 microsecond level. Today, 1 microsecond timekeeping is achievable with a modest amount of effort. In fact, the major timekeeping centers are keeping sub-microsecond level timing, in the 5-200 nanosecond range. Soon, we can expect nanosecond or, even, sub-nanosecond timekeeping. However, it will not be easily achieved or come cheaply.

These statements concerning timekeeping require certain assumptions and understandings. "Timekeeping capability" as used here is neither rigorously defined nor is there a generally accepted consensus on what it means. Some would justifiably say that if they can make sub-nanosecond measurements in a laboratory, they then have sub-nanosecond timekeeping. However, it may not be possible to predict how that time scale will compare with some accepted standard at some future epoch. This view provides the basis for the definition used in this paper. This definition takes into account a "standard" of comparison and includes the duration of the measurement. Therefore, in assessing timekeeping capability for a somewhat realistic case, it should include the ability to maintain a reference clock to within some prescribed tolerance to either a time scale determined by averaging a number of clocks or some external reference over some period of time. In this context, then, a 1 microsecond (us) timekeeping capability would mean that a laboratory could maintain a reference clock to within 1 microsecond of a mathematically derived time scale or some external reference, such as maintained by some navigation system for a reasonable period of time. In order to be concerned with operational systems, a reasonable period of time would be four weeks.

In regard to the earlier mentioned developments in timekeeping, it is obvious that the

introduction of the commercially available cesium beam frequency standard was a significant milestone which caused the first major improvement noted some 20 years ago. Improvements to the cesium beam frequency standard (improved tube), improvements in the computation of local time scales and improved monitoring and measurement systems contributed to the next two rounds of improvements. During the next 10 years, we can look forward to the introduction of several new devices, such as stored ion frequency standards and optically pumped cesium beam frequency standards, into our timekeeping systems to spearhead the next round of improved capabilities. In order to utilize these devices in a practical way, more robust statistical techniques and improved, more stable measurement systems will also have to be introduced. Table I summarizes in tabular form, while Figure I presents in graphical form the progress made in "timekeeping" over the last 20 years and projects forward an estimate of what can optimistically be expected during the next 10 years.

TIME TRANSFER TECHNIQUES

Very frequently, after a timekeeping system has been inaugurated, it becomes desirable to intercompare it with another system or systems. This desire may be based on real need, such as a requirement to maintain a system to within some specified tolerance, or intellectual curiosity, such as an interest in seeing the performance of one system with respect to another. It should be emphasized that this latter case is also a real need, for example, one can be trying to intercompare laboratory type cesium beam frequency standards as a basis for the definition of the System International (SI) second.

A time transfer comparison is usually achieved by the one or two-way exchange of timing data. One-way time transfer data is based on receiving a timed signal from some transmitting system, such as a satellite disseminating time signal or a navigational system. Usually, one is concerned with simultaneous reception of the same signal. In order to use these signals for precise time transfer, one must first carefully evaluate the propagation path delay from the transmitter and all electronic component delays of equipment used in the receiving system. One usually neglects delays in the transmitting system because all measurements are usually referenced to the time the signals leave the transmitting antenna. However, this does not rule out the need to know the delays through the transmitting equipment. Once the delays have been carefully estimated, they usually remain fixed until components are changed. The received signals are usually referenced to some local time standard. Two-way time transfer depends on the mutual exchange of some timed signals between the two stations involved. Because the mutually exchanged signals travel through the same atmosphere, propagation path delays do not affect the results as they are common to both sets of measurements and usually drop-out of the final comparison of the two-clocks. If there is some relaying device, such as a satellite, between the two stations, then it must be carefully investigated whether each signal suffers the same delay as it propagates through the relaying devices. For satellites, this means careful pre-launch calibration.

Obviously, the precision and accuracy of Time Transfer Techniques should be comparable with the accuracies of the timekeeping capabilities of the systems we are comparing. If not, it could take an inordinately long period of time to make the comparison. A measurement precision of I ns will yield a frequency measurement good to 1×10^{-12} in just 1000 secs (17 min). A measurement system good to I microsecond will need over a day to attain the same precision in frequency.

The capabilities and usage of several Time Transfer Techniques over the last two decades will be traced in order to develop a picture of future expectations in the field of Time Transfer. An historical approach to the categorization of the techniques (CCIR, 1982)

will be used. These categories include geographic area of coverage, frequency domain of the technique, and major system categorization, such as, navigation or communications systems.

One of the simplest methods of classification is through the specification of the frequency used to exchange timing data, such as radio or optical. In the former, we usually find sub-groups such as very low frequency (VLF), low frequency (LF), high frequency (HF), very high frequency (VHF) or microwave. Optical methods usually include laser pulses or optical fiber techniques. Various systems developed for special purposes such as navigation or communications can also be used for time transfer. These systems can be either land-based or satellite-based. The most obvious ones are the navigation systems, such as Loran-C, Transit, Omega and the Global Positioning System (GPS) and the communication systems, such as geostationary commercial communications satellites and the Defense Satellite Communications System (DSCS). Very Long Baseline Interferometry (VLBI), because it requires highly precise frequency standards which are used as a local reference oscillator and clock, can be used as a time transfer system over intermediate to intercontinental distances. Time transfer techniques which are local in coverage include both radio (TV, microwave, satellite systems) and optical (laser pulses and optical fibers). Methods which are intermediate in coverage include LF, HF and satellite systems. Hemispheric or intercontinental coverage in time transfer can be achieved through VLF or satellite systems. The latter are used for greatest precision. The satellite systems can be at either radio or optical frequencies.

During the last 20 years, the various systems mentioned above have been used in varying degrees by the timekeeping community to effect time transfers. Some systems have enjoyed more use than others, some have recent popularity. The choice of system is based on requirements and available funding. The popularity of some systems rests on the fact that over the years, they have shown an ability to increase system performance with time and use. Some systems have not and tend to be bounded in their time transfer capabilities. Hence, their usage quickly becomes limited. As it is with timekeeping systems, progress is marked by one of three items:

a) introduction of new devices, i.e. new technique;
b) improvements to fundamentals of technique, i.e. improved propagation theory or hardware;
or
c) technical improvements in ancillary or support systems, i.e., improved measurement components (SITREM modems).

As the capabilities of these systems for time transfer are traced over the last 20 years, the various factors which have caused enhancements in their capabilities will be mentioned as well as the factors which limit the technique.

RADIO TECHNIQUES FOR TIME TRANSFER

While optical methods, such as the dropping of a time ball at noon, dominated the early history of time transfer, their area of coverage was a limitation to their use. The introduction of the telegraph for time distribution brought about a major revolution in time transfer. The area of coverage of a time transfer system was greatly expanded. A significant increase in accuracy of time transfer was also achieved compared to the dropping of the time ball. We have here the case of an increase in time transfer capability through the use of a new technology.

A. VLF and LF Techniques

In 1904, the use of VLF transmissions from a U. S. Navy communication station for time distribution brought about another revolution in time transfer capabilities. A whole new region of the spectrum and a whole new technology was quickly seized-upon to effect intercontinental time transfer. By 1964 (Blair, 1974), time transfer techniques using VLF transmissions were good to about 50 us. in accuracy. The primary usage of VLF signals which has evolved over the last 20-30 years has been as a means of frequency control and stability measurement. Propagation path variations have proven to be the largest limitation to their use as a source of time. These variations are of a periodic nature, which can be modeled to a large extent, and a non-periodic nature, such as Sudden Ionospheric Disturbances (SID's) and Polar Cap Absorptions (PCA's), whose amounts can not be predicted. It was thought that the introduction of the Omega Navigation System, which used several VLF transmissions, would allow time to be recovered to about 1 us through the use of two-frequency techniques. More will be said about this in a later section. In any event, the non-predictable variations in both the periodic and non-periodic portions of propagation path variations have proven to be a limitation to the use of this technique to better than 10 us in accuracy. Extreme care and ideal laboratory conditions and equipment might reduce this number by 30-60 percent.

LF transmissions are subject to the same limitations in accuracy as the VLF systems. Dispersion, caused by the difference in the phase and group velocities of the VLF and LF waves, must be taken into account. As mentioned earlier, the primary effects in the VLF region are in the ionosphere. While in the LF region, the primary effects are caused by ground conductivity variations.

B. HF Techniques

The HF standard time and frequency transmissions have proven to be the most extensively used timing signals. While unmodelable ionospheric variations tend to limit their accuracy to about 0.2 ms., they are the most widely used and cost-effective means of time transfer. Their lack of great accuracy has not hampered their popularity and frequency of use because there are a large number of users who need time only to the accuracy necessary for everyday life, 1 sec. In fact, these HF signals are necessary for the initially setting most high precision time transfer systems in order to set their observing windows.

C. TV Techniques

While more limited in geographical coverage than other RF techniques, TV time transfer systems are capable of reasonably high degrees of accuracy and precision The original experiment of Tolman et al (1967) and its immediate applications were limited to about 100 ns in accuracy primarily because of receiver noise. Improved hardware has now reduced that number to about 10 ns. The atmosphere now seems to be the limiting factor for this technique. Geographic coverage is limited to primarily line-of-sight by the fact that the path the signals take are subject to large and unpredictable variations in order to compensate for the source of some network programming. Table 2 summarizes the development of the RF techniques for Time Transfer during the last 20 years.

NAVIGATION SYSTEMS FOR TIME TRANSFER

During the last 20 years, navigation systems have been the primary means for time transfer where wide geographic coverage and a relatively high degree of accuracy are required (Klepczynski, 1983). The four major systems in use for this purpose are Omega, Transit, Loran-C, and the Global Positioning System (GPS). In all but the Transit system,

the navigation signals emanating from their respective transmitters are controlled by redundant cesium beam frequency standards. This assures the reliability and stability of the signals.

The importance of these navigation systems to the timekeeping community cannot be overstated. Loran-C has been the primary vehicle which has allowed the Bureau International de l'Heure (BIH) to compute International Atomic Time (TAI) based on international representation. By noting the difference of contributing cesium clocks with respect to locally received Loran-C signals, it is possible to form a semi-global time scale through somewhat sophisticated averaging techniques (Granveaud and Guinot, 1976). The degree to which the various Loran-C chains can be coordinated (Charron, 1981) determines the geographic extent of contributing laboratories. The use of GPS for this purpose has been growing. Because of its precision and accuracy and because it is a truly global system, GPS can contribute significantly to this task. In fact, GPS timing receivers are now located on four continents and are allowing many more laboratories to contribute to the formation of TAI. It is thus becoming a truly international time scale.

A. Omega

As mentioned earlier, Omega suffers from the same limitatio.. ..t affect all VLF transmissions. Initial experiments with dual frequency timing receivers indicated that it was possible to build a receiver that could acheive a microsecond precision in timing. Unfortunately, ionospheric variations significantly degraded the transmitted signals to the 1-5 us level. More significantly, the frequency difference used in the experimental dual frequency timing receivers was not found among the frequencies actually transmitted by the operational Omega system, including the four navigation and one unique frequency transmitted by each member of the system. Thus, while Table 3 indicates a limit of 5 us for Omega time transfer, it cannot be achieved in practice.

B. Transit

The navigation solution in the Transit system analyzes the received Doppler shift of the signal transmitted from the spacecraft. The stability requirements of the transmitted navigation frequency translates into a timing requirement of about 500 us. These requirements can be met by a high quality crystal oscillator. However, the ground stations which control the spacecraft oscillator, all make their measurements with respect to cesium beam frequency standards. Thus, control of the spacecraft oscillator is operationally maintained at a higher level than required by the navigation requirements. In fact, Transit timing receivers can attain a precision of 25 us in their time transfer capabilities. The new Nova satellite, which was launched into orbit in 1982, contains a significantly better oscillator control system than the older Oscar satellites, consequently time transfers utilizing the Nova spacecraft can achieve a precision of between 3-20 us. In addition, the Nova spacecraft has built into it a PRN code modulation scheme which has the inherent capability to improve Transit time transfers to the sub-microsecond level. Unfortunately, this capability has not been operationally implemented.

C. Loran-C

Each of the 3-5 transmitting sites making up the stations of a Loran-C chain has 4 cesium beam frequency standards governing the timing of the transmitted pulse. Synchronization within a chain can be kept within 20 ns. However, this is a relative synchronization and relates to navigation. It does not pertain to time transfer accuracy. It is a measure of the ultimate accuracy limit for time transfers if all

systematic effects can be taken into account. The initial time transfer receivers developed for Loran-C were very awkward to use, requiring an oscilliscope and excellent judgement in locating the third zero crossover of the first pulse of the series of navigation pulses. The early seventies saw the emergence of the Austron 2000C Loran-C timing receiver. While it was not a completely automatic receiver and still a little cumbersome to use, it did help make the process of locking the receiver to the Loran-C signals a little easier. A good technician, with a little training, could set one up within an hour. However, the process still required the use of an oscilloscope and good judgment in locating the third zero crossover.

Our knowledge of the perplexities of the propagation path delay computations has improved. Computer programs, which computed the propagation path delay, began to take into account the conductivity of the surface over which the signals travelled. Thus, it became possible to achieve microsecond time transfers using Loran-C in certain parts of the world. With the advent of the Austron 2100, a microprocessor based Loran-C timing receiver in the early 80's, many of the problems associated with setting up a Loran-C timing receiver disappeared. The primary one being the selection of the third zero crossover. Inspection of time transfer data taken with these new receivers indicate a root mean square error of about 20-30 ns. Unfortunately, comparison of Loran-C time transfers with other techniques, in particular communication satellite time transfers (Costain et al, 1979) are supporting the conjectures that there is an annual variation in the propagation path delays on the order of about 1 us.

D. GPS

The GPS system is a satellite-based navigation system which will give 24 hour, world-wide, three dimensional position fixing capability to two levels of accuracy, 16m and 100m, respectively. The navigation signals transmitted from each of the 18 satellites in the final configuration will be controlled by cesium beam frequency standards or a rubidium frequency standard. GPS system time, which is based on the time kept at a ground station which has been designated as the master clock for the system, is physically kept to within 1 us of UTC(USNO). In addition, a set of coefficients is transmitted with the navigation message which allows the user to derive UTC(USNO) to within 100 ns.

Two portable clock verification trips in the mid-seventies showed that the GPS system would prove to be the major time distribution and time transfer system of the future. The first involved the acceptance testing of a single frequency time transfer unit (Putkovich, 1979) which showed that the set was capable of an accuracy of 50 ns. The second verified the time transfer capabilities of a specially modified dual frequency navigation receiver (Roth et al, 1979). This series of experiments showed an accuracy of 27 ns in time transfer capability. That these tests verified the time transfer capabilities of the GPS system at such an early stage of its development, indicated that the system had great potential.

Allan and Weiss (1980) pointed out the advantages of using common-view time transfer measurements. In this way, the limitations in precision of present single frequency GPS Time Transfer Units can be better overcome. By looking at the same satellite at the same instant, two stations could reduce the error budget in their time transfers by a significant amount because all errors common to the spacecraft clock and most of the error due to poor ephemerides would be eliminated from the measurements. The primary errors left in the measurements would be that due to the differential, unmodelled ionospheric path delays between the two stations. The differential unmodelled tropo-spheric corrections should be about a nanosecond or smaller, provided that the

tropospheric models are correct. Portable clock visits, which are also necessary for system calibration, have demonstrated that common-view GPS time transfers show u consistency of between 5-10 ns. Table 3 summarizes the development of navigation systems for Time Transfer during the last 20 years.

SATELLITE SYSTEMS FOR TIME TRANSFER

Besides the satellite-based navigation systems, there exist a number of satellite-based communications systems which are extremely effective for time transfer. The use of geostationary communication satellites for time transfer goes back to 1962 when clocks at USNO, NPL and RGO were compared to an accuracy of 1 us using two-way exchange of 5 us long pulses through the Telstar satellite (Steele et al, 1964). During the late 70's, a three-year long link was established between North America and Europe using the Symphonie satellite (Costain et al, 1979) at C-band (4/6 GHz). At the same time, experiments using the Hermes/CTS satellite at K-band (12/14 GHz) were commenced between USNO, NBS and NRC (Costain, 1979). Sub-nanosecond precision and accuracies of 20-50 ns were obtained by these techniques. Recently, a new PRN modem (SITREM), specially designed for time transfer (Hartl et al, 1983 a), has been used in some experiments (Hartl et al, 1983 b). While precisions in time transfer achieved with this ' RN modem are comparable to those achieved in the latter Hermes/CTS experiments, i.e., 600 ps, the main advantage of these modems lies in their simplicity of use and small power requirements. Only 1 watt of transmitting power is required. Because of the PRN coding technique and low power, the signals are non-interfering.

If care is not taken to carefully calibrate and measure all delays in the satellite being used before launch, these techniques suffer in attainable accuracy. Hence, portable clock trips are necessary to remove systematic errors between cooperating stations. Because these techniques use two-way exchange of signals, many common errors drop out of the time transfer mathematics. However, non-reciprocal delays through the channels and transponders of the satellite do not drop out, as well as differential ionospheric and tropospheric delays. The use of DSCS for time transfer is similar to that of using commercial communications satellites, in principle. Because of operational requirements, here are some technical differences in how the time transfers are made. However, the results are comparable.

The GOES satellite is primarily a weather and environmental monitoring platform. The data down-linked from the satellite contains a time code provided by and referenced to the NBS (Hanson et al, 1979). The system is used as a time distribution system in North America. If the user applies corrections for his location, an accuracy of 1 ms can be attained. If the user also applies corrections for the position of the satellite, an accuracy of 30-50 us can be achieved. Table 4 compares the capabilities of some satellite systems over the last 20 years.

SPECIAL SYSTEMS FOR TIME TRANSFER

While navigation and communication systems are significant contributors to the timekeeping field, several other systems, such as VLBI, laser ranging and Portable Clocks, also contribute significantly. There is no single unifying theme which brings these three techniques under one category. VLBI requires highly precise frequency standards at each station in a network. The VLBI correlation process, itself, determines the offsets in both epoch and frequency of the clocks within the network. Thus, a VLBI network is a self-contained synchronized network (but not in real-time). Very short laser pulses can form the basis of a highly precise time transfer system, because the time of arrival of a coded seque ? of extremely short laser pulses can be unambiguously and

precisely determined. Portable clocks are included in this category, because they have been the ultimate technique for verification and calibration of all other techniques. VLBI has shown itself to be an extremely precise time transfer system. Over the years, the data recording techniques used in various VLBI systems has grown and evolved into the present wide band system known as the Mark III system. The original Mark I sytem had a bandwidth of only 2 KHz. Allen Rogers (1976) has shown that the ultimate capability to synchronize two VLBI tapes is based on their bandwidth and S/N ratio of the observed sources. For the Mark I system, this is about 150 ps. For the Mark II system, whose bandwidth is 4 MHz, this number is typically about 100 ps. These numbers refer to the inherent precision which the correlation process can attain. However, there are many systematic effects which must be removed in order to achieve accuracy. Several experiments have attempted to verify the VLBI intrinsic capabilities by carefully calibrating and evaluating the many delays through the elements of a VLBI system (Clark et al, 1979; Spencer et al, 1981; and Johnston et al, 1983). The best results which have been obtained to date are those of Spencer et al (1981) and Johnston et al (1983) where verification was done at the 3 ns and 2 ns levels, respectively. It has become rather obvious that at these levels, present day verification and calibration techniques are marginally adequate. The ultimate limitation to VLBI time transfer appears to be the atmosphere and will limit the accuracy of VLBI time transfers to about 60 ps (Crane, 1976).

The two-way exchange of laser pulses should prove to be an extremely precise and accurate method for time transfer. When used to synchronize two ground stations over a distance of 35 km, a precision of 600 ps was achieved (Alley et al, 1982). Inter-continental time transfer, as proposed by the Lasso Program (Leschiutta, 1979), using a satellite with a retro-reflector and an on-board event timer should achieve similar results. However, this experiment has not been done as yet because the satellite planned for this purpose never made it into orbit. Use of very short laser pulses assures that the time of reception will be precisely recorded. Use of a reflecting surface, as opposed to a relaying transponder in the radio region, assures a reciprocal path. The differential variations in the propagation path delay during two-way exchange of laser pulses would become the limiting factor to the accuracy of this method. Thus, it seems that this technique should prove to be the verification and calibration system of the future. Unfortunately, laser stations which have sufficient capability both in regards to manpower and equipment are very few and very expensive to operate.

For the moment, the portable clock is the primary, although somewhat limited, verification and calibration system for certifying the accuracy of time transfers. Over the years, the capabilities of portable clock trips has improved. Initially, in the early 60's, one could only expect 1-5 us as the resulting accuracy of a PC trip. This improved dramatically with the introduction of the cesium clocks with the high performance beam tube. Since the early 70's (Putkovich, 1981), several factors have contributed to the further improvement in the accuracy attained with PC trips. Improved monitoring of the PC before and after the trip and care in minimizing the duration of the trip have helped the situation. For special critical experiments, an ensemble of clocks (Hafele & Keating, 1972 and Spencer et al, 1981) has been used. Presently, the best performance that can be expected from a PC trip is about 1 ns. This means a short trip and use of more than one PC. Table 5 shows the capabilities of these special systems during the last 20 years.

COST FACTORS OF VARIOUS TIME TRANFER TECHNIQUES

Many factors enter into the choice of selecting a time transfer system to meet a require-ment. Very often, cost is the single most important factor. Table 6 is presented in order to give a comparison of costs versus accuracy of technique. There is a general trend of

increased precision meaning increased costs. However, on considering GPS, it can be seen that for about twice the cost of a Loran-C timing receiver, one gets 8-10 times the performance. It should be pointed out that within a few short years, GPS timing receivers have dropped in price from their initial offering of about $55K to about $25K in 1985. It is expected that this trend should continue. It is also interesting to note that at $25K, GPS timing receivers are less than the price of a cesium beam frequency standard. The sub-nanosecond techniques, at this point in time, are still expensive. In order to utilize commercial communication satellites, an Earth station is needed. It would cost about $105K to outfit one. However, this may not be a significant problem as many laboratories almost have this capability if resources with sister institutions are combined. The use of VLBI requires the equivalent of a radio astronomical observatory. The cost of establishing one would be in excess of $1000K. A local, high-precision laser ranging system could be established for several hundreds of thousands of dollars. To expand to an intercontinental time transfer system would require the establishment of an observatory quality facility at a cost in excess of a million dollars. However, one should not look at askance at these techniques. It may not be necessary to commit these vast resources to utilize these techniques. Several observatories already participate in VLBI networks. Consequently, the building blocks for nodes in an organized time transfer system exist. As timekeeping capabilities evolve and there becomes a greater need to perform super-precise and accurate time transfers on a regular basis, the use of existing resources in a cost-effective manner will evolve.

DISCUSSION AND CONCLUSIONS

It does not seem that in the next ten years we will have any significant changes in time transfer instrumentation. Existing technology, with improvements, can probably keep up with timekeeping improvements, which will be based upon the introduction of hydrogen maser devices into time scales and also other new standards such as stored ion devices. Unless some serendipitous discovery allows a new type of technology to be applied to timekeeping, there appears to be no major quantum leap in time transfer technology capabilities in prospect. Most likely, we will witness a gradual evolution in the improvement of precision and accuracy of current techniques, some of which are in their developmental stage, i.e., laser-ranging. Most likely, these improvements will lead to the 10-100 ps range in time transfer capability. Satellite communications systems will play a larger role in time transfer techniques. These systems will go to higher frequencies with greater system bandwidths. Hopefully, we will see better pre-launch calibration in order to improve their accuracy. We will probably see the development of an intercontinental laser-ranging time transfer system. In order to utilize resources in a cost-effective manner we will see a developing hierarchy where some laboratories or observatories will become important nodes in an integrated time transfer network.

GPS will play a major role in worldwide time transfer. It will become one of the most cost-effective systems for a majority of users, in spite of the cloud of Selective Availability and Denial of Accuracy which hangs over the community of civilian users. There are effective ways to overcome some shortcomings, perhaps not in real time and perhaps not attaining all of the present day's precision attainable with the Standard Positioning Service. However, it still will be a viable cost-effective system. In the coming decade, there could arise a need for satellite-to-satellite time transfers. This would evolve from a need for the worldwide exchange of data through satellites or be driven by scientific reasons such as interferometry in space. There may be a demand for medium precision time transfer in order to synchronize networks of computers. The future will offer many challenges.

REFERENCES

D. W. Allan and M. A. Weiss

"Accurate Time and Frequency Transfer during Common-View of a GPS Satellite", Proceedings of 34th Annual Frequency Control Symposium, 1980.

C. O. Alley, J. D. Rayner, C. A. Steggerda, J. V. Mullendore, L. Small and S. Wagner

"Time Transfer Between the Goddard Optical Research Facility and the U. S. Naval Observatory Using 100 Picosecond Laser Pulses". Proceedings of the 14th Annual PTTI Applications and Planning Meeting, 1982.

B. E. Blair

"Time and Frequency Dissemination, An Overview of Principles and Techniques", NBS Monograph 140, Time and Frequency - Theory and Fundamentals, 1974, Chapter 10.

L. G. Charron

"Relationship Between U. S. Naval Observatory, Loran-C and Defense Satellite Communication System". Proceedings of the 13th Annual PTTI Applications and Planning Meeting, 1981.

T. A. Clark, C. C. Counselman, P. G. Ford, L. B. Hanson, H. F. Hinteregger, W. H. Klepczynski, C. A. Knight, D. S. Robertson, A. E. E. Rogers, J. W. Ryan, I. I. Shapiro and A. R. Whitney

Synchronization of Clocks by Very Long Baseline Interferometry", IEEE Trans. Instr. Meas., Vol IM_28, 184-187, September, 1979.

International Radio Consultation Committee (CCIR)

"Recommendation and Reports of the CCIR, 1982, Volume VII, Standard Frequencies and Time Signals". International Telecommunication Union, Geneva.

C. C. Costain, J. S. Boulanger, H. Deams, D. W. Hanson, R. E. Beehler, A. J. Clements, D. D. Davis, W. J. Klepczynski, L. Veenstra, J. Kaiser, B. Guinot, J. Azoubib, P. Parcelier, G. Freon and M. Brunet

"Two-Way Time Transfer via Geostationary Satellites NRC/NBS, NRC/USNO and NBS/USNO via Hermes and NRC/LPTF via Symphonic". Proceedings of the 11th Annual PTTI Applications and Planning Meeting, 1979.

R. K. Crane

"Refraction Effects in the Neutral Atmosphere" Methods of Experimental physics : Astrophysics, Part B - Radio Telescopes, Edited by M. L. Meeks, Academis Press, 1976.

D. M Granveaud and B. Guinot

"Atomic Time Scales", IEEE Trans. Instr. and Meas., Vol IM-21, 396, 1972.

J. C. Hafele and R. E. Keating

"Around the World Atomic Clocks : Observed Relativistic Time Gains", Edi.ed by M. L. Meeks, Academic Press, 1976.

D. W. Hanson, D. D. Davis and J. V. Cateora

"NBS time to the western hemisphere by satellite". Radio Science, Vol 14, 731-740, July-August, 1979.

P. Hartl, N. Gieschen, K. Mussener, ».. Schafer and C. Wende

"High Accuracy Global Time Transfer Via Geosynchronous Telecommunication Satellites with MITREX", Journal of Flight Sciences and Space Research, Vol 7, No. 5, 335-342, Sept-Oct, 1983.

P. Hartl, L. Veenstra, N. Gieschen, K. M. Mussener, W. Schafer, C. M. Wende, W. J. Klepczynski, H. H. Nau and R. Stoiber

"Spread Spectrum Time Transfer Experiment via Intelsat". Proceedings of the 15th Annual PTTI Applications and Planning Meeting, 1983.

K. J. Johnston, J. A. Buisson, M. J. Lister, O. J. Oaks, J. H. Spencer, W. B. Waltman, G. Elgered, G. Lundquist, A. E. E. Rogers, T. A. Clark. C. Ma, A. C. Johnson, K. Kingham, W. J. Klepczynski, G. Luther, A. J. Kubik and D. D. McCarthy

"Precise Time Transfer Using Mark III VLBI Technology". Proceedings of the 15th Annual PTTI Applications and Planning Meeting, 1983.

W. J. Klepczynski

"Modern Navigation Systems and their Relations to Timekeeping". Proceedings of the IEEE, Vol 71, 1193, October, 1983.

S. Leschiutta

"The Lasso Program - An Overview". Proceedings of the 11th Annual PTTI Applications and Planning Meeting, 1979.

K. Putkovich

"Time Dissemination - An Update". Proceedings of the 11th Annual PTTI Applications and Planning Meeting, 1979.

K. Putkovich

"Precise Time Dissemination via Portable Atomic Clocks". Proceedings of the 13th Annual PTTI Applications and Planning Meeting, 1981.

A. E. E. Rogers

"Theory of Two-Element Interferometers", Methods of Experimental Physics = Astrophysics, Part C - Radio Observations, Edited by M. L. Meeks, Academic Press, 1976.

B. Roth, W. J. Kiepczynski and R. G. Hall

"Time Transfer with the NAVSTAR Global Positioning System". Proceedings of the 11th Annual PTTI Applications and Planning Meeting, 1979.

J. H. Spencer, E. B. Waltman, K. J. Johnston, N. J. Santinis, W. J. Klepczynski, D. Matsakis, P. E. Angerhofer and G. Kaplan

"Comparison of VLBI, TV and Traveling Clock Techniques for Time Transfer". Proceedings of the 13th Annual PTTI Applications and Planning Meeting, 1981.

J. Tolman, V. Ptacek, A. Soucek and R. Stecher

"Microsecond clock comparisons by means of TV synchronizing pulses". IEEE Trans. Instr. and Meas., Vol IM-16, 247-254, December 1967.

L. E. Young

"Traveling Clock Verification of VLBI Clock Synchronization". Proceedings of the 11th Annual PTTI Applications and Planning Meeting, 1979.

Table I

TIMEKEEPING IN BETTER

TIMEKEEPING LABORATORIES

1984	1-100us	Commercial cesium just introduced (HP5060). Crystals start to be phased out.
1974	50-1000ns	High Performance Cesium Beam Tube introduced
1984	5-200ns	Time scale algorithm improved. Improved measurement and control systems. Active hydrogen masers introduced. Laboratory type cesiums being run as clocks.
1994	0.1-5ns	Improved optically pumped Cs tubes Stored Ion Devices Passive Hydrogen masers Cooled active hydrogen masers Robust techniques for algorithms Improved measurement systems

Table 2

RF TECHNIQUES FOR

TIME TRANSFER

	1964	1974	1984	SOURCES OF ERROR
VLF	500us	10us	10us	Variation in propagation path delay due to ionosphere
LF	50us	40us	20us	Variations in propagation path dealy due to Ionospheric variations and ground conductivity variations
HF	1ms	0.2ms	0.2ns	Propagation delays
TV	-	100ns	10ns	Atmosphere

Table 3

NAVIGATION SYSTEMS FOR

TIME TRANSFER

	1964	1974	1984	COMMENTS
LORAN-C	5-10us	0.5-5us	40-700ns	Seasonal Term
OMEGA	-	5us	5us	
TRANSIT	500us	25us	3-20us	Dependent on satellite used
GPS	-	100ns	5-40ns	Best results with common view

Table 4

SATELLITE SYSTEMS FOR

TIME TRANSFER

	1964	1974	1984	COMMENTS
GOES	-	50us	30us	Time distribution system
DSCS	-	100ns	50ns	Measurement System limited
Commercial Communication Satellite	1us	10ns	200-600ps	Spread Spectrum PRN modems

Table 5

SPECIAL SYSTEMS FOR

TIME TRANSFERS

	1964	1974	1984	
Portable Clocks	1-5us	30-1000ns	5-500ns	Limited by duration of trip
VLBI	–	150ps(15ns)	60ps(3ns)	Ultimately limted by atmosphere to about 60ps accuracy; values in parenthesis indicate verification
Laser-Ranging			200-600ps	

Table 6

COSTS OF VARIOUS

TIME TRANSFER TECHNIQUES

	Method	Cost for System (Receiver)	Accuracy
1)	GOES	$7K	20us
2)	TRANSIT	$12K	15us
3)	LORAN-C	$10K (receiver)	40-100ns
		$3K (micro-processor)	
4)	Portable Clock	$43K	10-100ns
5)	GPS	$20-32K	5-40ns
6)	Comm. Satellites	$30K (antenna) $15K (PRN Modem) $60K (other electronics)	1ns
7)	VLBI		1ns
8)	Laser Ranging		1ns

399
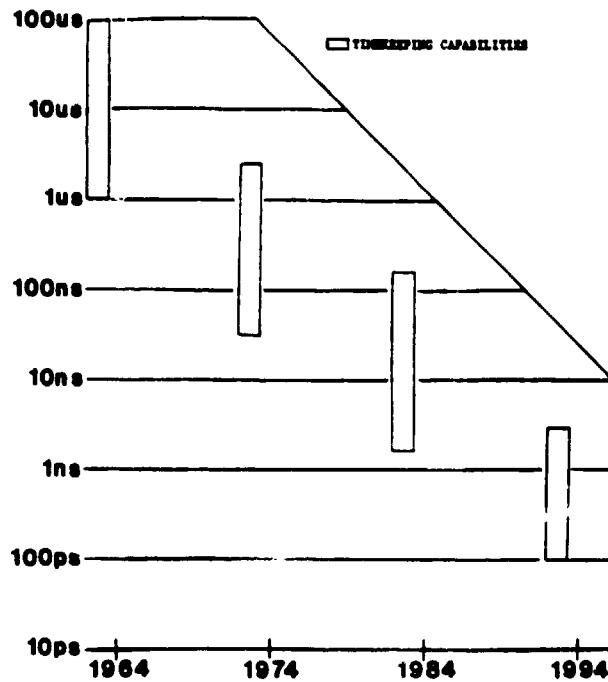
Figure 1   Range of values expected in timekeeping capabilities at better laboratories. The values for 1984 are author's estimates.
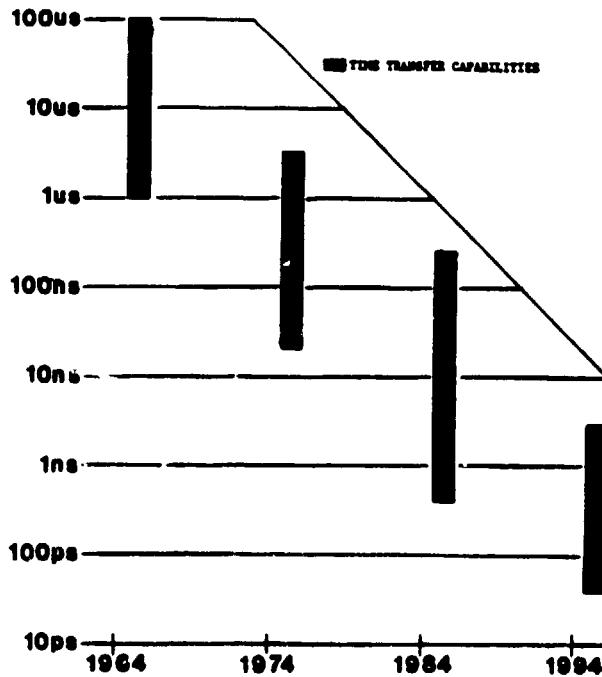
Figure 2   Range of Time Transfer capabilities. The values for 1984 are the author's estimates.
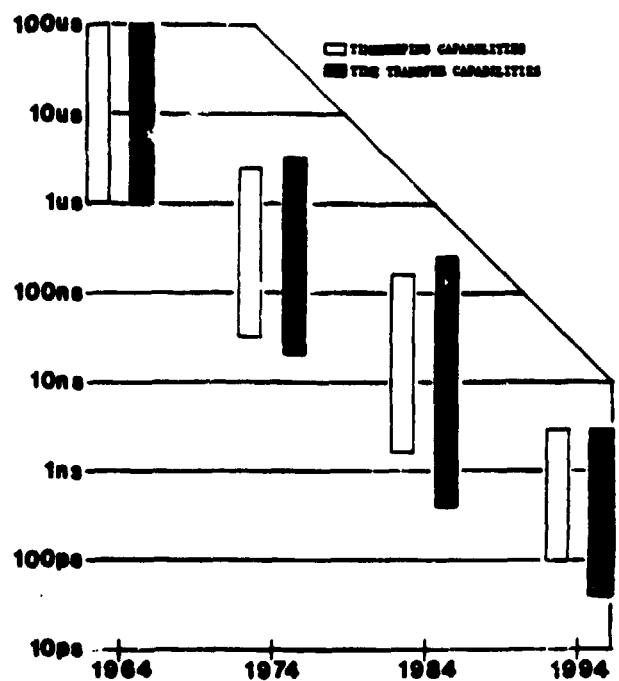
Figure 3   Composite of Figures 1 and 2

QUESTIONS AND ANSWERS

BOB BAKER, VANDENBERG AIR FORCE BASE, FEDERAL ELECTRIC CORPORATION, ITT: Would you say a few words about selective availability for GPS, please.

MR. KLEPCZYNSKI: That is a difficult subject. Right now the plan or policy is that, eventually at some time, when the system becomes operational, the current capabilities of the system for the CA code will be degraded to about a 100 meter precision for navigation purposes, which would mean that it would go down to about 300 nanoseconds for time transfer.

However, the common view mode would eliminate some of these problems.

In addition, not all of the satellites which are in orbit now would have that capability, would not be able to have the selective availability applied to them. It's only the last one or two satellites which have been launched which have that capability, as well as the future ones. Those already in orbit will still provide that capability for five or ten years -- their lifetime. There are some clouds on the horizon, but it's not that bad. The system will evolve and, I think, keep going.

MR. BUISSON: Let me add one thing. The selective availability capability will exist, but there is a chance that it will never happen.

MR. BAKER: Thank you. I have another question: On your commercial satellite, you didn't list the cost of the satellite usage.

MR. KLEPCZYNSKI: That is difficult to get a handle on. Some of the new techniques, in particular the spread spectrum modem, only need one four megahertz wide voice channel. You don't need the number of channels that you need for a TV broadcast or anything like that. Time costs about fifty dollars per hour or less but, for time transfer, you wouldn't be on the air for an hour. All you would have to be on would be five or ten seconds, or maybe five minutes if you wanted it to be really good.

That part of the cost is relatively minor. It's the initial capital cost which would be the biggest problem.

SAM WARD, JET PROPULSION LABORATORY: I think it should be emphasized also that, although highly precise, the laser and VLBI techniques carry a heavy burden in the a priori level of time synchronization that must be established before you can use the technique.

MR. KLEPCZYNSKI: There is no question about it. That's why I indicated that there are going to be very few centers with that capability.

MASTER AND SECONDARY CLOCK IN TELECOMMUNICATIONS NETWORKS

By

Allan Risley

Frequency and Time Systems, Inc.
34 Tozer Road
Beverly, MA 01915

ABSTRACT

Telecommunication networks of time division switches, interconnected by digital transmission are being put into place. At each switch, each incoming bit stream is brought into its own buffer. Then the clock in the switch "reads" each buffer to re-establish phase. Care must be taken to keep frequency differences between various clocks from becoming too large, other-wise buffers will under/over flow at an unacceptably high rate. Based on empirically defined data transmission requirements, one major network has determined that fractional frequency inequality between switches should be no worse than 1.7×10^{-9}.

A network needs near frequency equality between its own switches, and also between its switches and other networks with which it interfaces. Frequency accuracy - per se - is not required, but as a practical matter, the best way to achieve needed frequency equality is for each network to have master clock with an accuracy which is at least as good as 1×10^{-10}. To be certain that this accuracy is achieved the master clock in each network should be based on a signal from a cesium source.

Cesium sources for the purpose of providing master clock, fall into two categories:
1) Cesium standard on site.
2) Cesium based signal distributed via some transmission medium.

Concerns of systems designers are that:
A) The master signal be tied to a properly functioning cesium standard.
B) If master signal is lost, the secondary clocks be of sufficiently low aging that they free-run at least a week before their accuracy degrades below 1×10^{-9}.

The accuracy of a properly functioning commercial Cs beam standard is no worse than about 1×10^{-11}. The master/secondary system must be designed such that the accuracy of the master can be verified.

The paper discusses the relationship between the master and the secondary clocks. The questions of master clock accuracy and precision and the free-running capability of the secondary clocks will be examined.

INTRODUCTION

Until recently, the time and frequency (T&F) requirement of the commercial communications industry was almost totally limited to quartz oscillators of low to medium quality. This situation is changing very rapidly. There now exists a significant need for atomic standards and high-quality quartz oscillators. There are two reasons for this:

1. Vital portions of most major networks are now, or soon will be, digital.

2. The breakup (divestiture) of the Bell System and associated changes in the industry.

The breakup of the Bell System is a major additional step in the federal government's encouragement of competition in the telephone industry. This general encouragement plus one very specific aspect of the divestiture decision are of great importance in the industry's needs for T&F capability. Divestiture specifically requires "Equal Access." What this means is that, for any carrier, the cost of access to a long-haul (long distance) network and the quality of that access must be equal to that of any other carrier.

So competition and specifically, Equal Access, press for a widespread improvement in T&F capability and specific characteristics of digital communications define the quantitative requirement.

In most, if not all, existing and planned commercial networks, buffer interfaces are used on each incoming trunk of a digital switch. That is, it is not a totally synchronous network--phase is re-established at each switch. So even though the networks will be digital, the use of buffers at each switch means that it is only frequency equality (near equality) that is needed. (We think that this may not be true in the future because there are advantages to a totally synchronous system.) Since the network will be digital, the requirement is that, as they pass through the switches, the various bits must have a definite time (phase) relationship to one another. This is achieved at each switch by the local clock in the switch that sequentially "reads out" the buffers. If the rate of this local clock is not equal to that of the incoming bit stream, then the buffers will gradually under/over flow.

By empirical tests, the Bell System determined that data customers incurred unacceptable degradation if slip rates (buffer over/under flow rates) went beyond about one T-1 frame in 20 hours. [1] (A T-1 signal is communications traffic in a certain digital format whose rate is 1.544 Mb/s and whose frame length is 193 bits (125 microseconds) long.) This corresponds to an end-to-end fractional frequency difference of 1.7×10^{-9}. Assuming that the frequencies of the nodal clocks are randomly distributed about some nominal value, the probable offset is about 1×10^{-9} to cause slippage at the level where corrective action needs to be taken.

Frequency accuracy, per se, is not required. But, as a practical matter, achieving frequency accuracy is the most cost-effective means of acheiving the needed frequency equality. If all users take this approach, which they seem to be doing, then each one will achieve both compatability and autonomy.

If compatability is to be achieved, every node (switch) in a given network which is to interface with a node in another network must have fractional frequency accuracy of at least 1×10^{-9}. From a metrology viewpoint, one would like to have a reference whose accuracy is of the order of ten times better than those devices which are to be controlled/measured, i.e., about 1×10^{-10}.

FURTHER CONSIDERATIONS
ON NETWORK FREQUENCY REQUIREMENTS

For most users of T&F equipment, their major business is something else, e.g., telephony--and they want to keep it that way. This means that ideally, all equipment should arrive from the manufacturer on frequency, and it should stay within one part in 10^9 for many months. When recalibration is required, it should be performed at low cost by people who have no particular expertise with T&F technology.

The reality of the situation is that a quartz oscillator whose aging rate is about 1×10^{-10}/day will be out of frequency tolerance in a few weeks if left to free-run. Such an oscillator (known in the telephone industry as a Stratum 2 oscillator) is near the top of the line in commercially available quartz oscillators. As a pratical matter, this means that in any major network, there must be a minimum of at least one atomic frequency standard. We believe that these sources should be based on cesium. That is, it should be a cesium standard on site, a GPS (Global Positioning System) receiver, or a Loran-C receiver. With one such cesium master clock and suitable transmission lines to the other nodes that interface with the outside networks, an autonomous network of minimal frequency capability can be assembled. The remainder of this paper is a discussion of what is meant by "suitable transmission lines" and "minimal frequency capability." What we will sketch out is that the design of an optimum T&F network, based on the criterion of overall communications network profitability, is a rather general systems problem. One significant factor in the analysis is to try to account for the general unease of the telephony industry at having to deal with sophisticated T&F considerations.

Figure 1 is intended to make three points:

1. In a big network (e.g., a network covering most of the U.S.) some switches can be adequately slaved off a given master, but not all. In the figure, the solid lines joining nodes/ switches are short-haul (local distribution) paths that typically are less than 100 miles long. The broken paths are long-haul, for example, a satellite path. Whether a path is suitable to transfer master clock depends on four things--the

quality of the slave oscillator; the instability that the path adds to the transmitted signal; the co⌐ ⌐f using a portion of the bandwidth of that path for sending the T&F ⌐ ⌐al; and the realibility of the path. It is not our purpose to discuss these things in detail, both because of lack of space and because it could only be hypothetical since the optimum solution for each link of a given network depends on the present and future competitive situation for that network. It is useful, however, to give an example: Assume that the link between two nodes say, switches 1 and 2 of Network B, is a satellite path. If "clock" is to be passed from switch 2 to switch 1, then the slave clock at switch 1 must have a sufficiently low aging rate to average out the doppler shift due to satellite motion. The motion is approximately periodic with a period of one day. If the goal is that the clock at switch 1 never be more that 1×10^{-10} away from the master then its aging rate will have to be better than 1×10^{-10}/day. The reason is that the lock-loop time constant cannot be shorter than one day.

In summary, one of the major considerations in deciding whether to slave a clock located at the end of a given transmission path is to examine the trade-off between slave-clock quality/cost and stability/reliability of the path.

2. The figure is drawn to indicate that it is unadvisable for one major network to take its master clock from another major network. For example, with the connections as shown, consider what would happen if Network A took its clock from either Network B or C. If the signal goes away (for whatever reason) Network A will not be able to serve its own internal needs or have a connection of adequate quality to the still-functioning "other" network. We believe that every major long-haul network should have its own (autonomous) cesium-based master clock at at least one node.

3. We believe it will be very common for a switch of a large private network to be interconnected with two or more long-haul carriers. (See "Customer 4" in the figure). Such a customer may or may not wish to take clock from one of these commercial carriers. In any event, it again points up the need for good frequency equality between all parties--private as well as commercial.

What about the quality of the slave clocks? In the commercial networks, any digital switch site that directly interfaces with (no intervening switch) a digital switch of a competing carrier should have a clock that ages no worse than 1×10^{-10}/day, that is, a Stratum 2 clock. With a slave of this quality, if the master is lost, frequency accuracy at least as good as 1×10^{-9} will be maintained for at least one week. This will probably be sufficient time to restore the master.

We turn now to the idea of "minimal frequency capability" raised earlier. We said there that a single source of "cesium" at just one site was minimal. Later we indicated that, in a very large network, several sites would probably need their own master clock. We also think that, for at least one site in each of these networks, it will prove very valuable to have a dual "cesium" source.

The need for dual cesium is based on the idea that the master clock needs to be indisputably accurate. If Master clocks of any two switches, of different networks, are interconnected with one another, accuracy probably will be in question.

There are four major types of master clocks that are likely to be found. They are:

- Cesium Standard(s) on site
- The ubiquitous 1.544 Mb/s digital signal in the format known as DS1
- GPS receiver
- Loran-C reciver

The DS1, GPS, and Loran options are all, of course, based on cesium standards but the users' site is typically very remote from the source. Also, the signal arrives in a form (a format) which requires processing in order to extract the frequency of the cesium standards that lie behind them. (The T&F signal broadcast by Station WWVB of the National Bureau of Standards is also used in some cases. But, due to the nature of the signal, the averaging time needed to acheive the required precision will be longer than is convenient for most users.)

But, for a while at least, the means of obtaining master clock will probably divide into two major categories:

1. The Bell System Reference Frequency Network (BSRFN) and

2. Other, where "other" consists of on-site cesium, or GPS, or Loran, or some combination of these three.

The BSRFN, which is owned and operated by AT&T Communications, has been discussed in detail in other places.[1,2] It is important, however, to summarize its essential characteristics: It is based on a triad of cesium standards located in a single geographical location. The signal is transported in sinusoidal form to approximately 100 sites throughout the U. S., where it is terminated.

These sites are locations of #4ESS switches (the very large digital toll switches of the AT&T long-haul system). This signal becomes the master clock for each switch and, as such, its frequency is embedded in the DS1 traffic streams that emerge from these switches. Finally, some of these DS1 streams terminate in other digital switches which are part of the conventional telephone operating companies (These companies include the Bell Operating Companies (BOC's) and what, prior to divestiture, were known as the 'Independents.") The 8 kHz Fourier component of these streams becomes the master clock for these switches.

So now we have the situation of a great many BSRFN-derived master clocks interconnecting with each other and the "other" based clocks in neighboring networks, such as MCI and Sprint.

There have been and will be cases where there is--or appears to be--an out of tolerance frequency difference between switch pairs. It will not be easy to determine which, if either, of the switch clocks is in error. This is because the measurement needs to be made to an <u>accuracy</u> of at least $1X10^{-10}$ (and $1X10^{-11}$ at international gateway sites).
And it is because each and everyone of these master clocks will have been transformed at least once in its pathway from its originating cesium standard. (Almost without exception it will only be via an incoming DS1 traffic stream that a switch will be able to access the frequency of its neighbor.) The noise which accompanies these transformations, and the associated transmission processes, will require appropriate averaging times--typically from one to eight hours--to achieve a precision of $1X10^{-11}$.
We contend that, for at least one node in each major network, it will prove very cost effective to have a means of easily--unambiguously--determining the accuracy of your own and your neighbor's clock. The way to do this is with dual cesium capability of either the Cs/GPS or the Cs/Loran variety, and a DS1 interface that extracts the clock from the incoming traffic stream.
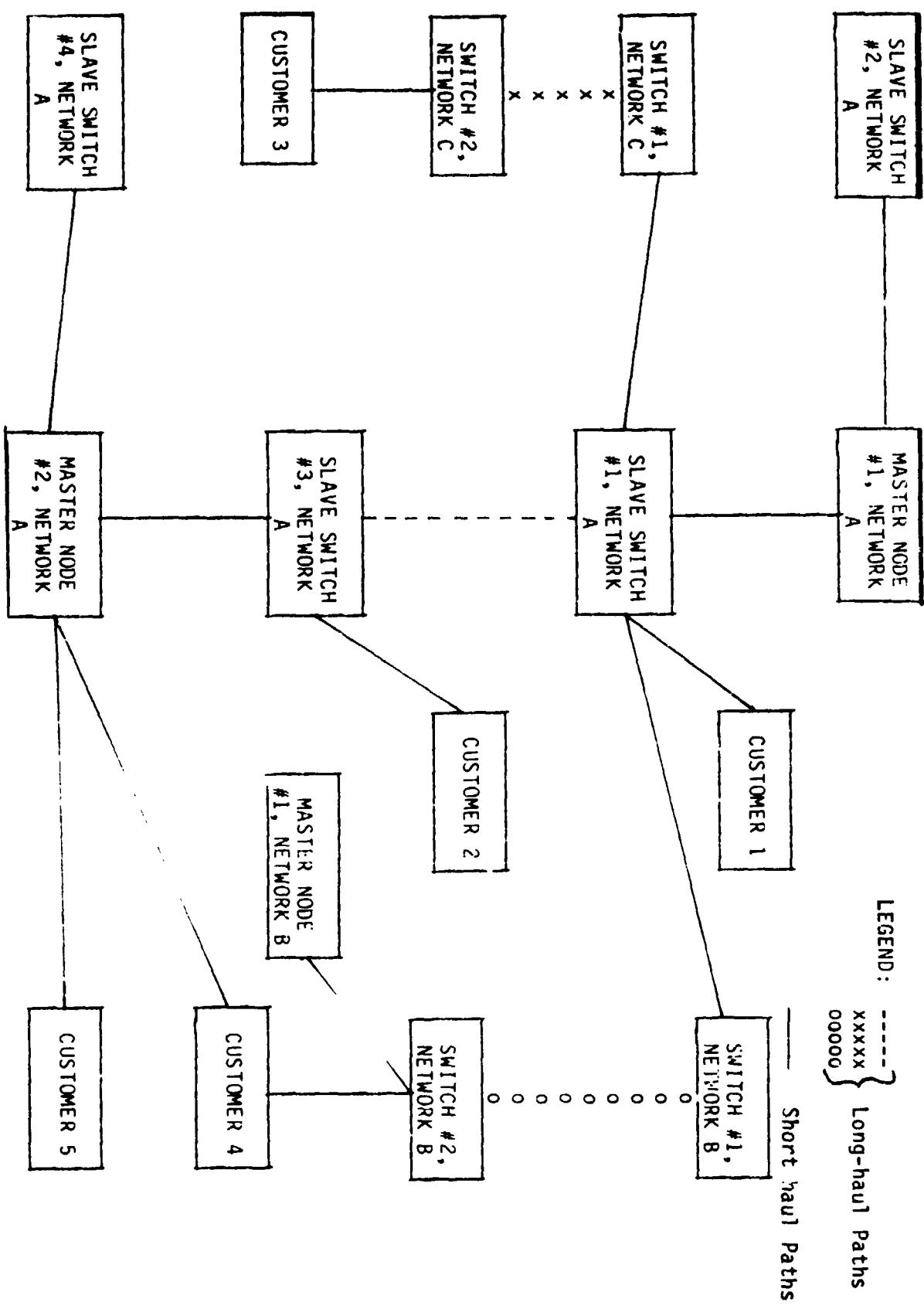
If the intercomparison of such a dual cesium system shows a fractional frequency difference not much larger than $1X10^{-11}$ then, to a very high probability, both sources are accurate approximately $1X10^{-11}$.
A check of the incoming clock against one of the members of the duo will then complete the tests. All-in-all, the resources spent to create a high-quality frequency reference system for a communications network will, in the long run, prove to be very cost effective.

Acknowledgement:

The author acknowledges the helpful review of this article by Mark H. Waite.

REFERENCES:

1. J. E. Abate, L. H. Brandenberg, J. C. Lawson, W. L. Ross, "The Switched Digital Network Plan," THE BELL SYSTEM TECHNICAL JOURNAL, 56, No. 7 (September 1977), pp. 1297-1320.

2. Allan Risley, "The Time and Frequency Requirements of Large Communications Networks," IEEE COMMUNICATIONS MAGAZINE, 22, No. 6, (June 1984), pp. 22-27.

SLAVE SWITCH #2, NETWORK A

SLAVE SWITCH #4, NETWORK A

CUSTOMER 3

SWITCH #2, NETWORK C

× × ×
× × ×

SWITCH #1, NETWORK C

MASTER NODE #2, NETWORK A

SLAVE SWITCH #3, NETWORK A

SLAVE SWITCH #1, NETWORK A

MASTER NODE #1, NETWORK A

CUSTOMER 2

CUSTOMER 1

MASTER NODE #1, NETWORK B

CUSTOMER 5

CUSTOMER 4

SWITCH #2, NETWORK B

SWITCH #1, NETWORK B

LEGEND:

-----
xxxxx } Long-haul Paths
ooooo

——— Short haul Paths

NEW GOES SATELLITE
SYNCHRONIZED TIME CODE GENERATOR

by

D. Earl Fossler and Roger K. Olson
TRAK Systems, a Division of TRAK Microwave Corp.
Tampa, Florida

ABSTRACT

This paper describes the TRAK Systems' GOES Satellite
Synchronized Time Code Generator. TRAK Systems has
developed this timing instrument to supply improved
accuracy over most existing GOES receiver clocks.
Integrating a classical time code generator with a
GOES receiver combining the best of both.

INTRODUCTION

During the last few years, several GOES Satellite Time
Receivers have been designed by various manufacturers. All
output time with accuracies of 2 milliseconds or better (at
least one has a reported accuracy of better than 100
microseconds) when locked to the satellite signal but all lack
several features desired by many users. All known designs
cannot output a usable time signal between power turn-on and
signal acquisition. When synchronization with the satellite
signal is lost, the accuracy of the time outputs degrades
rapidly in many designs. The 1PPS output in several designs
exhibits significant jitter during various microprocessor
activities. Output options are very limited and special
outputs are not economical.

There has been a significant interest to correct these
deficiencies by providing a manually presettable time code
generator which can operate as a stand alone generator or
fully synchronized to the satellite signal. Until now this
could only be accomplished by purchasing two separate units
from two suppliers. As a result of these problems, TRAK has
designed a new timing instrument to correct these deficiencies
in a single timing unit.

PRODUCT DESCRIPTION

TRAK Systems Model 8600 Satellite Synchronized Generator is a precision time signal generator with an internal GOES satellite receiver used to synchronize the generator. The single 1-3/4-inch high rack mountable instrument provides for both a satellite synchronized time signal generator or a manual front panel settable time signal generator.

This Synchronized Generator was designed to provide an accurate time source when synchronized to the GOES Satellite. It also will function as a local time source when synchronization is impossible.

This unit generates time by counting down either an external 1 MHz input or using its internal temperature controlled oven crystal oscillator. When synchronized to the satellite signal, these count down registers are continuously synchronized to the satellite 100 Hz reference. In this mode, the time of day accumulator will be set and periodically updated using the satellite data. Initial setting may also be done manually to provide usable time outputs before the satellite data is acquired.

The only required set-up mode parameters are Latitude and Longitude of the receiver site. These values are inputted via the front panel switches and stored in a non-volatile RAM. Time zone offset may also be entered to display and output local time.

The UHF receiver is a completely shielded coherent synchronous digital dual conversion receiver with automatic tuning for reception of both the GOES East and GOES West satellites. The receiver is fully enclosed in a metal case and located within the generator chassis. Signal enhancement and data detection is accomplished outside the receiver. Data and clock are inputted to the microprocessor for frame synchronization and data processing.

A microprocessor is used to control various operations of the unit. It is used to examine the detected satellite data, provide frame synchronization, test data for bit errors, select good data, calculate path delays, correct data for actual path delay, synchronize clocking frequency to the satellite clock, provide for synchronous time update and provide for interface with RS232 and IEEE 488.

Path delay calculations are performed on initial acquisition and each time a change of satellite position is observed. The signal path delay is calculated with a resolution of one microsecond and with an accuracy of better than 10 microseconds.

The time of year accumulator, its minor scaler (frequency dividers), the parallel time outputs and the serial time code generator(s) are all hardware to provide maximum time signal accuracy and coherency. The 1PPS is generated by a hardware divider chain from either the external 1 MHz or the internal temperature controlled oven crystal oscillator. A 100 Hz digital phase lock loop is corrected one microsecond at a time to maintain phase lock with the satellite 100 Hz signal.

Time signal outputs provided are:
    Fully synchronizes 1PPS output
    Parallel BCD with strobes
    IRIG B Modulated time code
    IRIG B DC time code
    IEEE 488 I/O interface
    RS 232 I/O interface
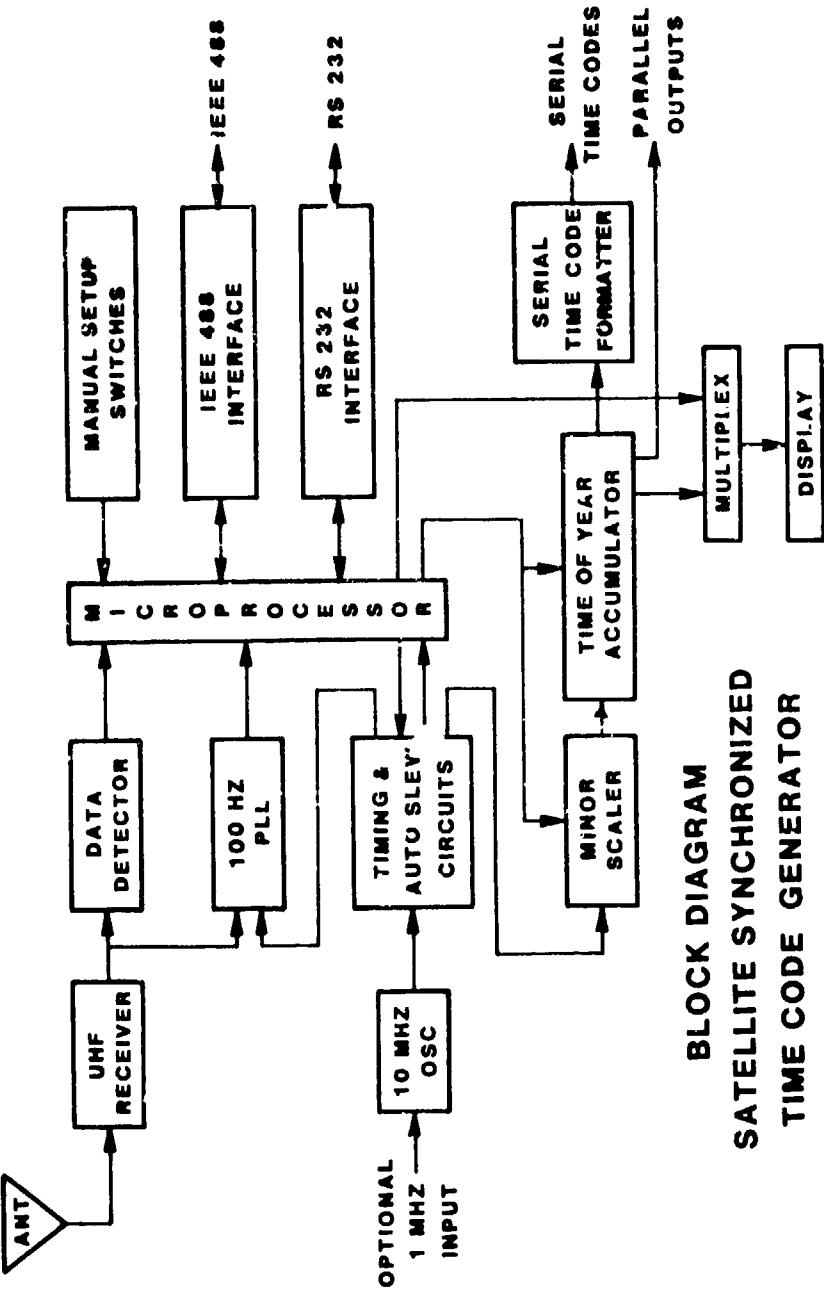
Optional outputs include:
    Additional serial time codes
    Parallel binary codes
    Additional precision rates

A list of features are given in Table 1 with a general specification following. A block diagram is in Figure 1.

REFERENCES

(1) GOES Satellite Time Code Dissemination by R.E. Beehler published in Proceeding of the Fourteenth Annual Precise Time and Time Internal (PTTI) Applications and Planning Meeting.

BLOCK DIAGRAM
SATELLITE SYNCHRONIZED
TIME CODE GENERATOR

TABLE 1

Model 8600 Satellite Synchonized Generator key features:

- Continuous Path Delay Correction

- Fully Synchronized 1 PPS Output

- Internal Drop-In Receiver

- Microprocessor Controlled

- Receiver Location Entered as Latitude and Longitude

- Hardware Frequency Divider, Time Accumulator and Time Code Generation Logic

- Displays UTC or Local Time

- Displays All Set-Up Parameters

- IRIG B Output

- Optional Additional Time Code Outputs

- Parallel BCD Time of Year Output

- Optional Special Parallel Outputs

- IEEE-488 and RS232 I/O Ports

- Single 1-3/4" Chassis

- Antenna Supplied

- Satellite Status Outputs

RECEIVER: Internal drop-in coherent synchronous digital UHF dual conversion receiver with automatic tuning for the reception of satellite generated signals at 468.8250 MHz and 468.8375 MHz.

ANTENNA: Outside mast mounted antenna furnished with unit.

SYSTEM SENSITIVITY: The sensitivity is suitable for proper operation when the viewing angle exceeds seven degrees above the horizon under normal conditions.

OPERATION MODES: A CPU section supervises internal operation and allows the Receiver to synchronize the generator only after analyzing the received data for acceptable content. Once synchronized, time is

415

continuously and smoothly corrected by tracking the
received 10^ Hz signal and by making path corrections
based on received data. Three operating modes are
provided:

 SETUP (SU): Permits entry of setup data such as
latitude, longitude, time zone, preset time.

GENERATE: Unit generates time, including all rate, time
code, and computer outputs, without satellite time
synchronization. Time accumulation starts from the time
entered during SETUP.

SYNC: Same as GENERATE except that Receiver provides
time and frequency updates to the Generator once the
Receiver is processing acceptable data.

TIME BASE: The Model 8600 has an internal crystal
oscillator and may also be operated from an external 1
MHz standard.

INTERNAL FREQUENCY STANDARD:

    Frequency: 10 MHz
    Aging rate: $\pm 2 \times 10^{-9}$ per day
    Temperature stability: $\pm 5 \times 10^{-8}$ (0 to 60 deg C)

EXTERNAL STANDARD INPUT:

    Frequency 1 MHz
    Impedance: 50 ohms
    Amplitude: 0.5 to 10 volts peak-to-peak
    Waveshape: Sinewave or squarewave.

TIME/DATA PRESETTING: Front panel thumbwheel switches
allows for presetting the time in seconds through days.
Latitude, longitude, and time zone correction data are
also entered by these switches.

TIME/SETUP/DISPLAY: Nine high-intensity 0.6 inch planar
LED indicators display time of year in days, hours,
minutes, and seconds. In the Setup mode, these decimal
indicators display setup parameters. Decimal points are
used to indicate operating modes and status.

TIME CODE OUTPUT:

    Format: IRIG B 122
    Mark/space ratio: 2:1 to 6:1 adjustable
    Levels/DRIVE: Adjustable 1 to 5 VPP into a 50 ohm
    level.

1PPS: OUTPUT:

    Fully synchronized to satellite data clock

Duty cycle: 10%., POSITIVE-GOING AT ON TIME
Levels/DRIVE: TTL levels into a 700 ohm load.

PARALLEL BCD OUTPUTS:

   Format: BCD   time   of   year   in   hundreds   of
   microseconds through hundreds of days

   Levels/Drive: TTL levels into a 700 ohm load.

BUILT-IN MONITOR:

A built in monitor program provides data outputs via both
IEEE-488 and RS-232 ports.   The   available output data
are:

   Time in milliseconds through days
   Time of last synchronization
   Last delay calculation
   Current data being received from satellite

RS-232 INTERFACE:

IEEE-488 INTERFACE: (IEEE-488-1978 CONVENTIONS)

POWER:

   105 TO 125 VAC 48 TO 440 Hz, 30 WATTS

PHYSICAL:

   Width: 19 inches standard rack mount
   Height: 1-3/4 inches
   Depth: 19 inches

QUESTIONS AND ANSWERS

BOB HESSLBERTH, SPECTRACOM: What's the price?

MR. FOSSLER: The introductory price is $7,500. If every thing goes well, we expect that price to drop. That includes the antenna.

MR. BUISSON: When you switch from the east satellites to the west satellites, do you have to adjust the antenna?

MR. FOSSLER: There are two ways to handle the antenna. If you are in the eastern part of the United States, and point it in the right direction, you get both satellites. If you are in the central or western part, we give you a second antenna and you would switch with a coaxial relay at the time when you switch satellites.

THE TIME AND FREQUENCY COMPARISONS VIA LORAN - C
AND NATIONAL TV NETWORK IN YUGOSLAVIA

Zoran M. Marković and Stijepo Hajduković

Federal Bureau of Measures and Precious Metals
Mike Alasa 14, 11000 Belgrade, Yugoslavia

ABSTRACT

Many years comparison results of the cesium clocks, which are done in the Laboratory of Federal Bureau of Measures and Precious Metals are presented in this paper. Regional standard frequency and time signals dissemination is over National TV network by so-called active TV system. International comparisons are performed via Loran-C system and by clock transportation.

The way of calculation and approximation of the time signal propagation delays in the aim of the clocks comparisons is given. Settled comparison results of the cesium clocks via TV network, Loran-C, both of them and by clock transportation are also discussed in this paper.

The aim of comparison and synchronisation is to form and maintain the Yugoslav time scale. The presented values of the UTC - UTC(YUZM) show the stability of frequency comparisons of 10^{-13} for the presented period.

INTRODUCTION

In the Laboratory of Federal Bureau of Measures and Precious Metals the Yugoslav primary standard of time and frequency is maintained for more than eight years. It consists of cesium beam tube standard and a rubidium gas cell standard as a backup. Comparisons of our primary standard is carried out with the international clocks as well as with the cesium clocks owned by certain

institutions in Yugoslavia. These comparisons are via Loran-C system, National TV network and by clock transportation.

The measurement process of comparisons is fully automatised by using the microcomputer which is for our purposes made in Yugoslavia. In that way the measurements of appropriate ti e intervals have been carried out every day a year.

The TV studio Belgrade, Yugoslavia began over ten years ago the experimental transmission of time and standard frequency signals by using the so-called active TV system, which secures the Time of Coincidence every second. In this system, second pulses, standard frequency and the coded time of day are all derived from the cesium clock which itself is located within the TV studio premisses. The principles of this system was reported on IX PTTI, November 1977. |1|

CLOCK COMPARISONS

For our UTC time comparison we used the signals transmitted from the master station of Mediterranean Sea chain of Loran-C system in Sellia Marina, Italy. In our everyday work we compare the clock in our Laboratory and the clock in TV studio Belgrade (TVB) with master clock of Mediterranean Sea chain, Figure 1, via Loran-C system. Also, via TV network our clock is compared with clock in TV studio Belgrade.

Figure 2. shows Coordinated Universal Time of our Laboratory UTC(YUZM) relative to UTC(BIH) for 1000 days at the intervals of ten days as it would be sent to BIH.

The origin of Coordinated Universal Time (UTC) Scale of the Federal Bureau of Measures and Precious Metals of Yugoslavia UTC(YUZM) is determined with the direct measurement by clock transportation in Geneve, Switzerland on December 21, 1981 (MJD 44959.59).

The second direct measurement of UTC(OP) - UTC(YUZM) by clock transportation was in Paris, France from June 26, 1984 (MJD 45877.8) till June 29, 1984 (MJD 45880.4). The time difference on MJD 45877.8 was UTC(OP) - UTC(YUZM) = -61.9 μs. With this direct measurement the calculated value of the total timing delay of Loran-C signals has been experimentally proved again. For the period of our experimental work, before the clock transportation to Geneve we used the calculated value of total timing delay for Loran-C signals which has been calculated in our Laboratory using USNO recomendations and Millington method for secondary phase corrections. |2|

To the data obtained by the time interval counter measurements we applied the corrections from USNO daily phase values and time differences Series 4 of UTC(USNO-MC) - Mediterranean Sea chain and from BIH Circular D of UTC - UTC(USNO-MC). Also, we subtracted the value of total timing delay with the assumption that the propagation delay between the Loran-C transmitter and our receiver are

constant for the time of observation.

The data plotted on this figure include the relative phase variations of received Loran-C signals and the frequency drift of our clock. From that data one can observe the seasonal variations of the phase of the received signals, which is the most stable in summer. The maximum value of the time difference between the plotted data and the approximated mean is 2.5 µs, and for the last year it is typically less than 0.5 µs. From this it is obvious that the long-term stability is better than 10^{-13}.

In this paper the comparison of cesium clocks using the time transmission of the active TV system is also analysed. The differences of time transmitted by TV Belgrade relative to the UTC(YUZM) for 1040 days are shown in Figure 3. The value of frequency drift of the clock in our Laboratory is removed from the data, and the drift shown on this figure is of the clock in TV studio Belgrade.

Together with the every day comparisons of our clock with the clock in TV studio Belgrade via TV network, clock transportations in certain time intervals (once a year) is used. The origin of time scale which is transmitted via TV network is determined by clock transportation. During the comparisons by clock transportation certain step time corrections are introduced in order to maintain the transmitted time within the ± 30 µs relative to the UTC(YUZM). By clock transportation the calculated value of total timing delay of TV signals is experimentally proved.

Data for ΔT are plotted at the intervals of ten days and they include the relative phase variations of the signals received via TV network.

Comparisons of the clock in TV studio Belgrade using the Mediterranean Sea chain of the Loran-C system and the National TV network obtain the difference of UTC - UTC(TVB). Figure 4. shows the time difference of UTC(TVB) relative to UTC(BIH) for 1000 days. To the data plotted at the intervals of ten days are applied the corrections from USNO Series 4 and BIH Circular D in the same way as it is previously described. The introduced steps in transmitted time were removed from the data by calculation in order to make easier observation of relative phase variations of the signals received via Loran-C and TV network. On this data there is no influence of the performance of the clock in our Laboratory, and the known drift is of the clock in TV studio Belgrade.

On that way, by simultaneous comparisons of clocks over each transmitting path, the particular performance of each cesium clock can be distinguished as well as the influence on stability of the particular transmitting path. The standard deviation (1σ) measured by the counter is typically 10 - 18 ns for the comparisons via Loran-C and TV network, 7 - 11 ns for the comparisons via Loran-C system and 7 - 10 ns for the comparisons via TV network. Due to the change of our TV receiver set with the newly

designed one this standard deviation for the comparisons via TV network is now 3 - 6 ns. Hence, it can be distinguished which transmitting path has the greater uncertainty.

CONCLUSION

In Federal Bureau of Measures and Precious Metals the international comparisons of our cesium clock are performed via Loran-C and by the clock transportation, and via National TV network it is compared with other cesium clocks in the country. The results of these comparisons for the time of observation from year 1981 till now are good enough for the maintaining of the Coordinated Universal Time Scale UTC(YUZM). Under such conditions it is possible to start sending our comparison results to and introduce our country in Bureau International de l´ Heure.

REFERENCES

1. B. Kovačević, "New ways of time and standard frequency dissemination over TV networks", Proc. 9th PTTI, pp. 277-287, November 1977.

2. Z. M. Marković, "Determination of the Loran-C signals propagation time from transmitter to receiver", Proc. 7th JUKEM, pp. 497-507, October 1976.

3. G. M. R. Winkler, "Path delay, its variation, and some implications for the field use of precise frequency standards", Proc. IEEE, Vol. 60, No. 5, pp. 522-529, May 1972.

4. A. R. Chi, "Performance of Loran-C chains relative to UTC", Proc. 6th PTTI, pp. 263-299, November 1974.

5. Conclusion de la reunion interimaire de la Commission d´etude 7 Doc. 7/77-F, CCIR Geneve, 1984.

6. BIH Annual Reports for 1981, 1982, 1983.

7. A. H. Morgan, "Precise time synchronization of widely separated clocks", NBS Technical Note 22, July 1959.
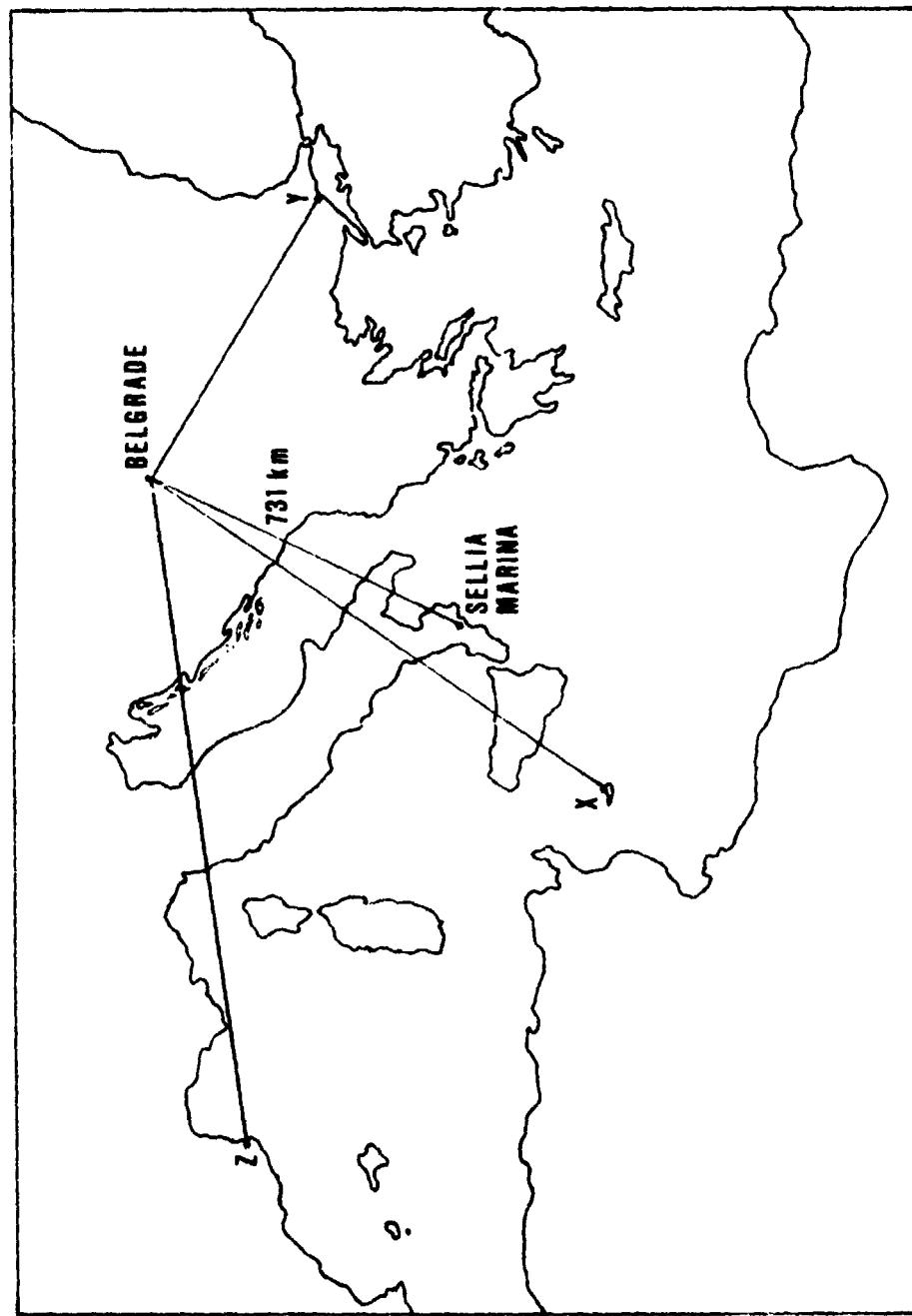
Figure 1. Mediterranean Sea Chain of Loran-C System
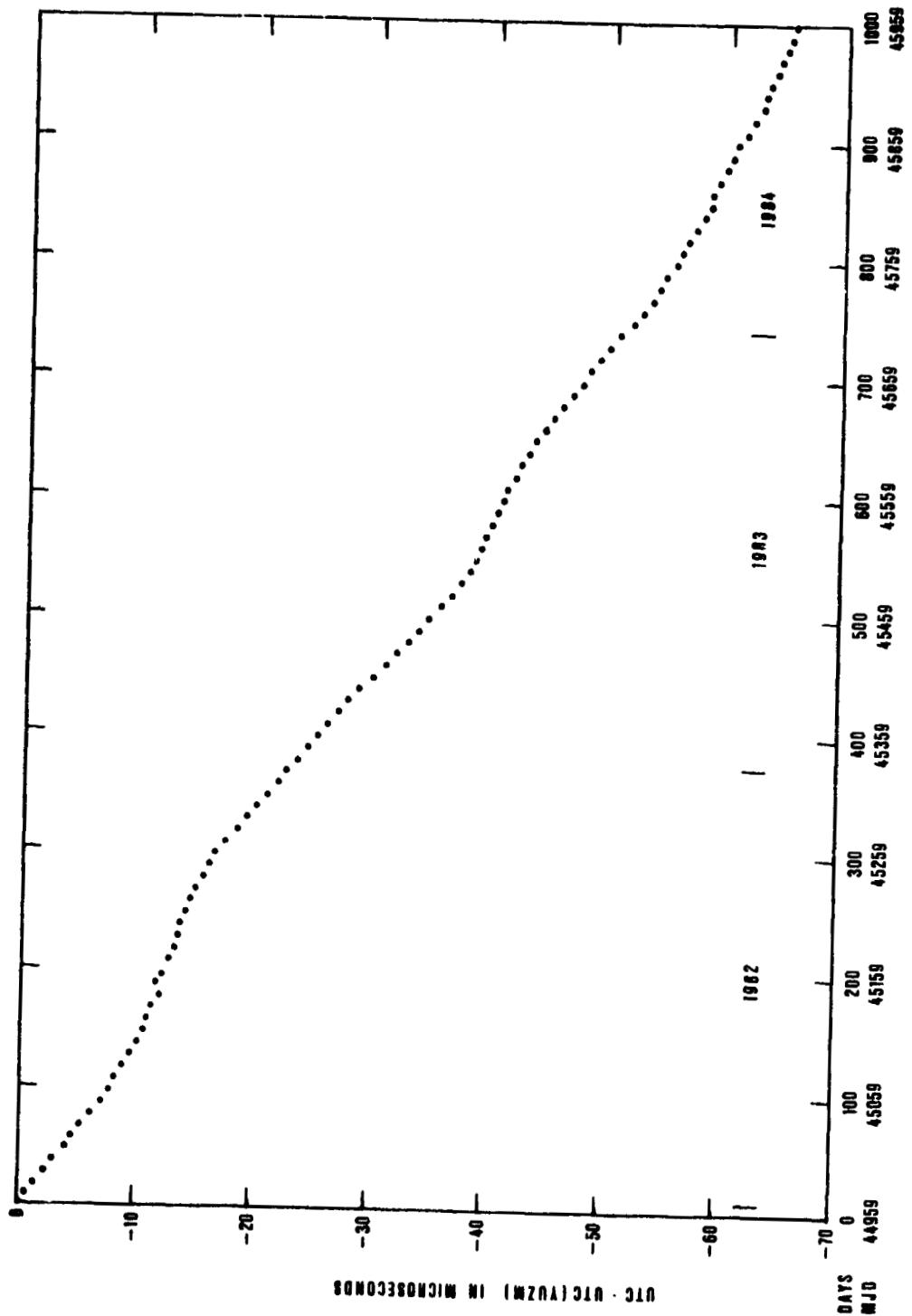
Figure 2. Coordinated Universal Time (UTC) Scale
of YUZM Laboratory Relative to UTC(BIH)
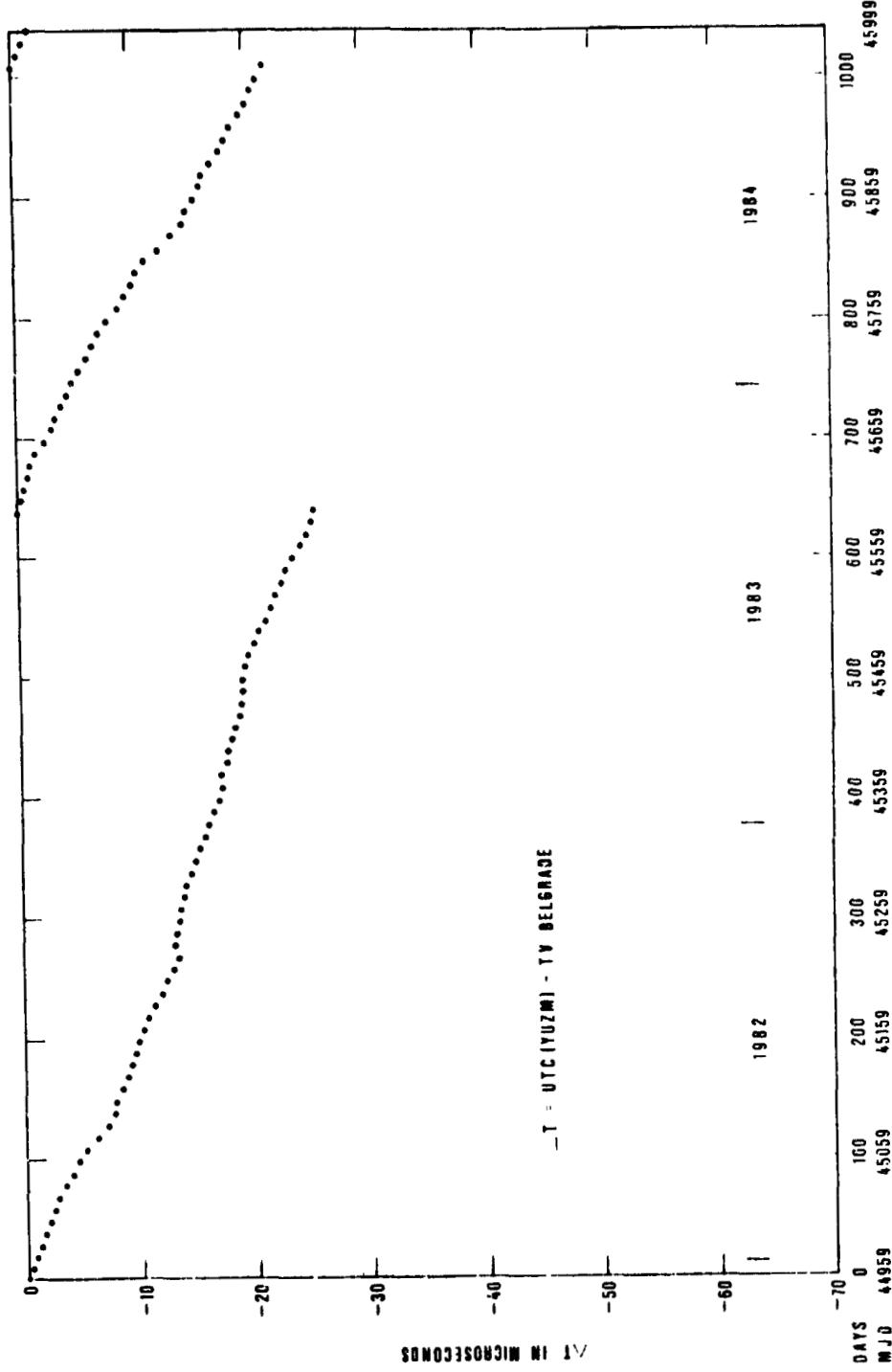
Figure 3. Comparison of Time Transmissions of
TV Belgrade Relative to the UTC(YUZM)
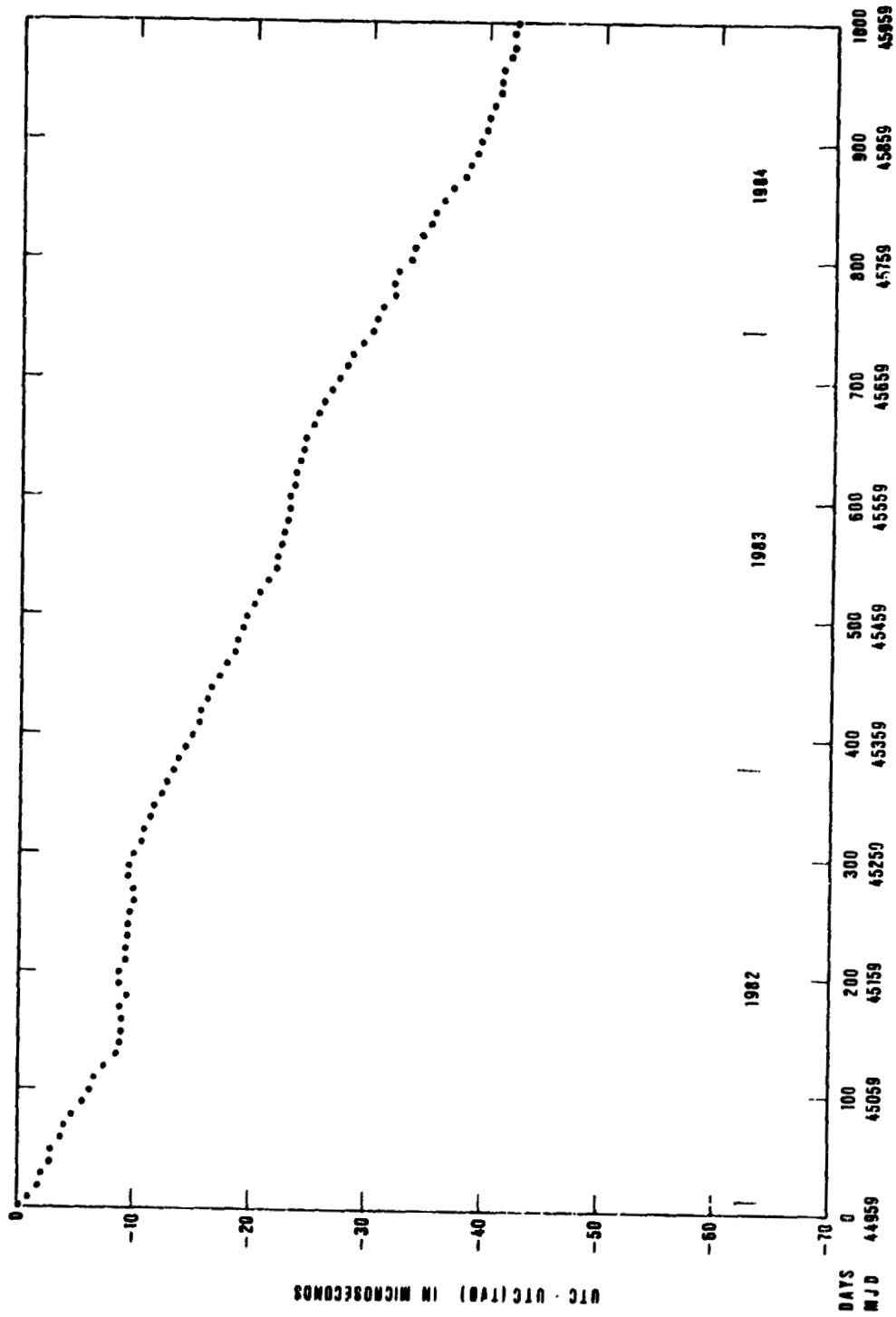
Figure 4. Comparison of Coordinated Universal Time
Scales Via Loran-C and National TV Network

MAINTENANCE OF TIME AND FREQUENCY IN THE JET PROPULSION LABORATORY'S DEEP SPACE NETWORK USING THE GLOBAL POSITIONING SYSTEM

by

P. A. Clements, S. E. Borutzki, and A. Kirk

Jet Propulsion Laboratory
California Institute of Technology
Pasadena, California

ABSTRACT

The Deep Space Network (DSN), managed by the Jet Propulsion Laboratory for NASA, must maintain time and frequency within specified limits in order to accurately track the spacecraft engaged in deep space exploration. The DSN has three tracking complexes, located approximately equidistantly around the earth. Various methods are used to coordinate the clocks among the three complexes. These methods include Loran-C, TV Line 10, Very Long Baseline Interferometry (VLBI), and the Global Positioning System (GPS). The GPS is becoming increasingly important because of the accuracy, precision, and rapid availability of the data; GPS receivers have been installed at each of the DSN complexes and are used to obtain daily time offsets between the master clock at each site and UTC (USNO/NBS). Calculations are made to obtain frequency offsets and Allan variances. These data are analyzed and used to monitor the performance of the hydrogen masers that provide the reference frequencies for the DSN Frequency and Timing System (DFT). This paper contains: (1) a brief history of the GPS timing receivers in the DSN, (2) a description of the data and information flow, (3) data on the performance of the DSN master clocks and GPS measurement system, and (4) a description of hydrogen maser frequency steering using these data.

I.   INTRODUCTION

The Deep Space Network (DSN), managed by the Jet Propulsion Laboratory for NASA, is a network of three complexes of antennas used to track spacecraft. These complexes are located approximately equidistantly around the earth at Goldstone, California; Canberra, Australia; and Madrid, Spain. Each of the complexes contains a frequency and timing system which provides the required frequencies and timing pulses throughout the complex. These three subsystems are a part of a network-wide DSN Frequency and Timing System (DFT).

The process of tracking spacecraft engaged in deep space exploration requires a highly accurate and stable timing system. Navigation parameters such as spacecraft range and relative velocity are obtained by measuring a radio signal's round-trip light time and the doppler frequency shift of the received signal. Since the long spacecraft distances involved result in long round-trip light times, one complex may need to hand over tracking to the next complex before these measurements are completed. In addition, Very Long Base-line Interferometry (VLBI) and the ongoing study of radio signal perturbations due to various causes (planetary occultations, solar wind electron density fluctuations, gravitational waves, etc.) necessitates further requirements for a highly synchronized and syntonized DFT.

Presently, DFT requirements are to maintain time to within ± 20 microseconds with a knowledge of ± 10 microseconds, and to maintain frequency to within $\pm 1 \times 10^{-12}$ $\Delta f/f$ with a knowledge of $\pm 3 \times 10^{-13}$ $\Delta f/f$. In addition, time synchronization must be maintained between the DSN and Universal Coordinated Time (UTC) to ± 20 microseconds, with a knowledge of ± 5 microseconds (see Fig. 1). The anticipated need of the DSN for 1986-1990 is for time synchronization of 10 nanoseconds between the stations (Ref. 1). While this may not be real-izable, it seems possible to have knowledge of the time offset to within 10 nanoseconds. In general, the DFT should be able to provide a value of time and frequency offset for any given past date. (Date is defined here as a specific point on a time scale; e.g., 1 January 1972, 0 h, 0 m, 10 s UTC is a date on the UTC time scale.) Therefore, the DFT must continually estimate the time and frequency offsets as well as keep past estimates and data archived.

II.   FREQUENCY AND TIMING CONTROL SYSTEM DESCRIPTION

Historically, the DFT has consisted of three fairly independent systems, each located at one of the three complexes. Various traditional methods (clock trips, VLBI, and Loran-C) were used in an attempt to keep these three systems synchronized and syntonized with respect to each other. In 1983, using the GPS timing receivers, a tighter control system was designed (see Fig. 2). The system consists of GPS measurements, an analysis of the output of daily offsets, and, if needed, a frequency adjustment and/or clock reset. Using the GPS receivers, the DFT is capable of identifying changes in frequency on the order of 1×10^{-13} $\Delta f/f$ in a matter of a few days.

The GPS receivers are queried weekly and a TWX message is issued with the calculations of time and frequency offset. The time offset of the Goldstone complex with respect to UTC realized at the National Bureau of Standards

[UTC (NBS)] is obtained fiom NBS so that a calculation of the other complexes with respect to UTC (NBS) can be made. The information is distributed about a week later. These data, as well as VLBI, Loran-C, and other measurements, are used to determine what action should be taken to keep the master clocks within their specified operating parameters.

III. GPS INSTALLATION AND COORDINATION

In 1982, JPL installed two GPS timing receivers in the DSN. The receivers were located in Goldstone, California and Madrid, Spain. The results of this installation were reported in the Proceedings of the 14th Annual Precise Time and Time Interval Applications and Planning Meeting (Ref. 2). Mutual view observations were made and the time offsets were compared to those offsets derived from VLBI measurements. (In the mutual view technique, two or more receivers take time offset data from a spacecraft at the same time; ideally, the elevation of the spacecraft above the horizon is the same when viewed from all of the receivers involved.)

In 1983, a receiver was installed at the Deep Space Station near Canberra, Australia. The plan was to use the Madrid receiver in Australia and provide only a single leg again, but the Madrid receiver proved so useful it was decided to lease a receiver from NBS so the two JPL-owned receivers could be deployed overseas. By early 1983, JPL had an operating worldwide network of GPS receivers. The primary 1983 effort was to evaluate the California-Australia line. The results of this effort were reported in the 15th Annual Precise Time and Time Interval Application and Planning Meeting (Ref. 3). Because of the great distances involved, both mutual view and flyover techniques were used, and comparisons were made using both VLBI and clock trips.

The GPS timing receivers at the complexes receive a timing pulse from the station's master clock, which is referenced to station time by the receiver. Each of th se receivers has a modem attached which may be queried remotely; at JPL a Hewlett Packard desk calculator (HP 9845) interfaces to a modem. (In the continental United States the regular phone system is used to query the receivers; the intercontinental queries are made using the voice communication system operated by NASA.) This calculator is used to store the receiver data on tape and to generate the weekly report of time offsets between the station clocks and between Goldstone and UTC (NBS).

JPL uses the NBS time coordination service (Ref. 4) to relate the station time at Goldstone, California to UTC (NBS). These data are obtained in two forms-- NBS provides a monthly report, and daily offsets are available by telephone from a computer at NBS. The NBS service provides the raw measurement data, a daily filtered estimate, a monthly filtered estimate, Allan variance plots, and other useful data about the performance of the JPL clock. This service eliminates the technical need for regular clock trips between JPL and NBS. The regular clock trips are still maintained, but they may be eliminated as operational confidence is gained in the pe formance of the GPS timing receivers.

In order to ensure that a time and frequency offset can be estimated for any past date, all of the data taken from the receivers are archived. Presently, the data accumulation rate amounts to about 2 megabytes per year. It is

429

estimated that a maximum rate would be 6 to 8 megabytes per year. This small amount of data is easily handled by a personal computer, while several years of data can be stored on a hard disk and backed up using either flexible diskettes or magnetic tape.

All of the data presented in this paper were taken using the common view technique. For the data taken between Goldstone, California and NBS (located at Boulder, Colorado), the elevation angles of the spacecraft were above 60 degrees. The Goldstone, California to Madrid, Spain angle was usually 40 to 45 degrees elevation—still quite high above the horizon. On the other hand, the mutual view between Goldstone, California and Canberra, Australia was approximately 18 degrees above the horizon, which presents a substantial problem with respect to variations in group delay due to the earth's atmosphere. While these problems could be largely overcome by using a flyover or long-arc technique (Ref. 3), because of computational difficulties, this method was not used as a normal procedure in 1984.

As Fig. 3 demonstrates, the application of a Kalman smoother filter substantially improves the standard deviation for shorter sampling times on the short baseline (less than 1000 km) between Boulder, Colorado and Goldstone, California. The longer baselines between California and Spain and between California and Australia promise to show the same sort of improvement with the application of appropriate Kalman smoothers.

Fig. 4 shows a comparison of the Allan variance of the data between California and Australia and California and Spain. At 8 days both of the standard deviations are near in value to that of the shorter Boulder-Goldstone baseline. Presumably, the greater amount of noise associated with the California to Australia measurement is caused by the low observation angles. An analysis shows a substantial amount of white phase noise, which implies that a Kalman smoother should help considerably.

IV.   ANALYSIS

The synchronization and syntonization of the DSN master clocks is accomplished by analyzing the time offset data obtained from all available sources. These sources include the GPS, VLBI (interstation), Loran-C (Goldstone and Madrid), TV line 10 (Canberra), and the local backup clocks at each station. (Time offset rates are also obtained from the GPS and VLBI measurements, but are not discussed in this paper.) These unfiltered time offset data and the data provided by the NBS Time and Frequency Bulletin, the USNO Series 4 Bulletin, and NATMAP Bulletin E are entered into a computer database at JPL. Any events, whether occurring at the station, NBS or USNO, are noted in the data files.

Estimates of frequency offsets for the clocks with respect to each other and to UTC (NBS/USNO) are made on a regular basis. These offsets are calculated by a least-squares linear fit on segments of the raw time offset data. The average time offset rate over the length of the fit segment is taken to be the relative frequency offset between the clock oscillators. The standard deviation of linear fit residuals is also calculated to determine the confidence of the calculation. Second-order effects (frequency drift) are estimated by the changes in the average time offset rate over a period of time; this is more

difficult to determine because it requires relatively long periods of unperturbed clock operation. Because there have been both explainable and inexplainable perturbations in the hydrogen maser operating frequency at all of the stations, accurate determination of frequency drift has not yet been possible.

The results of the measurements and calculations are studied to determine how the master clocks are performing with respect to the specification requirements. All known events are taken into account for this appraisal. For any unexplained time steps or frequency shifts, the station personnel are asked to provide any additional information which may help to uncover the reason for the behavior. Based on all of this information, time and/or frequency adjustments are proposed.

The decision to change the output frequency of a hydrogen maser is made by JPL personnel in charge of the standards. The method and the procedures to offset the frequency by the desired amount are determined using the history of that particular maser. The station activity schedule is consulted to find a time when there will be minimal impact on operations, then a TWX containing information on the proposed adjustment is issued to the station and to interested JPL personnel. This TWX includes a brief summary of the performance which prompted the action, the instructions for accomplishing the frequency adjustment, and the station clock reset instructions (if any). After the work has been completed, the station confirms the operation by TWX. The clock performance is watched closely after the procedure to determine hydrogen maser adjustment parameters and verify accuracy.

The results of the maintenance of time and frequency in the DSN using the GPS may be seen in the time offset data shown in Figs. 5 through 8. The particular timespan chosen (December 11, 1983 through June 28, 1984) is representative of what has been accomplished with this system. All events and the results of the linear fits on the time offset data are presented in Tables 1 through 3. [UTC (NBS) was chosen as a reference so that the events at each station may be seen more clearly.] As is evident from the data, the hydrogen maser frequency standard clock at each complex has been maintained to within the synchronization and syntonization requirements with respect to both an external time scale and to the other clocks in the DFT.

One goal in the implementation of the GPS was to allow more stringent frequency controls on each hydrogen maser. The results of four planned frequency adjustments may be seen in Table 4. As is discussed under clock correction methods, only a synthesizer adjustment will vary the operating frequency by a precisely known amount. Therefore, the results seen in the table were considered successful.

Of particular interest to JPL hydrogen maser standards personnel is the sensitivity of the standards to environmental changes in the field. The parameters most likely to vary and cause a disturbance are room temperature and the local magnetic field. Although the Deep Space Stations provide a controlled environment, there are occasional disturbances which are either unforeseeable or unavoidable. The events occurring at Goldstone on the 75th day of 1984 (84075) and at Madrid (84080) are examples of this. There was an unplanned temperature increase in the maser room at Goldstone, accompanied by

extensive equipment movement in the adjoining room, whic' may have affected the magnetic environment. At Madrid, a modification kit was installed in the maser and a cesium clock was removed from a neighboring rack. There was also some activity in the room in Canberra which may have affected maser behavior, although the effects are not as definite. As more data are collected and correlated to the changes in the operating environment, effects can be predicted and appropriate steps can be taken to prevent disturbances. Planned upgrades to the frequency standards rooms and more strictly limited access to these areas will improve these situations.

The maser failure in Madrid (84054) is fortunately a relatively rare occurrance. In this case, the problem was found to be a marginally low hydrogen pressure setting. After the pressure was increased, the maser returned to normal operation with no frequency change. Currently, the DSN has only one hydrogen maser at each site; backup is provided by a cesium standard. An additional hydrogen maser is planned for each location, and this will minimize the impact to data quality in the event of a prolonged maser failure.

The behavior of the hydrogen maser in Canberra is least understood. During this timespan there were no known events which would have produced frequency changes except for the frequency adjustments at NBS. This particular maser had undergone work at the Smithsonian Institution Astrophysical Observatory (SAO) and was returned to the station on 83320. From the GPS data, it appears to have decreased in frequency until approximately 84120. (In the past, the usual aging rate seen in an SAO maser was +3 to +5 x 10^{-15}/day.) Even with a frequency aging rate of only +1 x 10^{-15}/day, the frequency offset should have reached zero in about 60 days. But the time offset data and the associated linear fits show that it took approximately 150 days for this to happen, which would correspond to an aging rate of only +0.4 x 10^{-15}/day. When the NBS adjustments are taken into account (they were made in the negative direction for the most part), they show an even lower aging rate for the Canberra maser. Table 5 shows the relative frequency offsets when the NBS changes are removed. The results of this calculation show that the maser is not exhibiting the usual aging seen in this type of maser, at least not during this time period. It is possible that aging effects are appearing after 84122, but it is difficult to determine without comparison to another external standard.

The relative frequency offsets obtained by the calculations described above are complicated by several factors. First, it is essential that all time steps must be properly noted so that a fit is not made over any discontinuities. Second, the fit timespans must be chosen carefully so that misleading information is not obtained because of frequency shifts. Both the low and high frequency noise on the data will cause different frequency offset results, depending on the period chosen for the fit (see footnote 2, Table 2). This is especially important when determining the effects of any environmental changes on the operating frequency. There are situations where no cause can be found to explain a change in the maser frequency (such as the case in Madrid after the frequency adjustment on 84146) but the data cannot be included as part of the previous fit segment. Future GPS time synchronization

data should make it possible to see the more subtle changes in the behavior of a hydrogen maser. This information will allow more detailed analysis, leading to the development of a more accurate time and frequency system to meet more demanding future requirements.

V.   FREQUENCY ADJUSTMENT METHODS

An important parameter when using the hydrogen maser to drive the complex clock is its long-term stability (over several months). Due to cavity aging, most hydrogen masers have a small amount of long-term drift; drift due to a change in wall shift may add to or cancel part of the cavity drift. In addition, there are perturbations to the output frequency that are caused by changes in the ambient temperature, magnetic field, barometric pressure, humidity, etc. Constant monitoring and precise control of the maser's environment are essential to meet the DFT specifications.

Once a maser is installed in its environment, the magnetic field bias and receiver offset synthesizer are set to previously determined calibration values. The maser cavity is then carefully tuned by the spin exchange method and the frequency offset from UTC (NPS) is measured. The cavity frequency is then offset by a specified amount in the opposite direction of the drift (Fig. 9). This not only maximizes the frequency correction interval but also maintains the best average cavity frequency. Constant monitoring will then determine if nonscheduled frequency corrections are required.

The output frequency of a hydrogen maser may be changed by (1) cavity frequency adjustment, (2) receiver synthesizer offset adjustment, and (3) magnetic field bias adjustment. The range and resolution of the magnetic field adjustment are adequate to steer the output frequency. This adjustment is generally not used for this purpose because of its difficulty. Rather, an optimum magnetic field bias is initially determined and maintained for calibration. This adjustment offsets the hydrogen line frequency.

The receiver offset synthesizer adjustment is easily performed and does not disturb continuous operation of the maser if done in small increments (no phase steps are introduced). Resolution and range varies among maser types. The synthesizer is used to initially calibrate the maser's output frequency. Depending on the various systematic frequency offsets such as wall shift, each maser will have a unique synthesizer calibration setting. This adjustment offsets the receiver output from the hydrogen line frequency.

The cavity frequency adjustment is easily performed in the field and continuous operation of the hydrogen maser is not affected. Resolution is 2×10^{-16} to 2×10^{-14}, depending on the maser type. Range is 1×10^{-10} to 5×10^{-10}. Frequency change is instantaneous with varactor types or has a 5- to 24-hour time constant with thermal types. The cavity adjustment has a pulling effect on the line frequency (pulling factor Q-cavity/Q-line).

As previously mentioned, the cavity is initially tuned by the spin exchange method and the hydrogen maser is calibrated. Subsequent changes in hydrogen maser output frequency have been found to be due primarily to cavity aging and environmentally induced cavity shifts. Thus, it makes sense to correct a maser's frequency by readjusting the cavity only.

During 1984, the method described above was used to steer the hydrogen maser with reference to UTC (NBS) using the GPS. Spin exchange tuning was performed about once a year in order to determine total cavity shift and long-term behavior of the hydrogen line with respect to UTC.

VI. PROBLEMS ASSOCIATED WITH THE PRESENT CONTROL SYSTEM AND PROPOSED SOLUTIONS

A major problem is caused by noise factors and associated inaccuracies in the data. The GPS timing measurements have noise associated with them for several reasons. First, there is well-known noise that is intrinsic to the GPS (such as ephemeris errors, ionospheric errors, etc.). In addition, there is noise caused by the operation of the receivers; i.e., poor estimates of time offset are caused by an inexact mutual view, differences in elevation angles for the spacecraft at different receivers, and missing readings or readings averaged incorrectly. If a system of receivers is to be used to exploit the intrinsic accuracy and precision of the GPS, more accurate coordination among the receivers is required and more sophisticated analysis of the data is needed.

Over the course of the past year, about 20% of the days have had no GPS estimate of clock offset between the complexes provided by the GPS. The most common cause of missing data was power outages at the complexes. The receivers normally store less than a week's data in the failsafe memory, so if they are queried only once a week and there is a power failure, some of the data will probably be lost. The Goldstone receiver was relocated to a temporary location while major reconfigurations were being made at the Complex. This situation has now been changed and the receiver is presently in its permanent location, powered by an uninterruptible power system, as are the master clock and the frequency standards. It has become obvious that control must be improved over temperature and magnetic variations in the frequency standards environment. Security must be improved to limit personnel access to the area, and movement of equipment near the frequency standards.

VII. CONCLUSIONS

The GPS timing receivers have proven to be a cost-effective and reliable method to coordinate time and frequency to meet the requirements of the DSN. The performance of the master clocks was monitored on an almost daily basis. Frequency shifts and time jumps that were unexpected and in some cases unexplained were observed in the clocks. The hydrogen masers responded to frequency adjustments within the expected limits of knowledge of their performance behavior. Control of the time and frequency offset of the clocks was established to within the limits of the performance requirements of the DSN. It appears that with improved techniques the hydrogen maser master clocks can be controlled to much closer tolerances.

ACKNOWLEDGMENTS

REFERENCES

1. P. F. Kuhnle and R. L. Sydnor, "Present and Future Frequency and Timing Capabilities of the Deep Space Network," Journal De Physique, Colloque C8, Supplement No. 12, December 1981, pg. 42.

2. P. A. Clements, "Global Positioning System Receivers in the DSN," Proceedings of the Fourteenth Annual Precise Time and Time Interval (PTTI) Applications and Planning Meeting, NASA Conference Publ. 2265, 1982.

3. J. McK. Luck, J. R. Woodger, J. E. Wells, P. Churchill, and P. A. Clements, "First Results of GPS Time Transfer to Australia," Proceedings of the Fifteenth Annual Precise Time and Time Interval (PTTI) Applications and Planning Meeting, NASA Conference Publ. 7962, December 6-8, 1983.

4. S. R. Stein, G. Kamas, and D. W. Allan, "New Time and Frequency Services at the National Bureau of Standards," Proceedings of the Fifteenth Annual Precise Time and Time Interval (PTTI) Applications and Planning Meeting, NASA Conference Publ. 7962, December 6-8, 1983.

Table 1. Goldstone versus UTC (NBS) Relative Frequency Offsets

Event	Timespan (YYDDD)	$\Delta f/f$ (x 10^{-13})	Sigma	Comments
	83345-84008	2.36	0.04	Start
1	84009-84011	6.41	0.30	Backup cesium standard online during maser frequency adjustment (spin exchange tune); time step due to switchover
2	84012-84030	0.13	0.05	Maser prime and clock reset
3	84030-84060	0.20	0.02	NBS frequency adjustment of +0.88 x 10^{-14}
4	84061-84072	0.02	0.02	NBS frequency adjustment of -1.41 x 10^{-14}
5	84075-84091	2.58	0.12	Temperature change in maser room and equipment movement in adjoining room
6	84092-84113	2.81	0.07	NBS frequency adjustment of -2.31 x 10^{-14}
7	84115-84121	3.39	0.08	Maser maintenance in response to frequency change on DOY 75 (magnetic field bias adjustment); time step due to switchover
8	84122-84123	---	---	NBS frequency adjustment of -2.31 x 10^{-14}
9	84124-84152	5.65	0.04	GPS clock resynched to station clock (at this site only, the GPS uses a different frequency counter than the station)
10	84153-84163	6.68	0.10	NBS frequency adjustment of -2.31 x 10^{-14}
11	84167-84173	-1.33	0.06	Maser frequency adjustment (cavity) and clock reset

Table 2. Canberra versus UTC (NBS) Relative Frequency Offsets

Event	Timespan (YYDDD)	$\Delta f/f$ (x 10^{-13})	Sigma	Comments
	83346-84015	-0.61	0.03	Start
1	84033-84060	-1.34	0.05	NBS frequency adjustment of +0.88 x 10^{-14}
2	84061-84091[1]	-1.51	0.09	NBS frequency adjustment of -1.41 x 10^{-14}
3	84092-84121	-1.69	0.06	NBS frequency adjustment of -2.31 x 10^{-14}
4	84122-84152[2]	-1.22	0.05	NBS frequency adjustment of -2.31 x 10^{-14}
5	84153-84172[1]	0.19	0.07	NBS frequency adjustment of -2.31 x 10^{-14}

[1]Maintenance work was done on the backup cesium clock located in the same vicinity on days 83-86 and 157. The effect on the maser is unknown.

[2]The following is an example of how the results depend on the timespan chosen for the fit:

84122-84129	-0.86	0.17
84136-84141	-2.25	0.32
84146-84152	-0.49	0.44

Table 3. Madrid versus UTC (NBS) Relative Frequency Offsets

Event	Timespan (YYLDD)	$\Delta f/f$ (x 10^{-13})	Sigma	Comments
	83345-83360	7.19	0.04	Start
1	83364-84030	-0.15	0.04	Maser frequency adjustment (cavity) and clock reset
2	84033-84053	-0.08	0.10	NBS frequency adjustment of +0.88 x 10^{-14}
3	84055-84060	---	---	Maser source failure; maser restarted and clock reset
4	84061-84072	-0.15	0.04	NBS frequency adjustment of -1.41 x 10^{-14}
5	84080-84091	1.34	0.10	Maser modification kit installed; cesium standard removed from nearby rack
6	84092-84121	2.76	0.14	NBS frequency adjustment of -2.31 x 10^{-14}
7	84122-84142	2.83	0.19	NBS frequency adjustment of -2.31 x 10^{-14}
8	84146-84152	-1.74	0.28	Maser frequency adjustment (cavity)
9	84153-84173	-0.23	0.05	NBS frequency adjustment of -2.31 x 10^{-14}

438

Table 4. Results of the Hydrogen Maser Frequency Adjustments
(Change in Relative Frequency with Respect to NBS)

Date (YYDDD)	Complex	Goal	Result (x 10^{-13})	Method of Adjustment
83362	Madrid	-8.5	-7.3	Cavity frequency
84009	Goldstone	-3.0	-2.2	Magnetic field, receiver synthesizer, and cavity frequency (spin exchange tune)
84144	Madrid	-5.0	-4.6	Cavity frequency
84166	Goldstone	-8.4	-8.0	Cavity frequency

Table 5. Effect of the NBS Frequency Adjustments on the
Canberra Hydrogen Maser Relative Frequency Offsets

| Timespan (YYDDD)	NBS Adjustments Included $\Delta f/f$ (x 10^{-13})	NBS Adjustments Removed $\Delta f/f$ (x 10^{-13})
83346-84015	-0.61	-0.61
84033-84060	-1.34	-1.25
84061-84091	-1.51	-1.56
84092-84121	-1.69	-1.97
84122-84152	-1.22	-1.73
84153-84172	+0.19	-0.06
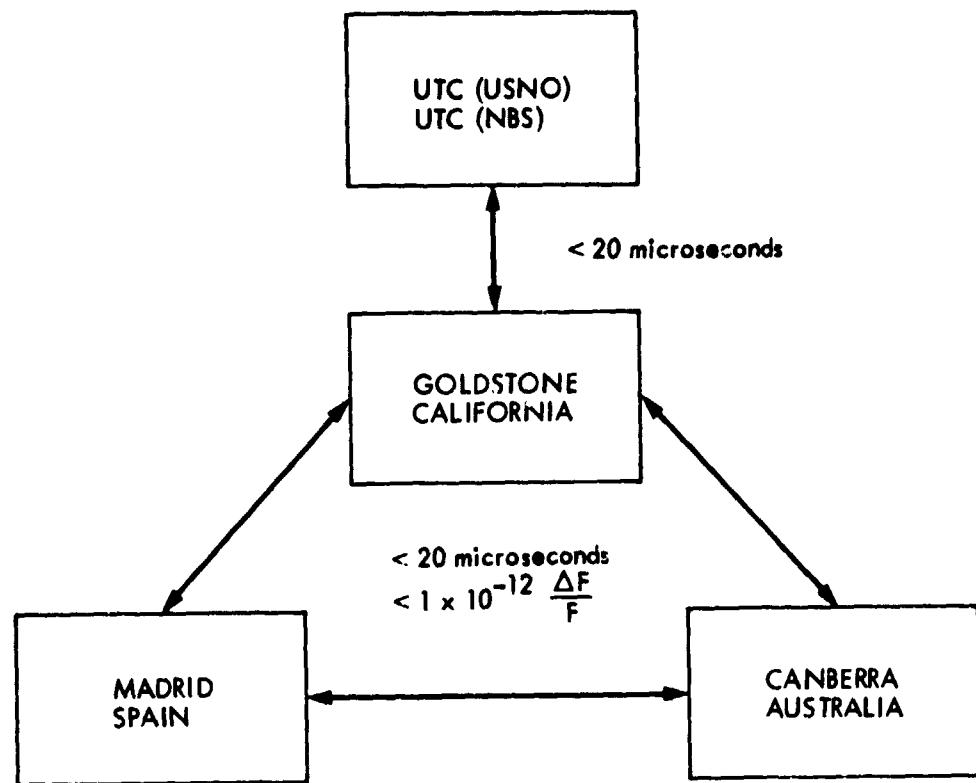
Figure 1. DFT System Functional Block Diagram
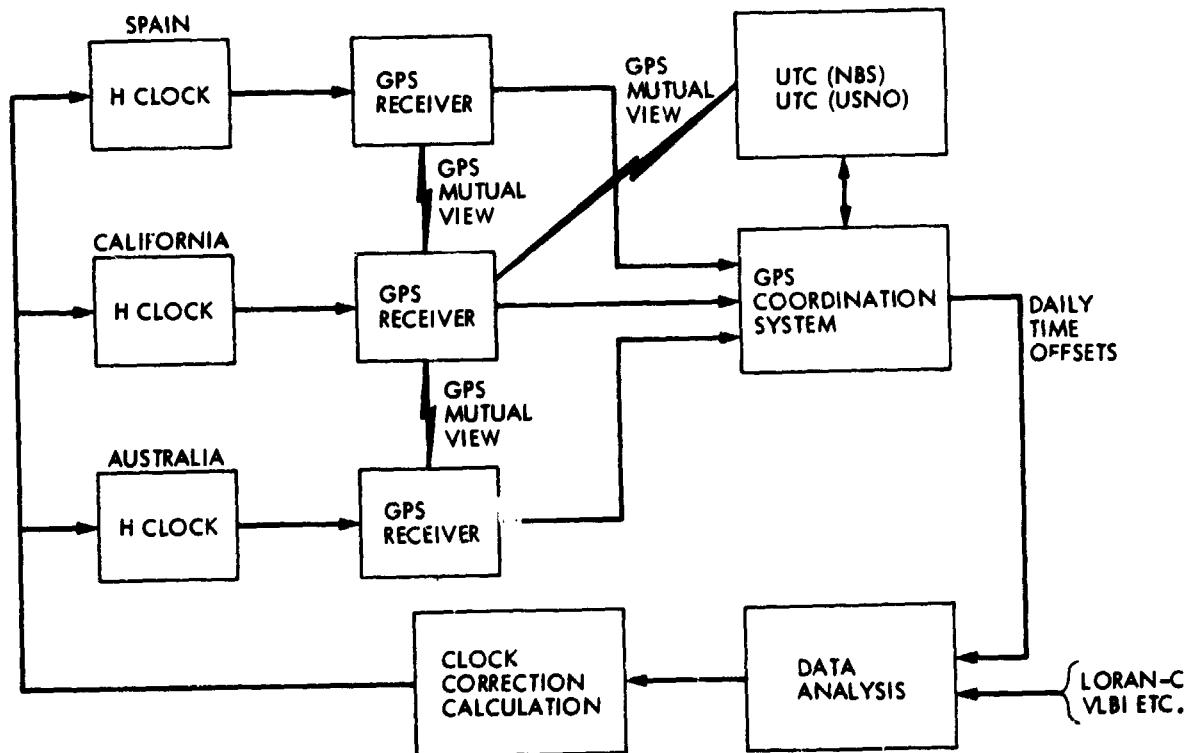
Figure 2. Frequency and Timing Control System
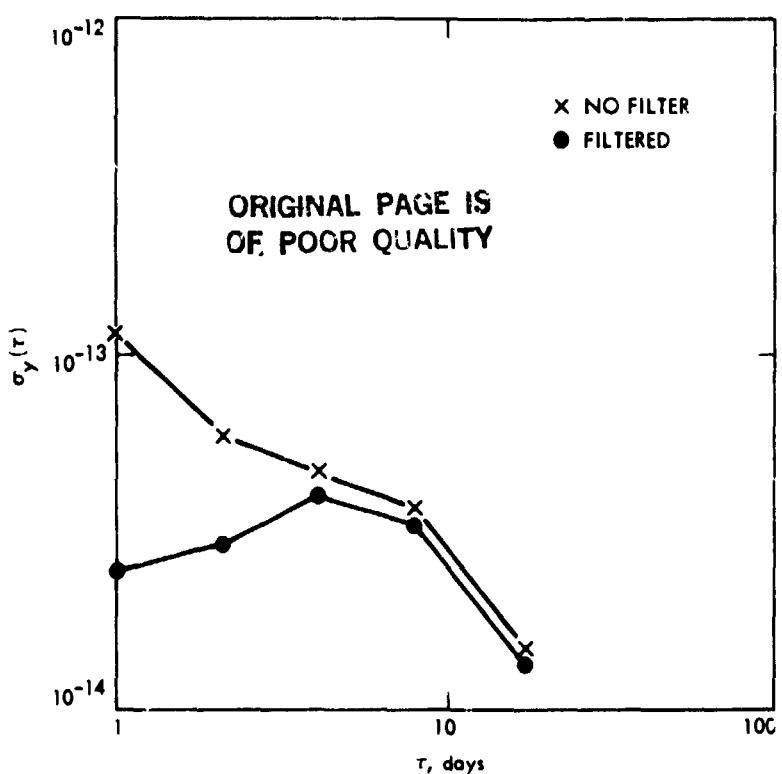
Figure 3.   Allan Variances of Goldstone-UTC (NBS)
Before and After Kalman Filter
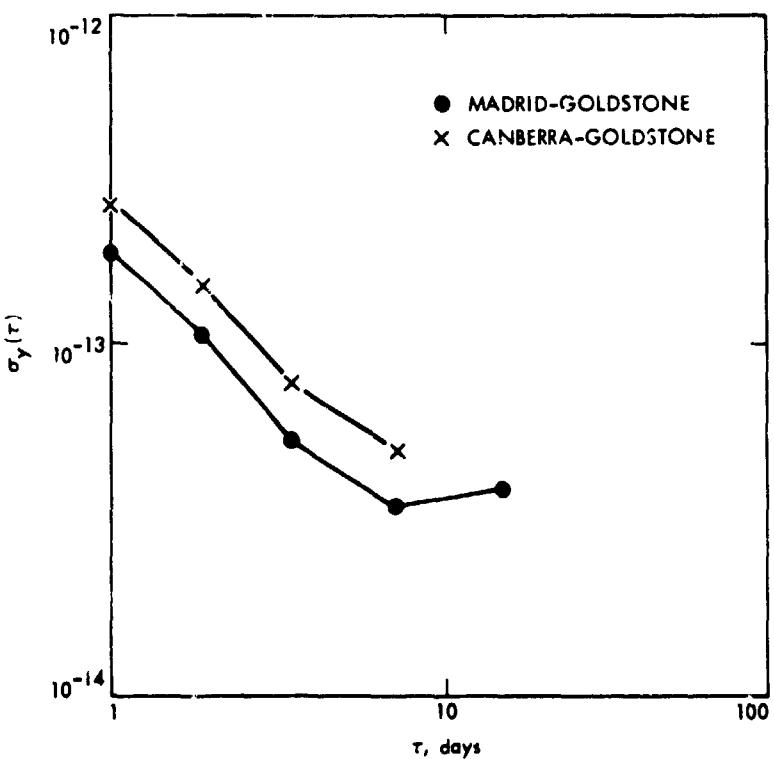
Figure 4.   Allan Variances of Spain-California and
Australia-California
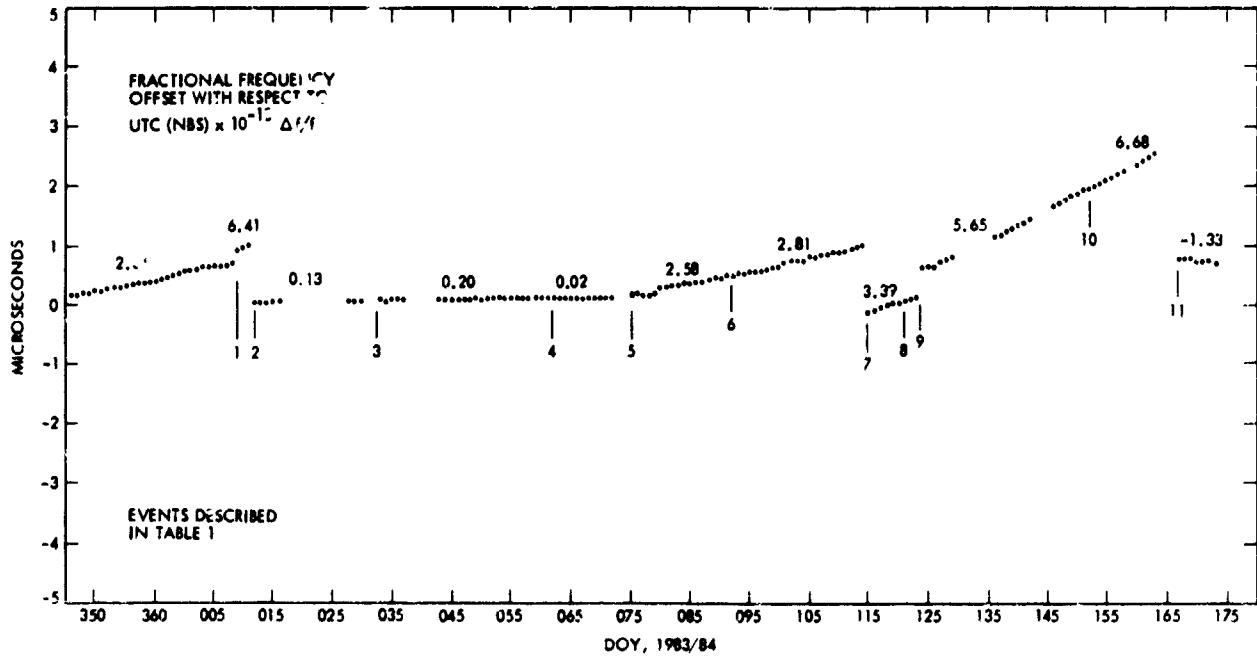
Figure 5. Time Offset, Goldstone versus UTC (NBS)
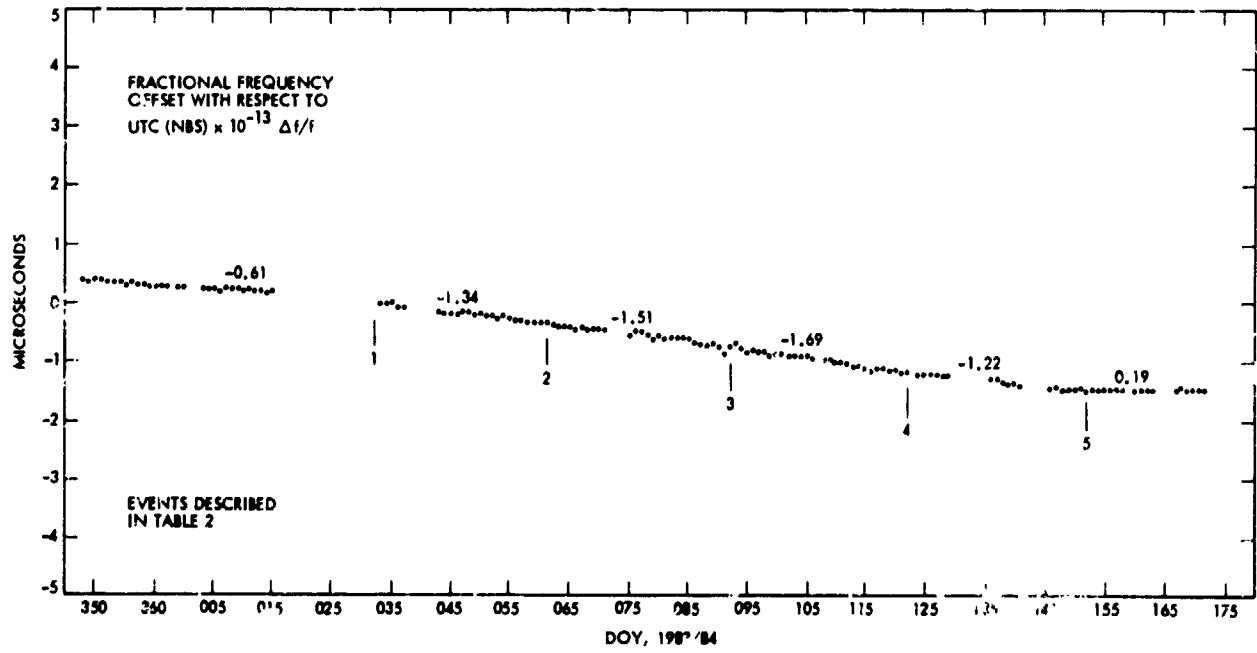
Figure 6. Time Offset, Cant   versus UTC (NBS)

442
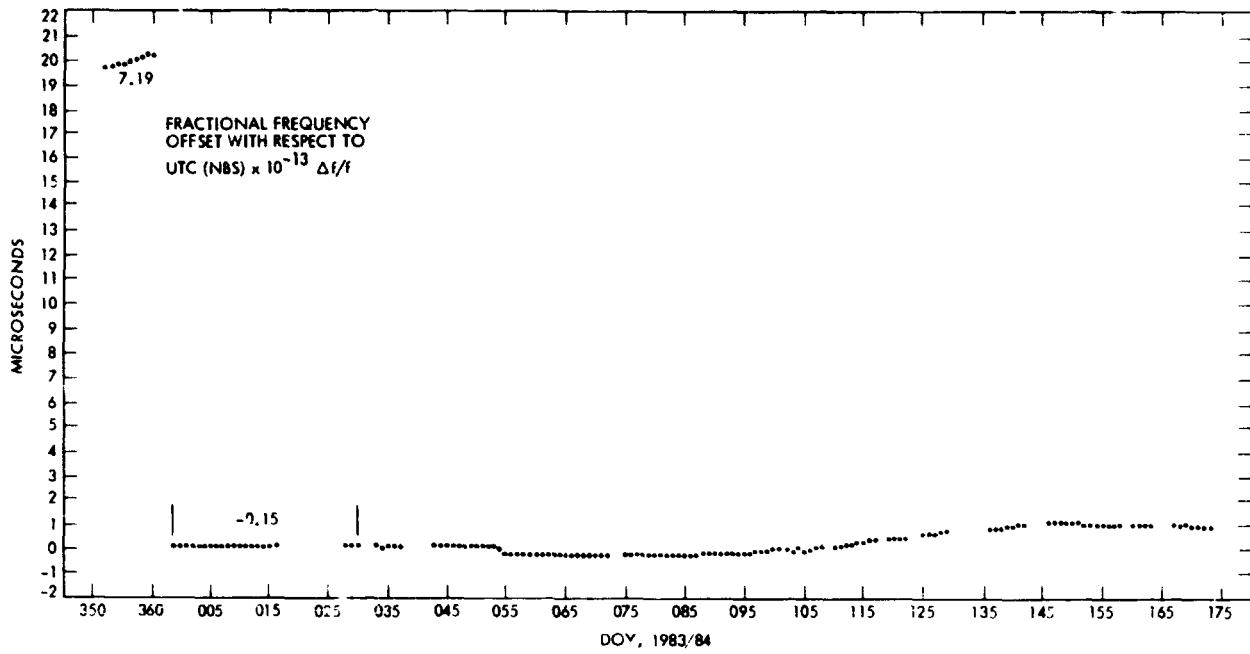
Figure 7a. Time Offset, Madrid versus UTC (NBS) Showing
Frequency Adjustment and Clock Reset (Note the
Different Ordinate Scale)
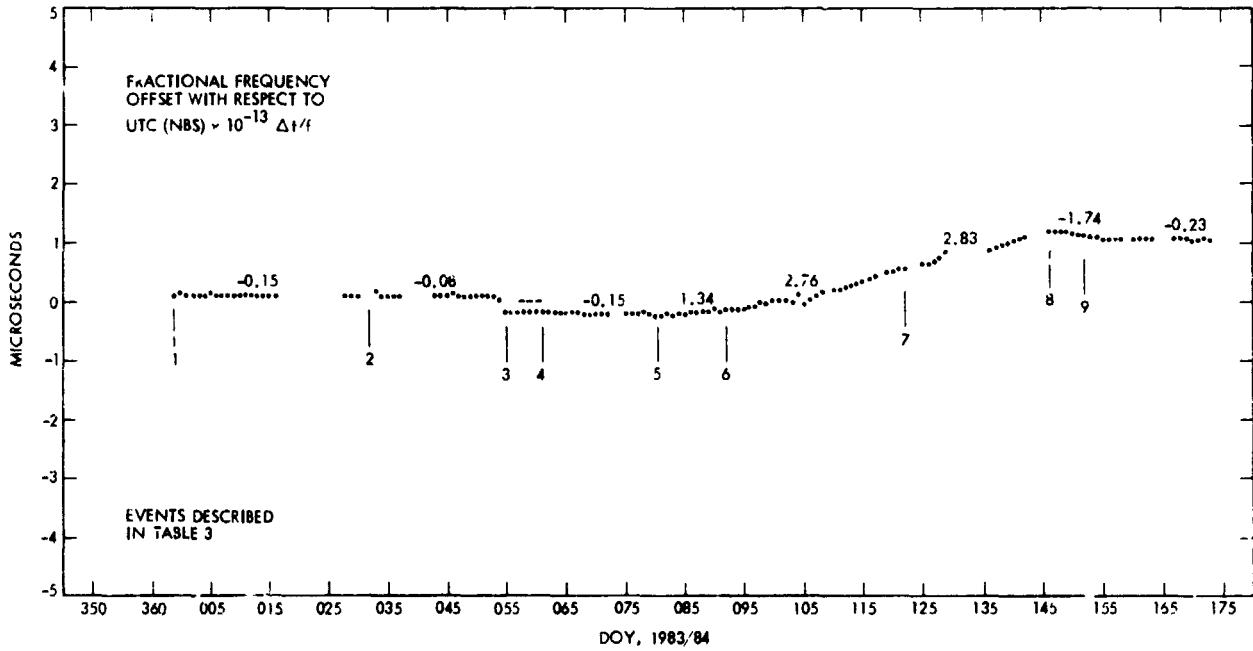
Figure 7b. Time Offset, Madrid versus UTC (NBS)

443
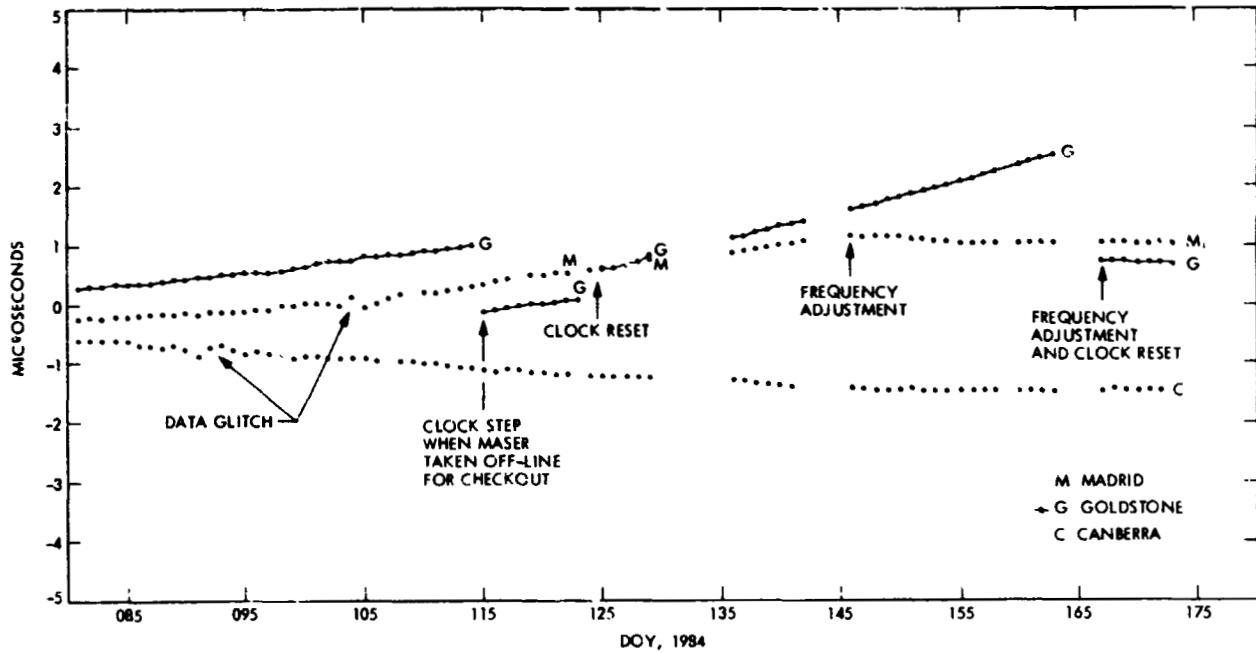
Figure 8.   Time Offset, DFT System versus UTC (NBS),
Showing All Three Stations
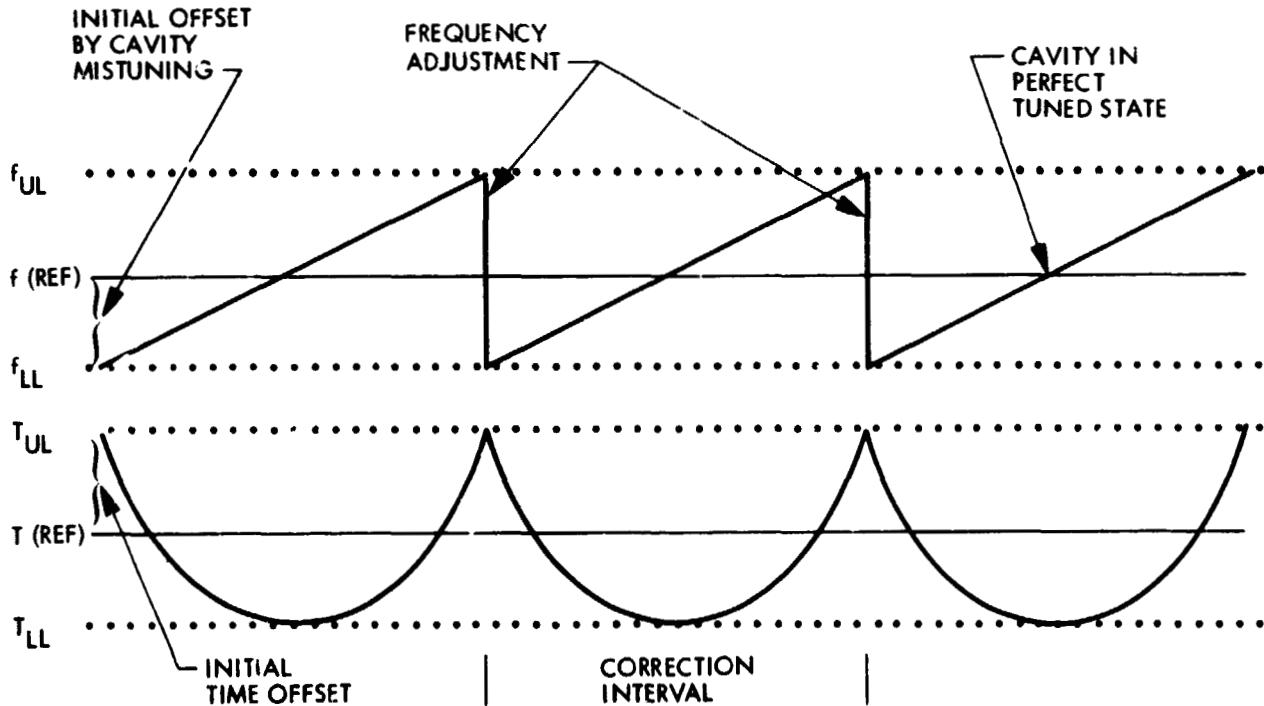
Figure 9.   Frequency Correction Intervals Based on
Known Cavity Drift and Allowable Limits

QUESTIONS AND ANSWERS

DAVID ALLAN, NATIONAL BUREAU OF STANDARDS: What was the temperature change, Phil, when you saw that frequency change on the Goldstone maser?

MR. CLEMENTS: Two degrees Celsius.

ANDY JOHNSON, U. S. NAVAL OBSERVATORY: Could you please tell the audience what kind of environment your masers are in?

MR. CLEMENTS: The masers are in a very well temperature controlled environment. There is a separate air conditioner that keeps the temperature to 22 degrees Celsius, plus or minus 0.1 Celsius.

MR. BUISSON: You presented mostly frequency. On the time aspect of it, do you have any feel, when you weren't adjusting frequency, how good your time comparisons would be between, say, Australia and Goldstone?

MR. CLEMENTS: That's hard. We made a clock trip last year, and reported it here. We had very good agreement, to within 25 to 50 nanoseconds.

What we are trying to do now -- Sam Ward will talk about it next -- is to use the weekly VLBI between the stations to check the accuracy of our time transfers.

ALBERT KIRK, JET PROPULSION LABORATORY: I didn't understand the last question. Could you explain?

MR. BUISSON: He showed a lot of plots of slopes of phase, and I was looking for absolute accuracy from a phase/time comparison.

MR. WARD: The filter data shows a rise in noise at a period of five days. What caused that?

MR. CLEMENTS: I don't know.

MR. BUISSON: That's an honest answer.

DAVID ALLAN, NATIONAL BUREAU OF STANDARDS: The Kalman smoother isn't a Kalman filter, it's really a smoother. We measure the characteristics of the propagation, the GPS noise if you will, and then we assume certain models for the clocks. These models are not perfectly well known. If you are not modeling the clock perfectly, you can get that kind of a hump in the sigma-tau plot, which may or may not be true to the clock. It' a model dependent characteristic. I wouldn't put too much stock in that humping.

I might mention that there have been several portable clock trips between the Goldstone clock and the Boulder clock, and they agreed -- and you can correct me if I am wrong -- by five nanoseconds.

MR. CLEMENTS: Yes, we make regular clock trips between the National Bureau of Standards and Goldstone, every two months supposedly, and we take the readings directly from the GPS receiver. We have come to within a few nanoseconds.

MR. BUISSON: That bothers me. Mr.Klobuchar talked yesterday. He talked about the difference in the ionosphere, and the holes, and having comparison that far with different times. Even though it's common view, you are looking at different parts of the sky, and it's hard to imagine that you are really down to the five nanosecond level if his drift rates are true, using a CA only code.

MR. CLEMENTS: We don't get down to the five nanosecond level with the overseas stations, only between NBS and Goldstone, which is less than a thousand kilometers.

MR. KLEPCZYNSKI: In regard to GPS time transfer, if you look at the data files that we have in the computer -- and I just did this a few days ago to compare Japan to the U.S.N.O -- if you take 780 second average points, for three or four days -- this is between Japan and the Observatory where you have a daytime situation on one end and a nighttime situation on the other -- you see a scatter of 40 to 50 nanoseconds between the points, which was right on the mark with the numbers that were quoted by Klobuchar yesterday.

MR. CAPLAN, NAVAL RESEARCH LABORATORY: Your graphs show that there were several apparent discontinuities in frequency. Did you correlate the data between the three stations in the network to try to isolate the cause of these changes in frequency?

MR. CLEMENTS: Yes, we compared the data and this clock was the only one with the change, so it was not in GPS.

USING GPS & VLBI TECHNOLOGY TO MAINTAIN
14 DIGIT SYNTONIZATION

Samuel C. Ward
Frequency and Timing System Cognizant Operations Engineer
Jet Propulsion Laboratory
Pasadena, California

ABSTRACT

To facilitate the navigation of spacecraft to the outer planets, Jupiter and beyond, the JPL-NASA Deep Space Network (DSN) has implemented three ensembles of atomic clocks at widely separated locations (Goldstone, California/Canberra, Australia/Madrid, Spain). These clocks must be maintained, syntonized, to within a few parts in 10^{13} of each other and, the entire group must be maintained, to a lesser degree, in synchronism with UTC (NBS/USNO).

Over the last 1 1/2 years the DSN has been using Global Positioning Satellites (GPS) and Very Long Baseline Interferometry (VLBI) technology to perform these critical Frequency and Time (F&T) synchronization tasks. Both techniques are required because: 1) Though VLBI techniques permit direct F&T measurements on widely dispersed clocks, it is relatively insensitive to drift. Drift of the group away from UTC and second order drift of individual member clocks. 2) The present constellation of GPSs is quite sensitive to clock offset from UTC and to second order drift but simultaneous direct measurements on widely separated clocks (Australia to Spain) cannot be made.

This report covers a year of F&T synchronization data collected from the intercomparison of 3 sets of cesium and hydrogen maser driven clock ensembles through the use of GPS and VLBI techniques. Also covered, are some of the problems met and limitations of these two techniques at their present level of technology.

In order to meet the increasingly higher accuracy demands of spacecraft navigation to the outer planets (Uranus and Neptune), Deep Space Network (DSN) Operations is implementing and testing improved and more accurate frequency and time (F&T) technology. These F&T requirements are an order of magnitude more stringent* than they were for the Jovian planetary encounter. The three hydrogen maser (HMA)/cesium (CS) driven clock ensembles were syntonized to each other and to UTC (NBS) in late 1980 [1,2]. Employing a technique developed by the author that first transfers the C_s133 hyperfine line to the hydrogen line then, all subsequent syntonization is accomplished through the use of the hydrogen hyperfine line [3]. The syntonization, so established, is being maintained through the combined use of five techniques (GPS, LORAN, TV, Traveling Clocks and VLBI). This paper reports the results from one years GPS and VLBI F&T data use to maintain syntonization via direct frequency measurements and, by the integration of time domain measurements.

The Larger Frequency and Time System

For the purposes of this report/study the Very Long Base Interferometer (VLBI) Time Sync System has been integrated into the Frequency and Time System. I refer the reader to Figure 1 which is an illustration of DSN's VLBI Time Sync Data System. At the present time, the Global Position Satelite (GPS) receivers are under an evaluation study as a high precision F&T data gathering system. Figure 2 illustrates how the GPS F&T sync ardware was configured during the period covered by this report. The Jesign was to provide for regular and routine F&T data collection, provide communication pathways to data reduction centers, provide for the distribution of the reduced data, in the form of "quick look reports" via TWXs to the collection points, to the F&T Network Operations Analyst (NOA) and to the F&T System Cognizant Operations Engineer (SCOE).

The 6 Month Test

Beginning early January, 1984, through mid-August a test was conducted for the purpose of: 1) Measuring the minimum level of effort required to meet the 1 sigma level of the four most critical F&T parameters (mutual syntonization between pairs of oscillators; syntonization of oscillators to the UTC rate; mutual synchronization between pairs of clocks; synchronization of clocks to the UTC epoch). These are listed in descending order of difficulty to meet and maintain. 2) Evaluating the comparative effectiveness of the GPS and VLBI techniques to measure these four F&T parameters.

First each of the three HMA were tuned (microwave cavity adjusted) in situ to the hydrogen line to bring the group into mutual syntonization. Next, each HMA synthesizer was adjusted to lower the output frequency to nullify the expected positive frequency pulling caused by accumulated cavity ageing. Last the master clock of each ensemble was reset to bring it within ± 1 microsecond of the UTC (USNO) epoch.

---

* The clock rates of the three globally distributed ensembles are to be maintained syntonized to the UTC rate within $\pm 1.7 \times 10^{-13}$. At Jupiter this requirement was implied to be within $\pm 1 \times 10^{-12}$.

Syntonization Tests

The mutual syntonization between the three pairs of oscillators was measured using both time domain and direct frequency domain measurements; employing both the GPS and VLBI instrumentation. The GPS time domain derivation of clock rate data (TABLE 1) were taken on multiple spacecraft in the pseudo simultaneous mutual view mode, and, is the 12 minute observation each sidereal day, averaged over the PERIOD indicated. The VLBI time domain derivation of clock rate (TABLE 1) is taken on multiple (6 to 20) Extra Galactic Radio Source (EGRS) observations taken every 6 to 10 days. The smaller values of STD DEV for the GPS data are more a reflection of the larger sample size than they are of instrumentation quality. The clock rate derived by the two techniques are always within less than 1 sigma variance over any common period.

If is significant to note that, since these are time domain data, they contain the noise of two clocks in addition to the noise of the two oscillators. The clock driven by oscillator #5 is significantly noisier than the others. This clock noise has adversely affected the VLBI data. But, since the GPS data on osc. #5 does not employ this clock (see Figure 2) there is no degradation from this cause. The data indicate we can meet the requirement within 2 sigma.

TABLE 2 contains oscillator vs oscillator syntonization data collected by direct frequency measurements of frequency (clock rate) by both the GPS and VLBI techniques. The GPS direct frequency data (TABLE 2) were taken only when one or more spacecraft were in true simultaneous mutual view. Note, that the measurement noise of the GPS data is more than an order of magnitude greater than that on the VLBI data.

TABLE 3 contains oscillator syntonization to UTC (NBS/USNO) data derived from time domain measurements. The VLBI time sync technique cannot measure this parameter therefore the table contains only GPS measurements. The data were derived from the relationship:
(UTC(NBS) - UTC(GPS) - (OSC/CLK - UTC(GPS)) = UTC(NBS) - OSC/CLK
The data were collected using the pseudo simultaneous mutual view technique. And so, the results still contain uncorrelated UTC(GPS) noise, uncalibrated path delays (Australia more noisy than Spain or USA) and, of course, the OSC/CLK noise. The largest contribution is that caused by OSC/CLK behavior. (i.e., unreported clock perturbations or resets and/or changes in the local magnetic or temperature environment* in which the oscillator is placed).

The 2ND ORDER DRIFT term data has not been filtered to remove the clock noise or, the affects of environmental changes. By use of eyeball integration upon the data presented in Figures 3, 4 and 5, the reader can easily detect non-linear oscillator performance. However, as the value of oscillator frequency offset decrease becomes <10-13) it becomes progressively more difficult to determine the 2no order term (frequency drift) because the GPS measurement noise (approximately 3x10-14) dominates the process.

---

* On 2 occasions (one in Spain April 1984 and one in USA March, 1984) local area environmental changes (magnetic and temperature) caused a step change in the oscillator frequency. These are visible in Figures 3 and 5.

TABLE 1

TIME DOMAIN MEASUREMENTS OSCILLATOR vs OSCILLATOR

(1) OSCILLATORS	MEAS. TECHNIQUE	PERIOD	AV CLK RATE OFFSET $\times 10^{-13}$	MEAN STD DEV $\times 10^{-13}$	2ND ORDER DRIFT $\times 10^{-15}$
#14 - #5	VLBI	5559-5651	1.3	20	14.1
#14 - #5	GPS	5544-5585	3.6	2.5	- 1.55
#14 - #5	GPS	5591-5645	5.89	3.0	21.5
#6 - #5	GPS	5706-5714	-0.299	2.9	-30
#6 - #5	VLBI	5712-5840	0.0952	14.6	- 3.0
#6 - #5	GPS	5732-5310	-2.48	4.3	- 7.1
#6 - #5	VLBI	5840-5860	NOT USEABLE		
#6 - #5	GPS	5814-5861	-6.1	8.5	- 4.8
#6 - #5	VLBI	5861-5914	2.79	3.7	-57.5
#6 - #5	GPS	5866-5896	0.9	8.7	-25.2
#7 - #5	VLBI	5511-5583	-0.824	39	-14.5
#7 - #5	VLBI	5587-5691	1.82	30	- 3.4
#7 - #5	GPS	5587-5644	4.5	13	1.6
#7 - #5	GPS	5654-5694	3.74	2.6	24.6
#7 - #5	GPS	5706-5715	-0.324	0.76	- 9.5
#7 - #5	VLBI	5721-5937	0.446	12.4	- 0.26
#7 - #5	GPS	5727-5865	-1.20	12.8	- 5.0
#7 - #5	GPS	5867-5897	-0.675	1.78	- 7.4
#7 - #6	GPS	5587-5645	-3.06	3.0	3.9
#7 - #6	GPS	5654-5691	3.96	4.6	42.2
#7 - #6	GPS	5732-5897	0.944	6.06	8.5

TABLE 2

DIRECT FREQUENCY MEASUREMENT - OSCILLATOR vs OSCILLATOR

(1) OSCILLATORS	MEAS. TECHNIQUE	PERIOD	FREQUENCY OFFSET $\times 10^{-13}$	MEAN STD DEV $\times 10^{-13}$
#14 - #5	VLBI	5533-5660	10.0	7
#14 - #5	GPS	5533-5675	59	140
#6 - #5	GPS	5721-5889	-19.8	470
#6 - #5	VLBI	5816-5861	- 0.28	7.5
#7 - #5	VLBI	5529-5679	6.5	7.9
#7 - #5	GPS	5584-5631	287.5	19
#7 - #5	GPS	5713-5895	64.5	104
#7 - #5	VLBI	5822-5903	- 6.6	7.5

Note: (1) All oscillators are Smithsonian Astrophysical Observatory hydrogen
masers. Serial numbers 5, 6 and 7 are model VLG-10B and, #14 is
model VLG-11. Serial #6 and 14 were located in Australia, serial
#5 in California and, serial #7 in Spain.

TABLE 3
TIME DOMAIN MEASUREMENTS REF UTC (NBS/USNO)

(1) OSCILLATOR	MEAS. TECHNIQUE	PERIOD	AV CLK RATE OFFSET $\times 10^{-13}$	MEAN STD DEV $\times 10^{-13}$	2ND ORDER DRIFT $\times 10^{-15}$
VLG-10B#5	GPS	5629-5659	-2.95	3.6	45.7
VLG-10B#5	GPS	5673-5710	-2.4	4.8	-10.7
VLG-10B#5	GPS	5727-5813	-1.14	2.3	- 5.4
VLG-10B#5	GPS	5814-5870	-3.97	1o.2	6.74
VLG-10B#5	GPS	5889-5897	-1.94	3.7	7.94
VLG-11B#14	GPS	5622-5653	5.37	82.7	-2.73
VLG-11B#14	GPS	5654-5659	NOT USEABLE		
VLG-10B#6	GPS	5675-5694	0.35	2.77	9.69
VLG-10B#6	GPS	5706-5714	0.50	2.94	46.7
VLG-10B#6	GPS	5732-5870	0.49	8.68	3.15
VLG-10B#7	GPS	5673-5694	-5.22	2.25	12.7
VLG-10B#7	GPS	5706-5715	0.084	1.04	4.1
VLG-10B#7	GPS	5727-5870	-0.568	9.5	0.34
VLG-10B#7	GPS	5883-5897	0.054	2.6	0.534

Note: (1) All oscillators are Smithsonian Astrophysical Observatory hydrogen masers. Serial numbers 5, 6 and 7 are model VLG-10B and, #14 is model VLG-11. Serial #6 and 14 were located in Australia, serial #5 in California and, serial #7 in Spain.

Time Synchronization to UTC

Neither the National Bureau of Standards nor the U.S. Naval Observatory is presently equipped to provide traceability to the UTC (NBS/USNO) epoch via the VLBI technique. Therefor all UTC referenced time sync data was acquired through the use of the GPS technique. The algorithm used for the Australian Clock sync measurement was:

$$[(NBS-GPS)-(USA\ CLK-GPS)]-[(AUS\ CLK-GPS)-(USA-GPS)]=NBS-AUS$$

This algorithm differs from that used for Spain's clock sync measurement, in that the (USA CLK-GPS) measurements, in the first half of the equation is not made at the same time as the (USA-GPS) measurement in the second half. However, the same GPS spacecraft is used for both measurements. This scheme had to be adopted because the large angular separation between the N.B.S., @ Boulder, Colo. and the Australian clock @ Tidbinbilla, Australian Capitol Territory (A.C.T.) makes mutual view very unlikely.

Figure 3 is a 150 day history of the time offset of the designated DSN Master Clock located @ Goldstone, Caifornia, USA. The permanent change in clock rate was induced by a permanent change in the local frequency standards room environment. The change in the magnetic environment appears to have also caused a change in the secondary drift term. The three steps in clock offset were all operator induced and, were not caused by mechanical failures.

Figure 4 is a plot of the performance of the DSN's Tidbinbilla Clock, located in the Australian Capitol Territory (A.C.T). There are no microsecond level clock steps. There appears to be no secondary drift and, the random wandering of the clock rate is due to lack of tight environmental* control.

Figure 5 is a plot of the performance of the DSN's Robledo Clock, located near Madrid, Spain. There were two "unrecovered" submicrosecond** level steps. Both were caused by FTS hardware failures. There were the occasions when the clockrate changed. The first change was caused by a failure of the HMA. The second and third were induced by changes*** in the magnetic environment. It appears that the secondary drift term is the same, in magnitude and sign, as that visible in Figure 3.

The data presented (Figures 3, 4 and 5) clearly shows that the three clocks (DSN Master Clock, Tidbinbilla Clock and Robledo Clock) maintained synchronization to the UTC (NBS/USNO) epoch within less than 6 microseconds over the test period.

Clock to Clock Synchronization

Both GPS and VLBI techniques were used to measure and maintain the synchronism between DSN clocks. Since there was but a single VLBI measurement

---

* A special frequency standards room, with very precise environment controls, has been constructed. But, the frequency standards cannot be moved until mid 1985.
** The design of the DSN's clocks is such that they can only be set to the nearest cycle of phase @ 1 MHz.
*** Hardware was removed from the frequency standards room then, later on, hardware was added.

on the Robledo/Tidbinbilla pair, all the data presented in Figure 8 was derived from the GPS technique. The VLBI and GPS time sync data points are from instrumentation connected directly to the DSN station Reference Clock, except @ Goldstone, California. Here the GPS time offset is taken from a phantom DSN Master Clock located in a building approximately 200 meters away (Figure 2), that is driven at the same rate as the DSN Master Clock, and, is synchronized to it through use of coaxial cables and a portable cesium clock.

Figure 6 is a plot of a 200 day history of the synchronism between the Tidbinbilla Clock and the DSN Master Clock as measured by both techniques (GPS and VLBI). The convention used is: Tidbinbilla minus the DSN Master. The large offset* between the two sets of data prior to Julian Day 5820 resulted from the lack of a convenient** means to synchronize the phantom clock in real-time.

Figure 7 is a plot of a 200 day history of the synchronism between the Robledo Clock and the DSN Master Clock as measured by both techniques (VLBI and GPS). The causes of the time offset prior to Julian Day 5820 are the same as for the Tidbinbilla vs DSN Master sync offset. The convention used is: Robledo Clock minus the DSN Master Clock.

Figure 8 is a plot of a 200 day history of the synchronism between the three pairs (Tidbinbilla vs DSN Master, Robledo vs DSN Master and Robledo vs Tidbinbilla) of DSN clocks. All three data sets were collected using the GPS time sync technique. The conventions used were: Robledo minus Tidbinbilla, Robledo minus DSN Master and Tidbinbilla minus DSN Master.

The data indicate that mutual time synchronization between all possible pairs of clocks has been maintained within less than 6 microseconds over the 200 day test period.

---

* The GPS time sync data reports are distributed within 14 days of the oldest measurement point date. The VLBI Time Sync System was in the process of a major block upgrade and the reporting lag sometimes approached 90 days. Therefore the offset was discovered long after the test began. The phantom clock was adjusted but, the problem of maintaining sync in real-time remained.
** The DSN Master Clock is "operationally" maintained 24 hours/day, every day. The phantom clock was maintained 8 hours/day, 5 days/week.

SUMMARY

Using GPS technology the frequency offset of four SAO VLG series hydrogen
masers were measured to be within a part in 10 to the 12th of the UTC(NBS)
rate, and, remained so for the entire test period of 200 days.

Using both GPS and VLBI technology the mutual syntonization between the 3
pairs of hydrogen masers was measured to be within 2 parts in 10 to .he
12th, and remained so over the entire test period.

Using GPS technology the time offset of three globally separated clocks
were maintained within less than 10 microseconds of the UTC(NBS/USNO) epoch
over the 200 day test period.

Using both GPS and VLBI technology the three pairs of globally separated
clocks were maintained in mutual synchronization within 6 microseconds
over the entire test period.

The tests revealed 3 problems: 1) The need to continually synchronize the
phantom clock 2) The need for prompt reporting 3) The need for more strin-
gent control of the frequency standards room environment. Problem #1
will go away when the GPS system is transferred from "experimental" to
"operational" status. Problem #2 has at present lessened considerably
(VLBI data turn around time is now 48 hours).

REFERENCES

1. Ward, S, "The Operational Performance of Hydrogen Masers in the DSN", Proceedings of the Twelfth Annual Precision Time & Time Interval Applications Planning Meeting, pp 616-617, December 2-4, 1980 Goddard Spaceflight Center, Greenbelt, Md.

2. Ward, S, "A Two Year History of Atomic Frequency Standards Syntonization in the Deep Space Network", DSN Progress Report, 42-72, pp 118-127, October-December 1982.

3. Ward, S, "Hydrogen Masers As Time and Frequency Standards", NASA Tech Brief NPO-15858.
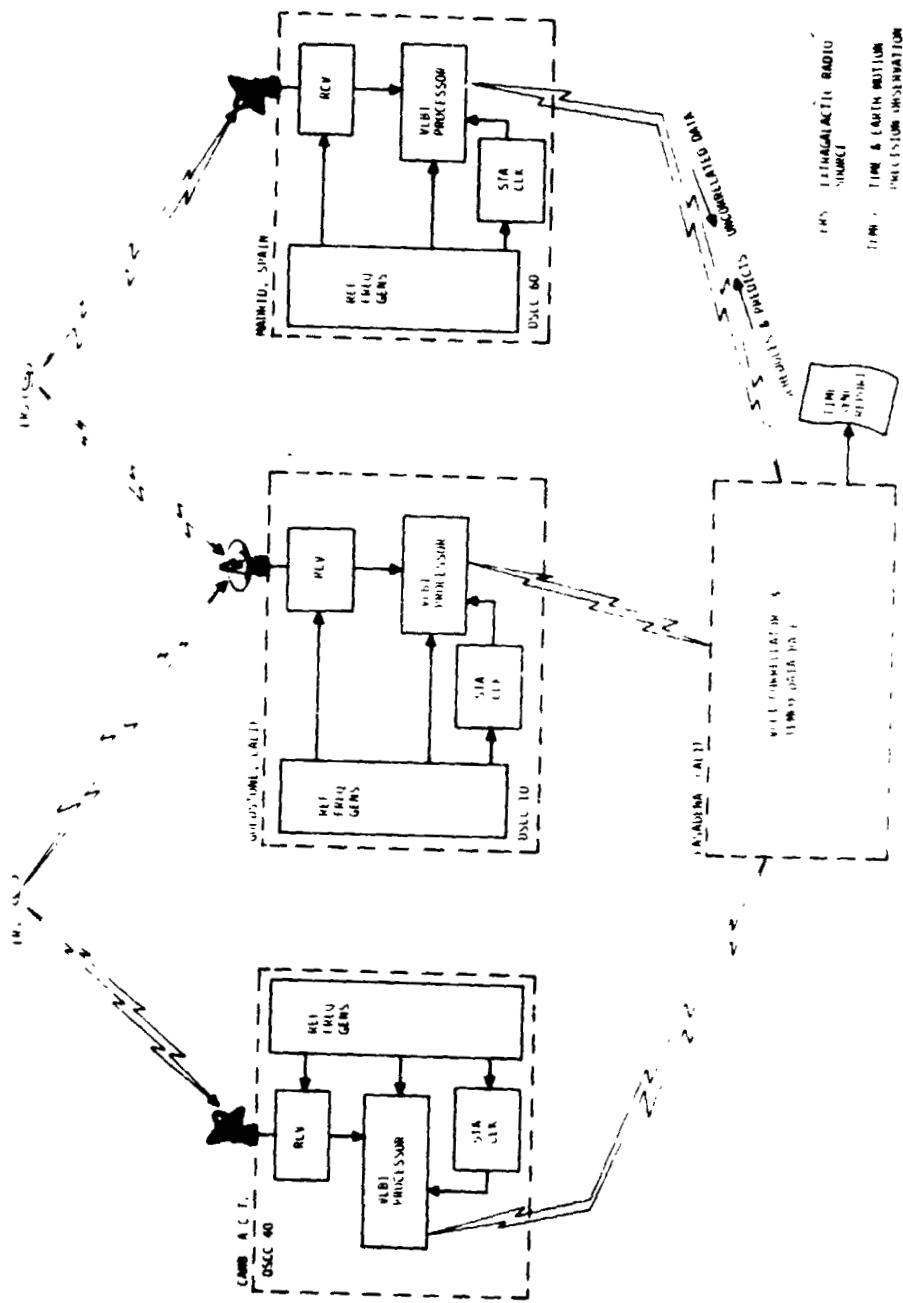
Figure 1. DSN VLBI Time Synchronization System
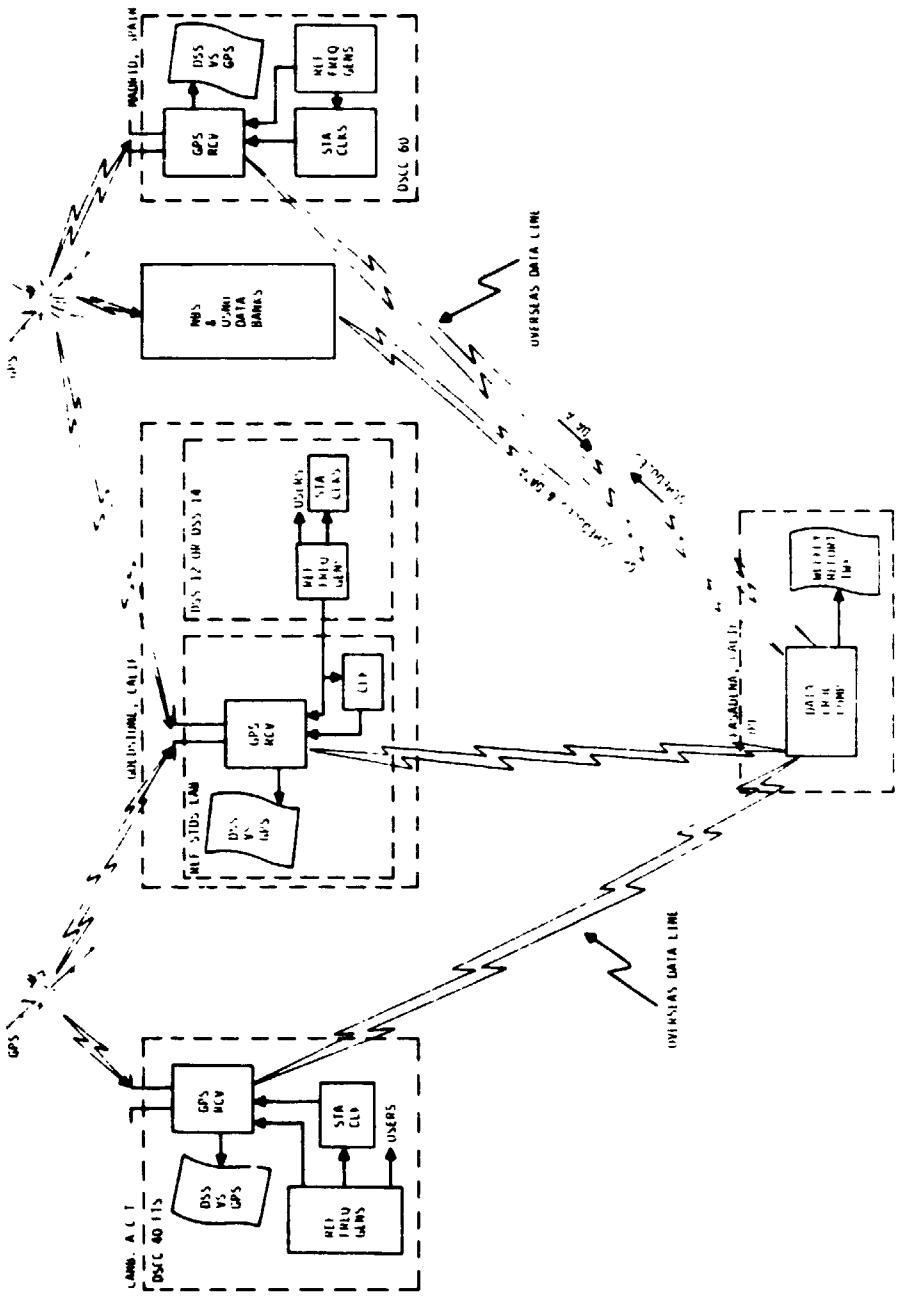
Figure 2. "S" GPS Experimental Time Sync System
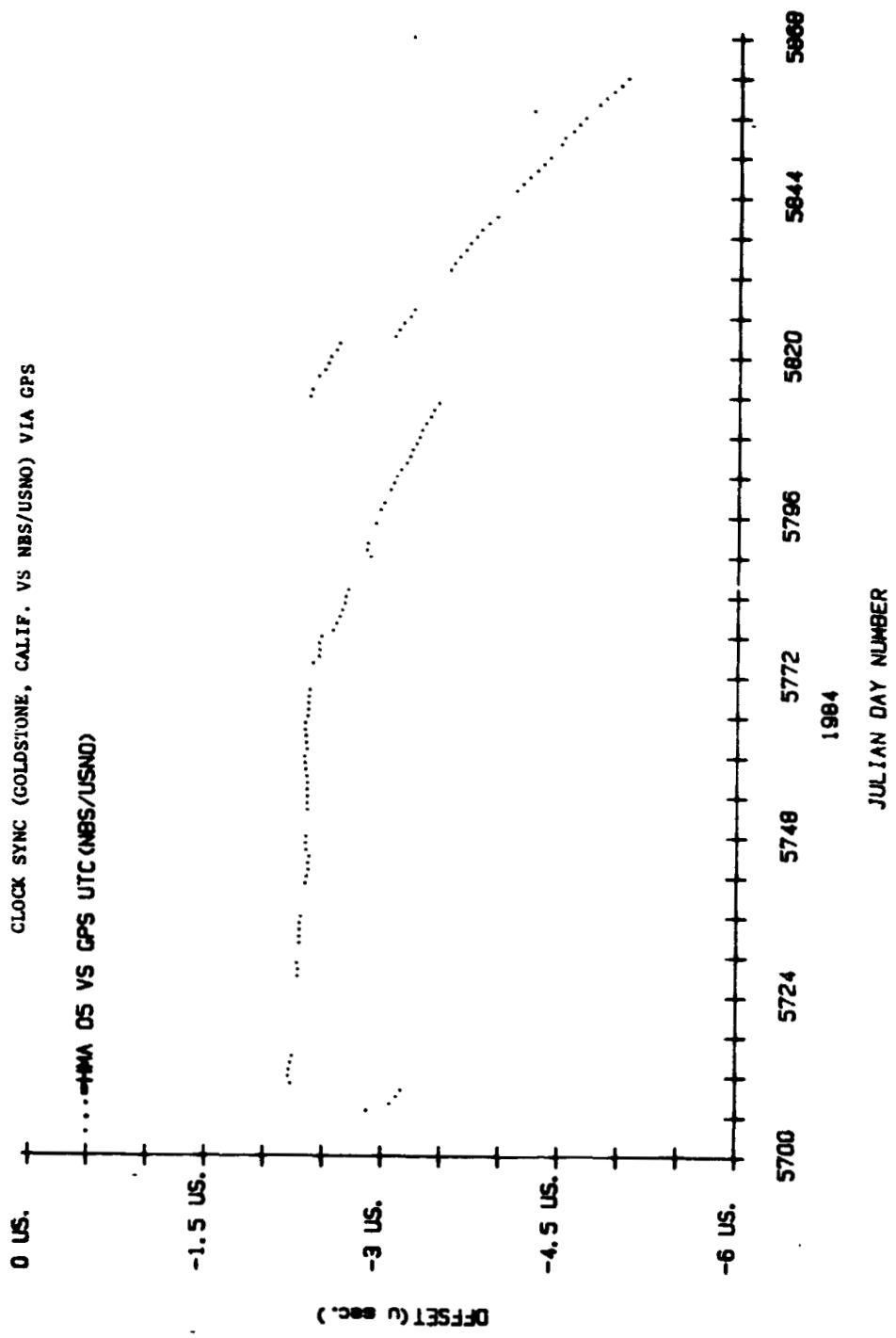
Figure 3. GPS Measurement of the Goldstone, Calif. DSN Master Clock Offset from UTC (NBS/USNO)

CLOCK SYNC (TIDBINBILLA, A.C.T. VS NBS/USNO) VIA GPS

HMA 06 VS GPS UTC (NBS/USNO)

OFFSET (u sec.)

0 US.

-1.5 US.

-3 US.

-4.5 US.

-6 US.

5700 5724 5748 5772 5796 5820 5844 5868

1984

JULIAN DAY NUMBER
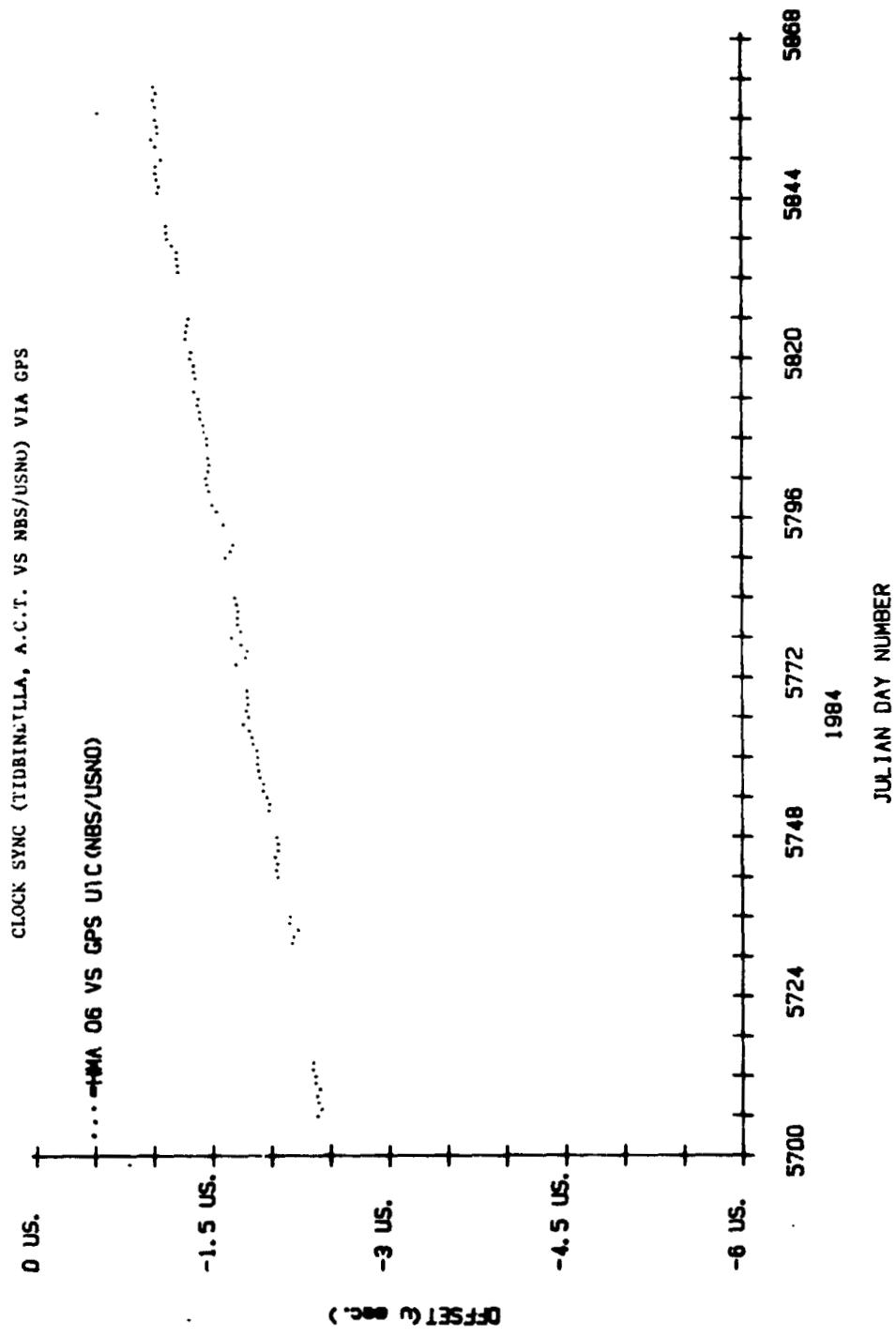
Figure 4. GPS Measurement of Tidbinbilla, A.C.T. Clock Offset from UTC (NBS/USNO)

459
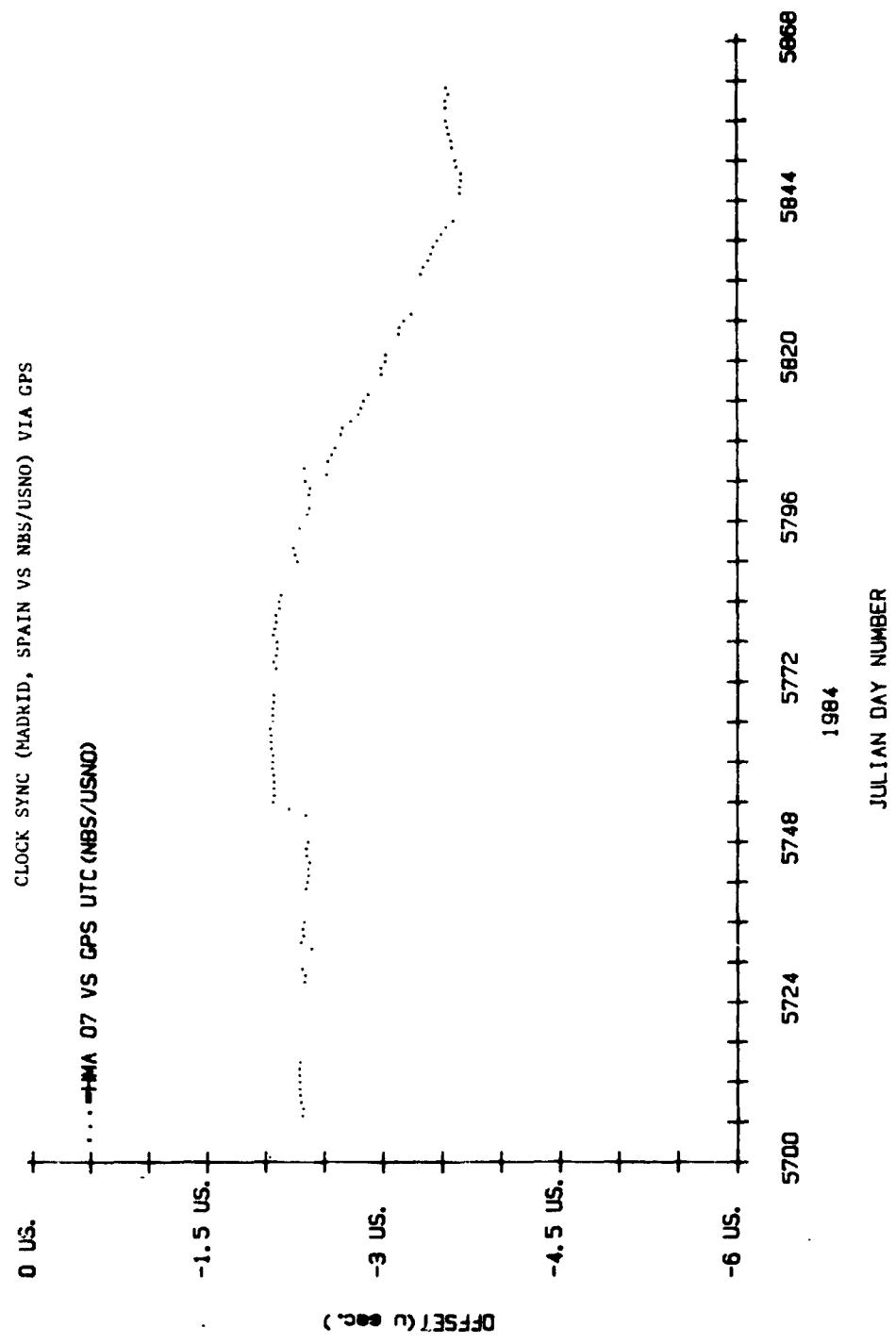
Figure 5. GPS Measurement of Robledo, Spain Clock Offset from UTC (NBS/USNO)
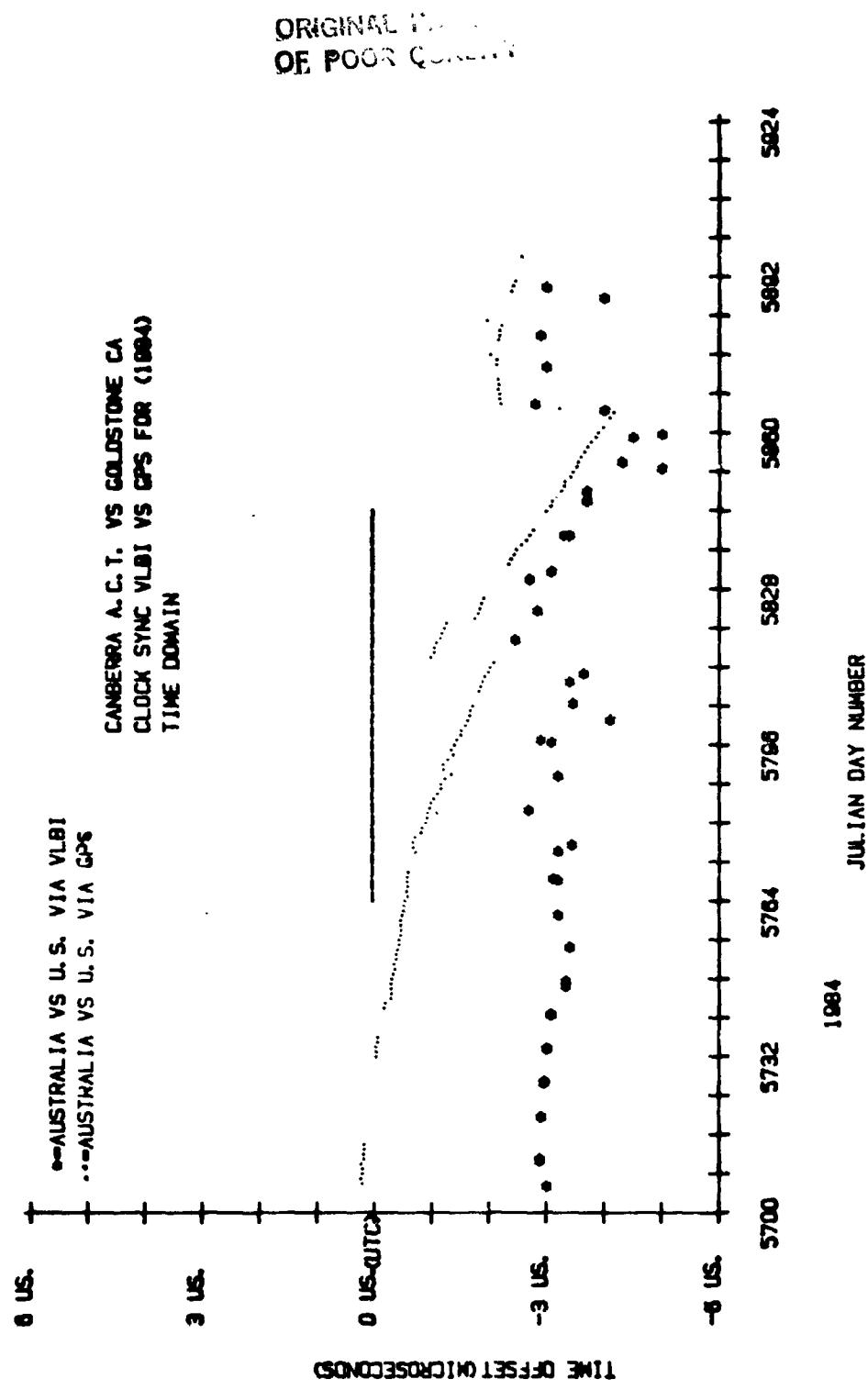
Figure 6. GPS & VLBI Measurement of the Tidbinbilla Clock Offset from the DSN Master Clock

461

MADRID VS U.S. VIA VLBI

MADRID VS U.S. VIA GPS

MADRID SPAIN VS GOLDSTONE CA
CLOCK SYNC VLBI VS GPS FOR (1984)
TIME DOMAIN

JULIAN DAY NUMBER

1984

TIME OFFSET (MICROSECONDS)

0 US.

5 US.

2 US.

0 US. (UTC)

-1 US.

-4 US.

5700 5732 5764 5796 5828 5860 5892 5924
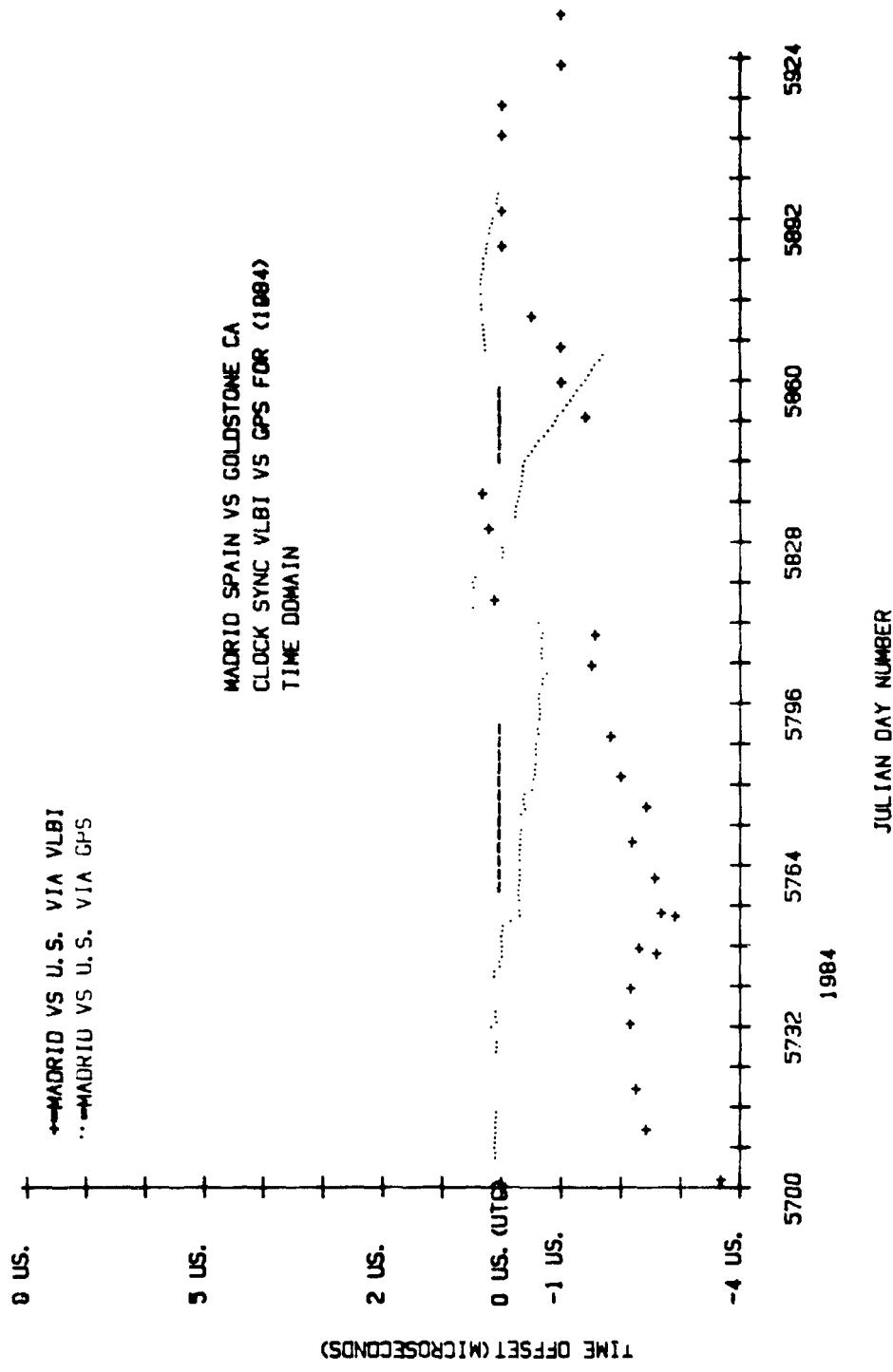
Figure 7. GPS & VLBI Measurement of the Robledo Clock Offset from the DSN Master Clock
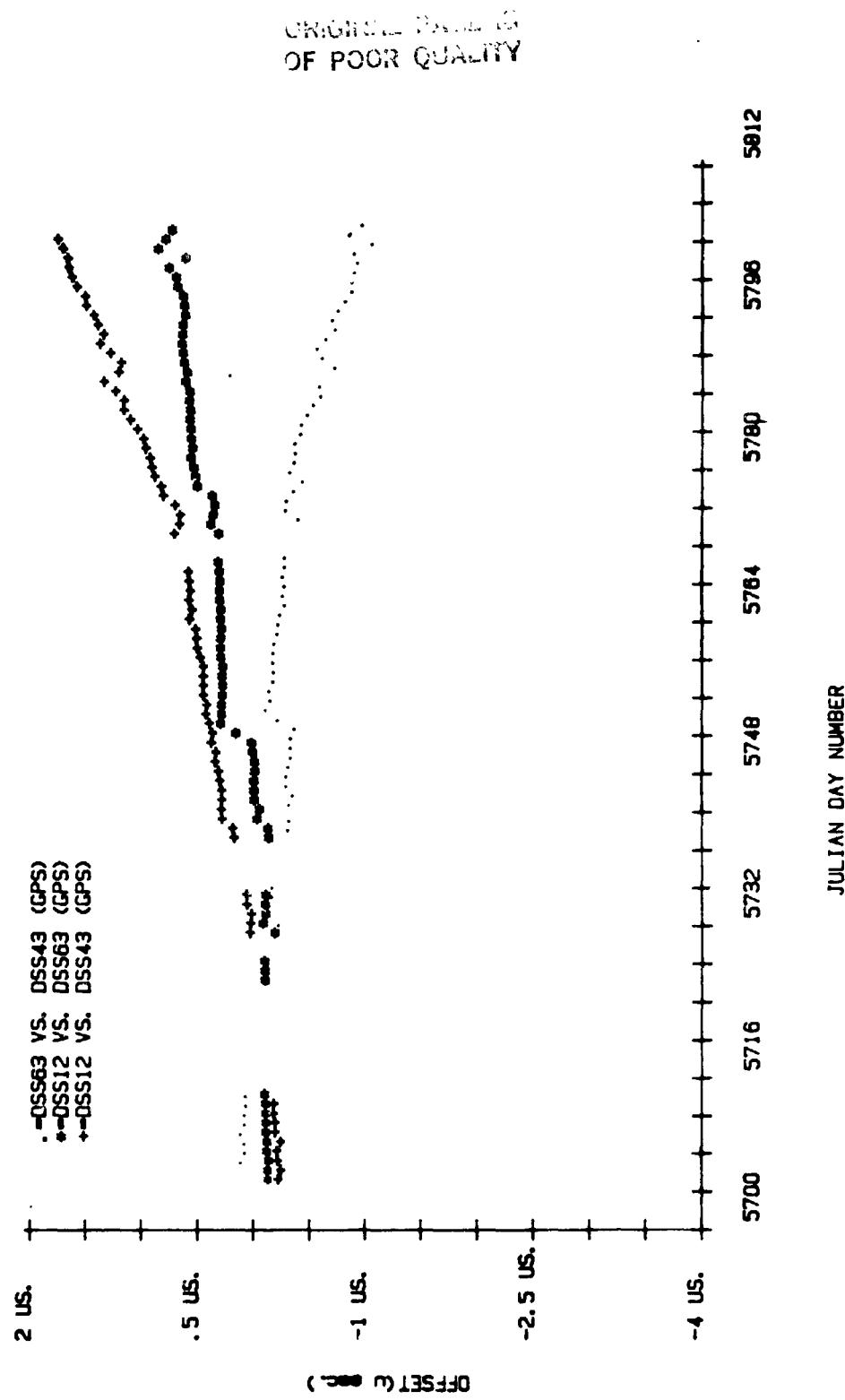
Figure 8. GPS Measurement of the Mutual Time Sync Between 3 Pairs of DSN Clocks

QUESTIONS AND ANSWERS

DAVID SHAFFER, INTERFEROMETRICS: what VLBI system are you using, and what frequency? Was it S band or X band at Goldstone and did you try to remove the ionosphere by using both frequencies?

MR. WARD: We haven't removed the ionosphere nor the cable drift problems since we don't have our calibrator yet.
    We are using both X band and S band. The VLBI system that we are using is about a Mark 2, or 1.5. During most of these observations we are using our Block Zero, which collects the data on wideband video tape. The rest of it used our Block One, which sends the data in digital form on wideband data lines back to the correlator in Pasadena.

GERNOT WINKLER, U.S.N.O.: Why these long delays in getting the VLBI data when you have transmitted the data back on wide band links?

MR. WARD: There is a big gap between doing things in the laboratory , and routinely doing it in the field. There is this business of getting procedures approved, and signed off, and getting software released.

MR. WINKLER: It is not a technical problem then, but an administrative one?

MR. WARD: Correct.

MR. WINKLER: The next question is: You show consistently that the GPS obtained values are very small in precision and, conversely, the VLBI's scatter about ten times more. Yet, when you show the rates, that is reversed. That is, the VLBI rates are much smoother from day to day than the GPS rates. I think that this is inconsistent.

MR. WARD: That again is part of the operations problem. There have been two occasions when the two systems were running on different clocks.

MR. ALLAN: I think that the reason for the difference is that if you average GPS over 12 minutes, as Klobuchar has shown in some work that he has done, you can be affected by multi-path. It's an excellent time point, but it's not a very good frequency measure over a few minutes. The scatter can be quite high. The frequency should be determined from day to day not over that short sample.

MR. WINKLER: I can't understand that, because GPS time values, day after day, are smooth. If you derive, from the time values, the rates -- or do you derive the rates directly from GPS?

MR. ALLAN: That's right.

MR. WINKLER: That's crazy!

MR. WARD: This is an evaluation period for us with GPS, and I just tried this to see which data type produced the greatest precision and accuracy. For instance VLBI has the greater precision, but it doesn't have the accuracy. Also, before you can use the VLBI, you have to use some other method to make sure that the two stations are within ten microseconds of each other to cut down the processing time at the correlator. It requires a priori synchronization and syntonization.

MR. REINHARDT: There is a very good reason for the big difference in VLBI between the rate data and the time data. There are two separate outputs in the VLBI processing. One is the fringe rate output, and one is the fringe output. They go through very different processing. I suspect the time data is highly contaminated by the fact that they don't have a cable calibrator.

My question is: Can you comment on the source of the large scatter in the time data? What do you think is causing it in the system, and do you expect that to be cleaned up?

MR. WARD: That is mostly an operational problem. That's strictly a matter of maintaining the clocks.

MR. REINHARDT: The scatter that I saw was a good fraction of a microsecond, and that is many orders of magnitude larger than you would expect from VLBI. You say that's not from the VLBI system?

MR. WARD: What you saw from the VLBI system is what the clocks were really doing. and the location of the equipment at Goldstone at Station 12 was an interim location while they were doing the antenna repair and upgrading the equipment at the 64 meter site.

MR. KLEPCZYNSKI: To calibrate the VLBI process, there are two areas you have to calibrate. One is cable delays in the system and the other is equipment delays. In addition, there is a very important delay with regard to the formater. That's the device that takes the tome from your local clock and puts it on the tape, so that you can tell when each bit of data was taken.

If the Block One or Block Zero system is similar to the Mark II system that is used elsewhere, it is an undetermined delay, which is very difficult to calibrate according to the clock time on the magnetic tape. Every time you start and stop your equipment, or turn it on from scratch, this delay changes. Unless you can calibrate every single time when you start you experiment, you can easily get delays of several microseconds.

A SIMPLIFIED GPS C/A RECEIVER FRONT END WITH LOW NOISE PERFORMANCE

D. D. Davis and A. D. J. Clements

Time and Frequency Division
National Bureau of Standards
Boulder, Colorado 80303

ABSTRACT

A redesign of the antenna electronics package for the NBS/GPS C/A receiver has resulted in significantly reduced cost and improved performance. Major improvements include a simplified and more reliable multiplier/mixer, elimination of all twelve piston trimmer tuning capacitors in the original design, elimination of expensive bandpass filters, less expensive antenna and a simplified packaging scheme.

BACKGROUND

Very early in the design of the NBS/GPS receiver (in 1979), we decided to include the first mixer and some IF amplification at the antenna. A local oscillator (LO) signal at 100 MHz, along with +15 Vdc, was sent to the antenna package on one cable. The LO was multiplied to 1500 MHz, and mixed with the GPS signal at 1575.42 MHz, generating an IF of 75.42 MHz. After amplification and filtering the IF signal is sent down to the receiver on a second coax cable.

Down conversion to the IF at the antenna package allows us to have almost unlimited cable lengths between the receive and antenna. Cable suitable for 75 to 100 MHz is inexpensive and easy to work with. Several NBS/GPS receivers are operating with RG-58 cables over 60 meters long. In contrast, a 60 meter cable suitable for operation at 1575 MHz would a "semirigid" air dielectric type and would not be easy to pull through raceways and ducts.

Unfortunately, down conversion at the antenna creates other problems, in that in addition to an RF amplifier, we have added a LO multiplier chain, mixer, and IF amplifier that must operate reliably from -25°C to +60°C. We have had some problems with the original multiplier chain design which convinced us that a complete redesign of the antenna package was necessary.

PHYSICAL PACKAGING

A comparison of the new and old antenna packages is shown in Figure 1. Both are drawn to the same relative scale. The new package is rectangular, 23 cm x 23 cm x 10 cm (9" x 9" x4"). The package consists of the 10 cm high aluminum cover with antenna and dome attached, with a 2.5 cm high inside fitting aluminum lid inserted in the bottom. A single fiberglass-epoxy G-10 printed circuit board is mounted to the lid with standoffs.

Figure 2 shows the major elements of the physical construction. One primary goal was to minimize cost of the antenna package while maintaining a rugged, reliable, reproducible unit.

The single G-10 printed circuit board with rf shields mounted on it where needed is much less expensive than the milled aluminum cases used in the original package. In fact, any one of the 3 milled aluminum cases in the original design was more expensive than the complete new physical package. The sections of aluminum heat sink extrusions used for rf shields require a minimum of machine work. The total cost of 4 shields and 3 covers is less than $20 per package, based on fabrication of 15 antenna packages.

No attempt was made to hermetically seal the antenna package, since our past experience indicates that water can always get in, and once inside, it stays. Rather, edges of the inside fitting lid were sanded with a belt sander so the lid was a loose fit in the cover. This allows the case to breathe and maintain the inside at ambient humidity. The lid is inset slightly so that water running down the sides of the cover will not "wick up" around the lid. All aluminum surfaces were given a protective chromate conversion surface treatment and sprayed with an aluminum metal sealer. After all components were mounted, the PC board was also sprayed with two coats of sealer, which also provides moisture proofing and fungus protection. All outside surfaces of the aluminum cover were sprayed with two coats of white epoxy paint.

ELECTRONICS

The electronics package shown in Figure 3 provides about 65 db of gain from antenna to IF output. All rf circuitry at 750 MHz and above is fabricated as microstripline on the main circuit board except for the single Ga As FET low noise amplifier. Since this stage determines the noise figure of the system, we decided not to attempt to build it on the relatively lossy G-10 circuit board. Our original intention was to fabricate the FET stage on a separate glass-teflon circuit board, but our second "point-to-point" wired prototype LNA board worked so well that we decided to use that approach. Because of the relatively simple construction a technician can easily fabricate ten LNA boards in one day.

The overall noise figure of the front end is adjusted by bending a small inductor in series with the gate of the LNA. The noise figure for the first ten units is between 1.0 and 1.25 dB, measured from LNA input to IF output. The noise figure is degraded 0.2 dB by losses in the cable connecting antenna and LNA.

One of our primary goals was elimination of all tuning capacitors in the new antenna package. Elimination of RF piston trimmers which cost a total of $160 in the old package also helps improve reliability. We avoid tuning of the 750 MHz and 1575 MHz microstrip bandpass filters by designing for 10% filter bandwidth. Our primary concern with the 1575 MHz filter is to insure that response is down at least 16 dB at the 1425 MHz IF image, so overall noise figure will not be degraded. Ultimate rejection of the stripline filter is a modest 30 dB which is not

nearly as high the $200 commercial lumped element filter used in the original antenna package. However it has proved adequate in this application.

All tuned circuits in the multiplier chain (50 MHz and 150 MHz) as well as the 75 MHz (±12 MHz) IF band pass filter are adjusted by bending the air wound coils. No mechanically adjusted tuning slugs are used in any circuit. All coils are wound using AWG-22 heat strippable wire, and are self-supporting on the circuit board. Besides cost reduction and improved reliability, we feel elimination of variable capacitors helps improve stability over the operating temperature range.

Group delay of the antenna package, an important parameter in a time transfer receiver, is primarily determined by the 75 MHz IF bandpass group delay of approximately 30 ns (total group delay for the RF section is under 5 ns). We have tested the IF section for changes in group delay over a temperature range of -25°C to +50°C and found the variation to be less than 1 ns. We hope to verify the overall group delay variation with temperature in the next few months, but expect that it will differ little from the I.F. group delay variation.

The multiplier chain and twin diode second harmonic mixer have been trouble free in this design. Use of this mixer cuts performance requirements of the multiplier chain substantially. First, the injection frequency is half that normally required by a mixer, 750 MHz in this case rather than 1500 MHz. Second, the power level required for the 750 MHz can be as low as -3 dBm, rather than the typical +6 dBm required by most double balanced mixers. Other than limited maximum signal level (-30 dBm) and limited bandwidth (20%) restrictions, the twin diode mixer is an excellent, low cost choice for a mixer. A more complete description can be found in the references [1].

The multiplier chain provides all necessary power gain at relatively low frequencies where gain is easy to obtain. The +15 dBm drive level at 150 MHz to the X 5 multiplier varies less than 1 dB as the 50 MHz input level is changed from +6 dBm to -15 dBm. The 150 MHz drive level is also constant (within 1 dB) over the full temperature range.

The X 5 diode multiplier was derived from the design of a similar multiplier in a Pay-TV down converter. The Pay-TV converter used a IN914 switching diode to multiply to 1100 MHz. We chose to use a more recent vintage switching diode, the IN4153, which worked very well in this circuit. Conversion efficiency is about 10%, including almost 3 dB loss in the 750 MHz bandpass filter.

The IF amplifier uses three wideband (dc to 400 MHz) integrated circuit gain blocks. Each circuit has a gain of 14 dB, providing a total of 42 dB gain. Low pass (150 MHz) filters before the first and after the second gain block, along with the bandpass filter between the first and second IF stages result in complete circuit stability with no tendency for spurious oscillation.

The antenna used with the new front end is a commercial implementation [2] of the volute or quadra-spiral helix, popularized by Kilgus [3]. It is relatively small (2.5 cm diameter by 5 cm high) and inexpensive to construct, consisting of three pieces of AWG-16 wire and one piece of miniature semi-rigid coax, the same diameter as AWG-16 wire. The radiation pattern response is right circular with near hemisphere coverage. Over a narrow frequency range near resonance (± 20 MHz) the VSWR is less than 1.4:1: however it becomes highly reactive outside of this narrow range.

Since the LNA, when adjusted for lowest noise figure, is not unconditionally stable at all frequencies up to the 60 GHz cutoff frequency of the FET, oscillations can occur due to the widely varying impedance of the antenna away from its resonant frequency. However, by carefully controlling the length of the cable connecting the antenna to the LNA, it is possible to present a stable set of source impedances. The same cable length has worked with all units, but a change in cable length of 2 cm will guarantee oscillation. A more elegant solution would be to provide a ferrite isolator in the LNA input, but this would both increase cost and degrade noise figure.

ACKNOWLEDGMENTS

REFERENCES

[1] Jim Dietrich, "Twin-Diode Mixer - A New Microwave Mixer", Ham Radio, Aug. 78, p.p. 84-86

[2] Kai P. Yiu, Richard Crawford and Ralph Eschenbach, "A Low-Cost GPS Receiver for Land Navigation", Navigation, Fall 82, p.p. 204-220

[3] C. C. Kilgus, "Resonant Quadrifilor Helix Design", Microwave Journal, Dec. 70, p.p. 48-52

POLYESTER FIBERGLASS ANTENNA COVER

29 cm DIA

53 cm

OLD PACKAGE

$1000

>2 dB (typical)

VERY DIFFICULT

SEVERAL FAILURES
AT LOW TEMP

23 cm

23 cm

10 cm

NEW PACKAGE

$200

<1.5 dB

YES

OPERATES FROM
-25°C to +60°C

PARTS COST

NOISE FIGURE

REPRODUCIBLE

TEMPERATURE RANGE

Figure 1. Comparison of Old and New Antenna Packages
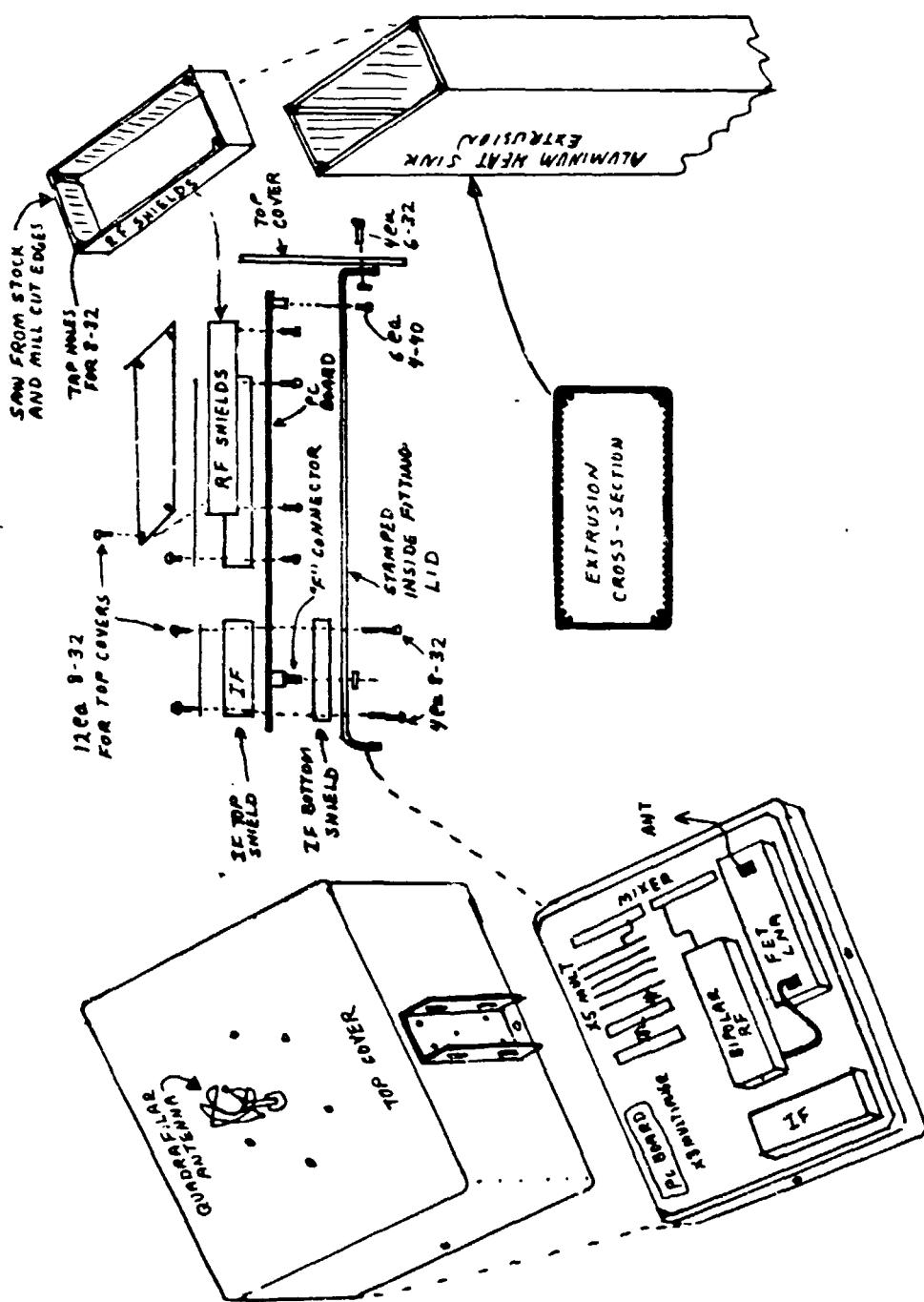
Figure 2. Physical Construction of Antenna Package
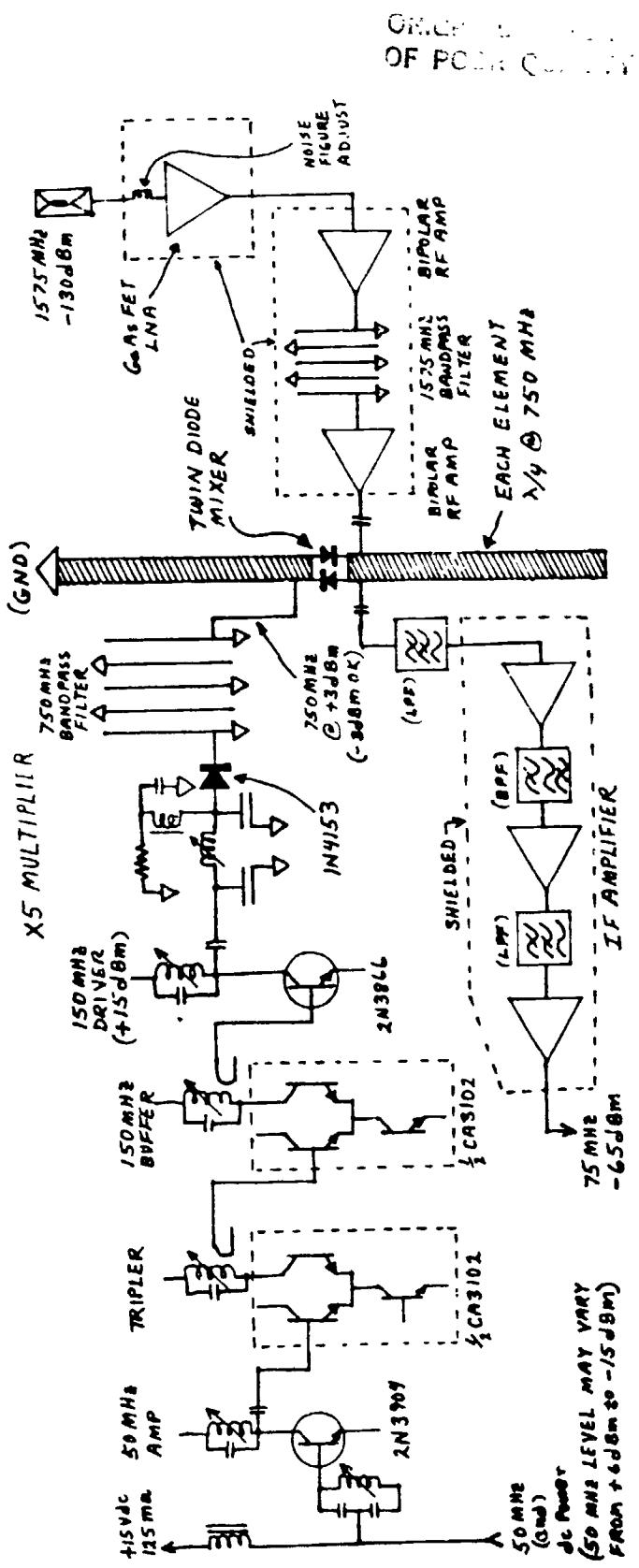
Figure 3. Antenna Electronics

473

QUESTIONS AND ANSWERS

VICTOR REINHARDT, HUGHES AIRCRAFT: That mixer that you used, is there any place where data is available on it?

MR. ALLAN: I am glad that you asked that question. In fact, the reason that we presented this paper, since N.B.S. is a standards laboratory service organization, we have had several requests for the circuit. Rather than give it out on a one at a time basis, we decided to go ahead and make it available to the public. Anyone who desires to have copies of it, we are now making it available, and we are changing out our old receivers with it as we have the opportunity. Certainly you are welcome to it. There is a fee in terms of labor and cost of parts and costs. It's very reasonable.

GEORGE RESCH, JET PROPULSION LABORATORY: What kind of scheme did you use in the last slide to correct for the ionosphere?

MR. ALLAN: It's the Klobuchar model that's in the data word.

PERFORMANCE TEST RESULTS
OF A LOW COST GPS
TIME AND FREQUENCY MONITOR

Ron C. Hyatt and Javad M. Ashjaee
Trimble Navigation
1077 Independence Avenue
Mountain View, CA 94043

ABSTRACT

Final prototype and pilot production performance test results will be presented on a single channel C/A code GPS receiver that has been optimized for time and frequency applications.

Timing accuracy and stability test results will be presented, as well as position determination results.

Summary of these results are as follows:

Timing accuracy:	better than 100 nsec
Timing stability:	better than 10 nsec rms for 10 sec averaging
Frequency stability:	better than 1 part in to the eleventh for 10 sec averaging
Position accuracy:	better than 50 meters when GDOP less than 8 and upload less than 5 hours old
Position stability:	Better than 10 meters rms when GDOP less than 8 for two minute averaging

This paper not received for publication.

QUESTIONS AND ANSWERS

DAVID ALLAN, NATIONAL BUREAU OF STANDARDS: do you know, Al, if the highest satellite lock condition can be overridden, if you wished, to lock it to a lower satellite?

MR. RISLEY: I am not familiar with the unit, but Mr. Mitchell will answer the question.

MR. MITCHELL: The answer to the question is yes. Any of the automatic features can be over ridden in the manual mode. It's simply a matter of selecting one control key on the front panel unit. That outputs you into a sub-menu.

You use the satellite-select for the particular satellite that you want to view. You can also override the automatic feature for the initial search. You could go to a sky search for a satellite that you know is in view to you, rather than letting it go through its entire catalog of satellites to set time.

You can also select the satellites that you want to do the positioning on. It will automatically go to the best satellite in view if you are in the automatic mode. You can override the automatic mode, and select the four satellites that you want to do the positioning on.

MR. KLEPCZYNSKI: Will the pricing structure which was announced for the Trimble receiver also be maintained by Datum and FTS?

MR. MITCHELL: The price is somewhat higher. Datum has purchased the exclusive rights to the unit. We don't feel that the price is that much different from the Trimble offering because we have made considerable improvements over the time since Trimble initially offered them at their introductory price. Trimble never sold any of them at the introductory price, by the way.

We do not consider the software updates to be an option, so it is included in the price. That way you have software updates for the next four years to protect you from any changes that might be made in the program, as well as to get any improvements that we find are necessary in the updating of the software to improve the operation.

The new price also includes the RS 232 and some other improvements. The unit is being introduced at around 25K.

MR. BUISSON: How many receivers are in the field?

MR. MITCHELL: Of the first production run of ten, I took the first unit to ITC. The second unit is here at this show. Two of the units are at the Plans meeting in San Diego this week, and four units are being delivered to Patrick in the next two or three weeks, and one unit is being delivered to Ampex, and the last unit goes to the Coast Guard. The second production run of ten is going into test this week. I believe that five of those units are already spoken for.

ATTENDEES

David W. Allan
National Bureau of Standards
Code 524.06
325 Broadway
Boulder, Colorado 80303

Carroll O. Alley
University of Maryland
Department of Physics and Astronomy
College Park, Maryland 20742

Edward E. Altshuler
RADC/EEPS
Hanscom Air Force Base, Massachusetts 01731

Charles R. Anderson
Hughes Aircraft Company
P. O. Box 31979
Aurora, Colorado 80041-0979

Stanley J. Andrzejewski
NASA/Westinghouse
8224 Burnley Road
Towson, Maryland 21204

John C. Arnold
Bendix Field Engineering Corporation
One Bendix Road
Columbia, Maryland 21045

Claude Audoin
Laboratoire de l'Horloge Atomique
Batiment 221
Universite de Paris-Sud
91405 Orsay, France

Robert L. Baker
Federal Electric Corporation - ITT
P. O. Box 5728, M/S OE600
Vandenberg Air Force Base, California 93437

John Bangert
Defense Mapping Agency
ATTN: HTC-GSGT
Washington, D. C. 20315

James A. Barnes
Austron, Inc.
737 29th Street
Boulder, Colorado 80303

Lawrence A. Bates
Weapons Station
2303 W. Bern Lane
Santa Anna, California 92706

Edward H. Beals
Naval Air Development Center
1825 Dover Road
Southampton, Pennsylvania 18966

Ronald L. Beard
Naval Research Laboratory
4555 Overlook Avenue, S. E.
Washington, D. C. 20375-5000

Roger E. Beehler
National Bureau of Standards
Code 524.00
325 Broadway
Boulder, Colorado 80303

Jose S. Benavente
Instituto y Observatorio de Marina
Cecilio Pujazon S/N
San Fernando (Cadiz) Spain

Albert Benjaminson
S. T. Research Corporation
8419 Terminal Road
Newington, Virginia 22022

Harry B. Bethke
Rockwell International
2600 Westminster Boulevard
(P. O. Box 3644)
Seal Beach, California 90746

Stephen C. Bigelow
Mitre Corporation
Burlington Road
Bedford, Massachusetts 01730

Fred M. Blanchette
Bendix
One Bendix Road
Columbia, Maryland 21045

Martin B. Bloch
Frequency Electronics Inc.
55 Charles Linbergh Boulevard
Uniondale, Long Island, New York 11553

John J. Bollinger
National Bureau of Standards
325 Broadway
Boulder, Colorado 80303

Susan E. Borutzki
Jet Propulsion Laboratory
4800 Oak Grove Drive
M/S 130-117
Pasadena, California 91016

Jean-Simon Boulanger
National Research Council of Canada
Montreal Road
Ottawa Canada K1A OR6

Ken F. Boutler
Jet Propulsion Laboratory
4800 Oak Grove Drive
Pasadena, California 91109

Helmut Brandenberger
Swiss Federal Office of Metrology
50 Lindenweg
Wabern Switzerland 3084

Archie W. Brown
Bendix Field Engineering Corporation
One Bendix Road
Columbia, Maryland 21045

Bert D. Brown
Hughes Aircraft Company
P. O. Box 31979
Aurora, Colorado 80041-0979

Kenneth R. Brown
IBM Federal Systems Division
21 Firstfield Road
Gaithersburg, Maryland 20878

R. Grover Brown
Iowa State University
Ames, Iowa 50011

Ellis H. Bryant, Jr.
The Weatherchron Company
5400 New Peachtree Road, N. E.
Atlanta, Georgia 30341

Melvin I. Burchwald
Los Alamos National Laboratory
MS D-466 Group ESS-7
Los Alamos, New Mexico 87501

James A. Buisson
Naval Research Laboratory
4555 Overlook Drive
Washington, D. C. 20375-5000

Giovanni Luigi Busca
Oscilloquartz
Neuchatel Switzerland

Jeffrey J. Byrnes
Hughes Aircraft Company
P. O. Box 31979
Aurora, Colorado 80041-0979

Jose E. Calavia
Bendix Field Engineering Corporation
One Bendix Road
Columbia, Maryland 21045

Robert W. Camp
Cinox
4914 Gray Road
Cincinnati, Ohio 45232

George T. Cannon, II
HQ ESMC/RSL AFSC
Air Force Eastern Test Range
ETR/RSL - Building 981
Patrick Air Force Base, Florida 32925

James A. Carlson
Naval Electronic Systems Command
PDE-106-2 NAVSTAR GPS
6506 Lamese Court
Springfield, Virginia 22152

Clifford F. Casey
Computer Sciences Corporation
6565 Arlington Boulevard
Falls Church, Virginia 22046

David Chalmers
U. S. Naval Observatory
1730 Preston Road
Alexandria, Virginia 22302

Mark J. Chandler
Bendix Field Engineering Corporation
One Bendix Road - Section TFO
Columbia, Maryland 21045

Laura G. Charron
U. S. Naval Observatory
Time Service Department
34th and Massachusetts Avenue, N. W.
Washington, D. C. 20390-5100

Randolph T. Clarke, III
U. S. Naval Observatory
Time Service Department
34th and Massachusetts Avenue, N. W.
Washington, D. C. 20390-5100

Mary C. Chiu
Johns Hopkins University
Applied Physics Laboratory
Johns Hopkins Road
Laurel, Maryland 21046

Philip A. Clements
Jet Propulsion Laboratory
4800 Oak Grove Drive
Pasadena, California 91109

Richard C. Coerse
U. S. Coast Guard
7323 Telegraph Road
Alexandria, Virginia 22310

Jimmie B. Collie
Naval Electronic Systems Command
National Center One, Room 5E44
Arlington, Virginia 20363

Walter Cote
RADC/DCCD
Griffiss Air Force Base, New York 13441

Stuart B. Crampton
Williams College
Department of Physics and Astronomy
Williamstown, Massachusetts 01267

John F. Crush
Hazeltine
Cuba Hill Road
Greenlawn, New York 11740

Peter R. Dachel
Bendix Field Engineering Corporation
One Bendix Road
Columbia, Maryland 21044

Larry R. D'Addario
National Radio Astronomy Observatory
2015 Ivy Road
Charlottesville, Virginia 22903

Edwin O. Danford
DMA HTC
Rt. 1, Box 270A
Sunderland, Maryland 20689

Fredrick Danzy
U. S. Naval Research Laboratory
4555 Overlook Avenue, S. W.
Washington, D. C. 20375-5000-5000

Charles L. Daues, Jr.
Hughes Aircraft Company
1665 Moline Street
Aurora, Colorado 80010

Duane G. Davis
Hughes Aircraft Company
6251 S. Ulster Street
Englewood, Colorado 80111

David G. Delgado
Embassy of Australia
1601 Massachusetts Avenue, N. W.
Washington, D. C. 20036

B. F. Dennison
Hughes Aircraft Company
6726 S. Spruce Drive West
Englewood, Colorado 80112

Edoardo Detoma
SEPA S.p.A.-Societa de
  Elettronica per l'Automazione
294 Corso Giulio Cesare
Turin Italy 10154

Robert A. DiFazio
Hazeltine Corporation
42 Plainfield Road
Albertson, New York 11507

Gian P. Dilawari
TDX Systems, Inc.
1920 Aline Avenue
Vienna, Virginia 22180

Christine Dise
U. S. Naval Observatory
Time Service Department
34th and Massachusetts Avenue, N. W.
Washington, D. C. 20390-5100

Lawrence E. Dodge
Bendix Field Engineering
P. O. Box 578
LaPlata, Maryland 20646

Lawrence Doepke
DMAAC
9418 Oakwood Manor
St. Louis, Missouri 63126

Robert W. Donaldscn
Westinghouse Electric Corporation,
Defense Electronics Systems
P. O. Box 1897, MS944
Baltimore, Maryland 21146

Robert J. Douglas
Nationl Research Council of Canada
Montreal Road, Building M-36
Ottawa, Canada KIA OR6

James M. Early
American Satellite Co
1801 Research Blvd
Rockville, Maryland 20850

James D. Echols
Austron, Inc
P. O. Box 14766
Austin, Texas 78761

Richard A. Eichinger
ITT Electro-Optical Products Divison
3700 Pontiac Street
Fort Wayne, Indiana

Robert F. Ellis
P. O. Box 14766
Austin, Texas 78761

Barry ELson
U. S. Naval Observatory
Time Service Department
34th and Massachusetts Avenue, N. W.
Washington, D. C. 20390-5100

Thomas C. English
Efratom Division of Ball Corp.
18851 Bardeen Avenue
Irvine. California 92715

Ferdinand K. Euler
Rome Air Development Center (RADC),
U.S. Air Force
RADC/ESE
Hanscom AFB, M   ausetts 01731

Bennie W. Falin
Jet Propulsion Laboratory
4800 Oak Grove Drive
Pasadena, California 91016

Jien Li Fanj
Beijing Institute of Radio Metrology
  and Measurement
3905 Yong ding lu
Beijing, China 810312

Sheila C. Faulkner
U. S. Naval Observatory
Time Service Department
34th and Massachusetts Avenue, N. W.
Washington, D. C. 20390-5100

Earl D. Fossler
Trak Systems-Division of Trak Microwave
4722 Elsenhower
Tampa, Florida 33615

Robert P. Frueholz
The Aerospace Corporation
P. O. Box 92957
Los Angeles, California 90009

Asbjorn M. Gjelsvik
The MITRE Corporation
Burlington Road
Bedford, Massachusetts 01730

Seymour Goldberg
EGFG LWC
35 Congress Street
Salem, Massachusetts 01970

Ehrard O. Graf
OSCILLOQUARTZ SA
16 Brevards
Neuchatel, Switzerland 2002

Gary B. Green
Aerospace Corporation
El Segundo, California 90245

Richard L. Greenspan
The Charles Stark Draper Laboatory, Inc.
555 Technology Square
Cambridge, Massachusetts 02139

William P. Hanrahan
Bendix Field Engineering Corporation
One Bendix Road
Columbia, Maryland 21045

Walter R. Harding
NAVELEX Portsmouth, Virginia
P. O. Box 55
Portsmouth, Virginia 23705

Samuel N. Harmatuk
Consultant
1575 Odell Street
Bronx, New York 10462

Allison J. Heaton
HQ ESMC/RSL Associate
Building 981
Patrick Air Force Base, Florida 32925

Helmut Hellwig
Frequency and Time System, Inc.
34 Tozer Road
Beverly, Massachusetts 01915

Charles P. Henry
Marktron/Frequency
1688 E. Gude Drive
Rockville, Maryland 20850

Robert J. Hesselberth
SPECTRACOM Corporation
101 Despatch Drive
East Rochester, New York 14445

Peter S. P. Hui
NASA/Goddard Space Flight Center
Code 712
Greenbelt, Maryland 20902

Jeffrey S. Ingold
Allied Bendix Aerospace
One Bendix Road
Columbia, Maryland 21045

James P. Jamison
TRACOR, Inc
Three Skyline Place
5201 Leeburg Pike
Falls Church, Virginia 22041

Alain R. Jendly
OSCILLOQUARTZ S.A.
16 Brevards
Neuchatel, Switzerland 2000

Charles J. Jensik
Pieto Crystal Co.
100 K
Carlislie, Pennsylvania 17013

Guy A. Jewett
TDX System Inc.
1920 Aline Ave
Vienna, Virginia 22180

Garry Jocham
GTE Spacenet
1700 Old Meadow Road
McLean, Virginia 22102

Andrew C. Johnson
U. S. Naval Observatory
Time Service Department
34th and Massachusetts Avenue, N. W.
Washington, D. C. 20390-5100

Alfred Kahan
USAF/RFB
Hanscom Air Force Base
Bedford, Massachusetts 01731

Peter Kartaschoff
Swiss PTT, R&D Division
Ostermundigenstrasse 3
Ostermundigen Switzerland 3072

Sang K. Kim
Hughes Aircraft Co.
2000 E El Segundo Bl
El Segundo Ca. 90245

Albert Kirk
Jet Propulsion Laboratory
4800 Oak Grove Drive
Pasadena, California 91016

William J. Klepczynski
U. S. Naval Observatory
Time Service Department
34th Street and Massachusetts Avenue, N. W.
Washington, D. C. 20390-5100

John A. Klobuchar
Air Force Geophysics Lab
AFGL-LIS
Hanscom Air Force Base
Bedford, Massachusetts 01731

Curt A. Knight
Interferometrics, Inc.
3150 Leesburg Pike
Vienna, Virginia 22180

Stephen H. Knowles
Naval Research Laboratory
Code 4183
Washington, D. C. 20375-5000

Anthony J. Kubik
U. S. Naval Observatory
Time Service Department
34th Street and Massachusetts Avenue, N. W.
Washington, D. C. 20390-5100

Ryszard R. K. Kunski
Applied Physics Laboratory
Johns Hopkins Route
Laurel, Maryland 20707

John A. Kusters
Hewett Packard
5301 Steven Creek Boulevard
Santa Clara, California 95050

Tae M. Kwon
Litton Guidance & Control Systems
55u0 Canoga Avenue, MS25
Woodland Hills, Ca. 913664

Marie M. Largay
Naval Research laboratory
Code 7773
4555 Overlook Avenue, S. W.
Washington, D. C. 20375-5000

Leonard R. Lathrem
Bendix Field Engineering Corporation
One Bendix Road
Columbia, Maryland 21061

Jean-Daniel Lavanceau
LT International Inc.
5106 Benton Avenue
Bethesda, Maryland 20814

Lionel Lipschultz
Applied Physics Laboratory
John Hopkins University
Laurel, Maryland 20707

Frank R. Loesel
Pacific Bell
85 2nd Street, 418A
San Francisco, California 94131

Bruce Lohrey
Department of Scientific and Industrial
  Research (DSIR) PEL
Gracefield Road (Private Bag)
Lower Hutt New Zealand

Carl F. Lukac
U. S. Naval Observatory
Time Service Department
34th Street and Massachusetts Avenue, N. W.
Washington, D. C. 20390-5100

Thomas J. Lynch
EG&G Inc.
35 Congress Street
Salem, Massachusetts 01970

Thomas B. McCaskill
Naval Research Laboratory
Code 7773
4555 Overlook Avenue, S. W.
Washington, D. C. 20375-5000

Edward M. Mattison
Smithsonian Astrophysical Observatory
60 Garden Street
Cambridge, Massachusetts 02178

Marvin P. Meirs
Frequency Electronics, Inc
55 Charles Lindbergh Boulevard
Mitchel Field, New York 11553

Edwin E. Mengal
Applied Physics Laboratory
Johns Hopkins University
John Hopkins Road
Laurel, Maryland 20707

Donald H. Mitchell
Datum Inc.
1363 S. State College Boulevard
Anaheim, California 92806

Billy B. Moon
U. S. Air Force
AGMC/MLEA
Newark Air Force Station, Ohio 43056

Derek Morris
National Research Council
Montreal Road
Ottawa, Canada KLA OR6

Brian G. Mousseau
Energy Mines & Resources
615 Booth Street
Ottawa, Ontario (Canada)

Lewis F. Mueller
Hewlett-Packard
5301 Stevens Creek Boulevard
Santa Clara, California 95051

Robert E. Murphy
Frequency & Time Systems, Inc.
34 Tozer Road
Beverly, Massachusetts 01930

James A. Murray Jr.
Naval Research Laboratory
Code 7771
Washington, D. C. 20375-5000

Thomas A. McClelland
Frequency Electronic Inc.
55 Charles Lindbergh Boulevard
Mitchel Field, New York 11553

R. J. McConahy
Applied Physics Laboratory
Johns Hopkins University
Laurel, Maryland 20707

Arthur O. McCoubrey
National Bureau of Standards
Building 221, Room B160
Gaithersburg, Maryland 20899

Janet B. McGraw
Stanford Telecommunications Inc.
2421 Mission College Boulevard
Santa Clara, California 95050

John E. McKeever
U. S. Coast Guard G-TES-4
8413 Ravenswood
New Carrollton, Maryland 20784

John S. McNabb
Trak Micowave Corporation
Tampa, Florida 33614

Christopher J. Madams
Admiralty Research Establishment UK
Portsdown
Cosmam, Hampshire
United Kingdom PO 64AA

Mark E. Manning
Bendix Field Engineering (Allied)
2922 Mayfield
La Cresenta, California 91214

Alan S. Markham
Bendix Field Engineering Corporation
One Bendix Road
Columbia, Maryland 21045

Zoran M. Markovic
Federal Bureau of Measures and
  Precious Metals
14 Mike Alasa
Belgrade, Yugoslavia 11000

Arvid E. Myers
U. S. Naval Observatory
Time Service Department
34th Street and Massachusetts Avenue, N. W.
Washington, D. C. 20390-5100

Jesse W. Myers
Bendix Field Engineer Corporation
925 E. Virginia Way
Barstow, California 92311

George Nard
Serce!
B.P. 64
Carquefou-Cedex, France 44471

Hung H. Nguyen
Bendix Field Engineer
4800 Oak Grove Drive
MS# 80-13
Pasadena, California 91109

Jerry R. Norton
Applied Physics Laboratory
Johns Hopkins University
Laurel, Maryland 20727

Klemens T. Nottarp
Institute for Applied Geodesy
11 Richard Strauss Allee
Frankfurt am Germany BRD D6000

Michael Nugent
DOD W36
9800 Savage Road
Ft. George G. Meade, Maryland 20755

Fernando Noel
Department of Astronomy, University of Chile
Casilla 36-D
Santiago, Chile

Michael Nusbaum
Hughes Aircraft Company
500 Superior Avenue
Building 700 M/S A2127
Newport Beach, California 92658-8903

John T. O'Hara
Marktron Inc.
54 Scott Adam Road, Suite 206
Hunt Valley, Maryland 21030-3280

Edward P. Oppenheimer
Applied Physics Laboratory
Johns Hopkins University
Johns Hopkins Road
Laurel, Maryland 20707

Terry N. Osterdock
Stanford Telecommunications, Inc.
2421 Mission College Boulevard
Santa Clara, California 95030

Iancu Pascaru
Frequency Electronics
55 Charles Lindbergh Boulevard
Uniondale, New York 11553

Peter Z. Paulovich
NAVELEXSYSENGCEN Portsmouth
PTTI Office, Building 16
U. S. Naval Observatory
34th Street and Massachusetts Avenue, N. W.
Washington, D. C. 20390

Paul Perl
TDX
1920 Aline Avenue
Vienna, Virginia 22180

Harry E. Peters
Sigma Tau Standards Corporation
P. O. Box 1877
Tuscaloosa, Alabama 35403

Edward L. Petroka
Kinemetrics/Truetime
3243 Santa Rosa Avenue
Santa Rosa, California 95407

Wolfgang R. Pflaum
Hughes Aircraft Company
500 Superior Avenue
Building 730, M/S-2127
Newport Beach, California 92658-8903

ATTENDEES, continued

David H. Phillips
2901 Accokeck Road West
Accokeek, Maryland 20607

Lewis Phillips
Defense Mapping Agency
Washington, D. C. 20315

John E. B. Ponsonby
University of Manchester, Jodrell Bank
Nuffield Radio Astronomy Laboratories
Macclesfield, Cheshire
United Kingdom

Joseph R. Preisig
NASA/Goddard Space Flight Center
State University of New York at Binghamton
Code 621.9
Greenbelt, Maryland 20771

Kenneth Putkovich
Voice of America
601 D Street, N. W.
Washington, D. C. 20547

Zhang Qin
Beijing Institute of Radio Methology
  and Measurement
3905 Yong ding lu
Beijing, China

James R. Ransom
Westinghouse Electric Comapny
107 E. Susquehanna Avenue
Towson, Maryland 21204

Wilson G. Reid
Naval Research Laboratory
4555 Overlook Avenue, S. W.
Washington, D. C. 20375-5000

Victor S. Reinhardt
Hughes Aircraft Company
P. O. Box 92919
M/S S12 W322
Los Angeles, California 90009

George M. Resch
Jet Propulsion Laboratory
MS 264-801
4800 Oak Grove Drive
Pasadena, California 91109

William J. Riley
EG&G, Inc.
35 Congress Street
Salem, Massachusetts 01775

Dale E. Ringer
Rockwell International
2600 Westminster Boulevard
Seal Beach, California 90740

Allan Risley
Frequency and Time Systems
34 Tozer Road
Beverly, Massachusetts 01915

Hugh G. Robinson
Duke University
Physics Department
Durham, North Carolina 27706

Vincent J. Rosati
U. S. Army ERADCOM
DELET-EQ
Fort Monmouth, New Jersey 07703

Paul M. Routly
U. S. Naval Observatory
Time Service Department
34th Street and Massachusetts Avenue, N. W.
Washington, D. C. 20390-5100

Lauren J. Rueger
Johns Hopkins University
Laurel, Maryland 20707

Robert E. Ryman
Austron, Inc.
1930 Isaac Newton Square, Suite 111
Reston, Virginia 22090

Peter Sabol
Comtech Government Systems Division
80 Oser Avenue
Hauppauge, New York 11788

Harry W. Sadler, III
Bendix Field Engineering Corporation
P. O. Box 116
Burtonsville, Maryland 20866

Jules Schlesinger
Hazeltine Company
Building 15
Greenlawn, New York 11740

Malvin C. Schwalje
EG&G, Inc.
35 Congress Street
Salem, Massachusetts 01970

John G. Seymour
Comtech, Inc.
80 User Avenue
Hauppauge, New York 11788

David B. Shaffer
Interferometrics, Inc.
Code 521.9
NASA/GSFC
Greenbelt, Maryland 21401

Herbert S. Sieler
PMTC - U. S. Navy
Projectory Instrumentation Division
Code 3421.3
Pt. Mugu, California 93042

Henry M. Sielski
Computer Sciences Corporation
4600 Powder Mill Road
Office C902
Beltsville, Maryland 20105

Alexander Skopetz
NASA/GSFC - Code 730.4
11911 Galaxy Lane
Bowie, Maryland 20715

James A. Slater
Defense Mapping Agency HTC
6500 Brookes Lane
Washington, D. C. 20315

Arthur E. Smith
Pacific Missile Test Center
Code 3421.3
Pt. Mugu, California 93048

Ira D. Smith
Arthur D. Little, Inc.
68 Charter Road
Acton, Massachusetts 01720

Les A. Smith
Kentron, Inc.
P. O. Box 64
APO San Francisco, California 96555

Robert S. Smythe
Piezo Technology, Inc.
P. O. Box 7859
Orlando, Florida 32804

Thomas M. Stalder
Bendix Field Engineering Corporation
5707 Thunderhill Road
Columbia, Maryland 21045

Sarah B. Stebbins
Naval Research Laboratory
Code 7773
4555 Overlook Avenue
Washington. D.C. 20375-5000

Sam R. Stein
Ball Efratom Division
P. O. Box 589
Broomfield, Colorado 80020

Ronald D. Stephens
Cinox Corp.
4914 Gray Road
Cincinnati, Ohio 45232

Robert B. Stitt
EG&G, Inc.
35 Congress Street
Salem, Massachuetts 01970

Harris A. Stover
Defense Communications Agency
DCA/DCEC
1860 Wiehle Avenue
Reston, Virginia 22090

David Y. Stowell
Mitre Corp.
1820 Dolly Madison Boulevard
W-640
McLean, Virginia 22102

John T. Strain
FEI
1680 E. Gude Drive
Rockville, Maryland 20850

Donald B. Sullivan
National Bureau of Standards
325 Broadway
Boulder, Colorado 80303

Jacques Vanier
National Research Council
Montreal Road
Ottawa, Ontario, Canada K1A0R6

M. J. Van Melle
Rockwell
P. O. Box 3644
Seal Beach, California 90740

J. R. Vetter
Applied Physics Laboratory
John Hopkins Road
Laurel, Maryland 20707

Dr. John R. Vig
Army Electronics R & D Cmd
Attn: DELET-EQ
Ft. Monmouth, New Jersey 07703

H. Beat Wackernagel
USAF Space Command
Peterson Air Force Base, Colorado 80914

Mark H. Waite
Frequency and Time Systems, Inc.
34 Tozer Raod
Beverly, Massachuetts 01915

William C. Walker
Pan American World Airways
Building 989, MU840
Patrick Air Force Base, Florida 32925

Harry T. Wang
Hughes Research Laboratories
3011 Malibu Canyon Road
Malibu, California 90265

Samuel C. Ward
Jet Propulsion Laboratory
4800 Oak Grove Drive
Pasadena, California 91109

S. Clark Wardrip
Bendix Field Engineering Corporation (BFEC)
726 Foxenwood Drive
Santa Maria, California 93455

Werner A. Weidemann
Ball/Efratom
18851 Bardeen Avenue
Irvine, California 92715

Denis S. Sutcliffe
National Physical Laboratory
Queens Road
Teddington
United Kingdom TW11 OLW

Everett R. Swift
Naval Surface Weapons Center
Dahlgren, Virginia 22448

Richard W. Sydnor
Jet Propulsion Laboratory
Cal Tech (238-420)
4800 Oak Grove Drive
Pasadena, California 91109

Morikawa Takao
Radio Research Laboratories
  Ministry of Posts and Telecommunications
2-1 Nukui-Kitamachi 4-chome
Koganei-shi Toyko, Japan 184

Philip E. Talley
Aerospace Corp.
550 Margo Avenue
Long Beach, California 90803

Lawrence R. Templin
Hughes Aircraft Company
500 Superior Avenue
Building 700 M/S A2127
Newport Beach, California 92658-8903

Douglas M. Tennant
Efratom/Ball
18851 Bardeen Avenue
Irvine, California 92715

Michel Tetu
Laval University
Electrical Engineering Department
Ste-Foy, Quebec, Canada G1K-7P4

Zin Thang
Beijing Institute of Radio Methology
  and Measurements
Beijing, China

Frank L. Valliant
U. S. Coast Guard
7323 Telegraph Road
Alexandria, Virginia 22310

ATTENDEES, continued

Joseph D. White
Naval Research Laboratory
Code 7771
4555 Overlook Drive, S. W.
Washington, D.C. 20375-5000

James W. Whelan
E-Systems, Inc., ECI Division
P. O. Box 12248
1501 72nd Street N.
St. Petersburg, Florida 33733

Gernot M. R. Winkler
U. S. Naval Observatory
Time Service Department
34th Street and Massachusetts Avenue, N. W.
Washington, D. C. 20390-5100

Frances Neville Withington
U. S. Naval Observatory
Time Service Department
34th Street and Massachusetts Avenue, N. W.
Washington, D. C. 20390-5100

Louis A. Williams, Jr.
Standard Frequency Measuring Service
2092 Arrowood Place
Cincinnati, Ohio 45231

Peter E. Williams
Royal Australian Navy
1601 Massachusetts Avenue, N. W.
Washington, D. C. 20036

Robert E. Wilson
Western Area Power Administration
U. S. Department of Energy
1800 S. Rio Grande Avenue
Montrose, Colorado 81401

Herman R. Wood
Kentron International, Inc.
2003 Byrd Spring Road
Huntsville, Alabama 35802

Warren K. Wordsworth
Austron, Inc.
1930 Isaac Newton Square, Suite 111
Reston, Virginia 22090

James L. Wright
Pan American World Airways
Building 989, MU840
Patrick Air Force Base, Florida 32925

Cheng Xi Xiong
Beijing Institute of Radio Methology
and Measurement
3905 Yong ding lu
Beijing, China

Yang Xiau Wei
Beijing Institute of Radio Methology
and Measurement
3905 Yong ding lu
Beijing, China

Fang Jiang Xi
Beijing Institute of Radio Methology
and Measurement
3905 Yong ding lu
Beijing, China

Nicholas F. Yannoni
Rome Air Development Center
Hanscom Air Force Base
Bedford, Massachusetts 01731

Thomas P. Yunck
Jet Propulsion Laboratory
4800 Oak Grove Drive
Pasadena, California 91109

Robert R. Zeigler
Piezo Systems
100 K Street
Carlisle, Pennsylvania 17013